STATICS, DYNAMICS AND STABILITY OF STRUCTURES

LODZ UNIVERSITY OF TECHNOLOGY

Editors:
Zbigniew KOŁAKOWSKI
Radosław J. MANIA

Vol. 5

Selected Problems of Solid Mechanics

A SERIES OF MONOGRAPHS
LODZ 2016

STATICS, DYNAMICS AND STABILITY OF STRUCTURES
OF STRUCTURES

Vol. 5

Selected Problems of Solid Mechanics

Authors of chapters:

Stanisław Burzyński 13	**Radosław Mania**............. 5,8,18
Jacek Chróścielewski.......... 13	**Bohdan Michalak**.................. 12
Katarzyna Ciesielczyk.......... 1	**Wiesław Nagórko** 2
Karol Daszkiewicz 13	**Piotr Ostrowski** 12
Veronika Demedetskaya 10	**Piotr Paczos** 9
Dan Dubina 20	**Wojciech Pietraszkiewicz** 13
Andrzej Garstecki 1	**Jacek Przybylski** 17
Ryszard Grądzki................. 18	**Jan Ravinger** 14
Katarzyna Jeleniewicz.......... 2	**Katarzyna Rzeszut**.................. 1
Jarosław Jędrysiak 3	**Agnieszka Sabik** 13
Monika Kamocka 8	**Shigeru Shimizu** 15
Sławomir Kędziora 4	**Bartosz Sobczyk** 13
Zbigniew Kołakowski 5	**Krzysztof Sokół** 17
Henryk Kopecki 6	**Janusz Szmidla** 17
Maria Kotełko 18	**Czesław Szymczak** 16
Vasily Krasovsky 7	**Łukasz Święch** 6
Marian Królak 8	**Andrzej Teter** 19
Muditha Kulatunga 11	**Lech Tomski** 17
Olga Lykhaczeva 7	**Viorel Ungureanu** 20
Martin Macdonald............. 11	**Sebastian Uzny** 17
Ewa Magnucka-Blandzi 9	**Jerzy Warmiński**................... 19
Krzysztof Magnucki 9	**Wojciech Witkowski** 13
Arkadiy Manevich 10	**Jan Zacharzewski** 6

STATICS, DYNAMICS AND STABILITY OF STRUCTURES

Vol. 5

Selected Problems of Solid Mechanics

Editors:
Zbigniew Kołakowski
Radosław J. Mania

LODZ UNIVERSITY OF TECHNOLOGY
A SERIES OF MONOGRAPHS
LODZ, September 2016

Reviewers:
Professor Tomasz Kapitaniak, **Professor Bogdan Posiadała**

Scientific Editor of the Faculty of Mechanical Engineering
Professor Tomasz Kapitaniak

Cover design: **Radosław J. Mania**
Text setting: **Radosław J. Mania**

© Copyright by Technical University of Lodz 2016

LODZ UNIVERSITY OF TECHNOLOGY PRESS
90-924 Lodz, 223 Wolczanska Street
phone//fax: +48 42 631-20-87; 42 631-25-38
e-mail: zamowienia@info.p.lodz.pl
www.wydawnictwa.p.lodz.pl

LODZ UNIVERSITY OF TECHNOLOGY
DEPARTMENT OF STRENGTH OF MATERIALS
Stefanowskiego Street 1/15, 90-924 Lodz
tel. +48 42 631 22 14, tel./fax: +48 42 636 49 85
www.kwm.p.lodz.pl e-mail: mechmat@info.p.lodz.pl

ISBN 978-83-7283-758-5

DOI 10.34658/9788372837585

Edition 150 copies. Offset papier 80 g 70 x 100
Printed by:
Offset printing „Quick-Druk" s.c. 90-562 Lodz, 11 Lakowa Street
No. 2176

This monograph is dedicated to commemorate
Professor **Katarzyna Kowal-Michalska**
and is an expression of our recognition of Hers achievements, Her inspiration. It is a selfless and professional support coming from Her friends and colleagues.

Professor Katarzyna Kowal-Michalska
1948-2015

Contents

In memoriam

'Our death is not an end if we can live on in our children and the younger generation. For they are us, our bodies are only wilted leaves on the tree of life' those comforting words of Albert Einstein were on the obituary which paid the last respect to Professor Katarzyna Kowal-Michalska, PhD, DSc, our dear, the late lamented friend, mentor, reputable scientist and academic teacher of Lodz University of Technology, who died on 7 August 2015 after losing several months struggle against serious illness.

Professor Kowal-Michalska was born on 25 September 1948 in Pabianice in the family of Barbara and Edward Kowal. Father was an mechanical engineer and for a short time he was professionally associated with the Lodz University of Technology where he led classes of machine construction. Professor Kowal-Michalska graduated Lodz University of Technology in 1972 with a distinction gained a degree in the specialization of 'combustion engines'. After graduation she stayed in TUL working in the team of Professor Jerzy Leyko at contemporaneous Institute of Applied Mechanics, later - after some organisational changes in The Department of Strength of Materials and Structures. Prof. Kowal-Michalska dedicated her entire professional life to the Lodz University of Technology as an academic teacher gaining further promotional ladder and additional academic degrees. Already in 1976, she defended her PhD (doctoral) thesis 'Dynamic stability of cylindrical shell subjected to simultaneous twisting and external pressure' whose supervisor was Professor Jerzy Leyko. In 1995, she submitted her DSc dissertation focused on the post-critical states in the elastic-plastic range 'Load capacity and post-critical state in elastic-plastic range of compressed orthotropic plates'. She filled the position of the associate professor in the Department of Strength of Materials in 1998, and received the title of professor in 2014.

At the turn of the years 1981-1982 she interned semi-annual scientific internship in the Netherlands, Delft University of Technology under the supervision of Professor Warner T. Koiter, and then twice in 1985 and 1987 several weeks internships at Strathclyde University in Glasgow. In 1999-2002 she was deputy dean for science in Faculty of Mechanical Engineering TUL. For many years - from 1978 to disband in 2009 she was secretary of the Team of Stability of the Section of Fundamentals of Construction of Polish Academy of Sciences contributing to a significant activation of its work.

The leading area of her scientific interests and research activities was the subject of stability of the structures - both static and dynamic, and issues of states in elastic-plastic range of thin-walled structures. The result of this activity was more than 130 scientific publications - including dozens of articles in prestigious scientific journals, five independent monographs and co-edited, and more than 60 scientific papers. For several editions of the Stability of the Structure Symposium she was active co-organiser. Over the years she served various functions, firstly in the organizing committee as the secretary, member of the organizing committee, to - from 1997 enter the Scientific Committee of the Symposium, and then repeatedly co-edit conference materials of Symposium. Not being a member of the Organizing Committee she still supported this work with a lot of care – I remember - she was choosing members of the plenary sessions and their chairmen with a high attention. Professor Katarzyna Kowal-Michalska was a member of numerous scientific committees regular conferences from 2000. Scientific-Technical Conference 'Problems of MES in computer assisted analysis, design and manufacturing', in 2006 and 2010 - Shell Structure Theory and Application Conference, the conference which was organized by Professor Wojciech Pietraszkiewicz. In 2011 she was the member of the Scientific Committee of the II Congress of Polish Mechanics and in 2008, co-organized the Jubilee Congress of PTMTS and VII conference 'New directions of mechanics' development'.

In the years 2003, 2007 and 2011 she was editor of special issues of the Journal of Thin-Walled Structures. Professor Kowal-Michalska was an active reviewer in scientific journals as: Thin-Walled Structures, Journal of Theoretical and Applied Mechanics, Mechanics and Mechanical Engineering, Fibers and Textiles, Journal of Kones, Bulletin of WAT and others. She reviewed dozen of doctoral (PhD 12) and postdoctoral (DSC 13) thesis and prepared 4 reviews of editorial postdoctoral thesis.

She took part in 11 science - research projects (grants) fulfilling active and leading role. Few of her science-research project results were applied in the industry.

As an academic teacher she took part in education process of mechanical engineers and in particular years of others specializations, leading all kinds of classes: lecturers, classes, laboratories and doctoral seminaries. She prepared also and modified the educational programs of strength of materials, solid mechanics, theory of plates and shells, introducing some innovations from her own research. All classes conducted in high level were very popular among students, also in English. She promoted three Doctor of Science (PhD) in the field of mechanics, two of them are professors at University of Technology. On behalf of the Council of the Faculty of Mechanical Engineering TUL she was a tutor in doctoral thesis from Faculty Mechanical Engineering Gdansk University of Technology.

Professor Katarzyna Kowal-Michalska was an active member of the Polish Society of Theoretical and Applied Mechanics, where since 2002 she was a member of Board of Lodz Division of PTMTS and in 2004-2010 she was a chair of Lodz Board. In 2009 she became a member of the Executive Committee of the Society. Since March 2009 she was Deputy of General Secretary and since June 2010 General Secretary of PTMS. She resigned from this function during last Congress in May 2015 due to her health. For scientific and organizational activity he was awarded the Bronze Cross of Merit and the badge Distinguished for Lodz University of Technology. In 1976 she obtained the prize of the Minister of III Degree and several dozen prize Rector of the Lodz University of Technology for research activities and publishing. She gained a genuine respect of the professional and scientific profession.

We could turn to her with all problems - scientific, professional or personal and Kasia always was able to find balanced and reasonable solution. We lost extraordinary teacher, reputable scientist, person with a great of authority and rules and also exceptional colleague, kind friend and repository. This friendship will be deeply missed.

In family life she was dear and loving wife, mother and grandmother. She was particularly proud of her grandchildren: Zuzia and Antoś. She paid significant attention on tradition and family relationship. She interested on literature and politics - both local Łodz and Pabianice, and also nationwide being up to date in the ongoing events. Animals were her special passion. Kasia bred with a big love horses and took a big care of dogs - mainly those which have needed help.

The news of the death of Professor Kowal-Michalska attracted a lot of condolences to the Head of the Department of Strength of Materials TUL, among which the e-mail versions were posted on the website of the Department.

For years we have published with Kasia and now it is a first time when we publish for Kasia. However, to have Her share even in this monograph we decided to cite directly Her text prepared for application in the procedure for awarding the title of full professor. Thus the Scientific Curriculum Vitae of professor Katarzyna Kowal-Michalska, mainly achievements in scientific, organization and teaching field are presented as described in details within Her original version of the summary of professional accomplishments elaborated by Professor Kowal-Michalska in the spring of 2013. On the 28th of July, 2014 the President of the RP conferred the title of professor, and the act of handing the nomination made the President on 24 October 2014, just the day before the tragic diagnosis of the disease. Therefore the supplement presents her research achievements since the spring of 2013 until her death in August 2015.

Kasia, thank you for everything we've been through over the years together. You have been etched permanently into our benevolent and respectful memory.

On behalf of all members of our Department and the co-authors

Editors

Editors would like to express the heartfelt thanks to all co-authors for accepting the invitation to contribute to this monograph as well as for their effort, patience and understanding.

Katarzyna Kowal-Michalska, DSc, PhD
Lodz University of Technology
Faculty of Mechanical Engineering
Department of Strength of Materials and Structures

List of professional achievements

(application for the full professor position;
stand on April 2013)

Professional career

In 1972 I graduated (with distinction) from the Faculty of Mechanical Engineering, Lodz University of Technology, in the specialization of turbomachinery and I started my professional career in the Institute of Applied Mechanics, TUL, as a junior assistant, assistant and then senior assistant.

In 1976 I defended a PhD dissertation entitled "Dynamic stability of a cylindrical shell under simultaneous torsion and external pressure" (published in *Archives of Mechanical Engineering*), which was granted a 3rd Class Ministry Award in 1977. In the same year I was employed as an assistant professor in the Institute of Applied Mechanics. Since the division of the Institute into three departments, which took place in 1991, I have been working in the Department of Strength of Materials and Structures.

A degree of Doctor of Science was conferred upon me in 1995 (DSc dissertation entitled 'Limit load carrying capacity and the post-buckling state of orthotropic beams under compression in the elasto-plastic range') and since 1998 I have been employed as an associate professor at the Faculty of Mechanical Engineering, TUL, in the Department of Strength of Materials and Structures.

On June 7th, 2002 the Board of the Faculty of Mechanical Engineering, on the presentation of positive opinions issued by Prof. Tomasz Kapitaniak, Lodz University of Technology, Prof. Stefan Joniak, Poznan University of Technology, and Prof. Czesław Szymczak, Gdansk University of Technology, unanimously accepted a resolution to apply for conferring a scientific title of professor in technical sciences on me to the Central Commission for Scientific Title and Scientific Degrees.

The application was rejected by the Central Commission in June 2004. Therefore, while describing my scientific activities after obtaining a DSc degree, I have highlighted the period after the year 2002.

Within the domain of my scientific activities, I deal with problems concerning stability loss, post-buckling states and load carrying capacity of thin-walled structures under static and dynamic loads. Among these issues, the following topics can be enumerated, namely:

- inelastic stability of thin-walled (iso- and orthotriopic) plate structures subject to pure and complex loading,
- investigations of performance curves of thin-walled plate structures within the whole range of loading (elastic and elasto-plastic states) and determination of limit load carrying capacity,
- application of various plasticity criteria in the stability analysis for iso- and anisotrorpic materials (Hill and Tsai-Wu criteria),
- analysis of stability, post-buckling states of multilayer plates (including composites and laminates) in the elastic and elasto-plastic state,
- investigations of the influence of load pulse duration, initial deflections, dynamic stability criteria, states above the yield point in a response analysis of thin-walled composite plate structures under pulse loading,
- stability of functionally graded plates under static and pulse, thermal and mechanical loads.

Within the years 1976-80 I took part in the investigations on topic of 03.3 "Stability and the post-bucking behaviour of thin-walled structures" of key problem 05.12 "Stability and optimization of machine and construction structures", whereas in the years 1981-85 I was involved in topic 3.1 "Post-buckling states in the elastic and elasto-plastic range of thin-walled structures under static and dynamic loads" of key problem 05.12 "Strength and optimization of machine and construction structures". Next, in the years 1986-90 I took part in the investigations devoted to topic 02.01-2-2.12 "Stability and the post-buckling behaviour of thin-walled grinders in the elastic and elastic plastic range" within CPBP 02.01 "Fundamentals of mechanics of materials, machines, structures and technological processes", whereas in the years 1986-91 I dealt with topic 02.04.01 "Development of calculation methods of limit load carrying capacity of elements of construction machinery" within CPBP 02.05 "Development of fundamentals of heavy machinery design, operation and tests, including construction machinery".

Then, my investigations were devoted to issues related to determination of critical stresses in the inelastic region of plates and grinders, in particular an analysis of the post-buckling behaviour of thin isotropic plates in the elastic plastic range. I co-authored (together with R. Grądzki) a method being a combination of analytical and numerical solution that allowed for determination of the complete performance curve of the isotropic plate structure, and further, on that basis, its limit load carrying capacity. During those investigations, an analysis of the influence of boundary conditions, material characteristics and geometrical inaccuracies was conducted.

The results of the above-mentioned investigations were widely reported. As a result, numerous publications authored or co-authored by me were issued. Among the most important, there are: chapters in two monographs, 10 papers (including 4 in foreign journals). The results were disseminated during home (13) and international (6) conferences.

In the beginning of the 1990s, my scientific interests started to be focused on stability problems of thin-walled structures made of orthotropic materials in the elasto-plastic range. My major achievement in that field was an analytical solution in the elastic range, which was the basis for a numerical solution, in which the Hill criterion of elasticity for orthotropic materials was considered and formulated in an incremental form of the Prandtl-Reuss equation. The derived relationships and the code developed allowed for analysis of the effect of orthotropy coefficients in the elastic range and various characteristics of orthotropic materials after yielding on limit load carrying capacity of plates with different boundary conditions. The analytical-numerical method for orthotropic materials, modified by me, enables determination of complete curves of performance (load-shortening) and yield regions. The results of the investigations were the basis for the DSc dissertation entitled "Limit load carrying capacity and the post-buckling state of orthotropic beams under compression in the elasto-plastic region" (1995).

After conferring a title of Doctor of Science on me, my scientific activities were related to problems of widely understood stability loss of plate structures made of orthotropic materials in the elastic and elasto-plastic range, including thin-walled multilayer and composite structures. Those works were conducted within three research projects financed by the Committee for Scientific Research, namely:

- "Stability, post-buckling states and limit load carrying capacity of thin-walled structures" (No. PB0923/P5/93/04);
- "Load carrying capacity of thin-walled composite beam-columns, including problems occurring in real structures" (No. PB-251/T07/97/12);
- "Stability, post-buckling states and load carrying capacity of thin-walled multilayer plate-shell structures made of orthotropic materials" (No. PB-0910/T07/99/17).

I was the main executor in the above-mentioned projects.

Within the above-listed projects, I dealt with the following issues:

- modal analysis of elastic and inelastic stability of isotropic and orthotropic plate structures - determination of critical stresses and local and global buckling modes; among original achievements, one can also mention an

application of the method developed for stability analysis in the elastic range of orthotropic beam-columns to inelastic problems - references [1.1], [2.1], [2.11], [2.12], 2.13];
- determination of performance curves of orthotropic beam-columns under eccentric compression within the whole range of loading; in the PhD dissertation (S. Kędziora, 2001) I supervised, it was shown that an elastic solution obtained on the basis of the asymptotic method could be effectively applied to analyze plate structures with open and closed cross-sections in the elasto-plastic range - references [1.1], [2.3];
- application of various criteria of plasticity (Hill criterion, Tsai-Wu criterion) in the stability analysis - references [2.2], [2.14];
- analysis of stability, post-buckling states in the elastic and elasto-plastic range of multilayer plates subject to complex loading; within this subject scope, in the PhD dissertation (R. Mania, 2002) I supervised, an effect of strength of the core materials on stability of three-layer plates in the plastic range was investigated; the post-buckling state in the elasto-plastic range for multilayer plates built of iso- and orthotropic layers, subject to pure and complex loading, was analyzed in references [2.2], [2.14]. Among my original achievements, I can mention the development of an analytical model that was used in the numerical solution.

The results of those investigations were disseminated in 27 publications, including 2 monographs, 8 papers and 12 contributions to home conference proceedings and 5 contributions to foreign conference proceedings.

From my viewpoint, the most important publications in that period were a monograph entitled "Selected problems of instabilities in composite structures" [1.1], where I authored or co-authored 5 chapters and was the editor of Part 2, as well as papers [2.1], [2.2],[2.3], [2.13],[2.14].

Moreover, in the period discussed I was an invited co-editor of "Thin-walled structures, advances and developments", Proceedings of the Third International Conference on Thin-Walled Structures [1.2].

My achievements after conferring a DSc degree on me until the first application for a title of professor covered 29 publications, including 3 monographs, 9 papers and 17 conference contributions, among them 5 published in foreign conference proceedings.

After 2002 I continued my investigations on post-buckling states of thin-walled plate structures made of iso- and orthotropic layers in the elasto-plastic range. I developed an analytical model for multilayered plates subjected to pure and complex loads that accounted for various plasticity criteria in the case of anisotropic materials. The results of those investigations were disseminated in [2.16]. Problems of proper implementation of plasticity criteria in professional

FEM software were discussed in [1.8]. A comparison of the results referring to the load carrying capacity of multilayered plates obtained with the analytical-numerical method, the FEM analysis and the kinematic approach was presented in [2.6].

A list of most significant investigation results from the publications on post-buckling states in elasto-plastic ranges was presented in monograph [1.14]. The monograph covers, among others, a summary of my scientific accomplishments in that field that followed from many-year long investigations presented in numerous former publications.

Since 2002 till now I have been involved as the main executor in the following research projects, namely:

– "Nonlinear dynamic stability of thin-walled composite structures" (KBN 5T07A 0125),
– "Load carrying capacity of thin-walled orthotropic beam-columns with multi-circumferential cross-sections" (KBN 4T07 A0289),
– "Dynamic response of thin-walled composite plate structures under pulse loading" (PB MNiSzW 1136/B/T02/2009/36),
– "Dynamic buckling of FGM plate structures subject to thermal and mechanical loads" (NCN-2011/01/B/ST8/0774) - ongoing project.

The continuation of my interests in modal analysis and coupled buckling is represented in co-authored publications (co-author: Z. Kołakowski) [2.9], [1.10a].

Within the field of analysis of dynamic stability of composite plate structures, I dealt with research on an effect of the following factors: duration and shape of the load pulse, initial deflections of structures, geometrical and strength parameters and criteria of dynamic stability applied - references [2.4], [2.17], [2.20], [1.11].

In the majority of works on dynamic loads, the investigations are conducted on the assumption of ideal elasticity of the material. It seems significant to extend them on the region exceeding the yield strength. I supervised a PhD dissertation devoted to this issue (L. Czechowski, 2007) and co-authored a series of publications on this topic [2.18], [1.12b], including works covering an effect of deformation velocity [1.10b].

The state of knowledge on the dynamic stability of composite plate structures and the investigation results of the research team conducting that project were presented in a monograph [1.5], where I was a co-author and a scientific editor.

Within my scientific interests related to determination of limit load carrying capacity of plate structures, I took part in the project "Load carrying capacity of orthotropic beam-columns with multi-circumferential cross-sections". The results of analytical, numerical and experimental investigations were presented in monographs [1.9a], [1.9b], [1.12a], papers [2.5], [2.7], [2.15], [2.19] and conference contributions presented both in Poland and abroad. In these publications, the attention was drawn, among others, to a proper description of the material characteristics in the computational codes based on the analytical-numerical method as well as in the professional FEM software.

At present, I deal with stability problems in FGM plates subject to compression and high temperatures, under static and dynamic loads. Functionally Graded Materials have been known for 30 years almost, they are composites built of two components (usually ceramics and metal). Their material properties vary continuously along their thickness. In the literature on this subject scope, one can find numerous publications on static loads and vibrations of FG plates, nevertheless, solutions to dynamic loads, especially the pulse ones, are lacking. In the initial stage of the project, I dealt with development of analytical solutions for static thermal and mechanical loads, effects of initial deflections at mechanical pulses [[1.9c]], as well as an influence of the boundary conditions of FG plates on the critical thermal load under time-variable temperature pulse [1.16]. The results of those investigations were discussed in the above-mentioned references, which I co-authored, in 1 paper under print, as well as were presented at 5 conferences, including 2 international ones.

I am an author or co-authored of 13 monographs, an author or co-author of 35 papers, including 15 from the JCR list. I presented my contributions at numerous scientific conferences, seminars and symposia, including 29 international conferences. I was an editor or co-editor of 14 monographs. The total number of my publications is 123.

I supervised three PhD dissertations defended at the Faculty of Mechanical Engineering, TUL in 2001, 2002 and 2007. I was a reviewer in 12 PhD procedures, including 6 at the Faculty of Mechanical Engineering, TUL.

In 2011 I was also a reviewer in a DSc procedure at the Faculty of Mechanical Engineering, TUL.

I acted as a publishing reviewer in DSc procedures four times (twice at Czestochowa University of Technology and twice at Lublin University of Technology).

I was a member of scientific committees of 8th-13th Symposium on Structure Stability (1997-2013) and 5th-11th Scientific Conference "FEM problems in computer-aided analysis, design and manufacturing" (2000-2013). I was a member of the scientific committee at the conference "Shell Structures Theory and Applications".

I prepared numerous reviews for scientific journals, among others, for two journals from the Thompson-Reuters list, namely: Thin-Walled Structures and Journal of Theoretical and Applied Mechanics. I wrote opinions as a publishing reviewer for 1 textbook and 1 monograph.

Since 1978 - until its dissolution, I acted as a Secretary to the Group on Stability of Structures of the Committee on Machine Building, Polish Academy of Sciences. I took part in preparation of all (since 1978) seminars and conferences, organized or co-organized by the Group on Stability. Before a title of DSc was conferred on me, I was a group tutor or a year tutor at the Faculty of Mechanical Engineering for many times. I took part in activities of the Organizing Committees of 3rd, 4th, 5th, 6th and 7th Symposium on Stability of Structures.

After a DSc degree was conferred upon me, I was a plenipotentiary of the Dean of the Faculty of Mechanical Engineering for the International Faculty of Engineering, I took part in the works of the Commission for Teaching and the Commission for Publishing of the Board of the Faculty of Mechanical Engineering.

In the term 1999-2002 I was the Vice-Dean for Science at the Faculty of Mechanical Engineering.

I have been a member of numerous commissions at the Faculty (for teaching, foreign cooperation, awards, teaching the Mechatronics major).

I was a co-organizer of the Third International Conference on Thin-Walled Structures, Cracow 2001 and the Jubilee Meeting of the Polish Association of Theoretical and Applied Mechanics and 7th Conference “New Directions in Development in Fluids Mechanics”, Rogów 2008.

Since 1978 I have been a member of the Polish Association of Theoretical and Applied Mechanics, in the years 2004-2010 I was the chairwoman of the Lodz Branch Board, and I have been a member of the Steering Committee of the Main Board since 2009; since 2010 I have been the General Secretary to the Polish Association of Theoretical and Applied Mechanics.

Before a DSc title was conferred upon me, I prepared numerous expertise and design projects for industry. Among most important engineering achievements, I can mention my participation in the project devoted to design and implementation of an automatic razor blade packing device prototype for the ”Wizamet” company in Lodz as well as development of a strength calculation method for transformer coils.

During my professional career, I had three foreign scholarships. From September 1980 to March 1981 I had on a 5-month long scholarship at Delft

University of Technology, where I dealt with modal stability analysis of beams and rod systems, under the supervision of Prof. W. Koiter. The results of those investigations were disseminated in 2 papers published in Delft University of Technology Reports. I had 2 scientific scholarships at Strathclyde University in Glasgow, at the Department of Mechanical Engineering (one-month long and two-week long), where I presented my investigations during scientific seminars. My cooperation with Prof. J. Rhodes from this university bore fruits in the fact that I was appointed editor of several special issues of Thin-Walled Structures.

Before a DSc degree was conferred upon me, I had tutorials and lab classes in strength of materials, lab classes in mechanics of deformable bodies and theory of plates and shells for the specialization Applied Mechanics. I co-authored a textbook for students entitled “Laboratory classes in theory of elasticity”.

After conferring a DSc degree on me, I have had lectures on mechanics of deformable bodies for the specialization Applied Mechanics, lectures and tutorials and lab classes in strength of materials for the Materials Science and Engineering, Energy Generation and Mechatronics degree courses. In all the above-mentioned cases, I always significantly modified programmes of studies for all types of classes (lectures, tutorials and lab classes). Moreover, for more than 10 years I have had tutorials in English at the International Faculty of Engineering, TUL.

I have supervised three MSc theses at the specialization Applied Mechanics.

In the years 1998-2000 I participated in the project TEMPUS UM_JEP 13117 "International Quality Education System" - as a member of the “Task Force” team who prepared an implementation of the quality education system at the Lodz University of Technology, I had two one-week long trainings at Twente University, the Netherlands, and University of Lund, Sweden, where I got acquainted with the didactic process and the quality education system at those universities.

I have been distinguished with 25 awards of the TUL Rector (the latest in 2012) for my scientific investigations, teaching and organizational activities, and in 1994 I was awarded a Bronze Cross of Merits.

List of Achievements in Scientific and Research Activities and Teaching Activities

I. Personal data

Date of birth:	September 25, 1948
Place of birth:	Pabianice
First names of parents:	Edward, Barbara
Address:	Pabianice

II. Education

1972 MSc in mechanics - diesel engines, Faculty of Mechanical Engineering, Lodz University of Technology

1976 PhD degree – mechanics, Faculty of Mechanical Engineering, Lodz University of Technology; the PhD dissertation title ”*Dynamic stability of a cylindrical shell under simultaneous torsion and external pressure”,* supervisor - Professor Jerzy Leyko

1995 DSc degree - mechanics; DSc dissertation *”Limit load carrying capacity and the post-buckling state of orthotropic plates under compression in the elasto-plastic range”*

The resolution of the Board of the Faculty of Mechanical Engineering, TUL, dated 25.09.1995, approved of by the Central Commission for Scientific Title and Scientific Degrees on 26.03.1996)

2002 application for a title of professor (the resolution of the Board of the Faculty of Mechanical Engineering, TUL, dated 7.06.2002)

2004 application rejected by the Central Commission for Scientific Title and Scientific Degrees on 13.06.2004.

III. Professional career

1972 - 1973 assistant at the Institute of Applied Mechanics, TUL

1973 - 1976 senior assistant at the Institute of Applied Mechanics, TUL

1976 - 1998 assistant professor at the Institute of Applied Mechanics, TUL, and after its division, at the Department of Strength of Materials and Structures, TUL since 1998 TUL associate professor, Department of Strength of Materials and Structures, TUL

IV. Scientific scholarships

- September 1981 - February1982 - scientific scholarship at the Delft University of Technology, the Netherlands (5 months)
- 1985 - scientific scholarship at the Strathclyde University, Glasgow, Great Britain (1 month)
- 1987 - scientific scholarship at the Strathclyde University, Glasgow, Great Britain (2 weeks)

V. Industrial placements

1986, 1990 - two 3-month long industrial placements at the Pabianice Bulb Factory "POLAM"

VI. Awards and distinctions

- 3rd Degree Ministry Award - 1976
- 21 awards of the Rector of Lodz University of Technology for research and scientific activities and publications
- 4 awards of the Rector of Lodz University of Technology for teaching activities

VII. Medals

Bronze Cross of Merits in 1994

VIII. Scientific activities

1.1.1. Participation in key problems and research projects of the Ministry for Science and Higher Education

A1. Before a DSc degree

1. 1976-80 - participation in the topic 03.3 "Stability and the post-bucking behaviour of thin-walled structures " of key problem 05.12 "Strength and optimization of the machine and construction structures".
2. 1981-85 - participation in the topic 3.1 "Post-buckling states in the elastic and elasto-plastic range of thin-walled structures under static and dynamic loads" of key problem 05.12 "Strength and optimization of the machine and construction structures".
3. 1986-90 - participation in the topic 02.01-2-2.12 "Stability and the post-buckling state of thin-walled girders in the elastic and elasto-plastic range" in CPBP 02.01 "Fundamentals of mechanics of materials, machines, structures and technological processes".
4. 1986-91 - participation in the topic 02.04.01 "Development of calculation methods for limit load carrying capacity of thin-walled elements of machines and construction equipment" in CPBP 02.05 "Development of fundamentals of heavy machinery design, operation and tests, including construction machinery".
5. 1993-1996 - main executor in the State Committee for Scientific Research project "Stability, post-buckling states and limit load carrying capacity of thin-walled structures" (No. PB0923/P5/93/04).

A2. After a DSc degree:

Main executor in the following research projects:

1. "Load carrying capacity of thin-walled composite beam-columns, including problems occurring in real structures"(No. PB-251/T07/97/12).
2. "Stability, post-buckling states and load carrying capacity of thin-walled multi-layer plate-shell structures made of orthotropic materials" (No. PB-0910/T07/99/17).
3. "Non-linear dynamic stability of thin-walled composite structures" (KBN 5T07A 0125).

4. ”Load carrying capacity of thin-walled orthotropic beam-columns with multi-circumferential cross-sections” (KBN 4T07 A0289).
5. ”Dynamic response of thin-walled composite plate structures under pulse loading” (PB MNiSzW 1136/B/T02/2009/36).
6. ”Dynamic buckling of FGM plate structures under thermal and mechanical loading” (NCN-2011/01/B/ST8/0774).

Publications

B1. before a DSc degree

– monographs	- 4
– papers	- 13
– contributions to international conference proceedings	- 6
– contributions to home conference proceedings	- 11

B2. after a DSc degree*)

– monographs	-	- 19 (3)
– papers		- 23 (8)
– contributions to international conference proceedings		- 23 (12)
– contributions to home conference proceedings		- 25 (6)

*)In brackets, there is a number of publications before 2002 - before the first application for a title of professor

Total number of publications - 123

Number of points according to the current list of the Ministry for Science and Higher Education (as regards p. B2) 172 points

Scientific reviews

C1: Reviews in journals:

– Thin-Walled Structures
– Journal of Theoretical and Applied Mechanics

– Mechanics and Mechanical Engineering
– Fibers and Textiles
– Journal of Kones
– Military Academy of Technology Bulletin

C2: Reviews of monographs and textbooks

– Publishing review of the textbook “Introduction to Engineering”, ed. R. Grądzki, Łódź, 2009
– Publishing review of the book “Mathematical modelling and analysis in continuum mechanics of microstructured media. Professor Margaret Woźniak pro memoria” ed. Cz. Woźniak, Silesian University of Technology Publishing House, 2010

More important research projects for industry

– Participation in the project ”Design of a new aggregate for cellophane wrapping of boxes containing razor blades and making 2 items of such devices in metal”, 1976-1981, implementation at the ”Wizamet” factory, Łódź (co-author of the project, 20% contribution)
– Participation in the project ”Development of the strength calculation method of transformer coils against effects of radial compression forces”, 1982, Institute of Power Engineering, Department of Transformers, (co-author of the calculation method of the coil strength model, approx. 35% contribution)
– Strength calculations of 5, 7, 10 and 15 ton vats, 1985, (co-author of the calculation model, approx. 30% contribution)

IX. Activities in the field of promotion of young scientists

– Supervisor of the PhD procedure of Sławomir Kędziora, MSc. Dissertation title: "Limit load carrying capacity of orthotropic thin-walled beam-columns with open and closed cross-sections in the elasto-plastic range". The dissertation defended and the PhD title conferred in 2001. The PhD dissertation obtained a distinction from the Board of the Faculty of Mechanical Engineering.
– Supervisor of the PhD procedure of Radosław Mania, MSc. Dissertation title: “Analysis of the effect of material properties of the core on stability

of a three-layer trapezoid plate". The dissertation defended and the PhD title conferred in 2002. The PhD dissertation obtained a distinction from the Board of the Faculty of Mechanical Engineering.

– Supervisor of the PhD procedure of Leszek Czechowski, MSc. Dissertation title: ”Dynamic stability of composite plates under complex pulse loading in the elasto-plastic range”. The dissertation defended and the PhD title conferred in 2007.

Reviews:

Reviews in PhD procedures

1. Ibrahim Kamal Mohamed El-Beshtawy, "Experimental and numerical analysis of sandwich construction deformations under thermal local load" - Wroclaw University of Technology, 1997
2. Tomasz Kubiak, "Nonlinear stability analysis of orthotropic thin-walled rods with various shapes of cross-sections" - Faculty of Mechanical Engineering, Lodz University of Technology, 1998
3. Michał Ciach, “Biomechanical aspects of analysis of the cervical and lumbar intervertebral disc with new implant systems” - Faculty of Mechanical Engineering, Lodz University of Technology, 2000
4. Piotr Stasiewicz, “Parametric optimization of dimensions of the horizontal circular cylindrical shell filled with a liquid, including stability analysis”, Faculty of Machine Design and Management, Poznan University of Technology, 2000
5. Miłosz Olejniczak, ”Influence of constitutive models on the evaluation of strength of thin-walled frame structures”, Faculty of Machine Design and Management, Poznan University of Technology, 2003
6. Piotr Paczos, ”Stability problem of an open orthotropic two-layer conical shell in the elasto-plastic range”, Faculty of Machine Design and Management, Poznan University of Technology, 2005
7. Mirosława Łęcka, ”Theoretical and experimental investigations of rigidity and strength of structures made of corrugated paper”, Faculty of Mechanical Engineering, Lodz University of Technology, 2005
8. Jacek Jankowski, ”Dynamic response of thin-walled composite thin-walled beam-columns with open and closed cross-sections”, Faculty of Mechanical Engineering, Lodz University of Technology, 2007
9. Michał Mariański, “Investigations of bus body strength against impacts at sideway rollover of the vehicle”, Faculty of Mechanical Engineering, Lodz University of Technology, 2009

10. Włodzimierz Werochowski, ”Static and strength analysis of cold bent Z-sections”, Faculty of Civil Engineering, Gdansk University of Technology, 2009
11. Michał Gajdzicki, ”Numerical determination of the anti-torsional rigidity of the flexural Z-section purlin”, Faculty of Architecture and Civil Engineering, Lodz University of Technology, 2011
12. Piotr Włuka, ”Modelling and analysis of composite structures with piezo-electrical elements for stress-strain control”, Faculty of Mechanical Engineering, Lodz University of Technology, 2013

Publishing reviews in DSc procedures

1. Jacek Przybylski, PhD, MSc ”Vibrations and stability of pre-coupled two-segment rod systems under non-conservative loads”, Czestochowa University of Technology, 2002
2. Janusz Szmidla, PhD, MSc ”Free vibrations and stability of slim objects under specific load”, Czestochowa University of Technology, 2009
3. Andrzej Teter, PhD, MSc ”Multimodal dynamic buckling of thin-walled structures with ribs under compressive pulse loading”, Lublin University of Technology, 2010
4. Hubert Dębski, PhD, MSc ”Numerical and experimental investigations of stability and load carrying capacity of composite thin-walled beams subject to compression”, Lublin University of Technology, 2013

Reviewer in the DSc procedure (appointed by the Faculty of Mechanical Engineering, TUL)

1. Dorota Pawlus PhD, MSc ”Dynamic stability of three-layer ring plates with a viscoelastic core”, Lodz University of Technology, 2011

Scientific tutor appointed by the Faculty of Mechanical Engineering, TUL, in the PhD procedure of Wiktoria Wojnicz, MSc, Faculty of Mechanical Engineering, Gdansk University of Technology, entitled: “Modelling and simulation of behaviour of the arm-forearm skeletal muscle system” (supervisor Prof. E. Wittbrot). The dissertation defended in 2009.

X. Teaching activities

Before a DSc degree

Textbook: Laboratory classes in theory of elasticity" - edited by J. Leyko, TUL Publishing House, 1982 (description of Laboratory Class no. 1)

Moreover, I conducted the following types of classes:

– tutorials and laboratory classes in strength of materials,
– laboratory classes for the specialization Applied Mechanics in: mechanics of deformable bodies and theory of plates and shells,
– laboratory classes in numerical analysis of structures,
– participation during preparation of didactic stands in the laboratory of mechanics of deformable bodies.

After a DSc degree

A. Teaching programmes:

– Preparation and modification of the teaching programme for the subject Strength of Materials for the Materials Science and Engineering degree programme and for the specialization Technology and Commerce (1999-2003)
– Preparation and modification of the teaching programme for the subject Strength of Materials for the Mechatronics degree programme and the Energy Engineering I degree programme (2009-2012)
– Preparation of a multimedia presentation of lectures for the subject Strength of Materials for the Mechatronics degree programme (2009-2011) and the Energy Engineering degree programme (2009-2012)
– Preparation and modification of the teaching programme for the subject Mechanics of Deformable Bodies for the Mechanics and Machine Design degree programme, specialization Applied Mechanics II (2009)

B. classes with students

– lectures in mechanics of deformable bodies for the specialization Applied Mechanics
– lectures, tutorials and lab classes in Strength of Materials for Mechatronics and Energy Engineering degree programmes
– lab classes (in English) in Basic Mechanical Engineering (mechanics and strength of materials)

C. Supervisor of MSc theses - 3 MSc theses in the field of stability and load carrying capacity of thin-walled structures (including FGMs) and strength analysis of structures for the Applied Mechanics degree programme

XI. Activities in scientific societies and scientific and technical associations

- Secretary to the Group on Stability of Structures at the Committee on Machine Building, Polish Academy of Sciences - from 1978 till its dissolution in 2009.
- Member of the Board of the Lodz Branch of the Polish Association of Theoretical and Applied Mechanics since 2002.
- Chairwoman of the Lodz Branch of the Polish Association of Theoretical and Applied Mechanics in the years 2004-2010.
- Member of the Steering Committee of the Polish Association of Theoretical and Applied Mechanics in the years 2009-2014.
- Secretary General to the Main Board of the Polish Association of Theoretical and Applied Mechanics in the years 2010-2014.

XII. Activities in favour of the scientific community

Since 1997 - member of the Scientific Committee of Symposia on Stability of Structures $7^{th} \div 12^{th}$

Since 2000 - member of the Scientific Committee of the periodic Scientific and Technical Conference "FEM problems in computer aided analysis, design and manufacturing"

2006-2010 - member of the Scientific Committee of the SSTA Conference

2011 - member of the Scientific Committee of 2^{nd} Congress of Polish Mechanics

2008 - co-organizer of the Jubilee Meeting of the Polish Association of Theoretical and Applied Mechanics and 7^{th} Conference "New directions in the development of mechanics"

XIII. Organizational activities at the Lodz University of Technology

A. before a DSc degree

- Plenipotentiary of the Dean of the Faculty of Mechanical Engineering for the International Faculty of Engineering – in the years 1993 –1998
- Member of Organizing Committees of 6^{th}, 7^{th}, 8^{th} and 9^{th} Symposium on Stability of Structures

B. after a DSc degree

1998-1999 plenipotentiary of the Dean of the Faculty of Mechanical Engineering for the International Faculty of Engineering,

1999-2002 Vice-Dean for Science, Faculty of Mechanical Engineering, TUL

1999-2003 member of the Commission for Science and the Commission for Foreign Cooperation of the Board of the Faculty of Mechanical Engineering

2001 member of the Organizational Committee of Third International Conference on Thin-Walled Structures (organized by Lodz University of Technology, Strathclyde University and Cranfield University, Great Britain)

1998-2000 participation in the project TEMPUS UM_JEP 13117 "*International Quality Education System"* - member of the Task Force team preparing implementation of the quality education system at the Lodz University of Technology

2002-2006 chairwoman of the Commission for Foreign Cooperation of the Board of the Faculty of Mechanical Engineering

2002- member of the Commission for Awards and Distinction, Faculty of Mechanical Engineering

1999- member of faculty commissions in PhD and DSc procedures

2008- member of the Didactic Commission for the Mechatronics degree program

SUMMARY

1. MONOGRAPHS - 23
– before a DSc degree 4
– after a DSc degree (until 2002)* 3
– after a DSc degree (after 2002) 16

2. PAPERS** - 36, including 15 from the Thompson-Reuters list
– before a DSc degree 13(6)
– after a DSc degree (until 2002)* 8(3)
– after a DSc degree (after 2002) 14(6)

3. IINTERNATIONAL CONFERENCES - 29
– before a DSc degree 6

– after a DSc degree (until 2002)* 12
– after a DSc degree (after 2002) 11

4. OTHERS - 26
– before a DSc degree 11
– after a DSc degree (until 2002)* 6
– after a DSc degree (after 2002) 19

*2002 r - first application for a title of professor

**In the brackets, there is a number of papers from Journal Citation Reports

TOTAL NUMBER OF PUBLICATIONS - 123

Number of points for publications after a title of DSc was conferred upon me, according to the Ministry for Science and Higher Education scoring - 172 points.

Hirsch Index:

– acc. to Web of Science h = 3,
– acc. to Scopus h = 5
– acc. to Publish or Perish h = 6.

SUPPLEMENT

List of Professor Katarzyna Kowal-Michalska publications April 2013 - August 2015

Monographs

- K. Kowal-Michalska, R. Mania (Eds.), Statics, dynamics and stability of structures, Vol. 3, Review and current trends in stability of structures, 50th anniversary of Stability of Structures Symposia, Lodz University of Technology, A Series of Monographs, Lodz 2013, p. 411.

Chapters in monographs

1. K. Kowal-Michalska, Wyboczenie płyt funkcjonalnie gradientowych przy statycznych i dynamicznych obciążeniach mechanicznych i/lub termicznych, In monograph: Modelowanie struktur i konstrukcji inżynierskich, Monografia jubileuszowa z okazji 45-lecia pracy profesora Wiesława Nagórko, Eds. G. Jemielita, M. Wągrowska, SGGW, Warszawa 2014, 163-175.
2. J. Jankowski, K. Kowal-Michalska, Dynamic response of FGM thin-walled plate structures subjected to a thermal pulse loading. In monograph: Shell Structures: Theory and Applications, Eds. W. Pietraszkiewicz, J. Górski, Vol. 3, Taylor&Francis Group, London 2014, 297-300.

Papers of JCR list

- L. Czechowski, K. Kowal-Michalska. Static and dynamic buckling of rectangular functionally graded plates subjected to thermal loading. Strength of Materials, 2013, 45, 6, 666-673.

Papers of list B of MNiSW

1. K. Kowal-Michalska, R.J. Mania, Static and dynamic thermo-mechanical buckling loads of functionally graded plates. Mechanics and Mechanical Engineering, 2013, 17, 1, 99-112.
2. J. Świniarski, K. Kowal-Michalska, T. Niezgodziński, Influence of foam filling on dynamic response of hemispherical shell subjected to blast pressure. Mechanics and Mechanical Engineering, 2013, 17, 2, 177-186.

International conference paperes

1. K. Kowal-Michalska, Z. Kołakowski, Inelastic buckling of thin-walled FML columns by elastic asymptotic solutions. SolMech 2014. 39th Solid Mechanics Conference, SolMech 2014, Zakopane 2014.
2. Z. Kołakowski, K. Kowal-Michalska, R.J. Mania, Global and local elastic-plastic stability of FML columns of open and closed cross-section. PCM-CMM-2015, September 2015, Gdańsk 2015.

Home conference papers

1. L. Czechowski, K. Kowal-Michalska, Statyczne i dynamiczne wyboczenie prostokątnych płyt funkcjonalnie gradientowych przy obciążeniach cieplnych. X Konferencja Nowe Kierunki Rozwoju Mechaniki, Jarnołtówek 2013.
2. M. Kotełko, K. Kowal-Michalska, Oszacowanie nośności granicznej płyt typu FML przy zastosowaniu metod analityczno-numerycznych. XI Konferencja Nowe Kierunki Rozwoju Mechaniki, Sarbinowo 2015.
3. Z. Kołakowski, K. Kowal-Michalska, R. Mania, Nonlinear stability of FML-FGM composite columns with square cross-section. Modeling of microstructured media IV, Lodz, October 2015.
4. K. Kowal-Michalska, Z. Kołakowski, Elastic-plastic stability of FML columns of open cross-section. XIV Sympozjum Stateczności Konstrukcji, Zakopane 2015.

List of Contributors

(in alphabetical order)

Stanisław BURZYŃSKI
Gdansk University of Technology
Faculty of Civil and Environmental Engineering
ul. Narutowicza 11/12,
80-233 Gdansk, Poland
stanislaw.burzynski@pg.gda.pl

Jacek CHRÓŚCIELEWSKI
Gdansk University of Technology
Faculty of Civil and Environmental Engineering
ul. Narutowicza 11/12,
80-233 Gdansk, Poland
jchrost@pg.gda.pl

Katarzyna CIESIELCZYK
Poznan University of Technology
Faculty of Civil and Environmental Engineering
ul. Piotrowo 5
60-965 Poznan, Poland
katarzyna.ciesielczyk@put.poznan.pl

Karol DASZKIEWICZ
Gdansk University of Technology
Faculty of Civil and Environmental Engineering
ul. Narutowicza 11/12,
80-233 Gdansk, Poland
karol.daszkiewicz@wilis.pg.gda.pl

Veronika DEMEDETSKAYA
Dniepropetrovsk National University
Department of Computational Mechanics and Strength of Structures
Gagarin av. 72
49010, Dniepropetrovsk, Ukraine
vdemendetskaya@yandex.ru

Dan DUBINA
Polytechnic University of Timisoara
Piata Victoriei No. 2
300006 Timisoara, Romania
dan.dubina@ct.upt.ro

Andrzej GARSTECKI
Poznan University of Technology
Faculty of Civil and Environmental Engineering
ul. Piotrowo 5
60-965 Poznan, Poland
andrzej.garstecki@put.poznan.pl

Katarzyna JELENIEWICZ
Warsaw University of Life Sciences – SGGW
Department of Mechanics
ul. Nowoursynowska 159
02-776 Warsaw, Poland
k.jeleniewicz@tlen.pl

Jarosław JĘDRYSIAK
Lodz University of Technology
Department of Structural Mechanics
Al. Politechniki 6
90-924 Lodz, Poland
jarek@p.lodz.pl

Monika KAMOCKA
Lodz University of Technology
Department of Strength of Materials
ul. Stefanowskiego 1/15
90-924 Lodz, Poland
monikakamocka_7@wp.pl

Sławomir KĘDZIORA
University of Luxembourg
Campus Kirchberg
6, rue Coudenhove-Kalergi
L-1359 Luxembourg
slawomir.kedziora@uni.lu

Zbigniew KOŁAKOWSKI
Lodz University of Technology
Department of Strength of Materials
ul. Stefanowskiego 1/15
90-924 Lodz, Poland
zbigniew.kolakowski@p.lodz.pl

Henryk KOPECKI
Rzeszow University of Technology
Department of Aircraft and Aircraft Engines
al. Powstancow Warszawy 8
35-959 Rzeszow, Poland
hkopecki@prz.edu.pl

Maria KOTEŁKO
Lodz University of Technology
Department of Strength of Materials
ul. Stefanowskiego 1/15
90-924 Lodz, Poland
maria.kotelko@p.lodz.pl

Vasily KRASOVSKY
Prydniprovs'ka State Academy of Civil Engineering and Architecture
Department of Structural Mechanics and Strength of Materials
Chernyshevsky str. 24,
49600, Dniepropetrovsk, Ukraine
stmeh@inbox.ru

Marian KRÓLAK
Higher Vocational State School
Department of Mechanics and mechanical Enginnering
ul. 3 Maja 17
87-800 Wloclawek, Poland
marian.krolak@p.lodz.pl

Muditha KULATUNGA
Glasgow Caledonian University
School of Engineering and Built Environment
Cowcaddens Road
Glasgow, G4 0BA, Scotland, UK
mmd3@gcu.ac.uk

Olga LYKHACZEVA
Prydniprovs'ka State Academy of Civil Engineering and Architecture
Department of Structural Mechanics and Strength of Materials
Chernyshevsky str. 24,
49600, Dniepropetrovsk, Ukraine
olga-likhacheva@mail.ru

Martin MACDONALD
Glasgow Caledonian University
School of Engineering and Built Environment
Cowcaddens Road
Glasgow, G4 0BA, Scotland, UK
mmd3@gcu.ac.uk

Ewa MAGNUCKA-BLANDZI
Poznan University of Technology
Institute of Mathematics
ul. Piotrowo 3A
60-965 Poznan, Poland
ewa.magnucka-blandzi@put.poznan.pl

Krzysztof MAGNUCKI
Poznan University of Technology
Institute of Applied Mechanics
ul. Piotrowo 3
60-965 Poznan, Poland
krzysztof.magnucki@put.poznan.pl

Arkadiy MANEVICH
Dniepropetrovsk National University
Department of Computational Mechanics and Strength of Structures
Gagarin av. 72
49010, Dniepropetrovsk, Ukraine
armanevich@yandex.ru

Radosław MANIA
Lodz University of Technology
Department of Strength of Materials
ul. Stefanowskiego 1/15
90-924 Lodz, Poland
radoslaw.mania@p.lodz.pl

Bohdan MICHALAK
Lodz University of Technology
Department of Structural Mechanics
Av. Politechniki 6
90-924 Lodz, Poland
bohdan.michalak@p.lodz.pl

Wiesław NAGÓRKO
Warsaw University of Life Sciences – SGGW
Department of Mechanics
ul. Nowoursynowska 159
02-776 Warsaw, Poland
wieslaw_nagorko@sggw.pl

Piotr OSTROWSKI
Lodz University of Technology
Department of Structural Mechanics
Al. Politechniki 6
90-924 Lodz, Poland
piotr.ostrowski@p.lodz.pl

Piotr PACZOS
Poznan University of Technology
Institute of Applied Mechanics
ul. Piotrowo 3
60-965 Poznan, Poland
piotr.paczos@put.poznan.pl

Wojciech PIETRASZKIEWICZ
The Szewalski Institute of Fluid-Flow Machinery Polish Academy of Sciences
ul. Fiszera 14
80-231 Gdansk, Poland
pietrasz@imp.gda.pl

Jacek PRZYBYLSKI
Technical University of Czestochowa
Institute of Applied Mechanics and Machine Design Foundations
ul. Dabrowskiego 73
42-200 Czestochowa, Poland
j.przybylski@imipkm.pcz.pl

Jan RAVINGER
Institute of Construction and Architecture, Slovak Academy of Sciences
Dúbravská cesta 9
845 03 Bratislava 45, Slovak Republic
smravi@svf.stuba.sk

Katarzyna RZESZUT
Posnan University of Technology
Faculty of Civil and Environmental Engineering
ul. Piotrowo 5
60-965 Poznan, Poland
katarzyna.rzeszut@put.poznan.pl

Agnieszka SABIK
Gdansk University of Technology
Faculty of Civil and Environmental Engineering
ul. Narutowicza 11/12,
80-233 Gdansk, Poland
agnieszka.sabik@wilis.pg.gda.pl

Shigeru SHIMIZU
Shinshu University
Department of Civil Engineering
Wakasato 4-Chome
380-8559 Nagano, Japan
shims00@shinshu-u.ac.jp

Bartosz SOBCZYK
Gdansk University of Technology
Faculty of Civil and Environmental Engineering
ul. Narutowicza 11/12,
80-233 Gdansk, Poland
bartosz.sobczyk@wilis.pg.gda.pl

Krzysztof SOKÓŁ
Technical University of Czestochowa
Institute of Applied Mechanics and Machine Design Foundations
ul. Dabrowskiego 73
42-200 Czestochowa, Poland
k.sokol@imipkm.pcz.pl

Janusz SZMIDLA
Technical University of Czestochowa
Institute of Applied Mechanics and Machine Design Foundations
ul. Dabrowskiego 73
42-200 Czestochowa, Poland
j.szmidla@imipkm.pcz.pl

Czesław SZYMCZAK
Gdansk University of Technology
Faculty of Ocean Engineering and Ship Technology
Department of Theory and Ship Design
ul. Gabriela Narutowicza 11/12
80-233 Gdansk, Poland
szymcze@pg.gda.pl

Łukasz ŚWIĘCH
Rzeszow University of Technology
Department of Aircraft and Aircraft Engines
al. Powstancow Warszawy 8
35-959 Rzeszow, Poland
lukasz.swiech@prz.edu.pl

Andrzej TETER
Lublin University of Technology
Mechanical Faculty
ul. Nadbystrzycka 38 D
20 – 618 Lublin, Poland
a.teter@pollub.pl

Lech TOMSKI
Technical University of Czestochowa
Institute of Applied Mechanics and Machine Design Foundations
ul. Dabrowskiego 73
42-200 Czestochowa, Poland
sekr@imipkm.pcz.czest.pl

Viorel UNGUREANU
Polytechnic University of Timisoara
Piata Victoriei No. 2
300006 Timisoara, Romania
viorel.ungureanu@upt.ro

Sebastian UZNY
Technical University of Czestochowa
Institute of Applied Mechanics and Machine Design Foundations
ul. Dabrowskiego 73
42-200 Czestochowa, Poland
s.uzny@imipkm.pcz.pl

Jerzy WARMIŃSKI
Lublin University of Technology
Mechanical Faculty
ul. Nadbystrzycka 38 D
20-618 Lublin, Poland
j.warminski@pollub.pl

Wojciech WITKOWSKI
Gdansk University of Technology
Faculty of Civil and Environmental Engineering
ul. Narutowicza 11/12,
80-233 Gdansk, Poland
wojciech.witkowski@wilis.pg.gda.pl

Jan ZACHARZEWSKI
Rzeszow University of Technology
Department of Aircraft and Aircraft Engines
al. Powstancow Warszawy 8
35-959 Rzeszow, Poland
jan.zacharzewski@prz.edu.pl

1.

Multi-aspect design methodology for steel skeleton multi-storey buildings

1.1. Introduction

From among structural materials steel is particularly attractive in application to light weight-structures and opens the way for architects to apply a wide range of technical and aesthetic structural solutions. A great variety of hot- and cold-formed steel sections is at designers' disposal. The choice of steel when designing multi-storey building means selection of a material having a low cost, strength, durability, design flexibility, adaptability and vulnerability to recycling. This decision also means the choice to engage in sustainable development. Modern highly automated cutting, drilling welding and corrosion protection make possible to design and prefabricate optimal structural elements, which can be easily assembled using unified welded or bolted connections. In case of steel skeleton multi-storey buildings the bearing structure consist of columns and beams which constitute support for different construction solutions of floors. Optimizing the number of points of load is an issue that is always discussed at the design stage, and its solution must take into account the intended use of the building. Considering the spatial layout, columns are always considered to be an obstacle, whose number should be reduced to a minimum. It must be underlined that the spatial layout of columns is important but not the only special aspects in design procedure of steel skeleton multi-storey buildings. Designers must seriously take into account such aspect as architectural preferences, constructional solutions of floors, configurations position relative to the structure of the facades, the cost of steel products, assembly costs, easiness of assembly and connections with secondary structural elements (in the case of the facade, walls, floors). Multi-storey building, regardless of the destination is made of a number elements or sub-elements influencing parameters: no only construction and building envelope, but also technical installations allowing to maintain the integrity of the building such heating and air conditioning, ventilation, power supply high and low voltage installations. Therefore, designers should ensure the possibility to control the interaction between installations and the structure of the building through an easy access to the system for maintenance, easy replacement of components whose service life is shorter than the durability of the building.

A modern form of inclusion of those aspects is Building Information Modelling (BIM) which distributed information in sub-sectoral studies and organized them in a transparent manner in the form of a model. The matrix is usually a model building created by architects. This model is supplemented by industry description, which accurately reflects the process that takes place on site. Modern open source software like Autodesk Revit or ArCADia BIM makes possible to conduct the design process in parallel way, and the designers of individual industries can watch the progress of work and they are constantly "up to date", which greatly simplifies the arrangements and eliminates the possibility of a collision. General availability of information and its readability increases the importance of all participants in the investment process from the initial design stages of investment. Specialists involved in the process have full knowledge of the project and can on a regular basis respond to emerging problems. They are fully aware of what limits the overall level of risk and number of errors. BIM model may also be associated with the data on the construction schedule, and the actual market, the materials and construction products. BIM design can become a tool for direct automated control of the investment, and can also provide invaluable assistance during the subsequent operation of the building. Moreover, the BIM allows designers to ensure the basic requirements of safety, not only because of construction namely bearing capacity, fire and corrosion protection but also because maintenance personnel in the field of facility management, which is at constant risk of electrical shock, falls, crushing, cuts and bruises. This issues are widely discussed in [1.10], where the authors present a BIM-based framework to support safe maintenance and repair practices during the facility management phase and rule-based decision making a user interface. In [1.9] information from BIM in conjunction with genetic algorithms was utilized to develop an optimization algorithm framework site layout models that consider the actual travel paths of on-site personnel and equipment. Furthermore, the paper presents a method to determine optimized dimensions for each facility, thus allowing for an increase in the efficiency of layouts.

It can be concluded that BIM enables the exchange of ideas and collaboration between the architect, builder and various other participants of the investment process. However, at each stage of the project, there is always a need for structural safety analysis in terms of static, strength and cost analysis. Accordingly, the constructor activity cannot be replaced by BIM but accompanied to it.

In this paper the multi-criteria analysis of steel skeleton multi-storey buildings was carried out. In the first step of the study the optimization was performed using the program ACE. Based on the conducted analysis the choice of the optimum concept based on assumptions flowing from the static and strength analysis supported by minimizing of cost and material consumption was made. Generated design solution and decisions taken on the basis of ACE have been verified in the second stage of the study. In this stage the verification of the optimal project was carried out using FEM and Eurocode recommendations for checking the ultimate and serviceability limit states.

1.2. Optimal designing

It is rather obvious that automated design supported by CAD and BIM should make possible arriving at optimal solutions in the design process. The optimal solution is considered here in general terms. Using the formalism of the optimization theory it means that a wide set of design variables including dimensional, material and topological ones should be accounted for. They are continuous or discrete. Fuzzy sets or interval variables can be faced, too. Moreover, a number of implicit constraints must be introduced. Surely, many local optima would appear. Nonlinear programming methods cannot be applied to a problem formulated in a such general way. Artificial neural networks (ANN) can handle the problem, but training the ANN would be rather difficult. There remain optimization solvers using genetic algorithms, however they would be extremely time consuming when applied to so built up problems. Therefore it seems reasonable to apply problem oriented methods of optimization, where the rational approach is combined with formal optimization.

In the present paper the application of Advanced Cost Estimator (ACE) system is demonstrated. In this system the decomposition of the problem, sub-structuring and simplified optimization methods e.g. fully stress design are used. The user can interact with the system by for example by limiting the range of design variables.

1.3. ACE - Advanced Cost Estimator

1.3.1. General information

There are many available tools which can be used for optimal designing of civil engineering structures. However, in the process of rational and optimal designing the most important issue is properly defining the optimization criterion, project parameters and constrains. Therefore, the choice of optimisation software is often considered of secondary importance. In fact the choice of optimisation software strongly affects the numerical efficiency of computation and what is more important, allows to find the global optimum. In this paper the authors decided to use Advanced Cost Estimator (ACE) [1.1, 1.2] because it allows introduction of a wide range of design variables, namely topological, material and dimensional.

The main aim of the ACE software is price or weight estimation of the steel constructions based on I-profiles. The tool allows to perform computations for the single beam, industrial hall, single module (analysis of one floor system) and multi-module (analysis of the whole floor system) both for single and multi-storey constructions (up to 20 storeys). After choosing one of the mentioned modulus and defining basic geometry of the model (width, length, column spacing, minimum height of the floor including free and service space, number of storeys) the next parameters of the construction should be specified. The ACE software allows the users to specify the following construction parameters:

– the value of permanent and variable load,
– steel and concrete class,
– type of the beam and slab (the possible beam-slab combinations were shown in Table 1.1),
– layers of the floor,
– bracing type,
– type of foundation (spread or plate footing),
– type of soil (sand 0.5MPa, gravel 0.6MPa or clay 0.35MPa).

Table 1.1. Available beam-slab connections

	Non composite			Composite	
I-profiles	steel deck	precast slab	hollow core slab	steel deck	precast slab
Cellular beam	steel deck	precast slab	hollow core slab	steel deck	precast slab
Slim floor IFB, SFB*	---	---	hollow core slab	---	---

* IFB - integrated floor beam; SFB - slim floors

Additionally the following data may be included in the analysis:

– type of fire protection (intumescing paint, sprayed material or rigid panels),
– fire resistance conditions R30 - R120,
– placement of splices (place of column cross-section change),
– cost of ground floor, roof, façade, internal finishing, service and other preliminary cost which may be defined as a percentage of the total cost of the structure.

It is worth to mention that ACE is not a software for accurate computation of the construction and the results obtained by it are based on the implemented databases. Therefore, the results should be verified using finite element computations.

1.3.2. Price estimation

ACE allows to estimate the total cost of the construction which is defined by the sum of the following components: steel frame (beam, columns, connections, bracing, roof construction, corrosion and fire protection, pre-cambering and propping, assembly and transport), concrete slab, ground floor, foundations and overheads. Additionally, in the cost estimation there is a possibility to include the price of: waterproofing membrane, façade, internal finishing and service.

The cost of a steel frame evaluated by ACE consists of the following constituents.

- Material: the weight of the component multiplied by the unit price (depended on the steel grade). An additional security cost is increased by 5%.
- Manpower: the cost of the manpower depends on the total weight of the steel elements.
- Connections: the price of a typical connection is multiplied by the number of the same joints (beam to beam, beam to column or column to column). Each type of the connection has a different price, which changes linearly as a function of beam weight and manpower.
- Studs: the price is a function depending on stud type, number of studs, type of the slab and manpower.
- Bracing: the price is represented by a nonlinear function depending on the height of the building.
- Corrosion protection: the price is calculated as a function of the external surface area of a steel profile. Two layers of corrosion protection (primer and finishing) are considered.
- Fire protection: the cost depends on the type of fire protection, shape and dimensions of the steel profile.
- Erection: the cost of the crane and erection manpower which depend on the weight of the construction element.
- Pre-cambering or propping: the price depends on slab type and span.
- Transport: the cost is a function of weight of the construction element. Additionally the cost of tower wagons is added.
- Overheads: steel contractors overheads expressed as a percentage of the sum of the above mentioned costs.

Table 1.2. The list of prices used in the analysis

Item description		Price
Steel quality	S235	0.812 €/kg
	S355	0.837 €/kg
	S460	0.837 €/kg
Steel for angels		0.699 €/kg
Bolts (grade 8.8)	M16-60	0.27 €/unit.
	M20-60	0.52 €/unit
	M22-60	0.94 €/unit
Propping	slab	3.50 €/m^2
	beam	10.0 €/m
Crane	40 tons	299.8 €/day
	100 tons	599.5 €/day
Tower waggons		15.0 €/h
Transport		0.03 €/kg
Overhead		15 %
Precast slab 5cm		20.0 €/m^2
Concrete chape		67.0 €/m^3
Reinforcement in precast slab		0.587 €/kg
Hollow core	12 cm	22.0 €/m^2
	16 cm	22.0 €/m^2
	20 cm	25.0 €/m^2
	27 cm	29.0 €/m^2
	32 cm	30.0 €/m^2
	40 cm	35.0 €/m^2
Steel decking		12.50 €/m^2
Concrete		85.0 €/m^3
Concrete - reinforcement		0.587 €/kg
Concrete - timbering		6.0 €/m^2
Manpower		7.5 €/h
Corrosion protection	primer	2.0 €/m^2
	finish	2.0 €/m^2
Fire protection	15 mm rigid panel	30.0 €/m^2
	material paint	6.5 €/kg
	material spray	0.65 €/kg

The price of the slab is estimated as follows:

- Concrete slab: the price is a function of concrete volume and reinforcement.
- Steel deck: cost is linearly dependent on the floor span.
- Precast slab: the price of a fixed amount of precast slab corresponding to the price with a thickness of 5 cm.

– Hollow core slab: the price depends on the thickness of the implemented slab.

Additionally the price of the slab is supplemented by the cost of manpower, which depends on the floor area.

The total price of the foundation includes the following costs:

– Concrete: the price depends on the volume.
– Reinforcement: the price is a function of weight of the reinforcement.
– Formwork: the cost is a function of needed formwork area expressed in m^2. The formwork area is determined by multiplying the area of foundation base by 5.
– Manpower: the price depends on the man-hours needed to perform the foundation.

In estimating the cost of the construction it is assumed that the cost of the roof is taken as 60% of the price of the floor system plus the price of the additional waterproofing. By default, the price of the ground floor is equal to the floor system (excluding the price of the steel frame). In the price estimation, both the roof and ground floor price can be typed in euro per square meter of usable area.

Moreover, in the ACE software it is possible to add to the total price of the building the following costs (by typing directly the prices):

– façade,
– internal finishing of the building,
– additional service costs.

The list of prices in Poland, which have been implemented in the ACE software, are used in the considered example and are presented in Table 1.2.

1.4. Optimal design of steel skeleton multi-storey buildings

1.4.1. Formulation of the optimization problem

The problem of the multi-aspect design is presented on the example of the steel skeleton 6-storey office building with the dimensions in plan 24×48 m. The visualisation of a segment part of the analysed construction were presented in Fig. 1.1. We assume that communication space (lifts, stairs) will be situated in the core, located in the centre of the construction.

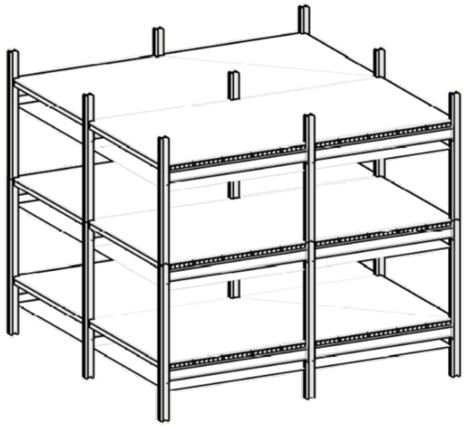

Fig. 1.1. Visualisation of a segment part of the analysed construction

As optimization criterion the total price of the construction is assumed. Moreover, the weight of the steel frame will also be analysed. It includes the following elements:

- beams and columns,
- bolts,
- other components of connection (the implemented connection types were presented in the Fig. 1.2),
- bracings,
- construction of the roof.

a)

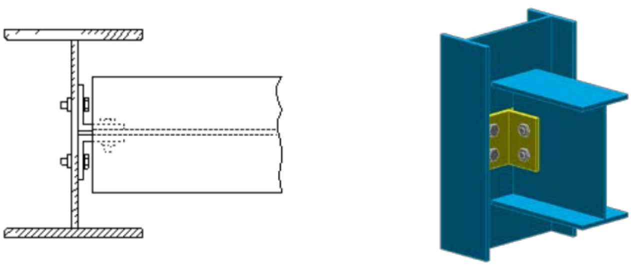

b)

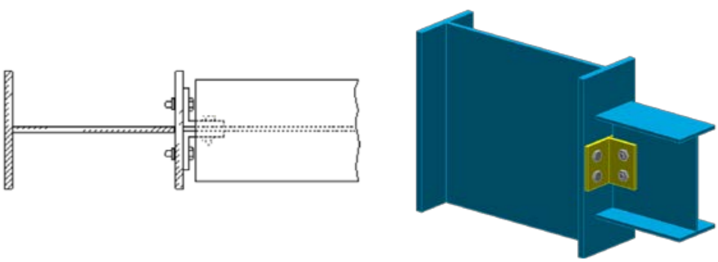

c)

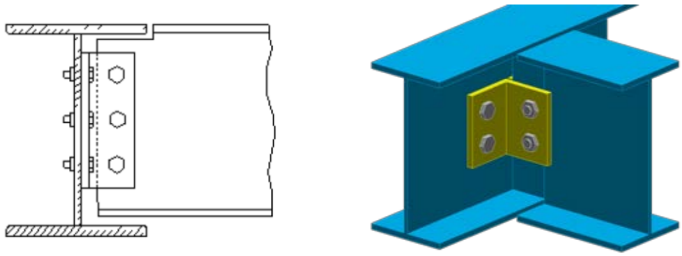

Fig. 1.2. Types of the available connections: a), b) beam-column, c) beam-beam

In the next step the characteristics that describe the structure were divided into design parameters and variances. To the design parameters which will be constant throughout the whole designing process, the following data were included:

– function of the building: office,
– soil: sand,
– number of storeys: 6,
– building plan dimensions: 24×48 m,
– floor type: hollow core slab, precast slab,
– type of foundation: spread foundation.

Directly with the established function of the building the following parameters are related:

– free spacing: 2.75 m,
– fire resistance: R120,
– permanent load: 3.00 kN/m^2,
– variable load: 3.00 kN/m^2.

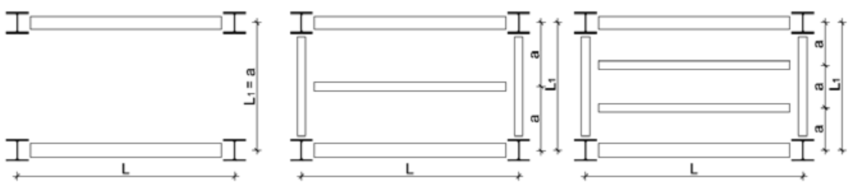

Fig. 1.3. Possible beam and column schemes (respectively with 0, 1 and 2 secondary beams)

Other parameters were classified in the group of design variables:

– beams and columns column cross-sections (IPE, HEA, HEB and HEM),
– beam and columns schemes (Fig. 1.3),

– beam orientation,
– steel class (S235, S355, S460),
– concrete class (C30/37, C40/45).

Moreover, each of the mentioned computations are performed for 6 variants of column spacing: 2 square and 4 rectangular column grid (see Fig. 1.4).

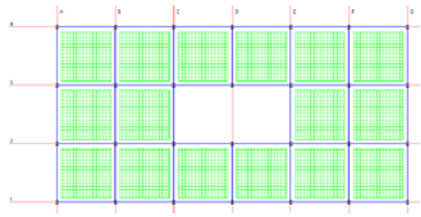

Variant 1: 8x8m

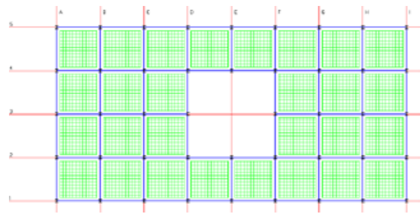

Variant 2: 6x6m

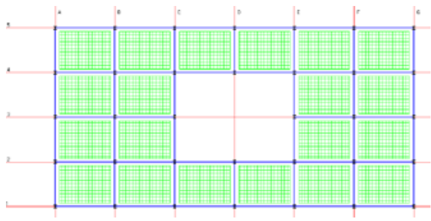

Variant 3: 6x8m

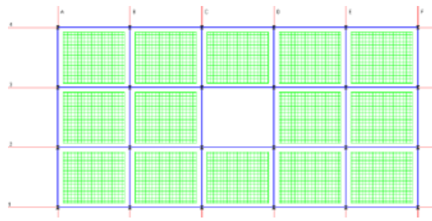

Variant 4: 8x9.6m

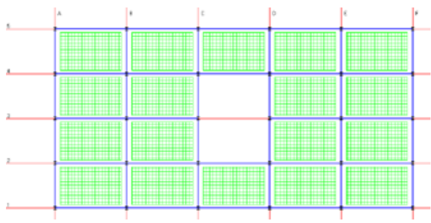

Variant 5: 6x9.6m

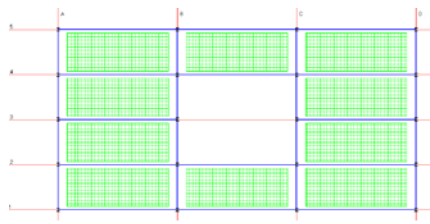

Variant 6: 6x16m

Fig. 1.4. Analysed dimensions of the column grid

In the last stage of the analysis the limitations are defined as the regulations specified by engineering codes (Eurocodes). In the computations the limit state methods are used.

1.4.2. Results of the analysis

As it was mentioned before, the analysis was performed using the ACE software in order to find the best (the cheapest) solution of the steel skeleton 6-storey office building. The results of the analysis were illustrated by three graphs (Fig. 1.5-Fig. 1.7). In the diagrams the total weight of the steel frame depending on the applied floor system was presented. The following notation for the floors was used: the first letter indicates the type of the floor beam (A: cellular beam, I: I-beam); the second letter N means that the only the non-composite type of floor system was taking into account; the third letter defined the type of the floor slab (H: hollow core slab, P: precast slab). Additionally, the total weight of the steel frame for each of the floor system was presented depending directly on the steel grade and indirectly on the concrete class. Three grades o steel were considered: S235, S355 and S460. For the first two steel grades, it was assumed that the slab is made of C30/37 concrete class and for the steel S460 the concrete C40/45 was introduced.

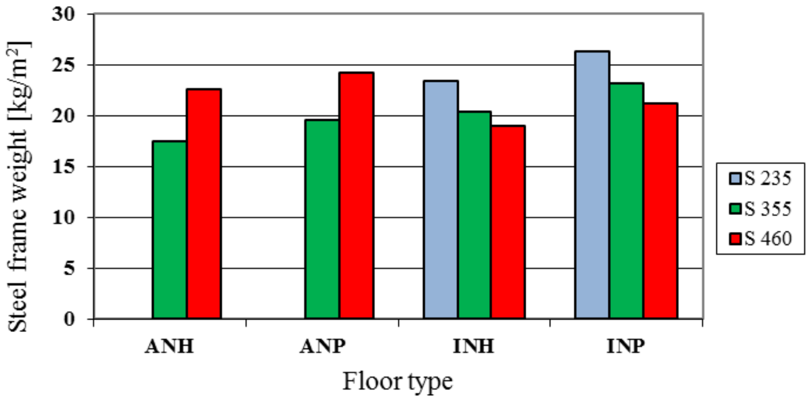

Fig. 1.5. The weight of the steel frame for the variant 2

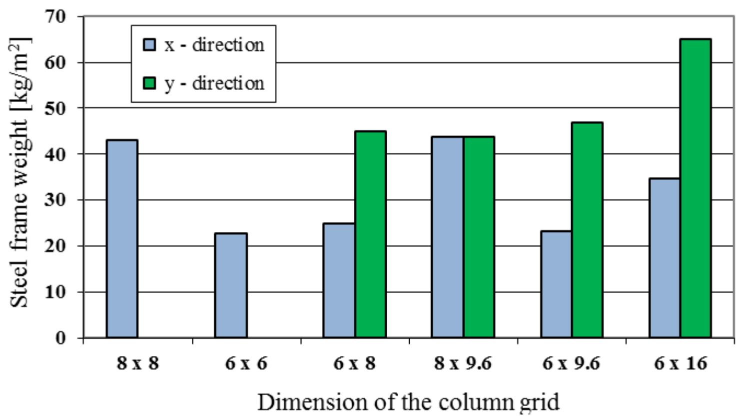

Fig. 1.6. The weight of the steel frame for the floor with cellular beam with non-composite hollow core slab

The above graph presents the total weight of the steel frame depending on the type of the floor system (for variant 2 - 6x6 m square column grid).

Additionally, three steel grades were analysed. In the case of the floor systems based on the I-beams (INH and INP), increasing the steel grades causes the reduction of the steel frame weight. It is a logical conclusion that increasing steel grades allows to use smaller cross-section. However, in the case of the floor systems based on the cellular beams (ANH and ANP) increasing the steel grades caused the increase of the steel frame weight. This results from the fact that ACE software, as the main optimization criterion assumed the cost of the structure not its weight. It turned out that it is cheaper to use other floor system configurations with stronger steel (despite the increase of the weight of the steel frame) than changing the steel grade without changing the floor system.

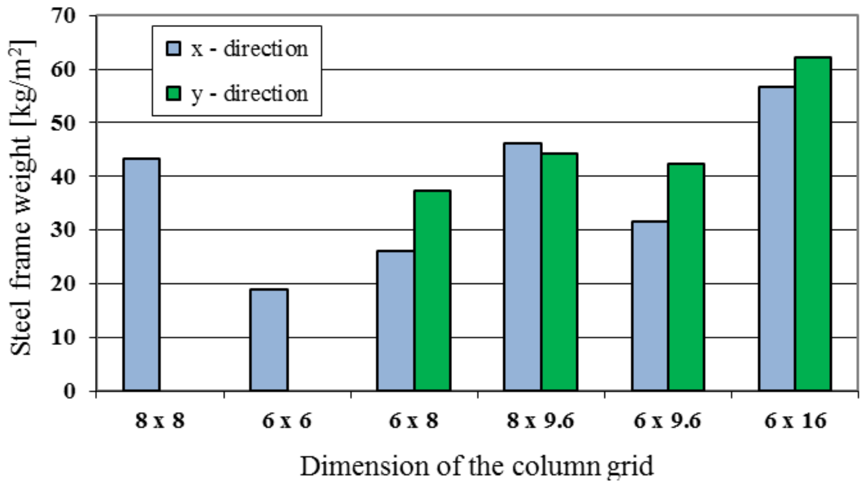

Fig. 1.7. The weight of the steel frame for the floor with I-profile beam with non-composite hollow core slab

The two next graphs present the total weight of the steel frame depending on the type of the beam (I-beam or cellular one) and the column grid spacing. Due to the fact that the first two variants were related to the square column grid, the result for both X and Y directions were the same. In other four variants, where the column grids were in the shape of rectangular, the results for the X and Y directions were different. Therefore, each analysis was performed for two beam orientations: both X and Y, where X direction determines the shorter side of the rectangular.

1.4.3. The optimal result

As a result of the foregoing considerations it was found that the optimal solution (the cheapest one) is variant 2, namely the square column grid which dimension of the side is equal to 6 meters. Incidentally, this is the minimum size of the column grid recommended for commercial buildings [1.8]. In the Fig. 1.8 the graph showing the distribution of cost in the considered example was presented. It can be concluded, that a significant impact on the total cost of the construction have costs of the slab (41%) and steel frame (28%). Wherefore, it is worth to mention that properly designing of slab, beams, columns and their connections leads to reduction of the cost of the entire construction.

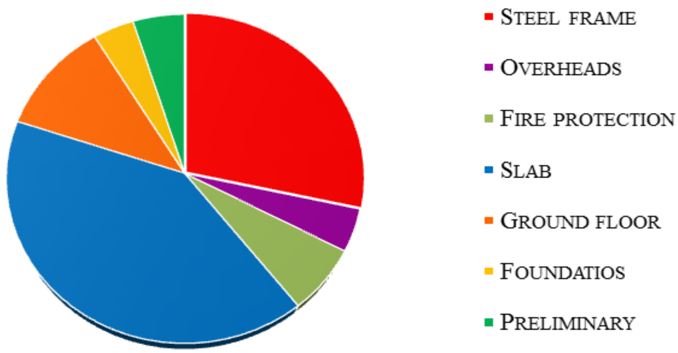

Fig. 1.8. The total cost distribution into cost components

Basing on the results of the foregoing analyses the square column grid 6 m was accepted for next design steps. In the Table 1.3 the detailed technical data of the optimal variant was presented.

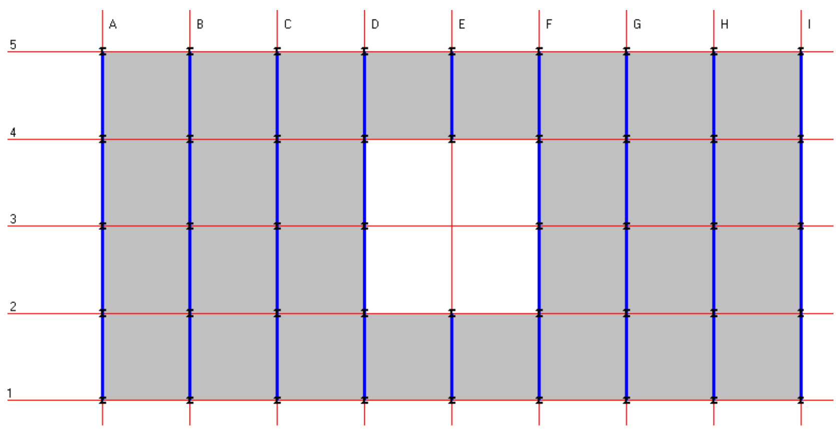

Fig. 1.9. Beam scheme in the optimal solution

Table 1.3. Technical details of the chosen conception

<table>
<tr><td colspan="3">Steel grade</td><td>S 460</td></tr>
<tr><td colspan="3">Concrete type</td><td>C 40/45</td></tr>
<tr><td colspan="3">Total height of the storey</td><td>3.81 m</td></tr>
<tr><td colspan="3">Total weight of the steel frame</td><td>110 365.50 kg</td></tr>
<tr><td colspan="3">Beam type</td><td>I-profiles</td></tr>
<tr><td colspan="3">Floor type</td><td>hollow core slab</td></tr>
<tr><td colspan="3">Beams (per one floor)</td><td>12 x IPE 330
22 x IPE 400</td></tr>
<tr><td rowspan="12">Columns</td><td rowspan="3">A1/A5/I1/I5</td><td>floor 1. 2</td><td>HEA 180</td></tr>
<tr><td>floor 3. 4</td><td>HEA 160</td></tr>
<tr><td>floor 5. 6</td><td>HEA 120</td></tr>
<tr><td rowspan="3">A2/A3/A4/B1/B5/C1/C5/D1 /D3/D5/E1/E2/E4/E5/F1/F3/ F5/G1/G5/H1/H5/I2/I3/I4</td><td>floor 1. 2</td><td>HEA 220</td></tr>
<tr><td>floor 3. 4</td><td>HEA 180</td></tr>
<tr><td>floor 5. 6</td><td>HEA 140</td></tr>
<tr><td rowspan="3">B2/B3/B4/C2/C3/C4/G2/G3/ G4/H2/H3/H4</td><td>floor 1. 2</td><td>HEA 260</td></tr>
<tr><td>floor 3. 4</td><td>HD 260 x 54</td></tr>
<tr><td>floor 5. 6</td><td>HEA 180</td></tr>
<tr><td rowspan="3">D2/D4/F2/F4</td><td>floor 1. 2</td><td>HD 260 x 54</td></tr>
<tr><td>floor 3. 4</td><td>HEA 220</td></tr>
<tr><td>floor 5. 6</td><td>HEA 180</td></tr>
<tr><td rowspan="16">Foundations</td><td rowspan="4">A1/A5/I1/I5</td><td>base</td><td>1.2 x 1.2 m</td></tr>
<tr><td>height</td><td>0.42 m</td></tr>
<tr><td>concrete</td><td>0.7 m^3</td></tr>
<tr><td>steel</td><td>66.2 kg</td></tr>
<tr><td rowspan="4">A2/A3/A4/B1/B5/C1/C5/D1 /D3/D5/E1/E2/E4/E5/F1/F3/ F5/G1/G5/H1/H5/I2/I3/I4</td><td>base</td><td>1.7 x 1.7 m</td></tr>
<tr><td>height</td><td>0.59 m</td></tr>
<tr><td>concrete</td><td>1.7 m^3</td></tr>
<tr><td>steel</td><td>174.2 kg</td></tr>
<tr><td rowspan="4">B2/B3/B4/C2/C3/C4/G2/G3/ G4/H2/H3/H4</td><td>base</td><td>2.3 x 2.3 m</td></tr>
<tr><td>height</td><td>0.82 m</td></tr>
<tr><td>concrete</td><td>4.7 m^3</td></tr>
<tr><td>steel</td><td>471.2 kg</td></tr>
<tr><td rowspan="4">D2/D4/F2/F4</td><td>base</td><td>2.1 x 2.1 m</td></tr>
<tr><td>height</td><td>0.72 m</td></tr>
<tr><td>concrete</td><td>3.3 m^3</td></tr>
<tr><td>steel</td><td>328.3 kg</td></tr>
</table>

Percent distribution of the steel frame weight in the optimal solution into components parts was presented in the Fig. 1.10.

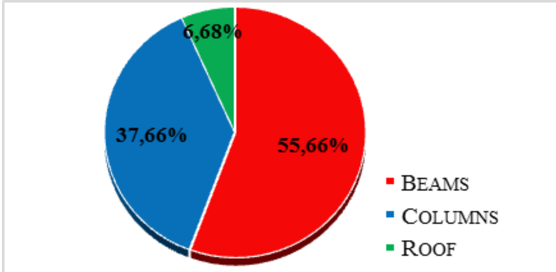

Fig. 1.10. Percent distribution of the total weight of the steel frame in the optimal solution

1.4.4. The numerical verification

In the following part of the study the numerical computations using Finite Element Method are performed in order to verify the results obtained from preliminary analysis (in ACE software). The computations are performed in two dimensional model for one of the middle frames (axis C). It was assumed to design the office building with the same dimensions, material parameters, column and beam cross-sections as those obtained from the analyses performed in ACE (Table 1.2). However, the authors adopted their own assumptions about the designed building.

In a first step the location of the designed office building was assumed. It is worth to mention that in the ACE software there is no possibility to define the location of the construction. The values of the climate loads are adopted on the base of the average statistic data collected for the countries of the European Union. The authors decided that the building is placed on Polish territory in the city of Poznan, which is located in the second zone of the snow load and the first zone of the wind load (according to the maps contained in [1.12, 1.13]. The climate loads were determined on the basis of these standards for the building located in an urban area. The value of the wind load was determined both for the exterior surfaces (wind blowing on the front wall or on the side wall) and for the interior surfaces.

The values of the permanent (*G*) and imposed loads were calculated. The permanent load was defined as a sum of the weight of the following elements:

- steel frame: included in the calculating program;
- concrete slab: specific load of the reinforced concrete multiplied by the thickness if the slab - 3.19 kN/m^2;
- other permanent load - 3.00 kN/m^2.

The value of imposed load is specified in the first part of European standards [1.4]. Value of the imposed load of the floors for the building of the B category (i.e. office space) should be taken from 2.00 to 3.00 kN/m^2. In the further calculation the value equal to 3.00 kN/m^2 was assumed.

Afterwards, the combinations of actions both in the ultimate limit state and the serviceability limit state were considered. The combinations were performed according to the Eurocode 0 [5.3]), they should be expressed either as (1.1) or alternatively as the lower value of (5.2a and 5.2b).

$$E_d = \sum_{j>1} \gamma_{G,j} G_{k,j} \text{"+"} \gamma_{Q,1} Q_{k,1} \text{"+"} \sum_{i>1} \gamma_{G,i} \psi_{0,i} Q_{k,i} \tag{1.1}$$

$$E_d = \min \begin{cases} \sum_{j>1} \gamma_{G,j} G_{k,j} \text{"+"} \gamma_{Q,1} \psi_{0,1} Q_{k,1} \text{"+"} \sum_{i>1} \gamma_{G,i} \psi_{0,i} Q_{k,i} \\ \sum_{j>1} \xi_j \gamma_{G,j} G_{k,j} \text{"+"} \gamma_{Q,1} Q_{k,1} \text{"+"} \sum_{i>1} \gamma_{G,i} \psi_{0,i} Q_{k,i} \end{cases} \tag{1.2a,b}$$

where: "+" - implies "to be combined with",
Σ - implies "the combined effect of",
γ - partial factor which depends on the situation and has the following values:
- permanent load: 1.00, 1.15 or 1.35,
- imposed, snow and wind load: 0.00 or 1.50,

ψ - factor for combination,
ξ - reduction factor for unfavourable permanent actions *G*.

The permanent and imposed loads were applied at each beam with the difference that the permanent load is always acting, whereas the imposed load does not need to appear or may be applied to one or several beams

The wind load was determined both for the external and internal surfaces of the building (according to the [1.11]. The walls and the roof were divided into special zones in order to calculate the value of the external wind load on each of the wall and roof slope. Moreover, the possibility of wind acting on each side of the building was considered.

Table 5.4. The values of factors for combinations

	Ψ_0	Ψ_1	Ψ_2
Imposed load	0.7	0.5	0.3
Snow load	0.5	0.2	0.0
Wind load	0.6	0.2	0.0

The values of factor for combination ψ were also adopted in accordance to the annex of this standard and were presented in the Table 1.4.

After calculating the loads acting on the designed structure, the internal forces (bending moment, shear force and axial force) were computed using FEM. The authors decided to design the rigid connection of columns into foundations (similarly as in ACE). We assumed, the rigid end-plated connections between columns and beams, in order to increase the stiffness of the construction and to reduce the values of the bending moment, though in ACE non-rigid connections were assumed.

In the next step the authors verified the safety and economy of the structure which had been the outcome of the ACE software. Therefore, basing on the cross sectional and material parameters of columns and beams following from ACE, the FEM analyses were carried out for various load combinations described above. For each element the resistance of cross-section and buckling resistance were computed according to the [1.5, 1.6]. For bending elements (beams) it was assumed that the adopted slab (hollow core slab) protected the element against the lateral-torsional buckling. Whereas, the effective length of the frame columns was determined on the basis of the graph presented in the Fig. 1.11. The values of the parameters: η_1 and η_2 are dependent on the moment of inertia of the columns and beams and their real length. They were determined separately for each element.

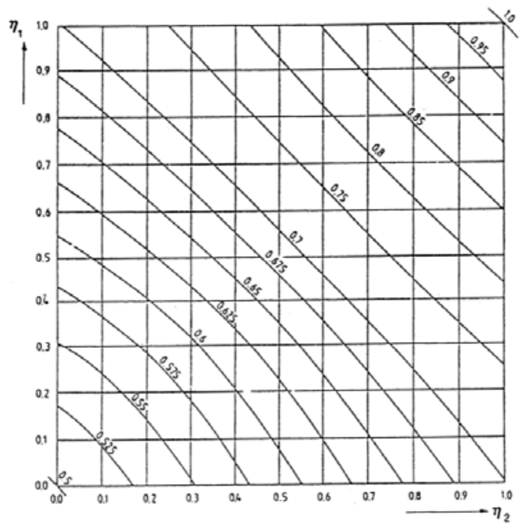

Fig. 1.11. The effective length coefficient of the columns [1.11]

The structural effort factors of all members are shown in Fig. 1.12. They express the relative load bearing capacity exhausted by the structural members.

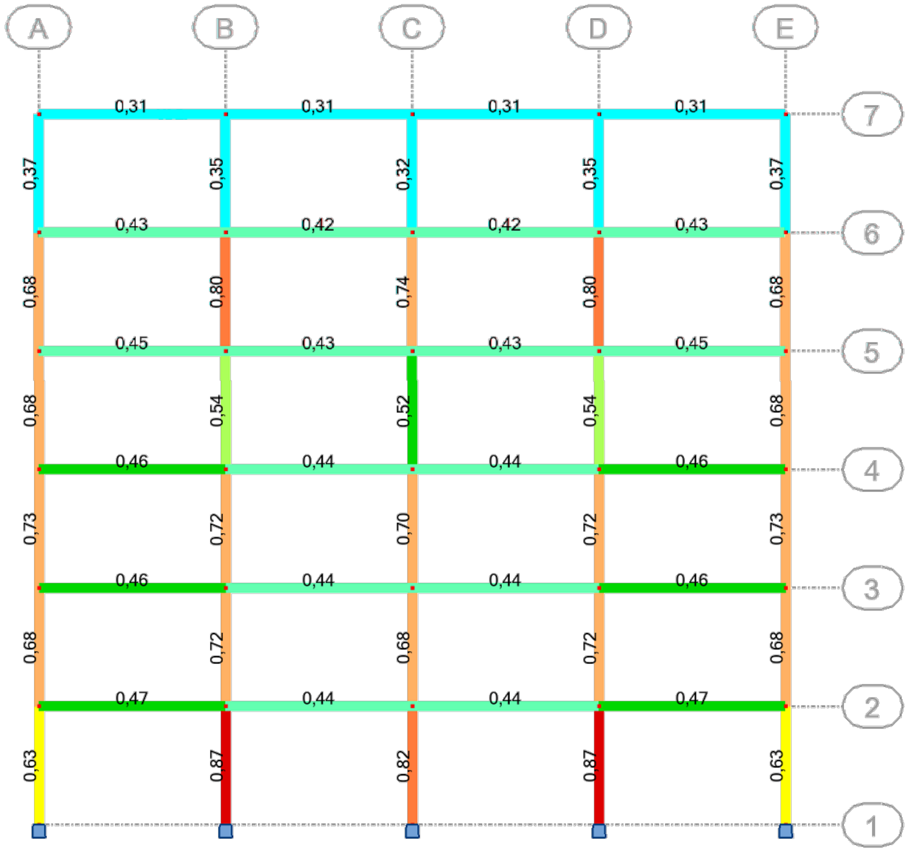

Fig. 1.12. The load bearing capacity factors

The presented results demonstrate that columns in the even storeys have smaller effort factors than the ones in the odd storeys, because it was assumed that a jump of the column cross-section took place in every second storey. At this point we leave it as an open question if it would be recommended the variation of column sections at each storey.

It is also evident that the beams have lower values of effort factors than the columns. There are two possible reasons. Firstly, we introduced rigid beam-to-column connections, whereas in ACE flexible connections had been assumed. Secondly, in ACE the technological conditions of minimal flange 180 mm in I section was introduced (Fig. 1.13a), to make possible the supporting of the hollow core slab. This is satisfied by the section IPE 400 which is too conservative. At this point an additional analysis might have been conducted by consideration another supporting of the slab, e.g. shown in Fig. 1.13b.

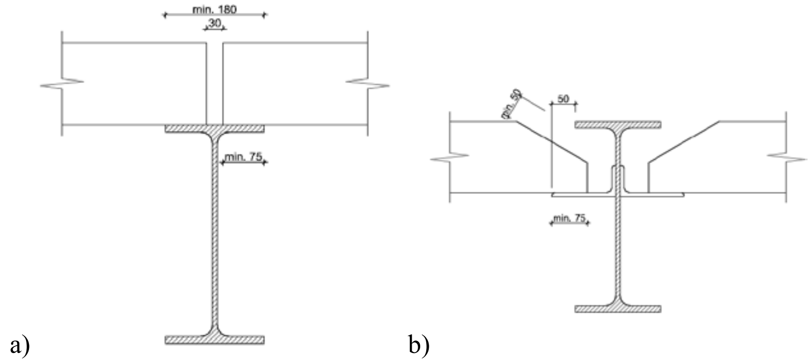

Fig. 1.13. The method of the placing the concrete slab on the beam: a) directly on the beam flange, b) by angle profiles fixed to the beam web

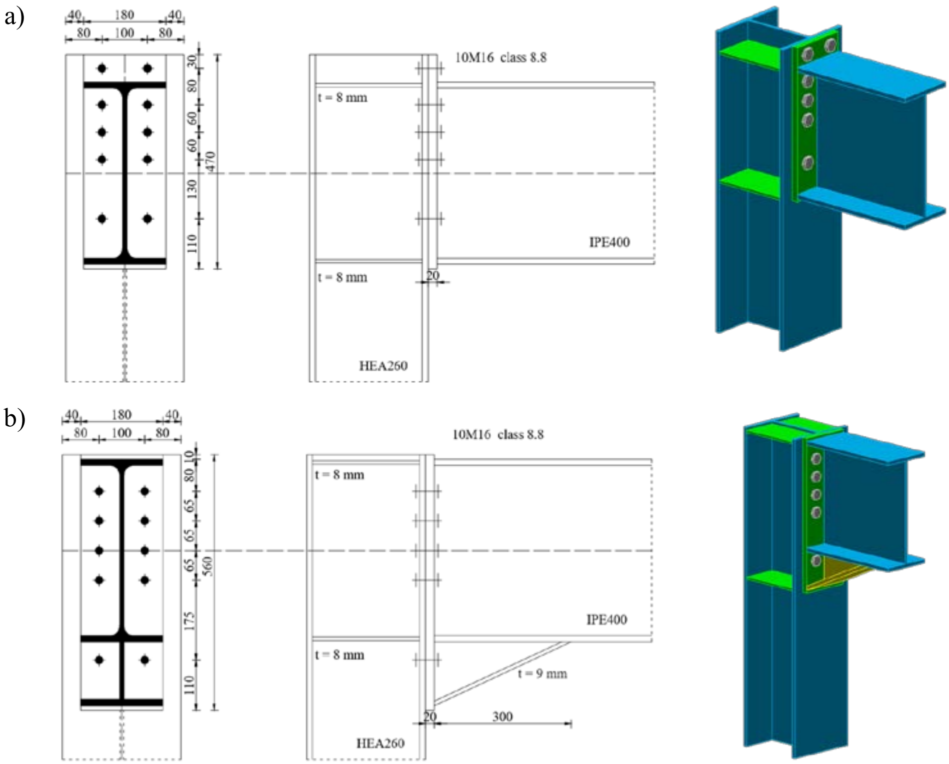

Fig. 1.14. The proposals of the construction of the rigid beam to column end-plated connection

Concluding these computational considerations it may be stated that the differences may also reflect the adoption of a rigid connection. The end-plated connection between the beam and column was calculated (according to the [1.7]). Two constructional solutions of the end-plated connection were proposed. Each of the solution consists of ten bolts (spaced in 5 rows) with the diameter equal to 16 mm and class 8.8, what means that the value of their ultimate tensile stress is equal to 800 MPa and the value of yield stress is equal to 640 MPa. Both joints were strengthened by two horizontal stiffening ribs with the thickness of 8 mm. The thickness of endplate is equal to 20 mm. In the first case (Fig. 1.14a) the endplate is 470 mm high and extends above the upper flange of the beam 60 mm where the first row of the bolts was placed. In the second example (Fig. 1.14b) the endplate extends below the lower flange of the beam 150 mm. In this case also the strengthen steel element in the shape of T-letter (located under the beam) was used. In both cases applied construction actions were performed in order to increase the bearing capacity of the connection on bending. Placing the assumed bolts only between the flanges of the beam was not enough.

Selection of one of the solutions depends on technological reasons of the designing floor construction. The first one definitely is a cheaper solution but the second one may additionally reduce the value of bending moment in the beam, what may also lead to decrease the beam cross-section.

1.5. Concluding remarks

1.5.1. Cost as the main optimization criterion

In the paper the cost expressed in €/m^2 of usable area was taken as the main optimization criterion. It was assumed that the price is a function of the main elements: steel frame, floor construction, fire and corrosion protection, foundations, transport and overheads. For detailed price estimation the contribution of all costs connected with designing and executing of the construction should also be taken into account. Additional costs arising during the designing and executing of the construction can play a significant role.

It seems rather obvious that the price is the principal criterion in selection of the design solution. However, due to complicated form of the cost function (depending on a number of components) specification of this function is not an easy task. For this reason formulation of the optimization problem as a cost criterion is used only at the stage of the preliminary designing. While, in the subsequent stages of the project, taking the cost as a main criterion is not recommended, because of a large number of design variables and implicit relations between these variables and the total cost.

It is worth to mention that the specific costs do not remain constant in time, but are influenced by variable economic conditions. Moreover, the design solution which in one country is taken as the optimal solution (the cheapest one) does not necessary have to be the best solution in another region or country. It is the result both of the different material cost and of the other value of the man-power rate. In the presented example the total price was calculated according to the price list in Poland. In the graph 1.15 the total price expressed in the €/m^2 of usable area of optimal solution (in Poland - Fig. 1.9) in different European countries was presented.

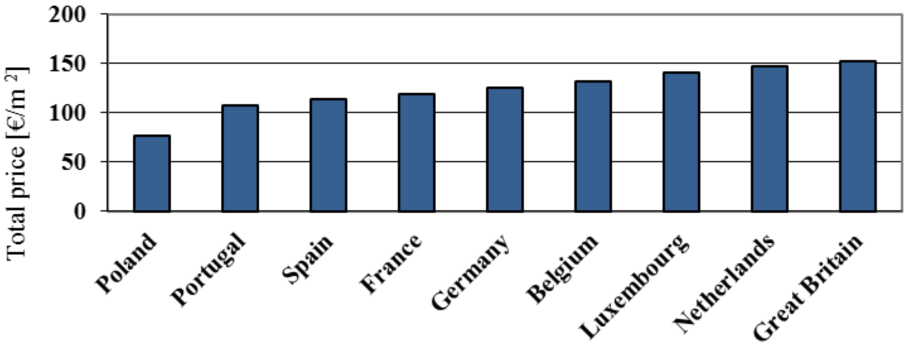

Fig. 1.15. The costs of the optimal solution in different European countries

1.5.2. Conclusions

The problem of optimal designing of steel skeleton multi-storey buildings was presented on the example of the office building which the dimensions in plan 24×48 m. The minimal construction cost in Poland was assumed as a main optimization criterion. The total cost was expressed as a price in € on the square meter of usable area. Six variants of column grid were analysed:

- variant 1 (8 x 8 m): 105,35 €/m^2,
- variant 2 (6 x 6 m): 77,16 €/m^2,
- variant 3 (6 x 8 m): 89,01 €/m^2,
- variant 4 (8 x 9,6 m): 113,74 €/m^2,
- variant 5 (6 x 9,6 m): 92,97 €/m^2,
- variant 6 (6 x 16 m): 113,04 €/m^2.

In the cheapest solution (variant 2) the non-composite hollow core slab based on the I-beams was applied.

The results of the performed analyses and computations allow to formulate the following conclusions:

1. The cost of executing the construction decreases with decreasing the spacing of columns.
2. The floor system contributes strongly to the total cost, hence inappropriate choice of the floor construction in one variant of column grid can cause an increase of the total cost up to 66%.
3. Changing the column grid can increase the cost of the construction by 47%:
   variant 2 (the cheapest one): 77,16 €/m^2,
   variant 4 (the more expensive): 113,74 €/m^2.
4. Executing of one foundation slab under the entire structure instead of separate footings under each of the column causes 2-3 fold increase of the total price of foundation. This difference decreases with increasing number of storeys of the building.
5. In the case of the rectangular column grid it is more cost effective to base the floor system on the beams orientated in the shorter dimension.

In order to verify the reliability of the ACE software the computations using Finite Element Method were performed. The computations algorithms on: collecting loads, statics and dimensioning were adopted from the European standards.

It can be concluded that software for cost estimation, like ACE, can be very helpful in a preliminary construction designing. ACE specified safe structure thou it was a little conservative. The output of the system similar to ACE is an excellent starting point to precise FEM analyses and final design.

1.6. References

1.1. “ACE - Advanced Cost Estimator, Introduction”. http://www.arcelormittal.com/sections/fileadmin/redaction/4-Library/2-Steel_research_reports/1-Steel_structures_EC/ESE/ACE_Getting_Started_EN.pdf.
1.2. “ACE - Advanced Cost Estimator, Technical Notes.”, Version 1,8,0, November 2011.
1.3. EN 1990: 2002 + A1, “Eurocode - Basis of structural design”.
1.4. EN 1991-1-1: 2002, “Eurocode 1: Actions on structures - Part 1-1: General actions - Densities, self-weight, imposed loads for buildings”.
1.5. EN 1993-1-1: 2005, “Eurocode 3: Design of steel structures - Part 1-1: General rules and rules for buildings”.
1.6. EN 1993-1-5: 2006, “Eurocode 3: Design of steel structures - Part 1-5: Plated structural elements”.
1.7. EN 1993-1-8: 2005, “Eurocode 3: Design of steel structures - Part 1-8: Design of joints”.

1.8. ”ESE - Strategies economic construction of steel framed building in Europe”, collected work edited by J. W. Rackham, December 2010. http://www.arcelormittal.com/sections/fileadmin/redaction/4-Library/2-Steel_research_reports/1-Steel_structures_EC/ESE/ESE_Strategies_Report_EN.pdf.
1.9. Kumar S., Cheng J.C.P., “A BIM-based automated site layout planning framework for congested construction sites”, Automation in Construction 59 (2015), pp. 24-37.
1.10. Wetzel E. M., Thabet W. Y., “The use of a BIM-based framework to support safe facility management processes”, Automation in Construction 60 (2015), pp. 12-24.
1.11. PN-B-03200, “Steel structures - Static and design” (in Polish).
1.12. PN-EN 1991-1-3: 2005, “Eurocode 1: Actions on structures - Part 1-3: General actions - Snow loads” (in Polish).
1.13. PN-EN 1991-1-4: 2008, “Eurocode 1: Actions on structures - Part 1-4: General actions - Wind actions” (in Polish).

2.

On the tolerance modelling of periodic inhomogeneous media

The aim of the paper is to provide a brief description of some tolerance modelling method (homogenization) of periodic inhomogeneous media. The method is based on the so-called tolerance averaging of coefficients of partial differential equations, which coefficients are discontinuous and highly oscillating. Unlike the classical method of asymptotic homogenization, where a microstructure size parameter (basic cell diameter) is formally equated to zero, the parameter in the tolerance modelling is constant, in accordance with his physical character. The basic concept in this method is a slowly varying function, i.e. the function, which can be considered as constant within the basic cell, along with its derivatives. The tolerance averaging technique is an averaging where the slowly varying function can be excluded outside an averaging operator, with the assumption that this operation is done within a certain tolerance. In result, the averaged equations of mechanics of periodic media have effective constants - the coefficients depending also on the microstructure size parameter.

2.1. Models and modelling of material media

The object of consideration are real material media, which have already been interpreted as mathematical objects. Therefore, we will consider their abstractive models, which we define as some relational structures, [2.2].

As *the model* or *the structure* we will call system $M = \langle X, R_1, R_2, ..., R_n \rangle$ where X is an established space, called *base space*, from a certain class of sets $\mathbf{A}$; R_i , $i = 1, 2, ..., n$, are relations, meant as subsets in the sets $X_i \in \mathbf{A}$; $R_i \subset X_i$. In the models which are considered in mechanics, it is generally assumed that X is the set of real numbers.

For example, a binary relation between elements $y \in Y \subset \mathbf{A}$ will be each subset $\rho \subset Y^2$. The elements $y_1, y_2 \in Y$ are in a relation ρ when $(y_1, y_2) \in \rho \subset Y^2$.

The model example is a system $M_{LS} =< R^1, U, F_0, M >$, which can be interpreted as an elastic body model. In this model, the basic space R is a set of real numbers, U, F_0 are spaces of functions determined in $\Omega \times I, \Omega \subset R^3$, $I = (t_0, t_1) \subset R^1$, having the values in R^3, and M is a relation in $U \times F_0$.

To determine M, we will assume $F_0 = B \times P \times F \times G \times H$, where the spaces *B*, *P*, *F*, *G*, *H* are functional spaces of functions $b : \Omega \times I \to R^3$, $p : \partial_1 \Omega \times I \to R^3$, $f : \partial_2 \Omega \times I \to R^3$ and $f = u|_{\partial_2 \Omega \times I}$, $u \in U$, $g = \Omega \times \{t_0\} \to R^3$ and $g = u|_{\Omega \times \{t_0\}}$, $u \in U$, $h = \Omega \times \{t_0\} \to R^3$ and $h = \dot{u}|_{\Omega \times \{t_0\}}$, $u \in U$, respectively.

The functions from the spaces *U* are interpreted as displacements of the body, whereas the functions from the spaces *B*, *P*, *F*, *G*, *H* are respectively: *B* - body forces, *P* - surface load on a part of the boundary $\partial_1 \Omega$, *F* - applied displacements on a part of the boundary $\partial_2 \Omega$, *G* - applied initial conditions for displacements and *H* - applied initial conditions for speed of displacements. Segmentation of the boundary $\partial \Omega$ on the regions $\partial_1 \Omega$, $\partial_2 \Omega$ fulfils the conditions $\partial \Omega = \partial_1 \Omega \cup \overline{\partial_2 \Omega}$, $\partial_1 \Omega \cap \partial_2 \Omega = \varnothing$.

Moreover, let us introduce a representation $T : U \to S$, $s = T(u)$, where S is a space of symmetric tensors $s : \Omega \times I \to R^{3\times 3}$, which representation describes the constitutive relation and *s* are stresses. A function $\rho : \Omega \times I \to R^1_+$ is a mass density.

Basic relations (equations of equilibrium or equations of motions with initial-boundary conditions) will take form of an operator $M : U \to F_0$, where

$$M(u) = [divT(u) - \rho \ddot{u}, T(u)n|_{\partial_1 \Omega \times I}, u|_{\partial_2 \Omega \times I}, u|_{\Omega \times \{t_0\}}, \dot{u}|_{\Omega \times \{t_0\}}] \tag{2.1}$$

With reference to the operator (2.1), a problem is formulated in the model M_{LS} in a following form

Let f_0 be a given element F_0. Find $u_0 \in U$ such as

$$M(u_0) = f_0 \tag{2.2}$$

Each function $u_0 \in U$ satisfying Eq. (2.2) is an exact solution and the approximate solution of Eq. (2.2) is an approximate solution in the model M_{LS}.

In similar way, in Point 2.4, we will define a multicomponent Kirchhoff plate model. The solution obtained within the frame of such model will be also an exact solution. This exact solution (a plate deflection) will be an approximate solution in a three-dimensional model of elastic body if we interpret it as three-dimensional displacements of the plate, using kinematic hypotheses or a proper form of displacement constraints.

It is an individual matter whether a plate model is simpler or not if compared to another model, for example the model M_{LS} of elastic body. We will assume that a simpler model is such a model which established from another model, as a result of a procedure recognized as *simplifying*.

It will turn out that the tolerance modelling which will be described in a further part of the paper, is such simplifying procedure, thus the models obtained as a result of application of this method will be simpler models.

The tolerance modeling was introduced to mechanics by Cz. Woźniak as *the microlocal parameter method* [2.8] and *the tolerance averaging technique* [2.5, 2.9]. In this paper we will base on the tolerance averaging technique.

2.2. Selected models of mechanics

The equation (2.1), presented above, is a particular case of the equation

$$\sum_{p=0}^{P}\sum_{r=0}^{R}(-1)^{r+1}\nabla^{(r)}\cdot\frac{\partial L_p}{\partial\nabla^{(r)}w^{(p)}}=0 \qquad (2.3)$$

where $P>0, R\geq 0$, $w=w(x,t), x\in\Omega\subset R^n, t\in(t_0,t_1)$, c,ρ,k_{kl},C_{klmn}, $(\nabla^{(r)}f(x))_{i_1\ldots i_r}\equiv\partial_{i_1}\ldots\partial_{i_r}f(x)$, $i,i_1,\ldots,i_r=1,2,\ldots,n$ and $\boldsymbol{w^{(p)}(x)}\square\frac{\partial \boldsymbol{w}}{\partial \boldsymbol{t^p}}$, $p=0,1,2,\ldots$, [2.5].

Objects L_p occurring in Eq. (2.3) are functionals $L_p=L_p(x,w^{(p)},\nabla w^{(p)},\ldots,\nabla^{(r)}w^{(p)})$. These functionals contain scalar or vectorial functions $w=w(x,t)$, $x\in\Omega\subset R^n$, $t\in(t_0,t_1)$ being sought.

If we assume that $P=0$ and the functional L_0 occurring in Eq. (2.3) is the Lagrangian, then Eq. (2.3) will be the Euler-Lagrange equations for this functional. Next functionals L_1, L_2, for $P>0$, can describe such properties of physical systems like, for example, plasticity etc.

If there is defined a functional $L=\sum_{p=0}^{P}\tau^p L_p$, where $\tau>0$ is a time dimension parameter, Eq. (2.3) takes the form

$$\sum_{p=0}^{P}\sum_{r=0}^{R}(-1)^{r+1}\tau^{-p}\nabla^{(r)}\cdot\frac{\partial L}{\partial\nabla^{(r)}w^{(p)}}=0 \tag{2.4}$$

The particular case of the functional L is a linear functional

$$L\equiv P=\frac{1}{2}\sum_{p=0}^{P}\sum_{r=0}^{R}\tau^{p}K_{pr}(x)\cdot\left[(\nabla^{(r)}w^{(p)})\otimes(\nabla^{(r)}w^{(p)})\right]+fw \tag{2.5}$$

Coefficients $K_{pr}(x)$ are functions $x\in\Omega\subset R^{n}$. For this reason, Eq. (2.4), in case of the functional (2.5), are linear differential equations with various coefficients.

As an example we will consider the functionals P for heat conduction and linear elasticity of inhomogeneous media.

Taking P in form

$$P=\frac{1}{2}(\tau c\dot{\theta}^{2}+k_{ij}\theta,_{i}\theta,_{j})+f\theta \tag{2.6}$$

Eq. (2.4) will be equal

$$\left[\frac{\partial P}{\partial(\theta,_{i})}\right]_{,i}-\frac{1}{\tau}\frac{\partial P}{\partial\dot{\theta}}-\frac{\partial P}{\partial\theta}=0 \tag{2.7}$$

Putting (2.6) to Eq. (2.7) we obtain the classical Fourier equation for inhomogeneous conductors

$$c\dot{\theta}-(k_{ij}\theta,_{i})_{j})+f=0 \tag{2.8}$$

If

$$P=\frac{1}{2}(\tau^{2}\rho\ddot{w}_{k}\ddot{w}_{k}+C_{klmn}w_{k},_{l}w_{m},_{n})+f_{k}w_{k} \tag{2.9}$$

then Eq. (2.4) will be equal

$$[\frac{\partial P}{\partial(w_{k},_{l})}],_{l}-\frac{1}{\tau^{2}}\frac{\partial P}{\partial\ddot{w}_{k}}-\frac{\partial P}{\partial w_{k}}=0 \tag{2.10}$$

Putting (2.9) to Eq. (2.10) we obtain $(C_{klmn}w_{m},_{n}),_{l}+f_{k}=\rho\ddot{w}_{k}$. Coefficients c,ρ,k_{kl},C_{klmn} occurring in Eq. (2.9)-(2.10) are specific heat, mass density, components of heat conduction tensor and components of elasticity tensor, respectively. By θ we denoted temperature and by w_{k}, $k=1,2,3$, displacements of the body.

2.3. Periodically inhomogeneous media

In further parts of the paper we assume that the objects under consideration are periodic inhomogeneous objects. This is an important class of material bodies, not only for cognitive reasons but also for utilitarian ones. In case of the periodic bodies presented in Eq. (2.5), the functions K_{pr} (not necessarily all) are periodic functions. In many problems, these functions can be periodic in one, two or three independent directions determined by vectors d^c from the three-dimensional space R^3, where $c=1$ or $c=1,2$ or $c=1,2,3$ (if more than one system is available, then such a system should be chosen where *c* is of the highest value and the sum of vector lengths is the lowest).

An arbitrary function $g(\cdot)$, determined in R^3 space, is *periodic*, if for every couple of arguments x and $x+k_c d^c$ of this function, holds

$$g(x)=g(x+k_c d^c)$$

where k_c are integer numbers.

Vectors d^c define in R^{c_0} sets of a form $\{x\in R^{c_0}: x=\eta_c d^c, \eta_c \in (-\tfrac{1}{2},\tfrac{1}{2})\}$, $c_0=1,2,3$, wherein if $c_0=1$ then this set takes a form of a section with a width $\left|d^1\right|$, if $c_0=2$ then the set is a parallelogram determined by d^c, $c=1,2$, whereas in case of $c_0=3$ - a parallelepiped determined by three vectors d^c, $c=1,2,3$.

These sets are called *representative elements* or *basic cells*. An arbitrary but ascertained representative element we will denote below by Δ and the functions $g(\cdot)$ we will call as Δ-*periodic*.

As it has been pointed out, in case of periodic media, in the Eq. (2.9) - (2.10) the coefficients $c, \rho, k_{kl}, C_{klmn}$, are periodic functions which are generally discontinuous and experience jumps in small domains of determinacy. The tolerance modelling allows to average these coefficients in the way that the obtained new model equations will contain constant coefficients, thus these models will be simpler.

If the medium under consideration is periodic in *micro*-scale - and such a situation occurs when the medium is densely periodic, i.e. there is plenty of repeatable elements - then a lot of difficulties arise when equations of statics or dynamics are being solved. Such situation seriously makes difficult and often even impossible to apply analytical and computer methods. The body heterogeneity in micro-scale is being modelled in macro-scale by using the homogenization technique. After the homogenization, the description of the body is usually homogeneous.

The basic concept in the tolerance modelling is a slowly varying function with respect to the periodicity cell.

Let us denote by d a trio of positive number $d \equiv (l, d_0, d_1)$. A scalar function f determined in a domain Ω, $f : \Omega \to R$, we will call a *slowly varying* function and will denote as $f \in SV_d^1(\Omega)$, if, for every $(x, y) \in \Omega^2$, it follows from $|x_k - y_k| \le l$ that $|f(x) - f(y)| \le d_0$ and $|f,_k(x) - f,_k(y)| \le d_1$, $k = 1,2,3$. By $|\cdot|$ we denote the absolute value.

Moreover, we will assume that the basic cell Δ consists of parts (finite elements) Δ_a, $a = 1,2,...,a_0$, such as $\overline{\Delta} = \bigcup_{a=1}^{a_0} \overline{\Delta}_a$, $\Delta_a \cap \Delta_b = \varnothing$, for every $a \ne b$. By $\eta_a = \dfrac{|\Delta_a|}{|\Delta|}$ we denote saturation of the periodicity cell with the components Δ_a. We assume that every part Δ_a is homogeneous, i.e. that the mass density ρ, c, k_{kl}, and tensor components C_{klmn} are constant within these parts $\rho^a = \rho\big|_{x \in \Delta_a} = const$, $c^a = c\big|_{x \in \Delta_a} = const$, $k_{kl}^a = k_{kl}\big|_{x \in \Delta_a} = const$, $C_{klmn}^a = C_{klmn}\big|_{x \in \Delta_a} = const$.

If such $a \ne b$ exist that at least one from the inequalities: $\rho^a \ne \rho^b$, $c^a \ne c^b$, $k_{kl}^a \ne k_{kl}^b$ or $C_{klmn}^a \ne C_{klmn}^b$, $a = 1,2,...,a_0$, $k,l,m,n = 1,2,3$, is fulfilled, then we will call the body as the *multicomponent* body (composite), [2.3, 2.7].

2.4. Model of multicomponent plates

A plate is a three-dimensional body but described by displacements, strains and stresses depending only on two variables determined on some space in this body, so-called mid-surface. It means that the plate, having some thickness, can be reduced to a plane area and the displacements (deflection) or stresses being sought are determined only on this area.

Attempts of description of three-dimensional state of strain and stress of plate by functions determined on its mid-surface were made by A. Cauchy and S. Poisson in years 1828-29. The suggestions which were presented at that time contained mistakes and only in 1850 G. Kirchhoff published a paper which now is recognized as the beginning of a theory which today is called as Kirchhoff's theory or Navier-Kirchhoff's theory [2.6].

The basic assumptions of this theory are hypotheses: kinematic and static. The kinematic hypothesis can be written in the form of limitations (constraints) in class of displacements

$$\begin{aligned} u_1(x_1,x_2,x_3,t) &= -x_3 w,_1(x_1,x_2,t) \\ u_2(x_1,x_2,x_3,t) &= -x_3 w,_2(x_1,x_2,t) \\ u_3(x_1,x_2,x_3,t) &= w(x_1,x_2,t) \end{aligned} \tag{2.11}$$

The function $w(x_1,x_2,t)$ is the plate deflection.

Moreover it is assumed that the functions describing elastic properties of the plate should be different than elastic constants C_{klmn}. These new functions $B_{\alpha\beta\gamma\delta}$, $\alpha,\beta,\gamma,\delta=1,2$ now depending on two variables (determined on the mid-surface), are called stiffness moduli and they are equal

$$B_{\alpha\beta\gamma\delta} = \int_{-\frac{h}{2}}^{\frac{h}{2}} \left(C_{\alpha\beta\gamma\delta} - \frac{C_{\alpha\beta33}C_{\gamma\delta33}}{C_{3333}} \right) x_3^2 dx_3, \quad \alpha,\beta,\gamma,\delta=1,2 \tag{2.12}$$

The relation connecting the introduced concepts is the following global relation

$$\left(\forall r \in \overline{V}\right)\left[\int_{\Pi} \left(\overline{B}_{\alpha\beta\gamma\delta} w_{,\alpha\beta} r_{,\gamma\delta}\right) da = \int_{\Pi_+ \cup \Pi_-} \left(p_+ + p_-\right) r da \right] \tag{2.13}$$

where $\overline{V}$ is a space of acceptable deflections $r:\Pi \to R$ which are compatible with the constraints (2.11), p_+, p_- are loads on the upper and lower plate area.

After application of the variational formalism for Eq. (2.13), we obtain the equation of thin plate for the plate deflection

$$(B_{\alpha\beta\gamma\delta} w,_{\alpha\beta}),_{\gamma\delta} + \rho h \ddot{w} = p \tag{2.14}$$

where $p = p_+ + p_-$.

A solution of Eq. (2.14) which fulfills appropriate initial-boundary conditions, is the exact solution within the frames of classical plate model. This exact solution (plate deflection) will be an approximate solution in the three-dimensional model described in Point 2.2, if we will interpret it as three-dimensional displacements of the plate with application of the constraints (2.11).

In case when a plate is periodically inhomogeneous, the model described by Eq. (2.14) can be simplified to a form where the coefficients $B_{\alpha\beta\gamma\delta}$ will be constant, not functions.

2.5. An averaged model of periodic inhomogeneous plates

We will assume that the plate is periodically inhomogeneous and the repeatable element - the basic cell, is a section with the length l_1, $\Delta \equiv (0,l_1)$ (periodicity in one direction) or a rectangle with the dimensions l_1, l_2, $\Delta = (0,l_1)\times(0,l_2)$ (periodicity in two directions). In that case the plate mid-plane Π will be divided - in the first case into layers $\Delta\times(0,L_2)$, in the second one into rectangles.

We assume about each layer and each rectangle that they have identical material properties, i.e. if a translation of one layer onto another or one rectangle onto another is done, then a result will be the identical inhomogeneous medium.

Another assumption is that the layers and rectangles in the plate are conglomerate of various homogeneous components. The system of these components will be described in a following way:

In case of layers the section $\Delta = (0,l_1)$ is divided into parts $\Delta^a \equiv \Delta(x_1^a) = (x_1^a - \frac{l_1}{2}, x_1^a + \frac{l_1}{2})$, where $x_1^a = a\frac{l_1}{2}$, $a = 1,2,...,a_0$. Hence, a layer $\Delta\times(0,L_2)$ consists of laminas $\Delta^a\times(0,L_2)$, $a = 1,2,...,a_0$, there is a_0 laminas in the layer.

Analogically, the rectangle is divided into parts $\Delta^{ab} \equiv \Delta(x_1^a, x_2^b)$, where x_1^a is determined as above and $x_2^b = b\frac{l_2}{2}$, $b = 1,2,...,b_0$. It's easy to notice that the points x_1^a are central points of the parts Δ^a and (x_1^a, x_2^b) - central points of the parts Δ^{ab} (i.e. the points dividing the rectangle sides into halves).

With reference to the parts Δ^a of the periodicity cell we assume that they are homogeneous, what means that

$$B^a_{\alpha\beta\gamma\delta} = B_{\alpha\beta\gamma\delta}\Big|_{\Delta^a} = \text{const}, \quad \rho^a\Big|_{\Delta^a} = \text{const} \tag{2.15}$$

and analogically for Δ^{ab}

$$B^{ab}_{\alpha\beta\gamma\delta} = B_{\alpha\beta\gamma\delta}\Big|_{\Delta^{ab}} = \text{const}, \;\; \rho^{ab}\Big|_{\Delta^{ab}} = \text{const} \tag{2.16}$$

The equation of motion (2.14) of the plate is also the equation of motion for the periodically inhomogeneous plates, described here. However, according to (2.15) and (2.16), if there is *a lot* of basic cells, the coefficients occurring in Eq. (2.14) are discontinuous and have fast changing values in small domains of determinacy.

We will construct a model where the coefficients (2.15)-(2.16) will be averaged. This averaging will retain an influence of inhomogeneous structure on the solutions and the solutions will depend on dimension of the basic cell.

An essential element of tolerance modelling is a decomposition of the values being sought (here the plate deflection) into two components

$$w(x_1, x_2, t) = u(x_1, x_2, t) + h^A(x_1, x_2) v^A(x_1, x_2, t) \tag{2.17}$$

where $(x_1, x_2) \in \Pi$, $t \in \langle t_0, t_1 \rangle$, $A = 1,2,3,...,N$.

In this decomposition, the functions u and v^A are being sought (there is $1+\mathrm{N}$ of them) and are interpreted as the averaged deflection and fluctuations describing an influence of plate heterogeneity on the deflection. The functions h^A are fluctuation shape functions - known, periodic and oscillating. We assume that these functions are dimensionless and take value which is of order of the cell dimension. In case of periodicity in one direction, h^A are only functions of x_1 but for periodicity in two directions h^A are functions of x_1, x_2. Moreover, we assume that u and v^A are slowly-varying.

We define the tolerance averaging of the functions determined in Π as

$$\langle f \rangle (x_1, x_2) = \frac{1}{l_1 l_2} \int_{x_1 - \frac{l_1}{2}}^{x_1 + \frac{l_1}{2}} \Big(\int_{x_2 - \frac{l_2}{2}}^{x_2 + \frac{l_2}{2}} f(y_1, y_2) dy_1 \Big) dy_2 \tag{2.18}$$

For the plate under considerations, let us take a functional *P* in the form

$$P = \frac{\tau^2}{2} \rho (\ddot{w})^2 - \frac{1}{2} B_{\alpha\beta\gamma\delta} w,_{\alpha\beta} w,_{\gamma\delta} - pw \tag{2.19}$$

where τ is parameter.

Substitution of the decomposition (2.17) of the plate deflection to the functional (2.19) and averaging it by (2.18) yields in the model equations having form of the Euler-Lagrange equations of this averaged functional

$$\begin{aligned} &\langle\rho\rangle\ddot{u} + \langle B_{\alpha\beta\gamma\delta}\rangle u,_{\alpha\beta\gamma\delta} + E^{A}_{\alpha\beta} v,^{A}_{\alpha\beta} = p \\ &E^{A}_{\alpha\beta} u,_{\alpha\beta} + E^{AB} v^{B} = 0 \end{aligned} \tag{2.20}$$

where $\langle\rho\rangle$ and $\langle B_{\alpha\beta\gamma\delta}\rangle$ are the averaged mass density and averaged material functions

$$\langle\rho\rangle = \eta^{ab}\rho^{ab},\ \langle B_{\alpha\beta\gamma\delta}\rangle = \eta^{ab} B^{ab}_{\alpha\beta\gamma\delta} \tag{2.21}$$

and $\eta^{ab} = \eta_{1a}\eta_{2b}$, $\eta_{1a} = \dfrac{l_{1a}}{l_1}$, $\eta_{2b} = \dfrac{l_{2b}}{l_2}$.

The remaining coefficients are equal

$$\begin{aligned} &E^{A}_{\alpha\beta} \equiv \langle B_{\alpha\beta\gamma\delta} h,^{A}_{\gamma\delta}\rangle = \eta^{abA}_{\gamma\delta} B^{ab}_{\alpha\beta\gamma\delta} \\ &E^{AB} \equiv \langle B_{\alpha\beta\gamma\delta} h,^{A}_{\alpha\beta}\, h,^{B}_{\gamma\delta}\rangle = \eta^{abAB}_{\alpha\beta\gamma\delta} B^{ab}_{\alpha\beta\gamma\delta} \end{aligned} \tag{2.22}$$

where $\eta^{abAB} = \dfrac{1}{l_1 l_2}\iint\limits_{\Delta^{ab}} h^{A} h^{B} d\Delta,\ \eta^{abAB}_{\alpha\beta\gamma\delta} = \dfrac{1}{l_1 l_2}\iint\limits_{\Delta^{ab}} h,^{A}_{\alpha\beta}\, h,^{B}_{\gamma\delta}\, d\Delta$.

In case if the matrix E^{AB} will be nonsingular, then from Eq. $(2.20)_2$ we can determine fluctuations v^{A}

$$v^{A} = -(E^{AB})^{-1} E^{B}_{\alpha\beta} u,_{\alpha\beta} \tag{2.23}$$

where $(E^{AB})^{-1}$ is the inverse matrix of E^{AB}, $A, B = 1,2,,...,N$, $\alpha,\beta = 1,2$.

Substituting (2.23) to Eq. $(2.20)_1$ we obtain

$$\langle\rho\rangle\ddot{u} + E^{0}_{\alpha\beta\gamma\delta} u,_{\alpha\beta\gamma\delta} = p \tag{2.24}$$

where

$$E^{0}_{\alpha\beta\gamma\delta} = \langle B_{\alpha\beta\gamma\delta}\rangle - E^{A}_{\alpha\beta}(E^{AB})^{-1} E^{B}_{\gamma\delta} \tag{2.25}$$

The quantities defined by Eq. (2.25) are effective stiffness moduli, obtained as a result of using the tolerance averaging technique.

Eq. (2.24) has an analogical form to the well known equation of plate deflection, but with the difference that Eq. (2.24) doesn't contain the stiffness moduli $B_{\alpha\beta\gamma\delta}$ (which are functions) but effective stiffness moduli which are constant. These moduli are not postulated but calculated, provided the fluctuation shape functions are known.

Eq. (2.22) describes dynamics of periodically inhomogeneous plates. In case of isotropic body the stiffness moduli (2.12) take the form

$$B^{ab}_{\alpha\beta\gamma\delta} = \frac{h^3}{12}\left(\lambda^{ab}\delta_{\alpha\beta}\delta_{\gamma\delta} + \mu^{ab}(\delta_{\alpha\delta}\delta_{\beta\gamma} + \delta_{\alpha\gamma}\delta_{\beta\delta}) - \frac{(\lambda^{ab})^2\delta_{\alpha\beta}\delta_{\gamma\delta}}{\lambda^{ab} + 2\mu^{ab}} \right).$$

In case of isotropic and homogeneous plate, the values occurring in (2.24) have a form $u = w$ and $E^0_{\alpha\beta\gamma\delta} = E_{\alpha\beta\gamma\delta}$ as well as are explained by means of the well known stiffness $D = \dfrac{Eh^3}{12(1-\nu^2)} = \dfrac{h^3(\lambda+\mu)\mu}{3(\lambda+2\mu)}$ where $E_{1111} = E_{2222} = D$ and $E_{1122} + E_{1212} + E_{2121} + E_{2211} + E_{1221} + E_{2112} = 2D$. Eq. (2.24) will get the classical form

$$\rho_0\ddot{w} + Dw,_{1111} + 2Dw,_{1122} + Dw,_{2222} = p\,.$$

2.6. Free vibrations of uniperiodic inhomogeneous plates

Let us consider a uniperiodic plate, simply supported on all edges.

Boundary conditions are assumed in the form

– $u = 0$ and $\dfrac{\partial^2 u}{\partial x_1{}^2} = 0$ at $x_1 = 0$ and $x_1 = L_1$

– $u = 0$ and $\dfrac{\partial^2 u}{\partial x_2{}^2} = 0$ at $x_2 = 0$ and $x_2 = L_2$

whereas initial conditions will be analogical as in [2.4];

$$- \quad \begin{aligned} & u(x_1, x_2, 0) = u_0(x_1, x_2) = c_0(1 - \cos\frac{2\pi}{L_1}x_1)(1 - \cos\frac{2\pi}{L_2}x_2) \\ & \dot{u}(x_1, x_2, t)\big|_{t=0} = v_0(x_1, x_2) = 0 \end{aligned}$$

where c_0 denotes an initial, sufficiently small deflection in a central point of the plate and v_0 is the velocity of displacement of the plate mid-surface in the time instant $t = 0$.

In this case, equation of motion (2.24) of the plate has the form

$$\ddot{u} + \frac{E^0_{1111}}{\rho^0}u,_{1111} + \frac{E^0}{\rho^0}u,_{1122} + \frac{E^0_{2222}}{\rho^0}u,_{2222} = 0 \tag{2.26}$$

The equation of a deformed plane of the plate - the eigenfunctions of the presented boundary problem - are assumed in the form

$$U_{mn}(x_1, x_2) = \sin\left(\frac{m\pi}{L_1}x_1\right)\sin\left(\frac{n\pi}{L_2}x_2\right) \tag{2.27}$$

where $m = 1,2,..,\ \ n = 1,2,..$.

The eigenvalue will be equal

$$\omega_{mn}^2 = \frac{1}{\rho^0}(E_{1111}^0\left(\frac{m\pi}{L_1}\right)^4 + E^0\left(\frac{m\pi}{L_1}\right)^2\left(\frac{n\pi}{L_2}\right)^2 + E_{2222}^0\left(\frac{n\pi}{L_2}\right)^4) \tag{2.28}$$

A solution of Eq. (2.26) has the form $w(x_1, x_2, t) = w_0(x_1, x_2, t) + w_1(x_1, x_2, t)$ where w_0 is the solution given by Kaliski in [2.4], for homogeneous plates

$$w_0(x_1, x_2, t) = -\frac{64\bar{c}_0}{\pi^2}\sum_{n=1}^{\infty}\sum_{m=1}^{\infty}\frac{\cos(\omega_{mn}t)\cdot\sin\left(\frac{m\pi}{L_1}x_1\right)\sin\left(\frac{n\pi}{L_2}x_2\right)}{mn(4-m^2)(4-n^2)}$$

where $m = 2k-1$, $n = 2j-1$, $k = 1,2,3,...$, $j = 1,2,3,...$ whereas w_1 is the solution obtained by Jeleniewicz in [2.3], describing the effect of periodic heterogeneity

$$w_1(x_1, x_2, t) = -w_0(x_1, x_2, t)\left(\frac{E_{11}^1}{E^{11}}\cdot\left(\frac{m\pi}{L_1}\right)^2 + \frac{E_{22}^1}{E^{11}}\left(\frac{n\pi}{L_2}\right)^2\right)h^1(x_1)$$

The fluctuation shape function $h^1(x_1)$ is assumed in this example in the form

$$h^1(x_1) = \begin{cases} c_1x_1(2x_1 - l), & x_1 \in \left(0, \frac{l}{2}\right) \\ -c_1(2x_1 - l)(x_1 - l), & x_1 \in \left(\frac{l}{2}, l\right) \end{cases}$$

where a constant c_1 is the order of l^2.

To show the solution in a graphical form, following plate parameters had been assumed: side lengths $L_1 = L_2 = 5\,m$, thickness $h = 0{,}2$ m, periodicity cell length $l_1 = l_2 = 0.3\,m$, material constants: $E_1 = 27 \cdot 10^9\,Pa$, $\nu_1 = 0.2$, $\rho_1 = 2200 \dfrac{kg}{m^3}$, $E_2 = 190 \cdot 10^9\,Pa$, $\rho_2 = 7900 \dfrac{kg}{m^3}$.

The plate is reinforced and its saturation with reinforcing rods is described by the function ν, $\nu_1 = 0.2$.

The dependence between the plate deflection, frequency of free vibrations and saturation of the basic cell with rods were analyzed. The basic cell dimension was assumed as $l = 0.05$ m and the saturation function - 0.9, 0.7 and 0.5. The dimensions and material constants of the matrix and rods remain unchanging.

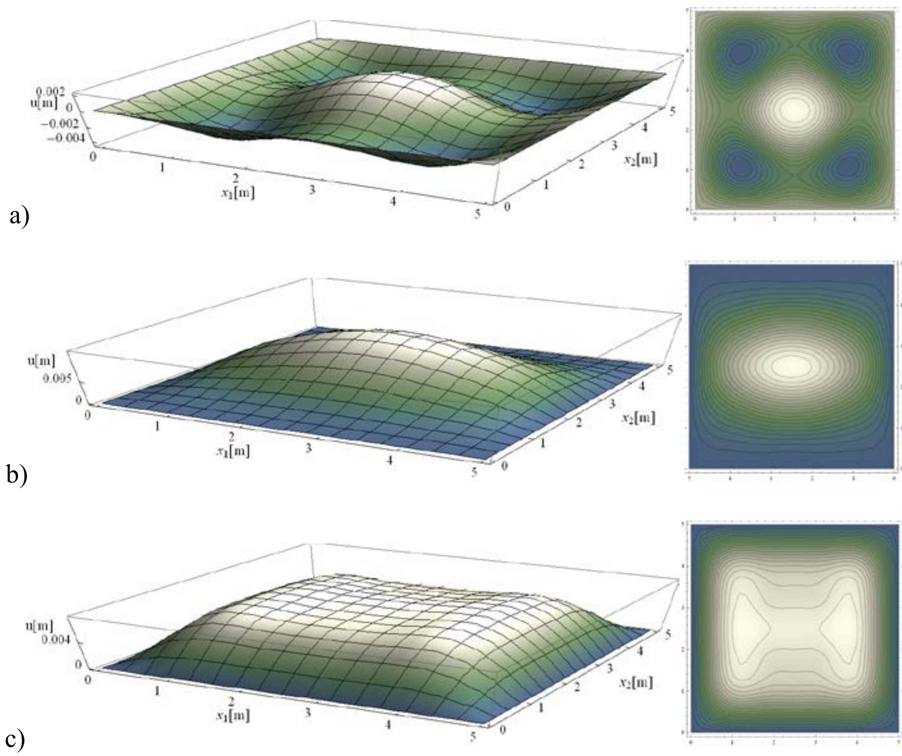

Fig. 2.1. The averaged plate deflection at time $t = 1.5$ s
for saturation a) 0.9, b) 0.7, c) 0.5

The figures 2.1 show the averaged plate defection for every case of saturation at the same time $t = 1.5$ s. The graphs were made as spatial figures and contour line figures. The contour line figures are characterized by various intensity of colour depending on position relative to the vertical axis.

The figure 2.2 shows the cross-section of the plate deflection w for three cases of saturation with rods for the same time.

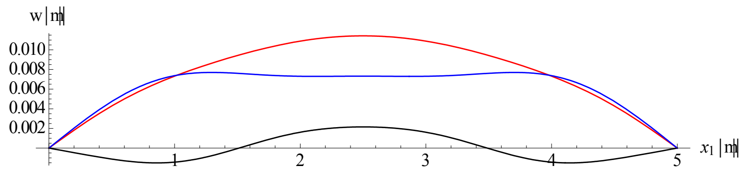

Fig. 2.2. Plate deflection - cross-section for x_2=L_2/2 at the time $t=1.5$ s for saturation 0.9 - black line, 0.7 - red line, 0.5 - blue line

Fig. 2.3 presents the deflection of the plate centre at the time 0.1 s. The graph was made for every values of saturation (0.9 - green line, 0.7 - red line, 0.5 - blue line) with the assumption of a certain free vibration frequency ω_{11}. As it results from the graph, reduction of the saturation causes reduction of the free vibration frequency. The vibration amplitude is the same in every cases.

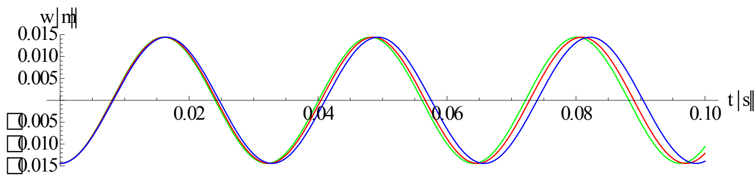

Fig. 2.3. The plate displacement in the point with coordinates $(L_1/2;\ L_2/2)$

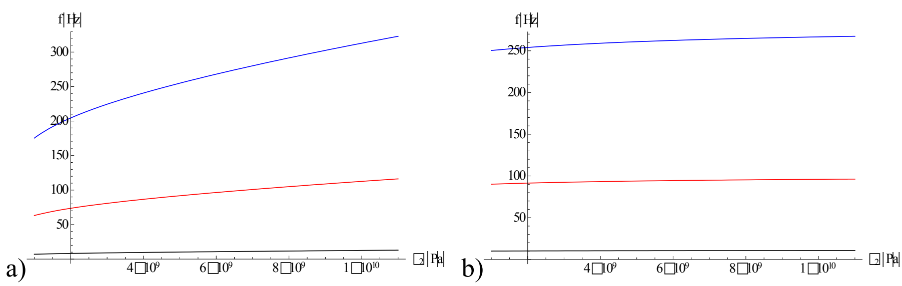

c)

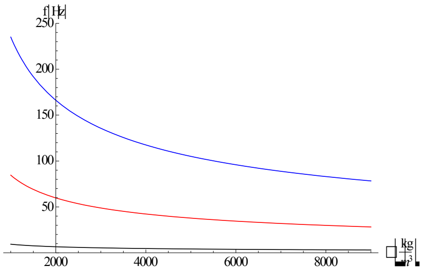

Fig. 2.4. The dependence between free vibrations frequency of the plate and Lamé constants (a, b) and mass density (c)

Fig. 2.4 shows a dependence between free vibration frequency of the plate and the Lamé constants as well as plate mass density. The graphs were made for three values of frequency: f_{11} - black line, f_{33} - red line , f_{55} - blue line. Basing on Fig. 2.4a we can conclude that along with increase of μ_2 (for the reinforcement) the free vibration frequency of the plate under consideration also increases. Moreover, we can notice that the higher frequency number is being considered, the stronger is the monotonicity of this dependence. The increase of value of λ_2 has a negligible effect on the increase of vibration frequency. The larger is the mass density, the lower is vibration frequency. In this case, we can also notice that the higher number of the frequency is being considered the stronger is the monotonicity of the dependence.

2.7. Summary

The methods of tolerance averaging, presented in this paper, concern the micro-periodic inhomogeneous media.

The tolerance averaging technique bases on the observation that the description of a material medium and properties of this medium is achieved by means of numbers obtained from an experiment, hence is not explicit. It depends on some „small" parameter $\varepsilon \geq 0$ which defines the precision of measurements and calculations. According to the tolerance technique, if $s_1 \in R$ is the result of measurement of a certain quantity $s \in R$, then we consider that this solution can be identified with s with a certain precision ε if $|s - s_1| \leq \varepsilon$. Every other number $s_2 \in R$ which satisfies the inequality $|s - s_2| \leq \varepsilon$ can be identified with the quantity s with the same precision. If a quantity being analyzed was equal 0, then all numbers from the set $\langle -\varepsilon, \varepsilon \rangle$ could be identified with this zero value with the precision ε.

The idea presented here was expressed in 1992 by Fichera, [2.1], in the following way: *in Physics the statement „the quantity s is equal to zero" has a different meaning than in Mathematics, since it expresses only the fact that* $|s| < \varepsilon$*, where the positive number* ε *must be regarded as a physical constant which should be determined before formulating any mathematical model of the physical phenomenon under consideration*.

The described methods of tolerance averaging can be generalized on account of functionally graded materials (FGM) if variability of functions, describing physical properties of the body, can be admitted for several neighboring representative elements as periodic with an established tolerance.

As a result of application of the tolerance modeling we can obtain both non-asymptotic models and asymptotic ones, i.e. such that the periodicity cell size is equated to zero. The asymptotic tolerance models contain microstructure parameters which occur in effective constants. These constants can be determined from appropriate equations.

The tolerance averaging techniques are convenient way of modelling of inhomogeneous media, alternative to classical methods of homogenization.

2.8. References

2.1 Fichera G., Is the Fourier theory of heat propagation paradoxical?, Rendiconti del Circolo Matematico di Palermo, 1992.

2.2 Grzegorczyk A., Zarys logiki matematycznej, PWN, Warszawa 1975.

2.3 Jeleniewicz K., Drgania konstrukcji sprężystych wzmocnionych prętami, SGGW, Warszawa 2014.

2.4 Kaliski S., Drgania i fale w ciałach stałych, PWN, Warszawa 1966.

2.5 Mathematical modelling and analysis in continuum mechanics of microstructured media, ed. Woźniak Cz. et al., Wyd. Politechniki Śląskiej, Gliwice 2013.

2.6 Mechanika sprężystych płyt i powłok, ed. Woźniak. Cz., PWN, Warszawa 2001.

2.7 Nagórko W., Wybrane metody modelowania płyt sprężystych, Wyd. SGGW, Warszawa 2008.

2.8 Woźniak Cz., Microlocal parameters in modelling of composites with internal constrains, Bull. Pol. Ac.: Techn., 35, 1987, pp. 7-8.

2.9 Woźniak Cz., A nonstandard method of modelling of thermoelastic periodic composites, Int. J. Engng Sci., 25, 1987, pp. 489-498.

3.

Tolerance modelling of medium thickness functionally graded plates

Various averaging approaches based on the known Hencky-Bolle-type plate assumptions are proposed in many papers to model medium thickness functionally graded plates with a microstructure. It can be shown that the effect of the microstructure size plays a crucial role in different thermomechanical problems of similar plates, cf. [3.2, 3.5, 3.7, 3.29, 3.68÷3.70]. However, governing equations of most of averaged models neglect the effect of the microstructure size on the overall behaviour of these plates. This lack of these models is supplemented in the tolerance model, which is based on the tolerance modelling approach, cf. [3.64, 3.65, 3.66].

3.1. Introduction

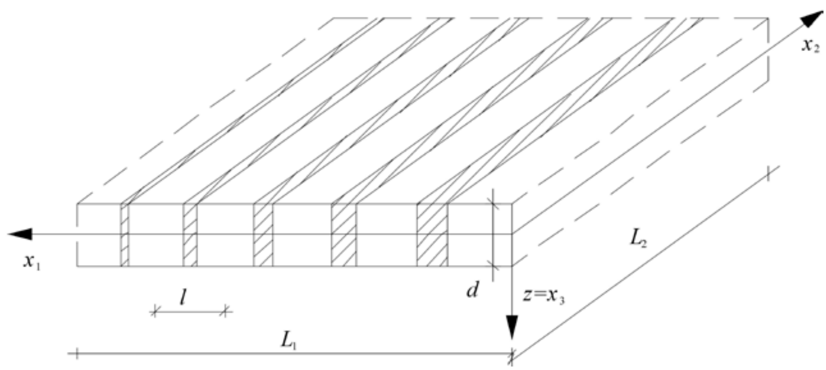

Fig. 3.1. A fragment of a functionally graded plate with a microstructure, cf. [3.23]

In this chapter vibrations of medium thickness functionally graded plates with a microstructure are considered. It is assumed that the plate has tolerance-periodic structure on the microlevel along only one direction parallel to the x_1-axis, but on the macrolevel it has functionally graded properties along this direction, cf. [3.21÷3.24, 3.57]. Material properties of the plate are assumed to be constant along the x_2-axis. In plates of this kind a “basic cell” can be distinguished, with a span l. The length l is assumed to be of an order plate thickness d, $d \sim l$. A fragment of the plate is shown in Fig. 3.1.

Composites and structures with functionally graded properties are usually described using the known methods, which are applied for periodic media. Some of them are shown in [3.57]. Similar approaches can be used for functionally graded plates with microstructure. Models based on the asymptotic homogenization method, cf. [3.4], are very interesting and useful, cf. [3.33]. Other modelling approaches for various periodically microstructured media are also proposed and applied in a series of papers, e.g. a homogenization based on microlocal parameters is used to model periodic plates by Matysiak and Nagórko [3.38] or to analyse temperature distributions in a periodically stratified layer by Matysiak and Perkowski [3.39]; natural frequencies of thick square plates made of orthotropic and hexagonal materials are considered by Batra et al. [3.3]; stability of multi-cell thin-walled columns is analysed by Królak et al. [3.34]; dynamic stability and buckling of beams or plates with metal foam core with variable mechanical properties are considered by Magnucka-Blandzi [3.36], Jasion et al. [3.16], Grygorowicz et al. [3.15].

In a series of papers there are shown many theoretical and numerical results of various problems of functionally graded structures. The modified Donnell type dynamic stability and compatibility equations are used to analyse stability of functionally graded cylindrical shells by Sofiyev and Schnack [3.56], where solutions are obtained by Galerkin's method. Natural frequencies are investigated applying some meshless methods in a few of papers, e.g. for functionally graded plates by Ferreira et al. [3.14], for sandwich beams with functionally graded core by Bui et al. [3.6]. A collocation method with higher-order plate theories is used to analyse vibrations of FG-type plates by Roque et al. [3.53]. A GDQ solution for free vibrations of shells is presented by Tornabene et al. [3.61]. Higher order deformation theories are used to analyse thermomechanical problems for plates, which are functionally graded along their thickness by Akbarzadeha et al. [3.1] and also for functionally graded plates and shells by Oktem et al. [3.47]. Tornabene and Viola [3.60] consider a static behaviour of functionally graded shells. Modal analysis of functionally graded beams with effect of the shear correction function is shown by Murin et al. [3.45]. A new low-order shell element is used to investigate shell-like structures with functionally graded material properties by Kugler et al. [3.35]. In the paper of Jha et al. [3.31] there are analysed free vibrations of functionally graded thick plates with shear and normal deformations effects. Higher-order shear and normal deformable plate theory is applied by Sheikholeslami and Saidi [3.55] to consider vibrations of functionally graded rectangular plates. A numerical analysis of heat transfer in polycrystalline composites, containing metallic or elastic interfaces is shown by Sadowski and Golewski [3.54]. A problem of single-pulse chaos for a functionally graded materials rectangular plate is considered by Yu-Gao Huangfu and Fang-Qi Chen [3.67]. Non-linear analysis of functionally graded plates based on a certain shear deformation theory is presented by Derras et al. [3.10]. Laminated plates are investigated by Fantuzzi et al. [3.13], where a strong formulation finite element method based on GDQ technique is shown.

It is necessary to observe that governing equations of these models neglect usually the effect of the microstructure size, cf. [3.5]. In order to analyse this problem it can be applied the tolerance averaging method, cf. [3.21, 3.64, 3.65, 3.66], which makes it possible to take into account this effect on the overall behaviour of microstructured media. Various problems of dynamics and stability for periodic structures and thermoelastic problems for periodic composites were analysed using this method in a series of papers, e.g. for thin periodic plates by Jędrysiak and Woźniak [3.29], Jędrysiak [3.17÷3.20]; for periodic fluid-saturated grounds by Dell'Isola et al. [3.9]; for plane periodic structures by Wierzbicki and Woźniak [3.62]; for periodic wavy-type plates by Michalak [3.42]; for thin plates reinforced periodically by a system of stiffeners by Nagórko and Woźniak [3.46]; for periodic medium-thickness plates by Baron [3.2]; for periodic thin plates with the microstructure size of an order of the plate thickness by Mazur-Śniady et al. [3.41]; for multiperiodic fibre reinforced composites by Jędrysiak and Woźniak [3.30]; for honeycomb lattice-type plates by Cielecka and Jędrysiak [3.8]; for periodic shells by Tomczyk [3.58, 3.59]; for microperiodic composite rods with uncertain parameters by Mazur-Śniady et al. [3.40]; for medium thickness plates resting on a periodic Winkler's foundation by Jędrysiak and Paś [3.27]; for thin periodic plates with large deflections by Domagalski and Jędrysiak [3.11]; for vibrations of geometrically nonlinear slender periodic beams by Domagalski and Jędrysiak [3.12]; for dynamics of periodic three-layered plates by Marczak and Jędrysiak [3.37].

The tolerance modelling can be successfully used to consider various thermomechanical problems of functionally graded structures, e.g. for stability of transversally and longitudinally graded plates by Jędrysiak and Michalak [3.26]; for heat transfer in transversally graded laminates by Jędrysiak and Radzikowska [3.28]; for dynamics of plates with longitudinally graded structure by Michalak and Wirowski [3.44], Wirowski [3.63], Perliński et al. [3.51]; for vibrations of transversally graded thin plates with the plate thickness small in compare to the microstructure size by Jędrysiak [3.21], Kaźmierczak and Jędrysiak [3.32], Jędrysiak and Kaźmierczak-Sobińska [3.25]; for dynamics of thin plates having the microstructure size of an order of the plate thickness by Jędrysiak [3.22-3.24]; for dynamic problems of a thin-walled structure with dense system of ribs by Michalak [3.43]; for non-stationary heat transfer in a hollow cylinder with functionally graded material properties by Rabenda [3.52]; for heat conduction in cylindrical composite conductors with non-uniform microstructure by Ostrowski and Michalak [3.48, 3.49]; for thermoelastic problems in transversally graded laminates by Pazera and Jędrysiak [3.50]. A lot of examples of applications of the tolerance method to analyse these composites and structures can be found in the books [3.21, 3.64, 3.65].

In this chapter there are derived the tolerance model equations of the medium thickness microstructured functionally graded plates with the microstructure size of an order of the plate thickness, which describe the effect of the microstructure size. Moreover, these equations and equations of the asymptotic model are applied to analyse vibrations for a simply supported microstructured plate band. Formulas of vibration amplitudes and resonance frequencies are obtained by using the Ritz method.

3.2. Modelling foundations

3.2.1. Preliminaries

A plate is considered in the orthogonal Cartesian coordinate system $Ox_1x_2x_3$. Let t be the time coordinate and subscripts i,k,l run over 1,2,3, but α,β,γ run over 1,2. Introduce $\mathbf{x}\equiv(x_1,x_2)$, $x\equiv x_1$, $z\equiv x_3$ and denote the region of the undeformed plate by $\Omega \equiv \{(\mathbf{x},z): -d/2 \le z \le d/2, \mathbf{x}\in\Pi\}$, where Π is the plate midplane and $d(\cdot)$ is the plate thickness, which can be a tolerance-periodic function in x. Derivatives of x_α are denoted by ∂_α and also $\partial_{\alpha\ldots\delta}\equiv\partial_\alpha\ldots\partial_\delta$. Let $\Delta\equiv[-l/2,l/2]\times\{0\}$ be the "basic cell" on Ox_1x_2, where l is its length dimension along the x_1-axis, which satisfies conditions $d\sim l$ and $l<<L_1$. Hence, it is called *the microstructure parameter*. Introduce also an interval $\Lambda\equiv[0,L_1]$. All material and inertial properties of the plate, as mass density $\rho=\rho(\cdot,x_2,z)$ and elastic moduli $a_{ijkl}=a_{ijkl}(\cdot,x_2,z)$, are assumed to be also tolerance-periodic functions in x, even functions in z and independent (constant) of x_2. Denote $c_{\alpha\beta\gamma\delta}\equiv a_{\alpha\beta\gamma\delta}-a_{\alpha\beta33}a_{\gamma\delta33}(a_{3333})^{-1}$, $c_{\alpha3\gamma3}\equiv a_{\alpha3\gamma3}-a_{\alpha333}a_{33\gamma3}(a_{3333})^{-1}$, where $a_{\alpha\beta\gamma\delta}$, $a_{\alpha\beta33}$, $a_{\alpha3\gamma3}$, a_{3333} are the non-zero components of the elastic moduli tensor. Denote also plate displacements by u_i (i=1,2,3) and total loadings in the z-axis direction by p.

3.2.2. Governing equations

The medium thickness plates under consideration have properties described by tolerance-periodic functions of x - a mass density per unit area μ, a rotational inertia ϑ and stiffnesses $b_{\alpha\beta\gamma\delta}$, $d_{\alpha\beta}$, defined by the following formulas

$$\begin{aligned}
&\mu(x) \equiv \int_{-d/2}^{d/2} \rho(x,z)dz, &&\vartheta(x) \equiv \int_{-d/2}^{d/2} \rho(x,z)z^2 dz,\\
&b_{\alpha\beta\gamma\delta}(x) \equiv \int_{-d/2}^{d/2} c_{\alpha\beta\gamma\delta}(x,z)z^2 dz, &&d_{\alpha\beta}(x) \equiv \tfrac{5}{6}\int_{-d/2}^{d/2} c_{\alpha 3\beta 3}(x,z)dz.
\end{aligned} \tag{3.1}$$

Using the kinematic assumptions of the Hencky-Bolle-type plate theory, the following action functional can be written

$$\mathsf{A}(u_i(\cdot), p(\cdot)) = \int_{\Pi}\int_{t_0}^{t_1} \mathsf{L}(\boldsymbol{y}, \nabla u_i(\boldsymbol{y},t), \dot{u}_i(\boldsymbol{y},t), u_i(\boldsymbol{y},t), p(\boldsymbol{y},t))dtd\boldsymbol{y}, \tag{3.2}$$

with Lagrangean $\mathcal{L}$ defined by the formula

$$\begin{aligned}
\mathcal{L} = &\tfrac{1}{2}(\mu\dot{w}\dot{w} + \vartheta\dot{\phi}_\alpha\dot{\phi}_\beta\delta_{\alpha\beta}) -\\
&-\tfrac{1}{2}(b_{\alpha\beta\gamma\delta}\partial_\alpha\phi_\beta\partial_\gamma\phi_\delta + d_{\alpha\beta}\partial_\alpha w\partial_\beta w + 2d_{\alpha\beta}\partial_\alpha w\phi_\beta + d_{\alpha\beta}\phi_\alpha\phi_\beta) + pw.
\end{aligned} \tag{3.3}$$

where: $w=u_3(\mathbf{x},t)$ is a plate deflection; $\phi_\alpha(\mathbf{x},t)$, $\alpha=1,2$, are plate rotations. It is assumed that $\mathcal{L}$ is tolerance-periodic, highly oscillating function of x. Using the principle of stationary action to functional $\mathcal{A}$, (3.2), and Lagrangean $\mathcal{L}$, (3.3), we arrive at the known system of partial differential equations for deflection $w(\mathbf{x},t)$ and rotations $\phi_\alpha(\mathbf{x},t)$ of the medium thickness plate:

$$\begin{aligned}
&\partial_\beta(b_{\alpha\beta\gamma\delta}\partial_\delta\phi_\gamma) - d_{\alpha\beta}(\partial_\beta w + \phi_\beta) - \vartheta\ddot{\phi}_\alpha = 0,\\
&\partial_\alpha[d_{\alpha\beta}(\partial_\beta w + \phi_\beta)] - \mu\ddot{w} = -p.
\end{aligned} \tag{3.4}$$

The above equations describe vibrations of medium thickness functionally graded plates with microstructure. Equations (3.4) have highly oscillating, non-continuous functional coefficients. Hence, an application of these equations to special problems is rather difficult and it is necessary to propose an averaged approach of them or Lagrangean $\mathcal{L}$, (3.3).

3.3. Tolerance modelling

3.3.1. Basic concepts

Basic concepts of the tolerance modelling method, which is used here, were defined in the books [3.21, 3.64÷3.66] and also in a series of papers, e.g. for transversally graded plates in [3.23÷3.24]. Here, these concepts can be only mentioned: the tolerance system, the tolerance-periodic function f, $f \in TP_\delta^r(\Lambda,\Delta)$, the slowly-varying function F, $F \in SV_\delta^r(\Lambda,\Delta)$, the highly oscillating function ϕ, $\phi \in HO_\delta^r(\Lambda,\Delta)$, the fluctuation shape function g,

$g \in FS_\delta^r(\Lambda,\Delta)$, where δ is a tolerance parameter, 0<δ<<1, *r* is a kind of the function, *r*>0.

Introducing a cell $\Delta(x) \equiv x + \Delta$ at $x \in \Lambda_\Delta$, $\Lambda_\Delta = \{x \in \Lambda : \ \Delta(x) \subset \Lambda\}$, the *averaging operator* for an integrable function *f* can be defined by

$$< f > (x, x_2) = \frac{1}{l} \int_{\Delta(x)} f(y, x_2) dy, \quad x \in \Lambda_\Delta. \tag{3.5}$$

The averaged value of a tolerance-periodic function *f*, calculated from (3.5), is a slowly-varying function in *x*.

3.3.2. Fundamental modelling assumptions

Using the introductory concepts two fundamental assumptions of the tolerance modelling can be formulated, cf. [3.64÷3.66] and for thin functionally graded plates in [3.23÷3.24].

The first assumption is *the micro-macro decomposition*, which lets to decompose medium thickness plate displacements in the form

$$\begin{aligned} u_3(\mathbf{x}, z, t) &= w(\mathbf{x}, t), \\ u_\alpha(\mathbf{x}, z, t) &= z[\varphi_\alpha(\mathbf{x}, t) + g(x)\theta_\alpha(\mathbf{x}, t)], \end{aligned} \tag{3.6}$$

where: new unknowns - *macrodeflection w*, *macrorotations* φ_α (α=1,2), and *fluctuation variables* θ_α (α=1,2), are slowly-varying functions in *x* ($w(\cdot,x_2,t), \varphi_\alpha(\cdot,x_2,t), \theta_\alpha(\cdot,x_2,t) \in SV_\delta^1(\Lambda,\Delta)$); the known fluctuation shape function *g*, $g(\cdot) \in FS_\delta^1(\Lambda,\Delta), g \in O(l)$, has the form of a saw-type function of *x*. Similar assumptions were introduced for periodic plates - thin, cf. [3.41], and medium thickness, cf. [3.2].

The next fundamental assumption is *the tolerance averaging approximation*, such that terms of an order of tolerance parameter δ are negligibly small in the modelling procedure, e.g. for functions $f \in TP_\delta^1(\Lambda,\Delta)$, $h \in FS_\delta^1(\Lambda,\Delta)$, $F \in SV_\delta^1(\Lambda,\Delta)$, in formulas: $< f > (x) = < \bar{f} > (x) + O(\delta)$, $< fF > (x) = < f > (x) F(x) + O(\delta)$, $< f\partial(hF) > (x) = < f\partial h > (x) F(x) + O(\delta)$, and they can be neglected.

3.3.3. Modelling procedure

The tolerance modelling procedure of thin functionally graded plates, having thickness *d*, which is small in comparing to the span of cell *l*, cf. [3.21, 3.32], can be easily adopted to consider plates with the span l being of an order of the plate thickness, cf. [3.22÷3.24].

In the first step Lagrangean $\mathcal{L}$ in the form (3.3) is formulated. The second step is the substitution of the micro-macro decomposition (3.6) into formula (3.3). In the next step the averaging operator (3.5) is used to the resulting equation. Applying in the fourth step the tolerance averaging approximation the tolerance averaged lagrangean $<\mathcal{L}_g>$ is derived in the following form

$$\begin{aligned} <\mathcal{L}_g> = {} & \tfrac{1}{2}(<\mu>\dot{w}\dot{w} + <\vartheta>\dot{\varphi}_\alpha\dot{\varphi}_\beta\delta_{\alpha\beta} + \underline{<\vartheta gg>\dot{\theta}_\alpha\dot{\theta}_\beta\delta_{\alpha\beta}}) - \\ & -\tfrac{1}{2}(<b_{\alpha\beta\gamma\delta}>\partial_\alpha\varphi_\beta\partial_\gamma\varphi_\delta + 2<b_{\alpha\beta 1\delta}\partial_1 g>\partial_\alpha\varphi_\beta\theta_\delta + \\ & + <b_{1\beta 1\delta}\partial_1 g\partial_1 g>\theta_\beta\theta_\delta + \underline{<b_{2\beta 2\delta}gg>\partial_2\theta_\beta\partial_2\theta_\delta}) - \\ & -\tfrac{1}{2}(<d_{\alpha\beta}>\partial_\alpha w\partial_\beta w + 2<d_{\alpha\beta}>\partial_\alpha w\varphi_\beta + \\ & + <d_{\alpha\beta}>\varphi_\alpha\varphi_\beta + \underline{<d_{\alpha\beta}gg>\theta_\alpha\theta_\beta}) + <p>w. \end{aligned} \tag{3.7}$$

From the principle of stationary action used to formula (3.7) the Euler-Lagrange equations for unknown functions $w(\cdot,x_2,t), \varphi_\alpha(\cdot,x_2,t), \theta_\alpha(\cdot,x_2,t)$ can be derived

$$\begin{aligned} &-\frac{\partial}{\partial t}\frac{\partial<\mathcal{L}_g>}{\partial\dot{w}} - \partial_\alpha\frac{\partial<\mathcal{L}_g>}{\partial\,\partial_\alpha w} + \frac{\partial<\mathcal{L}_g>}{\partial w} = 0, \\ &-\frac{\partial}{\partial t}\frac{\partial<\mathcal{L}_g>}{\partial\dot{\varphi}_\alpha} - \partial_\alpha\frac{\partial<\mathcal{L}_g>}{\partial\,\partial_\alpha\varphi_\beta} + \frac{\partial<\mathcal{L}_g>}{\partial\varphi_\alpha} = 0, \\ &-\frac{\partial}{\partial t}\frac{\partial<\mathcal{L}_g>}{\partial\dot{\theta}_\alpha} - \partial_2\frac{\partial<\mathcal{L}_g>}{\partial\,\partial_2\theta_\alpha} + \frac{\partial<\mathcal{L}_g>}{\partial\theta_\alpha} = 0. \end{aligned} \tag{3.8}$$

3.4. Governing equations

Substituting Lagrangean (3.7) into equations (3.8), after some manipulations governing equations for functions $w(\cdot,x_2,t), \varphi_\alpha(\cdot,x_2,t), \theta_\alpha(\cdot,x_2,t)$, α=1,2, are obtained

$$\begin{aligned} &\partial_\beta(<b_{\alpha\beta\gamma\delta}>\partial_\delta\varphi_\gamma) + \partial_\beta(<b_{\alpha\beta\gamma 1}\partial_1 g>\theta_\gamma) - <d_{\alpha\beta}>(\partial_\beta w + \varphi_\beta) - <\vartheta>\ddot{\varphi}_\alpha = 0, \\ &\partial_\alpha(<d_{\alpha\beta}>(\partial_\beta w + \varphi_\beta)) - <\mu>\ddot{w} = -p, \\ &-<b_{\alpha 1\gamma\delta}\partial_1 g>\partial_\delta\varphi_\gamma - \\ &-(<b_{\alpha 1\beta 1}\partial_1 g\partial_1 g> + \underline{\underline{<d_{\alpha\beta}gg>}})\theta_\beta + \underline{\underline{<b_{\alpha 2\gamma 2}gg>}}\partial_{22}\theta_\gamma - \underline{<\vartheta gg>}\ddot{\theta}_\alpha = 0, \end{aligned} \tag{3.9}$$

which are a system of partial differential equations. Equations (3.9) with micro-macro decomposition (3.6) stand *the tolerance model of medium thickness functionally graded plates with a microstructure*. Underlined terms of equations (3.9) depend on the microstructure parameter l. Hence, the tolerance model takes into account the effect of the microstructure size. Coefficients of (3.9) are slowly-varying functions in x. The basic unknowns - w, φ_α, θ_α, are slowly-varying functions in x. Boundary conditions should be formulated for macrodeflection w and macrorotations φ_α on all edges, but for fluctuation variables θ_α only for x_2=const.

In order to compare and evaluate obtained results an approximate model, which governing equations neglect the effect of the microstructure size, is introduced. The equations of this model can be derived from equations (3.9) after vanishing underlined terms and can be written as

$$\begin{aligned}
&\partial_\beta(<b_{\alpha\beta\gamma\delta}>\partial_\delta\varphi_\gamma)+\partial_\beta(<b_{\alpha\beta\gamma1}\partial_1 g>\theta_\gamma)-<d_{\alpha\beta}>(\partial_\beta w+\varphi_\beta)-<\vartheta>\ddot{\varphi}_\alpha=0,\\
&\partial_\alpha(<d_{\alpha\beta}>(\partial_\beta w+\varphi_\beta))-<\mu>\ddot{w}=-p, \qquad (3.10)\\
&-<b_{\alpha1\gamma\delta}\partial_1 g>\partial_\delta\varphi_\gamma-<b_{\alpha1\beta1}\partial_1 g\partial_1 g>\theta_\beta=0.
\end{aligned}$$

The above equations stand *the asymptotic model of medium thickness functionally graded plates with a microstructure*. On the contrary to equations (3.9) they do not describe the effect of the microstructure size on vibrations. Equations (3.10) have also slowly-varying coefficients.

3.5. Example - vibrations of medium thickness functionally graded plate band

3.5.1. Preliminaries

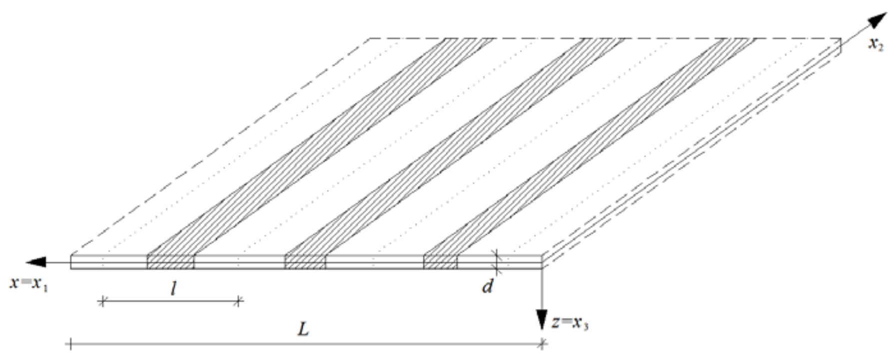

Fig. 3.2. A fragment of a functionally graded plate band

Let us consider vibrations of a simply supported plate band, with a span $L \equiv L_1$, cf. Figure 3.2. It is assumed that the plate band is made of two elastic isotropic materials, with Young's moduli E', E'', Poisson's ratios ν', ν'' and mass densities ρ', ρ''. Both materials are perfectly bonded across interfaces. It is assumed that $E(x), \rho(x), x \in \Lambda$, are tolerance periodic, highly oscillating functions in x, $E(\cdot), \rho(\cdot) \in TP^0_\delta(\Lambda, \Delta) \subset H^0(\Lambda)$, but Poisson's ratio $\nu \equiv \nu' = \nu''$ is constant. Under condition $E' \neq E''$ and/or $\rho' \neq \rho''$ the material structure of the plate can be treated as functionally graded in the x-axis direction. Hence, these plate properties can be assumed in the form

$$
\begin{aligned}
\rho(\cdot, z) &= \begin{cases} \rho', & \text{for} \quad z \in ((1-\gamma(x))\lambda/2, (1+\gamma(x))\lambda/2), \\ \rho'', & \text{for} \quad z \in [0, (1-\gamma(x))\lambda/2] \cup [(1+\gamma(x))\lambda/2, \lambda], \end{cases} \\
E(\cdot, z) &= \begin{cases} E', & \text{for} \quad z \in ((1-\gamma(x))\lambda/2, (1+\gamma(x))\lambda/2), \\ E'', & \text{for} \quad z \in [0, (1-\gamma(x))\lambda/2] \cup [(1+\gamma(x))\lambda/2, \lambda], \end{cases}
\end{aligned}
\tag{3.11}
$$

where $\gamma(x)$ is a distribution function of material properties, cf. Figure 3.3.

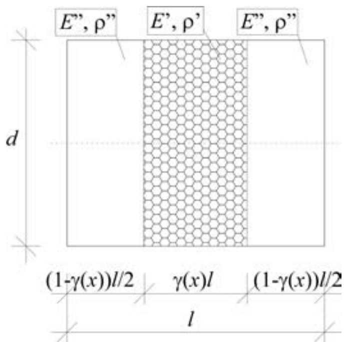

Fig. 3.3. A basic cell of a functionally graded plate under consideration, cf. [3.23]

Because the cell $\Delta(x)$, $x \in \Lambda$, of the plate band, has the form shown in Fig. 3.3 the periodic approximation of the fluctuation shape function can be assumed in as

$$
\tilde{h}(x, y) = \begin{cases} -2y[1-\tilde{\gamma}(x)]^{-1}, & y \in [0, (1-\tilde{\gamma}(x))\lambda/2], \\ (2y-l)\tilde{\gamma}(x)^{-1}, & y \in [(1-\tilde{\gamma}(x))l/2, (1+\tilde{\gamma}(x))l/2], \\ -2(y+l)[1-\tilde{\gamma}(x)]^{-1}, & y \in [(1+\tilde{\gamma}(x))l/2, l], \end{cases} \tag{3.12}
$$

where $x \in \overline{\Lambda}$, $y \in \Delta(x)$; $\tilde{\gamma}(x)$ is a periodic approximation of the distribution function of material properties $\gamma(x)$, cf. Fig. 3.4.

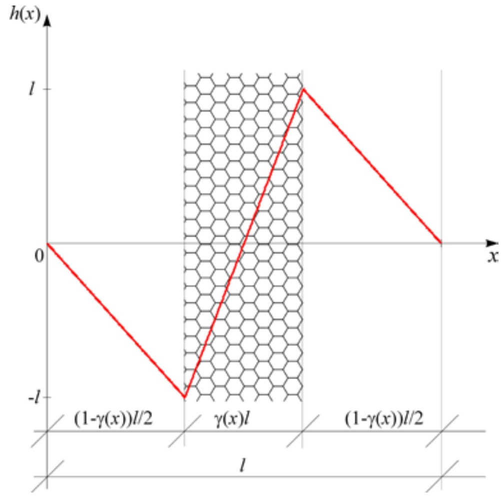

Fig. 3.4. A fluctuation shape function for the cell of the plate, cf. [3.23]

3.5.2. Governing equations of vibrations

Because vibrations of a medium thickness plate band are considered it is assumed that all basic unknowns are independent of argument x_2. Hence, the governing equations of *the tolerance model* (3.9) take the form

$$
\begin{aligned}
&\partial_1(<d_{11}>(\partial_1 w+\varphi_1))-<\mu>\ddot{w}=-<p>,\\
&\partial_1(<b_{1111}>\partial_1\varphi_1)+\partial_1(<b_{1111}\partial_1 g>\theta_1)-<d_{11}>(\partial_1 w+\varphi_1)-<\vartheta>\ddot{\varphi}_1=0,\\
&-<b_{1111}\partial_1 g>\partial_1\varphi_1-(<b_{1111}\partial_1 g\partial_1 g>+\underline{\underline{<d_{11}gg>}})\theta_1-\underline{<\vartheta gg>}\ddot{\theta}_1=0,\\
&\partial_1(<b_{2121}>\partial_1\varphi_2)+\partial_1(<b_{2121}\partial_1 g>\theta_2)-<\vartheta>\ddot{\varphi}_2=0,\\
&-<b_{2121}\partial_1 g>\partial_1\varphi_2-(<b_{2121}\partial_1 g\partial_1 g>+\underline{\underline{<d_{22}gg>}})\theta_2-\underline{<\vartheta gg>}\ddot{\theta}_2=0.
\end{aligned}
\tag{3.13}
$$

Equations (3.13) are decoupled on two systems of equations: the first of differential equations for unknown functions - macrodeflection w, macrorotation φ_1, fluctuation variable θ_1, and the second - for macrorotation φ_2 and fluctuation variable θ_2.

Obtained results can be evaluated using the governing equations of *the asymptotic model* (3.10), which have the form

$$\begin{aligned}
&\partial_1(<d_{11}>(\partial_1 w+\varphi_1))-<\mu>\ddot{w}=-<p>,\\
&\partial_1(<b_{1111}>\partial_1\varphi_1)+\partial_1(<b_{1111}\partial_1 g>\theta_1)-<d_{11}>(\partial_1 w+\varphi_1)-<\vartheta>\ddot{\varphi}_1=0,\\
&-<b_{1111}\partial_1 g>\partial_1\varphi_1-<b_{1111}\partial_1 g\partial_1 g>\theta_1=0,\\
&\partial_1(<b_{2121}>\partial_1\varphi_2)+\partial_1(<b_{2121}\partial_1 g>\theta_2)-<\vartheta>\ddot{\varphi}_2=0,\\
&-<b_{2121}\partial_1 g>\partial_1\varphi_2-<b_{2121}\partial_1 g\partial_1 g>\theta_2=0.
\end{aligned}\tag{3.14}$$

They are also decoupled on two systems of equations. It can be observed that for fluctuation variables θ_α, α=1,2, there are only algebraic equations $(3.14)_{3,5}$.

3.5.3. Approximate solutions to the governing equations

Equations (3.13), (3.14) have slowly-varying functional coefficients of x_1 argument. Hence, they are not a good tool to solve special problems of these plates. But some known approximate methods can be used, for instance the Ritz method, such for thin functionally graded plates in [3.21, 3.22÷3.25, 3.32]. For the plate band under consideration and using the following denotations

$$\begin{aligned}
&\widetilde{B}_{1111}=<b_{1111}>, && \widetilde{B}_{1212}=<b_{1212}>,\\
&\widetilde{B}_{111}=<b_{1111}\partial_1 g>, && \widetilde{B}_{122}=<b_{1212}\partial_1 g>,\\
&\widetilde{B}_{11}=<b_{1111}\partial_1 g\partial_1 g>, && \widetilde{B}_{22}=<b_{1212}\partial_1 g\partial_1 g>,\\
&\widetilde{D}_{11}=<d_{11}>, && \widetilde{D}_{22}=<d_{22}>,\\
&\overline{D}_{11}=l^{-2}<d_{11}gg>, && \overline{D}_{22}=l^{-2}<d_{22}gg>,\\
&\widetilde{\mu}=<\mu>, && \widetilde{p}=<p>\\
&\widetilde{\vartheta}=<\vartheta>, && \overline{\vartheta}=l^{-2}<\vartheta gg>,
\end{aligned}\tag{3.15}$$

Lagrangean $<\mathcal{L}_g>$, (3.7), takes the form

$$\begin{aligned}
<\mathcal{L}_g>=&\tfrac{1}{2}[\widetilde{\mu}\dot{w}\dot{w}+\widetilde{\vartheta}(\dot{\varphi}_1\dot{\varphi}_1+\dot{\varphi}_2\dot{\varphi}_2)+l^2\overline{\vartheta}(\dot{\theta}_1\dot{\theta}_1+\dot{\theta}_2\dot{\theta}_2)]-\\
&-\tfrac{1}{2}(\widetilde{B}_{1111}\partial_1\varphi_1\partial_1\varphi_1+\widetilde{B}_{1212}\partial_1\varphi_2\partial_1\varphi_2+\\
&\quad+2\widetilde{B}_{111}\partial_1\varphi_1\theta_1+2\widetilde{B}_{122}\partial_1\varphi_2\theta_2+\widetilde{B}_{11}\theta_1\theta_1+\widetilde{B}_{22}\theta_2\theta_2)-\\
&-\tfrac{1}{2}[\widetilde{D}_{11}(\partial_1 w\partial_1 w+\varphi_1\varphi_1+2\partial_1 w\varphi_1)+\widetilde{D}_{22}\varphi_2\varphi_2+\\
&\quad+\underline{l^2\overline{D}_{11}\theta_1\theta_1}+\underline{l^2\overline{D}_{22}\theta_2\theta_2})]+\widetilde{p}w.
\end{aligned}\tag{3.16}$$

Solutions to equations (3.13) can be assumed in the form satisfying proper boundary conditions for a simply supported plate band

$$\begin{aligned}
&w(x,t)=A_w\sin(\alpha x)\cos(\omega t),\\
&\varphi_1(x,t)=A_{\varphi_1}\cos(\alpha x)\cos(\omega t), \qquad \theta_1(x,t)=A_{\theta_1}\cos(\alpha x)\cos(\omega t),\\
&\varphi_2(x,t)=A_{\varphi_2}\cos(\alpha x)\cos(\omega t), \qquad \theta_2(x,t)=A_{\theta_2}\cos(\alpha x)\cos(\omega t),
\end{aligned}\tag{3.17}$$

where: α is a wave number; ω is a free vibration frequency; $A_w, A_{\varphi_1}, A_{\theta_1}, A_{\varphi_2}, A_{\theta_2}$ are amplitudes.

Using these solutions (3.17) and introducing the following denotations

$$
\begin{aligned}
&\breve{B}_1 = \widetilde{B}_{1111} = \tfrac{d^3}{12(1-\nu^2)}\int_0^L \{E''[1-\tilde{\gamma}(x)] + \tilde{\gamma}(x)E'\}[\sin(\alpha x)]^2 dx,\\
&\breve{B}_2 = \widetilde{B}_{1212} = \tfrac{d^3}{12(1+\nu)}\int_0^L \{E''[1-\tilde{\gamma}(x)] + \tilde{\gamma}(x)E'\}[\sin(\alpha x)]^2 dx,\\
&\widetilde{B}_1 = \widetilde{B}_{111} = \tfrac{-d^3}{6(1-\nu^2)}\int_0^L (E'-E'')\sin(\alpha x)\cos(\alpha x) dx,\\
&\widetilde{B}_2 = \widetilde{B}_{122} = \tfrac{-d^3}{6(1+\nu)}\int_0^L (E'-E'')\sin(\alpha x)\cos(\alpha x) dx,\\
&\widehat{B}_1 = \widetilde{B}_{11} = \tfrac{d^3}{3(1-\nu^2)}\int_0^L \tfrac{E''[1-\tilde{\gamma}(x)]+\tilde{\gamma}(x)E'}{\tilde{\gamma}(x)(1-\tilde{\gamma}(x))}[\cos(\alpha x)]^2 dx,\\
&\widehat{B}_2 = \widetilde{B}_{22} = \tfrac{d^3}{3(1+\nu)}\int_0^L \tfrac{E''[1-\tilde{\gamma}(x)]+\tilde{\gamma}(x)E'}{\tilde{\gamma}(x)(1-\tilde{\gamma}(x))}[\cos(\alpha x)]^2 dx,\\
&\breve{D}_1 = \breve{D}_{11} = \tfrac{5}{6}\tfrac{d}{1-\nu^2}\int_0^L \{E''[1-\tilde{\gamma}(x)] + \tilde{\gamma}(x)E'\}[\cos(\alpha x)]^2 dx,\\
&\breve{D}_2 = \breve{D}_{22} = \tfrac{5}{6}\tfrac{d}{1+\nu}\int_0^L \{E''[1-\tilde{\gamma}(x)] + \tilde{\gamma}(x)E'\}[\cos(\alpha x)]^2 dx,\\
&\overline{D}_1 = \overline{D}_{11} = \tfrac{5}{6}\tfrac{d}{3(1-\nu^2)}\int_0^L \{E''[1-\tilde{\gamma}(x)] + \tilde{\gamma}(x)E'\}[\cos(\alpha x)]^2 dx,\\
&\overline{D}_2 = \overline{D}_{22} = \tfrac{5}{6}\tfrac{d}{3(1+\nu)}\int_0^L \{E''[1-\tilde{\gamma}(x)] + \tilde{\gamma}(x)E'\}[\cos(\alpha x)]^2 dx,\\
&\breve{\mu} = d\int_0^L \{\rho''[1-\tilde{\gamma}(x)] + \tilde{\gamma}(x)\rho'\}[\sin(\alpha x)]^2 dx,\\
&\hat{\vartheta} = \tfrac{d^3}{12}\int_0^L \{\rho''[1-\tilde{\gamma}(x)] + \tilde{\gamma}(x)\rho'\}[\cos(\alpha x)]^2 dx,\\
&\breve{\vartheta} = \tfrac{d^3}{36}\int_0^L \{\rho''[1-\tilde{\gamma}(x)] + \tilde{\gamma}(x)\rho'\}[\cos(\alpha x)]^2 dx,\\
&P = \int_0^L p(x)\sin(\alpha x) dx,
\end{aligned}
\tag{3.18}
$$

the maximal kinetic energy $\mathrm{K}^{TM}_{\max}$ and the maximal potential energy $\mathcal{U}^{TM}_{\max}$ by the tolerance model can be written as:

– the maximal kinetic energy $\mathcal{K}^{TM}_{\max}$

$$
\mathcal{K}^{TM}_{\max} = \tfrac{1}{2}\omega^2[\breve{\mu}A_w{}^2 + \hat{\vartheta}(A_{\varphi_1}{}^2 + A_{\varphi_2}{}^2) + l^2\breve{\vartheta}(A_{\theta_1}{}^2 + A_{\theta_2}{}^2)], \tag{3.19a}
$$

– the maximal potential energy $\mathcal{U}^{TM}_{\max}$

$$\begin{aligned}\mathcal{U}^{TM}_{\max} = \tfrac{1}{2}[&\breve{D}_1\alpha^2 {A_w}^2 + 2\breve{D}_1\alpha A_w A_{\varphi_1} + (\breve{B}_1\alpha^2 + \breve{D}_1){A_{\varphi_1}}^2 + \\ &+2\widetilde{B}_1\alpha A_{\varphi_1}A_{\theta_1} + (\widehat{B}_1 + l^2\overline{D}_1){A_{\theta_1}}^2 + \\ &+(\breve{B}_2\alpha^2 + \breve{D}_2){A_{\varphi_2}}^2 + 2\widetilde{B}_2\alpha A_{\varphi_2}A_{\theta_2} + (\widehat{B}_2 + l^2\overline{D}_2){A_{\theta_2}}^2] + PA_w.\end{aligned} \tag{3.19b}$$

Similarly, these energies in the framework of the asymptotic model take the form:

– the maximal kinetic energy $\mathcal{K}^{AM}_{\max}$

$$\mathcal{K}^{AM}_{\max} = \tfrac{1}{2}\omega^2[\breve{\mu}{A_w}^2 + \widehat{\vartheta}({A_{\varphi_1}}^2 + {A_{\varphi_2}}^2)], \tag{3.20a}$$

– the maximal potential energy $\mathcal{U}^{AM}_{\max}$

$$\begin{aligned}\mathcal{U}^{AM}_{\max} = \tfrac{1}{2}[&\breve{D}_1\alpha^2 {A_w}^2 + 2\breve{D}_1\alpha A_w A_{\varphi_1} + (\breve{B}_1\alpha^2 + \breve{D}_1){A_{\varphi_1}}^2 + \\ &+2\widetilde{B}_1\alpha A_{\varphi_1}A_{\theta_1} + \widehat{B}_1{A_{\theta_1}}^2 + \\ &+(\breve{B}_2\alpha^2 + \breve{D}_2){A_{\varphi_2}}^2 + 2\widetilde{B}_2\alpha A_{\varphi_2}A_{\theta_2} + \widehat{B}_2{A_{\theta_2}}^2] + PA_w.\end{aligned} \tag{3.20b}$$

Using the conditions of the Ritz method

$$\begin{aligned}&\frac{\partial(\mathcal{U}_{\max} - \mathcal{K}_{\max})}{\partial A_w} = 0, \\ &\frac{\partial(\mathcal{U}_{\max} - \mathcal{K}_{\max})}{\partial A_{\varphi_1}} = 0, \qquad \frac{\partial(\mathcal{U}_{\max} - \mathcal{K}_{\max})}{\partial A_{\varphi_2}} = 0, \\ &\frac{\partial(\mathcal{U}_{\max} - \mathcal{K}_{\max})}{\partial A_{\theta_1}} = 0, \qquad \frac{\partial(\mathcal{U}_{\max} - \mathcal{K}_{\max})}{\partial A_{\theta_2}} = 0,\end{aligned} \tag{3.21}$$

to formulas (3.19) and (3.20) systems of linear algebraic equations for amplitudes $A_w, A_{\varphi_1}, A_{\theta_1}, A_{\varphi_2}, A_{\theta_2}$ can be obtained.

For the tolerance model these algebraic equations take the form of two decoupled systems:

– the first for amplitudes $A_w, A_{\varphi_1}, A_{\theta_1}$

$$\begin{aligned}&(\breve{D}_1\alpha^2 - \omega^2\breve{\mu})A_w + \breve{D}_1\alpha A_{\varphi_1} = -P, \\ &\breve{D}_1\alpha A_w + (\breve{B}_1\alpha^2 + \breve{D}_1 - \omega^2\widehat{\vartheta})A_{\varphi_1} + \widetilde{B}_1\alpha A_{\theta_1} = 0, \\ &\widetilde{B}_1\alpha A_{\varphi_1} + [\widehat{B}_1 + l^2(\overline{D}_1 - \omega^2\breve{\vartheta})]A_{\theta_1} = 0,\end{aligned} \tag{3.22a}$$

– the second for amplitudes $A_{\varphi_2}, A_{\theta_2}$

$$(\breve{B}_2\alpha^2+\breve{D}_2-\omega^2\hat{\vartheta})A_{\varphi_2}+\tilde{B}_2\alpha A_{\theta_2}=0,$$
$$\tilde{B}_2\alpha A_{\varphi_2}+[\hat{B}_2+l^2(\overline{D}_2-\omega^2\breve{\vartheta})]A_{\theta_2}=0. \tag{3.22b}$$

Below, our considerations are restricted only to equations (3.22a). Solving this system formulas of amplitudes $A_w, A_{\varphi_1}, A_{\theta_1}$ take the form

$$A_w=\frac{\{\omega^4 l^2\hat{\vartheta}\breve{\vartheta}-\omega^2[l^2(\breve{B}_1\alpha^2+\breve{D}_1)\breve{\vartheta}+(\hat{B}_1+l^2\overline{D}_1)\hat{\vartheta}]\}P}{l^2\breve{\mu}\hat{\vartheta}\breve{\vartheta}[(\varpi_{-1})^2-\omega^2][(\varpi_{-2})^2-\omega^2][(\varpi_{+1})^2-\omega^2]}+$$
$$+\frac{\{(\breve{B}_1\alpha^2+\breve{D}_1)(\hat{B}_1+l^2\overline{D}_1)-(\tilde{B}_1)^2\alpha^2\}P}{l^2\breve{\mu}\hat{\vartheta}\breve{\vartheta}[(\varpi_{-1})^2-\omega^2][(\varpi_{-2})^2-\omega^2][(\varpi_{+1})^2-\omega^2]},$$
$$A_{\varphi_1}=\frac{[\omega^2 l^2\alpha\breve{D}_1\breve{\vartheta}-\alpha\breve{D}_1(\hat{B}_1+l^2\overline{D}_1)]P}{l^2\breve{\mu}\hat{\vartheta}\breve{\vartheta}[(\varpi_{-1})^2-\omega^2][(\varpi_{-2})^2-\omega^2][(\varpi_{+1})^2-\omega^2]}, \tag{3.23}$$
$$A_{\theta_1}=\frac{\alpha^2\breve{D}_1\tilde{B}_1 P}{l^2\breve{\mu}\hat{\vartheta}\breve{\vartheta}[(\varpi_{-1})^2-\omega^2][(\varpi_{-2})^2-\omega^2][(\varpi_{+1})^2-\omega^2]},$$

where ϖ_{-1},ϖ_{-2} are *two lower* and ϖ_{+1} *the higher resonance frequencies*, respectively. Introducing the following denotations

$$\overline{a}\equiv\breve{\mu}\hat{\vartheta}\breve{\vartheta}l^2,$$
$$\overline{b}\equiv l^2\breve{\vartheta}[\breve{\mu}\breve{D}_1+\alpha^2(\breve{\mu}\breve{B}_1+\breve{D}_1\hat{\vartheta})]+\breve{\mu}\hat{\vartheta}(l^2\overline{D}_1+\hat{B}_1),$$
$$\overline{c}\equiv[\breve{\mu}\breve{D}_1+\alpha^2(\breve{\mu}\breve{B}_1+\breve{D}_1\hat{\vartheta})](l^2\overline{D}_1+\hat{B}_1)-\alpha^2(\breve{\mu}\tilde{B}_1^2-l^2\breve{B}_1\breve{D}_1\breve{\vartheta}\alpha^2), \tag{3.24}$$
$$\overline{d}\equiv\breve{D}_1[(l^2\overline{D}_1+\hat{B}_1)\breve{B}_1-\tilde{B}_1^2]\alpha^4,$$

and also

$$\overline{\alpha}\equiv 27\overline{d}\overline{a}^2+2\overline{b}^3-9\overline{a}\overline{b}\overline{c},$$
$$\overline{\beta}\equiv 3\overline{a}\overline{c}-\overline{b}^2, \tag{3.25}$$
$$\overline{\delta}\equiv\sqrt[3]{\overline{\alpha}+i\sqrt{-\overline{\alpha}^2-4\overline{\beta}^3}},$$

formulas of the abovementioned resonance frequencies take the following form

$$\varpi_{-1}=\sqrt{(3\overline{a})^{-1}[\overline{b}-(\sqrt[3]{2})^{-1}(\mathrm{Re}\,\overline{\delta}+\sqrt{3}\,\mathrm{Im}\,\overline{\delta})]},$$
$$\varpi_{-2}=\sqrt{(3\overline{a})^{-1}[\overline{b}-(\sqrt[3]{2})^{-1}(\mathrm{Re}\,\overline{\delta}-\sqrt{3}\,\mathrm{Im}\,\overline{\delta})]}, \tag{3.26}$$
$$\varpi_{+1}=\sqrt{(3\overline{a})^{-1}(\overline{b}+\sqrt[3]{4}\,\mathrm{Re}\,\overline{\delta})}.$$

It can be observed that formulas (3.26) are identical to these, which describe free vibration frequencies of medium thickness functionally graded plate band with microstructure in the framework of *the tolerance model*. There are two *fundamental lower frequencies* ϖ_{-1}, ϖ_{-2} *of free macro-vibrations* and one *higher frequency* ϖ_{+1} *of free micro-vibrations*.

On the other side, using the conditions of the Ritz method (3.21) to the asymptotic model formulas of the maximal energies (3.20) the systems of algebraic equations are obtained:

– the first for amplitudes $A_w, A_{\varphi_1}, A_{\theta_1}$

$$
\begin{aligned}
&(\breve{D}_1\alpha^2 - \omega^2\breve{\mu})A_w + \breve{D}_1\alpha A_{\varphi_1} = -P,\\
&\breve{D}_1\alpha A_w + (\breve{B}_1\alpha^2 + \breve{D}_1 - \omega^2\widehat{\vartheta})A_{\varphi_1} + \widetilde{B}_1\alpha A_{\theta_1} = 0,\\
&\widetilde{B}_1\alpha A_{\varphi_1} + \widehat{B}_1 A_{\theta_1} = 0,
\end{aligned}
\tag{3.27a}
$$

– the second for amplitudes $A_{\varphi_2}, A_{\theta_2}$

$$
\begin{aligned}
&(\breve{B}_2\alpha^2 + \breve{D}_2 - \omega^2\widehat{\vartheta})A_{\varphi_2} + \widetilde{B}_2\alpha A_{\theta_2} = 0,\\
&\widetilde{B}_2\alpha A_{\varphi_2} + \widehat{B}_2 A_{\theta_2} = 0.
\end{aligned}
\tag{3.27b}
$$

Restricting our considerations to equations (3.27a) and solving this system formulas of amplitudes $A_w, A_{\varphi_1}, A_{\theta_1}$ have the form

$$
\begin{aligned}
\widetilde{A}_w &= \frac{\{\omega^2\widehat{B}_1\widehat{\vartheta} - (\breve{B}_1\alpha^2 + \breve{D}_1)\widehat{B}_1 + (\widetilde{B}_1)^2\alpha^2\}P}{\breve{\mu}\widehat{\vartheta}\widehat{B}_1[(\widetilde{\varpi}_{-1})^2 - \omega^2][(\widetilde{\varpi}_{-2})^2 - \omega^2]},\\
\widetilde{A}_{\varphi_1} &= \frac{\alpha\breve{D}_1\widehat{B}_1 P}{\breve{\mu}\widehat{\vartheta}\widehat{B}_1[(\widetilde{\varpi}_{-1})^2 - \omega^2][(\widetilde{\varpi}_{-2})^2 - \omega^2]},\\
\widetilde{A}_{\theta_1} &= \frac{\alpha^2\breve{D}_1\widetilde{B}_1 P}{\breve{\mu}\widehat{\vartheta}\widehat{B}_1[(\widetilde{\varpi}_{-1})^2 - \omega^2][(\widetilde{\varpi}_{-2})^2 - \omega^2]},
\end{aligned}
\tag{3.28}
$$

where $\widetilde{\varpi}_{-1}, \widetilde{\varpi}_{-2}$ are *two lower resonance frequencies*. Introducing denotations similar to (3.24)

$$
\begin{aligned}
&\widetilde{b} \equiv \breve{\mu}\widehat{\vartheta}\widehat{B}_1,\\
&\widetilde{c} \equiv [\breve{\mu}\breve{D}_1 + \alpha^2(\breve{\mu}\breve{B}_1 + \breve{D}_1\widehat{\vartheta})]\widehat{B}_1 - \alpha^2\breve{\mu}\widetilde{B}_1^{\,2},\\
&\widetilde{d} \equiv \breve{D}_1(\widehat{B}_1\breve{B}_1 - \widetilde{B}_1^{\,2})\alpha^4,
\end{aligned}
\tag{3.29}
$$

formulas of the abovementioned resonance frequencies take the following form

$$\tilde{\omega}_{-1} = \sqrt{(2\tilde{b})^{-1}[\tilde{c} - \sqrt{\tilde{c}^2 - 4\tilde{b}\tilde{d}}\,]},$$
$$\tilde{\omega}_{-2} = \sqrt{(2\tilde{b})^{-1}[\tilde{c} + \sqrt{\tilde{c}^2 - 4\tilde{b}\tilde{d}}\,]}. \tag{3.30}$$

Formulas (3.30) are identical to these of free vibration frequencies of medium thickness functionally graded plate band with microstructure in the framework of *the asymptotic model*. They are only two *fundamental lower frequencies* $\tilde{\omega}_{-1}, \tilde{\omega}_{-2}$ *of free macro-vibrations*.

It can be observed that only in the framework of the tolerance model the effect of the microstructure size of the plate strip can be analysed in the form of higher vibration frequencies, $(3.26)_3$. However, in the asymptotic model this effect is neglected and the fundamental lower frequencies can be only investigated, (3.30).

3.6. Final remarks

The main problem considered in this chapter is modelling of vibrations of medium thickness functionally graded plates having a microstructure. Unfortunately, most averaging approaches applied to analyse these problems neglects phenomena related to the microstructure size of the plate. In order to take into account the effect of the microstructure size the tolerance method is used. Applying this method the known differential equations, based on the Hencky-Bolle-type plate assumptions, with tolerance-periodic, non-continuous, functional coefficients is replaced by governing equations with smooth, slowly-varying coefficients. The derived tolerance model equations describe the effect of the microstructure size on the overall behaviour of microstructured medium thickness functionally graded plates under consideration. However, the asymptotic model equations neglect this effect and describe these plates on the macrolevel only.

Following the obtained analytical results some general remarks can be formulated.

1 *The tolerance model* take into account *the effect of the microstructure size* in dynamic problems of microstructured medium thickness functionally graded plates, e.g. the “higher order” vibrations related to the plate microstructure;
2 *The asymptotic model* lets to investigate only lower order vibrations of these microstructured plates;

3 Solutions obtained in the framework of the tolerance model have to satisfy the condition to be slowly-varying functions in x_1. This condition stands *a posteriori* verification of results of this model.

Some other thermoelasticity problems of the medium thickness functionally graded plates will be considered in forthcoming papers, where certain evaluations and comparisons with other averaged models could be presented.

3.7. References

3.1 Akbarzadeha A.H., Abbasib M., Eslami M.R., Coupled thermoelasticity of functionally graded plates based on the third-order shear deformation theory, Thin-Walled Struct., 53, 2012, pp. 141-155.

3.2 Baron E., On dynamic behaviour of medium-thickness plates with uniperiodic structure, Arch. Appl. Mech., 73, 2003, pp. 505-516.

3.3 Batra R.C., Qian L.F., Chen L.M., Natural frequencies of thick square plates made of orthotropic, trigonal, monoclinic, hexagonal and triclinic materials, J. Sound Vibr., 270, 2004, pp. 1074-1086.

3.4 Bensoussan A., Lions J.-L., Papanicolaou G., Asymptotic analysis for periodic structures, North-Holland, Amsterdam 1978.

3.5 Brillouin L., Wave propagation in periodic structures, Dover Pub. Inc., Dover, 1953.

3.6 Bui T.Q., Khosravifard A., Zhang Ch., Hematiyan M.R., Golu M.V., Dynamic analysis of sandwich beams with functionally graded core using a truly meshfree radial point interpolation method, Eng. Struct., 47, 2013, pp. 90-104.

3.7 Cheng Z.B., Xu Y.G., Zhang L.L., Analysis of flexural wave bandgaps in periodic plate structures using differential quadrature element method, Int. J. Mech. Sci., 100, 2015, pp. 112-125.

3.8 Cielecka I., Jędrysiak J., A non-asymptotic model of dynamics of honeycomb lattice-type plates, J. Sound Vibr., 296, 2006, pp. 130-149.

3.9 Dell'Isola F., Rosa L., Woźniak C., A micro-structural continuum modelling compacting fluid-saturated grounds, Acta Mechanica, 127, 1998, pp. 165-182.

3.10 Derras M., Kaci A., Draiche K., Tounsi A., Non-linear analysis of functionally graded plates in cylindrical bending based on a new refined shear deformation theory, J. Theor. Appl. Mech., 51, 2, 2013, pp. 339-348.

3.11 Domagalski Ł., Jędrysiak J., On the tolerance modelling of geometrically nonlinear thin periodic plates, Thin-Walled Struct., 87, 2015, pp. 183-190.

3.12 Domagalski Ł., Jędrysiak J., Geometrically nonlinear vibrations of slender meso-periodic beams. The tolerance modelling approach, Comp. Struct., 136, 2016, pp. 270-277.

3.13 Fantuzzi N., Tornabene F., Viola E., Ferreira A.J.M., A strong formulation finite element method (SFEM) based on RBF and GDQ techniques for the static and dynamic analyses of laminated plates of arbitrary shape, Meccanica, 49, 2014, pp. 2503-2542.

3.14 Ferreira A.J.M., Batra R.C., Roque C.M.C., Qian L.F., Jorge R.M.N., Natural frequencies of functionally graded plates by a meshless method, Comp. Struct., 75, 2006, pp. 593-600.
3.15 Grygorowicz M., Magnucki K., Malinowski M., Elastic buckling of a sandwich beam with variable mechanical properties of the core, Thin-Walled Struct., 87, 2015, pp. 127-132.
3.16 Jasion P., Magnucka-Blandzi E., Szyc W., Magnucki K., Global and local buckling of sandwich circular and beam-rectangular plates with metal foam core, Thin-Walled Struct., 61, 2012, pp. 154-161.
3.17 Jędrysiak J., The length-scale effect in the buckling of thin periodic plates resting on a periodic Winkler foundation, Meccanica, 38, 2003a, pp. 435-451.
3.18 Jędrysiak J., Free vibrations of thin periodic plates interacting with an elastic periodic foundation, Int. J. Mech. Sci., 45, 2003b, pp. 1411-1428.
3.19 Jędrysiak J., The tolerance averaging model of dynamic stability of thin plates with one-directional periodic structure, Thin-Walled Struct., 45, 2007, pp. 855-860.
3.20 Jędrysiak J., Higher order vibrations of thin periodic plates, Thin-Walled Struct., 47, 8-9, 2009, pp. 890-901.
3.21 Jędrysiak J., Thermomechanics of laminates, plates and shells with functionally grades properties, No 1946, Pub. House Łódź Univ. Techn., Łódź 2010, [in Polish].
3.22 Jędrysiak J., Vibrations of microstructured functionally graded plates, Vibr. Physical Syst., 25, 2012, pp. 193-198.
3.23 Jędrysiak J., Modelling of dynamic behaviour of microstructured thin functionally graded plates, Thin-Walled Struct., 71, 2013, pp. 102-107.
3.24 Jędrysiak J., Free vibrations of thin functionally graded plates with microstructure, Engng. Struct., 75, 2014, pp. 99-112.
3.25 Jędrysiak J., Kaźmierczak-Sobińska M., On free vibration of thin functionally graded plate bands resting on an elastic foundation, J. Theor. Appl. Mech., 53, 2015, pp. 629-642.
3.26 Jędrysiak J., Michalak B., On the modelling of stability problems for thin plates with functionally graded structure, Thin-Walled Struct., 49, 2011, pp. 627-635.
3.27 Jędrysiak J., Paś A., Dynamics of medium thickness plates interacting with a periodic Winkler's foundation: non-asymptotic tolerance modelling, Meccanica, 49, 2014, pp. 1577-1585.
3.28 Jędrysiak J., Radzikowska A., Tolerance averaging of heat conduction in transversally graded laminates, Meccanica, 47, 2012, pp. 95-107.
3.29 Jędrysiak J., Woźniak C., On the elastodynamics of thin microperiodic plates, J. Theor. Appl. Mech., 33, 1995, pp. 337-349.
3.30 Jędrysiak J., Woźniak C., On the propagation of elastic waves in a multiperiodically reinforced medium, Meccanica, 41, 2006, pp. 553-569.
3.31 Jha D.K., Kant Tarun, Singh R.K., Free vibration response of functionally graded thick plates with shear and normal deformations effects, Comp. Struct., 96, 2013, pp. 799-823.

3.32 Kaźmierczak M., Jędrysiak J., A new combined asymptotic-tolerance model of vibrations of thin transversally graded plates, Engng. Struct., 46, 2013, pp. 322-331.
3.33 Kohn R.V., Vogelius M., A new model for thin plates with rapidly varying thickness, Int. J. Solids Struct., 20, 1984, pp. 333-350.
3.34 Królak M., Kowal-Michalska K., Mania R.J., Świniarski J., Stability and load carrying capacity of multi-cell thin-walled columns of rectangular cross-sections, J. Theor. Appl. Mech., 47, 2009, pp. 435-456.
3.35 Kugler St., Fotiu P.A., Murin J., The numerical analysis of FGM shells with enhanced finite elements, Engng. Struct., 49, 2013, pp. 920-935.
3.36 Magnucka-Blandzi E., Non-linear analysis of dynamic stability of metal foam circular plate, J. Theor. Appl. Mech., 48, 2010, pp. 207-217.
3.37 Marczak J., Jędrysiak J., Tolerance modelling of vibrations of periodic three-layered plates with inert core, Comp. Struct., 134, 2015, pp. 854-861.
3.38 Matysiak S.J., Nagórko W., Microlocal parameters in the modelling of microperiodic plates, Ing. Arch., 59, 1989, pp. 434-444.
3.39 Matysiak S.J., Perkowski D.M., Temperature distributions in a periodically stratified layer with slant lamination, Heat Mass Transfer, 50, 2014, pp. 75-83.
3.40 Mazur-Śniady K., Śniady P., Zielichowski-Haber W., Dynamic response of micro-periodic composite rods with uncertain parameters under moving random load, J. Sound Vibr., 320, 2009, pp. 273-288.
3.41 Mazur-Śniady K., Woźniak C., Wierzbicki E., On the modelling of dynamic problems for plates with a periodic structure, Arch. Appl. Mech., 74, 2004, pp. 179-190.
3.42 Michalak B., The meso-shape functions for the meso-structural models of wavy-plates, ZAMM, 81, 2001, pp. 639-641.
3.43 Michalak B., 2D tolerance and asymptotic models in elastodynamics of a thin-walled structure with dense system of ribs, Arch. Civ. Mech. Engng., 15, 2015, pp. 449-455.
3.44 Michalak B., Wirowski A., Dynamic modelling of thin plate made of certain functionally graded materials, Meccanica, 47, 2012, pp. 1487-1498.
3.45 Murin J., Aminbaghai M., Hrabovsky J., Kutiš V., Kugler S., Modal analysis of the FGM beams with effect of the shear correction function, Composites: Part B, 45, 2013, pp. 1575-1582.
3.46 Nagórko W., Woźniak C., Nonasymptotic modelling of thin plates reinforced by a system of stiffeners, Electr. J. Polish Agric. Univ. - Civil Engng., 5, 2002.
3.47 Oktem A.S., Mantari J.L., Guedes Soares C., Static response of functionally graded plates and doubly-curved shells based on a higher order shear deformation theory, Eur. J. Mech. - A/Solids, 36, 2012, pp. 163-172.
3.48 Ostrowski P., Michalak B., The combined asymptotic-tolerance model of heat conduction in a skeletal micro-heterogeneous hollow cylinder, Comp. Struct., 134, 2015, pp. 343-352.
3.49 Ostrowski P., Michalak B., A contribution to the modelling of heat conduction for cylindrical composite conductors with non-uniform distribution of constituents, Int. J. Heat and Mass Transfer, 92, 2016, pp. 435-448.

3.50 Pazera E., Jędrysiak J., Thermoelastic phenomena in transversally graded laminates, Comp. Struct., 134, 2015, pp. 663-671.

3.51 Perliński W., Gajdzicki M., Michalak B., Modelling of annular plates stability with functionally graded structure interacting with elastic heterogeneous subsoil, J. Theor. Appl. Mech., 52, 2014, pp. 485-498.

3.52 Rabenda M., Analysis of non-stationary heat transfer in a hollow cylinder with functionally graded material properties performed by different research methods, Engng. Trans., 63, 2015, pp. 329-339.

3.53 Roque C.M.C., Ferreira A.J.M., Jorge R.M.N., A radial basis function approach for the free vibration analysis of functionally graded plates using a refined theory, J. Sound Vibr., 300, 2007, pp. 1048-1070.

3.54 Sadowski T., Golewski P., Heat transfer and stress concentrations in a two-phase polycrystalline composite structure. Part I: Theoretical modelling of heat transfer, Mat.-wiss. u. Werkstofftech., 44, 2013, pp. 497-505.

3.55 Sheikholeslami S.A., Saidi A.R., Vibration analysis of functionally graded rectangular plates resting on elastic foundation using higher-order shear and normal deformable plate theory, Comp. Struct., 106, 2013, pp. 350-361.

3.56 Sofiyev A.H., Schnack E., The stability of functionally graded cylindrical shells under linearly increasing dynamic torsional loading, Engng. Struct., 26, 2004, pp. 1321-1331.

3.57 Suresh S., Mortensen A., Fundamentals of functionally graded materials, The University Press, Cambridge, 1998.

3.58 Tomczyk B., A non-asymptotic model for the stability analysis of thin biperiodic cylindrical shells, Thin-Walled Struct., 45, 2007, pp. 941-944.

3.59 Tomczyk B., Dynamic stability of micro-periodic cylindrical shells, Mech. Mech. Eng., 14, 2010, pp. 137-150.

3.60 Tornabene F., Viola E., Static analysis of functionally graded doubly-curved shells and panels of revolution, Meccanica, 48, 2013, pp. 901-930.

3.61 Tornabene F., Liverani A., Caligiana G., FGM and laminated doubly curved shells and panels of revolution with a free-form meridian: A 2-D GDQ solution for free vibrations, Int. J. Mech. Sci., 53, 2011, pp. 443-470.

3.62 Wierzbicki E., Woźniak C., On the dynamics of combined plane periodic structures, Arch. Appl. Mech., 70, 2000, pp. 387-398.

3.63 Wirowski A., Self-vibration of thin plate band with non-linear functionally graded material, Arch. Mech., 64, 2012, pp. 603-615.

3.64 Woźniak C., et al., (eds.), Mathematical modelling and analysis in continuum mechanics of microstructured media, Pub. House Silesian Univ. Techn., Gliwice 2010.

3.65 Woźniak C., Michalak B., Jędrysiak J., (eds.), Thermomechanics of heterogeneous solids and structures, Pub. House Łódź Univ. Techn., Łódź 2008.

3.66 Woźniak C., Wierzbicki E., Averaging techniques in thermomechanics of composite solids. Tolerance averaging versus homogenization, Pub. House Częstochowa Univ. Techn., Częstochowa 2000.

3.67 Yu-Gao Huangfu, Fang-Qi Chen, Single-pulse chaotic dynamics of functionally graded materials plate, Acta Mecha. Sinica, 29, 2013, pp. 593-601.
3.68 Zhi-Jing Wu, Feng-Ming Li, Yi-Ze Wang, Vibration band gap properties of periodic Mindlin plate structure using the spectral element method, Meccanica, 49, 2014, pp. 725-737.
3.69 Zhou X.Q., Yu D.Y., Shao X., Wang S., Tian Y.H., Band gap characteristics of periodically stiffened -thin-plate based on center-finite-difference-method, Thin-Walled Struct., 82, 2014, pp. 115-123.
3.70 Zhou X.Q., Yu D.Y., Shao X., Wang S., Zhang S.Q., Simplified-super-element-method for analyzing free flexural vibration characteristics of periodically stiffened-thin-plate filled with viscoelastic damping material, Thin-Walled Struct., 94, 2015, pp. 234-252.

4.

Application of structural topology optimisation for planetary carrier design

A planetary gear train is very common in automatic gearboxes nowadays as well as in manual gearboxes for a low range or reduces. The main advantage of this gear train is compactness with a connection to a high possible gear ratio. Additional advantages such as a possibility to change of the gear ration and direction of rotation with a very simple method by stopping one of three main components of the gear train can be found. Of course, the planetary gear train has disadvantages like a complex design that requires precise gears and a planet carrier with high torsional stiffness.

The presented work concerns a very important part of the planetary gear train, namely, a design of the planet carrier. An application of heavy-duty commercial gearboxes is selected because large torque levels dominate in this application and then the design of the carrier is crucial. One of the most important parameters of the plant carrier is its torsional stiffness, which has a direct influence on stress level gears. The low stiffness leads to uneven contact between the gears during loading which reduces pitting resistance of the gears. The next important parameter is the stress level in the planet carrier, because of varying torque the planet carrier is exposed to fatigue failure. These two parameters are taken in a design process as the main factors.

A topology optimization method [4.1, 4.3, 4.6] was used to find a direction to design the torsional stiff carrier also taking into account a size limit of the carrier.

The project is done with the purpose of showing that the usage of the optimization tool helps significantly to design a new part, which excels a standard part in terms of structural performance.

As it was said, a critical parameter in terms of working conditions between mating gears is the torsional stiffness of the planet carrier. The stiffer the carrier - the better results in terms of durability of the train gear are achieved. It is generally well known that quality of a contact between the mating gears has a significant influence on durability of the gears. The contact quality is effected by the low stiffness of the carrier because the contact is uneven characterising an edge-to-surface contact type instead of a surface-to-surface type. This leads directly to rising of contact stresses and therefore reducing pitting lifetime of the gears, especially the sun gear. The sun gear is loaded by more cycles resulting from a number of the mating planetary gears - normally they are from 3 to 5.

In order to reduce this effect of contact changes due to the low stiffness carrier, a simple method can be implemented, namely the gears can have very small helix angle to compensate the planet carrier deformation, see Figs.: 4.14 and 4.15. This solution looks brilliant at first glance. Unfortunately, the real implementation is more complex because it should reflect a particular torque level and then the correction is constant for all torque levels. However, this is meant to be only for selected torque levels, the gear train works in the optimum configuration and the rest of the time the contact is disturbed, the gears work in the conditions that are far from optimal. Therefore, the implemented correction cannot be suitable for a very much different duty cycle. The selection method of this additional helix angle correction is complex and an entire procedure can be found in the existing norms and standards. Hence, the best solution for the carrier is a very stiff design and then the correction can be neglected without any dramatic reduction of the pitting lifetime of the gears. At that time, an effect of the unwanted edge to surface contact is small in wide range of the used torque levels.

A second parameter - the maximum stress level is also important for the carrier but it is somehow driven by the carrier stiffness. The stiff design normally can be optimized quite easily to meet the required maximum stress level. To conclude, the torsional stiffness of the carrier is crucial for robustness of the planetary gear train and therefore critical during the design process.

The presented work is an attempt to design the carrier, which has the improved torsional stiffness with low stress levels in a predefined space envelope. The presented research corresponds to a typical design task of a design project of the planetary gear train.

To solve the established problem a design software SolidThinking Inspire for Altair Corporation [4.5] was utilized, this tool is developed to help engineers to find an initial shape of structures/ designs using topology optimization employing a finite element method among others. The usage of this tool can improve the design process significantly and it can bring measurable benefits as it is shown in this paper.

4.1. Goals

The purpose of this work is to create the carrier design with the improved torsional stiffness with less than 2.5 minutes of angular displacement at an input torque of 50% of a maximum nominal torque. The design is limited by the pre-defined space – the envelope in which the planet-carrier must be fitted see Fig. 4.4. For a comparative reason a standard design on the carrier was analysed as well and the new stiff carrier design must have the same mass as the standard one. The standard design is shown in Fig. 4.1 and it represents a typical design existing on the market in heavy-duty gearboxes.

Fig. 4.1. Standard design of planet carrier used as reference

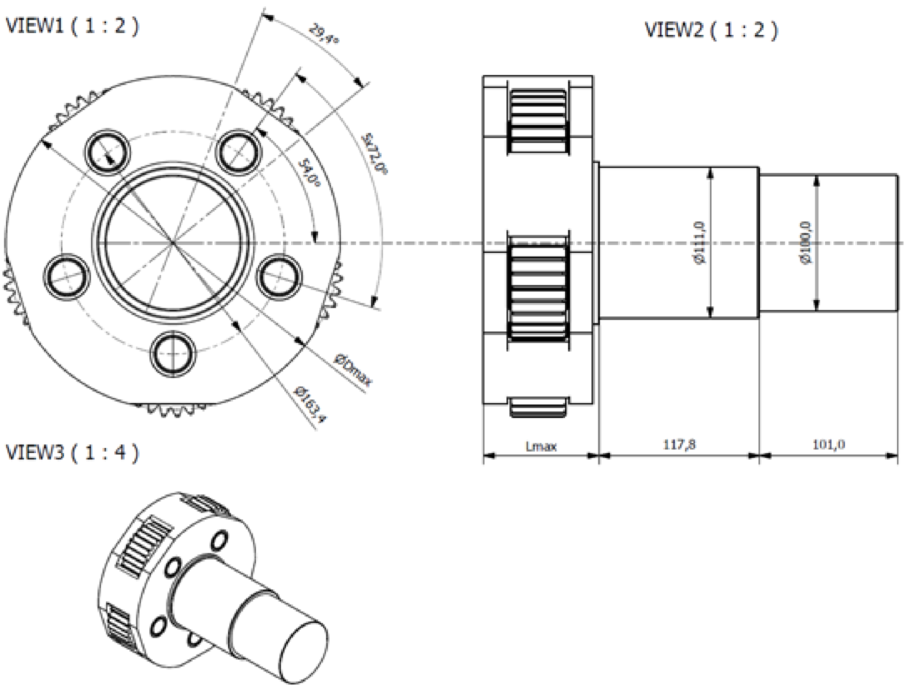

Fig. 4.2. Defined space envelope of planet carrier

The design of the carrier is very much determined by technology used to manufacture and it creates numerous design limitations. Therefore, in case of this work it is assumed that the both carriers are made from two forging pieces of alloy steel, then heat treated, machined and welded using a laser welding process. This welding technology is currently available on a market and a defined weld depth of 10 mm is completely feasible. Additionally, the laser welding ensures a stability in the manufacturing process, which translates directly to better product quality.

Table 4.1. Input data used to design planet carrier, see Figure 4.2

Input Data	Value	Remarks
Maximum input torque of the planetary gear train, Nm	9500	Fixed value
Number of the planet gears	5	Fixed value
Number of teeth of sun gear	25	Fixed value
Number of teeth of sun planet	28	Fixed value
Number of teeth of ring gear	85	Fixed value
Centre distance between sun and planet gears	81.7	Fixed value
Maximum diameter of plane carrier D_{max}, mm	248	Maximum material without planets gears
High of planet carrier L_{max}, mm	100	Maximum material
Minimum required safety factor against fatigue strength at 50% of maximum torque	1.2	Minimum required
Maximum angular displacement of planet carrier at 50% of maximum torque, min	2.5	For the planet carrier crown itself only.
Material of planet carrier	SAE 8620	Or similar material according EN standard

4.1.1. Input data

The following input data set in Table 4.1 and Fig. 4.2 was used to design the planet carrier; the data corresponds to the heavy-duty gearboxes and their manual versions. The commercial heavy-duty gearboxes are characterized by the input moment for 1400 Nm up 3300 Nm, and GCW (gross combination weight) between 20 - 60 tones.

4.1.2. Manufacturing aspects of planet-carrier

The carrier has a complex mechanical part; therefore, its production is expensive. Typically, the carrier is made by forging from two pieces, which are machining, then welding, and then again machining. The welding process can be different; it can be a standard arch welding method as well as a laser welding. It is assumed in the presented work that the planet carrier is made using the described process with the laser welding with a depth of maximum 10 mm. The location of the weld is placed in the middle of the carrier as it is shown in Fig. 4.3.

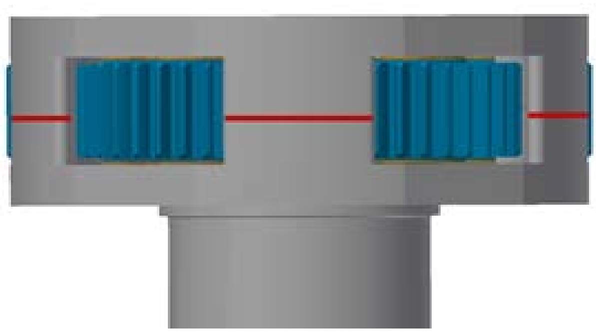

Fig. 4.3. Weld location in planet carrier reference

4.2. Analysis method

The analysis method depends on an estimation of a targeted shape of the planet carrier using the topology optimization with an objective to maximize the torsional stiffness. Then, steps of an interactive process of designing and FE analysis are done so to get the design of the carrier according to required constrains. In the presented work steps with shape and fatigue analyses were omitted because the elaborated design basing on the first step optimization is satisfactory in terms of the obtain stress levels, see Fig. 4.12. As further check, fatigue analysis could be done if a duty cycle is known. In the presented work the duty cycle is not defined therefore the fatigue analysis is not performed. The duty cycles are completely determined by used applications of the gearbox and without a deep analysis of the application is very hard to find the right cycle loading.

All calculations are done for two designs of the carrier; one called a standard design and the other one - the improved design defined basing on the topology optimization. The loads and the boundary conditions are the same for all analyses. Moreover, there is a requirement that the both designs must have the same mass. As a result, a comparison is made between them in terms of the stress levels and the torsional stiffness and the stiffness is metric, which is used to measure a design improvement.

The topology optimization was done using the commercial software SolidThinking Inspire (Altair Corporation) the rest of the calculations using the finite element methods were done ANSYS 15 [4.4] and 3D modelling was done using Autodesk Inventor 2015.

A material model is linear isotopic since allowable stresses must be lower than the fatigue strength. The nonlinearity is introduced in the FEA model through a contact definition. The fictional contact with friction coefficient of 0.1 is used.

The FEA was conducted only a one fifth of the carrier and asymmetry conditions were used in the cutting planes since the applied load is asymmetric. The FEA analysis is done in two steps first to get required press-fit between the carrier and the axle and then the bearing load is applied on the axle.

The details of the math models are presented in the next chapters of this paper.

Table 4.2. Material mechanical properties [4.2]

Material	Yield strength, [MPa]	Tensile strength, [MPa]	Fatigue strength at 10^6 Cycles, R=-1, [MPa]	Hardness, HRC	E, [MP]a	Poisson's ratio
Alloy steel, SAE 8620 (Quench Medium)	~690	~990	~380	35	2.12 10^5	0.3

4.2.1. Material properties

The planet carrier and the axles are made from alloy steel and the heat treatment of the planet carrier is planned to get the mechanical properties as shown in Table 4.2. The axle is not taken into any assessment, therefore the heat treatment and stress limits are not set up for the axle. The isotopic linear material model was used during calculations since the acceptable stress levels are limited only to elastic range. Alloy steel. SAE 8620 was selected as the material for the carrier as it is a standard material for gears and shafts in commercial vehicles. The material is assumed to be heat treated to get the required strength, which translates to hardness requirements of 35 HRC.

4.2.2. Topology optimization

An initial model shown in Fig. 4.4 is used to conduct the topology optimization analysis; a design space and a fixed design were predefined in order to fulfil requirements concerning boundary conditions, which should be applied on the fixed design only. The design space is a space, which is subjected to material removal during an optimization process and in fact, it defines the envelope of the planet carrier design. The fixed design is the part of the model that is not subjected to any changes.

The used boundary conditions are shown in the Fig. 4.5 and they reflect real working conditions of the carrier. The green arrow in the figure means a degree of freedom, which is free on a particular surface. The full model of the carrier is used during the optimization process to check if an expected symmetric shape of the optimal design is obtained and this is an additional check of the math model.

Optimization parameters are summarized in Table 4.3, and the objective of the optimization process is to find a shape of the planet carrier with maximum torsional stiffness for the defined loads and for the given boundary conditions. The obtained shape of the carrier serves only to create a conceptual model for the iterative CAD-FEA analysis.

Table 4.3. Topology optimization parameters employed during the calculations

Input Data	Value	Remarks
Maximum input torque of the planetary gear train, [Nm]	+/-9500	Fixed value
Objective	Maximize stiffness	No value
Thickness constrains minimum	10 mm	Fixed value
Total design space volume	30%	
Contacts	bounded	No separation
Applied gravity	no	

Stress constantans are not requested, because further FEA analyses of the designed carrier are conducted where the stress levels are precisely determined and controlled by the created geometry.

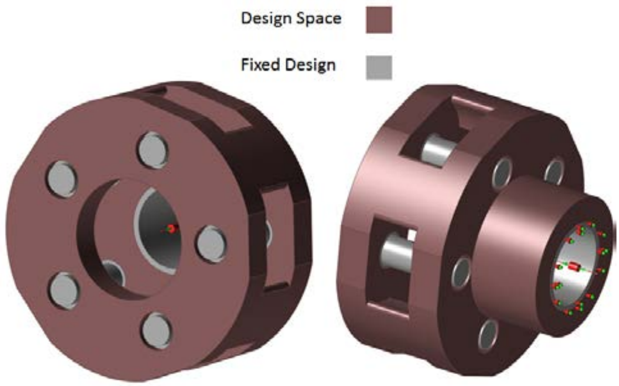

Fig. 4.4. Initial model for topology optimization

The contact definition between the design and fixed space is defined during the topology optimization employing a bounded contact see Fig. 4.5. This means that all bonding surfaces in the defined contacts are glued together.

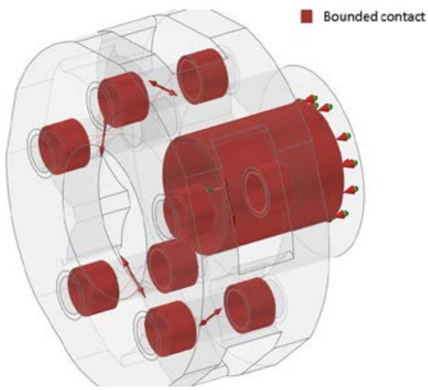

Fig. 4.5. Contact definition between model components

4.2.3. Results of topology optimisation

An obtained shape of the carrier is shown in Fig. 4.6 and this shape approximates somehow the real carrier design, because manufacturing constrains and the press-fit load should be taken into account. All these aspects are included in the final design of the carrier shown in Fig. 4.7.

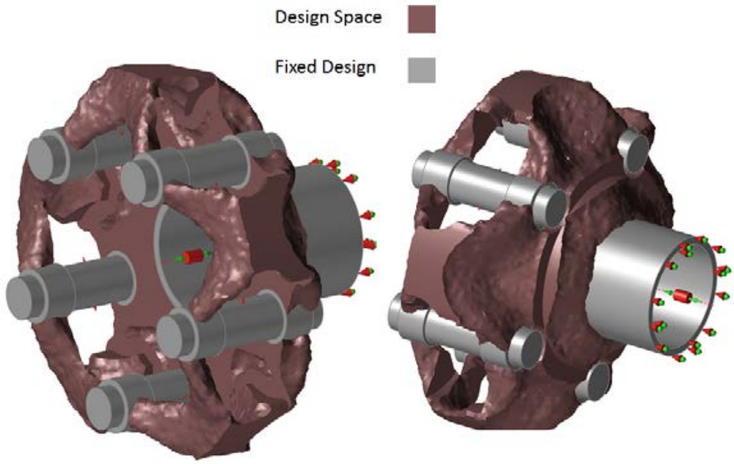

Fig. 4.6. Results of topology optimization with target of 30% of initial volume

4.2.4. Concept design based on topology optimization results

The obtained concept model of the carrier was used to design a realistic model where manufacturing and other requirements were taken into account. This model was analysed basing on a standard iteration process of FEA and redesigned in order to meet the requirements concerning stress levels and the manufacturing aspects. In the presented work, only two iterations are conducted to get the final carrier design. The elaborated design carrier is shown in Figure 4.7b and it can be seen that the shape is much different from the standard design shown in Fig. 4.7a.

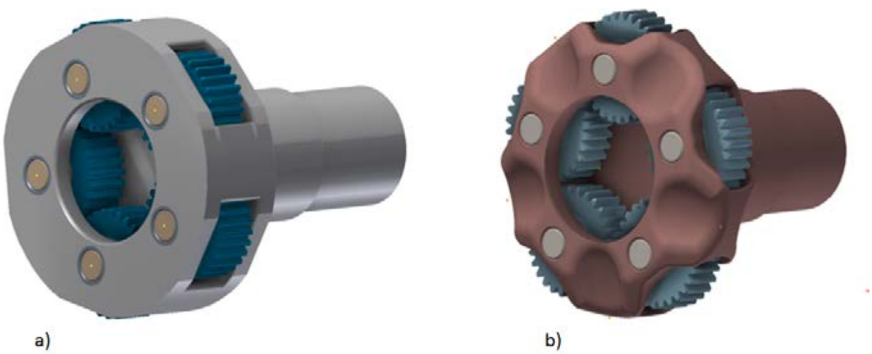

Fig. 4.7. Two concept designs: a) standard design, b) concept design basing on topology optimization

4.2.5. FEA models

The finite element model recalls the model used for the topology optimization in terms of the loads and the boundary conditions. A small change can be seen, namely the final model of the carrier is integrated with an output shaft, and this does not have any influence on the level of the stresses and the stiffness of the carrier. Additionally, only one-fifth of the model is used because the load is asymmetric and the geometry has five symmetry planes. This procedure helps speeding up the calculations without losing a precision see details in Figure 4.8. As well, second order elements are employed to get a precise stress estimation. The FEA configuration parameters are shown in Table 4.4. The load corresponding of 50% of the maximum torque is applied as a bearing load on the axle as shown in Fig. 4.9.

Table 4.4. Analysed components, assigned materials, and FEA element type

Materials	Material	Element Type
Planet Carrier	SAE 8620	Tet10
Axles	SAE 8620	Hex20, Wed15, Pyr13

Fig. 4.8. Finite element model of concept design of planet carrier

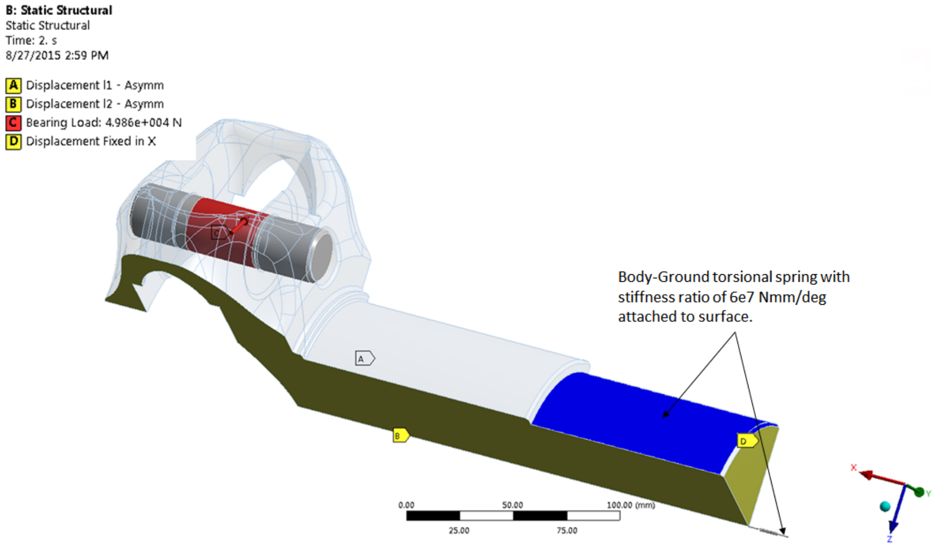

Fig. 4.9. Load and boundary conditions

4.2.6. Press-fit between planet axles and planet carrier

The press-fit connection between the planet axle and the carrier was modelled in order to take into account a stiffness benefit obtained by this connection. The calculations were made for two values of the interference fit: maximal and minimal interferences. Applied tolerances are shown in Table 4.5 and the maximum interference is 0.028 mm and the minimum one of 0.002 mm.

Table 4.5. Tolerance between planet carrier holes and axles

Parts	Planet carrier holes	Axles
Nominal dimension, [mm]	26	26
Top, [mm]	+0.013	+0.028
Low, [mm]	0	+0.015

4.2.7. Solution

The problem is numerically solved using the finite element method and the calculations are made using the commercial software ANSYS 15 [4.4]. The conducted analyses are nonlinear due to implementation of a realistic fictional contact between the carrier and the planet axle. The fiction coefficient of 0.1 is used in the defined contact between hard steel over hard steel.

The material model is linear because the acceptable stress level is below the yield strength, which unambiguously means that linear material model is sufficient.

As it was explained, the FE analysis was done in two steps in the first the interference fit is implemented and in the second step when the bearing is applied. This method allows calculating an alternating stresses due to the applied torque and a mean stress produced by the interference fit. The alternating stress is taken for the further structural assessment as a more dangerous for the carrier and causing fatigue failure. It is good to emphasize here that the carriers fail normally due to fatigue fracture. As it was said, in order to make any fatigue estimation, the duty cycle is required. In the presented case, the duty cycles is unknown therefore the safety factor of 1.2 for the alternating stress is requested in reference to fatigue strength.

4.3. Results and discussion

The shown design method basing on the topology optimization with the final tuning using the standard finite element method can be easily implemented for designing complex mechanical parts. Thanks to the topology optimization, the new carrier has the greater torsional stiffness adequately for maximum and minimum interference by 17.3% and 19.8% than the standard design keeping the same mass. The developed carrier is shown in Fig. 4.10.

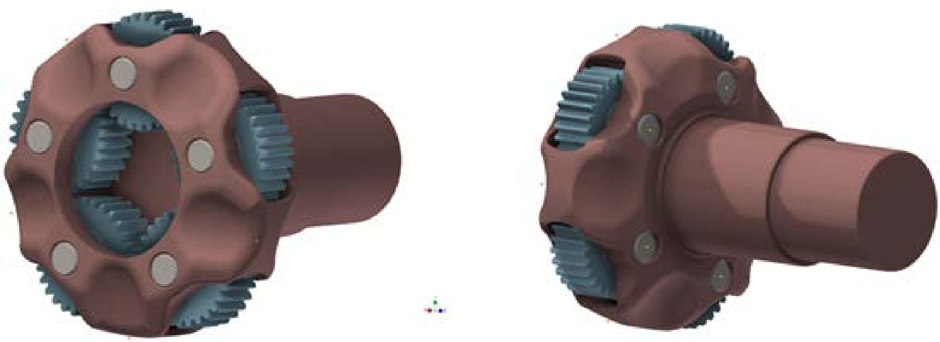

Fig. 4.10. Final concept design of the planet carrier

The obtained stiffness benefits may be unimpressive, but it should be taken into account that any stiffness gain of the carrier brings advantage in terms of a longer lifetime of planetary train gears. Moreover, the elaborated concept model has significantly a better stress distribution without any stress concentration, which also improves the lifetime of the carrier. The proposed shape of the carrier differs significantly from the standard design and without the topology optimization it is almost impossible to design it.

The standard design of the carrier has major stress concentrations due to the usage of the manufacturing process of welding and thus the defined geometry. The stress concentration locations are shown in Fig. 4.11. These areas can be places of an initiation of fatigue fractures and the worst location is the ending of the weld where the gradient of the stress is the largest. The best solution is to eliminate this problem if there is such a possibility. Unfortunately, very often the stress concentrations are accepted because the failure fatigues are not observed during a particular fatigue test. The tests are normally limited in number of cycles because of costs and they reflect only the selected duty cycles. Often, the fatigue tests are accelerated and a level of the load is inappropriate; that can make failure modes not realistic. Therefore, the best option is to remove the geometric stress concentrations especially if they are located close to the welds because the material is the weakest there.

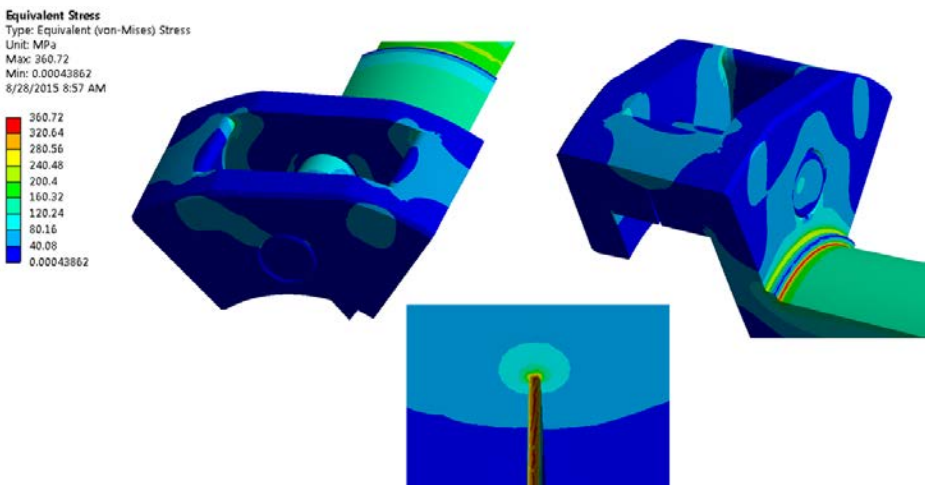

Fig. 4.11. Alternating von Mises stresses for maximum interference for standard planet carrier

The new carrier does not have this problem because its shape is properly designed to avoid any stress concentrations. Moreover, a thickness of the carrier in a place where the weld is located is reduced to get a full through wall weld. The required safety factor of 1.2 is achieved with the new carrier design as shown Fig. 4.13.

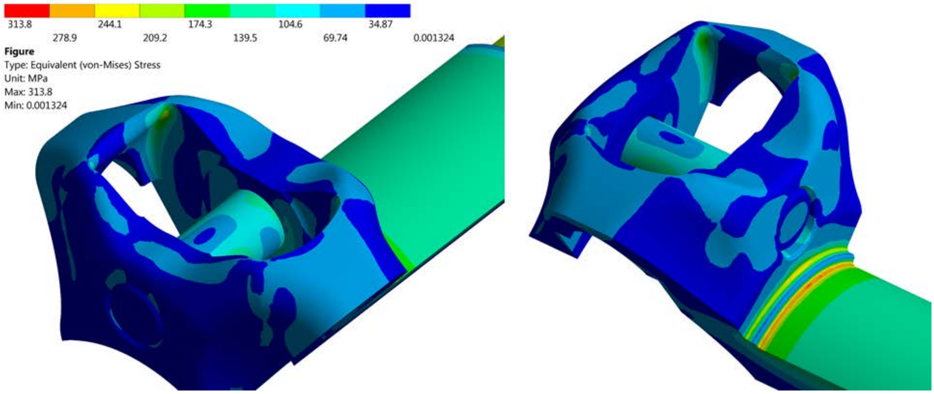

Fig. 4.12. Alternating von Mises stresses for maximum interference for new concept planet carrier

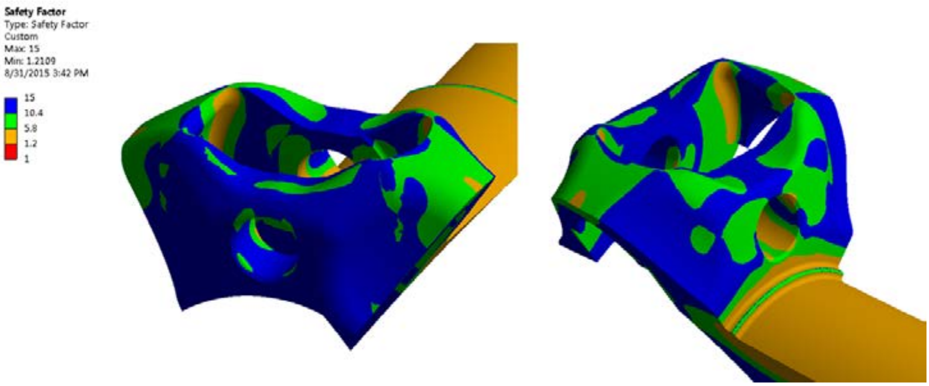

Fig. 4.13. Safety factor (alternating stress/fatigue strength) for new planet carrier

Fig. 4.14. Total displacement for maximum interference for new concept planet carrier

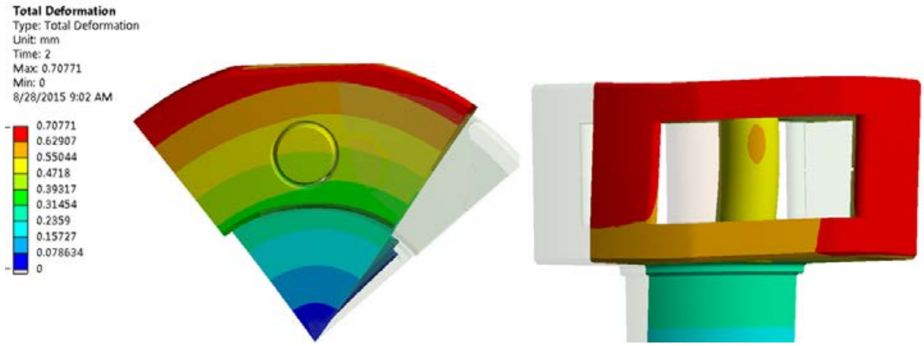

Fig. 4.15. Total displacement for maximum interference for standard planet carrier

The torsional stiffness is calculated as a ration of the applied torque divided by the relative twist angle between two axle holes of the planet carrier, Fig. 4.16.

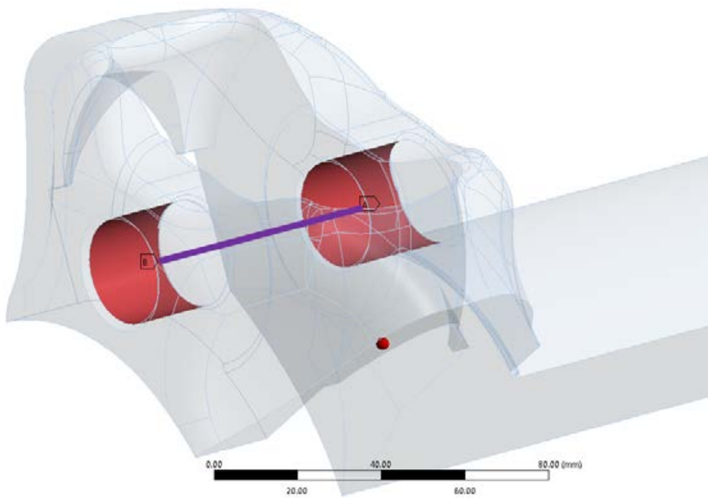

Fig. 4.16. Points: A and B used to calculate stiffness of planet carrier

The comparison results are presented in Tables 4.6 and 4.7, the torsional stiffness improvement is adequately 17.3% and 19.8% for the maximum and minimum interference is obtained. The obtained results are satisfactory taking into account the design stiffness requirement. The applied method gives the satisfactory results meeting the initial goals. The improvement can be seen as small but it should be considered that the torsional stiffness of the planet carrier is crucial for the sustainability of the planetary gear train. Therefore, the gain improvement is fully satisfactory. Moreover, the comparison is made with the very stiff standard design, which makes the new design more attractive.

Fig. 4.17 shows the comparison of the dimensionless torsional stiffness for both carriers and for the maximum and minimum interference fit between the axle and the carrier. It can be clearly seen that the new carrier has greater stiffness about 20% independently from the implemented interference fit. Obviously, the greater interference fit brings the extra stiffness improvement and this can be used to gain the additional stiffness by smart selection of the tolerances for the carrier and the axles.

Table 4.6. Torsional stiffness of both planet carrier designs

	Torsional stiffness, [N mm/deg]		Geometry parameters Table 4.1		
Design	Max interference	Min interference	D_{maxy}, [mm]	L_{max}, [mm]	Mass, [kg]
Standard design	1.785E6	1.473E5	245.0	84.5	27.9
New concept design	2.158E6	1.835E6	248.0	99.0	27.3

Table 4.7 Angular deformation

	Torsional angular deformation at 50% of maximum torque, [deg]	
Design	Max interference	Min interference
Standard design	2.66	3.23
New concept design	2.20	2.59

4.4. Conclusions

Based on the conducted analyses the following conclusions can be drawn:

- SolidThinking Inspire software is a topology optimization tool, which can significantly improve the concept design of mechanical parts aiding to design more robust and therefore better mechanical parts;
- Thanks to an application of the topology optimization, the stiffness of the proposed planet carrier can be improved by about 20%, see Fig. 4.17;
- The proposed analysis method is efficient and can be implemented in any design office. Calculation time and computer power are not any limitations. The whole analyses can be done on a CAE/CAD workstation in a few hours;

- The entire process is straightforward and therefore to be easily implemented in design offices. The method is of practical value for industrial interest;
- The extra torsional stiffness of the carrier can be achieved by the tighter tolerance between the axles and the carrier.

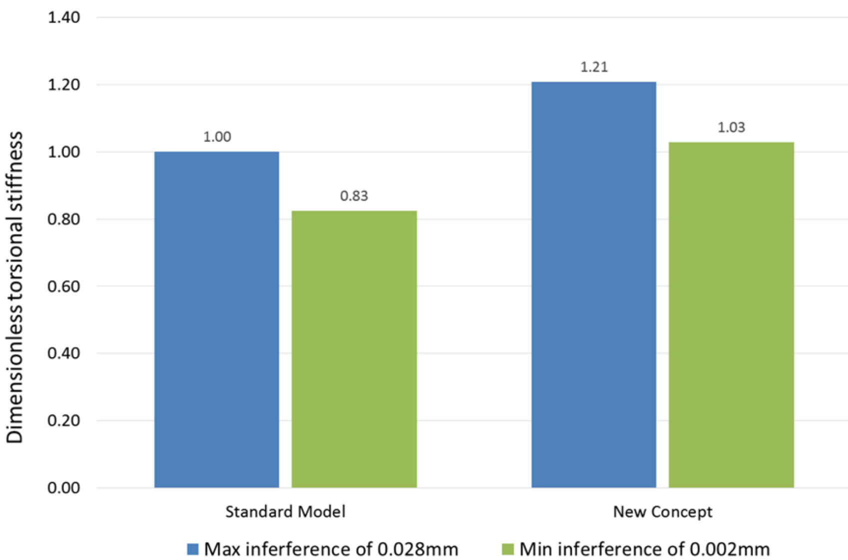

Fig. 4.17. Comparison between both designs of planet carrier at 50% of maximum torque

4.5. References

4.1 Belegumdu A.D., Chaandrupatla T.R., Optimization concept and application in engineering, second edition, Cambridge University Press, 2011.

4.2 Online material database, Steel Market Development Institute's Bar Steel Fatigue Database: http://barsteelfatigue.autosteel.org/

4.3 Online presentation of FE-DESIGN GmbH, Weight reduction of a planet carrier with stiffness requirements: http://resource.ansys.com/staticassets/ANSYS/staticassets/partner/FEDesign/Application_TOSCA_ANSYS_Optimization%20of%20a%20Planet-Carrier.pdf

4.4 User's guide ANSYS 15, ANSYS Inc., Houston, USA.

4.5 User's manual SolidThinking Inspire 2015.

4.6 Xie Y.M., Steven G P., Evolutionary Structural Optimization, Springer-Verlag, London 1997.

5.

Elastic-plastic stability of FML panel and columns of open and closed cross-section

5.1. Introduction

In the last few decades of the past century a rapid development of research on post-buckling behaviour of thin-walled structures in the elastic and elastic-plastic range until fracture took place. There are numerous publications concerning mainly singular isolated plates of different isotropic material properties. There are relatively few works dedicated to plate structures made of composite and/or laminate materials [5.2÷5.4, 5.7, 5.16]. In the last years, due to widespread of professional Finite Element Method software application, several publications appeared where full force-shortening curves of structures were determined. It concerns structures with a complex cross section made of different materials - also including orthotropic material [5.9, 5.14, 5.15].

In few works [5.6, 5.7, 5.13] the authors show the solution to the stability problem of thin-walled columns made of isotropic and orthotropic materials in elastic-plastic range. In the current study analogous issue for multi-layered materials of Fiber Metal Laminate type is considered.

Fiber Metal Laminates (FMLs) are hybrid materials, built of thin layers of metal alloy divided by layers of fiber reinforced epoxy resin. These materials are manufactured by bonding composite plies to metal ones mostly in an autoclave process. FMLs, when refers to metal layers, can be divided into FMLs based on aluminium alloys (ARALL - laminated with aramid fibers, GLARE - glass fibers, CARALL - carbon fibers) and others. Nowadays materials such as GLARE grades (glass fiber/aluminium) due to their very good fatigue and strength properties combined with the low density have been finding increasing application in an aircraft industry [5.17].

GLARE consists of alternate aluminium sheets and unidirectional high-strength glass fiber layers pre-impregnated with adhesive. Usually each glass composite layer is composed of a certain number of unidirectional (UD) plies which are stacked either unidirectionally, in a cross-ply or angle-ply arrangement. The number of layers, plies orientation and the stacking sequence of the UD plies in the entire FML panel depend on the GLARE grade. For example, a GLARE 2 has two UD plies in a particular composite layer with the same 0-degree orientation, while a GLARE 3 has two mutually perpendicular UD plies (cross-ply arrangement). The most common type of aluminium applied in GLARE is 2024-T3 Alloy.

In current investigation it is assumed that the material of particular structure is GLARE 3 [5.10, 5.11] with an even number of glass reinforced layers, whereas the outer layers are always of aluminium. Thus the number of glass prepreg layers is always one less than the number of metallic ones. The overall laminate is symmetric with reference to the midplane. The thickness of each UD GFRP ply is 0.125 mm, so that the doubled prepreg layers of both Glare 2 and 3 grades have a total thickness of 0.25 mm.

The orthotropic glass fiber prepreg properties of a 0/90 degree (cross-ply) combination allow in the conducted here analysis to consider the composite doubled layer as one isotropic layer. Furthermore, the small anisotropy of the rolled aluminium sheet observed only for yield limits is not taken into account.

The overall dimensions of considered structures are chosen in such a way that the stability loss occurs in the elastic-plastic range for aluminium layers. Elastic-plastic moduli are used for the aluminium layers in combination with the Ramberg-Osgood (RO) curve fitting method for the stress-strain behaviour [5.7, 5.14].

When the plate structure made of GLARE is subjected to in-plane uniform compression in the elastic-plastic range of stresses, the buckling occurs in such a way that the aluminium layers become plastic but the glass fiber layers remain elastic. Therefore the behaviour of such structures differs significantly from the behaviour of pure aluminium ones.

5.2. Method of solution

The problem of buckling in the elastic-plastic range of thin-walled FML columns, axially uniformly compressed, is examined using the analytical-numerical method (ANM) elaborated for the analysis of the elastic stability of multi-layered thin-walled columns [5.8]. The constitutive relationships between stress and strain for a singular elastic-plastic component layer is derived on the basis of the J2-deformation theory of plasticity (i.e. DT) or the J2-flow theory (incremental theory of plasticity i.e. IT) for Ramberg-Osgood formula.

An assumed for consideration material of FML metallic layers in the elastic range is simply defined as:

$$\sigma = E\varepsilon \quad \text{for} \quad \sigma \le \sigma_0 \tag{5.1}$$

whereas the elastic-plastic stress-strain behaviour of FML aluminium layer is described by a Ramberg-Osgood representation of the following type:

$$\sigma = \frac{(E-E_Y)\varepsilon}{\left[1+\left(\frac{(E-E_Y)\varepsilon}{\sigma_Y}\right)^N\right]^{\frac{1}{N}}} + E_Y\varepsilon \quad \text{for} \quad \sigma \geq \sigma_0 \tag{5.2}$$

where: σ - stress, ε - strain, E - Young's modulus, σ_0 - proportional limit, σ_Y - conventional yield limit, E_y - tangent modulus corresponding to the yield limit σ_Y, N - exponent in the Ramberg-Osgood formula. The orthotropic composite layers are assumed to have elastic properties due to linear stress-strain characteristic up to fracture.

For any orthotropic plate the constitutive relationships for the elastic range and the elastic-plastic range have very similar or even identical form (Eq. 5.3):

Elastic range	**Inelastic range**
$\sigma_x = K_{11}\varepsilon_x + K_{12}\varepsilon_y$	$\sigma_x = A_{11}\varepsilon_x + A_{12}\varepsilon_y$
$\sigma_y = K_{12}\varepsilon_x + K_{22}\varepsilon_y$	$\sigma_y = A_{12}\varepsilon_x + A_{22}\varepsilon_y$
$\tau_{xy} = K_{33}\gamma_{xy}$	$\tau_{xy} = A_{33}\gamma_{xy}$

(5.3)

Comparing the appropriate coefficients in both relations the instantaneous conventional parameters of 'elastic composite' for particular layers of entire FML structure can be found out. Thus the problem of inelastic stability of FML structures can be investigated in the analogous way as the problem of elastic composite structures. The coefficients $A_{11} - A_{33}$ (Eq. 5.3) determined on the basis of the J_2- deformation or J_2- flow theory of plasticity depend on the appropriate Young's modulus, secant and tangent moduli for the considered material layer characteristics in the inelastic range.

The analysed problem is solved in a numerical way. The elastic problem is solved by the asymptotic Koiter's theory [5.5], formulated by Byskov and Hutchinson [5.1]. The solution of the first order approximation enables one to determine the values of buckling global and local loads and the corresponding buckling modes. This analytical-numerical method [5.7, 5.8, 5.12] created to solve the elastic problem is applied here to calculate critical load values and buckling modes for inelastic thin-walled FML columns and panels. For a given geometrical parameters, material data constants of particular FML layer and for the assumed number of buckling half-waves, the elastic buckling stress for the considered composite structure is calculated. The most important advantage of this method is that it enables one to describe a complete range of a buckling behaviour of thin-walled structures from a global (i.e. flexural, flexural-torsional, lateral, distortional buckling and their combinations) to a local stability, including a mixed buckling modes [5.7, 5.8, 5.12].

Furthermore, a zero value of the function $f = f(\sigma - \sigma_e)$ is searched to apply the method of secants, where σ_e is the value of the critical stress of the “elastic orthotropic” structure. During the computations it is assumed that $\sigma \approx \sigma_e$, when $(\sigma - \sigma_e)\cdot 100\% / \sigma \le 0.01\%$.

The proposed method allows to consider the transition of buckling mode together with the increase of loading as distinct from the usual assumption that the elastic-plastic buckling mode is analogical to the elastic one.

For a given geometrical parameters, material constants of each FML layer and for the assumed number of buckling half-waves the elastic buckling stress for the considered composite structure is then calculated.

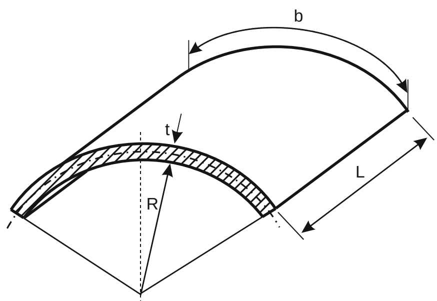

Fig. 5.1. Cylindrical shallow panel geometry

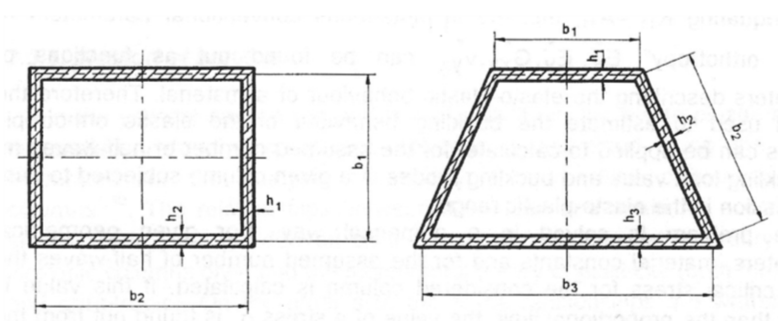

Fig. 5.2. Closed cross-sections analysed columns

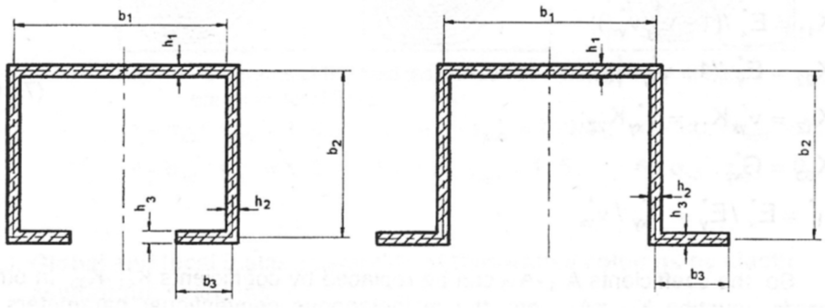

Fig. 5.3. Open cross-sections analysed columns

5.3. Some results of calculations

As some examples of proposed method of solution to the elastic-plastic problem of thin-walled FML hybrid composite structure a shallow cylindrical panel and a complex plate structure has been considered (Fig. 5.1÷5.3). It was assumed that the loaded edges of considered structure are simply supported at both ends. In order to account for all modes of global, local and coupled buckling, a plate model of thin-walled structure has been employed. As it was mentioned previously the overall dimensions of selected structures are chosen in such a way that the stability loss occurs in the elastic-plastic range for aluminium layers.

In presented work the detailed analysis was performed for the four chosen FML members which overall and cross-section parameters were as follows:

- a cylindrical panel simply supported along all edges subjected to axial compression (Fig. 5.1): $R = 430$ mm, $L = 860$ mm, $b = 430$ mm,
- a beam/column profile with a square cross-section (Fig. 5.2a) and $L = 1300$ mm, $b = 130$ mm,
- a beam/column profile with a trapezoidal cross-section (Fig. 5.2b) and $L = 1300$ mm, $b_1 = 100$ mm, $b_2 = 140$ mm, $b_3 = 140$ mm,
- a beam/column profile with a top-hat (Fig. 5.3a) and a lip channel cross section (Fig. 5.3b); $L = 1300$ mm, $b_1 = 130$ mm, $b_2 = 65$ mm, $b_3 = 15$ mm.

In all cases L indicates the column length. Constructions under investigation are built of alternate aluminium sheets and unidirectional high strength glass fiber layers so this stacking corresponds to GLARE 3 grade with 2024-T3 sheets [5.11, 5.18]. The total number of layers in considered material equals 13 what leads to the total wall thickness of column/panel wall equal to $t = 4.3$ mm where the thickness of singular aluminium sheets equals 0.4 mm and particular doubled fiber layer 0.25 mm. Mechanical properties of both isotropic layers are presented below in Table 5.1 [5.10, 5.18].

Table 5.1. Material data of GLARE 3-7/6-0.4 (13 layers) [5.18]

Material data of GLARE 3-7/6-0.4	Elastic properties			Plastic properties		
	Young's modulus	Poisson's ratio	Proportional limit	Yield limit	Tangent modulus	Exponent in Eq. (3)
	E	ν	σ_0	σ_Y	E_Y	N
	[GPa]	[-]	[MPa]	[MPa]	[MPa]	[-]
Al 2024-T3	700	0.3	170	290	12.1	1.8
Prepreg	30.75	0.144	-	-	-	-

Obtained results of the critical stress σ_{cr} calculations for the considered thin-walled FML structures (Figs. 5.1÷5.3) are shown in Figs. 5.4,5.7,5.10,5.13,5.17, respectively. Applied into the analysis three plasticity theories are distinguished in these figures as: elastic theory EL, J2-deformation theory DT and J2-incremental theory IT. For considered FML's cross-sections a stability loss can occur under symmetry (S) and anti-symmetry (A) conditions along symmetry axis of the cross-section. In the plots determined critical stress values are presented as a function of the number of half-waves m formed in the longitudinal direction. The lowest values of σ_{cr} are summarized in Tables 5.2÷5.6. The buckling modes of analysed FML structures are also presented in Figs. 5.5,5.6,5.8,5.9,5.11,5.12,5.14÷5.16,5.18÷5.20.

5.3.1. Cylindrical panel

In Figs. 5.4÷5.6 and Table 5.2 computation results for the cylindrical shallow panel are presented. According to defined above geometrical data analysed panels were of a short type because $L/R=2$ and $R/b=1$, respectively.

The lowest values of critical stresses σ_{cr} were obtained for $m=1$ in the case when the symmetry conditions at symmetry axis (i.e. S) were assumed, while for the assumption of asymmetry conditions (A) the number of half-waves was $m=2$. Determined values of critical stresses σ_{cr} for elastic-plastic range are lower than for elastic material behaviour. For deformation theory (DT) lower values of critical stresses were obtained in comparison to incremental theory (IT). This is a general, well-known from the literature relationship of results for both theories of elastic-plastic formulation.

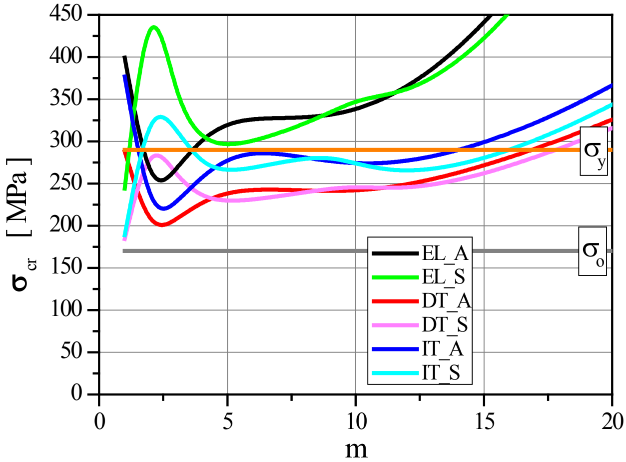

Fig. 5.4. Buckling stress σ_{cr} versus number of half-waves m for symmetry and antisymmetry conditions imposed along cross-section symmetry axis for shallow panel (σ_Y - aluminum yield limit, σ_0 - proportional limit)

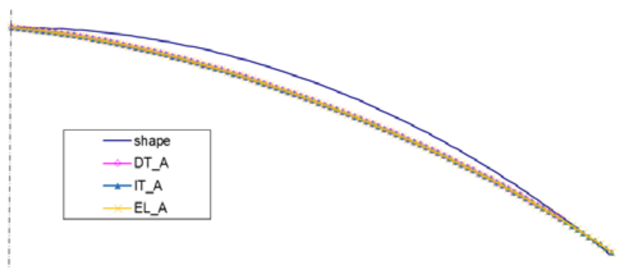

Fig. 5.5. Shapes of local antisymmetric (A) buckling modes for elastic (EL) and inelastic range (DT, IT) for panel

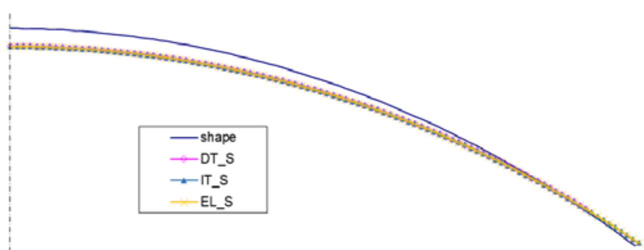

Fig. 5.6. Shapes of local symmetric (S) buckling modes for elastic (EL) and inelastic range (DT, IT) for panel

Revealed local buckling modes (Figs. 5.5, 5.6) of all three considered plasticity theories are very similar for each other for both assumed symmetry conditions at symmetry axis.

Table 5.2. Panel buckling stress and modes

Elastic range EL		Elastic-plastic range DT		Elastic-plastic range IT		Conditions along symmetry axis of cross-section
σ_{cr} [MPa]	m	σ_{cr} [MPa]	m	σ_{cr} [MPa]	m	
244	1	184	1	188	1	S
233	2	190	2	205	2	A

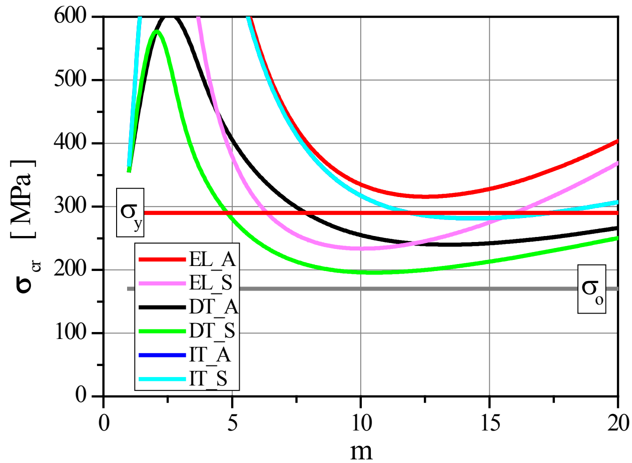

Fig. 5.7. Plots of buckling stress σ_{cr} versus number of half-waves m for a column of square cross-section

5.3.2. Closed cross-sections

In the following analysis the length of considered columns was assumed as $L = 1300$ mm. Thus for these overall dimensions (Fig. 5.2) only local buckling modes should be considered due to significantly higher values of global buckling critical stresses in comparison to the yield limit σ_Y (see Table 5.1).

Square cross-section

The plots in Fig. 5.7 present critical stress values σ_{cr} for the square cross-section from Fig. 5.2a. Particular curve corresponds to particular plasticity theory and gives the σ_{cr} value as a function of half-waves number in longitudinal direction of the compressed column. In Table 5.3 the lowest values of critical stresses for considered symmetry conditions on symmetry axis are shown for comparison. Critical stress values σ_{cr} for symmetry conditions (S) are lower than for anti-symmetry conditions, as it was expected. The lowest value of critical stress σ_{cr} was obtained with deformation theory (DT) application. From Table 5.3 it is clearly visible that the number of half-waves corresponding to the lowest value of σ_{cr} is different for elastic theory (i.e. $m = 14$) from those of deformation theory (i.e. $m = 13$). Both local buckling modes determined for considered theories are very similar for assumed boundary conditions (Figs. 5.8, 5.9).

Table 5.3. Square cross-section

Elastic range EL		Elastic-plastic range				Conditions along symmetry axis of cross-section
		DT		IT		
σ_{cr} [MPa]	m	σ_{cr} [MPa]	m	σ_{cr} [MPa]	m	
232	10	195	10	219	11	S
315	13	239	13	280	14	A

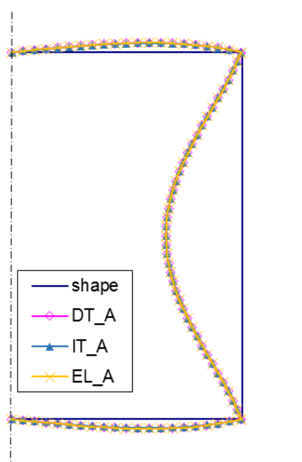

Fig. 5.8. Shapes of local antisymmetric (A) buckling modes for elastic (EL) and inelastic range (DT, IT) for square cross-section

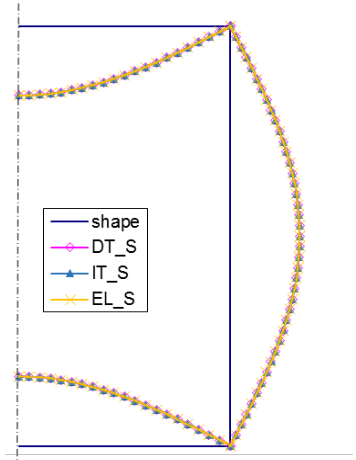

Fig. 5.9. Shapes of local symmetric (S) buckling modes for elastic (EL) and inelastic range (DT, IT) for square cross-section

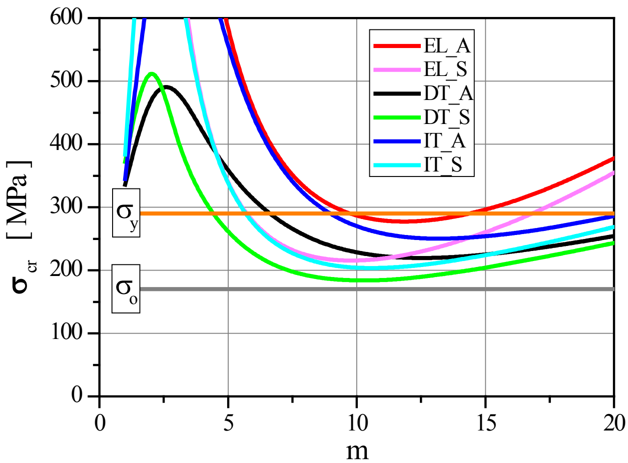

Fig. 5.10. Buckling stresses σ_{cr} versus number of axial half-waves *m* for trapezoidal cross-section

Trapezoidal cross-section

For the trapezoidal cross-section from Fig. 5.2b, there are critical stress values σ_{cr} as a function of half-waves number in longitudinal direction presented in Fig. 5.10 for all considered plasticity theories. Further, in Table 5.4 the lowest values of critical stresses for considered boundary conditions on symmetry axis are given. The local buckling modes for assumed boundary conditions are shown in Fig. 5.11 and 5.12. The conclusions from the elastic-plastic analysis of FML columns of the trapezoidal cross-section are very similar to the previous comments formulated for the square cross-section FML column. When the final results of square and trapezoidal cross-section columns are compared one can observed that the critical stress values are lower for a trapezoidal-cross section column.

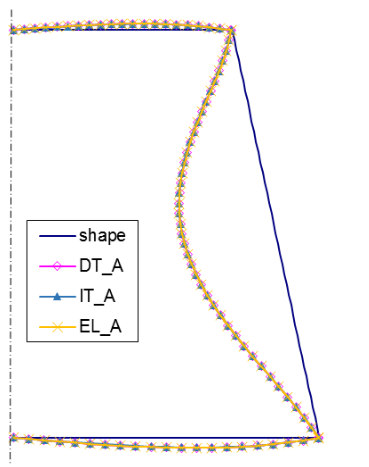

Fig. 5.11. Shapes of local antisymmetric (A) buckling modes for elastic and inelastic range for trapezoidal cross-section

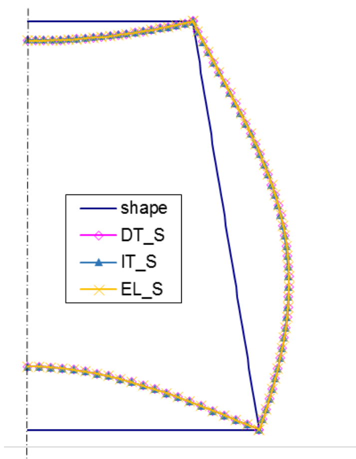

Fig. 5.12. Shapes of local symmetric (S) buckling modes for elastic and inelastic range for trapezoidal cross-section

Table 5.4. Trapezoidal cross-section results

Elastic range EL		Elastic-plastic range				Conditions along symmetry axis of cross-section
		DT		IT		
σ_{cr} [MPa]	m	σ_{cr} [MPa]	m	σ_{cr} [MPa]	m	
214	10	183	10	203	11	S
276	12	219	12	249	13	A

5.3.3. Open cross-sections

In the case of investigated open cross-section columns/profiles (presented in Fig. 5.3) i.e. top hat and lipped channel, for assumed overall dimensions all global buckling modes should be examined during the analysis. Thus flexural mode (S), distortional-flexural mode (S), flexural-torsional mode (A), distortion-flexural-distortional mode (A)) and local buckling mode including distortional-local modes, should be taken into account. Therefore additional indication is introduced for open cross-section profiles - global buckling mode (i. e. $m=1$) is denoted by G and local buckling mode (i.e. $m \geq 1$) by L.

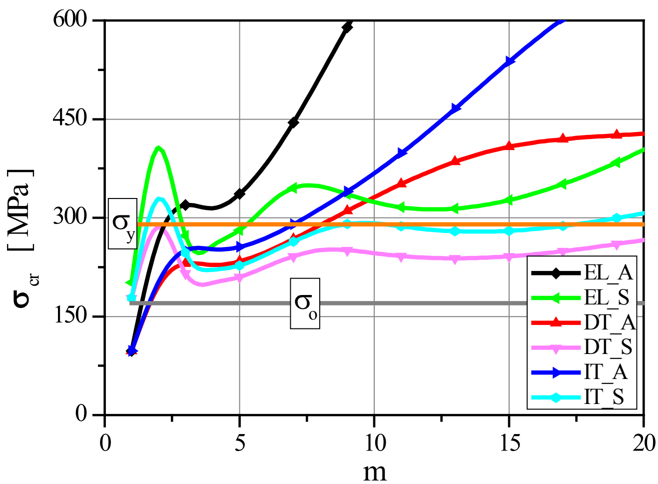

Fig. 5.13. Buckling stresses σ_{cr} versus number of axial half-waves m for top hat

Top hat

For the top hat cross-section columns/profiles (Fig. 5.3a) results of critical stresses as a function of half-waves number m are presented in Fig. 5.13. The lowest values of global and local critical stresses σ_{cr} are shown also in Table 5.5.

As it can be seen in this case a flexural-torsional global buckling mode (i.e. $m=1$, A) took place in the elastic range because the following relationship is fulfilled $\sigma_{cr}=97MPa<\sigma_0=170MPa$. While a flexural buckling is observed in the elastic-plastic range (i.e. $m=1$, S). Following this observation the flexural global buckling modes could be named as "pure bending" (Fig. 5.14) while anti-symmetry mode for elastic range is a distortional-flexural-torsional mode because the lips are not perpendicular to the flanges (see EL_A_G curve in Fig. 5.14).

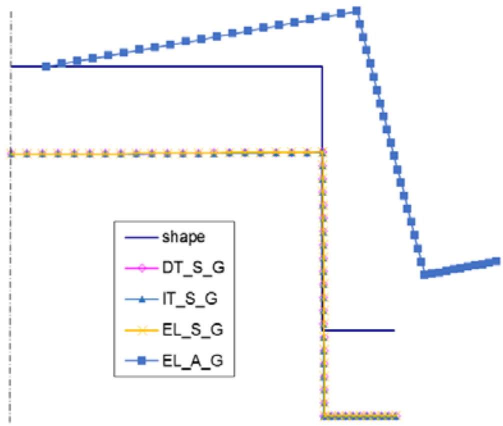

Fig. 5.14. Shapes of global buckling modes for top hat

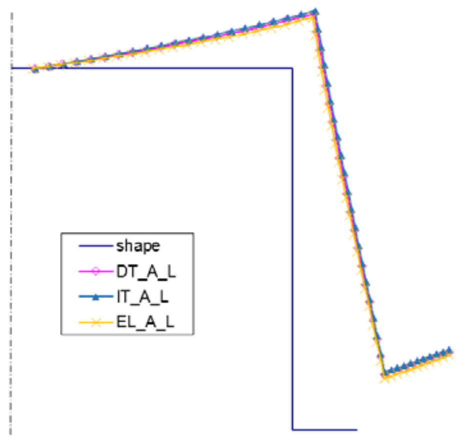

Fig. 5.15. Shapes of local anti-symmetric (A) buckling modes for a top hat profile

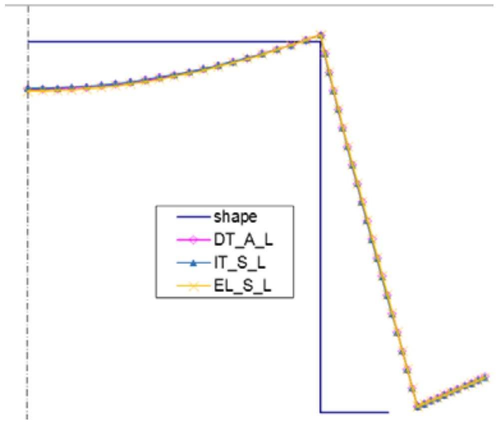

Fig. 5.16. Shapes of local symmetric (S) buckling modes for top hat profile

It can be seen in Table 5.5 that the value of the local critical stress σ_{cr} of symmetric mode (i.e. $m=4$, S) for elastic range is lower in comparison to a local anti-symmetric mode buckling stress (i.e. $m=2$, A) for elastic range. However, values of σ_{cr} for both elastic-plastic formulations and antisymmetrical modes are lower than the symmetric ones. For $m \geq 1$ buckling modes are distortional-local modes for both boundary conditions (Figs. 5.15, 5.16). Buckling modes are practically the same for each of applied theories.

Table 5.5 Top hat results

Elastic range EL		Elastic-plastic range				Conditions along symmetry axis of cross-section
		DT		IT		
σ_{cr} [MPa]	m	σ_{cr} [MPa]	m	σ_{cr} [MPa]	m	
201	1	177	1	178	1	S
257	4	201	4	220	4	S
97	1	-	-	-	-	A
267	2	196	2	202	2	A

Lipped channel

In Fig. 5.17 critical stress values σ_{cr} as a function of half-waves number m are presented for the FML column of lipped channel cross-section. Table 5.6 shows as well the lowest values of global and local σ_{cr} for both considered boundary conditions while corresponding to them buckling modes are given in Figs. 5.18÷5.20.

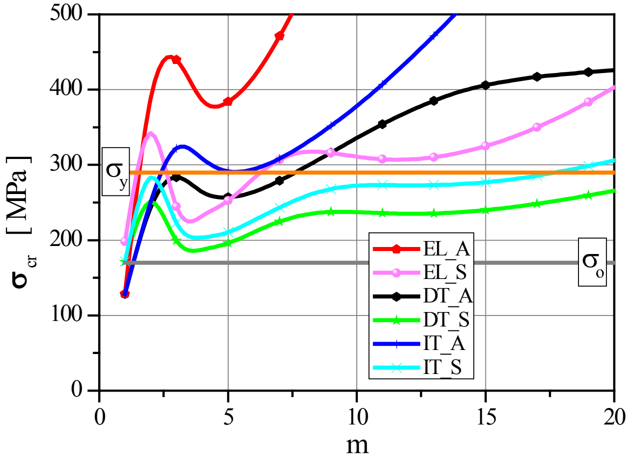

Fig. 5.17. Buckling stresses σ_{cr} versus number of axial half-waves m for lip channel column

The lowest value of critical stresses $\sigma_{cr} = 128$ MPa corresponds to a global flexural-torsional mode (i.e. $m = 1$, A) in elastic range (see EL_A_G line in Fig. 5.18). The global buckling stress value $\sigma_{cr} = 198$ MPa ($m = 1$, S) corresponds to a distortional-flexural buckling mode for elastic range (Fig. 5.18). Symmetric global buckling modes are similar for considered constitutive theories. Local buckling stress values are lower for symmetric modes in comparison to anti-symmetry ones.

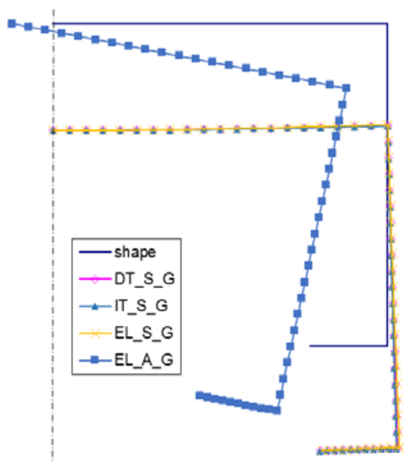

Fig. 5.18. Shapes of global buckling modes for lip channel

Presented in Figs. 5.19 and 5.20 buckling modes are of distortional-local symmetric and anti-symmetric type. It should be emphasized that local symmetric buckling modes (Fig. 5.20) differ slightly between themselves at the junction of flanges with the lips. In works [5.6, 5.11] for one-layered isotropic and orthotropic structures there was a lot of variety local and global buckling modes obtained which differed significantly between themselves for elastic and elastic-plastic range.

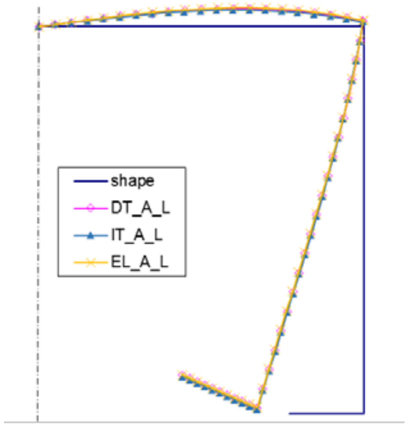

Fig. 5.19. Shapes of local anti-symmetric (A) buckling modes for lip channel

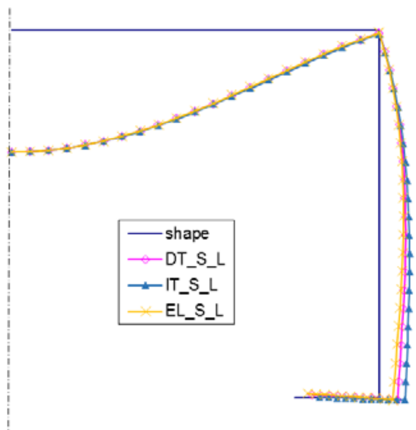

Fig. 5.20. Shapes of local symmetric (S) buckling modes for lip channel

As it can be seen from presented in current work buckling modes for FML multi-layered structures determined buckling modes differ at least slightly between themselves because particular elastic glass fibre layers work within elastic range. Thus mechanical properties of glass fibre layer remain unchanged in elastic-plastic range of entire FML wall, when aluminium layer changes own properties from isotropic to orthotropic. It makes that multi-layered structures are not as sensitive to changes of buckling modes as one-layered structures. The latter change their mechanical properties across whole thickness in the elastic-plastic range [5.6, 5.13].

Table 5.6. Lipped channel results

Elastic range EL		Elastic-plastic range				Conditions along symmetry axis of cross-section
		DT		IT		
σ_{cr} [MPa]	m	σ_{cr} [MPa]	m	σ_{cr} [MPa]	m	
198	1	176	1	177	1	S
232	4	187	4	203	4	S
128	1	-	-	-	-	A
383	5	256	5	291	5	A

5.4. Conclusions

In work the comparison of critical stresses for thin-walled FML structures in elastic and elastic-plastic range is presented. Two plasticity theories were considered i.e. J2-deformation theory and J2-incremental theory. The lowest values of critical stresses for all analysed structures were obtained in elastic-plastic range for the deformation theory. It is fully consistent with results presented in literature survey. Moreover it ought to be pointed out that:

- the solutions given here are valid in the cases of the uniform compression of the thin-walled FML structure. Other types of loadings would need further investigation,
- the usual assumption, made in many works in the field, that the buckling modes in the elastic and elastic-plastic range are identical cannot be true in some cases,
- it should be noted that the buckling modes in elastic and elastic-plastic range can be not always cover-up.

Acknowledgment

This contribution is a part of the project funded by the National Science Centre Poland, allocated on the basis of the decision No. 2012/07/B/ST8/0409.

5.5. References

5.1 Byskov E., Hutchinson J.W., Mode interaction in axially stiffened cylindrical shells, AIAA J., 15 (7), 1977, pp. 941-48.

5.2 Grądzki R., Kowal-Michalska K., Post-buckling analysis of elastic-plastic plates basing on the Tsai-Wu criterion, JTAM, 4, 37, 1999, pp. 893-908.

5.3 Grądzki R. Kowal-Michalska K., Ultimate load of laminated plates subjected to simultaneous compression and shear, The Archives of Mechanical Engineering, XLVIII, 3, 2001, pp. 249-264.

5.4 Grądzki R., Kowal-Michalska K., Stability and ultimate load of three layered plates - a parametric study, Engineering Transactions, 51,4, 2003.

5.5 Koiter W.T., General theory of mode interaction in stiffened plate and shell structures, WTHD Report 590, Delft 1976, 41.

5.6 Kołakowski Z., Kowal-Michalska K., Kędziora S., Determination of inelastic stability of thin walled isotropic columns using elastic orthotropic plate equations, Mechanics and Mechanical Engineering, 1997, 1 (1), pp. 79-90.

5.7 Kolakowski Z, Kowal-Michalska K. (Eds.), Selected problems of instabilities in composite structures, A Series of Monographs, Technical University of Lodz, Poland, 1999.

5.8 Kolakowski Z., Krolak M., Modal coupled instabilities of thin-walled composite plate and shell structures, Composite Structures, 2006, 76, pp. 303-313.

5.9 Kołakowski Z., Kowal-Michalska K. (Eds.), Statics, dynamics and stability of structures, Vol. 2, Statics, dynamics and stability of structural elements and systems, Lodz University of Technology, A Series of Monographs, Lodz 2012.

5.10 Kowal-Michalska K., Kolakowski Z., Inelastic buckling of thin-walled FML columns by elastic asymptotic solutions, 39th Solid Mechanics Conf. Zakopane, Poland, 2014.

5.11 Kolakowski Z, Kowal-Michalska K., Mania R.J., Global and local elastic-plastic stability of FML columns of open and closed cross-section, Proc. of Polish Congress of Mechanics, 2015, pp. 907-908.

5.12 Kolakowski Z., Mania J.R., Semi-analytical method versus the FEM for analysis of the local post-buckling. Composite Structures, 97, 2013, pp. 99-106.

5.13 Kowal-Michalska K., Kołakowski Z., Kędziora S., Global and local inelastic buckling of thin-walled orthotropic columns by elastic asymptotic solutions, Mechanics and Mechanical Engineering, 1998, 2 (2) pp. 209-231.

5.14 Kowal-Michalska K., Stany zakrytyczne w obszarach sprężysto-plastycznych konstrukcji płytowych, Lodz University of Technology, A Series of Monographs, Lodz 2013 /in Polish/.

5.15 Kowal-Michalska K., Problem of modeling in the non-linear stability investigation of thin-walled plated structures, Part II - Elasto-plastic range, pp. 157-180, in monograph "Mathematical models in continuum mechanics" (Eds. K. Wilmański, B. Michalak, J. Jędrysiak), Lodz University of Technology, A Series of Monographs, 2011.

5.16 Mania J.R., Kolakowski Z., Bienias J., Jakubczak P., Majerski K., Comparative study of FML profiles buckling and postbuckling behaviour under axial loading, Composite Structures, Vol. 134, 2015, pp. 216-225.
5.17 Vermeeren C. (ed.), Around GLARE, A new aircraft material in context, Kluwer Academic Publishers. 2004.
5.18 Wittenberg T.C., de Jonge A. Plasticity correction factors for buckling of flat rectangular Glare plates. DUT, Int. Council of the Aeronautical Sciences, 2002, 482.1-482.13.

6.

Crack propagation in thin-walled structures under cyclic variable loads. The numerical and experimental studies

6.1. Introduction

The modern design of load-bearing structures is accompanied by constant multiple improvements of the theoretical concepts verified through experimental studies. Among the many engineering calculation methods of today, which make it possible to solve complex problems related to the design of load-bearing structures in a way worthy of today's requirements, the numerical methods remain the dominant ones. Like any other computational methods, the numerical ones require experimental verification. Because, without underestimating the many opportunities and the practical usefulness offered by the numerical methods, one should take into account that they involve rough calculations and their results refer to no real structures but to their idealized models.

The wider in respect of formulated assumptions and the more rigorous in respect of assumed technical conditions the problem under consideration becomes, the more complex is the form taken by its calculation model, and the results obtained remain in many cases dubious. In similar situations, an experiment appropriate for the problem concerned is the only reliable source of information about the behaviour of the structure. On the other hand, verification of prototypal solutions for load-bearing structures is a costly and time-consuming undertaking, and needs to be carried out in due course as part of the design process as well. These limitations are often the cause of the delay in receiving information on to what extent the structural solution under implementation remains in concordance with the said assumptions, especially in respect of the crucial details. That is why improvements in computational methods are observed along with a process of systematic refinement of the methods and concepts for conducting experimental studies which could be a form of verification of calculations and which could be applied as part of the design of load-bearing structures when substantial corrections can be made prior to the costly and laborious implementation of a prototypal solution. The tests refer to complete structures (global tests) but can also be local in character, covering selected, crucial areas of the planned structure. The purpose of the latter is primarily to identify imperfect detail solutions and to eliminate them sufficiently in advance as they could be the cause of premature failure of the structure.

Within the broad spectrum of experimental testing methods that meet the above requirements, those relating to model mechanics are of major significance. The assumption that, based on the model similarity theory, the quantitative conclusions can be - in the broad sense - transferred from the observation of physical phenomena in a certain mechanical system onto another system of a different scale, is fundamental to those methods. The notion of a scale does only not refer to the object geometry here. Enabling mechanical properties to be programmed, the development of the chemistry of plastics, including the plastics with an effect of temporary double refraction in polarized light, has become an important factor affecting the domain of application of model tests. Apart from the widely used epoxy resins, examples of representative materials include polycarbonate, optically active material with a wide range of uses as construction material with its instantaneous characteristic showing elastic and inelastic deformation phases. Model tests can also be carried out on objects made of the actual construction materials. Both the scale and the selection of the model material is the outcome of striving to obtain results which give the basis for their transposition into the real object based on the model similarity theory.

Because of the above-mentioned factors and economic considerations, which are not negligible, model tests as the reasonably economical expansion of the domain of experimental testing find broad application in the physically and geometrically nonlinear analyses of states of stress and deformation of load-bearing structures, thus becoming an effective tool for verifying the results of numerical analyses.

It is common for all theoretical concepts related to the design of load-bearing structures to idealize the structures to a greater or lesser degree. If we expect experimental studies to provide more information on to what extent the adopted calculation model for the planned load-bearing structure remains in concordance with the actual state confirmed in an experiment, irrespective of the type and scope of the tests, and, when the experimental verification function is fulfilled by model tests, the object - the model intended for use in experimental testing must strictly meet all the requirements, from those on geometric similarity and on similarity of a material’s physical characteristics to, in some situations, the requirements on similarity in reflecting the effects of a manufacturing process, e.g. the state of assembly stress. Preparing objects for the tests that meet the requirements in question is no simple undertaking in technical terms. Fatigue tests on thin-walled structures require special attention and considerable experience as well. When the planned structure is composed of a number of sub-assemblies (and in practice this is usually the case), it is necessary to reproduce the mechanical properties of the structure tested including the required variable load resistance, and in particular when the operation process starts with a local defect.

The versatility of thin-walled load-bearing structures has shaped an equally extensive area of constructional solutions and testing methods. This special category of structures covers thin-walled aircraft structures, for which broad experimental studies determine the competent authority's decisions to certify the aircraft fit for flying tests. During the design and construction of a prototype, its load-bearing structures are subjected to extensive tests, from segment, static and fatigue tests on the constructional solution details, through global static tests, fatigue and resonance tests, to factory-based and national flying tests.

When it comes to the role of model tests, then, as a rule, they function as a tool for testing selected areas of elements. They are no validation tests. Their purpose is to analyze, in particular with regard to the verification of the calculation model adopted, those elements or areas of the planned structure, in which strong discontinuities relating to the structure stiffness may appear because of the geometry resulting from the functionality. The discontinuities may be due to the passes, local reinforcements, press-formed stiffening and points of connection between elements made of materials with diverse moduli of elasticity, and due to local defects as well. These areas are crucial to the structure, or the major factors determining its service life and reliability.

These determinants are reflected in all the design stages of load-bearing structures, in particular in the procedures involving the determination of fatigue life which can today be determined numerically, and thus as early as in the structure design stage. Extreme allowable stresses corresponding to post-buckling deformations form the basis for the calculation of fatigue life. The determination of stress fields in advanced stages of post-buckling deformation of thin-walled structures, in particular those with high geometric complexity is only feasible by numerical methods.

Not understating the significance of numerical analyses as unquestionably effective tools and not ignoring the problems related to the certain measure of result unreliability that is always present, and in the end, given that for engineering practice, which requires absolute confidence in the results of every numerical analysis, it is reasonable, and in a number of situations even necessary to introduce special tests to support the design which could considerably enhance the reliability of numeral analysis results.

The many years' experience of a number of centres show that this function is increasingly taken over by appropriately configured special experimental studies that enable ongoing evaluation of the calculation models adopted and their reasonable correction. Therefore, it becomes reasonable to continue the modernization of the design process of load-bearing structures based on continuously improved calculation models and aimed at enhancing the reliability of the numerical calculation results verified through experimental studies.

This paper attempts to assess the result relevance for the study of propagation of fatigue cracks in thin-walled structures made of a model material into structures of real materials. The model material was chosen to be polycarbonate which is today widely used in many fields of technology, also as a constructional material, the instantaneous characteristic of which exhibits elastic and inelastic deformation phases. The attainment of the aims of the study required the determination of stresses in the components of the structures with the passes and cracks subjected to variable loads. The problem was solved on the grounds of numerical methods and experimental studies.

6.2. Structure fatigue

The loads acting on the structure change with time and are often random in character because of the service conditions (Fig. 6.1). Variable stresses induce a complex state of stress in the material. These are phenomena that favour premature failure of the structure.

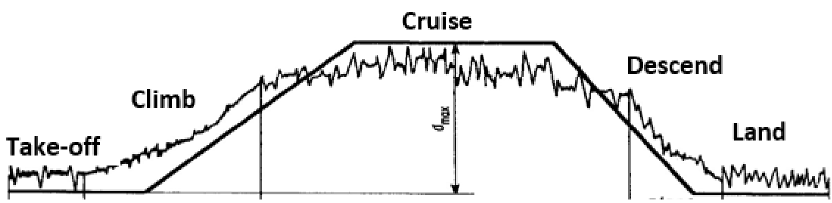

Fig. 6.1. Examples of distribution of stresses in an aircraft's wing

The material fatigue process is commonly characterized by a graph called the Wöhler curve (Fig. 6.2). The curve is obtained by bringing a specific number of model samples to failure through changing the stress amplitude of the cycle σ_a for the established value of the steady-stress component σ_m. Each value of σ_a or σ_{max} has a corresponding number of load cycles causing fatigue damage N, provided stress σ_a does not decrease to the fatigue limit Z_G once the basic number of cycles N_G is reached.

In the most common system of coordinates σ, log N, the graph appears to be a curved line (Fig. 6.2). The turn point, or the point of intersection of both the graph segments defines the theoretical limiting number of cycles N_0 which to a varying degree can deviate from the adopted basic number of cycles N_G [6.4, 6.6, 6.8].

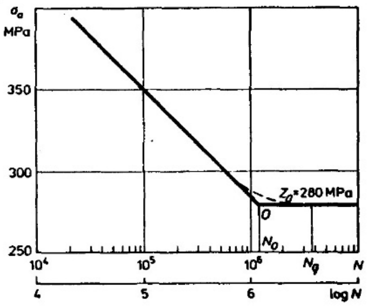

Fig. 6.2. Example of a Wöhler curve for a sample of normalized steel 45 subjected to rotational bending, in the system of σ, log N

On account of the multitude of load factors, the process of destruction may take on various forms: from gently plastic destruction to sudden brittle cracking. There is a wide range of intermediate forms between the types of destruction mentioned above. And so, plastic or ductile cracking is always preceded by plastic macro-strains and is caused by slip. Crack surfaces are characterized by systems of pits and bulges that impart to the surfaces a honeycomb or scaly structure.

Brittle cracking goes quite differently. It develops at a speed close to the speed of sound, which is typical of a given material within the conventionally elastic range, and thus without any macroscopic elastic deformations, in the normal direction to the largest material elongation. Cracking arises along certain crystallographic planes, so called cleavage planes. Such cracking is called cleavable transcrystalline cracking. Another type of brittle cracking is one that goes along the grain boundaries, forming intercrystalline scrap.

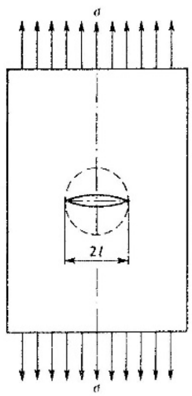

Fig. 6.3. A diagram of a plate with a centre crack for the description of Griffith's criterion

Mixed cracking, that is partially brittle and partially plastic cracking is very common. Out of the cracking types, brittle cracking is the most dangerous due to the lack of clear signs of cracking directly prior to the destruction.

The basis for the calculation of a material's resistance to brittle cracking is formed by Griffith's theory [6.8]. The theory is based on the energy balance of an elastic disc with an elliptic hole under uniaxial tension.

With an infinitely small growth of the crack length (cracking initiation), the elastic deformation energy decreases. It is:

$$\Delta U_s = -\frac{c}{2}\pi\sigma^2 l^2 \tag{6.1}$$

where

$$c = \begin{cases} 2(1-\nu^2)/E \\ 2/E \end{cases}$$

Eq. (6.1) denotes the so-called crack opening work.

At the same time, the energy related to overcoming the cohesive forces (the phenomenon of adhesion of two surfaces), i.e. the surface energy increases U_γ.

$$U_\gamma = 4l_\gamma \tag{6.2}$$

Where γ is the energy needed to form a free surface unit.

The sum of the above energy makes up the total energy for crack development

$$\Delta U = U_\gamma - \Delta U_s \tag{6.3}$$

A decrease of the total energy U is a sine qua non for cracking initiation, so it is required that the first derivative of this function goes to zero in relation to the crack surface *A=2l x 1*.

$$\left.\frac{dU}{dA}\right|_{l=l_{kr}} = 0$$

Considering equations (6.1), (6.2) and (6.3), we will obtain

$$\left.\frac{dU_\gamma}{dA}\right|_{l=l_{kr}} = -\left.\frac{dU_s}{dA}\right|_{l=l_{kr}} \tag{6.4}$$

$$\left.\frac{dU_\gamma}{dA}\right|_{l=l_{kr}} = 2\gamma = R \tag{6.5}$$

$$\left.\frac{dU_s}{dA}\right|_{l=l_{kr}} = -\frac{c}{2}\pi\sigma^2 l = G \tag{6.6}$$

Relationship, Eq. (6.6) represents the ***energy criterion of cracking***, which states that a crack will start propagating when the energy release rate G is equal to the material's crack resistance R. Therefore, spontaneous development of a crack is only possible when its length reaches a critical value $l = l_{kr}$. To a critical crack length corresponds buckling stress σ_{kr}. This value results directly from formula (6.6)

$$\sigma_{kr} = \sqrt{\frac{4\gamma}{c\pi l_{kr}}} \tag{6.7}$$

After transformation, from equation (2.6) we receive

$$\sigma\sqrt{\pi l} = \sqrt{\frac{4\gamma}{c}} = K \tag{6.8}$$

The value K is a stress intensity factor which for the critical values l_{kr} and σ_{kr} becomes a critical value K_c and is called *crack resistance*.

The interpretation of the phenomena occurring in fracture mechanics requires a knowledge of the stress field and the displacement in the front of and around the crack. The three main cases of crack development are considered. Case 1 was described as normal crack opening. Case 2 refers to transverse shear, while case 3 to longitudinal shear of a crack.

In practice, case 1 is most significant. Our further discussion is limited to this case.

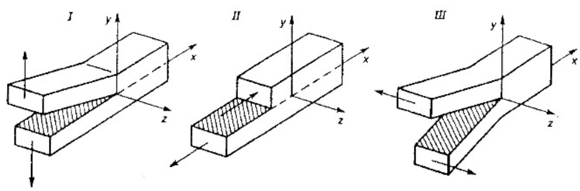

Fig. 6.4. Three main cases of crack development

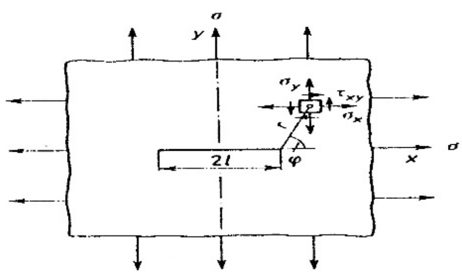

Fig. 6.5. A plate with a centre crack and a system of coordinates marked for equations (6.9)

As a result of his study, Irwin formulated the following equations for the diagram as in Fig. 6.5:

$$\left.\begin{aligned}\sigma_x &= \frac{\sigma\sqrt{\pi l}}{\sqrt{2\pi r}} cos\frac{\varphi}{2}\left(1 - sin\frac{\varphi}{2}sin\frac{3}{2}\varphi\right)\\ \sigma_y &= \frac{\sigma\sqrt{\pi l}}{\sqrt{2\pi r}} cos\frac{\varphi}{2}\left(1 - sin\frac{\varphi}{2}sin\frac{3}{2}\varphi\right)\\ \tau_{xy} &= \frac{\sigma\sqrt{\pi l}}{\sqrt{2\pi r}} cos\frac{\varphi}{2}sin\frac{\varphi}{2}cos\frac{\varphi}{2}\\ \sigma_z &= \nu(\sigma_x + \sigma_y)\\ \tau_{yz} &= \tau_{xz} = 0\end{aligned}\right\} \tag{6.9}$$

$$\left.\begin{aligned}u &= \frac{\sigma\sqrt{\pi l}}{2G_{sp}}\sqrt{\frac{r}{2\pi}} cos\frac{\varphi}{2}\left(\kappa - 1 + sin^2\frac{\varphi}{2}\right)\\ v &= \frac{\sigma\sqrt{\pi l}}{2G_{sp}}\sqrt{\frac{r}{2\pi}} sin\frac{\varphi}{2}\left(\kappa - 1 + cos^2\frac{\varphi}{2}\right)\\ w &= 0\end{aligned}\right\} \tag{6.10}$$

In formulae (6.10), the value **k** for plane stress is

$$\kappa = \frac{3-\nu}{1+\nu} \tag{6.11a}$$

and for the plane state of strain, it is

$$\kappa = 3 - 4\nu \tag{6.11b}$$

ν denotes Poisson's ratio here, while the symbol G_{sp} represents a rigidity modulus.

The value $\sigma\sqrt{\pi l}$ appearing in the equations is a pre-defined stress intensity factor K and makes up a measurement of stress growth rate for the cracking zone. The factor K depends on external loads, the crack geometry and the element geometry. The effect of an element's edges on the stress fields increases with the growth of the crack length in relation to the width of the element. A correction factor β, accounting for the finiteness of the element's dimensions, is then introduced into the formula. Depending on the computational methods adopted, different forms of the formulae for determining the factor β are obtained.

Generally, we can write:

$$K = \beta\sigma\sqrt{\pi l} \tag{6.12}$$

Sudden development of a crack occurs when the stress intensity factor K_I reaches a critical value K_{Ic}, so, the value of critical stresses σ_{kr} for known dimensions of the crack can be defined for the plane state of strain as

$$\sigma_{kr} = \frac{K_{Ic}}{M_{kI}\sqrt{\pi l_{kr}}} \tag{6.13}$$

The value of factor K depends substantially on the element's thickness as shown diagrammatically in Fig. 6.6. However, from the thickness determined for a given material, the factor K does not change. It is just the lowest critical value of the stress intensity factor that was adopted as crack resistance K_{Ic}.

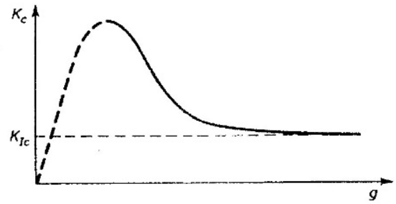

Fig. 6.6. The effect of the element's thickness on the stress intensity factor

The stress intensity factor K is a criterion of local cracking as formulated by Irwin. This is a force-related criterion that corresponds to Griffith's energy criterion, which was discussed earlier in this paper and the exponent of which is the unit energy of crack development G. The above factors are basic values in linear fracture mechanics and are interrelated as follows

$$G = \frac{K^2 c}{2} \tag{6.14}$$

Crack development in real metal materials is closely linked to the plastic strain zone before the front of the crack and considerably limits the applicability of the principles of classical fracture mechanics. According to Irwin's theory, the size of this zone for plane stress (r_{pl}) and the plane state of strain (r_{plo}) respectively is, for a diagram as in Fig. 6.7, the following

$$r_{pl} = \frac{K_{Ic}{}^2}{2\pi R_e^2} cos^2 \frac{\varphi}{2}\left(1 + 3sin^2 \frac{\varphi}{2}\right) \tag{6.15}$$

and

$$r_{plo} = \frac{K_{Ic}{}^2}{2\pi R_e^2} cos^2 \frac{\varphi}{2}\left(1 + 3sin^2 \frac{\varphi}{2} - 4\nu(1-\nu)\right) \tag{6.16}$$

The dissimilarity of the state of stress along the crack width causes differences in the zone sizes on the surface of the plate (plane stress) and in its centre (plane state of strain). The quotient $r_{pl}/r_{plo} = 1/(1-2\nu)^2$ for ν=1/3 is as the ratio of 9:1. This demonstrates a serious impact of stress on crack development.

The plastic strain zone affects the stress intensity factor K, so it becomes necessary to make appropriate corrections. According to Irwin, the correction comes down to the adoption of the apparent crack length consisting of the real length extended by the size of the plastic zone, that is

$$K_I = \sigma\sqrt{(l + r_{pl})\pi} \tag{6.17}$$

Along with an increase in the quotient σ/R_e, there will also be an increase in the factor K calculation error. For example, for $\sigma/R_e \approx 0.7$, the error is over 20%, thus limiting the application of linear fracture mechanics. For $\sigma/R_e \leq 0.4$, virtually no correction is required because the calculation error does not exceed 5%.

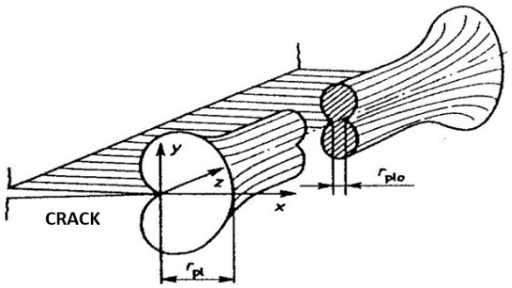

Fig. 6.7. The shape of a plastically deformed zone in the front of a crack in a thick-walled plate

A crack growth is to be understood as a crack growing longer at stable rate, from length l_o to critical length l_{kr}, the reach of which is assumed to be damage to the element. In fracture mechanics, damage or destruction as a consequence of variable loads is known as "fatigue failure".

Fatigue crack development takes place in stages (Fig. 6.8). The initial stage is nucleation (initiation) of a macrocrack with a length that is large enough for the description of the crack behaviour to be accurate enough on the grounds of deformable body mechanics. Cyclic variable loads make energy accumulate near the internal material discontinuities. This in turn causes the microdefects to grow and connect with each other until a macrocrack, called a fatigue crack, is formed after a certain number of cycles N. The second stage is growth (propagation) of the fatigue crack from length l_i to length l_{kr}. The duration of this stage is determined by the number of cycles Np. The last stage is unstable growth of the crack, equated with fatigue failure. The total number of load cycles that can be safely transferred by a structural element is a sum of the number of cycles prior to crack initiation N and the number of cycles corresponding to crack propagation N_p . The numerical values of both these quantities depend on many factors, i.a. the type of material, the quantities describing the load and the crack geometry; hence it is difficult to state any general regularities. It is all the more difficult because the first stage, the initiation of a fatigue crack is still poorly understood, both in terms of experiment and theory. However, it is in many cases accepted that the determining factor for the evaluation of the service life of a structure is the fatigue crack propagation phase, so, a knowledge of the number of cycles is enough.

The independent parameters that describe stresses caused by cyclic variable loads with constant amplitude are: steady-stress component σ_m, stress amplitude σ_a and frequency ω.

The typical curve representing the dependence of the crack length from the number of cycles is shown in Fig. 6.8. The real initial crack length l_0 must be large enough in order to apply the principles of fracture mechanics to the description of behaviour of the crack. The smallest crack length that can be detected in non-destructive testing is marked as l_d. This length is adopted as the initial length. Crack length l_d is determined by a so-called inspection range, i.e. a range, within which experimental observation of the crack is possible). As a result of the changing load, the crack grows slowly from the initial length until it reaches a certain length l_r. Then, the crack growth clearly accelerates. This period of the work of the element with the crack is regarded as useful service life. Once the crack has reaches the critical length, its growth becomes very rapid and uncontrollable, and is equated with destruction of the element. The number of cycles corresponding to destruction is N_f. The determination of the element's lifetime, defined by the number of cycles prior to destruction N_f, and of curve $l=l(N)$ is the basic objective of the analysis of crack growth at fatigue.

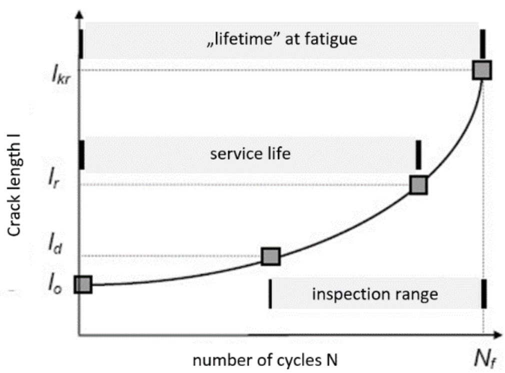

Fig. 6.8. Example of a fatigue crack propagation curve

The mechanics behind the crack growth under variable loads is connected with the local stress field near the crack top. Plastic strains can occur even under very light loads as a result of high stress concentration in the crack top region.

The fatigue crack growth is connected with local stress concentration. It can therefore be presumed that crack growth is connected with stress intensity factor (SIF) K. For any configuration, this factor can be written as

$$K = \beta\sigma\sqrt{\pi l} \tag{6.18}$$

where β is a (numerical or functional) coefficient related to finite body dimensions and σ denotes the load applied. Previously introduced as a parameter controlling the process of destruction, the stress variability range can be replaced with an SIF variability range. Considering that for the particular cycle as defined by variability of stress between σ_{min} and $\sigma_{max,}$ the following relationships occur

$$K_{min} = \beta\sigma_{min}\sqrt{\pi l} \tag{6.19}$$

$$K_{max} = \beta\sigma_{max}\sqrt{\pi l} \tag{6.20}$$

the SIF variability range can be expressed by the following equation

$$\Delta K = \beta\Delta\sigma\sqrt{\pi l} \tag{6.21}$$

while stress ratio R is

$$R = \frac{K_{max}}{K_{min}} \Rightarrow \Delta K = (1 - R)K_{max} \tag{6.22}$$

The **fatigue crack propagation rate** is defined as ***an increase in the crack length felling on one cycle*** - so, it is expressed by derivative dl/dN with a dimension of [mm/cycle]. The equation for the fatigue crack propagation rate can be written as

$$\frac{dl}{dN} = f(\Delta K, R) \tag{6.23}$$

It can be shown that function *f* is an increasing function on account of both arguments. Because of the considerable difficulty in formulating a mathematical description by way of theoretical analysis, function *f* is determined based on experimental methods.

It has become customary in fracture mechanics to use the very propagation rate curve (and not the growth curve l (N)) to describe the growth of fatigue cracks, although the curve is not obtained directly through experience but through transformation of the growth curve.

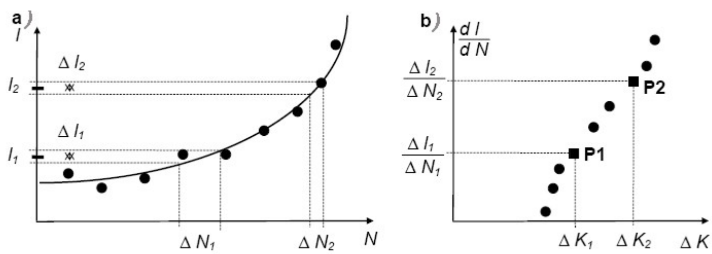

Fig. 6.9. Fatigue crack growth: a) experimental crack growth curve, b) constructed crack propagation rate curve

The fatigue crack growth curve is obtained during a fatigue test performed on any given sample with known factor β. During the test, the current crack length is recorded in the function of the number of load cycles (Fig. 6.9). This is the entire information obtained through experiment and nothing but the processing of this information allows us to determine the function, Eq. (6.9).

The curve shown in Fig. 6.10b is characterized by three distinct phases: in phase 1, the crack propagation rates are low and stay within the range of $0 \div 10^{-5}$ mm/cycle, in phase 2, the rates are medium, within the range of $10^{-5} \div 10^{-3}$ mm/cycle, and in phase 3 - high, over 10^{-3} mm/cycle. These are indicative values which can vary according to materials, loads, environmental conditions and so on.

On a double-logarithm scale for phase 2, the graph dl/dN vs ΔK is almost linear, which is reflected in the empirical formulae defining function, eq. (6.10).

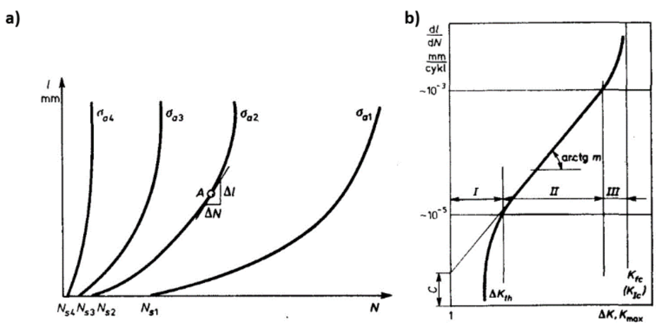

Fig. 6.10. A schematic description of the nature of fatigue crack development at different stress amplitudes $\sigma_{a1} < \sigma_{a2} < \sigma_{a3} < \sigma_{a4}$ a) and a logarithmic graph for cracking rate dl/dN according to range ΔK or the highest K_{max} of the stress intensity factor b)

Fatigue crack growth is not possible if a certain threshold value ΔK_{th} is not exceeded. It is assumed that ΔK_{th} corresponds to ca. 10^6 cycles. From Eq. (6.22) it appears that the critical value is

$$\Delta K_{kr} = (1 - R)K_{Ic} \tag{6.24}$$

Our qualitative observations resulting from the experimental tests covering crack propagation under fatigue loads allow us to understand the "structure" of the numerous suggestions to formulate a detailed equation for crack propagation rate eq. (6.23). For the linear phase 2 on graph log(dl/dN) vs logΔK, the crack propagation rate equation is formulated as follows [6.2, 6.7, 6.10]. For one specific cycle asymmetry coefficient R, we can, using the general equation for straight line $y = m_p x + b$, where $y = \log(dl/dN)$; $x = \log(\Delta K)$, write an equation for this straight line in the form

$$log\left(\frac{dl}{dN}\right) = m_p\, log(\Delta K) + log(C_p) \tag{6.25}$$

Considering the logarithmic function properties, we will obtain, after simple transformations, an equation in the form

$$\frac{dl}{dN} = C_p(\Delta K)^m \tag{6.26}$$

Equation (6.26), known as Paris' law or the Paris-Erdogan law, was introduced into the literature jointly by Paris and Erdogan [6.8] The constants m_p and C_p are determined based on experimental data. A knowledge of two points (ΔK, dl/dN) is obviously enough but better results are obtained if the constants are determined based on a greater number of measuring points.

For most materials, constant m_p stays within the range of 3÷5, constant C_p depends more strongly on the material, and what is more, it depends on the units used for the calculation.

Indicative constant values for some materials are compiled in Table 6.1. The data relate to a load cycle with asymmetry coefficient $R = 0$; crack propagation rate dl/dN is expressed in mm/cycle, while variability range ΔK - in $MPa\sqrt{m}$.

There is a number of empirical dependencies for specific material classes which associate constants m and C in Paris' equation with the values of yield point R_e and ultimate tensile strength R_m. They allow us to determine m and C, at least approximately, when it is necessary to make fatigue calculations and no experimental data relative to the material are available [6.7].

Table 6.1. Indicative constant values in Paris' equation (2.25)

Material	Yield strength R_e [MPa]	Tensile strength R_m[MPa]	C_p	m_p
Aluminium alloy PA7	420	510	7×10^{-11}	4

With a description of the non-linear phase 3 of this graph in mind, in which phase for $\Delta K = \Delta K_c = K_c(1\text{-}R)$, (Fig. 6.10b), Forman et al. [6.7] suggested the following adaptation of Paris' equation

$$\frac{dl}{dN} = C_F \frac{(\Delta K)^{m_F}}{(1-R)K_C - \Delta K}, \tag{6.27}$$

K_c denotes crack resistance under specific load conditions. If relevant data are not available, K_{Ic} should be used. Forman's equation enables determination of the crack growth rate with any cycle asymmetry coefficient R.

A large group of equations refers to the initial phase on the crack propagation rate curve. They all contain the threshold value for the variability range of stress intensity factor ΔK_{th} as one of the parameters.

$$\frac{dl}{dN} = C(\Delta K - \Delta K_{th})^m \tag{6.28}$$

A knowledge of the threshold value ΔK_{th} is crucial for the possibility to use this equation. Usually, the form as below, is used for this calculation

$$\Delta K_{th} = (1 - R)^{\gamma} \Delta K_{th0} \tag{6.29}$$

where ΔK_{th0} is the threshold value for a cycle characterized by coefficient RR = 0 and γ is a parameter relating to the material and staying within the range of 0.5÷1.0.

The formulae suggested by Vosikovsky, which link ΔK_{th}z to yield strength R_e and tensile strength R_m, are considered relations giving a good estimation of the threshold value for different grades of steel and asymmetry coefficient R = 0. The formulae have the following forms

$$\Delta K_{th0} = 11.17 - 0.0032\, R_m \tag{6.30}$$

$$\Delta K_{th0} = 11.40 - 0.0046\, R_e \tag{6.31}$$

For cycles with coefficient $R \neq 0$, the following equation can be used

$$\Delta K_{th} = \Delta K_{th0} - BR \tag{6.32}$$

where

$$B = 10.39 - 0.0052\, R_e \tag{6.33}$$

An equation describing the threshold value for aluminium alloys was given by Mackay

$$\Delta K_{th} = \left(\frac{1-R}{1+R}\right)^{0,5} \Delta K_{th0} \tag{6.34}$$

The aim of the analysis of the issue of fatigue crack growth is to determine a crack propagation curve and the number of load cycles, after which the element tested fails. This number, marked in Fig. 6.8 with symbol N_f, defines the service life of an element with a fatigue crack. For cyclic loads with constant amplitude, the service life can be determined on condition that the load parameters and the form of stress intensity factor (6.18) are known. Equation (6.23) implies the following relation

$$dN = \frac{dl}{f(\Delta K, R)} \tag{6.35}$$

Hence, after integration, a number of cycles prior to destruction or a number determined by test requirements is obtained in the form

$$N_f = \int_{l_0}^{l_k} \frac{dl}{f(\Delta K, R)} \tag{6.36}$$

where l_o denotes the crack's initial length assumed or found in the element, and l_k denotes the crack's final length which is often equated with critical length l_{kr} determined based on one of cracking criteria.

When a necessity arises to make quick calculations, instead of the integral formula (6.36), a rough formula in the following form can be used

$$N_f = \sum_{l_0}^{l_k} \frac{dl}{f(\Delta K, R)} \tag{6.37}$$

6.3. Experimental and numerical studies

6.3.1. A plate strip weakened by a crack

The service life of thin-walled structures is determined by different forms of damage, like cracks, fractures, passes etc. Although local defects, in and of themselves, constitute no direct hazard to the structure, they can under certain conditions lead to its premature damage. In plates and coatings whose thickness is small compared to the characteristic dimensions in the proximity of fractures, cracks or passes, local buckling can occur, also in the process of tension [6.3]. The occurrence of local buckling defined as structure wrinkling, caused by the occurrence of local compression zones, results in a change in the state of stress within the distorted geometry zone because apart from the membrane state that prevails on the plate, also a flexural state occurs in some places.

The subject of the study was a thin rectangular plate with a centrally located crack with an initial length of 30 mm (Fig. 6.11), subjected to cyclic variable tension loads within the range: $P_{min} = 0$, $P_{max} = 1500$N. The crack propagates in the presence of local buckling with an increase in the number of load cycles, until it reaches the critical length. The crack growing over time causes the local buckling zone to expand which has an impact on the crack propagation rate.

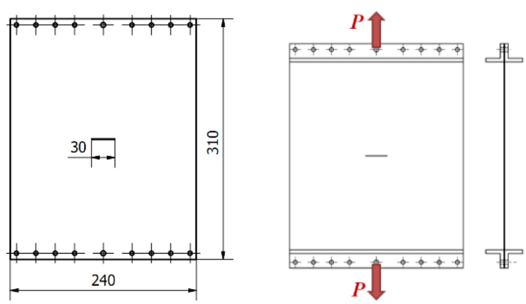

Fig. 6.11. Overall dimensions of the sample and the method of fastening and loading

The studies involved the analyses of propagation of fatigue cracks carried out for samples with identical geometry. Figs. 6.12 present crack growth for a demonstration sample. The first cracks were observed after about 11,000 load cycles. The cracks then propagated in the direction perpendicular to the longer plate edge until the plate failed.

During the fatigue tests, the lengths of fatigue cracks were monitored. On this basis, graphs were drawn to present the dependence of fatigue crack propagation in the function of the number of load cycles (an example of the graph in Fig. 6.13).

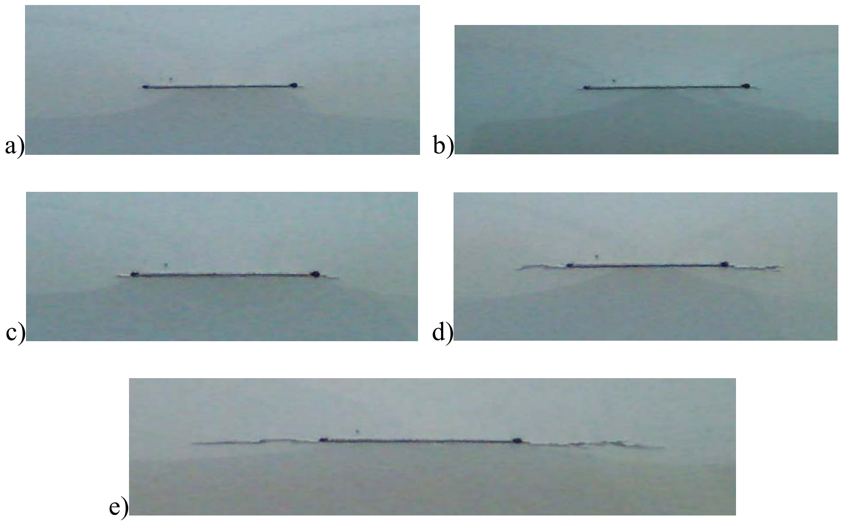

Fig. 6.12. Crack growth during experiment after number of load cycles: a)10 812 (first crack), b)11 303, c) 16 205, d) 49 800, e) 83 309

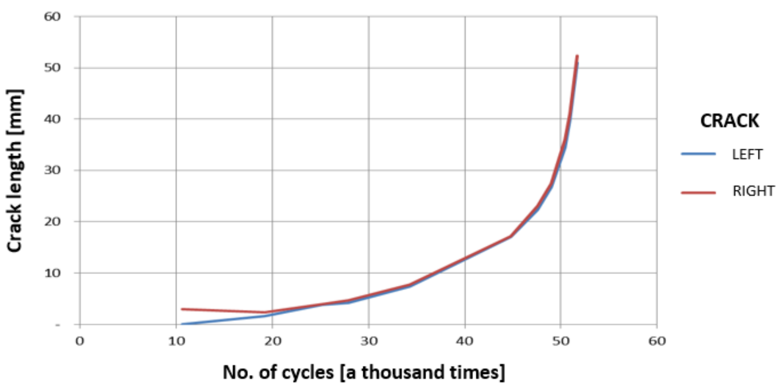

Fig. 6.13. Fatigue crack growth in the function of the number of load cycles

Based on the test results, graphs for crack growth rate Δl/ΔN in the function ΔK (Fig 6.14) were drawn, where

$$\Delta K = K_{max} - K_{min}$$

$$K_{max} = \sigma_{max}\sqrt{\pi l} \cdot \beta$$

$$K_{min} = \sigma_{min}\sqrt{\pi l} \cdot \beta$$

$$\beta = \left[1 + 0.128\frac{l}{w} - 0.288\left(\frac{l}{w}\right)^2 + 1.529\left(\frac{l}{w}\right)^3\right]$$

Using the relationships Δl/ΔN vs ΔK on a logarithmic scale, the constants m_p and C_p in the Paris-Erdogan equation were identified

$$\frac{dl}{dN} = C_p(\Delta K)^{m_p}$$

The "service life", or the number of cycles, after which the sample fails, was calculated

$$N_f = \frac{2}{\beta(m_p - 2)C_p(\Delta\sigma)^{m_p}\pi^{0.5m_p}}\left[\frac{1}{l_0^{\,0.5(m_p-2)}} - \frac{1}{l_k^{\,0.5(m_p-2)}}\right]$$

Table 6.2. Calculated values N_f

Sample no.	C_p	m_p	N_f
1	$4.315\cdot10^{-9}$	7.06	61155
2	$2.415\cdot10^{-8}$	3.94	60637
3	$9.35\cdot10^{-9}$	5.35	53110

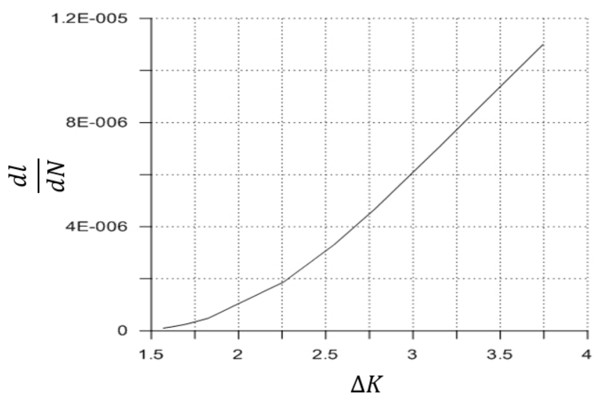

Fig.6.14. Dependence: $\frac{dl}{dN}$ in the function ΔK

6.3.2. Numerical analysis

Modern software enables numerical determination of the Stress Intensity Factor (SIF) [6.5]. For this purpose, a crack is to be modelled and an area for the determination of SIF values is to be selected. Fig. 6.15 presents an area of a degenerate finite element grid marked out by a circle with a radius of 5 mm. The aim of the degeneration of the grid consisting in the modification of the elements in the immediate proximity of the crack front is to force occurrence of a singularity to enable determination of a stress pattern in such a zone with higher accuracy than that achieved with a traditional method of modelling. Fig. 6.16 presents examples of distribution patterns for effort near the crack top obtained as a result of using the above-described method of modelling and of application of the traditional division into finite elements.

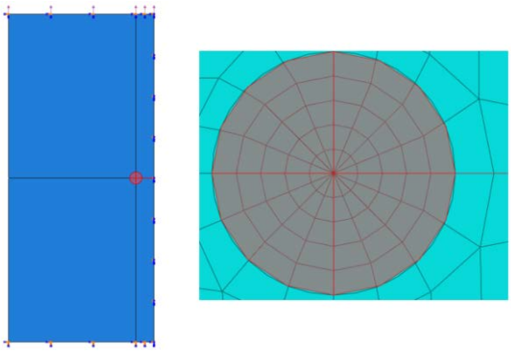

Fig. 6.15. Numerical model geometry and boundary conditions. Area of a degenerate finite element grid

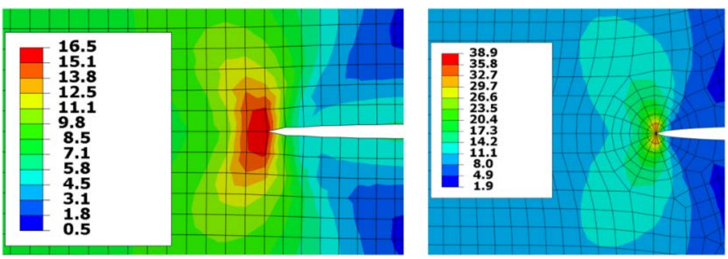

Fig. 6.16. Example of a comparison of effort distribution patterns
a) normal grid b) fragment of a degenerate grid

The SIF value is determined in consecutive so-called contours covering a larger and larger area in the region of the crack front. Fig. 6.17. shows the areas equated with consecutive contours.

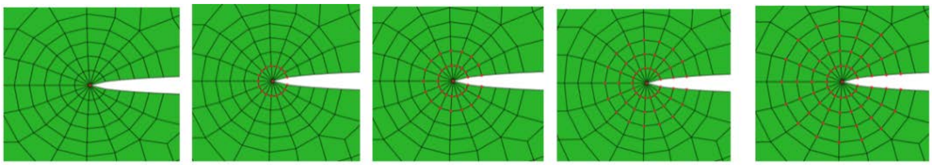

Fig. 6.17. Finite element nodes within consecutive contours

Three modelling versions were considered on account of the finite elements used and of the procedure to find a solution. Table 6.3 contains information about the numerical models created. Model A was digitized by means of disc elements of plane stress CPS8R with four nodes, each characterized by three degrees of freedom (two translational and one rotational). In Model A, no large deformations were allowed (the Newton-Raphson procedure option related to the definition of a strain tensor).

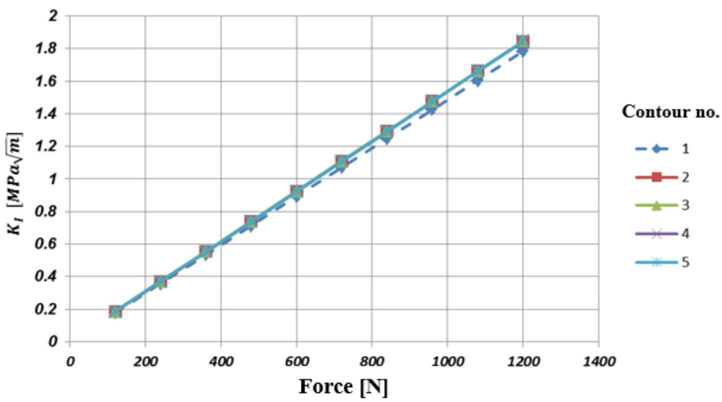

a)

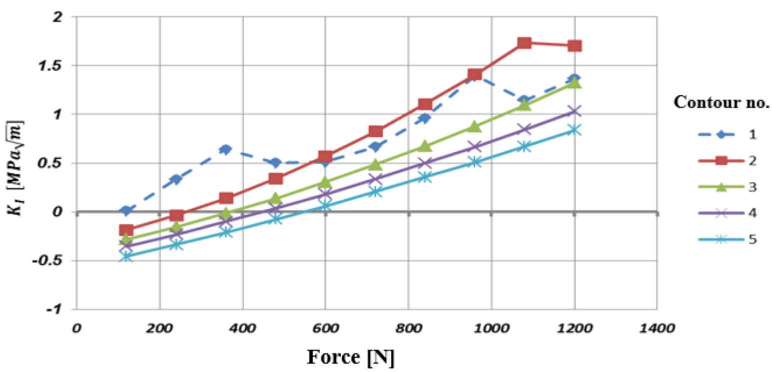

b)

Fig. 6.18. Dependence of SIF from the acting load
a) Model A, b) Model B2

Models B1 and B2 were built from plate/shell elements S4R, each having four nodes with five degrees of freedom. The difference between Models B1 and B2 lay in enabling (for Model B2) the option of large deformations. The aim of the verification of the results obtained under the assumption of finite deformations was to assess the possibility of determining SIF when modelling plate wrinkling.

Table 6.3. Numerical models

Marking	Type of element	Element name	Large deformations
Model A	2D disc	CPS8R	None
Model B1	3D plate	S4R	None
Model B2	3D plate	S4R	Enabled

Below are presented the results for the models considered in the form of displacement and effort fields as well as the graphs demonstrating SIF (for consecutive contours) changing with increasing loads.

For Model A that was treated as a reference case, the value obtained for stress intensity factor (under maximum load) was nearly the same in all the contours used for the calculation (a difference of ca. 3%). For Model B1, the SIF value did not show any differences greater than 4%in particular contours but compared to Model A, the SIF value obtained was 25% higher.

Different results were obtained for Model B2, for which the differences in SIF reached 3% to 39% between consecutive contours. The graph in Fig. 6.18b further indicates nonlinear nature of the SIF changes for contours 1 and 2. The comparison of the results obtained for Model A shows that the differences reach even 43%. This forces a statement that the available strategy to find SIF values by way of numerical analyses may turn out to be ineffective if it assumes finite deformations to occur in the case of analyzing a plate strip with wrinkling taken into account.

Table 6.4. Stress intensity factor values for the models under consideration

K_I [MPa m^1/2] for loading of 1200 N					
	Contour 1	Contour 2	Contour 3	Contour 4	Contour 5
Model A	1.428576	1.475392	1.47809	1.477331	1.476208
Model B1	1.783119	1.845156	1.847594	1.846334	1.846334
Model B2	1.366232	1.702543	1.322278	1.030216	0.836329

Table 6.5 presents the crack opening sizes during the application of force of 1200 N, obtained through numerical analyses. According to the previous analysis of deformation fields, the opening sizes were similar for Models B1 and B2.

Whereas, in spite of lower stiffness, Model A indicated a 20% smaller crack opening than that in models built from plate/shell elements.

Table 6.5. Crack opening size (load of 1200 N)

	Model A	Model B1	Model B2
Crack opening [mm]	0.132	0.165	0.165

6.3.3. Stress pattern for a crack-weakened structure

In terms of their character, the effort distribution patterns obtained by numerical methods are in concordance with the results of the experimental studies. During the experimental studies, the phenomenon of wrinkling was observed. It is extremely troublesome to reproduce the phenomenon numerically. As a plane structure in numerical calculations, it does not buckle spontaneously. Initial bending of the plate is smoothed away by a load in the form of tensile force that “tries” to straighten the element in question. The following figures show a qualitative comparison of the numerical analysis and experimental results. For polymer samples, the numerically calculated effort distribution is, according to the hypothesis τ_{max} , concurrent enough, in terms of quality, with the picture of isochromatic lines making up the result of photoelastic tests [6.9].

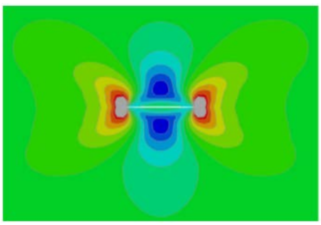
b)
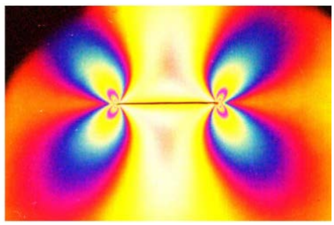

Fig. 6.19. A comparison of effort distribution patterns according to the hypothesis τ_{max} obtained by FEM a) and the picture of optical effects obtained by way of photoelastic tests b)

a)
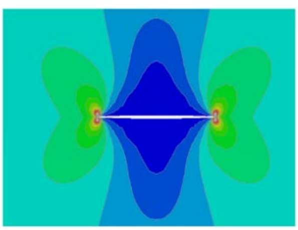
b)
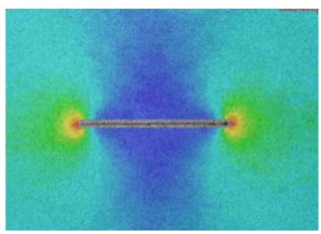

Fig. 6.20. A comparison of main strain distribution patterns - the maximum strains a) FEM result, b) DIC experimental results

Aluminium structures were tested using the digital image correlation (DIC) method [6.1, 6.11]. The photos presenting a comparison of the results obtained by this way and the results of numerical analyses also indicate high concurrence.

a) 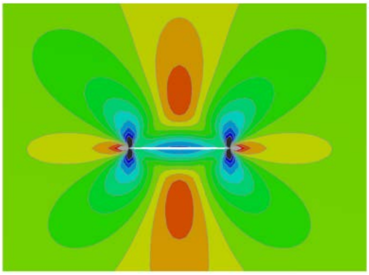 b) 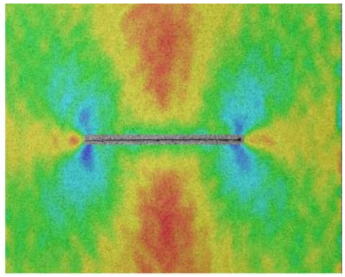

Fig. 6.21. A comparison of main strain distribution patterns - the minimum strains
a) FEM result, b) DIC experimental results

Also pictures of isochromatic lines in the crack front zone were recorded using a reflection polariscope. For this purpose, a coat of fluorescent paint was applied to one side of the test plate. Fig. 6.22. presents the isochromatic fields in advanced stages of crack propagation.

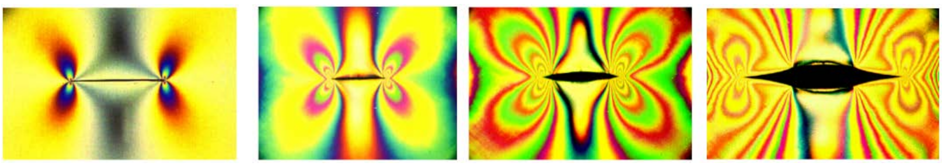

Fig. 6.22. Isochromatic field for the centre crack

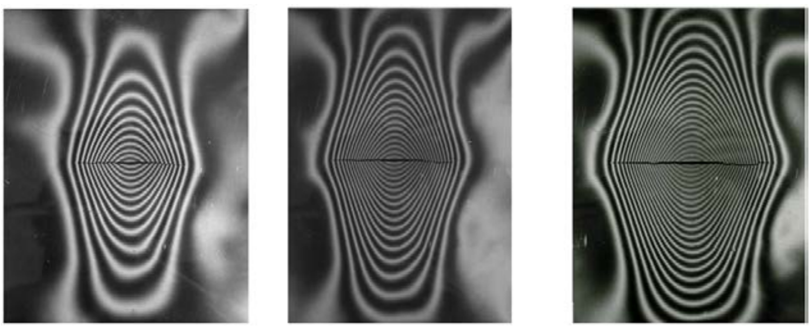

a) 2a=30 mm b) 2a=50 mm c) 2a=70 mm

Fig. 6.23. Pictures of moiré fringes illustrating the quantitative
character of transverse strains

The crack grows and the plate stiffness decreases as the number of load cycles increases. This is expressed by the visible growth of the wrinkling effect.

In order to quantitatively determine transverse strains (bending) in the particular phases of deformation, the shadow moiré method was applied.

Fig. 6.23 shows the contour lines for identical bending values in the buckling zone. The distance between the neighbouring lines corresponds to 0.26 mm bending. So, the maximum bending values are, respectively: 3.12 mm, 4.42 mm, 5.72 mm.

6.3.4. Fatigue crack development in a plate subjected to shear

When taking up the issues of fatigue crack development in the structure under consideration, a monocyclic load spectrum was adopted (Fig. 6.24). The lower limit for a load cycle was minimally raised in relation to the spectrum pulsating from zero in order to avoid the troublesome loading force sign inversion that can occur in similar situations. In order to shorten the duration of the fatigue tests, a rate of force development of 3 kN/s was adopted.

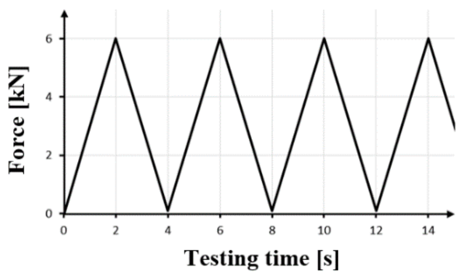

Fig. 6.24. Load spectrum for the plate tested

For the purposes of the experiment, a plate fastening system was designed and made in the form of a stiff four-jointed frame. The frame consisted of eight flat steel bars, four on each side of the plate, joined in the corners with bolts. The frame components were connected with the plate with screw-nut gears, monitoring uniformity of pressure over the entire edge length during the assembly. This type of connection ensured occurrence of friction force between the contacting surfaces.

The sufficiently high stiffness of the flat steel bars did not enable the plate edges to rotate. This created fastening conditions close to ideal restraint.

The schematic diagram of the test stand is shown in Fig. 6.25. The lower frame node was connected to the testing machine base. The upper node with the machine's traverse enabled introduction of loading force. This method of introducing external forces ensured occurrence of internal loads on the plate edges in the form of tangential expenditure constituting the impact of the frame components on the plate (Fig. 6.25).

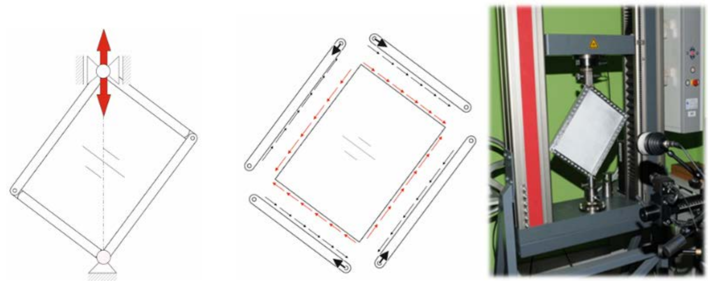

Fig. 6.25. Schematic diagram for the load and the test stand

The tests on the plate revealed the first 0.5 mm long fatigue cracks after 45,000 load cycles at points of connection with the frame (Fig. 6.26). The cracks indicate that there occurs extreme effort in these areas. After about 55,000 load cycles, cracks on the plate diagonal appeared. After about 73,000 cycles, formation of four cracks with similar lengths and angle orientation in relation to the plate edges was observed. During the subsequent 6,000 load cycles, those cracks formed two large cracking zones. Fig. 6.27 shows the development of the cracks described till the plate failure.

Fig. 6.26. The first fatigue cracks and their locations on the plate surface

No significant changes in the global stiffness of the structure were found during the first 83,000 cycles. During that cycle period, the fatigue cracks reached as large lengths as 50 mm. The last 2,500 cycles caused distinct gradual degradation of the structure which manifested itself in loss of stiffness, i.e. in an increase in the displacement of the upper plate attachment point, from the value of 2.6 mm to over 10 mm.

The failure occurred as a result of reaching a critical length by one of the fatigue cracks. The crack propagation rate suddenly increased, causing the crack to reach the critical length (Fig. 6.28).

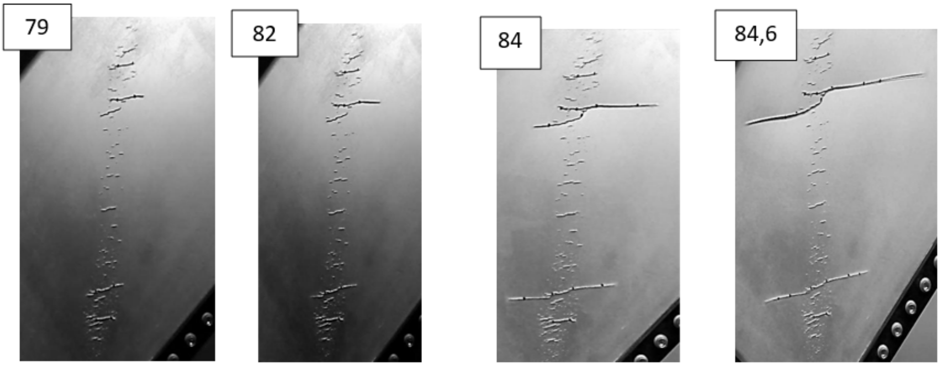

Fig. 6.27. Fatigue crack development (in frames: number of load cycles times 10^3)

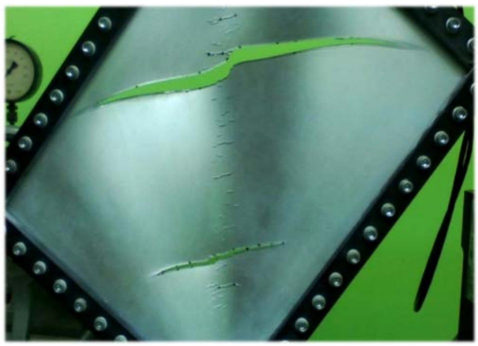

Fig. 6.28. Failure of the plate (84,658 load cycles)

6.4. Summary

It seems clear that the modern testing and calculation methods not only enable but simply require consideration of factors that have been often passed over in the design of thin-walled load-bearing structures because of mathematical or equipment-related difficulties. The modern tools in the form of computer programs and broad laboratory equipment enabling static and dynamic testing (fatigue, resonance tests, flight tests) form the primary basis for the design and implementation of new, original concepts. The better and better availability of the tools obliges the designer to take a closer look at the opportunities offered by the contemporary technology in this regard.

This paper raised a number of issues that have a significant effect on the service life of thin-walled load-bearing structures, both those planned and those in use (periodic repairs, repairs after damage etc.).

The above issues include, first and foremost, the occurrence of cracks that do not mean failure of the structure but require the determination of critical lengths.

The experimental study and numerical calculation methodology was presented in the form of suggestions about choosing the appropriate tool for studying the aforementioned phenomenon. The suggestions are based on the modern generation measuring technology. Attention was also drawn to the effectiveness of conventional photoelasticity.

The experimental studies and numerical analyses carried out enabled us to formulate detailed remarks which may be important for the design process. For example, the comparison of the experiment results (photoelasticity, moiré method, DIC method) allows us to state that the phenomenon of wrinkling has virtually no effect on premature destruction of thin-walled structures weakened with advanced cracks.

6.5. References

6.1 ARAMIS - User manual, GOM mbH, 2010.

6.2 Chrzanowski M., Kolczuga M., Continuous damage mechanics applied to fatigue failure, Mech. Research Communic., Vol. 7/1,1980.

6.3 Czerepanow C.P., Halmov H., On the theory of crack growth, Eng. Fract. Mech., Vol. 4, 1992.

6.4 Dyląg Z., Orłoś Z., Wytrzymałość zmęczeniowa materiałów, WNT, Warszawa 1978.

6.5 Forman H.G., Kearny V.G., Numerical analysis of crack propagation in cyclic loaded structures, J. Basic Eng. Trans. ASME, D, Vol. 81, 1997.

6.6 Kocańda S., Zmęczeniowe niszczenie metali, WNT, Warszawa 1978.

6.7 Kuroda M., Extremely low cycle fatigue life prediction based on a new cumulative fatigue damage model, Int. Journal of Fatigue, 24, 2001.

6.8 Neimitz A., Mechanika Pękania, PWN, Warszawa 1998.

6.9 Szczepiński W., Mechanika Techniczna – metody doświadczalne mechaniki ciała stałego, PWN, Warszawa 1984.

6.10 Troszczenko B.T., Deformirowanije i razruszenije metallow pri mnogocikłowom nagrużenii, Izd. Nauka Dumka, Kijew 1981.

6.11 Zafar A., Digital image correlation, CEE 498 KUC – Experimental methods in structures and materials, 2008.

7.

Deformation and buckling of axially compressed cylindrical shells with transversal cut in numerical and physical experiments

7.1. Introduction

Difficulties of the design of axially compressed smooth circular cylindrical shells are connected with an essential effect of small perturbations of idealised models of shells on their bearing capacity. Additional problems appear in the case of various discontinuities of shells (openings, cut-outs) which can be consequences of the design and technological nature or structural damages. A great number of researches (experimental, analytical and numerical) deal with the study of stability of shells with cut-outs. A particular problem of definition of buckling loads for cylindrical shells with cut-outs became separate in 1947 after the studies made by A.I. Lurie [7.14] and devoted to the stress concentration around circular openings. Early researches by R.C. Tennyson [7.24] that included experimental results of the buckling problem of axially compressed elastic shells with a small circular cut-out were one of the pioneer investigations. The first theoretical research performed by P. Van Dyke [7.25] provided a very good agreement with the experimental data [7.24]. Detailed information on the initial stage of the stability investigation of shells with openings is presented in the reviews of I.N. Preobrazhenskii [7.17-7.18], E.I. Grigolyuk and L.A. Filshinskii [7.5], A.N. Guz and Yu.A. Ashmarin [7.2], G.J. Simitses [7.20], J.G. Teng [7.23], C.-Y. Song [7.21], I. Elishakoff [7.4].

The research [7.8] of J.F. Jullien and A. Limam should be related to the works of “modern” times associated with an intensive implementation of program codes based on the finite element method (FEM) for problems of the shell buckling. The paper contained results of an original experiment as well as results of numerical simulations of the stability problem of shells with singular or several cut-outs. Among variable parameters there were different shapes (rectangular or circular) of openings, their locations and sizes in the circumferential and longitudinal directions. Besides, two types of the loading conditions (kinematic compression with possible or restrained edges rotations, [7.10]) and the effect of initial imperfections on the shells bearing capacity were studied. One of the most important conclusions of the authors was an estimation of the coupling effect between initial geometrical imperfections and openings on the buckling loads.

The monograph [7.16] of N.I. Obodan, A.G. Lebedev, V.A. Gromov discussed the buckling problem of shells with large cut-outs subjected essentially to external pressure as well as to axial compression. Stability of short reinforced and smooth shells with singular damages was studied in the work of R.M.K. Kwok [7.13].

Researches [7.3] performed by A.P. Dzyuba, E.F. Prokopalo, P.A. Dzyuba generalised the experimental data of numerous tests of shells with openings of various shapes and number under different types of loading: axial compression, flexion, torsion, and some their combinations.

We should also mention a cycle of studies [7.6, 7.7, 7.12] of the stability of composite cylindrical shells that were carried out by the scientists of NASA with the participation of M.W. Hilburger in the last two decades. The researches included testing and numerical results for the shells with reinforced and unreinforced openings. The influence of geometrical imperfections, effect of delamination and non-uniform loading provoked by imperfect edges of a shell were estimated.

Despite numerous experimental and theoretical researches of the buckling of axially compressed cylindrical shells with cut-outs, this problem cannot be considered as solved. In particular, a singular opening or cut generates essential non-uniform stress-strain state (SSS) of a shell in the longitudinal and circumferential directions with consequent possible larges deflections. Moreover, because of non-uniform SSS, the buckling behaviour and bearing capacity of the shell can be influenced by the nature of loading (force or kinematic loading), as well as by the conditions of load application to shell edges. Obviously, a linear model of shells behaviour may be insufficient in this case. Meanwhile, the theoretical analysis of geometrically nonlinear problem reflects the essence of the real buckling process. But in the presence of an essential non-uniform pre-critical SSS a successful analysis turns out very difficult.

The realisation of such analyses appears possible just recently due to an intensive development of computer technologies and universal FEM-based program codes. The most important aspect of analyses in the environments of software is an evaluation of possible analysis realisation, as well as estimation of the accuracy of numerical approaches. In this case, recognised criteria of the evaluation are comparisons of numerical results with experiments and analytical solutions. Proceeding from the above, a combined numerical and experimental research of insufficiently studied buckling behaviour of circular cylinders with one transversal cut of various lengths under certain loading nature and loading conditions of axial compression is a very important and actual problem.

7.2. Methodology and results of the experimental research

7.2.1. Experiment preparation

All experiments were carried out on small size specimens produced of drawing paper Goznak of mark “B” (GOST 597-73, former Soviet Union state standard specification) with following mechanical characteristics: modulus of elasticity E_y=6.9 GPa, E_x=3.45 GPa (hereinafter y corresponds to the direction along shell generatrix and x corresponds to the circumferential direction according to the coordinate system of ANSYS software); shear modulus G=1.92 GPa; Poisson’s ratio ν_y=0.3, ν_x=0.15; ultimate strengths σ_y=45 MPa, σ_x=30 MPa. The test diagram of the paper is presented in Fig. 7.1. Geometrical parameters of the shells were: radius R = 37.5 mm, length L = 75 mm, thickness h = 0.23 mm (R/h = 163, L/R = 2.0). The longitudinal size of cuts was preliminary determined and designed equal a=2 mm (see Fig. 7.3) to avoid touching of cut boards in the loading process. The cut length l varied from 3.0 mm to 60 mm and corresponded to angles γ from 4°.6 to 92°. The total number of tested specimens comprised 24 shells: two specimens of the same geometry including two shells without cuts.

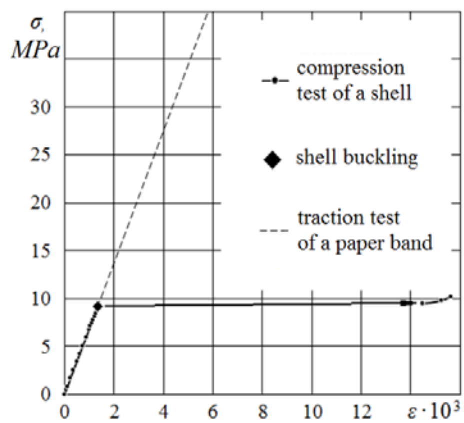

Fig. 7.1. Test diagram of the paper (Whatman paper, GOST 597-73)

Shells were made of flat rectangular sheets of 240×115 mm. Boards of sheets were joined with the glue BF-2 (GOST 12172-74) around metal cylinders of diameter equal to 75 mm. The width of glue over-lapped joints was about 5 mm.

The centre of a cut was located in the middle section of each shell diametrically opposite to the centre of a joint. After glue joints polymerisation finished shells were set on massive steel test disks that had central circular openings. A tight contact of shell and disk was also kept by the glue BF-2.

An axial compressive force was applied to the upper disk through the central spherical joint. This joint was connected with a long steel rod that extended through the opening of fixed bottom disk and was attached to a flat circular platform. The loading was applied by means of a system of weights placed on the platform. General view of the test installation is presented in Fig. 7.2a. It is obvious that the concerned loading scheme corresponds to the force loading. Besides, the transfer of loads to a shell allowed free rotations of its rigid disks (see Fig. 7.2).

The loading of shells was realised till their general (overall) buckling occurred. To prevent a total specimens collapse, the restriction of sharp vertical displacements of the upper disk caused by reaching the limit load was envisaged (see the support in Fig. 7.2a). The test process of shells was video filming.

a)  b) 

Fig. 7.2. Test installation: a) general view, b) tested specimen

7.2.2. Quality of shells

Because of the lack of special facilities, the control of shells quality consisted in the visual inspection of specimens. Shells which were taken off technological cylinders had some geometrical deviations observed with the naked eye. In particular, cross-sections of shells were different from circular and similar to drop-shaped thus the pointed end of “drops” was nearby the glue joint. The other initial imperfection was clearly observed only for shells with large cuts.

Edges of cuts were not mirror images of each other, so they formed a little stair in the middle of their length.

Fitting shells on the rigid disks almost completely eliminated drop-shaped cross-sections. At the same time, they had no influence on imperfections of the offset edges of cuts. On the other hand, rigid disks initiated some other imperfection. Particularly, generatrices of cylinders bended, and shells became barrel-shaped. As well under the weight of disks, rotations of the top shell edge occurred to the centre of cuts; thus, longitudinal sizes in the middle of cuts decreased $a' < 2$ mm (see Fig. 7.3).

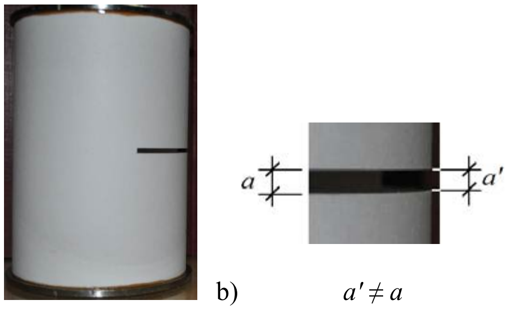

a) b) $a' \neq a$

Fig. 7.3. Initial imperfections of patterns

Results of the preliminary tests of shells without cuts showed that buckling loads were equal $N = (0.56 \div 059)N^{cl}$. According to the classification [7.9] of shells quality, considered specimens of the cylinders without cuts should be referred as quality shells.

7.2.3. Results of the experiment

The deformation of intact shells and shells with small cuts l=3÷4 mm occurred in the same way. During the loading no changes were visually detected. The buckling happened instantly with the formation of a closed belt of circumferential dents (see Fig. 7.4b). Sometimes the cut turned out to be in the buckle between two dents (see Fig. 7.4a). To distinguish the location of the first dents formation was only possible by means of a slowed video of the loading process. The analysis of sweeps of tested buckled shells showed that the total number of circumferential dents was between 6 and 8. Dimension of the biggest dents were about from 35×40 mm to 40×45 mm (hereinafter the first number indicates the height of a dent).

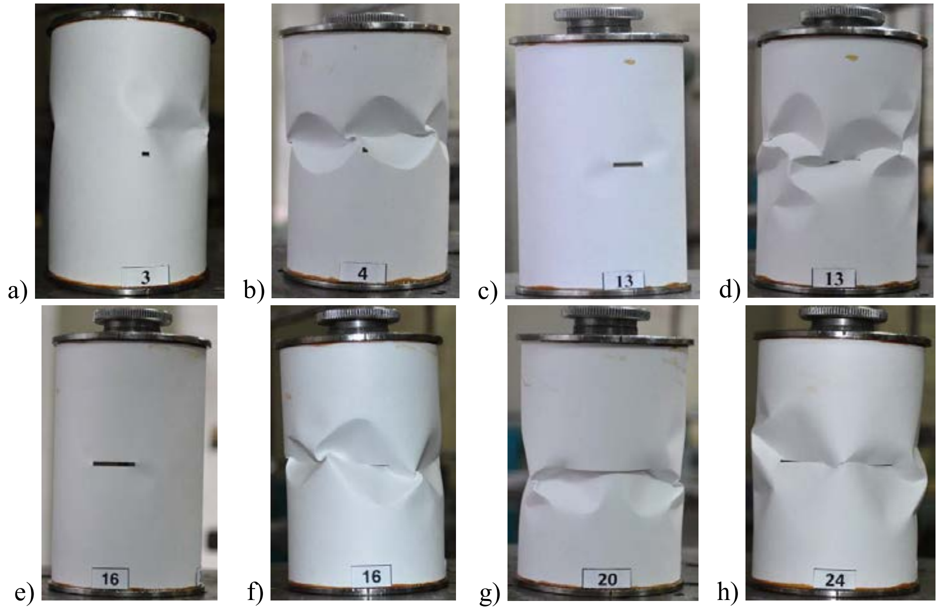

Fig. 7.4. Experimental buckling modes: c), e) local, a)-b), d), f)-h) overall

Buckling of the most of shells with cuts l=5÷60 mm (except two specimens that we discuss further) was characterised by formation of one or two local dents asymmetric in relation to the cut line (see Fig. 7.4e and Fig. 7.4c, respectively). Then, there were two possible ways of the deformation evolution. In the first case with constant axial compression N^{loc}, a local dent (or two local dents) slowly developed and formed the overall buckling mode (see Fig. 7.4f). In the second case the transformation of the initial dent to the post-critical buckling mode occurred when axial compression increased (see Fig. 7.4d). But independently of the deformation evolution, overall buckling modes were significantly developed nearby the cut. There was almost no buckling along the glue joint. The total number of dents was between 8 and 13. For the buckled shells with cuts l = 5÷14 mm the cut was situated in the area of the biggest post-critical dent of dimension about from 25×50 to 40×50 mm. For the shells with cuts l = 20÷60 mm the biggest post-critical dent with dimensions from 30×40 to 40×50 mm was located away from the cut, and there were also two separate dents along the cut lines (see Fig. 7.4h).

For some shells with large cuts l = 30 and 40 mm there were no local buckling modes detected. During the loading initial “barrel-shaped” imperfections increased and developed. The buckling of these shells was accomplished with asymmetric displacements of the cut edges (see Fig. 7.4g). The total number of dents was n = 13 for the shell with l=30 mm, and n = 10 for the shell with l = 40 mm. The biggest post-critical dent formed away from the cut and covered the area with diagonals 35×45 mm and 45×45 mm, respectively.

The Table 7.1 contains results of considered tests. Depending on a cut size (given in millimetres and in degrees) there are presented following values: local (N_1^{loc} and N_2^{loc}) and general (N_1 and N_2) buckling loads for two specimens of the same geometry, arithmetic average values of general buckling loads (N_{av}) and their relative values $\overline{N} = N_{av} / N^{cl}$, where $N^{cl} = 2\pi E h^2 / \sqrt{3(1-\nu^2)}$ is the classical critical axial compression found for an isotropic shell with average mechanical characteristics of the paper E = 5.175 MPa and ν = 0.225.

Table 7.1. Results of the tests

l, [mm]	γ, °	N_1^{loc}, N	N_1, N	N_2^{loc}, N	N_2, N	$N_{av} = \frac{N_1 + N_2}{2}$, N	$\overline{N} = N_{av} / N^{cl}$
0	0	-	570	-	595	582.5	0.572
3	4.6	-	575	-	628	601.3	0.590
4	6.1	-	625	-	590	607.5	0.596
5	7.6	-	565	530	530	547.5	0.537
7	10.7	495	495	545	550	522.5	0.513
10	15.3	490	522	515	532	527.0	0.517
14	21.4	475	515	465	490	502.5	0.493
20	30.6	488	488	470	470	478.8	0.470
30	45.8	420	428	-	472	450.0	0.442
40	61.2	378	378	-	367	372.5	0.365
50	76.4	320	329	285	290	309.5	0.304
60	91.7	268	268	285	285	276.3	0.271

7.3. Methodology and results of the numerical study

The numerical analysis of SSS and buckling of axially compressed cylindrical shells with considered cuts was accomplished in ANSYS software. Below there are proposed methods of a creation of geometrical and finite element (FE) models, methodology of applying loads and boundary conditions, and technics of the results processing.

7.3.1. Numerical finite element modelling

Numerical models were created using standard options of ANSYS software. First, three-dimensional geometrical models of circular cylindrical shells without any cut or with one transversal cut of different length were generated by means of up-going modelling procedure. Then mechanical characteristics of shells material were set. These elastic constants strictly conformed to real experimental data taking into account principal orthotropy directions of the paper. Missing material parameters along the thickness were assumed equal to the smallest values known for the paper. Thus, the material of shells was orthotropic and elastic.

Geometrical models also included two rigid disks. The disks imitated end testing devices that were attached to the upper and bottom edges of shells. Rigid disks were simulated as short cylinders of the diameter equal to the diameter of shells (75 mm) and of the height equal to 3 mm. The rigidity of disks were similar to the rigidity of end testing devices and were defined by a high value of modulus of elasticity of an homogeneous elastic isotropic material ($E = 2 \cdot 10^{15}$ Pa and $\nu = 0.3$).

FE mesh of shells was created with a four-node element SHELL181 from the standard ANSYS element library. Each node of elements has six degrees of freedom: three translations and three rotations about local axes (see Fig. 7.5a). This element is well-suited for linear and geometrically non-linear analyses of shell structures of small and moderate thickness taking into account large displacements and rotations that are governed by the first-order shear-deformation theory (referred to as Mindlin-Reissner shell theory [7.1]). Using FE SHELL181 considers the application of a full integration option for possible asymmetric deformation with incompatible modes [7.1].

FE modelling of the rigid disks was carried out by means of three-dimensional element SOLID185 (see Fig. 7.5b) having eight nodes with three degrees of freedom at each node that represented three translations in the nodal directions of local axes.

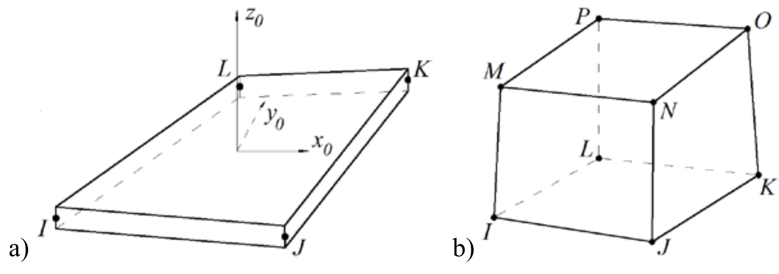

Fig. 7.5. Geometry of FE in ANSYS software: a) SHELL181, b) SOLID185

FE discretisation was realised on the base of standard ANSYS generator – MESHING. At first, geometrical models of the shells were covered with FE. Then created shell meshes were refined along free edges of the cut lines. At the end, solid FE filled the volumes of the rigid disks (see Fig. 7.5b). FE mesh of an entire shell surface (except refined areas around the cut) was built of regular square in plan elements with a side of 1.5 mm. The size of elements was chosen by the procedure of successive mesh refinements based on criteria of stable results of critical and limit loads for an ideal shell. Moreover, the size of FE was checked in the edge effect zone equal to $1.72\sqrt{Rh}$. There were four FE at least.

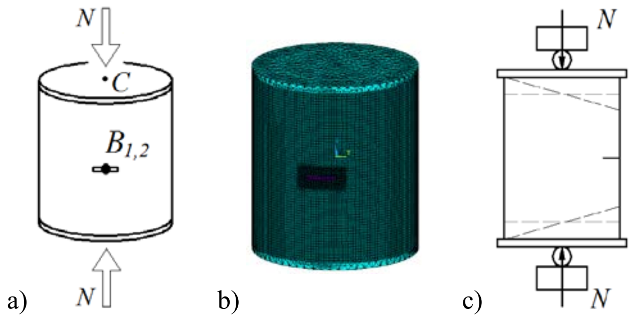

Fig. 7.6. Scheme of the force loading of a shell with one transversal cut a), its FE model including rigid disks b), scheme of pre- and post-critical behaviour of a shell caused by possible out-of-plane rotations of its edges c)

Meshes of the rigid disks were free and proportional to FE meshes of the shells. Arbitrary elements were referred to special points (points C in Fig. 7.6a) in the centre of disks where loads were applied. So, the total number of FE varied between 35000 and 37500, including between 13600 to 16000 shell elements depending on the cut length.

Loads and boundary conditions were performed in ANSYS processor DEFINE LOADS. Fixing of an entire shell in the longitudinal direction was realised in the middle section of the shell height. An axial compression was applied as axial compressive forces N (force loading) with possible out-of-plane rotations of shell edges during the loading (Fig. 7.6c). Exactly this loading scheme was implemented in the experiment. For its accurate realisation by means of ANSYS facilities there were two special “hard points” created on the external surfaces of rigid disks and situated on the axe of the shell. Concentrated forces N were applied to the “hard points”. The boundary conditions considered restrained radial and tangent displacements (in ANSYS designations - $ux = 0$, $uy = 0$ in the nodal coordinate system of FE) on the top edge of the upper disk and on the bottom edge of the lower disk. Besides, on the upper and lower edge of the shell rotations were limited (in ANSYS designations - $roty = 0$ in the nodal coordinate system of FE). Restricted rotations corresponded to clamped edges of the shell. This clamped connection between shells and disks distinguished the loading scheme 1 of the present study from the scheme 1 proposed in [7.11].

7.3.2. Types of analyses and numerical procedure

All solutions were specified as STATIC. During static analyses we studied the influence of time-constant static loads (loads and reactions could change slowly in time [7.1]) on considered shells. While the loading process of the shells, values of displacements and internal forces were determined, as well as values of stresses were controlled.

Depending on considered problems we performed three following types of numerical analyses for generated FE models of the shells without or with cuts:

1 geometrically linear buckling analysis taking into account linear pre-critical deformations in order to define minimal eigenvalues (N^{cr}) and eigenmodes (analysis *I*);
2 geometrically nonlinear static analysis of SSS for the definition of limit loads (N^{lim}) and corresponding deformations (analysis *II*);
3 geometrically nonlinear analysis with initial imperfections. These imperfections corresponded to the first eigenmode obtained out of a preliminary linear buckling analysis of shells without or with cuts (Fig. 7.7a,b). The magnitude of imperfections was assumed to be depending on the shells quality, i.e., it was equal to the magnitude that provided buckling loads of a shell without cuts adequate to average loads found in the experiment [7.9] (analysis *III*).

It should be noted here that a simultaneous comparative research of three mentioned types of analyses is extremely important for certain localisations and sizes of cuts (as opposite to the investigation of deformation and buckling of cylindrical shells without any openings and dissections). This fact is easy to be explained by the physical nature of the buckling of shells with a cut. Particularly, the first bifurcation (as a result of the analysis *I*) appears in this case like a separation of cut edges during the loading. Obviously, this distortion of shell near a cut can occur for rather low loads. Therefore, a judgment on total exhaustion of the bearing capacity of a shell is possible valid only in comparison with the results of geometrically nonlinear analyses *II* and *III*.

As far as any measurement of initial imperfections of tested specimens was not carried out, the magnitude of "bifurcational" imperfections for the analysis *III* was imposed in the following way. In geometrically nonlinear analyses we found limit loads for considered specimens without cuts and with "bifurcational" imperfections of different magnitudes $w_0 = w/h$. Results of these simulations were generalised as the dependence of limit loads on magnitudes of imperfections "$N^{\lim} - w_0$" (see Fig. 7.7c).

By the results of tested shells without cuts, an average value of experimental buckling loads $N^{\exp} = 0.572 N^{cl}$ (see table 1). According to the dependence "$N^{\lim} - w_0$" (Fig. 7.7c), this limit load was realised for the magnitude of imperfections $w_0 = 0.12h$. That was the value of imperfections which was put in the analysis *III* for the definition of limit loads of the shells with cuts and initial imperfections.

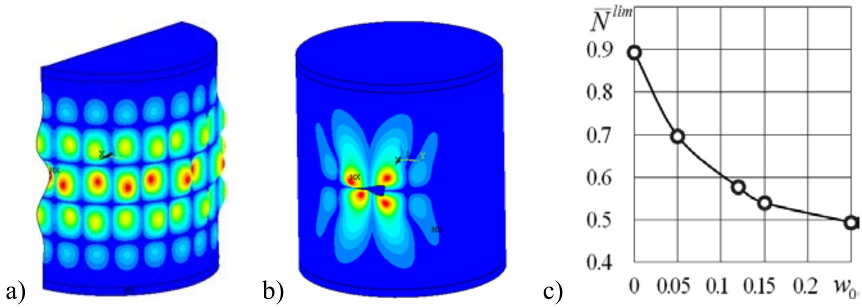

Fig. 7.7. Eigenmodes of axially compressed shells: a) without cut, b) with a cut, c) the dependence of limit axial compressive forces on magnitudes of "bifurcational" imperfections

The eigenvalues were determined by Lanczos method [7.1].

During the nonlinear analyses we plotted pre- and post-critical equilibrium paths "load-deflection".

Both types of nonlinear analyses were accomplished by arc-length method. That was connected with loading particularities. For the force schemes of compression, forces are applied step by step. But in the vicinity of limit points a change of the loading parameter is required to obtain a post-critical branch that is only possible in the case of the arc-length method.

Another important feature of geometrically nonlinear analyses of shells with cuts was that the best way for selection of main solution parameters (number of substeps, maximal and minimal multiplier of the reference arc-length radius – MAXARC, MINARC) based only on the results of nonlinear deformation of an ideal cylindrical shell was insufficient. Moreover, we ought to increase the number of substeps for each series of shells with a cut versus their number for a shell without cuts (approximately in two times). Finally we admitted the parameters that provided smooth post-critical branches without snap-backs to the initial equilibrium paths [7.19, 7.22]. Note that too many substeps may essentially increase the solution time with no accuracy changes. Besides, size and shape of FE are not the least of factors for correct post-critical paths. Irregular shapes of FE can cause not only poor convergence of the solution, but also lead to wrong, overrated values of critical and limit loads on the pre-critical equilibrium paths.

7.3.3. Processing and presentation of numerical results

The processing of numerical results was performed in GENERAL POSTPROCESSOR of ANSYS software. For the most comprehensive and convenient analysis it is recommended to save results after each substep. In this case a result file contains the most complete information on executed nonlinear solutions: parameters of strains, stresses, efforts in all nodes and elements in appropriate form (tables, contours, graphs, etc.).

The evaluation of obtained results was carried out on the basis of correspondence of numerical solutions with the experimental data. Because of the experiment scantiness, along with buckling modes, buckling loads were the main criteria of results evaluation. A complete picture of the buckling behaviour of shells with cuts were reconstructed by means of the plotting dependences of displacements of special points (points *B*, *C*, see Fig. 7.6a) on loads level. We also registered stresses which corresponded to special loads on the pre- and post-critical branches of equilibrium paths.

Note the particular importance of the post-processing review and evaluation of results. The influence of applied loads and boundary conditions, validation of FE mesh, substeps value, etc. can be estimated only at this stage of the numerical research.

7.3.4. Analysis of numerical results, comparison with experimental data and discussion

For a demonstrable comparison of the numerical simulation results with experimental data in Fig. 7.8 the buckling loads are presented as the dependences on the cut length l (γ). Here, “one” of the y-axis corresponds to the value of the critical axial compressive force of an isotropic shell with average mechanical characteristics of the paper ($E = 5.175$ MPa and $\nu = 0.225$). In Fig. 7.8 red triangles correspond to general buckling loads of the experiment. Local experimental loads N^{loc} appear as red rhombs. White dots represent critical loads of the geometrically linear solution *I*; black dots show limit loads of the geometrically nonlinear solution *II*; blue and white dots show limit loads of the geometrically nonlinear solution *III*.

Studying the graph presented in Fig. 7.8 shows that for a small size of cuts (l<7 mm) the geometrically linear analysis *I* is higher than geometrically nonlinear analysis *II*, but increasing the cut leads to inversion of limit and critical loads. However, in the small cut region the experimental values of buckling loads are much lower than numerical buckling loads due to the initial imperfections observed for real structures, which are absent in FE models of numerical analyses *I* and *II*. A sharp drop of both limit and critical loads for small cuts till the value of $0.62N^{cl}$ can be explained by an extreme sensitivity of buckling loads to local perturbing factors, in particular to the transversal cut in this case. In the region of large cuts a smooth decrease of limit and critical loads is distinguished till the value of $0.39N^{cl}$ caused by progressive reduction of the working area of a shell.

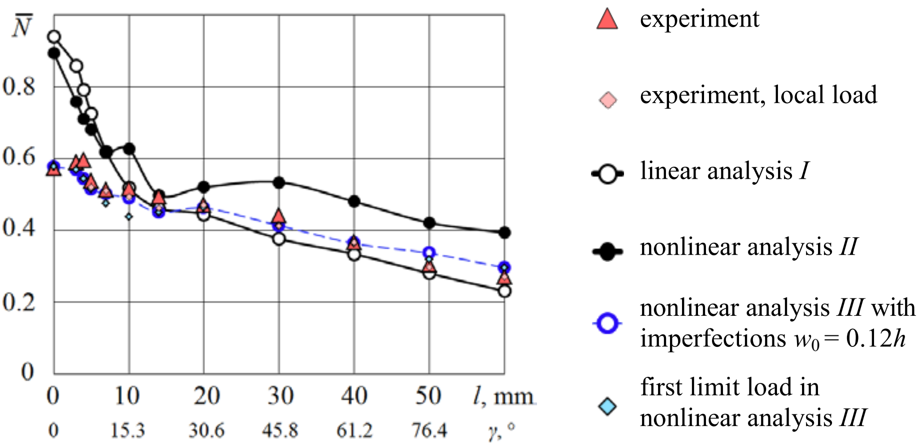

Fig. 7.8. Dependences of relative experimental and numerical critical and limit loads on the cut length l (γ)

Mention two local maximums in the region of decreasing limit loads of the analysis *II* near the cuts l=10 and 30 mm which can be also observed in a smooth form for the experiment. The first rise is connected with a constrained deformation near the cut. In the second case, a certain strengthening of shells leads to the increase of deformation zone. A pre-critical dent (Fig. 7.9a; hereinafter framed buckling modes correspond to the maximal value of limit loads) is not able to cover the entire cut, and as a result it transforms into two separate local post-critical dents at the edges of the cut (Fig. 7.9b,c). On the other hand, imperfections of the analysis *III* eliminate both rises of loads.

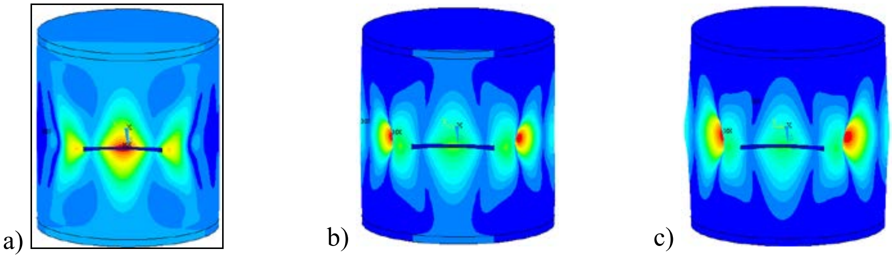

Fig. 7.9. Deformations of the shell with $l = 30$ mm in the analysis *II*:
a) pre-critical, b, c) post-critical

The best agreement of numerical results with the experimental data is observed for the limit loads obtained in the nonlinear analysis *III*. The maximal difference between the analysis *III* and experimental data is less than 10%. On the one hand, it indicates an excellent qualitative and good quantitative correspondence of the numerical analysis and experiment. And, on the other hand, this lets us complete the lack of the experimental data with numerical results concerning pre- and post-buckling behaviour of the shells with the cuts.

Fig. 7.10a-b,d-e describes typical dependences of displacements on load values in the analysis *III* for the shells with cuts $l = 5$ mm and $l = 30$ mm. Studying these graphs lets us determine that at the buckling moment the relative longitudinal displacement ΔZ of point *C* (see Fig. 7.6a; *C* is situated in the middle of external surfaces of rigid disks) is equal to $0.24h$ and $0.21h$, respectively. For the entire series of shells $\Delta Z = 0.20h \div 0.27h$. Relative radial displacements $\overline{w}$ of points *B* (points B are situated in the vertical line of symmetry on the edges of cuts; positive translations $\overline{w}$ are out of the centre of a shell curvature) are equal up to $1.24h$ and $2.32h$, respectively. For the entire range of considered shells $\overline{w} = 0.10h \div 2.51h$.

Thus for real shells with one transversal cut produced according to the considered technology, the cut presence leads to initial geometrical imperfections similar to the first eigenmode (bifurcation) that is revealed like symmetric distortions of the cut edges. During the loading this initial pre-deformation develops intensively near the cut, and the shell buckling occurs after reaching a limit point. Note that the bearing capacity of shells with large cuts is determined by reaching the first limit load (Fig. 7.10d). And in the case of small cuts the buckling happens after overloading the first limit point (Fig. 7.10a).

Numerical experiments realised according to the proposed methodology in the frame of geometrically nonlinear analysis *III* with "bifurcational" imperfections (preliminary obtained in the buckling linear solution *I*) allow a complete study of the buckling behaviour of cylindrical shell with singular transversal cuts. This fact is confirmed by a good qualitative and quantitative correspondence between numerical results and data of the physical experiment.

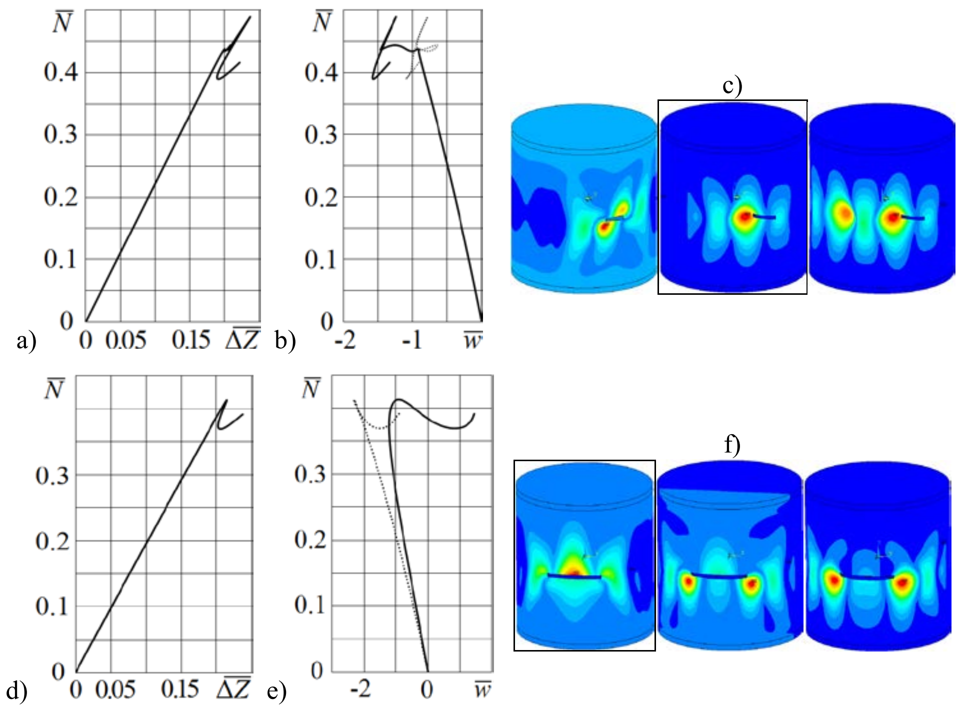

Fig. 7.10. Typical behaviour in the analysis *III* and buckling modes for the shells with cuts: a-c) l = 5 mm, d-f) l = 30 mm

7.3.5. Stress state around the cuts

It is known that cut-outs and openings provoke stress concentrations which can significantly influence on the pre- and post-critical deformation of a shell. Therefore, we control stresses along dissections in the geometrically nonlinear buckling analyses of considered shells (in the experiment stresses were not measured). The main results of this study are following.

The most important characteristics of the strength assessment of a shell are membrane stresses (in ANSYS designations – stresses in the middle layer of FE). As a rule, they use to evaluate the strength of shells produced of plastic materials by equivalent von Mises membrane stresses (energetic strength theory). In Fig. 7.11 there are contours of equivalent von Mises membrane stresses at different levels of loads. Framed stress states of the shells (full pictures and near concentrations) correspond to limit loads. Furthermore there is a coloured scale of stresses (in pascals) measured at the buckling moment for each shell with a cut. Nodes of maximal stresses in the shell are automatically marked with the symbol “*MX*”.

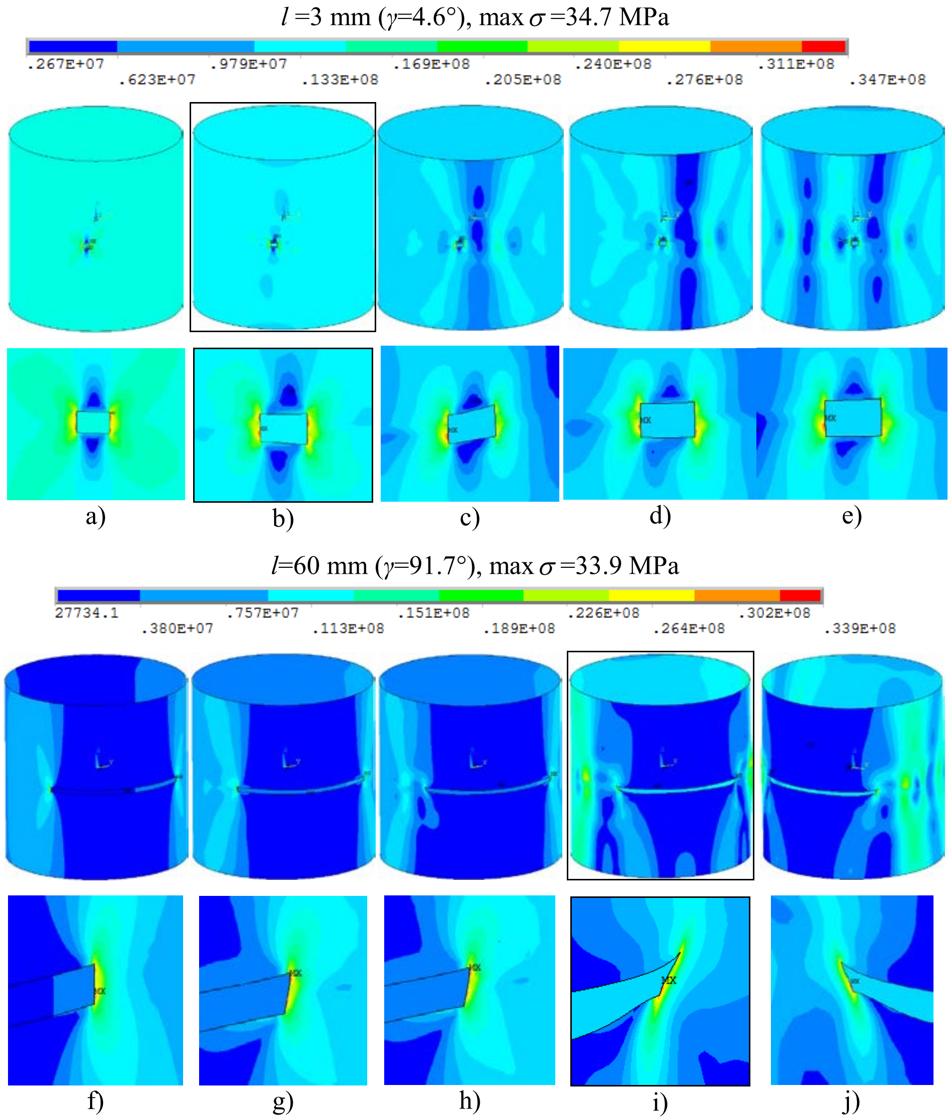

Fig. 7.11. Distribution of von Mises membrane stresses (Pa) at different loading time

A detailed analysis of the stress distribution indicates that the highest stresses appear near cuts at one node situated along the height of cut edges (see Fig. 7.11b,i). Maximal buckling stresses are equal about 35 MPa, and they are obviously results of the concentration as far as average values of the stress fields are 2.5-3.0 times lower.

The stress distributions as well as registered values of membrane stresses, which do not exceed dangerous stresses for the material, prove that the buckling of tested axially compressed cylindrical shells with singular transversal cuts happens in the elastic stage of material deformation. Besides, a pronounced concentration of stresses is observed around the cut irrespective of its length.

7.4. Conclusions

A series of tests of axially compressed identical circular cylindrical shells with singular transversal cuts in the middle section were carried out. The cut length varied in the wide range (angle sizes of cuts in the circumferential direction were between 4.6° and 92°). Shells were produced of sheets of the dense paper (Whatman paper) with a weak orthotropy of its elastic properties (the longitudinal modulus of elasticity was two times higher than circumferential one). The pre-critical deformation and buckling occurred in the elastic stage of the material work.

Numerical simulations of the experiment (concerning deformation and buckling of axially compressed orthotropic shells with transversal cuts and without cuts) were realised in ANSYS software according to the methodology proposed by authors. The analysis was based on three types of solutions: 1) linear buckling problem (bifurcations of linear pre-critical deformation); 2) geometrically nonlinear problem for the definition of limit loads of perfect shells with cuts; 3) geometrically nonlinear analysis of considered shells with initial geometrical imperfections of the middle surface. Initial imperfections imposed like a family of buckles and dents corresponded to the first eigenmode of an axially compressed shell with a cut of considered length. The magnitude of imperfections was equal to $0.12h$. This proper magnitude provided that the numerical limit compressive force matched with an average value of buckling loads found for shells without cuts in the experiment.

The best agreement, both quantitative and qualitative, of numerical results with the experimental data is observed in the case of the third analysis for all considered cuts. The buckling of shells with transversal cut, which occurs in this analysis, corresponds to the values of limit loads about $0.295 \div 0.576$ from the classical critical force of an isotropic shell with average elastic constants. The maximal difference between the third analysis and experiment is less than 10%. Such a good result is the consequence of taking into account of all important features of the physical experiment in the numerical analysis. These features include: material orthotropy, initial geometrical imperfections, loading nature (force loading), and conditions of load application (loading through the rigid disks with their unrestricted rotations during the pre-critical deformation and buckling of a shell). According to the classification in [7.10], this loading is referred to the “loading scheme 1”.

In the region of medium and large cuts $\gamma > 15°$ a very good agreement with the experiment is provided by linear bifurcational analysis *I* without initial imperfections. However, numerical values of critical loads are lower than the bearing capacity of tested shells in this region.

Furthermore, the performed numerical analysis allows completing the testing results with missing data on the pre- and post-critical behaviour of shells with considered cuts. Particularly, in numerical buckling analyses we detected up-going post-critical branches of equilibrium paths for the shells with medium and large cuts.

The numerical study of von Mises membrane stresses shows that an essentially pronounced stress concentration takes place near the longitudinal edges of cuts. Maximal stresses exceed the average values of stress fields in 2.5-3.0 times, and for the maximal limit loads they are equal about 35 MPa.

All above mentioned proves an extremely high applicability of ANSYS software for the problems of deformation and buckling of shells with essentially non-uniform stress-strain state.

Acknowledgements

This research was supported by the Alexander von Humboldt Foundation (Institutional academic cooperation program, grant no. 3.4 - Fokoop - UKR/1070297).

7.5. References

7.1 ANSYS Inc. Academic Research, Release 13.0, Help System of Mechanical Analysis Guide.

7.2 Ashmarin Yu.A., Guz A.N., Stability of a shell weakened by holes (review), Soviet Applied Mechanics, Vol. 9, iss. 4, 1973, pp. 349-358 (translated from Prikladnaya Mekhanika, Vol. 9, iss. 4, 1973, pp. 3-15).

7.3 Dzyuba A.P., Prokopalo E.F., Dzyuba P.A., Bearing capacity of cylindrical shells with the perforations, Oles Honchar Dnipropetrovsk National University, Dnipropetrovsk, Lira, 2014, 224 p (in Ukrainian). (Дзюба А.П., Прокопало Є.Ф., Дзюба П.А., Несуча здатність циліндричних оболонок з отворами,

Дніпропетровський національний університет імені Олеся Гончара, Дніпропетровськ, Ліра, 2014, 224 с.).
7.4 Elishakoff I., Probabilistic resolution of the twentieth century conundrum in elastic stability, Thin-Walled Structures, Vol. 59, 2012, pp. 35-57.
7.5 Grigolyuk E.I., Filshinskii L.A., Perforated plates and shells, Moscow, Nauka, 1970, 556 p. (in Russian). (Григолюк Э.И., Фильшинский Л.А., Перфорированные пластины и оболочки, Москва, Наука, 1970, 556 p.).
7.6 Hilburger M.W., Buckling and failure of compression-loaded composite laminated shells with cutouts, AIAA Journal, Vol. 21, 99, 2007, pp. 1-13.
7.7 Hilburger M.W., Starnes Jr. J.H., Effects of imperfections on the buckling responce of compression-loaded composite shells, Journal of Non-linear Mechanics, Vol. 37, 2002, pp. 623-643.
7.8 Jullien J.-F., Limam A., Effect of openings on the buckling of cylindrical shells subjected to axial compression, Thin-Walled Structure, Vol. 31, 1998, pp. 187-202.
7.9 Krasovsky V., Experimental investigation of buckling of compressed cylindrical shells (quality of shells and mechanisms of buckling), In: Static, dynamics and stability of structures, Z.Kolakowski, K.Kowal-Michalska (eds.), Lodz University of Technology, A series of Monographs, Lodz, Vol. 2, 18, 2012, pp. 447-476.
7.10 Krasovsky V.L., Lykhachova O.V., Numerical buckling solutions of cylindrical shells with one transversal cut under different conditions of axial compression, Stability of Structures, Zakopane, Vol. 14, 2015, pp. 61-62.
7.11 Krasovsky V.L., MarchenkoV.A., Influence of edges reinforcement of longitudinal compressed cylindrical shell on its behaviour at local cross-section impact, Stability of Structures, Zakopane, Vol. 14, 2015, pp. 63-64.
7.12 Kriegesmann B., Hilburger M.W., Rolfes R., The effect of geometric and loading imperfections on the response and lower-bound buckling load of a compression-loaded cylindrical shell, AIAA Journal, 2012, pp. 1-10.
7.13 Kwok R.M.K., Mechanics of damaged thin-walled cylindrical shells: PhD thesis; University of Surrey, Guildford, 1991, 468 p.
7.14 Lurie A.I., Static of thin-walled elastic shells, Moscow, Godtechizdat, 1947, 252 p. (in Russian). (Лурье А.И., Статика тонкостенных упругих оболочек, Москва, Гостехиздат, 1947, 252 p.).
7.15 Lykhachova O.V., Schmidt R., Deformation and buckling of axially compressed elastic cylindrical shells with transversal cut in experiments and numerical simulations, Shell Structures: Theory and Applications, W.Pietraszkiewicz and J.Gorski (eds.), London, Taylor & Francis Group, Vol. 3, 2014, pp. 219-222.
7.16 Obodan N.I., Lebedev O.G., Gromov V.A., Nonlinear behaviour and stability of thin-walled shells – Solid Mechanics and its applications, G.M.L. Gladwell (ed.), New York-London, Springer Dordrecht Heidelberg, 199, 2013, 178 p.
7.17 Preobrazhenskii I.N., Stability of thin-walled shells with holes (survey). Part 1, Strength of Materials, Vol. 14, iss. 1, 1982, pp. 23-35 (translated from Problemy Prochnosti, 1, 1982, pp. 21-32).

7.18 Preobrazhenskii I.N., Stability of thin shells with cutouts (review). Part 2, Strength of Materials, Vol. 14, iss. 2, 1982, pp. 218-225 (translated from Problemy Prochnosti, 2, 1982, pp. 74-81).

7.19 Rotter J.M., Shell structures: the new European standard and current research needs, Thin-Walled Structures, Vol. 31, iss. 1-3, 1998, pp. 3-23.

7.20 Simitses G.J., Buckling and postbuckling of imperfect cylindrical shells. A review, Applied Mechanics Review, Vol. 39, 10, 1986, pp. 1517-1524.

7.21 Song C.-Y., Buckling of cylindrical shells under non-uniform axial compressive stress, Journal of Zhejang University, Vol. 3, 5, 2002, pp. 520-531.

7.22 Song C.-Y., Teng J.G., Rotter J.M., Imperfection sensitivity of thin elastic cylindrical shells subject to partial axial compression, International Journal of Solids and Structures, Vol. 41, 2004, pp. 7175-7180.

7.23 Teng J.G., Buckling of thin shells. Recent advances and trends, Applied Mechanics Review, Vol. 49, 4, 1996, pp. 263-274.

7.24 Tennyson R.C., The effect of unreinforced circular cutouts on the buckling of circular cylindrical shells under axial compression, Journal of Engineering for Industry, Vol. 90, 4, 1968, pp. 541-546.

7.25 Van Dyke P., Stress about a circular hole in a cylindrical shell, AIAA Journal, Vol. 3, 1965, pp. 1733-1742.

8.

Corner radius effect in the thin-walled columns of regular polygon cross-section on the local buckling and load carrying capacity

It is a common observation that the thin-walled columns of flat walls are widely used in engineering practice. However, despite high strength materials applied for their manufacturing, those structures couldn't be fully exploit due to mostly low values of critical stress of a local buckling. In the stability of structures it is obvious that increasing the local stability could be gained by simple treatments: as thicker walls, stiffeners or by changing the cross-section shape. But those methods lead to making a structure larger and heavier. Nowadays, the optimization of the material distribution is the crucial factor during projecting and design process. It encourages to find the best coherence between a local buckling load or an ultimate load and cross section shape of specific structure without enlarging its cross-section area i.e. its total mass. As an example in [8.4] authors proof that the load carrying capacity of thin-walled multi-cell columns can be increased by changing their cross-section shape but not its entire area. Tillman and Williams [8.11] were searching for an agreement between the tests and the theory for the problems associated with defining the buckling loads of practical columns. The performed comparison tests gave results to be good in the main with theory. Camotim at all [8.2] applied the generalised beam theory (GBT) formulation to perform first-order and buckling analyses of arbitrary thin-walled members, namely members with cross-sections that combine closed cells with open branches. Królak at all [8.6] analysed multicell closed cross-section columns and girders to determine their critical load and postbuckling response. There isotropic structures were considered whereas in [8.4, 8.7] orthotropic properties of column walls were assumed. The same authors team investigated analogous problem in laboratory experiments to validate the previous analytical approach with satisfactory results [8.5]. The problem of an influence of corner radii of square cross-section short thin-walled columns on the buckling and postbuckling response was introduced in [8.9].

It should be emphasize that the question of the local buckling of thin-walled columns has a numerous and well-known literature and has been thoroughly investigated. In particular within the literature survey, one can find some studies presented the influence of a cross section shape i.e. open or closed, on the local stability [8.3, 8.8]. However, one can still find issues worth to be studied. Authors of this work have been investigated a corner radius effect on the local buckling of thin-walled structures. For each considered regular cross-section shapes (i.e. triangular, square, regular pentagon or hexagon) different values of corner radii were applied taking into account a constant area of a column cross-section. This study appears to be some kind of an optimizing analysis of thin-walled members without fundamental formulation.

8.1. Introduction

During axial-compression of a plate thin-walled steel column of regular polygon cross-section (mainly column with an even number of walls - it is square, regular hexagon or octahedron), we can determine the local buckling critical stress from the formula valid for a long uniformly-compressed rectangular plate simply supported at all edges (Eq. 8.1) [8.3, 8.8, 8.13]

$$\sigma_{kr} = 4\frac{\pi^2 D}{\mathrm{b}_0^2 t} = \frac{\pi^2 E}{3\left(1-\nu^2\right)}\left(\frac{t}{b_0}\right)^2 \tag{8.1}$$

where: E - Young's modulus of column material,

ν - Poisson's ratio,

b_o - width of column single wall or a long rectangular plate,

t - wall thickness (or plate thickness).

Assuming that for steel E = 200 GPa, $\nu = 0.3$ and b_o = 1 m, t = 1 mm, t = 2 mm, t = 3 mm and t = 4 mm, respectively, we got the following results

$\sigma_{cr} =$ 0.723 MPa for t = 1 mm,

$\sigma_{cr} =$ 2.894 MPa for t = 2 mm,

$\sigma_{cr} =$ 6.507 MPa for t = 3 mm,

$\sigma_{cr} =$ 11.57 MPa for t = 4 mm.

As we can see, these are very small values of critical stresses in comparison to the structural steel yield limit. Thus, the strength mechanical properties of applied material cannot be fully utilized in considered columns [8.8].

8.2. The problem formulation

We consider the local stability and load carrying capacity of thin-walled columns of a regular polygon (equilateral triangle, square, regular pentagon, hexagon, heptagon, octahedron etc.) cross-section with corner radii. In the frame of this analysis critical stresses of local buckling and load carrying capacity of thin-walled columns of various (mentioned) cross-sections subjected to axial-compression are considered. Among these cross-sections there are some with introduced radius corner ($r \neq 0$) and some without radius corner (i.e. $r = 0$, $b = b_0$). For comparison reasons we assume that the material, column length, wall thickness and cross-section perimeter of all columns are the same. The radius of a corner between two adjacent walls could be changed between $0 \leq r_n \leq r_c$, where r_c - radius of a circle with total circumference equal to a total perimeter of each considered of columns (it is the radius of cylindrical shell).

8.3. Column cross-section geometry description

In Fig. 8.1 some basic cross section dimensions of considered columns are presented and designated. They are respectively: r_n - a corner radius of regular polygon columns, b_{0n} - a single wall width of regular polygon cross section column with n walls and with radius $r_n = 0$, b_n - a flat wall element width ('net' width between radii) of regular polygon cross section with n walls and a corner radius $r_n \neq 0$.

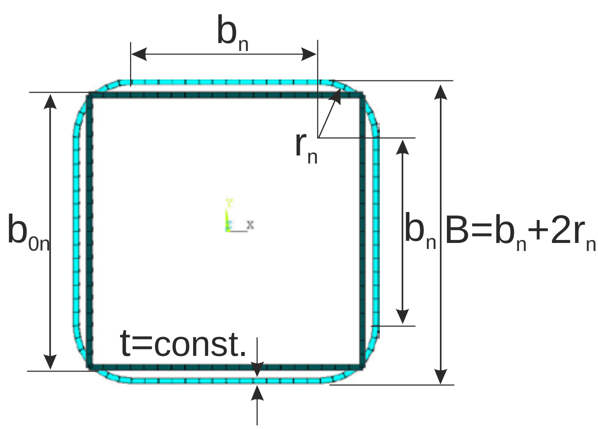

Fig. 8.1. Cross-section of a square section column with corner radii

We consider columns with a global number of walls $n = 3 \div 8$. The single wall width b_{on} of any regular polygon without corner radii is referred to a square column cross-section ($n = 4$), where a single wall width is marked as - b_{04} .

From the equality of a column perimeter it follows that $nb_{on} = 4b_{04}$. Therefore

$$b_{on} = 4b_{04}/n \tag{8.2}$$

After comparing perimeter of columns without corner radii and with corner radius r_n, we simply got $nb_{0n} = nb_n + 2\pi r_n$. From the later relationship it follows that

$$b_n = b_{0n} - \frac{2\pi}{n} r_n \tag{8.3}$$

For each of considered columns we obtain a cylindrical shell in the case when $b_n = 0$ - thus for walls without flat parts. This shell radius equals to

$$r_n = \frac{n}{2\pi} b_{0n} = \frac{2}{\pi} b_{04} \tag{8.4}$$

and it is identical for all considered columns (it is not dependable on n a total number of walls of regular polygon). Thus after a simple recalculation $r_n = 2/\pi\, b_{04} = 0.63662 b_{04}$ and therefore corner radius between adjacent walls could be changed between the limits of $0 \le r_n \le 0.63662 b_{04}$.

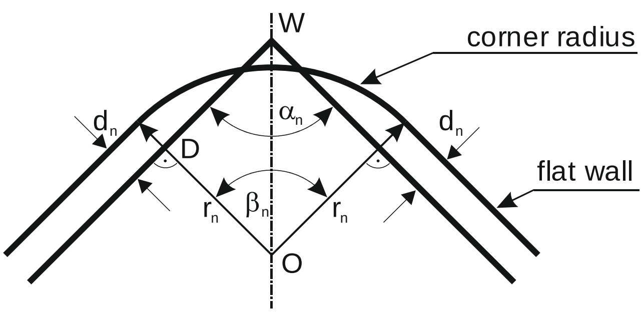

Fig. 8.2. Vertex geometry

In Fig. 8.2 an exemplary vertex of a regular polygon cross-section is shown. We indicate as α_n an angle between adjacent (corner) walls because this angle depends on n the number of column walls. For a regular polygon with n component walls we can define these distinctive angles as follows

$$\alpha_n = \pi - \frac{2\pi}{n} = \frac{\pi(n-2)}{n}$$

and also

$$\beta_n = \pi - \alpha_n = \frac{2\pi}{n}$$

In Fig. 8.2 the distance between flat part of a wall in the polygon with corner radius and without corner radius is denoted by d_n. As it is also shown in this figure, the length of segment $\overline{WD}$ equals to $\overline{WD} = \frac{1}{2}(b_{0n} - b_n) = \frac{\pi}{n} r_n$. Moreover, $r_n - d_n = \overline{WD} \cdot ctg\frac{\beta_n}{2}$, and finally one gets

$$d_n = r_n(1 - \frac{\pi}{n} ctg\frac{\pi}{n}) \tag{8.5}$$

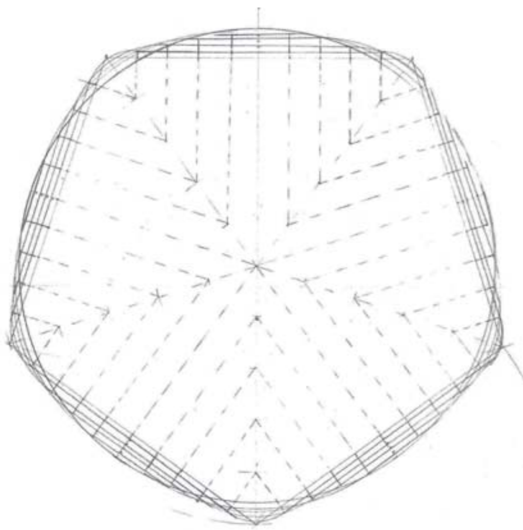

Fig. 8.3. Family of pentagon cross-sections

The position of the centre of any corner radius (point O in Fig. 8.2) counted from node W, results from a sine function of the angle $\frac{\beta_n}{2} = \frac{\pi}{n}$:

$$\sin\frac{\beta_n}{2} = \frac{\overline{WD}}{\overline{WO}} = \frac{\frac{\pi}{n} r_n}{\overline{WO}}$$

$$\overline{WO} = \frac{\frac{\pi}{n} \cdot r_n}{\sin\frac{\pi}{n}} = \frac{\pi \cdot r_n}{n \cdot \sin\frac{\pi}{n}}$$

To limit the range of considered possibilities the following data quantity has been assumed for computations:

- material modulus: $E = 2 \cdot 10^5$ MPa, $\nu = 0.3$;
- to maintain the same perimeter of all considered cross-section shapes it was assumed that the 'starting' width of a particular wall without corner radius is: $b_{03} = \frac{4}{3} m$, $b_{04} = 1m$, $b_{05} = \frac{4}{5} m = 0.8m$, $b_{06} = \frac{2}{3} m$, $b_{07} = \frac{4}{7} m$, $b_{08} = \frac{1}{2} m$, respectively.
- four wall thicknesses: $t_1 = 1\ mm$, $t_2 = 2\ mm$, $t_3 = 3\ mm$, $t_4 = 4\ mm$ - for all columns.

Among all possible corner radius values one can indicate few common radii lengths undependable on n number of column walls so the same dimension for particular column. Assuming again that $b_{04} = 1\ m$ these radii are given below and will be further applied for comparative juxtaposition:

$r_0 = 0$ - for columns without corner radius,

$r_1 = \frac{1}{5} r_c = \frac{1}{5} \cdot \frac{2}{\pi} b_{04} = \frac{2}{5\pi} b_{04} = \frac{2}{5\pi} 1 = 0.1273m$,

$r_2 = \frac{2}{5} r_c = \frac{4}{5\pi} b_{04} = \frac{4}{5\pi} 1 = 0.25465m$,

$r_3 = \frac{3}{5} r_c = \frac{6}{5\pi} b_{04} = \frac{6}{5\pi} 1 = 0.38197m$,

$r_4 = \frac{4}{5} r_c = \frac{8}{5\pi} b_{04} = \frac{8}{5\pi} 1 = 0.5093m$,

$r_5 = r_c = \frac{2}{\pi} b_{04} = \frac{2}{\pi} 1 = 0.63662m$ - a cylinder with radius r_c.

For the comparative analysis presented above radii values will be given in plots with numerical results.

8.4. Numerical model

To illustrate the impact of the corner radius insertion on the buckling stress and load carrying-capacity extent some computations were performed. The Finite Element Method was employed as an efficient tool for that purpose. The solution to the considered problem of a nonlinear buckling analysis of short thin-walled columns might be solved by application of a chosen variational method. However, the governing differential equations would be a mixture of a flat plate and a curved shell formulations with required junction conditions, what would lead to rather complex expressions. In a consequence the solution to that equation set would require numerical integration or generally numerical methods application. It all explains the FEM advantage and reasons of our choice to it application.

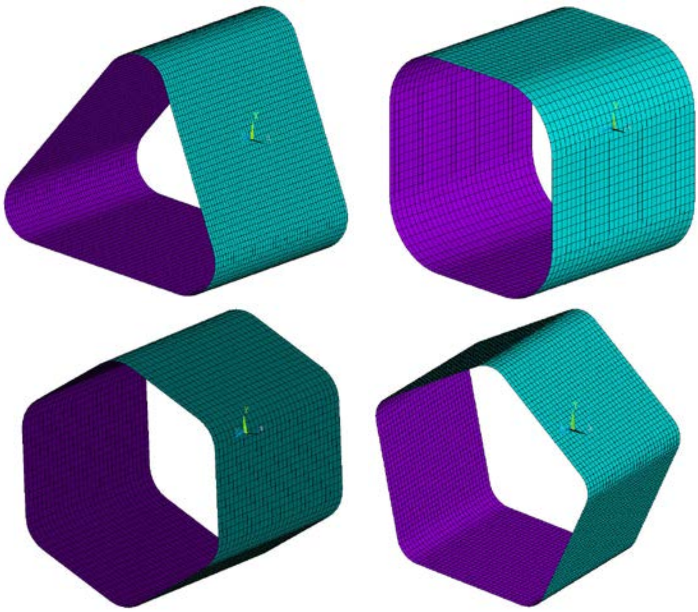

Fig. 8.4. Exemplary numerical models

The parametric numerical models of considered closed profile cross-section shapes were prepared in commercial package ANSYS [8.14] which is based on the FEM. The presented study concerns a thin-walled structure and the plane stress state, therefore a shell finite element was chosen to discretization and to formulate the finite element model. It was the SHELL181 - finite quadrilateral shell element of ANSYS software library. This element is suitable to nonlinear applications (strain and material) and is governed by the first order shear deformation theory in the case of multilayered composite cross-section. Each of its four nodes has six degrees of freedom i.e. translations in the x, y, and z directions, and rotations about the x, y, and z-axes of a local coordinate system. Hereby the in-plane rotational (drill) stiffness is added at the nodes for solution stability. A penalty method is then used to relate this independent rotational degree of freedom about the normal to the shell surface with the in-plane components of displacement. That formulation offers excellent accuracy in curved-shell-structure simulations.

The developed numerical models of considered columns were discretized with an uniform mesh of finite elements (Fig. 8.4) and the full geometry was used to simulate assessed buckling and post-buckling response of a particular column. Despite of the existing geometrical symmetry of a considered structure, it was resigned from modelling only part of it to be able to analyse different deformation modes which could be lost in opposite case. The total number of finite elements approached ten thousands. It was a series of additional tests performed to check if the produced finite element model gives a reliable representation of the structure being analyzed. These tests are not described here due to limited scope of the paper.

The boundary conditions at loaded column edges followed the analytical assumption of simply supported type (Fig. 8.5). They were attained through constrained displacement of model edges in normal to a wall surface direction. For the limit shape i.e. cylindrical columns not only the radial but tangential displacements of column loaded edges were restricted. To fulfil additionally the condition of loaded edges being rectilinear the coupling constrains were introduced. Therefore, the applied system of displacement constrains allowed a replication of a column edge behaviour of a classical structural strength approach. It recalls also the standard conditions during a static compression test in a strength test machine.

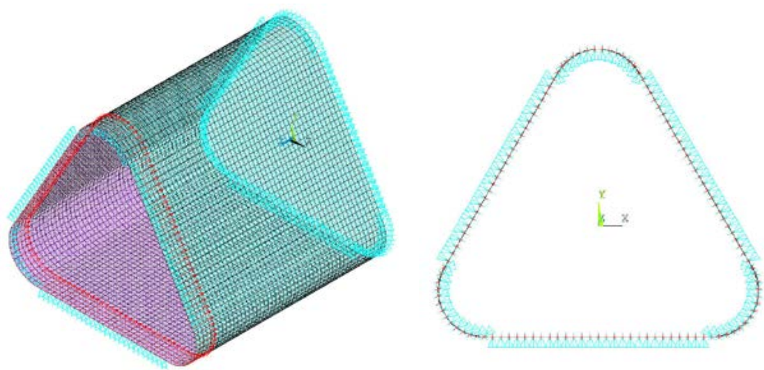

Fig. 8.5. Simply support BC defined in FEM model

Conducted analysis concerned an axial compression of studied short closed cross-section profiles/columns thus the loading was obtained by uniform nodal force distribution along ‘upper’ column edge where the ‘lower’ one was constrained against axial displacement.

The main interest of a nonlinear buckling analysis was the load carrying-capacity of an individual column which was preceded by the linear eigenbuckling analysis. From the first one, the critical load was determined as well as the first buckling mode. Obtained in this way eigenbuckling mode was introduced into the numerical model as initial imperfection. The eigenmode mapping technique was here applied. The magnitude of this out of flatness imperfection referred to a column wall thickness was in the range of 0.01÷0.1. The full Newton-Raphson iteration procedure was used as the incremental technique in the finite element structural analysis [8.1].

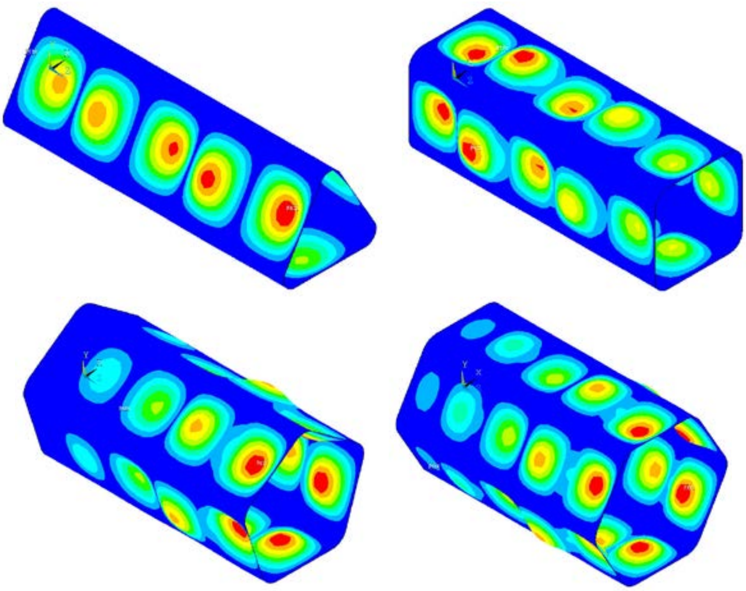

Fig. 8.6. First buckling modes for b_{04} = 500 mm and equal r length

The material model assumed in computations was defined by a bilinear characteristic with isotropic hardening. The static yield limit was taken as equal to σ_y = 200 MPa with a tangent modulus E_t = 2000 MPa, with the Young’s modulus and Poisson ratio defined within the text above. Some considerations of applying the Needelman-Tvergard formula for approximation of material characteristic [8.10] or an input of a real material characteristic as multi-linear curve to eliminate the abrupt slope change in bilinear material description were performed but their results did not improve the numerical process in a visible way and were skipped therefore. The yield surface was established with Huber-Mises-Hencky criterion hence the same yield stresses value in uniaxial tension and compression for ductile isotropic material was assumed.

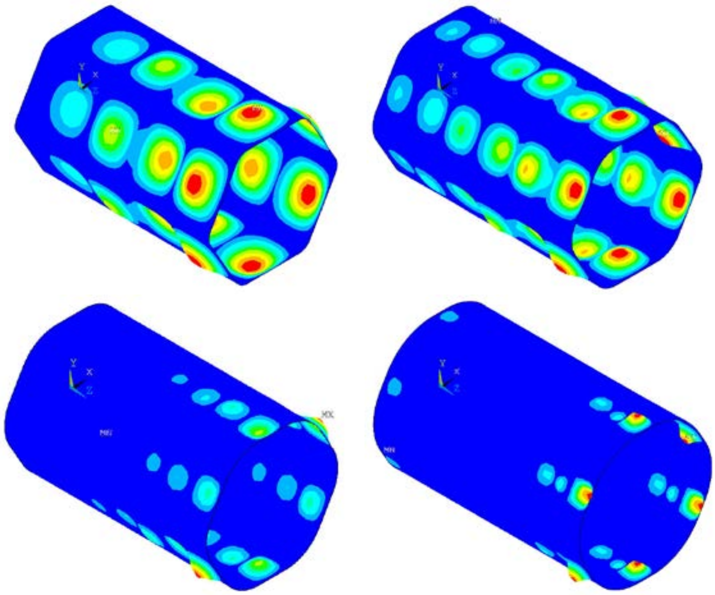

Fig. 8.7. First buckling modes of hexagon cross-section column for a series of r length (0.2; 0.4;…0.8 of r_c)

8.5. Results of buckling stress computations

A lot of numerical analysis was performed with reference to four chosen cross-section shapes of thin-walled columns. These were regular polygons, i.e. equilateral triangle, square, regular polygon and regular hexagon. For comparison reasons it was assumed the equal perimeter of each polygon and then the formulas for the length of particular polygon side - defined above within the data for computations - were fulfilled. Two perimeter lengths were considered 4m and 2m, with four cases of column wall thickness. For particular column cross-section type a series of computations were performed where the buckling load - buckling stress, buckling modes and the load carrying-capacity were determined. To focus the attention on a local buckling phenomenon the total length of all considered columns were assumed three times a side length of a considered regular polygon. Thus all investigated thin-walled profiles were of a short column class. Exemplary results are presented below in the following graphs and figures.

Within the first step of buckling analysis it was critical load determined as well as buckling modes. Some exemplary first modes of considered column shapes are presented in Figs. 8.6 and 8.7. In Fig. 8.6 there are presented buckled shapes of all profile cross-section types when the reference $b_{04} = 0.5\,m$ and the same value of corner radius $r_n = b_{04}/2\pi$ was assumed. One can observe the same number of halve waves along all column walls with visible modulation effect of buckles magnitude between loaded column ends. This effect is more pronounced when a cross-section shape tends to a cylinder (see Fig. 8.7). The length of a single buckle is shorter than b_{0n} the flat part of a column wall. The very characteristic of detected modes is the fact that despite the cross-section shape and corner radius dimension, buckles occurred only throughout the flat part of walls. Buckling deformations of curved parts of column walls were never observed.

The predictable effect of buckling wave number and length connected with the increase of corner radius length is presented in Fig. 8.7. It corresponds to the previous conclusion that the width of a flat part of column wall influences the length thus a number of buckles along the column length. Also the modulation effect is visible too. However, for almost cylindrical columns the few first eigenbuckling values are very close each other (difference up to 5%) and their modes are similar with small difference in buckles magnitude only.

The impact of corner radius on the buckling load is presented on plots in subsequent figures for different juxtapositions.

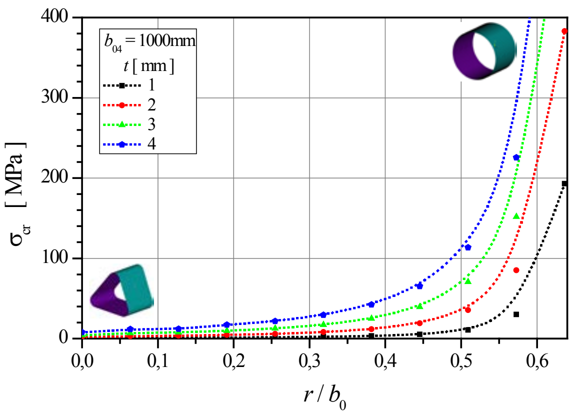

a)

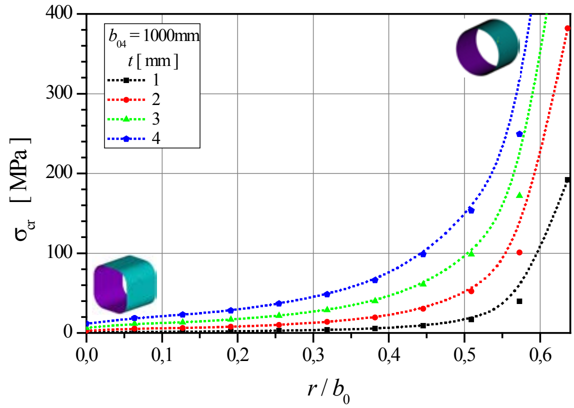

b)

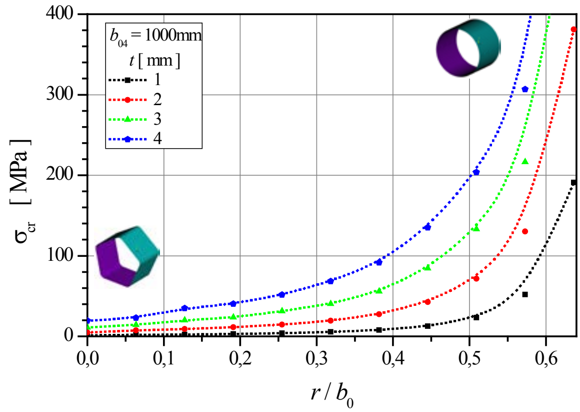

c)

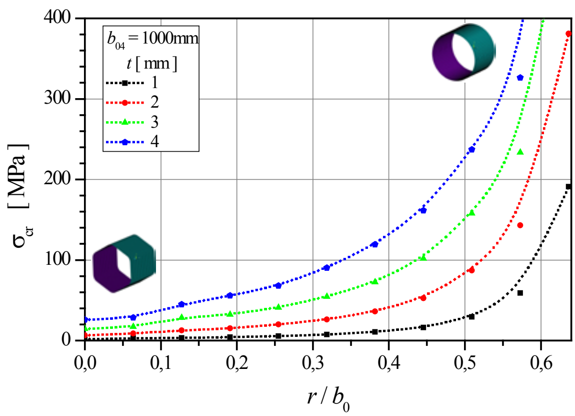

d)

Fig. 8.8. Critical stress value as a function of corner radius value for different cross-section shapes of $3\times b_{0n}$ columns

In Fig. 8.8 there are charts presenting the influence of corner radius length on the critical stress value increase for columns of four chosen cross-section shapes where the reference width of square cross-section wall is equal to $b_{04}=1\,m$. The pronounced jump of critical stress value between regular polygon and cylindrical cross-section is up to almost 400 times for regular triangle of $t_1=1\,mm$. This effect decreases when the number of polygon walls increases as well as the wall thickness does. The increasing effect of stress value is observed even for low dimensions of corner radii for polygons of greater number of walls whereas for triangle or square is visible for cross-section shapes closer to cylindrical shell.

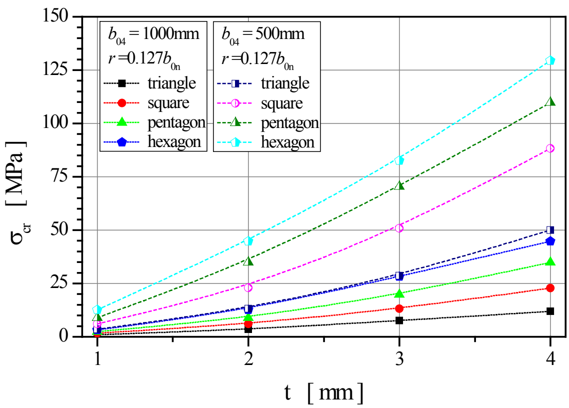

a)

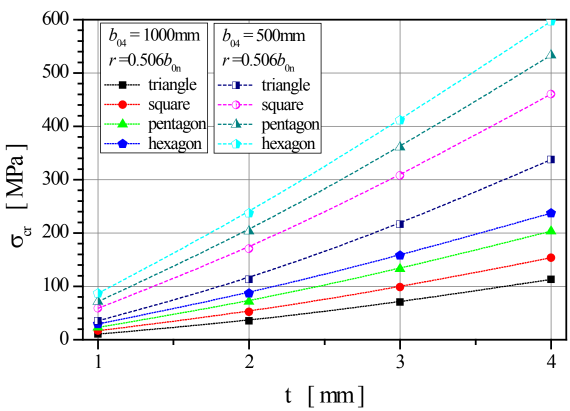

b)

Fig. 8.9. Critical stress value as a function of wall thickness for different corner radius values and cross-section shapes

Similar conclusions are valid for columns which reference cross-section perimeters differ (are greater or lower) to $4 \times b_{04} = 4\ m$. Then the critical stress relationship for regular polygon column and cylindrical column are in similar relationships as the their perimeters are to $4 \times b_{04} = 4\ m$.

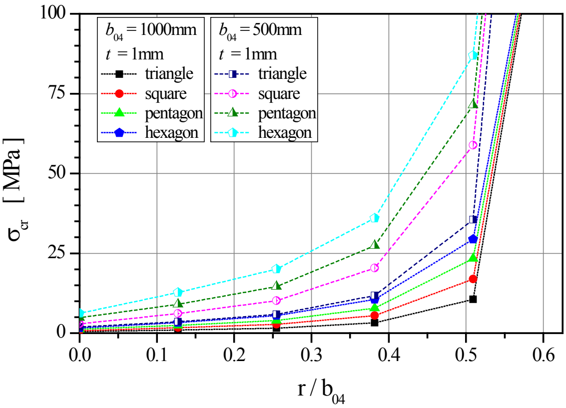

a)

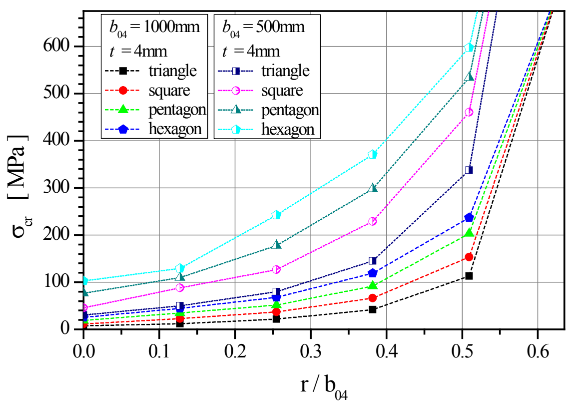

b)

Fig. 8.10. Critical stress value as a function of corner radius values for different cross-section shapes

Analyzing an impact of corner radius introduction between adjacent column walls on the buckling load one can compare this effect when changing the cross-section shape for constant wall thickness and the same perimeter length. From Fig. 8.9 it is visible that this effect is connected in greater degree with number of column walls (see triangle and hexagon) and it is more efficient for bigger corner radius length. However, the increase of critical stress value for the column of triangle cross-section when compared to a hexagon cross-section is greater for thinner walls (i.e. $t_1 = 1\,mm$) than thicker on approximately 30%. This statement can also be referred to a shorter perimeter case and is more potent for a shorter radii (Fig. 8.9a). The changes in inclinations of the lines on the graphs in Fig. 8.9 are grater for an increasing number of column walls.

The conclusions drawn above are again confirmed by both scatter plots in Fig. 8.10, where exemplary results for two limit wall thicknesses $\mathrm{t}_1 = 1\,mm$ and $\mathrm{t}_1 = 4\,mm$ are presented. Despite the widespread ranges of critical stress absolute values for increasing corner radius dimension the relative relations between the buckling loads vary in a narrower range. However these ranges are broader for shorter perimeter length multiwall cases.

Table 8.1. Critical load and ultimate load for some column cases

pentagon	t = 1 mm		t = 2 mm		t = 3 mm		t = 4 mm	
r/b_{04}	σ_{cr} [MPa]	$\frac{N_{ult}}{N_{cr}}$	σ_{cr} [MPa]	$\frac{N_{ult}}{N_{cr}}$	σ_{cr} [MPa]	$\frac{N_{ult}}{N_{cr}}$	σ_{cr} [MPa]	$\frac{N_{ult}}{N_{cr}}$
0	4.8	5.691	19.2	2.690	43.1	1.760	76.4	1.329
0.063662	7.3	4.121	22.8	2.304	46.5	1.640	79.1	1.277
0.127324	9.0	4.028	34.9	1.869	70.4	1.633	109.8	1.054
0.190986	11.2	3.489	40.2	1.737	86.8	1.224	151.3	1.012
0.254648	14.5	2.843	51.5	1.500	105.3	1.167	177.5	0.999
0.31831	19.4	2.311	68.2	1.291	139.6	1.033	226.2	0.834
0.381972	27.3	1.830	91.6	1.098	184.0	0.896	297.6	0.635
0.445634	42.6	1.597	135.0	1.033	256.9	0.726	401.6	0.485
0.509296	71.4	1.346	203.4	0.867	360.8	0.532	533.5	0.366
0.572958	130.2	1.075	306.5	0.617	491.7	0.394	681.0	0.286

For assumed column overall dimensions and shapes in the most cases the calculated critical stress values are very low when compared to the yield limit for assumed structural steel. Thus the load carrying-capacity of these columns gives a broad reserve of loading. Higher critical stress values were determined for thicker column walls and greater corner radius dimensions what makes a column stiffer. The later values determined in the linear eigenbuckling analysis are in many cases above the yield limit for assumed material properties. In the nonlinear buckling analysis - in a geometrical approach and in terms of a real material characteristic, a critical load is restricted by the structural steel yield strength. This type of analysis requires too two steps and time consuming computations. Hence the assessment of an impact of corner radii effect on the ultimate load of considered columns was performed for limited number of structures. The exemplary results of this analysis are summarized in Table 8.1. Nevertheless, the drawn conclusions can be extended to all investigated short columns of regular polygon cross-sections.

The representative results presented in Table 8.1 were obtained for a column of a pentagonal cross-section with the reference width of a single wall $b_{04} = 0.5\,m$, what makes $b_{05} = 0.4\,m$ and the profile total length equal to $3 \times b_{04} = 1.2\,m$. A critical stress determined for a thin wall solution of analysed columns allows a post-buckling work of a column in a much wider range than for thicker walls structure. The available excess of loading up to the ultimate load reaches few times the critical stress. This relationship reduces with the increase of corner radius length and with the wall thickness. Then from obvious reasons the quotient N_{ult}/N_{cr} of ultimate force and critical force is lower than one. Here again it should be emphasized that also in the post-buckling range local buckling deformations are observed over the 'flat' parts of column walls. For a small reserve of axial compression (N_{ult}/N_{cr} a bit greater than 1) local buckles follow the eigenbuckling pattern and enter the curved parts of column walls in deep post-buckling range. This phenomenon is shown in Fig. 8.11. In the far post-buckling stage the wall deformations are shifted towards the loaded edge and form deep inside deflections. Due to relatively flat hardening part of stress-strain diagram assumed for computations (E_t = 2000 MPa) the equivalent stress value gained 221 MPa in the region close to the column loaded end.

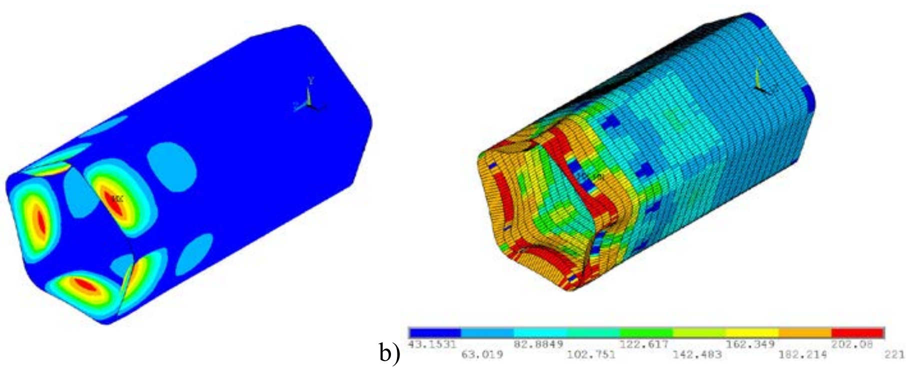

a) b)

Fig. 8.11. a) Post-buckling displacements, b) stress map of a short pentagon column

8.6. Conclusions

The performed investigations confirmed the impact of corner radii solution on the thin-walled column local buckling load value. The buckling strength of a column can be controlled (increased) by introduction of a curved radial junction of adjacent walls. This statement is valid for different cross-section shapes. However, the increase effect is more visible for columns of greater number of walls. In the performed FEM computations, where the buckling shapes of analysed structures were possible to watch both at critical load state as well as in the post-buckling range, it has been never observed buckles over curved parts of column walls, only flat strips of walls exhibited deformations.

Application of medium values of corner radii for columns of thinner walls has given better effect for ultimate load surplus. For thicker walls the yield stress value was crucial for restricting the axial column load. This effect was enhanced by greater dimension of corner radius.

Columns of greater number of walls exhibit better properties as it goes on local buckling load and react in a more profitable or useful way on the corner radius introduction.

8.7. References

8.1 Bathe K.J., Finite element procedure, Prentice-Hall Inc., New Jersey 1996.

8.2 Goncalvesa R., Dinis P.B., Camotim D., GBT formulation to analyse the first-order and buckling behaviour of thin-walled members with arbitrary cross-sections, Thin-Walled Structures, Vol. 47, 5, 2009, pp. 583-600.

8.3 Królak M. (Ed.), Buckling, postbuckling and load carrying capacity of thin-walled orthotropic structures, Monographs, Technical Univ. of Lodz 1995 (*in Polish*).

8.4 Królak M., Kowal-Michalska K., Stability and ultimate load of multi-cell orthotropic columns subjected to compression, in Shell Structures Theory and Application, Pietraszkiewicz W., Szymczak Cz. (eds.), Taylor&Francis Gr., London 2006, pp. 235-239.

8.5 Królak M., Kowal-Michalska K., Mania R.J, Świniarski J., Experimental tests of stability and load carrying capacity of compressed thin-walled multi-cell columns of triangular cross-section Thin-Walled Struct.,Vol. 45, 10-11, 2007, pp. 883-887.

8.6 Królak M., Kowal-Michalska K., Mania R.J, Świniarski J., Stability and load carrying capacity of multicell thin-walled columns of rectangular cross-section, J. of Theoretical and App. Mechanics, 47, 2, 2009, pp. 435-456.

8.7 Królak M., Mania R.J., Critical and postcritical behavior of thin-walled multicell column of open profile, Mechanics and Mechanical Eng., Vol. 14, No. 2, 2010, pp. 281-290.

8.8 Królak M., Mania R. J. (eds), Stability of thin-walled plate structures, Vol. 1 of Statics, Dynamics and Stability of Structures, Series of Monographs, Technical Univ. of Lodz 2011.

8.9 Królak M., Mania R.J., Kamocka M., Corner radius effect in thin-walled square section columns on the local buckling of walls under axial compression, Proceedings of the XIV Symp. on the Stability of Struct., Mania R.J. (ed.), 2015, pp. 63-64.

8.10 Mania R.J., Kowal-Michalska K., Parametryczna analiza stateczności dynamicznej konstrukcji cienkościennych Metodą Elementów Skończonych, in: Analizy numeryczne wybranych zagadnień mechaniki, Niezgoda T. (ed.), Wyd. WAT, Warszawa 2007, pp. 227-243 (in Polish).

8.11 Tillman S.C., Williams A.F., Buckling under compression of simple and multicell plate columns, Thin-Walled Structures, Vol. 8, 2, 1989, pp. 147-161.

8.12 Timoshenko S., Gere J., Theory of elastic stability, McGraw-Hill, 1961.

8.13 Volmir A.S., Ustoiczivost deformirujemych system, Nauka, Moskwa 1967.

8.14 ANSYS Help, Release 15.0, SAS IP, Inc., 2013.

9.

Local and global elastic buckling of I-beams under pure bending

9.1. Introduction

Thin-walled beams are main parts of contemporary machines. The main constraints of structural design are strength, stability and geometric conditions. The basis of calculation of local and global elastic buckling and optimization problems of thin-walled beams, plates and shells are described in many monographs, for example by Bažant and Cedolin [9.5], Brzoska [9.7], Iwicki [9.24], Kołakowski and Kowal-Michalska [9.29, 9.30], Kotełko [9.32], Kowal-Michalska [9.35, 9.36, 9.38], Kowal-Michalska and Mania [9.37], Królak [9.40], Kubiak [9.46], Magnucka-Blandzi [9.54], Magnucki and Ostwald [9.59], Murray [9.67], Mutermilch and Kociołek [9.68], Paczos [9.76], Trahair [9.90], Ventsel and Krauthammer [9.91], Vlasov [9.92], Volmir [9.93], Weiss and Giżejowski [9.95]. The detailed study related to buckling problems of thin-walled beams with open cross sections, in particular I-beams, are presented in many papers, by: Andrade and Providência [9.1], Aydin [9.2], Basaglia et al [9.3], Batista [9.4], Bacque and Rasmussen [9.6], Camotim et al [9.8, 9.9], Cheng and Schafer [9.10], Chróścielewski et al [9.12], Chu et al [9.13], Davies [9.14], Dinis nad Camotim [9.15], 9.16], Dubina and Ungureanu [9.17], El-Mahdy and El-Saadawy [9.18], Gonçalves [9.19], Hancock [9.20, 9.21, 9.22], Hancock and Rasmussen [9.23], Lewiński and Magnucki [9.47], Li and Chen [9.48], Loughlan and Yidris [9.49], Ma and Hughes [9.50], Macdonald et al [9.51, 9.52], Magnucka-Blandzi and Magnucki [9.55, 9.57], Magnucki and Monczak [9.58], Magnucki et al [9.62, 9.63], Manevich and Raksha [9.65], Mohri et al [9.66], Naderian et al [9.69], Narayanan and Mahendran [9.70], Ozbasaran et al [9.72], Paczos et al [9.73, 9.74, 9.75], Pala [9.77], Pastor and Roure [9.78, 9.79], Rasmussen [9.80], Rondal [9.82], Samanta and Kumar [9.83], Schafer and Peköz [9.84], Schafer [9.85], Silvestre and Camotim [9.86], Song et al [9.87], Szymczak [9.89], Wang and Ikarashi [9.94], Young [9.96] and Zirakian [9.99, 9.100].

To a special group of the thin-walled constructions belong the beams with non-classical structures. The important studies concerning the buckling and ultimate load problems of these beams are presented by: Kołakowski [9.25], Kołakowski et al [9.26], Kołakowski and Królak [9.27], Kołakowski and Kowal-

Michalska [9.28], Kotełko [9.31], Kotełko and Królak [9.33], Kowal-Michalska and Grądzki [9.34], Królak [9.39], Kólak and Młotkowski [9.41], Królak et al [9.42, 9.44, 9.45], Królak and Kowal-Michalska [9.43]. Ovesy et al [9.71] and Zaraś et al [9.97, 9.98].

The problems presented in these monographs and papers are to-day extensively studied in many specialist teams. The results of these studies are applied to practice and, in consequence, are conducive to improvement of contemporary thin-walled structures in mechanical and civil engineering.

The subject of the chapter includes three types of I-beams: the first one - a standard beam (B-1), the second - a non-standard beam (B-2) with lipped flanges, and the third one - a non-standard beam (B-3) with sandwich flanges. Local and global buckling problems of these beams are studied.

9.2. Buckling of the standard-universal I-beam (B-1)

The cross-section of the first I-beam (B-1) is shown in Fig. 9.1.

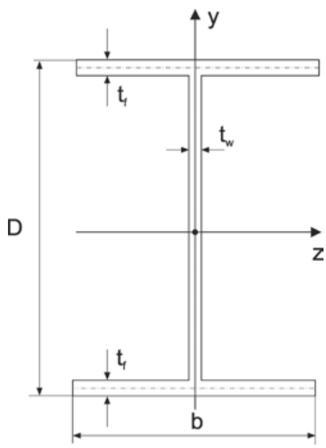

Fig. 9.1. The cross-section of the standard I-beam (B-1)

The sizes of the cross-section are as follows: D - total depth, b - width of the flanges, t_f - thickness of the flanges, t_w - thickness of the web.

9.2.1. Local buckling

Analytical study. The upper flange of the I-beam under pure bending is axially compressed, however the lower flange is tensioned. The simple theoretical model of the half of the flange is a rectangular plate with three edges simply supported and one edge free. The critical stress of this plate - half upper flange, taking into account the papers [9.5, 9.54, 9.59, 9.91, 9.93], is in the following form

$$\sigma_{CR,flan}^{(B-1,An)} = \frac{\pi^2 E}{12(1-\nu^2)}\left(2\frac{t_f}{b}\right)^2 k_{flan}^{(B-1)} \tag{9.1}$$

where: $k_{flan}^{(B-1)} = \frac{6}{\pi^2}(1-\nu) + \left(\frac{b}{2L_w}\right)^2$ - dimensionless parameter, L_w - half-wavelength. E,ν - material constants,

Then, the critical bending moment of I-beam for the local buckling

$$M_{CR,flan}^{(B-1,An)} = \frac{2J_z}{D-t_f}\sigma_{CR,flan}^{(B-1,An)} \tag{9.2}$$

where J_z - moment of inertia with respect to the *z* axis (Fig. 9.1).

The dimensionless measure of the quality of the I-beam is assumed based on the paper [9.56] in the following form

$$\Phi_{flan}^{(B-1,An)} = \frac{M_{CR,flan}^{(B-1,An)}}{EA^{3/2}} \tag{9.3}$$

where A - total area of the cross-section.

Example 1. The first beam (B-1) with the following sizes of the cross-section: $D = 210\,\text{mm}$, $b = 134\,\text{mm}$, $t_f = 10\,\text{mm}$, $t_w = 6.4\,\text{mm}$. Then, the geometrical properties of the cross-section are as follows: total area $A = 3960\,\text{mm}^2$, torsion constant $J_t = 10.681\cdot 10^4\,\text{mm}^4$, and moments of inertia $J_z = 31.067\cdot 10^6\,\text{mm}^4$, $J_y = 4.010\cdot 10^6\,\text{mm}^4$, $J_\omega = 40.102\cdot 10^9\,\text{mm}^6$.

Thus, the values of the characteristic quantities are as follows:

$\sigma_{CR,flan}^{(B-1,An)} = 2002.8\,\text{MPa}$ for $L_w = 250\,\text{mm}$ - the critical stress (9.1);

$M_{CR,flan}^{(B-1,An)} = 622.2\,\text{kNm}$ - the critical bending moment (9.2);

$\Phi_{flan}^{(B-1,An)} = 0.01248$ - the dimensionless measure of quality (9.3).

Numerical study - finite strip method (CUFSM 3.12). The numerical model FSM of the standard I-beam (B-1) (Fig. 9.1) is elaborated for the sizes as in the *Example 1*. The results of numerical calculations and the shape of local buckling of the beam are shown in Fig. 9.2. The mathematical bases of the finite strip method (FSM) and its application in structural analysis is described by Cheung [9.11], while the CUFSM system was developed by Schafer [9.85].

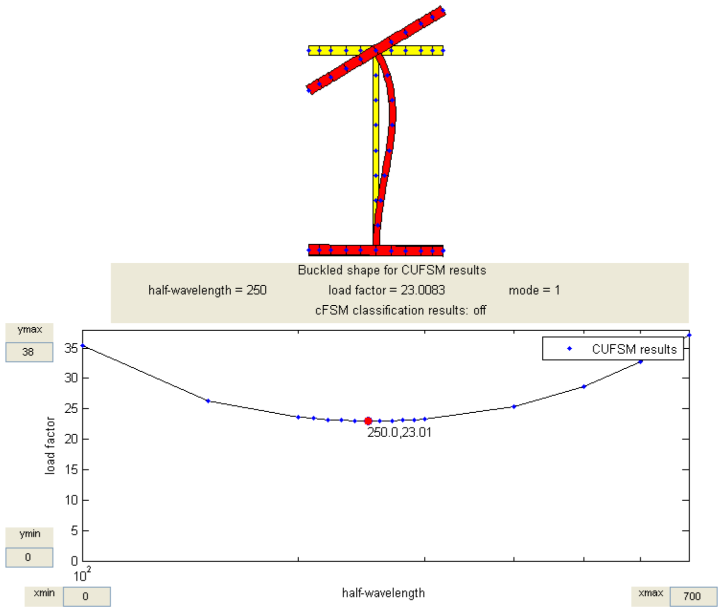

Fig. 9.2. The local buckled shape - the flange of the first I-beam (B-1)

The value of the critical stress for local buckling of the standard I-beam calculated with the use of the FSM is $\sigma_{CR,flan}^{(B-1,FSM)} = 2300.8\,\text{MPa}$ for $L_w = 250\,\text{mm}$ and exceeds the analytical value by 15%. The analytical model gives the lower estimation of the critical stress for the local buckling, because the interaction with the web is ignored. It should be noticed that the local buckling of the beam related to the flange does not occur in elastic range.

9.2.2. Global buckling

Analytical study. The analytical models of the global buckling - lateral buckling of the thin-walled beams are described in details in the papers: [9.5, 9.53, 9.54, 9.59, 9.95, 9.99, 9.100]. The critical moment for the lateral buckling is in the following form

$$M_{CR,glob}^{(B-1,An)} = \pi \frac{E}{L} \sqrt{\frac{J_y J_t}{2(1+\nu)} \left[1 + 2\pi^2 (1+\nu) \frac{J_\omega}{J_t L^2} \right]} \tag{9.4}$$

where: L - length of the beam, J_ω - warping moment of inertia.

Then, the critical stress of the I-beam for global – lateral buckling

$$\sigma_{CR,glob}^{(B-1,An)} = \frac{M_{CR,glob}^{(B-1,An)}}{2J_z}\left(D - t_f\right) \tag{9.5}$$

and the dimensionless measure of quality

$$\Phi_{glob}^{(B-1,An)} = \frac{M_{CR,glob}^{(B-1,An)}}{EA^{3/2}} \tag{9.6}$$

Thus, the values of the characteristic quantities for the data of *Example 1* are as follows:

$M_{CR,glob}^{(B-1,An)} = 80.69\,\mathrm{kNm}$ - the critical bending moment for $L = 4\mathrm{m}$ (9.4);

$\sigma_{CR,glob}^{(B-1,An)} = 259.8\,\mathrm{MPa}$ - the critical stress (9.5);

$\Phi_{glob}^{(B-1,An)} = 0.001619$ - the dimensionless measure of quality (9.6).

Numerical study – finite strip method (CUFSM 3.12). The results of numerical calculations with consideration of the data of *Example 1* are shown in Fig. 9.3.

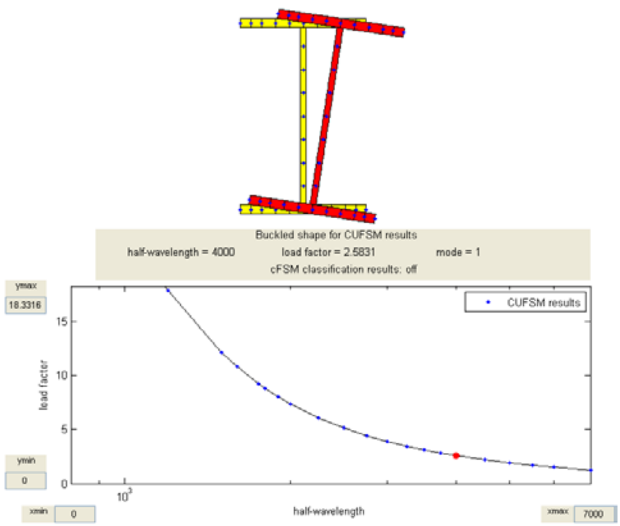

Fig. 9.3. The global buckled shape of the first I-beam (B-1)

The value of the critical stress for global buckling of the standard I-beam calculated based on the Finite Strip Method is $\sigma_{CR,glob}^{(B-1,FSM)} = 258.3\,\mathrm{MPa}$ for the length of the beam $L = 4\,\mathrm{m}$ and is by 0.6% smaller than analytical value.

9.3. Buckling of the non-standard I-beam with lipped flanges (B-2)

The cross-section of the second I-beam (B-2) is shown in Fig. 9.4.

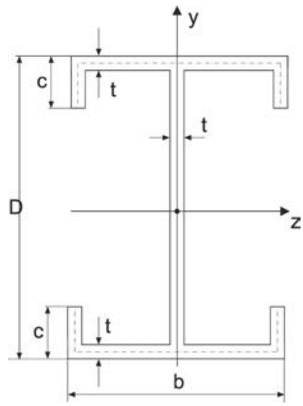

Fig. 9.4. The cross-section of the I-beam with lipped flanges

The sizes of the cross-section are as follows: D - total depth, b - width of the flanges, c depth of the bend, t - thickness of the flanges and the web.

9.3.1. Local buckling

Analytical study. The upper flange of the I-beam under pure bending is axially compressed, however the lower flange is tensioned. The simple theoretical model of the half of the lipped flange is described as rectangular plate with three simply supported edges and one edge free. Taking into account the papers [9.54, 9.60, 9.61, 9.81, 9.86, 9.90, 9.93, 9.99, 9.100] the critical stress of the upper lipped flange is formulated in the following form

$$\sigma_{CR,flan}^{(B-2,An)} = \left[2\frac{1+x_2}{1+\nu}\left(\frac{t}{b-t}\right)^2 + \frac{\pi^2}{4}\left(1-\frac{3}{4}\frac{x_2}{1+x_2}\right)x_2^3\left(\frac{b-t}{L_w}\right)^2 \right]\frac{E}{1+3x_2} \tag{9.7}$$

where: $x_2 = \dfrac{2c-t}{b-t}$ - dimensionless parameter, L_w - half-wavelength.

Therefore, the critical bending moment of this beam for the local buckling

$$M_{CR,flan}^{(B-2,An)} = \frac{2J_z}{D-t}\sigma_{CR,flan}^{(B-2,An)} \tag{9.8}$$

and the dimensionless measure of quality

$$\Phi_{flan}^{(B-2,An)} = \frac{M_{CR,flan}^{(B-2,An)}}{EA^{3/2}} \tag{9.9}$$

Example 2. The second beam (B-2) with sizes of the cross-section: $D = 206.4\,\mathrm{mm}$, $b = 134\,\mathrm{mm}$, $c = 44.2\,\mathrm{mm}$ $t_f = t_w = t = 6.4\,\mathrm{mm}$. Then, the geometrical properties of the cross-section are as follows: total area $A = 3960\,\mathrm{mm}^2$, torsion constant $J_t = 5.407 \cdot 10^4\,\mathrm{mm}^4$, and moments of inertia $J_z = 27.371 \cdot 10^6\,\mathrm{mm}^4$, $J_y = 6.478 \cdot 10^6\,\mathrm{mm}^4$, $J_\omega = 84.587 \cdot 10^9\,\mathrm{mm}^6$.

Thus, the values of the characteristic quantities are as follows:

$\sigma_{CR,flan}^{(B-2,An)} = 1751.6\,\mathrm{MPa}$ for $L_w = 625\,\mathrm{mm}$ - the critical stress (9.7);

$M_{CR,flan}^{(B-2,An)} = 479.4\,\mathrm{kNm}$ - the critical bending moment (9.8);

$\Phi_{flan}^{(B-2,An)} = 0.009620$ - the dimensionless measure of quality (9.9).

Numerical study – finite strip method (CUFSM 3.12). The numerical model FSM of the second I-beam (B-2) (Fig. 9.4) is elaborated for the sizes as in the *Example 2*. The results of numerical calculations and the shape of local buckling of the beam are shown in Fig. 9.5.

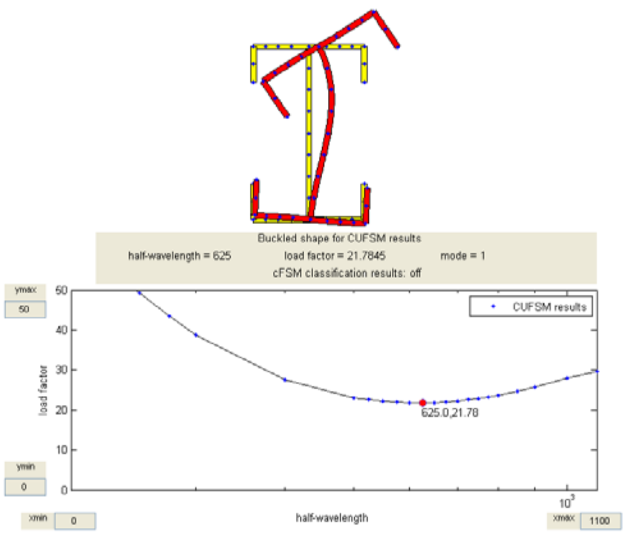

Fig. 9.5. The local buckled shape - the flange of the second I-beam (B-2)

The value of the critical stress for local buckling of the standard I-beam calculated based on the finite strip method is $\sigma_{CR,local}^{(B-2,FSM)} = 2178.5\,\text{MPa}$ for $L_w = 625\,\text{mm}$ and is by 24% greater than the analytical value. The analytical model gives the lower estimation of the critical stress for the local buckling, without the interaction with the web. It should be noticed that the local buckling of the beam of the flange does not occur in elastic range.

9.3.2. Global buckling

Analytical study. The analytical models of the global buckling – lateral buckling of the thin-walled beams are described in the papers: [9.5, 9.53, 9.54, 9.59, 9.95, 9.99, 9.100]. The critical moment for the lateral buckling is in the following form

$$M_{CR,glob}^{(B-2,An)} = \pi \frac{E}{L} \sqrt{\frac{J_y J_t}{2(1+\nu)} \left[1 + 2\pi^2 (1+\nu) \frac{J_\omega}{J_t L^2} \right]} \tag{9.10}$$

where: L - length of the beam, J_ω - warping moment of inertia.

Then, the critical stress of the I-beam for global - lateral buckling

$$\sigma_{CR,glob}^{(B-2,An)} = \frac{M_{CR,glob}^{(B-2,An)}}{2J_z} (D-t) \tag{9.11}$$

and the dimensionless measure of quality

$$\Phi_{glob}^{(B-2,An)} = \frac{M_{CR,glob}^{(B-2,An)}}{EA^{3/2}} \tag{9.12}$$

Thus, the values of the characteristic quantities for the data of *Example 1* are as follows:

$M_{CR,glob}^{(B-2,An)} = 108.0\,\text{kNm}$ - the critical bending moment for $L = 4\text{m}$ (9.10);

$\sigma_{CR,glob}^{(B-2,An)} = 394.6\,\text{MPa}$ - the critical stress (9.11);

$\Phi_{glob}^{(B-2,An)} = 0.002167$ - the dimensionless measure of quality (9.12).

Numerical study – finite strip method (CUFSM 3.12). The results of numerical calculations of the global buckling – lateral buckling with the data of *Example 2* are shown in Fig. 9.6. The cross section of the beam rotates, while the shape of the cross section after lateral buckling remains unchanged. The value of the critical stress for global buckling of the standard I-beam calculated with the use of the FSM is $\sigma_{CR,glob}^{(B-2,FSM)} = 391.1\,\text{MPa}$ for the length of the beam $L = 4\,\text{m}$ and is by 0.9% smaller than the analytical value.

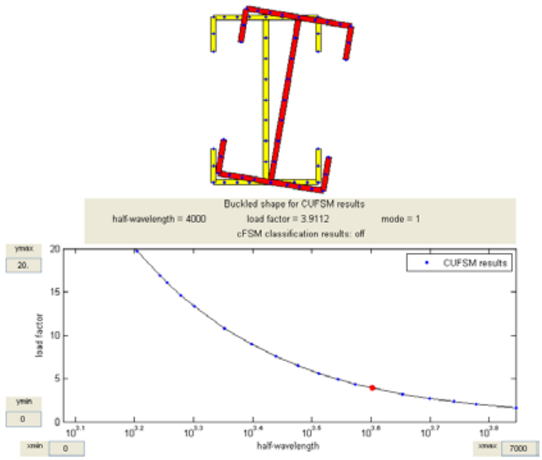

Fig. 9.6. The global buckled shape of the second I-beam (B-2)

9.4. Buckling of non-standard I-beam with sandwich flanges

The cross-section of the third I-beam (B-3) [9.64] is shown in Fig. 9.7.

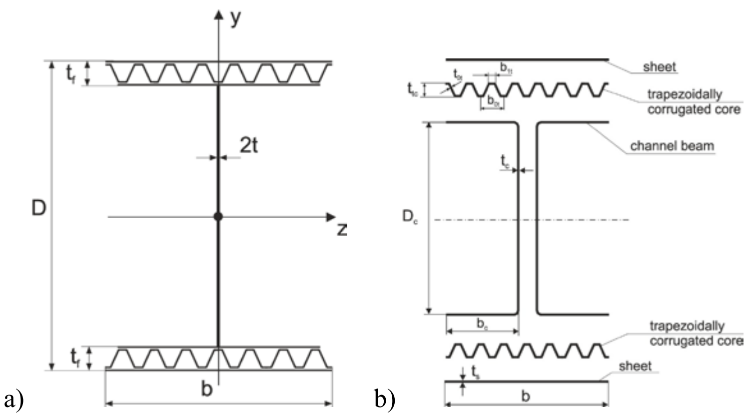

Fig. 9.7. The cross-section of the I-beam with sandwich flanges:
a) front view of the I-beam, b) component parts of the I-beam

The sizes of the cross-section are as follows: D - total depth, b - width of the flanges, t_f - total thickness of the sandwich flanges, t - thickness of the sheets.

9.4.1. Local buckling

Analytical study. **The upper flange** of the I-beam under pure bending is axially compressed. The simply buckle shape of this flange is shown in Fig. 9.8.

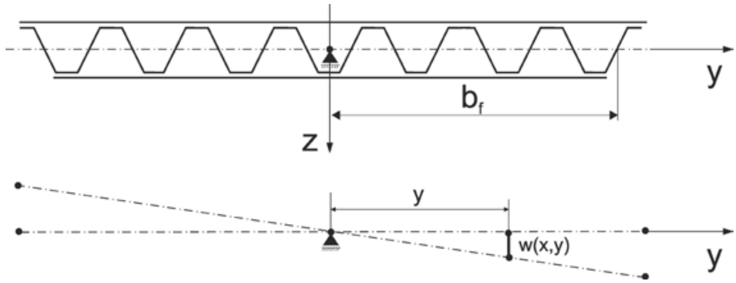

Fig. 9.8. The sandwich upper flange and the scheme of the buckle shape

The theoretical model of the flange is described as rectangular orthotropic plate with three simply supported edges and one edge free. Taking into account the papers [9.7, 9.56, 9.60, 9.61, 9.64, 9.91, 9.93] the following analytical model is elaborated. The elastic strain energy for orthotropic plate

$$U_\varepsilon = \frac{1}{2}\int_0^L\int_0^{b_{pf}}\left[D_x\left(\frac{\partial^2 w}{\partial x^2}\right)^2 + 2H\left(\frac{\partial^2 w}{\partial x\partial y}\right)^2 + D_y\left(\frac{\partial^2 w}{\partial y^2}\right)^2\right]dxdy \tag{9.13}$$

where: D_x, H, D_y - flexural and torsional rigidities of the plate-flange, and $w(x,y) = w_a\dfrac{y}{b_{pf}}\sin\left(\dfrac{\pi x}{L}\right)$ - the deflection, b_{pf} width of the half plate (Fig. 9.8).

The work of the load

$$U_\varepsilon = \frac{1}{2}N_x^o\int_0^L\int_0^{b_{pf}}\left(\frac{\partial^2 w}{\partial x^2}\right)^2 dxdy \tag{9.14}$$

where N_x^o - intensity of the load - longitudinal compression.

The critical intensity of the load and the critical stress are obtained based on the principle of stationary total potential energy in the form

$$N_{x,CR}^{o}=\frac{1}{b_{pf}^{2}}\left[\left(\pi\frac{b_{pf}}{L}\right)^{2}D_{x}+6H\right] \text{ and } \sigma_{CR,flan}^{(B-3,An)}=\frac{b_{pf}}{A_{pf}}N_{x,CR}^{o} \tag{9.15}$$

where A_{pf} - area of the cross section of the half plate-flange.

Then, the critical bending moment of this beam for the local buckling

$$M_{CR,flan}^{(B-3,An)}=\frac{2J_{z}}{D-t_{f}}\sigma_{CR,flan}^{(B-3,An)} \tag{9.16}$$

and the dimensionless measure of quality

$$\Phi_{flan}^{(B-3,An)}=\frac{M_{CR,flan}^{(B-3,An)}}{EA^{3/2}} \tag{9.17}$$

Example 3. The third beam (B-3) with sizes of the cross-section: $D=220\,\text{mm}$, $b=140\,\text{mm}$, $b_{mf}=134\,\text{mm}$, $t_{f}=10\,\text{mm}$, $t_{w}=2\,\text{mm}$, $t=1\,\text{mm}$. Then, the geometrical properties of the cross-section: total area $A=1391\,\text{mm}^{2}$, torsion constant $J_{t}=4.830\cdot10^{4}\,\text{mm}^{4}$, moments of inertia $J_{z}=12.298\cdot10^{6}\,\text{mm}^{4}$, $J_{y}=1.396\cdot10^{6}\,\text{mm}^{4}$, $J_{\omega}=16.358\cdot10^{9}\,\text{mm}^{6}$, and the rigidities of the plate-flange [9.91] $D_{x}=131.32\cdot10^{5}\,\text{Nmm}$, $H=71.4\cdot10^{5}\,\text{Nmm}$.

Thus, the values of the characteristic quantities are as follows:

$\sigma_{CR,flan}^{(B-3,An)}=2660.2\,\text{MPa}$ for $L_{w}=850\,\text{mm}$ - the critical stress (9.15);
$M_{CR,flan}^{(B-3,An)}=311.6\,\text{kNm}$ - the critical bending moment (9.16);
$\Phi_{flan}^{(B-3,An)}=0.03003$ - the dimensionless measure of quality (9.17).

The web of the I-beam under pure bending is loaded by linearly distributed in-plane compression. The critical stress of the web [9.7]

$$\sigma_{CR,web}^{(B-3,An)}=\frac{3\pi^{2}E}{1-\nu^{2}}\left(\frac{t_{w}}{D-2t_{f}}\right)^{2} \tag{9.18}$$

Then, the values of this critical stress $\sigma_{CR,web}^{(B-3,An)}=650.7\,\text{MPa}$.

Numerical study – finite strip method (CUFSM 3.12). The numerical model FSM of the third I-beam (B-3) (Fig. 9.7) is elaborated for the sizes as in the *Example 3*. The results of numerical calculations an the shape of local buckling of the flange of the beam are shown in Fig. 9.9. The value of the critical stress for local buckling of the third I-beam calculated with the FSM is $\sigma_{CR,flan}^{(B-3,FSM)} = 2826.8\,\text{MPa}$ for $L_w = 625\,\text{mm}$ and is by 6% greater than the analytical value. The analytical model gives the lower estimation of the critical stress for the local buckling, without the interaction with the web. The rigidities of the sandwich flanges are decidedly greater as compared to the rigidities of the web.

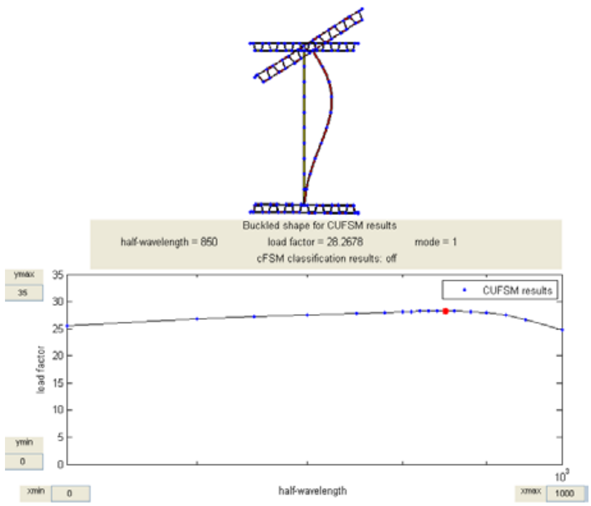

Fig. 9.9. The local buckled shape - the flange of the third I-beam (B-3)

The local buckling of the web is shown in Fig. 9.10.

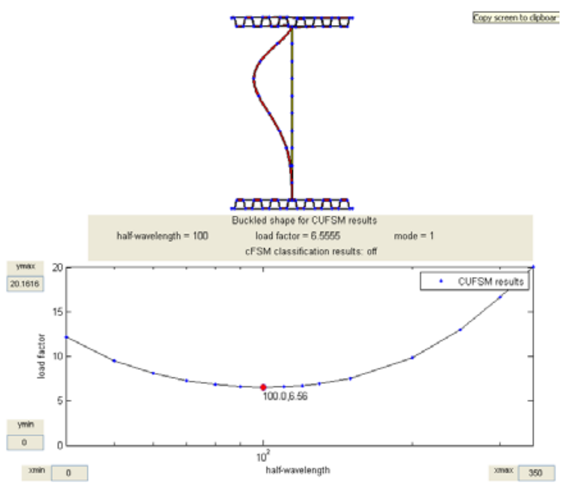

Fig. 9.10. The local buckled shape - the web of the third I-beam (B-3)

The value of the critical stress for local buckling of the web based on the Finite Strip Method is $\sigma_{CR,web}^{(B-3,FSM)} = 655.6\,\text{MPa}$ for $L_w = 100\,\text{mm}$ and is by 0.8% greater than the analytical value. It should be noticed that the local buckling of the beam of the flange and the web does not occur in elastic range.

9.4.2. Global buckling

Analytical study. The critical moment for the lateral buckling is similar to the first and second beams, and is in the following form

$$M_{CR,glob}^{(B-3,An)} = \pi \frac{E}{L}\sqrt{\frac{J_y J_t}{2(1+\nu)}\left[1+2\pi^2(1+\nu)\frac{J_\omega}{J_t L^2}\right]} \tag{9.19}$$

Then, the critical stress of the I-beam for global – lateral buckling

$$\sigma_{CR,glob}^{(B-3,An)} = \frac{M_{CR,glob}^{(B-3,An)}}{2J_z}\left(D - t_f\right) \tag{9.20}$$

and the dimensionless measure of quality

$$\Phi_{glob}^{(B-3,An)} = \frac{M_{CR,glob}^{(B-3,An)}}{EA^{3/2}} \tag{9.21}$$

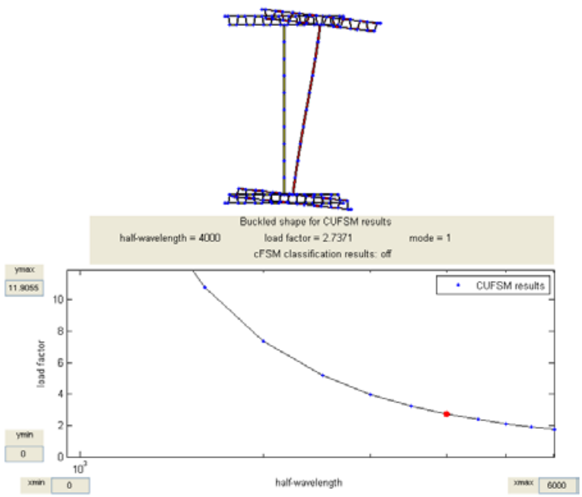

Fig. 9.11. The global buckled shape of the third I-beam (B-3)

Therefore, the values of the characteristic quantities for the data of *Example 3* are as follows:

$M_{CR,glob}^{(B-3,An)} = 32.83\,\text{kNm}$ - the critical bending moment for $L = 4\text{m}$ (9.19);

$\sigma_{CR,glob}^{(B-3,An)} = 280.3\,\text{MPa}$ - the critical stress (9.20);

$\Phi_{glob}^{(B-3,An)} = 0.003164$ - the dimensionless measure of quality (9.21).

Numerical study - finite strip method (CUFSM 3.12). The results of numerical calculations with the data of *Example 3* are shown in Fig. 9.11.

The value of the critical stress for global buckling of the third I-beam calculated with the Finite Strip Method is $\sigma_{CR,glob}^{(B-3,FSM)} = 273.7\,\text{MPa}$ for the length of the beam $L = 4\,\text{m}$ and is by 2.4% smaller than the analytical value.

9.5. Conclusions

The three considered types of the I-beams are distinguished by significant resistance to the local buckling of the flanges or webs which does not depend on the total length of the beam. The local buckling of these beams occurs only in the elastic-plastic range. The global buckling depends on the length of the beam. The shape of the flanges affects the value of the critical moment of the global – lateral buckling. The assumed dimensionless measure of quality discloses the effect of the flange shape on the global buckling resistance (Table 9.1).

Table 9.1. The values of the dimensionless quality measure for global buckling beams

Beam type	B-1	B-2	B-3
$\Phi_{glob}^{(B-i,An)}$	0.001619	0.002167	0.003164

The I-beam with sandwich flanges (B-3) (Fig. 9.7) is nearly twice as resistant as the standard I-beam (B-1) (Fig. 9.1).

The dimensionless measure of quality (9.3), (9.6) and similar next expressions enable comparison of the resistance values for local or global buckling of the beams with various cross sections.

9.6. References

9.1 Andrade A., Providência P., Camotim D., Elastic lateral-torsional buckling of restrained web-tapered I-beams, Computers & Structures, Vol. 88, 2010, pp. 1179-1196.

9.2 Aydin M.R., Elastic flexural and lateral torsional buckling analysis of frames using finite elements, KSCE Journal of Civil Engineering, Vol. 14 (1), 2010, pp. 25-31.

9.3 Basaglia C., Camotim D., Silvestre N., Global buckling analysis of plane and space thin-walled frames in the context of GBT, Thin-Walled Structures, Vol. 46, 2008, pp. 79-101.

9.4 Batista E.M., Local-global buckling interaction procedure for the design of cold-formed columns: Effective width and direct method integrated approach, Thin-Walled Structures, Vol. 47, 2009, pp. 1218-1231.

9.5 Bažant Z.P., Cedolin L., Stability of structures, Oxford University Press, New York, Oxford 1991.

9.6 Becque J., Rasmusen K.J.R., A numerical investigation of local-overall interaction buckling of stainless steel lipped channel columns, Journal of Constructional Steel Research, Vol. 65, 2009, pp. 1685-1693.

9.7 Brzoska Z. Static and stability of thin-walled structures. PWN, Warszawa 1965.

9.8 Camotim D., Silvestre N., Basaglia C., Bebiano R., GBT-based buckling analysis of thin-walled members with non-standard support conditions, Thin-Walled Structures, Vol. 46, 2008, pp. 800-815.

9.9 Camotim D., Dinis P.B., Coupled instabilities with distortional buckling in cold-formed steel lipped channel columns, Thin-Walled Structures, Vol. 49, 2011, pp. 562-575.

9.10 Cheng YU, Schafer B.W., Simulation of cold-formed steel beams in local and distortional buckling with applications to the direct strength method, Journal of Constructional Steel Research, Vol. 63, 2007, pp. 581-590.

9.11 Cheung Y.K., Finite strip method in structural analysis, Pergamon Press, New York 1976.

9.12 Chróścielewski J., Lubowiecka I., Szymczak C., Witkowski W., On some aspects of torsional buckling of thin-walled I-beam columns, Computers & Structures, Vol. 84, 2006, pp. 1946-1957.

9.13 Chu X., Kettle R., Li L., Lateral-torsional buckling analysis of partial-laterally restrained thin-walled channel-sections beam, Journal of Constructional Steel Research, Vol. 60, 2004, pp. 1159-1175.

9.14 Davies J.M., Recent research advances in cold-formed steel structures, Journal of Constructional Steel Research, Vol. 55 (1-3), 2000, pp. 267-288.

9.15 Dinis P.B., Camotim D., Local/distortional mode interaction in cold-formed steel lipped channel beams, Thin-Walled Struct., Vol. 48, 2010, pp. 771-785.

9.16 Dinis P.B., Camotim D., Post-buckling behaviour and strength of cold-formed steel lipped channel columns experiencing distortional/global interaction, Computers & Structures, Vol. 89, 2011, pp. 422-434.

9.17 Dubina D., Ungureanu V., Effect of imperfections on numerical simulation of instability behaviour of cold-formed steel members, Thin Walled Structures, Vol. 40, 2002, pp. 239-262.

9.18 El-Mahdy G.M., El-Saadawy M.M., Ultimate strength of singly symmetrical I-section steel beams with variable flange ratio. Thin Walled Structures, Vol. 87, 2015, pp. 149-157.
9.19 Gonçalves R., Dinis P.B., Camotim D., GBT formulation to analyse the first-order and buckling behaviour of thin-walled members with arbitrary cross-sections, Thin Walled Structures, Vol. 47, 2009, pp. 583-600.
9.20 Hancock G.J., Local, distortional, and lateral buckling of I-beams, Journal of the Structural Division, Vol. 104 (ST11), 1978, pp. 1787-1798.
9.21 Hancock G.J., Design for distortional buckling of flexural members, Thin-Walled Structures, Vol. 27, 1997, pp. 3-12.
9.22 Hancock G.J., Cold-formed steel structures, Journal of Constr. Steel Research, Vol. 59, 2003, pp. 473-487.
9.23 Hancock G.J., Rasmussen K.J.R., Recent research on thin-walled beams-columns, Thin-Walled Structures, Vol. 32, 1998, pp. 3-18.
9.24 Iwicki P., Selected problems of stability of steel structures, Monografia 105, Wyd. Politechniki Gdańskiej, Gdańsk 2010.
9.25 Kołakowski Z., Static and dynamic interactive buckling regarding axial extension mode of thin-walled channel, Journal of Theoretical and Applied Mechanics, Vol. 48 (3), 2010, pp. 703-714.
9.26 Kołakowski Z., Królak M., Kowal-Michalska K., Modal interactive buckling of thin-walled composite beam-columns regarding distortional deformation, International Journal of Eng. Science, Vol. 37 (12), 1999, pp. 1577-1596.
9.27 Kołakowski Z., Królak M., Modal coupled instabilities of thin-walled composite plate and shell structures, Composite Structures, Vol. 76 (4), 2006, pp. 303-313.
9.28 Kołakowski Z., Kowal-Michalska K., Interactive buckling regarding the extension mode of thin-walled channel under compression in the first nonlinear approximation, International Journal of Solids and Structures, Vol. 48, 2011, pp. 119-125.
9.29 Kołakowski Z., Kowal-Michalska K., (Eds.), Selected problems of instabilities in composite structures, A series of monographs, Technical University of Lodz, Łódź 1999.
9.30 Kołakowski Z., Kowal-Michalska K. (Eds.) Static, dynamics and stability of structural elements and systems. A Series of Monographs, Vol. 2, Lodz 2012.
9.31 Kotełko M., Ultimate load and post-failure behavior of thin-walled orthotropic beams, Intl Journal of Applied Mechanics and Engineering, Vol. 6 (3), 2001, pp. 693-717.
9.32 Kotełko M., Ultimate load and crashing of thin-walled structures. Wyd. Naukowo-Techniczne, Warszawa 2011.
9.33 Kotełko M., Królak M., Collapse behaviour of triangular cross-section girders subject to pure bending, Thin-Walled Struct., Vol. 15 (2), 1993, pp. 127-141.
9.34 Kowal-Michalska K., Grądzki R. The post-buckling behaviour of thin-walled columns in the elastic-plastic range. Rozprawy Inżynierskie, Vol. 34, 1986.

9.35 Kowal-Michalska K. Nośność graniczna i stan zakrytyczny w obszarze sprężysto-plastycznym ściskanych płyt ortotropowych. Zeszyty Naukowe Politechniki Łódzkiej, Rozprawy Naukowe, z. 214, Łódź 1995.
9.36 Kowal-Michalska K (Eds.) Dynamic stability of composite plate structures. Wyd. Naukowo-Techniczne, Warszawa 2007.
9.37 Kowal-Michalska K., Mania R.J. (Eds.) Review and current trends in stability of structures. A Series of Monographs, Vol. 3, Lodz 2013.
9.38 Kowal-Michalska K. Stany zakrytyczne w obszarach sprężysto-plastycznych konstrukcji płytowych. Seria Monografie, Politechnika Łódzka, Łódź 2013.
9.39 Królak M., Influence of the flexural rigidity of diaphragms on the stability of thin-walled box columns subjected to uniform compression, Thin-Walled Structures, Vol. 8 (1), 1989, pp. 63-71.
9.40 Królak M. (Red.), Stany zakrytyczne i nośność graniczna cienkościennych dźwigarów o ścianach płaskich, PWN, Warszawa-Łódź 1990.
9.41 Królak M., Młotkowski A., Experimental analysis of post-buckling and collapse behaviour of thin-walled box-section beam, Thin-Walled Structures, Vol. 26 (4), 1996, pp. 287-314.
9.42 Królak M., Kołakowski Z., Kotełko M., Influence of load-non-uniformity and eccentricity on the stability and load carrying capacity of orthotropic tubular columns of regular hexagonal cross-section, Thin-Walled Structures, Vol. 39 (6), 2001, pp. 483-498.
9.43 Królak M., Kowal-Michalska K., Stability and ultimate load of multi-cell orthotropic columns subjected to compression, 8th Conference on Shell Structures, Theory and Applications, 235-239, Taylor & Francis, London, Leiden, New York, Philadelphia, Singapore 2005.
9.44 Królak M., Kowal-Michalska K., Mania R. J., Świniarski J., Experimental tests of stability and load carrying capacity of compression thin-walled multi-cell columns of triangular cross-section, Thin-Walled Structures, Vol. 45 (10-11), 2007, pp. 883-887.
9.45 Królak M., Kowal-Michalska K., Mania R. J., Świniarski J., Stability and load carrying capacity of multi-cell thin-walled columns of rectangular cross-sections, Journal of Theoretical and Applied Mechanics, Vol. 47 (2), 2009, pp. 435-456.
9.46 Kubiak T. Static and dynamic buckling of thin-walled plates structures. Springer 2013.
9.47 Lewinski J., Magnucki K., Optimization of anti-symmetrical open cross-section of cold-formed thin-walled beams, Journal of Theoretical and Applied Mechanics, Vol. 47 (3), 2009, pp. 553-571.
9.48 Li L., Chen J., An analytical model for analysis distortional buckling of cold-formed steel sections, Thin-Walled Structures, Vol. 46, 2008, 1430-1436.
9.49 Loughlan J., Yidris N., The post-local buckling mechanics and ultimate carrying capability of uniformly compressed thin-walled I-section struts and columns, Proc. Stability of Structures, XII-th Symposium, K. Kowal-Michalska, R.J. Mania (Eds.), Zakopne 2009, pp. 33-48.

9.50 Ma M., Hughes O., Lateral distortional buckling of monosymmetrical I-beams under distributed vertical load, Thin-Walled Structures, Vol. 26 (2), 1996, pp. 123-145.
9.51 Macdonald M., Heiyantuduwa M.A., Rhodes J., Recent developments in the design of cold-formed steel members and structures, Thin-Walled Structures, Vol. 46, 2008, 1047-1053.
9.52 Macdonald M., Heiyantuduwa M.A., Kotełko M., Rhodes J., Web crippling behaviour of thin-walled lipped channel beams, Thin-Walled Structures, Vol. 49, 2011, pp. 682-690.
9.53 Magnucka-Blandzi E., Critical state of a thin-walled beam under combined load, Applied Mathematical Modelling, Vol. 33, 2009, pp. 3093-3098.
9.54 Magnucka-Blandzi E. Stability of sandwich beams and plates and cold-formed thin-walled beams. Wyd. Politechniki Poznańskiej, Poznań 2010.
9.55 Magnucka-Blandzi E., Magnucki K., Buckling and optimal design of cold-formed thin-walled beams: Review of selected problems, Thin-Walled Structures, Vol. 49, 2011, 554-561.
9.56 Magnucki K., Maćkiewicz M., Lewiński J., Optimal design of a mono-symmetrical open cross section of a cold-formed beam with cosinusoidally corrugated flanges, Thin-Walled Structures, Vol. 44, 2006, pp. 554-562.
9.57 Magnucki K., Magnucka-Blandzi E., Variational design of open cross section thin-walled beam under stability constraints, Thin-Walled Structures, Vol. 35, 1999, pp. 185-191.
9.58 Magnucki K., Monczak T., Optimum shape of open cross section of thin-walled beam, Engineering Optimization, Vol. 32, 2000, pp. 335-351.
9.59 Magnucki K., Ostwald M., Optimal design of selected open cross sections of cold-formed thin-walled beams, Publishing House of Poznan University of Technology, Poznan 2005.
9.60 Magnucki K., Paczos P., Theoretical shape optimization of cold-formed thin-walled channel beams with drop flanges in pure bending, Journal of Constructional Steel Research, Vol. 65, 2009, pp. 1731-1737.
9.61 Magnucki K., Paczos P., Kasprzak J., Elastic buckling of cold-formed thin-walled channel beams with drop flanges, Journal of Structural Engineering, Vol. 136 (7), 2010, pp. 886-896.
9.62 Magnucki K., Rodak M., Lewiński J., Optimization of mono- and anti-symmetrical I-section of cold-formed thin-walled beams, Thin-Walled Structures, Vol. 44, 2006, pp. 832-836.
9.63 Magnucki K., Szyc W., Stasiewicz P., Stress state and elastic buckling of a thin-walled beam with monosymmetrical open cross-section, Thin-Walled Structures, Vol. 42, 2004, pp. 25-38.
9.64 Magnucki K., Paczos P., Elastic buckling of an I-beam with sandwich flanges. *Nord Steel 2015 Construction Conference*, Finland, Tampere, 23-25 September 2015.
9.65 Manevich A.I., Raksha S.V., Two-criteria optimization of H-section bars-beams under bending and compression, Thin-Walled Structures, Vol. 45, 2007, pp. 898-901.

9.66 Mohri F., Bouzerira C., Potier-Ferry M., Lateral buckling of thin-walled beam-column elements under combined axial and bending loads, Thin-Walled Structures, Vol. 46, 2008, pp. 290-302.
9.67 Murray N.W. Introduction to the theory of thin-walled structures, Clarendon Press, Oxford 1986.
9.68 Mutermilch J., Kociołek A., Strength and stability of thin-walled bars with open cross sections. Wyd. Politechniki Warszawskiej, Warszawa 1972.
9.69 Naderian H.R., Ronagh H.R. Azhari M., Elastic distortional buckling of doubly symmetric steel I-section beams with slender webs. Thin Walled Structures, Vol. 84, 2014, pp. 289-301.
9.70 Narayanan S., Mahendran M., Ultimate capacity of innovative cold-formed steel columns, Journal of Const. Steel Research, Vol. 59, 2003, pp. 489-508.
9.71 Ovesy H.R., Loughlan J., GhannadPour S.A.M., Morada G., Geometric non-linear analysis of box section under end shortening, using three different versions of the finite-strip method, Thin-Walled Structures, Vol. 44, 2006, pp. 623-637.
9.72 Ozbasaran H., Aydin R., Dogan M., An alternative design procedure for lateral-torsional buckling of cantilever I-beam. Thin Walled Structures, Vol. 90, 2015, pp. 235-242.
9.73 Paczos P., Zawodny P., Magnucki K., Stress state and displacements of cold formed thin-walled channel beams. The Ninth Intl Conference on Computational Structures Technology, Athens, Greece, Paper 217, Civil-Comp Press, Stirlingshire, Scotland 2008.
9.74 Paczos P., Magnucki K., Experimental investigations of cold-formed thin-walled C-beams with drop flanges, Proc. Sixth Intl Conference on Advances in Steel Structures, The Hong Kong Institute of Steel Construction, Chan S.L. (Editor), Hong Kong, China, 2009, pp. 395-400.
9.75 Paczos P., Wasilewicz P., Experimental investigations of buckling of lipped, cold-formed thin-walled beams with I-section, Thin-Walled Structures, Vol. 47, 2009, pp. 1354-1362.
9.76 Paczos P. Stability and load capacity of cold-formed channel beams. Wyd. Politechniki Poznańskiej, Poznań 2014.
9.77 Pala M., A new formulation for distortional buckling stress in cold-formed steel members, Journal of Constructional Steel Research, Vol. 62, 2006, pp. 716-722.
9.78 Pastor M.M., Roure F., Open cross-section beams under pure bending. I. Experimental investigations, Thin-Walled Struct., Vol. 46, 2008, pp. 476-483.
9.79 Pastor M.M., Roure F., Open cross-section beams under pure bending. II. Finite element simulation, Thin-Walled Structures, Vol. 47, 2009, pp. 514-521.
9.80 Rasmussen K.J.R., Bifurcation of locally buckled point symmetric columns – Analytical developments, Thin-Walled Structures, Vol. 44, 2006, 1161-1174.
9.81 Rogers C.A., Schuster R.M., Flange/web distortional buckling of cold-formed steel sections in bending, Thin-Walled Structures, Vol. 27(1), 1997, pp. 13-29.

9.82 Rondal J. Cold formed steel members and structures. General Reports, Journal of Constructional Steel Research, Vol. 55 (1-3), 2000, pp. 155-158.

9.83 Samanta A., Kumar A., Distortional buckling in monosymmetrical I beams, Thin-Walled Structures, Vol. 44, 2006, pp. 51-56.

9.84 Schafer B.W., Peköz T., Laterally braced cold-formed steel flexural members with edge stiffened flanges, Journal of Structural Engineering, Vol. 125(2), 1999, pp. 118-127.

9.85 Schafer B.W., Review: The direct strength method of cold-formed steel member design, Journal of Constructional Steel Research, Vol. 64, 2008, pp. 766-778.

9.86 Silvestre N., Camotim D., On the mechanics of distortion in thin-walled open sections, Thin-Walled Structures, Vol. 48, 2010, pp. 469-481.

9.87 Song Q-Y., Heidarpour A., Zhao X-L., Han L-H., Post-earthquake fire behavior of welded steel I-beam to hollow column connections: An experimental investigation. Thin Walled Structures, Vol. 98, 2016, pp. 149-153.

9.88 Stasiewicz P., Magnucki K., Lewiński J., Kasprzak J.: Local buckling of a bent flange of a thin-walled beam. Proceedings in Applied Mathematics and Mechanics, PAMM, Vol. 4, 2004, pp. 554-555.

9.89 Szymczak C., Sensitivity analysis of thin-walled members, problems and applications, Thin-Walled Structures, Vol. 41, 2003, pp. 271-290.

9.90 Trahair N.S., Flexural-torsional buckling of structures, F&FN Spon, an imprint of Chapman & Hall, London, Glasgow, New York, Tokyo, Melbourne, Madras 1993.

9.91 Ventsel E., Krauthammer T. Thin plates and shells. Marcel Dekker, Inc. New York, Basel, 2001.

9.92 Vlasov V.Z., Thin-walled elastic rods. Fiz-Mat-Lit, Moscow 1959.

9.93 Volmir A.S., Stability of deformation systems. "Nauka". Moscow 1967.

9.94 Wang T., Ikarashi K., Coupled buckling strength of H-Shaped steel beams under bending-shear, Proc. 5th Intl Conference on Coupled Instabilities in Metal Structures, Vol. 1, K. Rasmussen, T. Wilkinson (Eds), The University of Sydney, Australia, 2008, pp. 341-348.

9.95 Weiss S., Giżejowski M., Stability of metal structures, Rod systems. Arkady, Warszawa 1991.

9.96 Young B., Research on cold-formed steel columns, Thin-Walled Structures, Vol. 46, 2008, pp. 731-740.

9.97 Zaras J., Rhodes J., Królak M., Buckling and post-buckling of rectangular-plates under linearly varying compression and shear. 1. Theoretical-analysis, Thin-Walled Structures, Vol. 14 (1), 1992, pp. 59-87.

9.98 Zaras J., Rhodes J., Królak M., Buckling and post-buckling of rectangular-plates under linearly varying compression and shear. 2. Experimental investigations, Thin-Walled Structures, Vol. 14 (2), 1992, pp. 105-126.

9.99 Zirakian T., Elastic distortional buckling of doubly symmetric I-shaped flexural members with slender webs, Thin-Walled Structures, Vol. 46, 2008, pp. 466-475.
9.100 Zirakian T., Lateral-distortional buckling of I-beams and the extrapolation techniques, Journal of Constructional Steel research, Vol. 64, 2008, pp. 1-11.

10.

Forced oscillations of a viscoelastic Timoshenko beam with dampers and dynamic vibration absorbers

Steady-state forced oscillations of viscoelastic Timoshenko beam with dampers, dynamic vibrations absorbers and point masses under harmonic excitation are studied. An analytical series solution has been obtained with using natural modes of elastic Timoshenko beam (without dampers, absorbers and point masses). A numerical parametric analysis is performed with particular emphasis on cantilever beams. Effects of shear flexibility, viscous internal and external friction and the absorber parameters on characteristics of forced oscillation are studied. Special attention is paid to appearance of running waves.

10.1. Introduction

Investigation of forced vibration of beams equipped with dampers or/and dynamical vibration absorbers (DVA) is of great practical interest in view of the problem of oscillations suppression for various civil engineering structures (towers, bridges and others). For many such structures one-dimensional (beam) model is applicable but it is necessary to take into account the shear deformability, as well as the internal and external viscous damping (especially in the vicinity of resonances). The relatively simple and sufficiently exact approach to this problem is provided by Timoshenko beam model (TB) and Kelvin-Voigt model for a viscoelastic material.

Beams with dampers and DVAs are distributed parameters systems which undergo, along with distributed or concentrated external loads, local forces applied at certain points and depended on the motion of the beam itself. It is often argued (Korenev, Reznikov [10.5]) that in such problems the method of expanding the solutions on natural modes of free oscillations is too cumbersome as at account of damping the natural modes become complex; and they should be recomputed iteratively at presence of the frequency-dependent forces. So the authors [10.5] claim that in these problems more preferable are methods of civil engineering (method of initial parameters, methods of forces and displacements).

One of the objectives of this article is to show that the series method is rather effective if to use the expansion on natural modes of the *elastic* Timoshenko beam *without* dampers, DVAs and point masses. Such an approach allows one to escape the recalculation of eigenmodes and eigenfrequencies, retaining the advantages of the method - simplicity of determination of basic modes, exact satisfying boundary conditions.

For the elastic TB a general scheme of solution of the forced oscillation problem using superposition of the natural modes has been worked out in early papers by Anderson [10.1], Dolph [10.2], Hermann [10.4]. The principal distinction and main difficulty for the TB (in comparison with the classical Euler-Bernoulli (E-B) mode) lies in orthogonality conditions. In distinction to the classical model where the stress-strain state is entirely defined by the displacement function $y(x,t)$, the deformation in TB is defined by a two dimensional vector [$y(x,t)$, $\psi(x,t)$], where $\psi(x,t)$ is the angle of the cross-section rotation (or by other two independent variables, e.g., bending and shear deflections). Correct orthogonality conditions, which have vector form, have been obtained by Dolph in 1951 (see [10.2]) and then have been used in [10.2, 10.4].

For viscoelastic TB (without local frequency-dependent loads) the forced oscillations problem was studied by Newman [10.11] (by use of a Laplace transformation technique) and by Lee [10.6] (steady-state motions). Both these authors consider the material which is viscoelastic only in extension, not in shear. A solution for more exact formulation of the problem has been obtained by Pan [10.12]. Further references can be found in Grigoluk, Selezov [10.3] and in other reviews.

In our previous work [10.10] we consider steady-state vibration of the viscoelastic TB with DVAs for simply supported beams where due to sinusoidal natural modes the orthogonality conditions were not required. Here the solution is presented for a wide class of boundary conditions for which the orthogonality conditions play an important role (special attention is paid to case of cantilever beam).

In distinction on [10.10], where a single four-order PDE has been used, here we employ a set of two second-order PDEs. This enables us to simplify essentially the theoretical scheme and to present more transparent and usable solutions. In the numerical parametric analysis the effects of shear flexibility, viscous internal and external friction and the absorber parameters on characteristics of forced oscillation are studied on the example of the cantilever beam. Special attention is paid to studying running waves which appear due to the viscous friction and become significant in presence of local loads.

10.2. Governing equations for viscoelastic Timoshenko beam loaded by a distributed load

Bearing in mind that in analysis of forced oscillations of the viscoelastic TB we should account for different loads (from external forces, dampers, dynamic vibration absorbers, point masses, Fig. 10.1), we start from differential equations of oscillations of TB loaded by an arbitrary distributed load $q_0(x,t)$. Such equations for viscoelastic TB were obtained in several works, from earlier papers [10.6, 10.11, 10.12] till recent works [10.7÷10.10] where the equations have been presented in rather convenient dimensionless form. These equations are extended below to take into account also distributed moments $m_0(x,t)$ (due to inertia forces moments in attached masses) and external damping (concentrated forces will be described by δ -functions). For the viscoelastic material we use the Voigt model.

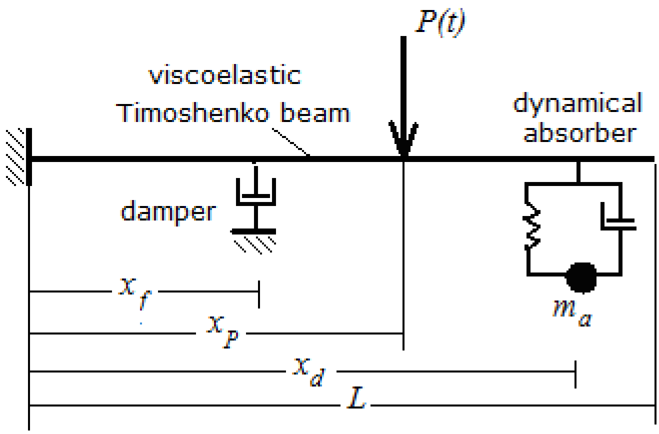

Fig. 10.1. The mechanical model

Deformations of TB are specified by two independent functions –total displacement $y(x,t)$ and the angle of cross section rotation $\psi(x,t)$. Total slope of the bent axis is $\partial y / \partial x = \psi + \gamma$ (γ is the shear angle).

Constitutive relations are assumed according to the Voigt law for normal stresses as well as for shear ones in the form

$$\sigma_x = E\left(1+\mu_1\frac{\partial}{\partial t}\right)\varepsilon_x \qquad \tau = G\left(1+\mu_2\frac{\partial}{\partial t}\right)\gamma \tag{10.1}$$

where μ_1 and μ_2 are internal viscous friction parameters. The bending moment and the transverse shear force in the cross section are specified by known expressions

$$M = -EJ\left(1+\mu_1\frac{\partial}{\partial t}\right)\frac{\partial\psi}{\partial x} \qquad Q = k'AG\left(1+\mu_2\frac{\partial}{\partial t}\right)\left(\frac{\partial y}{\partial x}-\psi\right) \tag{10.2}$$

where k' is the shear factor depended on the cross-section shape.

The equations of forces balance for the beam loaded by a distributed load $q_0(x,t)$ and a distributed moment $m_0(x,t)$ with account of the rotatory inertia and viscous external friction (associated with linear velocity $-\beta_1\partial y/\partial t$ and angular velocity $-\beta_2\partial\psi/\partial t$) are as follows

$$\begin{gathered}\frac{\partial Q}{\partial x}-\rho A\frac{\partial^2 y}{\partial t^2}-\beta_1\frac{\partial y}{\partial t}+q_0(x,t)=0\\ -\rho J\frac{\partial^2\psi}{\partial t^2}+Q-\frac{\partial M}{\partial x}-\beta_2\frac{\partial\psi}{\partial t}+m_0(x,t)=0\end{gathered} \tag{10.3}$$

These equations with account of relations (10.2) result in two differential equations of motion in y and ψ:

$$\begin{gathered}k'GA\left(1+\mu_2\frac{\partial}{\partial t}\right)\frac{\partial}{\partial x}\left(\frac{\partial y}{\partial x}-\psi\right)-\rho A\frac{\partial^2 y}{\partial t^2}-\beta_1\frac{\partial y}{\partial t}+q_0(x,t)=0\\ -\rho J\frac{\partial^2\psi}{\partial t^2}+k'AG\left(1+\mu_2\frac{\partial}{\partial t}\right)\left(\frac{\partial y}{\partial x}-\psi\right)+EJ\left(1+\mu_1\frac{\partial}{\partial t}\right)\frac{\partial^2\psi}{\partial x^2}-\beta_2\frac{\partial\psi}{\partial t}+m_0(x,t)=0\end{gathered} \tag{10.4}$$

In dimensionless variables and parameters

$$\begin{gathered}\xi=\frac{x}{r_0},\quad Y=\frac{y}{r_0},\quad \tau=\frac{c}{r_0}t,\quad \chi=\frac{E}{k'G},\quad \mu_j^*=\frac{c}{r_0}\mu_j,\quad q=\frac{q_0r_0}{EA}\\ m=\frac{m_0}{EA},\quad \beta_1^*=\frac{cr_0}{EA}\beta_1,\quad \beta_2^*=\frac{c}{EA}\beta_2\end{gathered} \tag{10.5}$$

where $r_0^2=J/A$, $c=\sqrt{E/\rho}$, Eqs (10.4) take the form

$$\left(1+\mu_2^*\frac{\partial}{\partial\tau}\right)\frac{\partial}{\partial\xi}\left(\frac{\partial Y}{\partial\xi}-\psi\right)-\chi\frac{\partial^2 Y}{\partial\tau^2}-\beta_1^*\chi\frac{\partial Y}{\partial\tau}+\chi q(\xi,\tau)=0$$

$$-\chi\frac{\partial^2\psi}{\partial\tau^2}+\left(1+\mu_2^*\frac{\partial}{\partial\tau}\right)\left(\frac{\partial Y}{\partial\xi}-\psi\right)+\chi\left(1+\mu_1^*\frac{\partial}{\partial\tau}\right)\frac{\partial^2\psi}{\partial\xi^2}-\beta_2^*\chi\frac{\partial\psi}{\partial\tau}+\chi m(\xi,\tau)=0 \tag{10.6}$$

We consider the following boundary conditions (in dimensionless variables):

1. Simply supported edge:

$$Y=0,\quad M=0\ \rightarrow\ \frac{\partial\psi}{\partial\xi}=0 \tag{10.7}$$

2. Clamped edge:

$$Y=0,\quad \psi=0 \tag{10.8}$$

3. Free edge:

$$M=0,\quad Q=0\ \rightarrow\ \frac{\partial\psi}{\partial\xi}=0;\quad \frac{\partial Y}{\partial\xi}-\psi=0 \tag{10.9}$$

10.3. Natural modes of elastic TB and conditions of their orthogonality

In the analysis of non-autonomic dynamics of viscoelastic TB with viscous friction, point masses, dampers and DVAs we use expansions of the forced oscillations modes on natural modes of TB without internal and external damping and concentrated influences. Such an approach allows one to satisfy boundary conditions for TB, using simply derived functions. So below we briefly present equations which provide orthogonal natural modes of free oscillations for the elastic TB.

10.3.1. Natural modes of elastic TB

For free oscillations of elastic TB ($q=0$, $m=0$, $\mu_1=\mu_2=0$, $\beta_1=\beta_2=0$) Eqs. (10.6) yield

$$\frac{\partial}{\partial\xi}\left(\frac{\partial Y}{\partial\xi}-\psi\right)-\chi\frac{\partial^2 Y}{\partial\tau^2}=0 \tag{10.10}$$

$$-\chi\frac{\partial^2\psi}{\partial\tau^2}+\left(\frac{\partial Y}{\partial\xi}-\psi\right)+\chi\frac{\partial^2\psi}{\partial\xi^2}=0$$

Putting for free oscillations

$$Y(\xi,\tau)=e^{i\omega\tau}\tilde{Y}(\xi) \qquad \psi(\xi,\tau)=e^{i\omega\tau}\Psi\ (\xi) \tag{10.11}$$

we reduce set (10.10) to the set of ordinary differential equations (wave symbol above Y further is dropped)

$$\frac{d}{d\xi}\left(\frac{dY}{d\xi}-\Psi\right)=-\chi\omega^2 Y \qquad \chi\frac{d^2\Psi}{d\xi^2}+\frac{dY}{d\xi}=\Psi\ (1-\chi\omega^2) \tag{10.12}$$

from which one can obtain eigenfrequencies ω_j and eigenmodes (Y_j, Ψ_j), $j=1,2,\ldots$. This problem was solved in many earlier works. But in view of new form of the governing equations we present here solutions which will be used below.

The characteristic equation for set (10.12) (obtained after substitution $Y_j(\xi)=y_j\,e^{k\xi}$, $\Psi_j(\xi)=\psi_j\,e^{k\xi}$) is as follows (index “*j*” at ω_j, as well as at quantities β, $k_{1,2}$ and the constants below is dropped)

$$k^4+\omega^2\left(1+\chi\right)k^2+\omega^2\left(\chi\omega^2-1\right)=0 \tag{10.13}$$

In case $\chi\omega^2<1$ (“low frequencies”) two roots $k_{1,2}=\pm\alpha_1$ are real and two $k_{3,4}=\pm i\alpha_2$ are imaginary, where

$$\alpha_{1,2}=\sqrt{\frac{\omega}{2}\left[\sqrt{\omega^2\left(1+\chi\right)^2+4\left(1-\chi\omega^2\right)}\mp\omega\left(1+\chi\right)\right]} \tag{10.14}$$

In case $\chi\omega^2>1$ (“high frequencies”) all roots are imaginary: $k_{1,2}=\pm i\,\alpha_3$, $k_{3,4}=\pm i\,\alpha_2$, where

$$\alpha_3=\sqrt{\frac{\omega}{2}\left[\omega\left(1+\chi\right)-\sqrt{\omega^2\left(1+\chi\right)^2+4\left(1-\chi\omega^2\right)}\right]} \tag{10.15}$$

Solution to set (10.12) for case $\chi\omega^2<1$ is

$$\begin{aligned}Y_j(\xi)&=C_1\operatorname{ch}\alpha_1\xi+C_2\operatorname{sh}\alpha_1\xi+C_3\cos\alpha_2\xi+C_4\sin\alpha_2\xi\\ \Psi_j(\xi)&=D_1\operatorname{ch}\alpha_1\xi+D_2\operatorname{sh}\alpha_1\xi+D_3\cos\alpha_2\xi+D_4\sin\alpha_2\xi\end{aligned} \tag{10.16}$$

The constants C_m and D_m are coupled through the first Eq. (10.12)

$$C_1 = \nu_1 D_2, \quad C_2 = \nu_1 D_1, \quad C_3 = \nu_2 D_4, \quad C_4 = -\nu_2 D_3 \tag{10.17}$$

where

$$\nu_1 = \frac{\alpha_1}{\alpha_1^2 + \chi\omega^2} \qquad \nu_2 = \frac{\alpha_2}{\chi\omega^2 - \alpha_2^2} \tag{10.18}$$

The four remaining unknown constants are determined by boundary conditions (10.7)-(10.9).

Solution for case $\chi\omega^2 > 1$ can be written similarly (or obtained from (10.16) by transferring from hyperbolic functions to trigonometric ones).

10.3.2. The case of elastic cantilever beam

As an example which is important for the following analysis let us consider a cantilever beam ($Y = 0$, $\psi = 0$ at $\xi = 0$ and $\partial\psi / \partial\xi = 0$; $\partial Y / \partial\xi - \psi = 0$ at $\xi = L / r_0$). It follows from conditions (10.17) together with the boundary conditions that

$$Y_j(\xi) = \nu_2 D_4 (\cos\alpha_2\xi - \operatorname{ch}\alpha_1\xi) - D_3(\nu_2 \sin\alpha_2\xi + \nu_1 \operatorname{sh}\alpha_1\xi) \tag{10.19}$$

$$\Psi_j(\xi) = D_3(\cos\alpha_2\xi - \operatorname{ch}\alpha_1\xi) + D_4\left(\sin\alpha_2\xi - \frac{\nu_2}{\nu_1}\operatorname{sh}\alpha_1\xi\right)$$

where constants D_3, D_4 satisfy the set of linear homogeneous equations

$$D_3\left(\alpha_1 \operatorname{sh}\frac{\alpha_1 L}{r_0} + \alpha_2 \sin\frac{\alpha_2 L}{r_0}\right) + D_4\left(\frac{\nu_2}{\nu_1}\alpha_1 \operatorname{ch}\frac{\alpha_1 L}{r_0} - \alpha_2 \cos\frac{\alpha_2 L}{r_0}\right) = 0 \tag{10.20}$$

$$D_3\left[(1 - \nu_1\alpha_1)\operatorname{ch}\frac{\alpha_1 L}{r_0} - (1 + \nu_2\alpha_2)\cos\frac{\alpha_2 L}{r_0}\right] + D_4\left[\frac{\nu_2}{\nu_1}(1 - \nu_1\alpha_1)\operatorname{sh}\frac{\alpha_1 L}{r_0} - (1 + \nu_2\alpha_2)\sin\frac{\alpha_2 L}{r_0}\right] = 0$$

Condition of vanishing determinant of this set determines, with account of (10.14), natural frequencies ω_j in terms of parameters L / r_0 and χ. Ratio D_3 / D_4 is specified from (10.20)

$$\frac{D_3}{D_4} \equiv \nu_3 = \frac{\alpha_2 \cos\frac{\alpha_2 L}{r_0} - \frac{\nu_2}{\nu_1}\alpha_1 \operatorname{ch}\frac{\alpha_1 L}{r_0}}{\alpha_1 \operatorname{sh}\frac{\alpha_1 L}{r_0} + \alpha_2 \sin\frac{\alpha_2 L}{r_0}} \tag{10.21}$$

Then the eigenmodes can be written as follows (C is an amplitude factor)

$$Y_j(\xi) = C\left[\nu_2(\cos\alpha_2\xi - \cosh\alpha_1\xi) - \nu_3(\nu_2 \sin\alpha_2\xi + \nu_1 \sinh\alpha_1\xi)\right] \tag{10.22}$$

$$\Psi_j(\xi) = C\left(\nu_3(\cos\alpha_2\xi - \operatorname{ch}\alpha_1\xi) + \sin\alpha_2\xi - \frac{\nu_2}{\nu_1}\operatorname{sh}\alpha_1\xi\right) \tag{10.23}$$

10.3.3. Conditions of orthogonality

Orthogonality conditions for eigenmodes in TB which hold for three boundary conditions (10.7)-(10.9) [10.2], in the dimensionless variables and parameters are as follows

$$\int_0^{l/r_0} (Y_m Y_n + \Psi_m \Psi_n) d\xi = 0 \tag{10.24}$$

If to consider eigenmodes of TB as vector-functions Z_j=(Y_j, Ψ_j), then these orthogonality conditions are written as $\int_0^{l/r_0} Z_m Z_n d\xi = 0$.

The natural modes are normalized by the conditions

$$\int_0^{l/r_0} Z_j^2 d\xi = 1 \quad \text{or} \quad \int_0^{l/r_0} \left(Y_j^2 + \Psi_j^2\right) d\xi = 1 \tag{10.25}$$

The following statement is necessary in order to use series on the natural modes of elastic TB for presentation of forced scillations of viscoelastic TB (with damping and concentrated forces) [10.2]

Two arbitrary functions $f(x)$ and $g(x)$ on interval (0, l) can be expanded in natural modes Y_j, Ψ_j in the form

$$f(x) = \sum_{j=1}^{\infty} \zeta_j Y_j(x) \qquad g(x) = \sum_{j=1}^{\infty} \varsigma_j \Psi_j(x) \tag{10.26}$$

Possibility of such expansion (with the same coefficients ζ_j for both functions) and expressions for coefficients ζ_j yield from property of completeness of sets of natural modes and from the following consideration. If to introduce vector-function $\mathrm{E}(x) = [f(x), g(x)]$ with scalar product

$$\mathrm{E}_1(x)\bullet\mathrm{E}_2(x) = \int_0^l [f_1(x)\, f_2(x) + g_1(x)\, g_2(x)]dx$$

then expansions (10.26) are equivalent to expansion of the vector-function

$$E(x) = \sum_{j=1}^{\infty} \zeta_j\, Z_j(x) \tag{10.27}$$

Multiplying (10.27) by $Z_j(x)$ and integrating from 0 to l, one obtains with account of orthogonality conditions (10.24) and normalization (10.25)

$$\zeta_j = \int_0^l E(x)\cdot Z_j(x)dx \quad \text{or} \quad \zeta_j = \int_0^l \left[f(x)Y_j(x) + g(x)\Psi_j(x) \right] dx \tag{10.28}$$

Thus coefficients ζ_j are uniquely determined for arbitrary pair of functions $f(x)$ and $g(x)$.

10.4. A series solution for steady-state forced oscillations of viscoelastic TB

10.4.1. General solution

We consider forced oscillations of the TB under action of the harmonic external load

$$q = q(\xi)e^{i\,\Omega\tau} \qquad m = m(\xi)e^{i\,\Omega\tau} \tag{10.29}$$

where Ω is the frequency in time τ. We will seek only steady-state (stationary) solutions which are also harmonic oscillations with the same frequency:

$$Y(\xi,\tau) = e^{i\,\Omega\tau}Y_s(\xi) \quad \psi(\xi,\tau) = e^{i\,\Omega\tau}\Psi_s(\xi) \tag{10.30}$$

Then the set (10.6) reduces to ordinary differential equations

$$\left(1+i\,\mu_2^*\,\Omega\;\right)\frac{d}{d\xi}\left(\frac{dY}{d\xi}-\psi\right)+\Omega^2\chi\,Y-i\Omega\;\beta_1\,\chi\,Y+\chi\,q\;(\xi)=0$$

$$\chi\,\Omega^2\psi+\left(1+i\mu_2^*\Omega\right)\left(\frac{dY}{d\xi}-\psi\right)+\chi\left(1+i\mu_1^*\Omega\right)\frac{d^2\psi}{d\xi^2}-i\,\Omega\beta_2\,\chi\,\psi+\chi\,m(\xi)=0 \tag{10.31}$$

Further the normalized coefficients of internal friction for linear and angular velocities are assumed to be equal: $\mu_1^*=\mu_2^*=\mu^*$, as well as those for external friction: $\beta_1^*=\beta_2^*=\beta^*$.

Functions $Y(\xi)$ and $\Psi(\xi)$ are expanded on the eigenfunctions Y_j, Ψ_j of the elastic TB

$$Y(\xi)=\sum_{j=1}^{\infty}\zeta_j\,Y_j(\xi)\qquad \Psi(\xi)=\sum_{j=1}^{\infty}\varsigma_j\,\Psi_j(\xi) \tag{10.32}$$

All terms in these expansions satisfy the above specified boundary conditions for TB, so we have to satisfy only the set of ODEs (10.31). Substitution of (10.32) into (10.31) gives

$$\sum_{j=1}^{\infty}\zeta_j\left[\left(1+i\,\mu^*\Omega\;\right)\left(-\frac{d^2Y_j}{d\xi^2}+\frac{d\Psi_j}{d\xi}\right)-\Omega^2\chi Y_j+i\Omega\;\beta^*\chi\,Y_j\right]=\chi q\;(\xi)$$

$$\sum_{j=1}^{\infty}\zeta_j\left[\left(1+i\mu^*\Omega\;\right)\left(-\frac{\partial Y_j}{\partial\xi}-\chi\frac{\partial^2\Psi_j}{\partial\xi^2}+\Psi_j(\xi)\right)-\Omega^2\chi\,\Psi_j+i\Omega\beta^*\chi\,\Psi_j\right]=\chi\,m(\xi) \tag{10.33}$$

This set of equations in view of Eqs (10.12) for eigenmodes can be written in the form

$$\sum_{j=1}^{\infty}\zeta_j\left(\omega_j^{\,2}-\lambda\right)Y_j(\xi)=\frac{q\;(\xi)}{1+i\,\mu^*\Omega} \tag{10.34}$$

$$\sum_{j=1}^{\infty}\zeta_j\left(\omega_j^2-\lambda\right)\Psi_j(\xi)=\frac{m(\xi)}{1+i\,\mu^*\Omega}$$

where

$$\lambda=\frac{\Omega\;\left(\Omega-i\,\beta^*\right)}{1+i\Omega\;\mu^*} \tag{10.35}$$

Now we multiply both Eqs. (10.34) by $Y_k(\xi)$ and $\Psi_k(\xi)$, respectively, for $k=1,2,\dots$, integrate the obtained equalities above the beam length and add both the equalities. With account of orthogonality conditions (10.24) we obtain

$$\zeta_k\left(\omega_k^2-p\right)\int_0^{l/r_0}(Y_k^2+\Psi_k^2)d\xi=\frac{1}{1+i\mu^*\Omega}\int_0^{l/r_0}\left(q(\xi)Y_k+m(\xi)\Psi_k\right)d\xi \quad (10.36)$$

whence in view of normalization (10.25) coefficients of the expansion are

$$\zeta_k=\frac{1}{1+i\mu^*\Omega}\frac{\int_0^{l/r_0}\left(q(\xi)Y_k+m(\xi)\Psi_k\right)d\xi}{\omega_k^2-\lambda}=\frac{\int_0^{l/r_0}\left(q(\xi)Y_k+m(\xi)\Psi_k\right)d\xi}{(\omega_k^2-\Omega^2)+i\Omega\left(\mu^*\omega_k^2+\beta^*\right)}$$

(10.37)

This expression can be written in polar form:

$$\zeta_k=a_ke^{i\theta_k},\quad a_k=\frac{\int_0^{l/r_0}\left(q(\xi)Y_k+m(\xi)\Psi_k\right)d\xi}{\sqrt{(\omega_k^2-\Omega^2)^2+\Omega^2\left(\mu^*\omega_k^2+\beta^*\right)^2}},\quad tg\,\theta_k=-\frac{\Omega\left(\mu^*\omega_k^2+\beta^*\right)}{\omega_k^2-\Omega^2}$$

(10.38)

The amplitude functions of total deflection and angle of cross-section rotation (10.32) are

$$Y(\xi)=\sum_{k=1}^{\infty}a_ke^{i\theta_k}\,Y_k(\xi)\qquad \Psi(\xi)=\sum_{k=1}^{\infty}a_ke^{i\theta_k}\,\Psi_k(\xi) \quad (10.39)$$

Finally the solution to steady-state forced oscillation of viscoelastic TB (10.30) is as follows:

$$Y(\xi,\tau)=e^{i\Omega\tau}\sum_{k=1}^{\infty}a_ke^{i\theta_k}\,Y_k(\xi)\qquad \Psi(\xi,\tau)=e^{i\Omega\tau}\sum_{k=1}^{\infty}a_ke^{i\theta_k}\,\Psi_k(\xi) \quad (10.40)$$

or in algebraic form ($Y_{Re}(\xi,\tau), Y_{\mathrm{Im}}(\xi,\tau)$ and $\Psi_{Re}(\xi,\tau)$, $\Psi_{\mathrm{Im}}(\xi,\tau)$ are real and imaginary parts of $Y(\xi,\tau)$ and $\Psi(\xi,\tau)$)

$$Y(\xi,\tau)=Y_{Re}(\xi,\tau)+iY_{\mathrm{Im}}(\xi,\tau)\qquad \Psi(\xi,\tau)=\Psi_{Re}(\xi,\tau)+i\Psi_{\mathrm{Im}}(\xi,\tau) \quad (10.41)$$

where

$$Y_{Re}(\xi,\tau)=\sum_{k=1}^{\infty}a_k Y_k(\xi)\cos\left(\Omega\tau+\theta_k\right) \quad Y_{\mathrm{Im}}(\xi,\tau)=\sum_{k=1}^{\infty}a_k Y_k(\xi)\sin\left(\Omega\tau+\theta_k\right)$$

$$\Psi_{Re}(\xi,\tau)=\sum_{k=1}^{\infty}a_k \Psi_k(\xi)\cos\left(\Omega\tau+\theta_k\right) \quad \Psi_{\mathrm{Im}}(\xi,\tau)=\sum_{k=1}^{\infty}a_k \Psi_k(\xi)\sin\left(\Omega\tau+\theta_k\right)$$

(10.42)

The real and imaginary parts of (10.41) are solutions to the problem for excitation force with time functions $\cos\Omega\tau$ or $\sin\Omega\tau$, respectively.

10.4.2. Action of a concentrated harmonic force

If the external load is a concentrated harmonic force with amplitude P, applied at point $x_P = r_0\,\xi_P$, then $q_0(x) = P\delta(x - x_P)$. In dimensionless parameters with account of known identity for δ- function of $x = r_0\,\xi$: $\delta(x) = \delta(\xi)/r_0$ we have

$$q(\xi) \equiv \frac{q_0 r_0}{E\,A} = \widehat{P}\delta(\xi-\xi_P) \qquad (\widehat{P} = \frac{P}{EA}) \tag{10.43}$$

The nominator in formulas (10.37), (10.38) with account of $m = 0$ equals to

$$\int_0^{l/r_0} q(\xi)Y_k(\xi)d\xi = \widehat{P}\int_0^{l/r_0} Y_k(\xi)\delta(\xi-\xi_P)d\xi = \widehat{P}Y_k(\xi_P) \tag{10.44}$$

and (10.37), (10.38) yield

$$\zeta_k = \frac{\widehat{P}Y_k(\xi_P)}{(\omega_k^2-\Omega^2)+i\Omega\,\left(\mu^*\omega_k^2+\beta^*\right)}, \quad a_k = \frac{\widehat{P}Y_k(\xi_P)}{\sqrt{(\omega_k^2-\Omega^2)^2+\Omega^2\left(\mu^*\omega_k^2+\beta^*\right)^2}}$$

(10.45)

(formulas (10.39)-(10.42) remain the same).

10.4.3. Single-mode approximation

It is apparent that in certain cases the single-mode approximation might be sufficient, e.g., in case when the load frequency is close to (or less than) the first eigenfrequency, and the second and other eigenfrequencies are considerably higher. Then only the first term in expansion (10.32) is significant (except of special cases of application of a concentrated force), and other terms can be neglected. Similarly, if the frequency of external load is very close to a certain eigenfrequency ω_k one can expect that the forced oscillation mode will be close to the k-th eigenmode.

For the single-mode approximation, e.g., with $k=1$, solution (10.40)-(10.42) reduces to

$$Y(\xi,\tau)=a_1 e^{i(\Omega\tau+\theta_1)}Y_1(\xi) \quad \Psi(\xi,\tau)=a_1 e^{i(\Omega\tau+\theta_1)}\Psi_1(\xi) \tag{10.46}$$

where

$$a_1=\frac{\int_0^{l/r_0}\left(q(\xi)Y_1+m(\xi)\Psi_1\right)d\xi}{\sqrt{(\omega_1^2-\Omega^2)^2+\Omega^2\left(\mu^*\omega_1^2+\beta^*\right)^2}} \qquad tg\,\theta_1=-\frac{\Omega\,\left(\mu^*\omega_1^2+\beta^*\right)}{\omega_1^2-\Omega^2} \tag{10.47}$$

In the case of action of a concentrated force, one has

$$a_1=\frac{\hat{P}Y_1\,(\xi_P)}{\sqrt{(\omega_1^2-\Omega^2)^2+\Omega^2\left(\mu^*\omega_1^2+\beta^*\right)^2}} \tag{10.48}$$

It is convenient to introduce the dynamic amplification factor as

$$k_{dyn}=\frac{a_1 p_1^2}{\hat{P}Y_1\,(\xi_P)}=\frac{p_1^2}{\sqrt{(\omega_1^2-\Omega^2)^2+\Omega^2\left(\mu^*\omega_1^2+\beta^*\right)^2}} \tag{10.49}$$

where p_1 is the first eigenfrequency in classical E-B model. Introducing in (10.49) new dimensionless parameters

$$\tilde{\Omega}=\Omega/p_1 \qquad \tilde{\omega}_1=\omega_1/p_1 \qquad \tilde{\mu}=\mu^* p_1 \qquad \tilde{\beta}=\beta^*/p_1 \tag{10.50}$$

we obtain

$$k_{dyn}=\frac{1}{\sqrt{(\tilde{\omega}_1^2-\tilde{\Omega}^2)^2+\tilde{\Omega}^2\left(\tilde{\mu}\,\tilde{\omega}_1^2+\tilde{\beta}\right)^2}} \tag{10.51}$$

This expression is similar to usual formula for the dynamic amplification factor in one-degree-of-freedom system ($\tilde{\omega}_1=\omega_1/p_1$ is rather close to 1), with replacement of a damping coefficient by the “effective damping factor“ $\tilde{\mu}\,\tilde{\omega}_1^2+\tilde{\beta}$ embracing internal and external damping.

10.4.4. Qualitative comparison of undamped and damped beams

For forced oscillations of undamped elastic beam ($\tilde{\mu} = \tilde{\beta} = 0$, $\tilde{\omega}_1 = 1$) all $tg\theta_k$ in formula (10.39) vanish, and $\theta_k = 0$ or $\theta_k = \pi$, respectively if $\Omega < \omega_k$ or $\Omega > \omega_k$ (this is seen from 5(37)). Correspondingly $e^{i\theta_k}$ equals to 1 or -1. Formulas (10.40) reduce to

$$Y(\xi,\tau) = e^{i\Omega\tau}\sum_{k=1}^{\infty}(\pm a_k)Y_k(\xi) \qquad \Psi(\xi,\tau) = e^{i\Omega\tau}\sum_{k=1}^{\infty}(\pm a_k)\Psi_k(\xi) \tag{10.52}$$

This means that in the shape of forced oscillations all constituent modes for which $\Omega > \omega_k$ oscillate in phase with the load, and all constituent modes with lower frequencies ($\Omega < \omega_k$) oscillate in anti-phase with the load. In cases of excitation force with time functions, e.g., $\cos\Omega\tau$, solution (10.52) takes the form

$$Y(\xi,\tau) = \cos\Omega\tau\sum_{k=1}^{\infty}(\pm a_k)Y_k(\xi) \qquad \Psi(\xi,\tau) = \cos\Omega\tau\sum_{k=1}^{\infty}(\pm a_k)\Psi_k(\xi) \tag{10.53}$$

Here the variables are separated in real form, so this is a standing wave.

At forced oscillations of damped beams (with internal and/or external friction), as is seen from the above solution (10.38)-(10.41), each constituent mode has certain phase shift θ_k with respect to the external harmonic load (which depends not only on the effective damping factor $\mu^*\omega_k^2 + \beta^*$, but also on ω_k). In real form, for excitation time function $\cos\Omega\tau$ solution (10.40) is

$$Y(\xi,\tau) = \sum_{k=1}^{\infty}a_kY_k(\xi)\cos\left(\Omega\tau + \theta_k\right) \qquad \Psi(\xi,\tau) = \sum_{k=1}^{\infty}a_k\Psi_k(\xi)\cos\left(\Omega\tau + \theta_k\right)$$

Here the variables are not separable in view of different phase shifts θ_k, except of case of the single-mode approximation (note that in complex form (10.30) the variables are separated). This means that in general case the mode shapes of beam are not similar in various time moments, so they are not standing waves. In a damped beam the oscillating bent axis includes a certain running wave. This holds for any model of beam (E-B, Rayleigh, TB).

It is obvious that the running component will be intensified with the rise of the numbers of significant modes and magnitudes of phase shifts θ_k .

10.5. Viscoelastic Timoshenko beam with a damper, point mass and dynamical vibration absorber

10.5.1. Viscoelastic TB with a damper

Let the TB is equipped with a damper of viscous friction at point x_f. Then the concentrated force P_f, applied at this point, is proportional to its velocity: $P_f = -g_f \,\partial y / \partial t$ (g_f is the viscous friction coefficient). In dimensionless parameters (10.5) at harmonic oscillation (10.30) one has

$$\widehat{P}_f = -i\Omega\, g_f^* Y(\xi_f) \quad (g_f^* = \frac{r_0\, c}{E\,A} g_f) \qquad (10.54)$$

This force can be accounted for in the above solution (10.37)-(10.40) by adding it to the external load, i.e. presenting the load as a sum of the given load $q_e(\xi,\tau)$ and a force from the damper. Then the amplitude load function (normalized) with account of expansion (10.33) is equal to

$$q(\xi) = q_e(\xi) - i\Omega\, g_f^* Y(\xi_f)\delta(\xi-\xi_f) = q_e(\xi) - i\Omega\, g_f^* \sum_{j=1}^{\infty} \zeta_j\, Y_j(\xi)\delta(\xi-\xi_f) \qquad (10.55)$$

Substitution of (10.55) into integral in r. h. side of (10.37) (with $m=0$) gives

$$\int_0^{l/r_0} q(\xi) Y_k\,(\xi)\,d\xi = \int_0^{l/r_0} q_e(\xi) Y_k\,(\xi)\,d\xi - i\Omega\, g_f^* Y_k\,(\xi_f) \sum_{j=1}^{\infty} \zeta_j Y_j(\xi_f) \qquad (10.56)$$

After rewriting the last term as

$$i\Omega\, g_f^* Y_k\,(\xi_f) \sum_{j=1}^{\infty} \zeta_j Y_j(\xi_f) = \sum_{j=1}^{\infty} e_{k\,j} \zeta_j \qquad (10.57)$$

where

$$e_{k\,j} = i\Omega\, g_f^* Y_k\,(\xi_f)\,Y_j(\xi_f) \qquad (10.58)$$

the set of Eqs. (10.36) in view of normalization (10.25) reads

$$\zeta_k \left[(\omega_k^2 - \Omega^2) + i\Omega\, \left(\mu^* \omega_k^2 + \beta^* \right) \right] + \sum_{j=1}^{\infty} e_{k\,j} \zeta_j = \int_0^{l/r_0} q_e(\xi) Y_k\,\left(\xi\right) d\xi \,, \quad k = 1,2,\ldots \qquad (10.59)$$

We come to infinite set of linear algebraic equations with matrix

$$\begin{pmatrix} \omega_1^2\left(1+i\mu^*\Omega\right)-\Omega\left(\Omega-i\beta^*\right)+e_{11} & e_{12} & e_{13} & \ldots \\ e_{21} & \omega_2^2\left(1+i\mu^*\Omega\right)-\Omega\left(\Omega-i\beta^*\right)+e_{22} & e_{23} & \ldots \\ e_{31} & e_{32} & \omega_3^2\left(1+i\mu^*\Omega\right)-\Omega\left(\Omega-i\beta^*\right)+e_{33} & .. \\ \ldots & \ldots & \ldots & \ldots \end{pmatrix} \tag{10.60}$$

determining coefficients ζ_k in (10.32) and then solution (10.30). In case when the external load is a concentrated force, applied at point ξ_P, r. h. sides in (10.59) in accordance with (10.45) are replaced with $\widehat{P}\,Y_k\left(\xi_P\right)$. Then set (10.59) reads

$$\zeta_k\left[\omega_k^2-\Omega^2+i\Omega\;(\mu^*\omega_k^2+\beta^*)\right]+\sum_{j=1}^{\infty}e_{kj}\zeta_j=\widehat{P}Y_k\;(\xi_P) \qquad k=1,2,\ldots \tag{10.61}$$

The forced oscillation mode in the complex form is determined by expressions (10.32), and the general solution for stationary oscillations is given by (10.30).

In the single-mode approximation (with $k=1$) for arbitrary load one has

$$\zeta_1=\frac{\int\limits_0^{l/r_0}\left(q(\xi)Y_1+m(\xi)\Psi_1\right)d\xi}{\left(\omega_1^2-\Omega^2\right)+i\Omega\left(\mu^*\,\omega_1^2+\beta^*+g_f^*Y_1^2(\xi_f)\right)} \tag{10.62a}$$

and for a concentrated force

$$\zeta_1=\frac{\widehat{P}Y_1\;(\xi_P)}{\left(\omega_1^2-\Omega^2\right)+i\Omega\left(\mu^*\,\omega_1^2+\beta^*+g_f^*Y_1^2(\xi_f)\right)} \tag{10.62b}$$

or, in the polar form $\zeta_1=a_1e^{i\theta_1}$,

$$a_1=\frac{\int\limits_0^{l/r_0}\left(q(\xi)Y_1+m(\xi)\Psi_1\right)d\xi}{\sqrt{(\omega_1^2-\Omega^2)^2+\Omega^2\left(\mu^*\,\omega_1^2+\beta^*+g_f^*Y_1^2(\xi_f)\right)^2}} \tag{10.63}$$

$$tg\,\theta_1=-\frac{\Omega\left(\mu^*\,\omega_1^2+\beta^*+g_f^*Y_1^2(\xi_f)\right)}{\omega_1^2-\Omega^2}$$

10.5.2. Viscoelastic TB with a dynamic vibration absorber

Let a Timoshenko beam is equipped with a dynamic vibration absorber of mass m_a at point x_d, Denote $y_a(t)$ the absorber mass displacement, $y_d(t) = y(x_d, t)$ - the displacement of point of the absorber attachment to the beam. Force P_d, acting from the absorber to the beam and applied at point x_d, equals to the inertial force of the absorber

$$P_d = F_a^i = -m_a \frac{d^2 y_a}{d t^2} \tag{10.64}$$

Deflection $y_a(t)$ is connected with the displacement of point of the absorber attachment to the beam $y_d(t)$ by the differential equation of absorber

$$m_a \frac{d^2 y_a}{dt^2} = -k_a \left(y_a - y_d \right) - \beta_a \left(\frac{dy_a}{dt} - \frac{dy_d}{dt} \right) \tag{10.65}$$

Here k_a and β_a are stiffness and viscosity coefficients for the absorber (the viscous friction is assumed to be proportional to displacement of the mass m_a with respect to the attachment point). From this equation the displacement $y_a(t)$ can be expressed through $y_d(t)$ in the form

$$y_a = h_a y_d \tag{10.66}$$

where h_a is a linear operator (in particular case of single-frequency oscillation h_a is reduced to a complex number, which has meaning of the absorber's dynamic amplification factor and is presented below). Then the inertial force for the absorber equals to

$$P_d = -m_a h_a \frac{d^2 y_d}{d t^2} \tag{10.67}$$

In dimensionless variables (10.5) equation of absorber oscillations (10.65) takes the form

$$\frac{d^2 Y_a}{d \tau^2} + \omega_a^{*2} \left(Y_a - Y_d \right) + \frac{\beta_a}{m_a} \frac{r_0}{c} \left(\frac{d Y_a}{d \tau} - \frac{d Y_d}{d \tau} \right) = 0 \tag{10.68}$$

where $Y = y / r_0$, $\tau = c\,t / r_0$, $\omega_a^* = \omega_a \dfrac{r_0}{c}$, $\omega_a = \sqrt{k_a / m_a}$ is the partial frequency of the absorber.

For steady-state harmonic oscillations, substituting $Y_d(\tau) = Y_d\, e^{i\Omega\tau}$ (where $Y_d \equiv Y(\xi_d)$) and $Y_a(\tau) = Y_a\, e^{i\Omega\tau}$ into (10.68) we obtain the relationship between amplitudes Y_a and Y_d in the form

$$Y_a = h_a Y_d \qquad h_a = \frac{1 + i\,\beta_a^* \widehat{\Omega}}{1 - \widehat{\Omega}^2 + i\,\beta_a^* \widehat{\Omega}} \tag{10.69}$$

where the tuning parameter $\widehat{\Omega}$ and the normalized damping parameter β_a^* are

$$\widehat{\Omega} = \frac{\Omega}{\omega_a} \qquad \beta_a^* = \frac{\beta_a}{m_a \omega_a} \tag{10.70}$$

For harmonic oscillations in the dimensionless variables and parameters we now have from (10.67)

$$\widehat{P}_d = \widehat{m}_a h_a \Omega^2\, Y(\xi_d) \qquad (\widehat{P}_d = \frac{P_d}{EA}, \quad \widehat{m}_a = \frac{m_a}{\rho A r_0}) \tag{10.71}$$

Then the amplitude function of the total load (including inertial force from the absorber) with account of expansion (10.32) equals to

$$q(\xi) = q_e(\xi) + \widehat{m}_a h_a\ \Omega^2 \sum_{j=1}^{\infty} \zeta_j\, Y_j(\xi_d)\delta(\xi - \xi_d) \tag{10.72}$$

Integral in (10.37) is equal to

$$\int_0^{l/r_0} q(\xi) Y_k\,(\xi)\, d\xi = \int_0^{l/r_0} q_e(\xi) Y_k\,(\xi)\, d\xi + \widehat{m}_a h_a\ \Omega^2 Y_k\,(\xi_d) \sum_{j=1}^{s} \zeta_j\, Y_j(\xi_d) \tag{10.73}$$

With denotation

$$f_{k\,j} = \widehat{m}_a h_a\ \Omega^2 Y_k\,(\xi_d) Y_j(\xi_d) \tag{10.74}$$

set of equations (10.37) in view of (10.25) takes the form

$$\zeta_k \left[\omega_k^2 \left(1 + i\,\mu^* \Omega\ \right) - \Omega\ \left(\Omega\ - i\,\beta^*\right) \right] - \sum_{j=1}^{\infty} f_{k\,j} \zeta_j = \int_0^{l/r_0} q_e(\xi) Y_k\,\left(\xi\right) d\xi \qquad k = 1,2,.. \tag{10.75}$$

The set (10.75) is similar to set (10.59) - its matrix yields from matrix (10.60) after replacing $e_{k\,j}$ (10.58) by $-f_{k\,j}$. In case when the external load is a concentrated force, applied at point ξ_P, r.h. sides in (10.75) are replaced with $\widehat{P}\,Y_k\left(\xi_P\right)$.

10.5.3. Viscoelastic TB with point mass, damper and dynamic vibration absorber

The case of a concentrated mass M attached to the beam at point x_M is a particular case of the above considered beam with a DVA. The inertial force P_M, acting at this point, is $P_M = -M\,\partial^2 y_M / \partial t^2$ ($y_M = y(x_M)$); this corresponds to (10.67) with $h_a = 1$. So it is sufficient to replace $f_{k\,j}$ in set (10.75) with

$$g_{k\,j} = \widehat{M}\,\Omega^2 Y_k\,(\xi_M)\,Y_j(\xi_M) \qquad \widehat{M} = \frac{M}{\rho A r_0} \tag{10.76}$$

In general case of TB with various attached bodies and devices - mass, damper and DVA - one should to add all forces induced by them to the external load. Then we come to the set of linear algebraic equations similar to (10.59)

$$\zeta_k\left[(\omega_k^2 - \Omega^2) + i\Omega\,\left(\mu^*\omega_k^2 + \beta^*\right)\right] + \sum_{j=1}^{\infty}\left(e_{k\,j} - g_{k\,j} - f_{k\,j}\right)\zeta_j = \int_0^{l/r_0} q_e(\xi)Y_k\,\left(\xi\right)d\xi \tag{10.77}$$

where $e_{k\,j}$, $f_{k\,j}$ and $g_{k\,j}$ are specified by expressions (10.58), (10.74) and (10.76).

If there are multiple concentrated loads (e. g., several point masses), the corresponding term in (10.77) is replaced with the sum of all these forces.

In any case, the action of concentrated loads, depended on motion of the system, results in coupling different natural modes (coupling set of equations).

10.6. Results of numerical analysis for a cantilever TB

Dynamics of TB is determined by a large number of parameters of the beam, damper, DVA and external excitation. Here we briefly consider the effect of some parameters on forced oscillation of cantilever beams under action of a concentrated force.

10.6.1. Eigenmodes and eigenfrequencies

As a basic variant for the analysis we took a cantilever beam with parameters $L/r_0 = 10$, $\chi = 3$. In Table 10.1 the first three normalized natural frequencies ω_j for this beam are presented, and for comparison there are also given corresponding frequencies at $\chi = 0$, i.e. for Rayleigh model (results for E-B and Rayleigh models here practically coincide; noticeable discrepancies appear only for higher modes).

Table 10.1. Normalized eigenfrequencies ω_j for elastic cantilever beam ($L/r_0 = 10$)

	ω_1	ω_2	ω_3
$\chi = 3$	0.0323	0.1459	0.3183
$\chi = 0$	0.0344	0.1913	0.4649

(ω is the frequency in time τ (10.5); frequency ω_0 in real time t equals to $\omega_0 = (c/r_0)\omega$). The eigenfrequencies for TB are noticeably lower than in E-B model, beginning already from the second one.

Corresponding three natural modes (total deflection $Y(\xi)$ and angle $\Psi(\xi)$) are shown in Fig. 10.2 for TB (*a*, *b*, *c*), and for comparison the third natural mode is shown for E-B model on Fig. 10.2 *d* (the 1st and 2nd modes in E-B model almost coincide with those of TB and are not shown here).

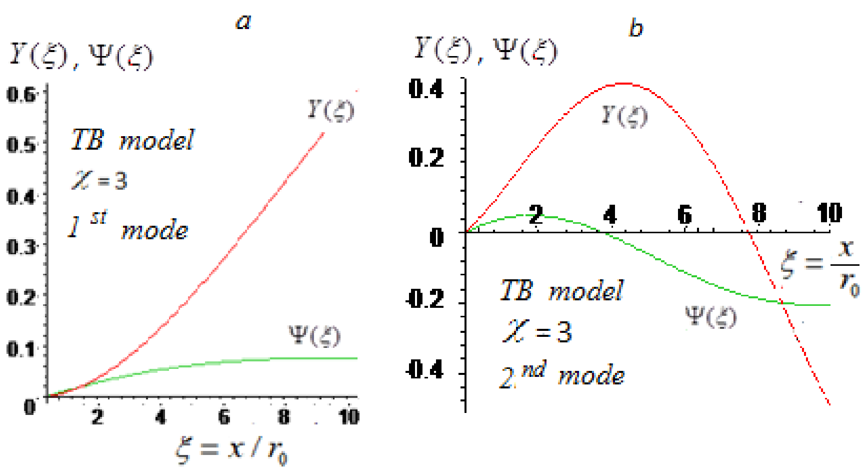

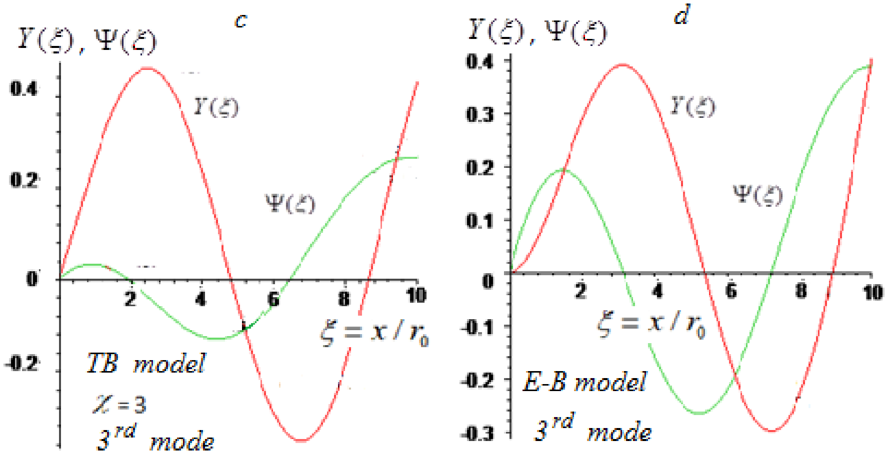

Fig. 10.2. Natural nodes of oscillation of elastic cantilever beam with parameters: $L/r_0 = 10$; (*a*), (*b*), (*c*) - the 1st, 2nd and 3rd eigenmodes $Y(\xi)$, $\Psi(\xi)$ of TB ($\chi = 3$); (*d*) - the 3rd eigenmode for classical beam model

In distinction on the natural frequencies, the presented natural modes are rather close for the both models; significant differences are observed only near the clamped end, where in TB model the total slope of the bent axis does not vanish, in distinction on E-B model (only condition $\Psi(0) = 0$ is satisfied).

10.6.2. Shapes of forced oscillations of an elastic TB (without dampers and DVAs)

Consider now modes of forced oscillations at different frequencies of the external force, first for the elastic beam ($\mu = 0$, $\beta = 0$) without dampers, DVAs and additional point masses. The concentrated force with normalized magnitude $\hat{P} = p_1^2$ was applied at different points of the beam $x_P = \xi_P r_0$. Various values of the force frequency were assumed, less and larger than the first eigenfrequency $\omega_1 = 0.0323$ (at $L/r_0 = 10$, $\chi = 3$).

For the considered beam coefficients ζ_j in expansion of the dynamical deflection in eigenmodes of elastic TB (real in case of elastic beams) are presented in Table 10.2.

In the pre-resonance range ($\Omega/\omega_1 < 1$) the first mode predominates in the forced oscillation shape, contribution of other modes can be ignored, regardless of location of the force application point. In case of $\Omega/\omega_1 > 1$ (but $\Omega < \omega_2$) the second mode component increases and gradually becomes predominant, but the third mode does not become noticeable even at normalized frequency $\Omega = 5\omega_1 = 0.1616 > \omega_2$. Simultaneously with increasing Ω difference between TB and E-B beam increases.

Table 10.2. Coefficients ζ_j in expansion (10.32) for elastic TB at various excitation frequencies Ω and different location of the force ξ_P ($L / r_0 = 10, \hat{P} = p_1^2, \chi = 3$)

Ω / ω_1	$0.1\xi_P$	ζ_1	ζ_2	ζ_3
0.9	1	8.0781	-0.0287	0.0051
	0.7	4.9711	0.0092	-0.0041
	0.5	2.9786	0.0237	-0.0007
2.5	1	-0.1125	-0.0419	0.0054
	0.7	-0.0692	0.0135	-0.0043
	0.5	-0.0415	0.0346	-0.0007
5.0	1	-0.0250	0.0708	0.0071
	0.7	-0.0154	-0.0228	-0.0057
	0.5	-0.0092	-0.0585	-0.0009

Thus, in the pre-resonance range only the first term in series (10.32) may be taken into account (the single-mode solution). Here the shear deformability does not affect noticeably the forced oscillation mode. In the post-resonance range the single-mode approximation, as a rule, is insufficient, but two- or three- modes approaches are rather correct. In post-resonance range the effect of shear becomes more significant, and E-B and Rayleigh models, as a rule, are inapplicable.

In Fig. 10.3 the forced oscillations shapes $Y(\xi)$ are presented for considered elastic TB ($\hat{P} = p_1^2$) at various excitation frequencies Ω; the force acts at the middle cross-section of the beam. The curves are obtained in the first, second and third approximations (curves 1, 2, 3, respectively). The first plot (*a*) relates to pre-resonance excitation frequency $\Omega = 0.0291 = 0.9\omega_1$; here the curve practically coincides with the first eigenmode. The second plot (*b*) - for $\Omega = 0.097 = 3.0\omega_1$; here the shape in the single-mode approximation (with the first mode) is rather far from the curve, obtained in two- and three-mode solutions (the second mode predominates, and two last curves coincide). The third plot (*c*) - for frequency $\Omega = 0.1616 = 5.0\omega_1$, exceeding ω_2; here also the 2nd and 3rd eigenmodes are sufficient for good presentation of the forced oscillation shape.

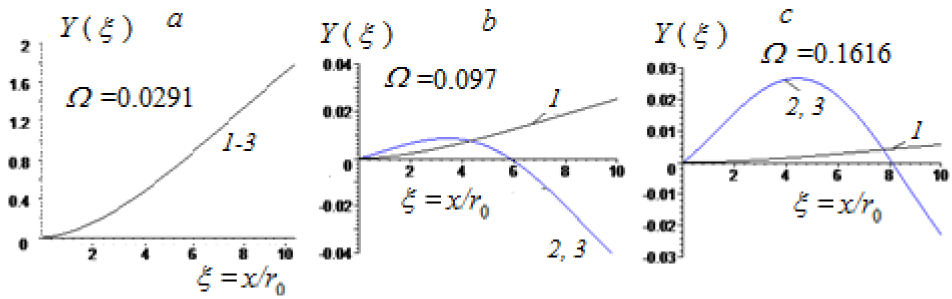

Fig. 10.3. Forced oscillations shapes $Y(\xi)$ in elastic TB ($L/r_0 = 10$, $\chi = 3$, $\hat{P} = p_1^2$) at various excitation frequencies Ω; the force acts at the middle of the beam; 1, 2, 3 - curves in the single-, two- and three modes approximations; (a) excitation frequency $\Omega = 0.0291$; three shapes coincide; (b) $\Omega = 0.097$ and (c) $\Omega = 0.1616$ (curves in the two- and three modes approximations coincide)

Thus the forced oscillation shape depends mainly on the excitation frequency. The location of the force can also affect the shape (if the point of the force application is close to a node of some mode, then the corresponding component does not contribute to this shape).

10.6.3. Forced oscillations of a viscoelastic TB (without dampers and DVAs)

To analyze the influence of the internal and external viscous friction on forced oscillation shapes of TB we take the beam $L/r_0 = 10$, $\chi = 3$ with following values of the friction dimensionless parameters (10.50) $\tilde{\beta} = 0.1$, $\tilde{\mu} = 0.1$. The external force with magnitude $\hat{P} = p_1^2$ and various frequencies $\tilde{\Omega} \equiv \Omega / p_1$ was applied at points $\xi_P (r_0 / L) = 0.5$ (middle of the beam) or $\xi_P (r_0 / L) = 0.7$. Values of the computed coefficients ζ_k in expansions (10.32) are presented in Table 10.3.

The main peculiarity of the damped beam is that the coefficients of expansion of the forced oscillations shape in the eigenmodes are complex. Complexity of the coefficients ζ_k means the appearance of a phase shift between the force and the oscillation mode, and different phase shifts θ_k for various eigenmodes destroy standing wave and generate a running wave component. As is seen from Table 3, for the assumed parameters of the external and internal friction (rather moderate) the imaginary parts of ζ_k are sufficiently small with respect to the real parts, so one might expect that the running wave component will be small with respect to the standing wave component. Strictly speaking, in case of damped beam the profile of forced oscillation mode loses its definiteness, the nodes are not fixed, and similarity at various time moments is violated.

Table 10.3. Coefficients ζ_k in expansions (10.32) for viscoelastic TB at different frequencies and locations of the force ($L/r_0=10$, $\chi=3$, $\widehat{P}=p_1^2$, $\tilde{\beta}=0.1$, $\tilde{\mu}=0.1$)

Ω/ω_1	$0.1\xi_P$	ζ_1	ζ_2	ζ_3
0.9	1	1.3124 – 2.9798 *i*	-0.0284 + 0.0028 *i*	0.0051 – 0.0005 *i*
	0.7	0.8076 – 1.8337 *i*	0.0091 - 0.0009 *i*	-0.0040 + 0.0004 *i*
	0.5	0.4839 – 1.0987 *i*	0.0234 – 0.0023 *i*	-0.0007+0.0001 *i*
2.5	1	-0.1116 - 0.0098 *i*	-0.0361 + 0.0146 *i*	0.0051 – 0.0014 *i*
	0.7	-0.0687 - 0.0060 *i*	0.0116 – 0.0047 *i*	-0.0040 + 0.0011 *i*
	0.5	-0.0412 – 0.0036 *i*	0.0298 – 0.0120 *i*	-0.0007 + 0.0002 *i*
5.0	1	-0.0250 - 0.0010 *i*	0.0248 + 0.0338 *i*	0.0047 – 0.0034 *i*
	0.7	-0.0154 – 0.0006 *i*	-0.0080 – 0.0109 *i*	-0.0038 + 0.0027 *i*
	0.5	-0.0092 – 0.0004 *i*	-0.0204 – 0.0279 *i*	-0.0006 + 0.0004 *i*

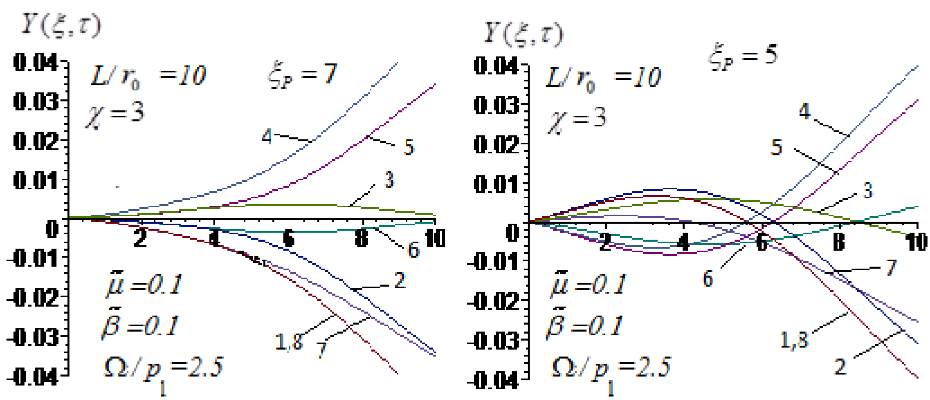

Fig. 10.4. Bent axis of the TB in various times at excitation frequency $\Omega/p_1=2.5$ for two locations of the force: (*a*) $\xi_P(r_0/L)=0.7$; (*b*) $\xi_P(r_0/L)=0.5$ ($\tilde{\mu}=0.1$, $\tilde{\beta}=0.1$). Curves 1-$\Omega\tau$ =0, 2-$\Omega\tau=\pi/4$, 3-$\Omega\tau=\pi/2$, 4-$\Omega\tau=\pi$, 5- $\Omega\tau=5\pi/4$, 6-$\Omega\tau=3\pi/2$, 7-$\Omega\tau=7\pi/4$, 8-$\Omega\tau=2\pi$

In Fig. 10.4 the bent axes of the considered beam ($\tilde{\beta}=0.1$, $\tilde{\mu}=0.1$) in various time moments are shown at excitation frequency $\Omega/p_1=2.5$ for two locations of the force: $\xi_P(r_0/L)=0.7$ (*a*) and $\xi_P(r_0/L)=0.5$ (*b*).

When the force is applied in a vicinity of the free end of the cantilever beam ($\xi_P(r_0/L)=0.7$), the bent axes are almost similar, i. e. the running component is rather small. But at $\xi_P(r_0/L)=0.5$ the node of axis moves in a wide interval, and the running component is noticeable.

10.6.4. TB with a concentrated mass

Consider some results of the solution in the single-mode approximation (which applicable at excitation frequencies not exceeding considerably the first eigenfrequency) for TB with parameters $L/r_0=10$, $\chi=3$, $\widehat{P}=p_1^2$, $\tilde{\beta}=0$, $\tilde{\mu}=0.1$, with a point mass and a force on free end ($\xi_M=L/r_0$). In Fig. 10.5 the frequency response curves (FRC), i.e. dynamical amplification factors k_{dyn} (50) via the frequency parameter $\tilde{\Omega}=\Omega/p_1$, are shown for various values of the normalized mass $\widehat{M}$.

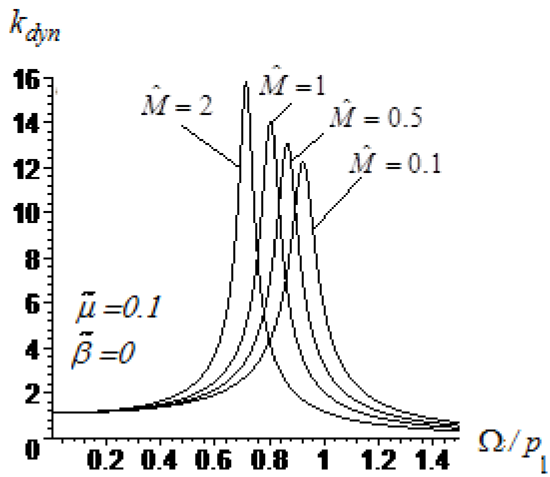

Fig. 10.5. Frequency response curves for various values of normalized mass $\widehat{M}$ on free edge of the beam ($L/r_0=10$, $\chi=3$, $\tilde{\beta}=0$, $\tilde{\mu}=0.1$, $\widehat{P}=p_1^2$, $\xi_P=L/r_0$)

The concentrated mass increases the maximum on the FRC and displaces it to lower value of Ω (due to increasing inertia force and decreasing natural frequency).

10.6.5. Viscoelastic TB with dynamical vibration absorber

In the numerical analysis there are studied:

- influence of the beam and the absorber parameters on amplitude-frequency characteristics (within framework of the single-mode approximation);
- influence of the excitation frequency and location of the absorber and the force on the qualitative picture of forced oscillations.

The influence of absorber parameters on frequency-response curves (single mode approximation)

A dynamic vibration absorber is characterized with three dimensionless parameters: normalized mass $\widehat{m}_a$ (10.71), the viscous friction parameter β_a^* (10.70) and the tuning parameter ω_a / p_1 (ratio of the DVA partial frequency to the 1st eigenfrequency of the elastic TB). In the following analysis we took beam with the same parameters $L / r_0 = 10$, $\chi = 3$, $\tilde{\mu} = 0.1$; $\tilde{\beta} = 0$, $\widehat{P} = p_1^2$; for the absorber following basic parameters were taken: $\widehat{m}_a = 0.1$, $\omega_a / p_1 = 0.9$.

Figs. 10.6, *a-f*, illustrate the influence of the absorber friction parameter β_a^* on FRCs at given tuning (in the single-mode approximation). Plot *a* relates to the beam without absorber, other plots (*b-f*) to the beam with absorber having different β_a^* values, from $\beta_a^* = 0.06$ till $\beta_a^* = 0.6$. At small friction (plots *b, c*, $\beta_a^* = 0...0.15$) the FRCs have two distinct maxima, but with rising β_a^* they merge into a single maximum (plots *e, f*). So the viscous friction in DVA (as well as internal friction in beam) can lead to fusion of two maxima on FRC into a single one. Maxima on FRC reach the minimal value in range β_a^*=0.2 - 0.3 (for given beam parameters). After the fusion at further increasing β_a^* the maximal amplitude rises monotonously. Such dependence of maximal dynamic amplification factor from viscous friction parameter is similar to well known dependence of dynamic amplification factor on viscous friction in one-degree-of-freedom systems. The optimal β_a^* values are of special interest, as well as the quantitative effect of the DVA on the beam oscillation (decrease of amplitude about two times for mass ratio $\widehat{m}_a = 0.1$ (compare plots (*a*) and (*d*)).

The next plots (Fig. 10.7) illustrate the impact of absorber tuning parameter ω_a / p_1 on the maximum of k_{dyn} for given friction value $\beta_a^* = 0.15$ ($\widehat{m}_a = 0.1$). The tuning parameter varied in range (0.6 …1.2).

Here again the optimum value of parameter ω_a / p_1 corresponds to equality of two local maxima on the FRC. At small ω_a / p_1 value the global maximum is determined by the right peak (the left peak at plot (*a*) is almost invisible); with rising ω_a / p_1 these peaks converge and become equal at $\omega_a / p_1 \approx 0.9$. At further increasing ω_a / p_1 the left peak becomes global. So value $\omega_a / p_1 \approx 0.9$ ensures the minimax value of k_{dyn} for the assumed parameters L / r_0, $\chi, \tilde{\mu}; \tilde{\beta}, \tilde{m}_a, \beta_a^*$.

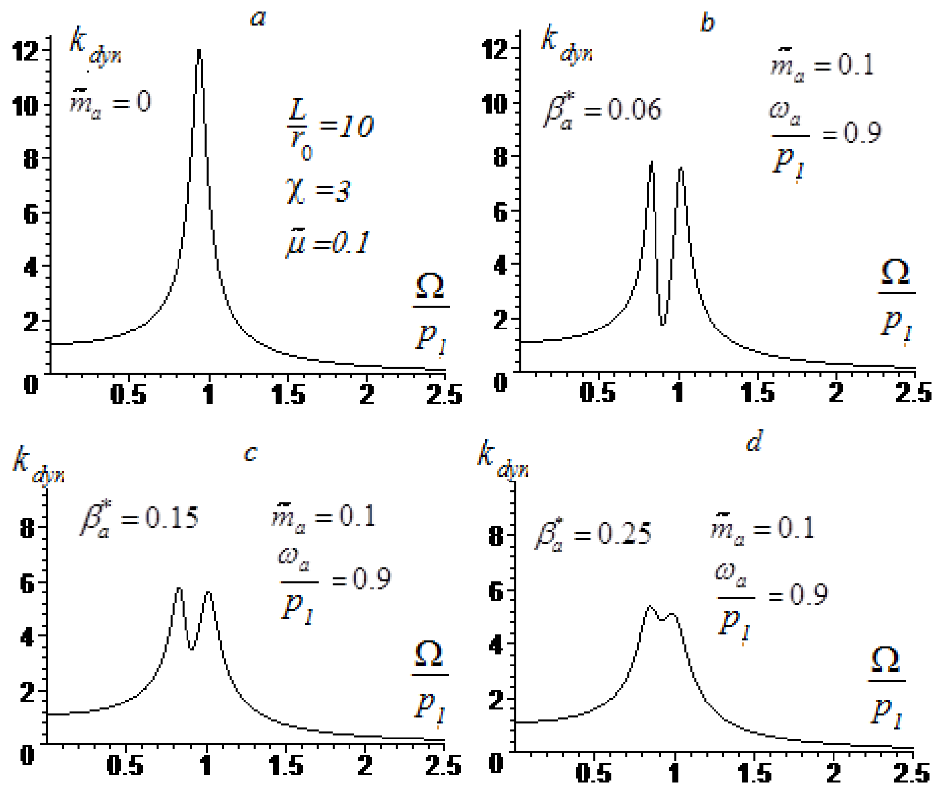

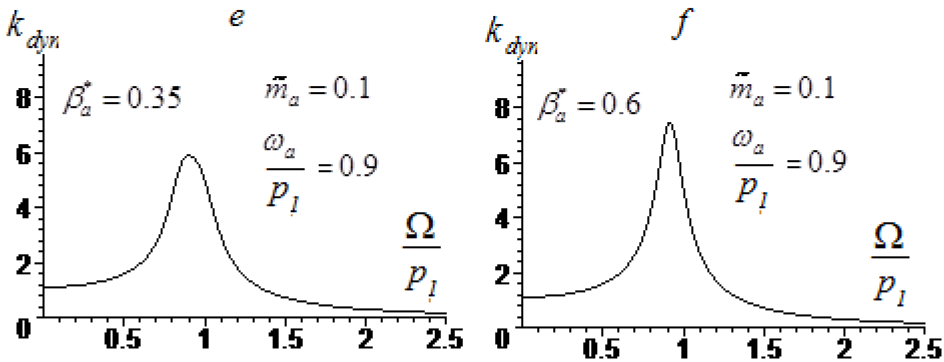

Fig. 10.6. Influence of the absorber viscous friction parameter β_a^* on FRC's for viscoelastic Timoshenko beam ($L/r_0 = 10$, $\chi = 3$, $\tilde{\mu} = 0.1$; $\tilde{\beta} = 0$, $\hat{P} = p_1^2$); *a*) beam without DVA, *b*) $\beta_a^* = 0.06$, *c*) $\beta_a^* = 0.15$, *d*) $\beta_a^* = 0.25$, *e*) $\beta_a^* = 0.35$, *(f)* $\beta_a^* = 0.6$.

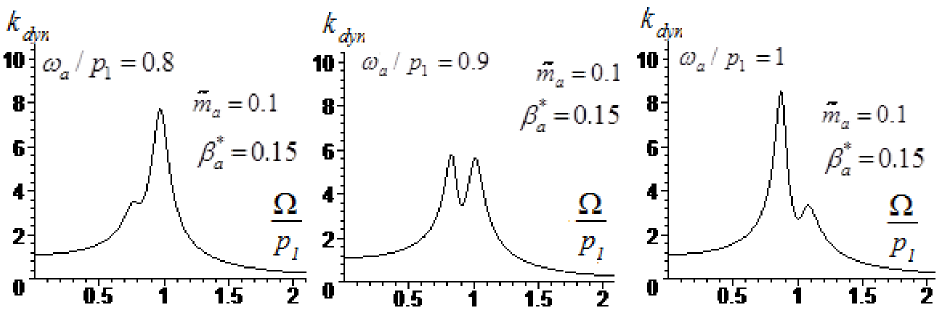

a) b) c)

Fig. 10.7. Influence of tuning parameter ω_a / p_1 on the FRCs for the viscoelastic TB; (*a*) $\omega_a / p_1 = 0.8$; (*b*) $\omega_a / p_1 = 0.9$; *(c)* $\omega_a / p_1 = 1.0$;.($L/r_0 = 10$, $\chi = 3$, $\tilde{\mu} = 0.1$; $\tilde{\beta} = 0$, $\hat{P} = p_1^2$; $\hat{m}_a = 0.1$, $\beta_a^* = 0.15$).

Multi-mode solution. Running waves

In order to study qualitative effects due to distinctions between forced oscillations shapes of the viscoelastic TB with DVAs and natural modes of the elastic TB we took into account three terms of the expansion (10.32) (such solution is applicable for excitation frequency up to the third eigenfrequency). There were assumed the former parameters of TB ($L/r_0 = 10$, $\chi = 3$, $\tilde{\mu} = 0.1$; $\tilde{\beta} = 0$) , DVA ($\hat{m}_a = 0.1$, $\beta_a^* = 0.35$, $\omega_a / p_1 = 0.9$); and various excitation frequencies $\Omega / p_1 = 0.9$, 2.5, 5.0 were put. The absorber was located on the free end, and the force was applied either at the end or in the middle cross-section (Fig. 10.8, schemes I and II respectively).

In Fig. 10.9 the force oscillation shapes are presented for these two schemes at various excitation frequencies.

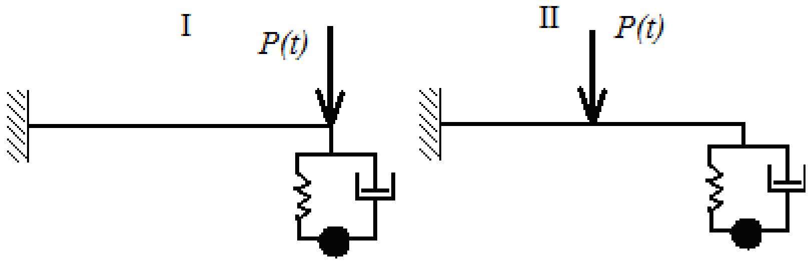

Fig. 10.8. Two variants of location of DVA and external force

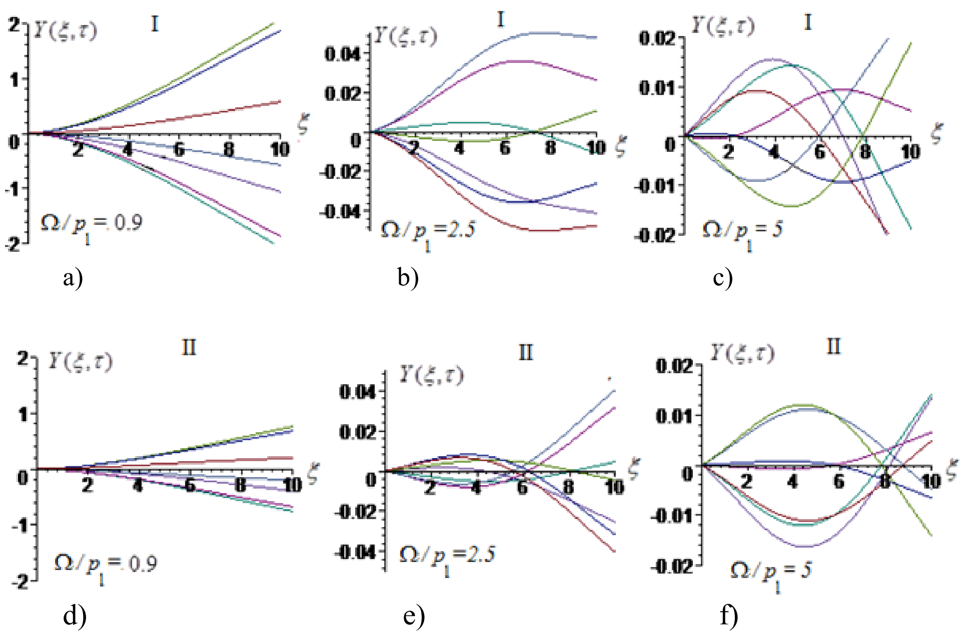

Fig. 10.9. Dynamic deflection of the beam $Y(\xi,\tau)$ with DVA at various time moments; plots *a,b, c* - scheme I, $\omega_a / p_1 = 0.9$, 2.5 and 5, respectively; plots *d*, *e*, *f* - scheme II, $\omega_a / p_1 = 0.9$, 2.5 and 5, respectively ($L / r_0 = 10$, $\chi = 3$, $\tilde{\mu} = 0.1$; $\tilde{\beta} = 0$, $\hat{m}_a = 0.1$, $\beta_a^* = 0.35$)

It is seen from Fig. 10.9 that the excitation frequency is a decisive factor determining the dynamic response of the beam. For frequency parameter $\Omega / p_1 = 0.9$ (pre-resonance range) in both the cases I and II the shapes of the bent axis are similar, and the dynamic deflection can be considered as a standing wave. In post-resonance ranges (frequency parameter $\omega_a / p_1 = 2.5; 5.0$ lies in the interval between the first and second eigenfrequencies) the traveling wave component is significant and increases with increasing excitation frequency. At location of the force and DVA in different cross-sections (case II) this tendency becomes stronger.

Note that these results related to cantilever beams well correspond qualitatively with the analysis of simply supported beams presented in [10.10], but there are quantitative differences, in particular, due to absence of symmetry in case of cantilever beams. The running component of the dynamic deflection can result in significant changes in the bent axis curvature and bending stresses. So account of running waves can be necessary at design of beams and choice of DVAs parameters.

10.7. Conclusion

The general solution for the steady-state forced oscillations of viscoelastic Timoshenko beams with dampers, dynamical vibration absorbers and point masses under harmonic (in time) external loads is obtained. The solution is based on expanding the dynamic deflection and the angle of cross-section rotation in the natural modes of elastic TB (without dampers, absorbers and point masses) and employing the appropriate orthogonality conditions. The dampers, DVAs and point masses are included in the general solution within the uniform scheme as concentrated influences which themselves depend on the beam motion.

At presence of internal and external viscous friction the dynamical deflection of the beam undergoes qualitative changes - there appears a running wave component which is superimposed on a standing wave. The trend to appearance of the running wave can be amplified by the local forces due to the dampers, absorbers or point masses.

In the numerical analysis there are studied subsequently effects of parameters of the beam, mass and of dynamical absorbers on forced oscillations of cantilever beams. In particular, optimal ranges of the tuning and viscous friction parameters of DVAs are assessed.

10.8. References

10.1 Anderson R.A, Flexural Vibrations in Uniform Beams According to the Timoshenko Theory, J. Appl. Mech., Vol. 20, 1953, N 4, pp. 504-510.

10.2 Dolph C.L., On the Timoshenko theory of transverse beam vibrations, Quarterly of Applied Mathematics, Vol. 12, 1954, pp. 175-187.

10.3 Grigoluk E.I., Selezov I.T., Nonclassical theories of oscillations of rods, plates and shells. In: “Itogi nauki i tekhniki”, Series: Mekhanika tviordykh deformiruemykh tel, Vol. 5, Moscow, VINITI, 1973, 272 p. (in Russian). (Григолюк Э. И., Селезов И. Т., Неклассические теории колебаний стержней, пластин и оболочек. Итоги науки и техники. Серия Механика твёрдых деформируемых тел. Т. 5. М,, ВИНИТИ, 1973, 272 с.).

10.4 Hermann G., Forced Motions of Timoshenko Beams, J. Appl. Mech., Trans. of ASME, Vol. 22, 1955, N 1, pp. 33-56.

10.5 Korenev B.G., Reznikov L.M.. Dynamic vibration absorbers: Theory and technical applications. Chichester, W. Sussex, Eng.; New York, Wiley, 1993, 296 p. (Коренев Б. Г., Резников Л. М., Динамические гасители колебаний: Теория и технические приложения. М.: Наука, ГРФМЛ, 1988, 304 с.).

10.6 Lee H.C., Forced Lateral Vibration of a Uniform Cantilever Beam with Internal and External Damping, J. Appl. Mech., Vol. 27, 1960, pp. 551-556.

10.7 Manevich A.I., Transverse waves in viscoelastic Timoshenko beam. In: Theoretical Foundations of Civil Engineering - XVII, Polish-Ukrainian Transactions, Warsaw, PW, 2009, Vol. 17, pp. 209-216 (In Russian).

10.8 Manevich A., Demedetskaya V., Forced oscillations of a beam with viscous dampers and concentrated masses. In: Theoretical Foundations of Civil Engineering - XI,. Polish-Ukrainian Transactions, Warsaw, PW, 2011, Vol. 19, pp. 161-168. (In Russian).

10.9 Manevich A., Kolakowsky Z., Free and forced oscillations of Timoshenko beam made of viscoelastic material, J. Theor. Appl. Mech., 49, N 1, Warsaw 2011, pp. 3-16.

10.10 Manevich A., Demedetskaya V., Oscillation of viscoelastic Timoshenko beam with dynamic vibration absorber and concentrated masses. In: “Statics, Dynamics and Stability of Structures”. Vol. 3, Kowal-Michalska K., Mania R.J. (eds.), “Review and Current Trends in Stability of Structures”, Lodz University of Technology. A Series of monographs, Lodz, 2013, pp. 147-178.

10.11 Newman M.K., Viscous Damping in Flexural Vibrations of Bars, J. Appl. Mech., N. Y., Vol. 26, 1959, pp. 367-376.

10.12 Pan H.H., Vibration of a Viscoelastic Timoshenko beam, J. of Engineering Mechanics Division, Proc. of ASCE, Vol. 92, No. EM2, 1966, pp. 213-234.

10.13 Panovko Ya.G., Internal friction at oscillations of elastic systems, GIFML, Moscow, 1960, 194 p. (in Russian). (Пановко Я.Г., Внутреннее трение при колебаниях упругих систем, ГИФМЛ, Москва, 1960, 194 с.).

10.14 Timoshenko S., Young D.Y., Vibration Problems in Engineering, third ed., D. van Nostrand Co, New York, 1961, 440 p.

11.

The modifications proposed to the buckling design recommendations of cold-formed column members of lipped channel section with perforations

This chapter describes the results obtained from numerical, experimental and theoretical investigations into the load capacity of column members of lipped channel cross-section with perforations of different arrangements subjected to compression loading.

Most structural cold-formed steel members are manufactured with pre-punched perforations to accommodate, for example, electrical, plumbing and heating services. Due to the position, orientation and the shape of perforations, the elastic stiffness and ultimate strength of a structural member can vary.

The buckling behaviour of cold-formed steel structural column members with lipped channel cross-section, with perforations of different shapes were studied and comparisons of the finite element results and the test results are also made with existing design specifications and conclusions are drawn on the basis of the comparisons.

11.1. Introduction

Cold-formed steel sections are widely used in storage racks, building structures, transportation machineries, domestic equipment, and other applications. The uses of cold-formed steel products are many and varied due to various characteristics such as their high strength-to-weight ratio, reliability and accuracy of profile, and ease of manufacture [11.3, 11.10, 11.12, 11.19]. The behaviour of a structural member with perforations can vary with perforation size, position, shape and number of perforations and can limit the advantages of these structures [11.2, 11.7, 11.15]. Hence, these can make the design and analysis of these members more complex.

In evaluation of the section properties of cold-formed members in compression or bending, perforations made specifically for fasteners such as bolts, screws, etc. may be neglected as perforations are filled with material. However, for any other perforations, the reduction in cross sectional area caused by these perforations should be taken into account. Shown in Figure 11.1 are some common section geometries of cold-formed structures [11.16].

a)

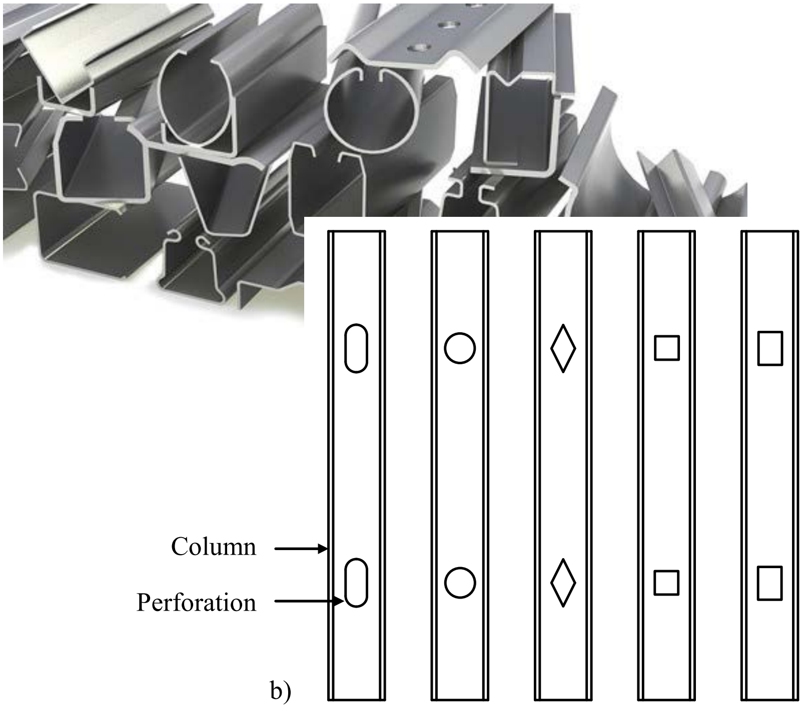

b)

Fig. 11.1. a) Examples of cold-formed members & b) Colum members with different shape perforations

The thickness of light gauge steel sheets or strips that can be cold-formed into structural shapes normally ranges from 0.3 mm to about 6 mm. Cold-formed steel structures have many advantages over conventional hot-rolled sections. In general, the following advantages of cold-formed steel structural members are identified in building construction: versatility of profile shape, reliability and accuracy of profile, pre-galvanised or pre-coated materials can be formed, variety of materials which can be formed, variety of connection methods, increase in yield strength, high strength-to-weight ratio and etc [11.5, 11.13, 11.19].

Cold-formed thin-walled sections tend to buckle locally at stress levels lower than the yield strength of the material when they are subjected to compression loading conditions. However, failure modes are not commonly encountered in normal structural steel design specifications, and therefore, extensive testing is required to provide a guideline for the design of cold-formed thin-walled structural members. As illustrated in Fig. 11.2, compared with conventional structural column members, cold-formed thin-walled steel open cross-section column members have at least three competing buckling modes namely, local, distortional, and Euler (flexural or torsional-flexural) buckling [11.8, 11.14, 11.17, 11.18,].

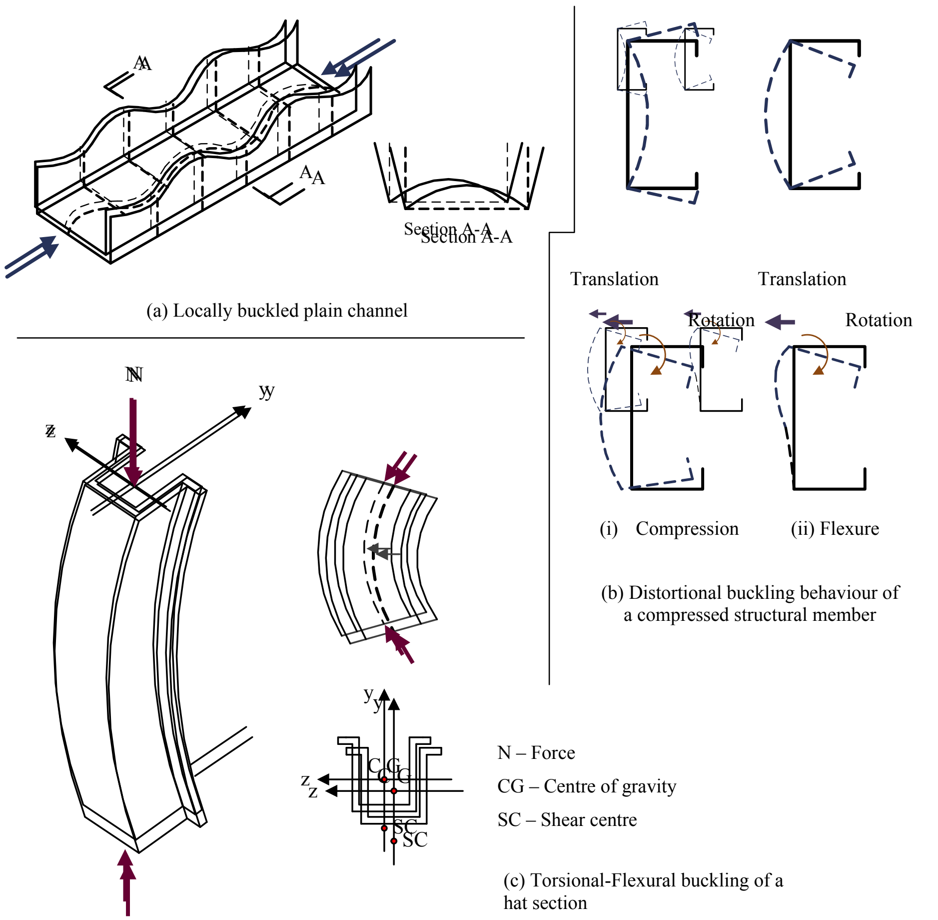

Fig. 11.2. a) Locally buckled plain channel in compression, b) Distortional buckling modes and c) Torsional-Flexural buckling of a hat section, when the section is weak in tension column leads to the rotation about the force axis

The load capacity of cold-formed column members of lipped channel cross-section subjected to compression loading mainly depends on overall buckling. In general, buckling modes interact with each other. The relevant literature reveals that the proper incorporation of various buckling modes is imperative for accurate and reliable buckling strength predictions of cold-formed steel members [11.9].

11.2. Numerical investigation

A general finite element procedure with a particular emphasis on analysing thin-walled members using ANSYS finite element software package is presented here. Finite element analysis is now commonly used early in the design process to try out new concepts and optimise before any physical prototypes are made and tested. The numerical results presented have been determined through the non-linear buckling analysis of column members of lipped channel cross-section with perforations using ANSYS shell element SHELL181 [11.1]. Figure 11.3 illustrates SHELL181 geometry. SHELL181 is one of the shell elements in the ANSYS element library along with many other shell elements such as SHELL43, SHELL93, etc.

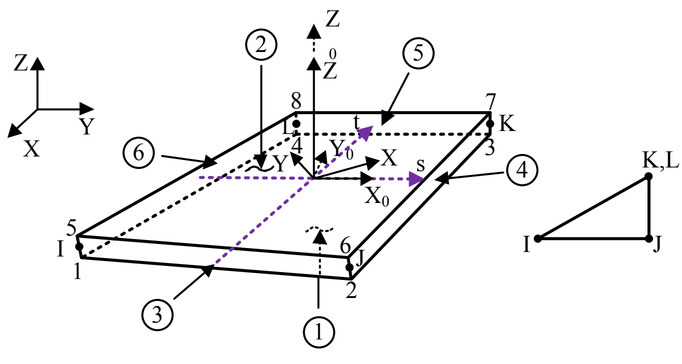

Fig. 11.3. SHELL181 geometry

Finite element models were developed using exact dimensions of the web, flange, and lip of the member and perforations. They were then modified by including the material properties obtained from tensile tests. In this study, only one-half of the section was modelled using symmetry of the sections, loading, and support reactions about the vertical plane [11.6].

The loading was applied through a load bearing plate, suitable to represent the true compression load used in the experiments. Displacement control method was used, and contact elements were created by defining a pair of contact surfaces at the bottom of the load bearing plate and the top cross-section of the column. This scenario simulates the actual contact situation existing during the tests. At the location where the top end fixture exists, nodes were constrained in UX, UY, ROTX, ROTY and ROTZ. The nodes located at the bottom end fixture were constrained in UX, UY, UZ, ROTX, ROTY and ROTZ as shown in Figure 11.4, to represent the actual test conditions in the experimental investigations [11.11].

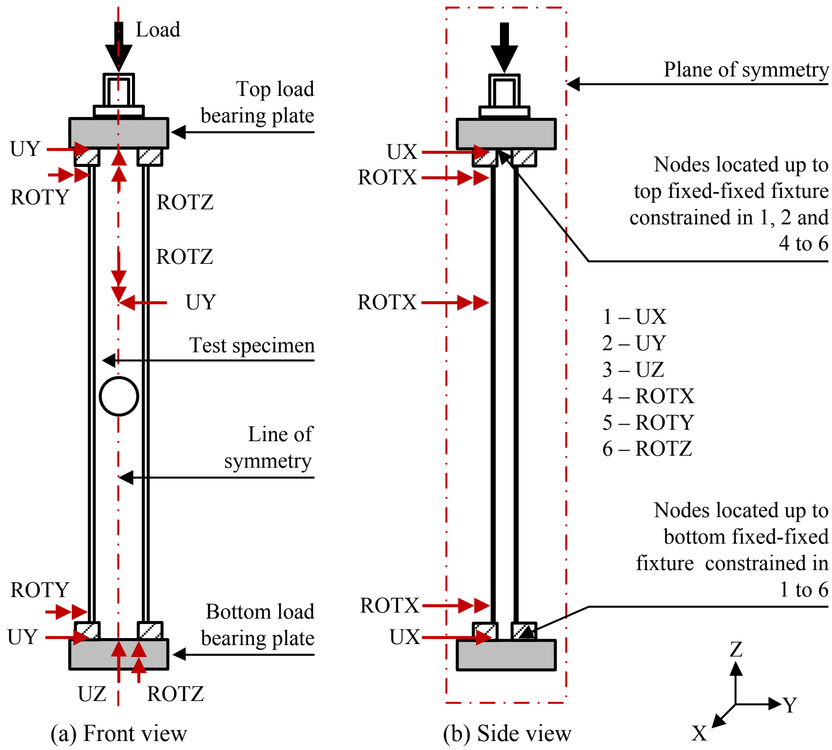

Fig. 11.4. Boundary conditions for fixed-fixed condition

Finite element analysis (FEA) is an accurate and flexible technique, which can be used to predict the performance of a structure, mechanism or process under different loading conditions. The accuracy of results obtained from a finite element analysis is greatly dependent on material properties. A number of material-related factors can cause a structure's stiffness to change during the course of an analysis. Three tensile tests were conducted for each different steel sheet and average yield stress was determined with the 0.2% strain offset method and engineering stress vs. engineering strain graphs were computed using load-displacement curves obtained from the tensile tests. Figure 11.5 shows symmetry boundary and fixed-fixed support conditions.

The finite element modelling was undertaken using ANSYS general post-processor /POST1 and time history post-processor /POST26. The static non-linear solution technique was employed. Ultimate loads and load vs. displacement graphs were reported using time-history post-processor POST26. In this investigation, half models were validated with results obtained from experimental studies.

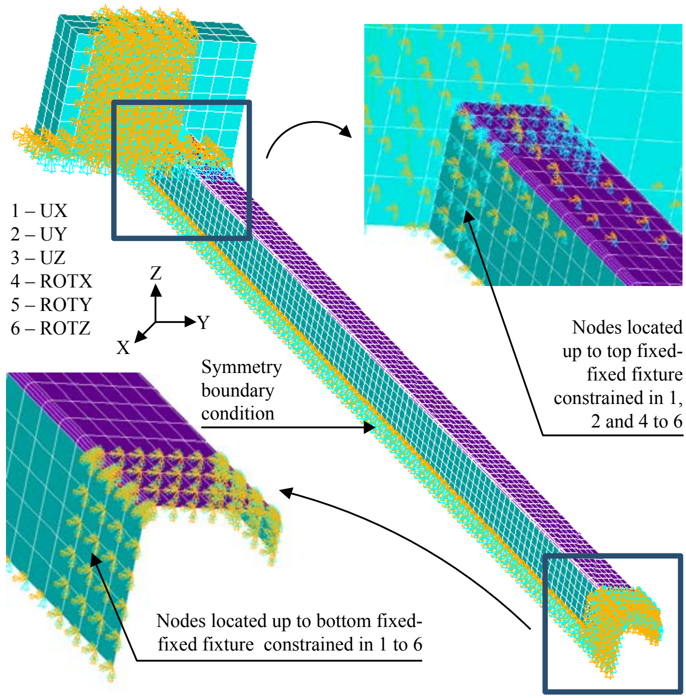

Fig. 11.5. Symmetry boundary and fixed-fixed support conditions

11.3. Experimental investigation

11.3.1. Different types of columns specimens tested

In this study, a set of specimens of the same cross-section but with different perforation positions were tested as shown in Figure 11.6. Column lengths were kept constant at 1000mm, with perforations located at the mid-height of the column. Five cold-formed steel columns were tested to failure with fixed-fixed end conditions. For the specimens tested with fixed-fixed end conditions, two sets of identical clamping attachments were manufactured as shown in Figure 11.7. Each set mainly consists of two parts namely inside end attachment and outside end attachment. In this investigation, inside and outside end attachments prevented a change in shape of the cross-section. The design of the end attachments was made for ease of manufacture and effective grip on the specimens. The inner surfaces of the load bearing plates were milled to provide extra frictional gripping on the specimens. The column testing parameters are shown in Table 11.1.

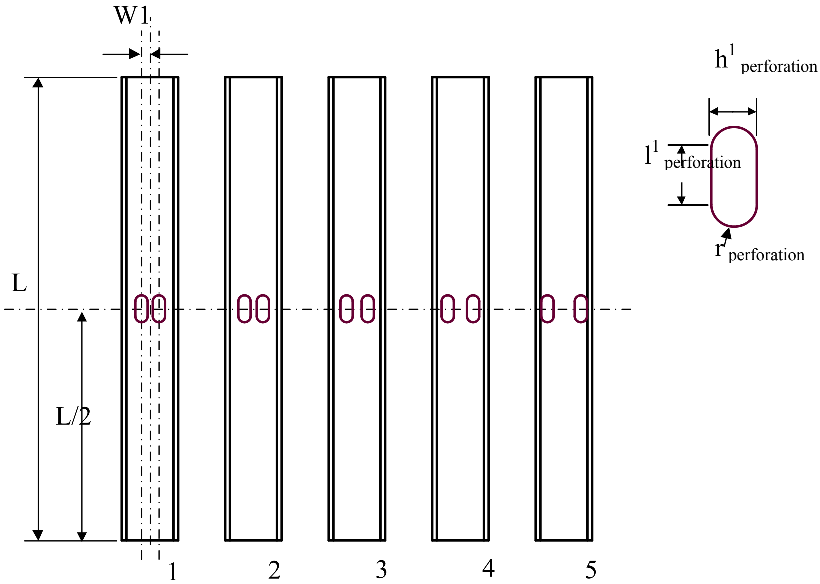

Fig. 11.6. Perforation shapes and positions

Table 11.1. Nominal section dimensions

Specimen		Length of the specimen	$h^1_{perforation}$	$l^1_{perforation}$	W1
1	SIII/S1/P/F-F	L	1 b	2 b	4 c
2	SIII/S2/P/F-F	L	1 b	2 b	5 c
3	SIII/S3/P/F-F	L	1 b	2 b	6 c
4	SIII/S4/P/F-F	L	1 b	2 b	7 c
5	SIII/S5/P/F-F	L	1 b	2 b	8 c
		L = 1000 mm, b = 30 mm, c = 5 mm			

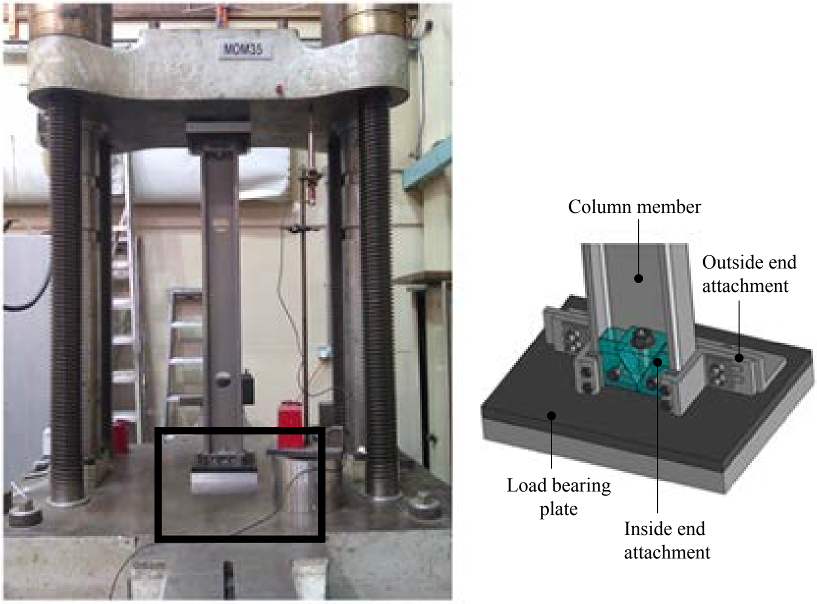

Fig. 11.7. Fixed-end fixture and test setup

11.3.2. Fixed-fixed end fixture

Figure 11.8 shows the details of the inside fixed-fixed end attachment. Blocks (a, b, c, and d) in Y-direction could be controlled using two screws (g, h). The movement of blocks (a, b, c, and d) in X-direction could be controlled using the nut, i. This attachment was designed to facilitate quick adjustment for accurate positioning and to avoid the deformation of the cross-section during the loading process. The inside end attachment was also designed such that it would fit into all cross-sections.

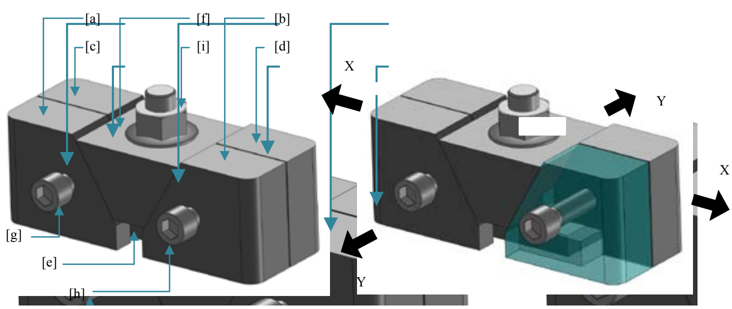

Fig. 11.8. Fixed-fixed inside end attachment

The details of the fixed-fixed outside end attachment are shown in Figure 11.9. The outside end attachment was designed such that it would fit into all cross-sections. The holding blocks (g) could be moved in X-direction, inward and outward to suit with the size of the outside dimension of the cross-section. Parts (h) can be moved in Y-direction, providing support to avoid the deformation of the lips of the cross-section during the loading process.

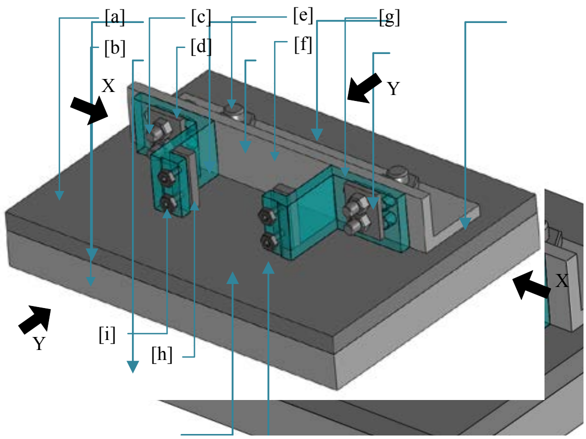

Fig. 11.9. Fixed-fixed outside end attachment

In this study column specimens were tested on a Tinius-Olsen material and structural testing machine. All column specimens were loaded with displacement control at a constant rate, and a high level of accuracy of the Tinius-Olsen testing machine crosshead displacement was achieved using a linear variable displacement transducer (LVDT).

11.3.3. Geometric imperfections

The effect of geometric imperfections on the ultimate strength of cold-formed steel members has been studied by numerous researchers [11.7]. In general, the larger the initial imperfections, the smaller the ultimate failure load, and thus the effect of initial imperfections on the buckling behaviour should be taken into consideration. In this study, measurements were recorded along three lines in the longitudinal direction in both web and flanges at 20 mm intervals as shown in Figure 11.10.

The geometric imperfections were measured using a coordinate measuring machine to a precision of 0.01 mm. The specimen was supported horizontally using clamps.

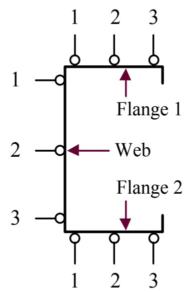

Fig. 11.10. Locations on the web and flanges to measure geometric imperfections

11.3.4. Material properties testing

Tensile coupon tests were performed to obtain the steel stress-strain curve and yield stress of steel sheets which were used for the manufacture of test specimens in this study. The tests were conducted in accordance with British Standard BS EN 10002-1:2001 "Metallic materials – Tensile testing – Part 1: Method of test at ambient temperature" (BSI 2001). BS EN 10002-1:2001 specifies the method for tensile testing of metallic materials and defines the mechanical properties which can be determined at ambient temperature. The average yield stress, σ_y was determined with the 0.2 % strain offset method and the results are summarized in Table 11.2.

Table 11.2. Measured material properties

Average Yield Stress, σ_y [N/mm^2]	Modulus of Elasticity, E [N/mm^2]
195	210,500

11.4. Theoretical investigation

For the specimens tested with fixed-fixed end conditions, the European Standard EN 1993-1-3, Eurocode 3: Design of Steel Structures: Part 1-3 General rules - Supplementary rules for cold-formed members and sheeting, provides design recommendations for cold-formed members and sheeting. In this standard, design equations and conditions are given for cold-formed steel products that have been cold-formed by forming processes such as forming or press-braking. Eq. (11.1) highlights the design equation for calculating the buckling resistance, $N_{b,Rd}$ of a compression member.

$$N_{b,Rd} = \frac{xA_{eff}f_y}{\gamma_{M1}} \tag{11.1}$$

where x is the reduction factor for the relevant buckling mode, A_{eff} is the effective area, f_y is the yield strength and γ_{M1} is the general partial factor [11.4].

11.5. Comparisons between numerical, experimental and theoretical investigations

11.5.1. Deformation behaviour of the specimens

The outcome of this investigation has shown that the ultimate load varied with the position of the perforations. The buckled shape is three half-waves in the longitudinal direction with a half-wave length approximately equal to the one third of the height of the specimen. It was noticed that the deformation around perforations was found to be higher than that of the areas without web openings.

Interaction of local and distortional buckling modes was observed adjacent to the perforations. The load capacity of the perforated cross-sections showed a reduction of 33.52% with the increase of the distance of two perforations. This observation was accomplished to prove the strength increase around bends due to the cold forming process.

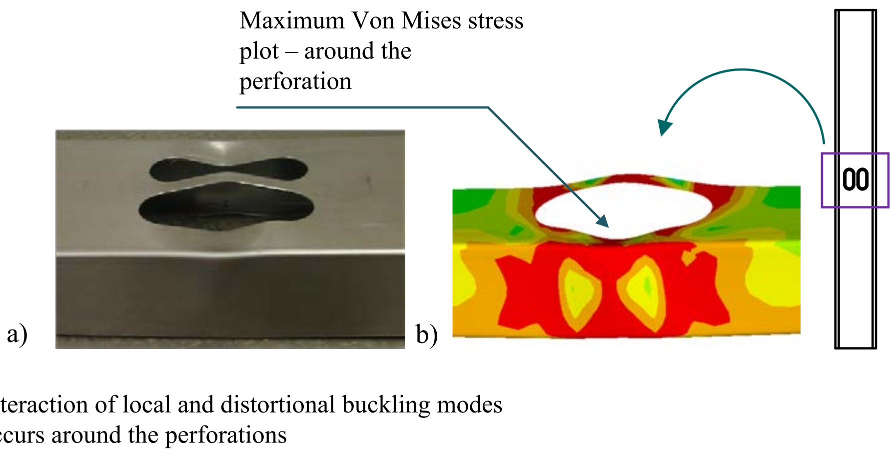

Fig. 11.11. Comparison of experimental and finite element analysis deformed shape: a) experimental deformed shape around the perforation and, b) ANSYS deformed shape around the perforation, equivalent half section for the section SIII/S2/P/F-F

11.5.2. Numerical, experimental and theoretical results

The results obtained from numerical, experimental, and theoretical investigations are presented here. The allowable and ultimate strength values of compression members obtained from experimental and numerical tests are shown. . Comparison of experimental and finite element analysis deformed shape is shown in Figure 11.11.

Table 11.3. Comparisons of numerical and experimental results

	Specimen	Experimental Buckling Strength [kN]		Numerical Buckling Strength [kN]		$P_{FEA,A}/P_{exp,A}$	$P_{FEA,U}/P_{exp,U}$
		Allowable, $P_{exp,A}$	Ultimate, $P_{exp,U}$	Allowable, $P_{FEA,A}$	Ultimate, $P_{FEA,U}$		
1	SIII/S1/P/F-F	27.62	31.74	23.43	31.42	0.85	0.99
2	SIII/S2/P/F-F	24.13	27.19	24.85	29.01	1.03	1.07
3	SIII/S3/P/F-F	23.72	30.06	27.28	31.27	1.15	1.04
4	SIII/S4/P/F-F	22.75	27.87	19.15	27.02	0.84	0.97
5	SIII/S5/P/F-F	17.56	21.10	16.68	22.52	0.95	1.07
Mean, $\overline{X}$						0.96	1.03
Standard Deviation, S						0.13	0.04
Coefficient of Variation, COV						0.13	0.04

Table 11.4. Comparisons of design code predictions with experimental results

	Specimen	Ultimate Buckling Strength [kN]		Ultimate Load Ratio
		Test, $P_{exp,U}$	Eurocode, $N_{b,Rd}$	$N_{b,Rd}/P_{exp,U}$
1	SIII/S1/P/F-F	31.74	38.33	1.21
2	SIII/S2/P/F-F	27.19	38.60	1.42
3	SIII/S3/P/F-F	30.06	38.26	1.27
4	SIII/S4/P/F-F	27.87	38.69	1.39
5	SIII/S5/P/F-F	21.10	38.04	1.80
Mean, $\overline{X}$				1.42
Standard Deviation, S				0.23
Coefficient of Variation, COV				0.16

Design code approach: Eurocode 3 - ENV 1993-1-3:2009 was used to obtain the nominal buckling strength of cold-formed lipped channel sections with perforations. Load vs. specimen graphs obtained from the finite element analysis, the experimental investigation and the theoretical investigation, and also full details of results including comparisons of the buckling strength between numerical and experimental investigations are presented in Table 11.3. Further, design code results compared with experimental results are given in Table 11.4.

Table 11.5. Comparisons of numerical results and design code predictions with experimental results

	Specimen	Ultimate Load Ratio: Numerical $P_{FEA,U}/P_{exp,U}$	Ultimate Load Ratio: Design Code Predictions $N_{b,Rd}/P_{exp,U}$
1	SIII/S1/P/F-F	0.99	1.21
2	SIII/S2/P/F-F	1.07	1.42
3	SIII/S3/P/F-F	1.04	1.27
4	SIII/S4/P/F-F	0.97	1.39
5	SIII/S5/P/F-F	1.07	1.80
	Mean, $\overline{X}$	1.03	1.42
	Standard Deviation, S	0.04	0.23
	Coefficient of Variation, COV	0.04	0.16

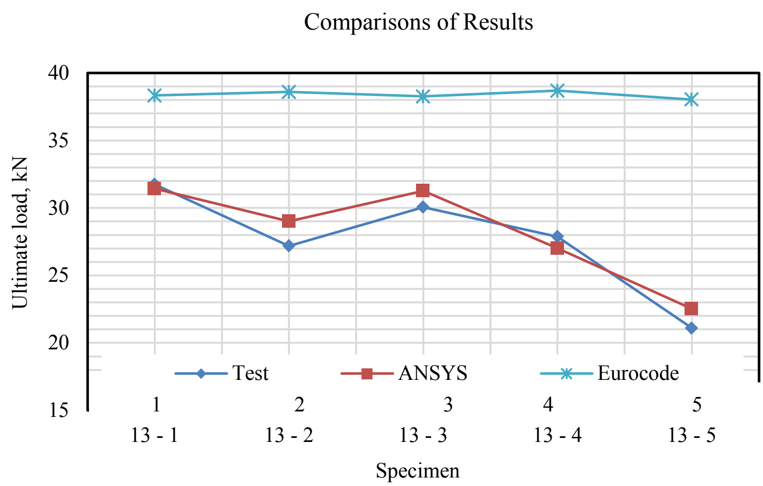

Fig. 11.12. Comparison of numerical, experimental, and theoretical ultimate buckling strength results

Comparisons of numerical results and design code predictions with experimental results are shown in Table 11.5 and Comparisons of experimental, numerical, and theoretical ultimate buckling strength results are given in Figure 11.12 respectively.

11.6. Proposals for the Eurocode specification

The Eurocode specification provides equations to calculate the ultimate buckling strength of cold-formed lipped channel sections with perforations. These design rules show highly unreliable results for the sections with larger perforations and hence, design modifications are proposed as listed below. The alternative design rule proposed in this section is valid only for channel sections with perforations located as shown in Figure 11.13.

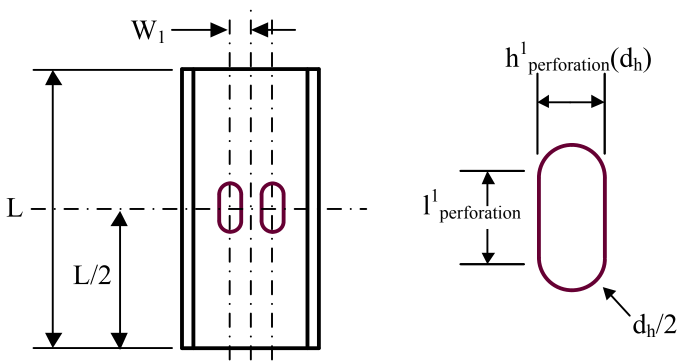

Fig. 11.13. Illustration showing perforation parameters

The effective width is given tin Eq. (11.2).

– Calculate effective width, b

$$b = \rho * (w - d_h - W_1) \tag{11.2}$$

where ρ is the local reduction factor, w is the flat width of the section, d_h is the width of the perforation, and W_1 is the perforation position on web measured from the centre (transverse direction).

– Calculating reduction factor, ρ

Reduction factor, ρ can be computed with the modified $\bar{\lambda}_p$ as indicated in Eq. (11.3) and (11.4).

$$\bar{\lambda}_p = \frac{\bar{b}/t}{28.4\varepsilon\sqrt{k_\sigma}} \tag{11.3}$$

where
$$\bar{b} = w - 2d_h + \left(2W_1 + \frac{h}{d_h}\right) \tag{11.4}$$

where w is the flat width of the section, d_h is the width of the perforation, W_1 is the perforation position on web measured from the centre (transverse direction), and h is the overall web depth.

The comparisons of current and proposed Eurocode ultimate buckling strength predictions with experimental results for a sample set are shown in Figure 11.14.

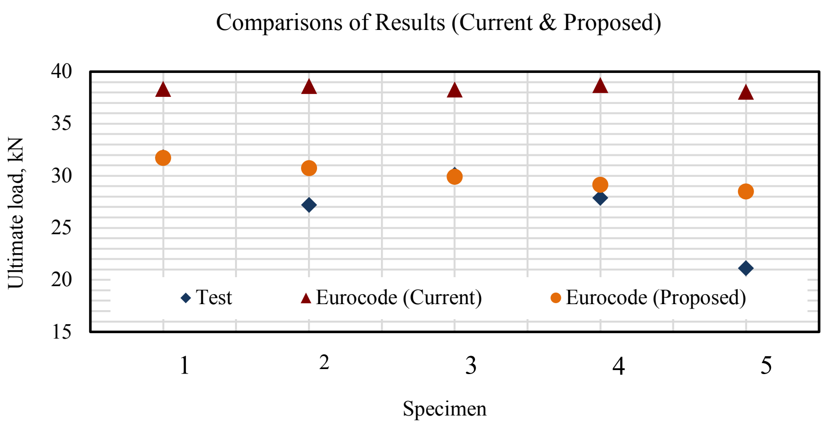

Fig. 11.14. Comparisons of current and proposed Eurocode ultimate buckling strength predictions with experimental results

11.7. Conclusion

The literature and the comprehensive description of cold-formed steel members, including buckling behaviour have shown that the use of cold-formed steel structures has increased over the past sixty years. However, investigations have shown that the use of cold-formed steel as a structural building material has limitations due to the lack of knowledge of structural behaviour of these members. The complicated structural behaviour and the limitations regarding experimental investigations result in a lack of a full understanding of cold-formed steel and applications.

Both local and elastic buckling failure modes were noticed in the tests. It was also observed that the all column members are susceptible to local buckling at relatively low compressive stress, approximately 45% of the ultimate load. Further, the presence of perforations has a great impact on the buckling load and deformed shape. The presence of perforations leads to complex structural failure, and hence, complicates the expected distortional buckling mode. Unlike local buckling, distortional buckling is influenced by end boundary conditions. The failure load of the column member, the interaction of the local and distortional buckling modes was observed in many cases.

The accuracy of finite element analysis is influenced greatly by the selection of finite element type and mesh density, particularly controlling the element mesh. Therefore, selecting the element mesh may be a more complicated process and thereby depends strongly on the experience and the knowledge of the user. However, this was overcome through identifying the high and low stress areas, and modelled with fine and coarse mesh respectively.

Eurocode recommendations provide many more possibilities for analysis of buckling strength of thin-walled sections, but these codes used today are limited for the use of structural members with perforations. Eurocode recommendations present design provisions to accommodate the influence of perforations on the buckling strength of lipped channel sections which are, in general, conservative and provide a more general description regarding the perforation parameters such as shape, position, orientation, etc.

The finite element analysis results into the load capacity of column members of lipped channel cross-section, subjected to compression loading, were compared against the experimental investigations results, and the comparison was used to validate the FE models. Tensile tests of the lipped channel column materials were carried out to determine the material properties which were incorporated into the FE model. It was shown that experimental and numerical investigations can be used to obtain a better understanding of failure mechanisms of buckling with a reasonable degree of confidence. Further, the study indicated that the ultimate load of the structure under compression load varied greatly with the perforation shape, size, orientation, and etc.

As noticed in in the investigation the presence of slotted holes on the web reduces the axial stiffness and also it can be clearly seen that a higher reduction in axial stiffness can be observed when the perforations are located near to the corners. The buckling investigation conducted has proven that the cold worked flat portions of the cross-section have lower yield strength compared to the corners.

Modifications were proposed to the current buckling design predictions studied in this study. Additionally, alternative design rules were suggested based on the results of the experimental investigation. The recommended design rules were indicated to closely predict the ultimate buckling strength of the lipped channel section. Furthermore, buckling strength values remained well within ± 5% limits of the experimental buckling strength values for the fixed-fixed end conditions.

The buckling investigation conducted has proven that the cold worked flat portions of the cross-section do have lower yield strength compared to the more highly worked corners and this affected the buckling behaviour. The FEA model, in conjunction with the modifications proposed to the buckling design recommendations studied in this research work and based on the parametric study findings, enables engineering judgements to be made about cold formed structural members before manufacturing the final product.

11.8. Future work

There are still some areas of the buckling behaviour of cold-formed lipped channel sections which need further extensive investigation and development in terms of the factors such as cross-section, column length, thickness, corner radius, forming method, and perforation parameters: size, shape, position, and orientation. For better classification of buckling results, a comprehensive and detailed study to determine under what conditions perforations influence the buckling modes is needed.

11.9. References

11.1 ANSYS., ANSYS Mechanical APDL Structural Analysis Guide: ANSYS Release 13.0. USA, 2010.

11.2 Cristopher D.M., Direct Strength Design of Cold-Formed Steel Members with Perforations. The Johns Hopkins University, Department of Civil Engineering, Baltimore, USA, 2009.

11.3 Cristopher D.M., Schafer B.W., Experiments on Cold-Formed Steel Columns with Holes, Thin-Walled Structures, Vol. 46(10), 2008.

11.4 ENV 1993-1-3:2006. Eurocode 3, Design of Steel Structures; Part 1.3: General rules - supplementary rules for cold formed thin gauge members and sheeting, 2009.

11.5 Ghersi A., Landolfo., R., Mazzolani., F.M., Design of Metallic Cold-Formed Thin-Walled Members, London: Taylor & Francis Group. ISBN 0-203-16451-2, 2005.

11.6 Hutton D.V., Fundamentals of Finite Element Analysis. USA: McGraw-Hill Companies, Inc. ISBN 0-07-239536-2, 2004.

11.7 Kulatunga M., Macdonald M., Harrison D.K., and Rhodes J., Load Capacity of Cold-Formed Column Members of Lipped Channel Cross-Section with Perforations Subjected to Compression Loading. Thin-Walled Structures, 2014.

11.8 Kulatunga M., Macdonald M., Investigation of Cold-Formed Steel Structural Members with Perforations of Different Arrangements Subjected to

Compression Loading, Thin-Walled Structures, Vol. 67, pp. 78-87, ISSN: 0263-8231, 2013.

11.9 Loughlan J., Yidris N., Jones K., The Failure of Thin-Walled Lipped Channel Compression Members due to Coupled Local-Distortional Interactions and Material Yielding, Thin-Walled Structures, Vol. 61, pp. 14-21, 2012.

11.10 Macdonald M., Heiyantuduwa Don M.A., Kotelko M., Rhodes J., Web Crippling Behaviour of Thin-Walled Lipped Channel Beams, Thin-Walled Structures [online]. Vol. 49(5), pp. 682-690, 2011.

11.11 Macdonald M., Kulatunga M., The Effects of End Conditions on the Load Capacity of Cold-Formed Steel Column Members of Lipped Channel Cross-Section with Perforations Subjected to Compression Loading. In: 22nd International Specialty Conference on Cold-Formed Steel Structures, 5-6 November, Missouri, USA, 2014.

11.12 Rhodes J., Design of Cold-Formed Steel Members: Elsevier Applied Science, 1991.

11.13 Rondal J., Cold Formed Steel Members and Structures General Report. Journal of Constructional Steel Research [online]. Vol. 55(1), pp. 155-158, 2000.

11.14 Schafer B.W., Peköz T., Local and Distortional Buckling of Cold-Formed Steel Members with Edge Stiffened Flanges. New York: Cornell University, 2011.

11.15 Shanmugam N.E., Evans H.R., Structural Response and Ultimate Strength of Cellular Structures with Perforated Webs, Thin-Walled Structures, Vol. 3, 1985.

11.16 Shanmugam N.E., Dhanalakshmi M., Design for Openings in Cold-Formed Steel Channel Stub Columns. Thin-Walled Structures, Vol. 39(12), 2001.

11.17 Yang D., Hancock G.J., Compression Tests of Cold-Reduced High Strength Steel Stub Columns. Research Report R815. Australia: Department of Civil Engineering Sydney NSW, 2002.

11.18 Yang D., Hancock G.J., Rasmussen K.J.R., Compression Tests of Cold-Reduced High Strength Steel Long Columns. Research Report R816. Australia: Department of Civil Engineering Sydney NSW, 2002.

11.19 Yu W.W., Cold-Formed Steel Structures, 3rd Ed. Canada: John Wiley & Sons Inc. ISBN 0-471-34809-0, 2000.

12.

Tolerance modelling of stability of thin composite plates with dense system of beams

12.1. Introduction

The subject of the contribution are thin functionally graded skeletal plates with dense system of beams. The considered skeletal plate is made of two families of thin homogeneous beams with axes intersecting under the right angle. The regions situated between the beams fills a homogeneous matrix material (Fig. 12.1). It is assumed that the width of the beams can vary slowly in the midplane of the plate. Thus, we deal with composite plate that has space-varying microstructure. Since, the apparent properties of the plate are graded in space, we deal with a special case of a functionally graded material. The generalized period $l=\sqrt{l_1 l_2}$ of heterogeneity is assumed to be sufficiently small comparing to the measure of the midplane of the plate. The fundamental feature of proposed model is that the microstructure length parameter l is similar compared to thickness h of the plate. From a formal point of view, the plate with microstructure of this kind can be described in the framework of the well-known theories for thin elastic plates. However, due to the inhomogeneous microstructure of the plate, this direct description of the structure leads to plate equations with discontinuous and highly oscillating coefficients. These equations are not a good tool to be applied to numerical solutions of specific engineering problems.

The aim of the presented analysis is to derive and apply the macroscopic mathematical model describing stability of the composite plate under consideration. The macroscopic model for the plate dynamic analysis of this kind we can find in [12.5]. The formulation of the macroscopic mathematical model for the analysis of stability of these plates will to be based on the tolerance averaging approach. The general modelling procedures of this technique are given by Woźniak et al. in books [12.8], [12.9]. The applications of this technique for the modelling of stability of various periodic composites are given in a series of papers. Baron [12.1] analyzed dynamic stability of an uniperiodic medium thickness plate. In the paper of Michalak [12.3] the stability of elastic slightly wrinkled plates is analyzed. The stability of thin periodically stiffened cylindrical shells was analyzed by Tomczyk [12.6]. In the paper of Wierzbicki et al. [12.7], stability of micro-periodic materials under finite deformations is discussed. The approach, based on the tolerance averaging technique, formulating macroscopic model of stability of functionally graded plates was presented by Jędrysiak and Michalak [12.2]. In the paper of Perliński et al. [12.4] stability of functionally graded annular plate interacting with elastic micro-heterogeneous subsoil is presented.

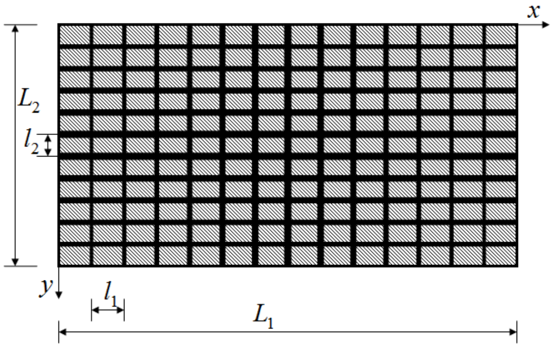

Fig. 12.1. Rectangular plate with varying width of the beams

In the above mentioned papers the thickness h of the considered plates is supposed to be much smaller comparing to the microstructure length parameter l. In the presented contribution we deal with the plates which are reinforced by two dimensional system of beams, where the microstructure length parameter $l = \sqrt{l_1 l_2}$ (l_1, l_2 - dimensions of cell in Fig. 12.1) is similar compared to the plate thickness h.

Throughout the contribution, indices $i,k,l \ldots$ run over $1,2,3$, indices $\alpha,\beta,\gamma,\ldots$ run over $1,2$ and $A,B,C,\ldots$ run over $1,2$. The summation convention holds all aforementioned sub-and superscripts.

12.2. Direct description

The subject of presented considerations are rectangular plates shown in Fig. 12.1. Let us introduce the orthogonal Cartesian coordinate system $Ox_1x_2x_3$. Setting $\mathbf{x} \equiv (x_1, x_2)$ and $z = x_3$ we assume that the undeformed plate occupies the region $\Omega \equiv \{(\mathbf{x}, z) : -h/2 \le z \le h/2, \mathbf{x} \in \Pi\}$, where Π is the plate midplane and h is the plate thickness. The starting point of this contribution is the direct description of the composite plate in the framework of the well-known second order non-linear theory of thin plates. The displacement field of the arbitrary point of the plate we write in form:

$$w_3(\boldsymbol{x},z)=w_3(\boldsymbol{x}), \qquad w_\alpha(\boldsymbol{x},z)=w_\alpha^0(\boldsymbol{x})-z\cdot\partial_\alpha w_3(\boldsymbol{x}) \tag{12.1}$$

Denoting by $\mathbf{p}(x_\alpha)$ the external forces, setting $\partial_k=\partial/\partial x_k$ we also introduce gradient operators $\nabla\equiv(\partial_1,\partial_2)$, in the framework of the linear approximated theory for thin plates, we obtain the following system of equations:

(i) strain-displacement relations

$$\begin{aligned} &e_{\alpha\beta}(\boldsymbol{x},z)=\varepsilon_{\alpha\beta}(\boldsymbol{x})+\kappa_{\alpha\beta}(\boldsymbol{x})\cdot z \\ &\varepsilon_{\alpha\beta}=\nabla_\beta w_\alpha^0+\tfrac{1}{2}\partial_\alpha w_3\ \partial_\beta w_3 \qquad \kappa_{\alpha\beta}=-\nabla_{\alpha\beta}w_3 \end{aligned} \tag{12.2}$$

(ii) strain energy averaged over the plate thickness

$$E(\boldsymbol{x})=\tfrac{1}{2}B^{\alpha\beta\gamma\delta}\,\kappa_{\alpha\beta}\,\kappa_{\gamma\delta}+\tfrac{1}{2}D^{\alpha\beta\gamma\delta}\varepsilon_{\alpha\beta}\ \varepsilon_{\gamma\delta} \tag{12.3}$$

where $D^{\alpha\beta\gamma\eta}=\dfrac{E\,h}{(1-\nu^2)}H^{\alpha\beta\gamma\eta}$ is the tensile stiffness and $B^{\alpha\beta\gamma\eta}=\dfrac{E\,h^3}{12(1-\nu^2)}H^{\alpha\beta\gamma\eta}$ with $H^{\alpha\beta\gamma\eta}=0.5(g^{\alpha\eta}\,g^{\beta\gamma}+g^{\alpha\gamma}g^{\beta\eta}+\nu(\in^{\alpha\gamma}\in^{\beta\eta}+\in^{\alpha\eta}\in^{\beta\gamma})$ is the bending stiffness.

(iii) work of external forces

$$F=p^\alpha\ w_\alpha^0+p^3\ w_3 \tag{12.4}$$

In order to derive governing equations of considered plate we shall define the stationary action functional:

$$\mathrm{A}\big(\mathbf{w}(\cdot)\big)=\int_\Pi L(\mathbf{w},\nabla\mathbf{w},\nabla^2\mathbf{w})\,d\mathbf{x} \tag{12.5}$$

where Lagrangian $L=F-E$.

From stationary action principle ($\delta\mathrm{A}=0$) we obtain

$$\begin{aligned} &\partial_{\alpha\beta}m^{\alpha\beta}-\partial_\alpha(n^{\alpha\beta}\,\partial_\beta w_3)=p^3 \\ &\partial_\beta n^{\alpha\beta}=-p^\alpha \end{aligned} \tag{12.6}$$

where generalized forces

$$\begin{aligned} &n^{\alpha\beta}=\int_{-h/2}^{h/2}\sigma^{\alpha\beta}dz=D^{\alpha\beta\gamma\delta}e_{\gamma\delta} \\ &m^{\alpha\beta}=\int_{-h/2}^{h/2}\sigma^{\alpha\beta}z\,dz=B^{\alpha\beta\gamma\delta}\kappa_{\gamma\delta} \end{aligned} \tag{12.7}$$

This direct description leads to plate equations with discontinuous and highly oscillating coefficients, which are too complicated to be used in the engineering analysis. The above equations will be used as a starting point of the modelling procedure.

12.3. Modelling concept

Let the midplane of the considered plate (Fig. 12.1) occupy the region $\Pi \equiv [0, L_1] \times [0, L_2]$. We assume in considered composite plate that the number of beams in x_1 and x_2 direction is n and m, respectively $(1/n << 1, 1/m << 1)$. Hence $l_1 = L_1/n$ and $l_2 = L_2/m$ are dimensions of the cell $\Delta \equiv (-l_1/2, l_1/2) \times (-l_2/2, l_2/2)$, cf. Fig. 12.2. For the arbitrary cell $\Delta(\mathbf{x}) \equiv \Delta + \mathbf{x}$ with centre situated at point $\mathbf{x} = (x_1, x_2)$ we introduce the orthogonal local coordinate system Oy_1y_2 which is local with its origin at $\mathbf{x} \in \overline{\Pi}_\Delta$, where $\Pi_\Delta \equiv (l_1/2, L_1 - l_1/2) \times (l_2/2, L_2 - l_2/2) \subset \Pi$. The beams width is functional $a_\alpha = a_\alpha(\mathbf{x}), \alpha = 1,2$ but constant for every fixed $\mathbf{x} \in \overline{\Pi}_\Delta$.

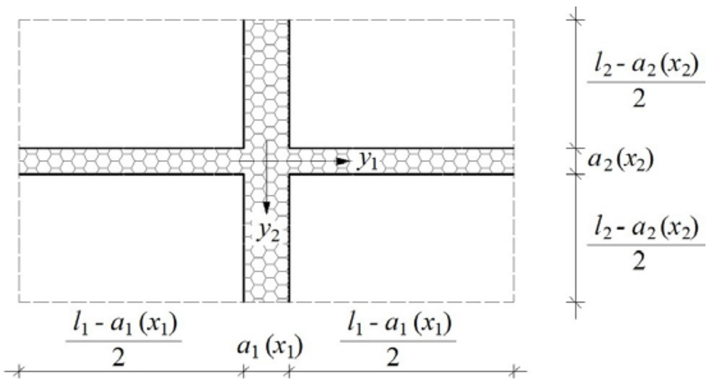

Fig. 12.2. A unit cell Δ geometry

In order to derive averaged equations for the plate under consideration we apply tolerance averaging approach [12.8, 12.9]. We mention here some basic concepts of this technique, as a tolerance periodic function, a slowly varying function, a highly oscillating function and an averaging operator.

The first concept of the modelling technique is *the averaging operation*:

$$< f > (\mathbf{x}) = \frac{1}{|\Delta|} \int_{\Delta(\mathbf{x})} f(\mathbf{y}, \mathbf{x}) d\mathbf{y}, \quad \mathbf{x} \in \overline{\Pi} \tag{12.8}$$

We shall refer (12.8) to as averaging of arbitrary integrable function $f(\cdot)$ for every $\mathbf{x} \in \overline{\Pi}$.

Periodic approximation. Let H^r be the Sobolev space for fixed $r \geq 0$. Function $\widetilde{f}^{(k)}(\mathbf{x},\cdot) \in H^0(\Pi)$, $\mathbf{x} \in \Pi$, $k = 1,2,...,r$ will be referred to as the periodic approximation of $\partial^k f(\cdot)$ in $\Delta(\mathbf{x})$ (where ∂^k - k-th gradient in Π). For $k = 0$ we define $\partial^0 f \equiv f$, $\widetilde{f}^{(0)} \equiv \widetilde{f}$.

Tolerance periodic function. Function $f \in H^r(\Pi)$ will be called *the tolerance periodic function* (with respect to cell $\Delta(\mathbf{x})$ and tolerance parameter ε), $f \in TP_\varepsilon^r(\Pi,\Delta)$, if for $k = 0,1,...,r,$ the following conditions hold:

$$\begin{aligned} &(\forall \boldsymbol{x} \in \Pi)\left(\exists \widetilde{f}^{(k)}(\boldsymbol{x},\cdot) \in H^0(\Delta)\right)\left[\left\| \partial^k f(\cdot)\big|_{\Pi_x} - \widetilde{f}^{(k)}(\boldsymbol{x},\cdot)\right\|_{H^0(\Pi_x)} \leq \varepsilon\right] \\ &\int_{\Delta(\cdot)} \widetilde{f}^{(k)}(\cdot,\boldsymbol{y})\, d\boldsymbol{y} \in C^0(\overline{\Pi}) \end{aligned} \tag{12.9}$$

In the above definition we introduced the so called *cluster of cells*:

$$\Pi_x := \bigcap_{\mathbf{z} \in \Delta(\mathbf{x})} \Delta(\mathbf{z}), \quad \mathbf{x} \in \Pi_\Delta \tag{12.10}$$

Slowly varying function. Function $F \in H^r(\Pi)$ will be called *the slowly varying function* (with respect to the cell $\Delta(\mathbf{x})$ and tolerance parameter ε), and denoted by $F \in SV_\varepsilon^r(\Pi,\Delta)$, if for $k = 0,1,...,r,$ the following conditions hold:

$$F \in TP_\varepsilon^r(\Pi,\Delta) \text{ and } (\forall \mathbf{x} \in \Pi)\,[\widetilde{F}^{(k)}(\mathbf{x},\cdot)\,|_{\Delta(\mathbf{x})} = \partial^k F(\mathbf{x})] \tag{12.11}$$

It can be observed that periodic approximation $\widetilde{F}^{(k)}(\mathbf{x},\cdot)$ of $\partial^k F(\mathbf{x})$ in $\Delta(\mathbf{x})$ is a constant function for every $\mathbf{x} \in \Pi$. In other words, if $F \in SV_\varepsilon^r(\Pi,\Delta)$ then:

$$(\forall \mathbf{x} \in \Pi)\left(\left\| \partial^k F(\cdot) - \partial^k F(\mathbf{x})\right\|_{H^0(\Delta(\mathbf{x}))} \leq \varepsilon,\ k = 0,1,...,r\right) \tag{12.12}$$

Highly oscillating function. Function $\phi \in H^r(\Pi)$ is called *the highly oscillating function* (with respect to the cell $\Delta(\mathbf{x})$ and tolerance parameter ε), and denoted by $\phi \in HO_\varepsilon^r(\Pi,\Delta)$, if for $k = 0,1,...,r,$ the following conditions hold:

$$\begin{gathered} \phi \in TP_\varepsilon^r(\Pi,\Delta) \\ (\forall \boldsymbol{x} \in \Pi)\,[\widetilde{\phi}^{(k)}(\boldsymbol{x},\cdot)\,|_{\Delta(x)} = \partial^k \widetilde{\phi}(\boldsymbol{x},\cdot)] \\ \forall F \in SV_\varepsilon^r(\Pi,\Delta)(f \equiv \phi F \in TP_\varepsilon^r(\Pi,\Delta)) \wedge \widetilde{f}^{(k)}(\mathbf{x},\cdot)\,|_{\Delta(\mathbf{x})} = F(\mathbf{x})\,\partial^k \widetilde{\phi}(\mathbf{x})\,|_{\Delta(\mathbf{x})} \end{gathered} \tag{12.13}$$

Let by $\varphi(\cdot)$ denote a highly oscillating function, $\varphi \in HO_\varepsilon^2(\Pi,\Delta)$, defined on $\overline{\Pi}$, continuous together with gradient $\partial^1\varphi$. Its second derivative $\partial^2\varphi$ is a piecewise continuous and bounded. Function $\varphi(\cdot)$ is called *the fluctuation shape function* of the 2-nd kind, if it depends on l as a parameter and satisfies conditions:

1° $\partial^k \varphi \in O(l^{\alpha-k})$ for $k = 1,...,\alpha,\ \alpha = 2$,

2° $< \varphi > (\mathbf{x}) \approx 0$ for every $\mathbf{x} \in \Pi_\Delta$.

Set of all fluctuation shape functions of the 2-nd kind is denoted by $FS_\varepsilon^2(\Pi, \Delta)$.

12.4. Averaged model equations

The modelling technique will be based on the tolerance averaging approximation and on the restriction of the displacement field under consideration given by:

$$\begin{aligned} &w_3(\boldsymbol{x}, z) = V_3(\boldsymbol{x}) \\ &w_\alpha(\boldsymbol{x}, z) = V_\alpha(\boldsymbol{x}) + g^A(\boldsymbol{y}, \boldsymbol{x}) V_\alpha^A(\boldsymbol{x}) + (-\partial_\alpha V_3(\boldsymbol{x}) + g^A(\boldsymbol{y}, \boldsymbol{x}) u_\alpha^A(\boldsymbol{x})) \cdot z \end{aligned} \tag{12.14}$$

for $\mathbf{x} \in \Pi$, $z \in (-h/2, h/2)$ and $A = 1,2$.

The basic tolerance modelling assumption states that macro-displacements $V_3(\cdot), V_\alpha(\cdot)$ and fluctuation amplitudes of displacements $V_\alpha^A(\cdot)$, $u_\alpha^A(\cdot)$ are slowly varying functions together with all partial derivatives. Functions $V_3(\cdot) \in SV_\varepsilon^2(\Pi, \Delta)$, $V_\alpha(\cdot) \in SV_\varepsilon^1(\Pi, \Delta)$, $u_\alpha^A(\cdot) \in SV_\varepsilon^1(\Pi, \Delta)$, $V_\alpha^A(\cdot) \in SV_\varepsilon^1(\Pi, \Delta)$ are the basic unknowns of the modelling problem. Functions $g^A(\cdot)$ are known, dependent on the microstructure length parameter $l = \sqrt{l_1 l_2}$ (l_1, l_2 - dimensions of the cell Δ), fluctuation shape functions.

Let $\tilde{g}^A(\mathbf{x},\cdot)$, $\partial_\alpha \tilde{g}^A(\mathbf{x},\cdot)$ stand for periodic approximation of $g^A(\cdot)$, $\partial_\alpha g^A(\cdot)$ in cell $\Delta(\mathbf{x})$, respectively. Due to the fact that $w_3(\cdot)$, $w_\alpha(\cdot)$ are tolerance periodic functions, it can be observed that the periodic approximation of $w_{3g}(\cdot, \mathbf{x})$, $w_{\alpha g}(\cdot, \mathbf{x})$ and their derivatives in $\Delta(\mathbf{x})$, $\mathbf{x} \in \Pi$ have the form:

$$\begin{aligned} &w_{3g}(\boldsymbol{y}, \boldsymbol{x}) = V_3(\boldsymbol{x}) \\ &\partial_\alpha w_{3g}(\boldsymbol{y}, \boldsymbol{x}) = \partial_\alpha V_3(\boldsymbol{x}) \end{aligned} \tag{12.15}$$

$$w_{\alpha g}(\boldsymbol{y}, \boldsymbol{x}, z) = V_\alpha(\boldsymbol{x}) + g^A(\boldsymbol{y}, \boldsymbol{x}) V_\alpha^A(\boldsymbol{x}) + \left(g^A(\boldsymbol{y}, \boldsymbol{x}) u_\alpha^A(\boldsymbol{x}) - \partial_\alpha V_3(\boldsymbol{x})\right) z$$

$$\partial_\gamma w_{\alpha g}(\boldsymbol{y}, \boldsymbol{x}, z) = \partial_\gamma V_\alpha(\boldsymbol{x}) + \partial_\gamma g^A(\boldsymbol{y}, \boldsymbol{x}) V_\alpha^A(\boldsymbol{x}) + \left(\partial_\gamma g^A(\boldsymbol{y}, \boldsymbol{x}) u_\alpha^A(\boldsymbol{x}) - \partial_{\alpha\gamma} V_3(\boldsymbol{x})\right) z$$

Setting $w_3 = w_{3g}$ and $w_\alpha = w_{\alpha g}$ into Lagrangian $L(\mathbf{w}, \nabla \mathbf{w}, \nabla^2 \mathbf{w})$ we can assume that $L_g(\mathbf{w}_g, \nabla \mathbf{w}_g, \nabla^2 \mathbf{w}_g) \in HO_\varepsilon^0(\Pi, \Delta)$. Hence the periodic approximation of

$L_g(\cdot)$ in every $\Delta(\mathbf{x})$ we denote by $\widetilde{L}_g(\mathbf{x},\mathbf{y},w_{3g},w_{\alpha g},\partial_\alpha w_{3g},\partial_\alpha w_{\beta g})$. In order to derive the governing equations we shall define tolerance averaged Lagrangian $<L_g>=<F_g>-<E_g>$:

$$
\begin{aligned}
&<L_g>(\mathbf{x},\nabla_{\alpha\beta}V_3,\nabla_\alpha V_\beta,\nabla_\alpha V_3,V_3,V_\alpha,V_\alpha^A,u_\alpha^A)=\\
&=\frac{1}{|\Delta|}\int_{\Delta(\mathbf{x})}\widetilde{L}_g(\mathbf{x},\mathbf{y},w_{3g},w_{\alpha g},\partial_\alpha w_{3g},\partial_\alpha w_{\beta g})\,d\mathbf{y}
\end{aligned}
\tag{12.16}
$$

Substituting the right-hand sides of equations (12.15) into (12.8), on the basis of tolerance averaging approximation, we arrive the strain energy averaged over the cell $\Delta(\mathbf{x})$:

$$
\begin{aligned}
&<E_g>=\tfrac{1}{2}<B^{\alpha\beta\gamma\delta}>\nabla_{\alpha\beta}V_3\,\nabla_{\gamma\delta}V_3-<B^{\alpha\beta\gamma\delta}\,\partial_\gamma g^A>u_\delta^A\,\nabla_{\alpha\beta}V_3+\\
&+\tfrac{1}{2}<B^{\alpha\beta\gamma\delta}\partial_\beta g^A\partial_\delta g^B>u_\alpha^A\,u_\gamma^B+\tfrac{1}{2}<D^{\alpha\beta\gamma\delta}>\nabla_\beta V_\alpha\,\nabla_\delta V_\gamma+\\
&+<D^{\alpha\beta\gamma\delta}\,\partial_\gamma g^A>V_\delta^A\,\nabla_\beta V_\alpha+\tfrac{1}{2}<D^{\alpha\beta\gamma\delta}\partial_\beta g^A\partial_\delta g^B>V_\alpha^A\,V_\gamma^B+\\
&+\tfrac{1}{2}<D^{\alpha\beta\gamma\delta}>\nabla_\beta V_\alpha\,\nabla_\gamma V_3\nabla_\delta V_3+\tfrac{1}{2}<D^{\alpha\beta\gamma\delta}\partial_\beta g^A>V_\alpha^A\nabla_\gamma V_3\nabla_\delta V_3+\\
&+\tfrac{1}{8}<D^{\alpha\beta\gamma\delta}>\nabla_\alpha V_3\nabla_\beta V_3\,\nabla_\gamma V_3\nabla_\delta V_3
\end{aligned}
\tag{12.17}
$$

External load energy averaged over the cell $\Delta(\mathbf{x})$

$$
<F_g>=<p^3>V_3+<p^\alpha>V_\alpha+<p^\alpha\,g^A>V_\alpha^A \tag{12.18}
$$

From principle of stationary action of the averaged Lagrangian $<L_g>$ we obtain equations responsible for:

a) plane stress state

$$
\begin{aligned}
&\nabla_\beta N^{\alpha\beta}+<p^\alpha>=0\\
&<n^{\alpha\beta}\,\nabla_\beta g^A>-<p^\alpha\,g^A>=0
\end{aligned}
\tag{12.19}
$$

where normal forces

$$
N^{\alpha\beta}=<n^{\alpha\beta}>=<D^{\alpha\beta\gamma\delta}>\nabla_\delta V_\gamma+<D^{\alpha\beta\gamma\delta}\,\nabla_\delta g^A>V_\gamma^A+\tfrac{1}{2}<D^{\alpha\beta\gamma\delta}>\nabla_\gamma V_3\,\nabla_\delta V_3 \tag{12.20}
$$

b) bending state

$$
\begin{aligned}
&\nabla_{\alpha\beta}\left(\widetilde{B}^{\alpha\beta\gamma\delta}\nabla_{\gamma\delta}V_3-\widetilde{B}^{\gamma A\alpha\beta}u_\gamma^A\right)-\nabla_\alpha\left(N^{\alpha\beta}\,\nabla_\beta V_3\right)-\left\langle p^3\right\rangle=0\\
&\widetilde{B}^{\alpha A\gamma\delta}\nabla_{\gamma\delta}V_3-\widetilde{B}^{\alpha A\gamma B}u_\gamma^B=0
\end{aligned}
\tag{12.21}
$$

where we have denoted:

$$\widetilde{B}^{\alpha\beta\gamma\delta} =< B^{\alpha\beta\gamma\delta} >, \widetilde{B}^{\alpha A\gamma\delta} =< B^{\alpha\beta\gamma\delta} \nabla_{\beta} g^{A} >, \widetilde{B}^{\alpha A\gamma B} =< B^{\alpha\beta\gamma\delta} \nabla_{\beta} g^{A} \nabla_{\delta} g^{B} > \tag{12.22}$$

From (12.21) we can obtain direct representation of oscillation amplitudes u_{γ}^{B}. Let $K_{\alpha\beta}^{AB}$ stands for linear transformation operator such that $K_{\alpha\tau}^{AC} \widetilde{B}^{\alpha A\gamma B} = \delta_{\tau\gamma}\delta^{BC}$. Thus

$$u_{\mu}^{B} = K_{\mu\alpha}^{BA} \widetilde{B}^{\alpha A\gamma\delta} \nabla_{\gamma\delta} V_{3} \tag{12.23}$$

Denoting

$$B_{eff}^{\alpha\beta\gamma\delta} = \widetilde{B}^{\alpha\beta\gamma\delta} - \widetilde{B}^{\mu B\alpha\beta} K^{\mu B\tau A} \widetilde{B}^{\tau A\gamma\delta} \tag{12.24}$$

stability equation takes a form

$$\nabla_{\alpha\beta}(B_{eff}^{\alpha\beta\gamma\delta} \nabla_{\gamma\delta} V_{3}) - \nabla_{\alpha}(N^{\alpha\beta} \nabla_{\beta} V_{3}) = 0 \tag{12.25}$$

The above equation has an identical form as stability equation for thin plate with functional coefficients. Coefficients in the above equation are functional but smooth in contrast to equation in direct description.

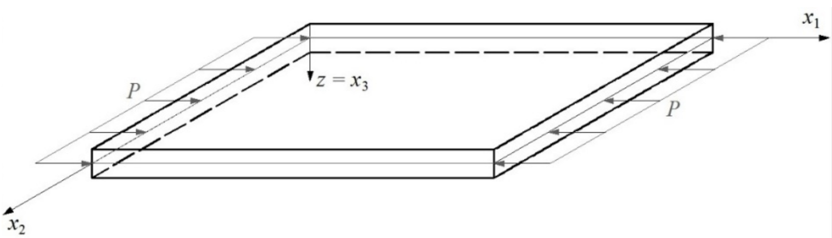

Fig. 12.3. Simply supported plate under pressure

12.5. Applications

Let us consider a rectangular plate simply supported on all edges and suppressed in one direction only, cf. Fig. 12.3. The stability equation (12.25) transforms then into:

$$\begin{aligned} &\partial_{11}\left(B_{eff}^{1111} \partial_{11} V_{3} + B_{eff}^{1122} \partial_{22} V_{3}\right) + 4\partial_{12}\left(B_{eff}^{1212} \partial_{12} V_{3}\right) \\ &+ \partial_{22}\left(B_{eff}^{1122} \partial_{11} V_{3} + B_{eff}^{2222} \partial_{22} V_{3}\right) - N^{11} \partial_{11} V_{3} = 0 \end{aligned} \tag{12.26}$$

where $N^{11} = -P$. The above equation in all subsequent examples will be solved with Galerkin method using the following assumed form of solution:

$$V_3(\mathbf{x}) = \sum_{m=1}^{\infty}\sum_{n=1}^{\infty} V_{mn} \cdot \sin(\alpha_m x_1) \cdot \sin(\beta_n x_2) \tag{12.27}$$

where $\alpha_m = m\pi / L_1$, $\beta_n = n\pi / L_2$.

Since coefficients in (12.26) explicitly depend on assumed fluctuation shape functions, we must first define them, what is done next.

12.5.1. Fluctuation shape function

During tolerance modelling few assumptions had to be state. One of them is the form of given fluctuation shape functions. They should satisfy conditions mentioned in former sections and they are in number of two. Both of them are assumed as a product of linear and quadratic function

$$g^A(\mathbf{y},\mathbf{x}) = \varphi_1^{(A)}(\mathbf{y},\mathbf{x}) \cdot \varphi_2^{(A)}(\mathbf{y},\mathbf{x}) \tag{12.28}$$

where $A = 1,2$. Graphs of these functions are shown below (Fig.12.4a,12.4b).

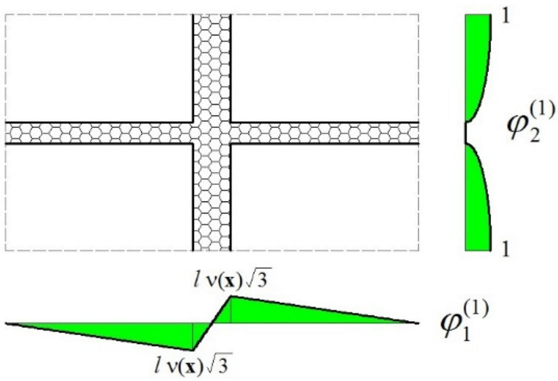

Fig. 12.4a. Fluctuation shape function g^1

Fluctuation shape functions depend on microstructure parameter l as well as on the distribution of heterogeneity:

$$v(\mathbf{x}) = \frac{1}{l^2}\sqrt{(l_1 - a_1(\mathbf{x}))(l_2 - a_2(\mathbf{x}))(l_1 a_2(\mathbf{x}) + l_2 a_1(\mathbf{x}) - a_1(\mathbf{x}) a_2(\mathbf{x}))} \tag{12.29}$$

Such properties and characteristics assure continuity of displacement field overall and stress field continuity along the beams.

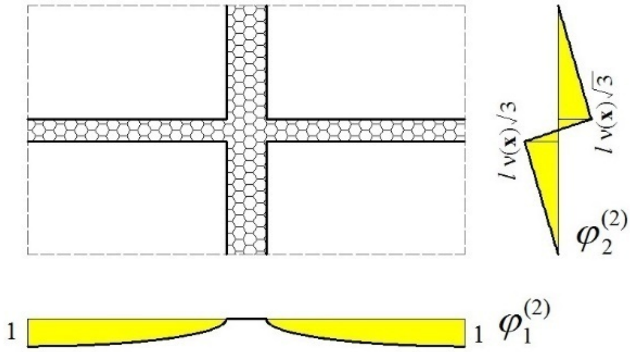

Fig. 12.4b. Fluctuation shape function g^2

The exact formulas of these functions:

$$\varphi_1^{(1)}(y_1,\mathbf{x})=\begin{cases}\dfrac{2lv\sqrt{3}}{l_1-a_1}\left(y_1+\dfrac{l_1}{2}\right) & \text{for } y_1\in\left[-\dfrac{l_1}{2},-\dfrac{a_1}{2}\right]\\ -\dfrac{2lv\sqrt{3}}{a_1} & \text{for } y_1\in\left[-\dfrac{a_1}{2},\dfrac{a_1}{2}\right]\\ \dfrac{2lv\sqrt{3}}{l_1-a_1}\left(y_1-\dfrac{l_1}{2}\right) & \text{for } y_1\in\left[\dfrac{a_1}{2},\dfrac{l_1}{2}\right]\end{cases} \tag{12.30}$$

$$\varphi_2^{(2)}(y_2,\mathbf{x})=\begin{cases}\dfrac{2lv\sqrt{3}}{l_2-a_2}\left(y_2+\dfrac{l_2}{2}\right) & \text{for } y_2\in\left[-\dfrac{l_2}{2},-\dfrac{a_2}{2}\right]\\ -\dfrac{2lv\sqrt{3}}{a_2} & \text{for } y_2\in\left[-\dfrac{a_2}{2},\dfrac{a_2}{2}\right]\\ \dfrac{2lv\sqrt{3}}{l_2-a_2}\left(y_2-\dfrac{l_2}{2}\right) & \text{for } y_2\in\left[\dfrac{a_2}{2},\dfrac{l_2}{2}\right]\end{cases} \tag{12.31}$$

$$\varphi_2^{(1)}(y_2,\mathbf{x})=\begin{cases}1-\left(\dfrac{l_2+2y_2}{l_2-a_2}\right)^2 & \text{for } y_2\in\left[-\dfrac{l_2}{2},-\dfrac{a_2}{2}\right]\\ 0 & \text{for } y_2\in\left[-\dfrac{a_2}{2},\dfrac{a_2}{2}\right]\\ 1-\left(\dfrac{l_2-2y_2}{l_2-a_2}\right)^2 & \text{for } y_2\in\left[\dfrac{a_2}{2},\dfrac{l_2}{2}\right]\end{cases} \tag{12.32}$$

$$\varphi_1^{(2)}(y_1,\mathbf{x}) = \begin{cases} 1-\left(\dfrac{l_1+2y_1}{l_1-a_1}\right)^2 & \text{for } y_1 \in \left[-\dfrac{l_1}{2},-\dfrac{a_1}{2}\right] \\ 0 & \text{for } y_1 \in \left[-\dfrac{a_1}{2},\dfrac{a_1}{2}\right] \\ 1-\left(\dfrac{l_1-2y_1}{l_1-a_1}\right)^2 & \text{for } y_1 \in \left[\dfrac{a_1}{2},\dfrac{l_1}{2}\right] \end{cases} \tag{12.33}$$

12.5.2. Validation of proposed model

In order to find out the correctness of the proposed mathematical model and its applicability, some benchmark analysis should be first made. Suppose the beams (Fig. 12.2) are made of steel, i.e. for Young's modulus $E'' = 210\,GPa$ and Poisson's ratio $\nu'' = 0.3$, meanwhile the matrix is made of concrete for which has $E' = 20\,GPa$ and $\nu' = 0.3$. Consider a biperiodic square plate with $L_1 = L_2 = 4\,m$ and $l_1 = l_2$ of thickness $h = 0.1\,m$, which consists of beams (20 in each direction) of the same thickness: $a_1 = a_2$. Due to such a microstructure, all averaged coefficients in stability equation are constant and (12.26) reduces to:

$$B_{eff}^{1111}\partial_{1111}V_3 + 2\left(B_{eff}^{1122} + 2B_{eff}^{1212}\right)\partial_{1122}V_3 + B_{eff}^{2222}\partial_{2222}V_3 + P\,\partial_{11}V_3 = 0 \tag{12.34}$$

Now, substituting (12.27) we obtain:

$$P = \frac{\pi^2 B_{eff}^{1111}}{L_1^2}\cdot\frac{\sum_{m=1}^{\infty}\sum_{n=1}^{\infty}\left(m^4 + \eta\cdot m^2n^2 + n^4\right)\cdot V_{mn}}{\sum_{m=1}^{\infty}\sum_{n=1}^{\infty} m^2\cdot V_{mn}} \tag{12.35}$$

where

$$\eta = \frac{2\left(B_{eff}^{1122} + 2B_{eff}^{1212}\right)}{B_{eff}^{1111}} \tag{12.36}$$

Hence the critical force for the *m*-th and *n*-th buckling mode:

$$P_{cr} = \frac{\pi^2 B_{eff}^{1111}}{L_1^2}\cdot\frac{m^4 + \eta\cdot m^2n^2 + n^4}{m^2} \tag{12.37}$$

If $m = n = 1$ then we deal with the first mode of buckling.

Let us introduce a parameter $\beta = a_1 / l_1$, $\beta \in [0,1]$ as a volume fraction of beams material but in this example only. Case of $\beta = 0$ stands for an uniform plate made of matrix material (concrete) for which $P_{cr\_c} = 4.519 \cdot 10^3\ kN/m$, and case of $\beta = 1$ stands for uniform plate made of beams material (steel) for which $P_{cr\_s} = 4.745 \cdot 10^4\ kN/m$. These values for critical forces are obtained from the exact solution.

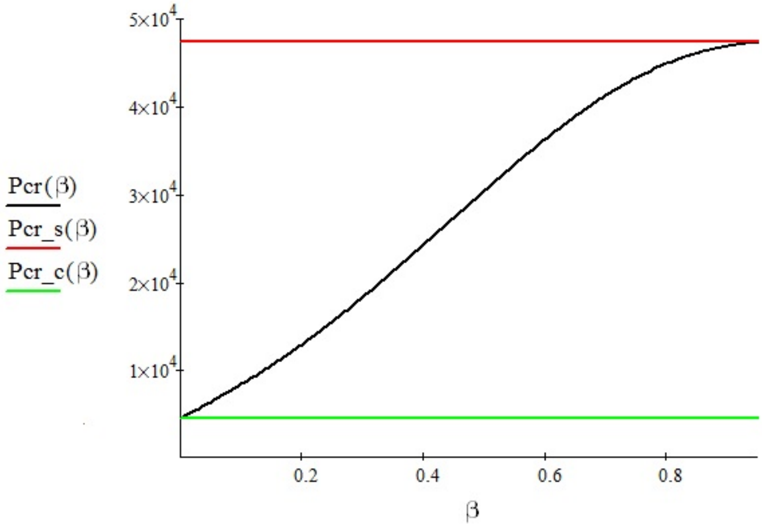

Fig. 12.5. Critical forces in square biperiodic plate as a function of parameter β

As we can see in Fig. 12.5, the graph is situated precisely between two values for uniform plate. Therefore, there exists a smooth passage from biperiodic to uniform plate which proofs the correctness of the proposed model.

12.5.3. Influence of geometrical and material properties on stability of plates

This section is devoted to some model applications presented in few numerical examples. Suppose the material properties of plate components are invariant in all following examples, i.e. we deal with concrete matrix and steel beams. Square plates ($L_1 = L_2 = 4\ m$) are only investigated.

Example 1. Suppose the width of the "vertical" beams $a_1 = l_1/4$, and width of the "horizontal" beams

$$a_2(\mathbf{x}) = a_2\left(\frac{l_2}{2}\right) \cdot \left[1 + (\beta_2 - 1) \cdot \sin\left(\frac{\pi}{2} \cdot \frac{2x_2 - l_2}{L_2 - l_2}\right)\right] \tag{12.38}$$

for $x_2 \in [l_2/2, L_2 - l_2/2]$, where $a_2(l_2/2) = l_2/4$ and $\beta \equiv \beta_2 = a_2(L_2/2)/a_2(l_2/2)$ is a tested in this example parameter. Such width function implies uniperiodic plate with functionally graded effective properties in one of directions, cf. Fig. 12.6.

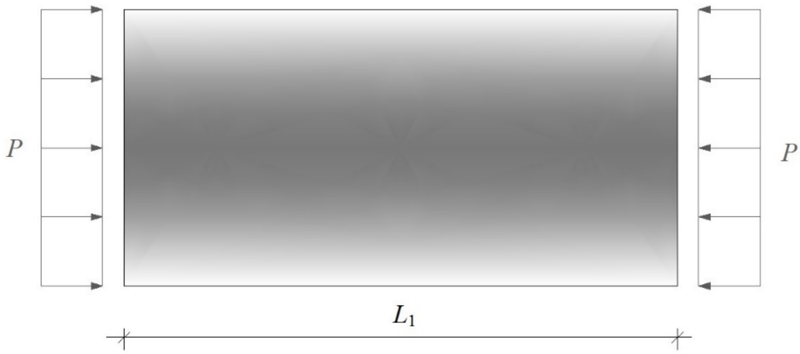

Fig. 12.6. Distribution of effective material properties in uniperiodic plate

Case of $\beta = 1$ stands here for biperiodic plate. If $\beta < 1$ then we deal with a situation where “horizontal” beams are getting wider moving away from the centre of the plate. Case of $1 < \beta \leq 4$ is the opposite one.

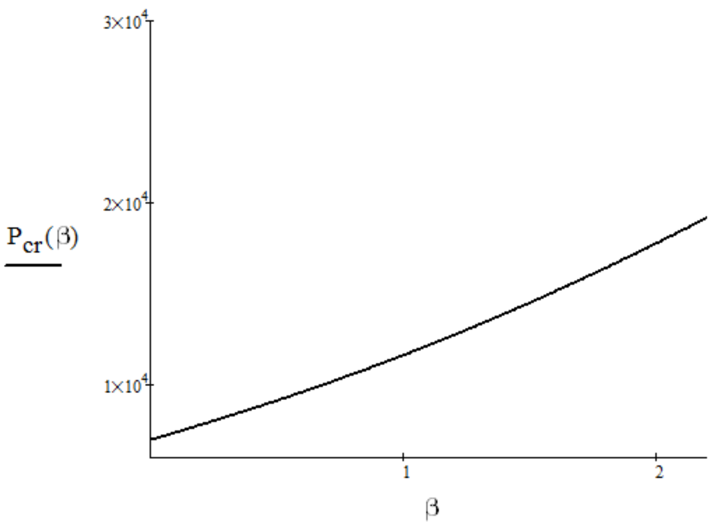

Fig. 12.7. Diagram of critical force in uniperiodic plate

The critical force as a function of parameter β is a strictly monotone (strictly increasing) function (Fig. 12.7). It means that concentration of beams material in the centre of the plate essentially enlarges the value of critical force.

Example 2. Suppose now that the width of vertical beams is not constant but expressed by similar form to (12.38):

$$a_1(\mathbf{x}) = a_1\left(\frac{l_1}{2}\right)\cdot\left[1+(\beta_1-1)\cdot\sin\left(\frac{\pi}{2}\cdot\frac{2x_1-l_1}{L_1-l_1}\right)\right] \tag{12.39}$$

for $x_1 \in [l_1/2, L_1-l_1/2]$, where $a_1(l_1/2)=l_1/4$ and $\beta_1 = a_1(L_1/2)/a_1(l_1/2)$. The width of the “horizontal” beams is as in Example 1. Moreover, the same parameter β is investigated. Physical interpretation of β_1 is quite similar to β.

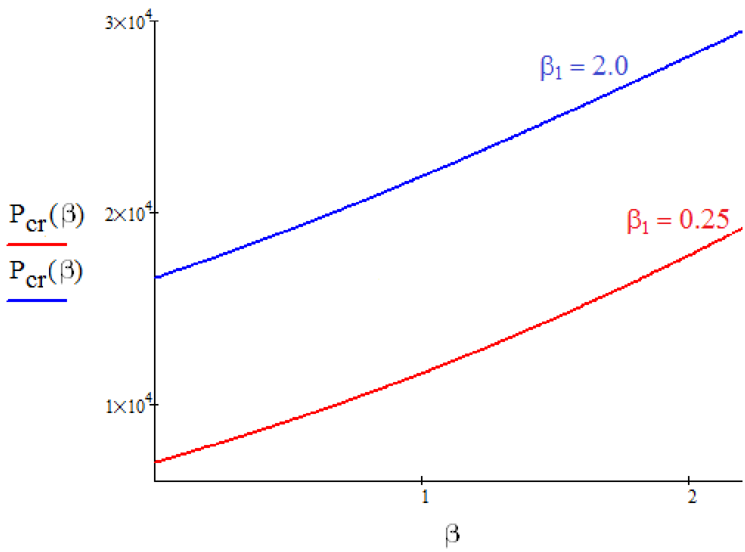

Fig. 12.8. Diagram of critical force in functionally graded plate

As we can see in Fig. 12.8, two graphs of critical force dependence for two different values of β_1 are displayed. Critical force is also strictly increasing with respect to parameter β_1. Thus, it suffices to have more beams material in the centre of the plate to obtain a greater value of critical force.

Example 3. The final example is most interesting in our opinion. Suppose

$$a_\alpha(\mathbf{x}) = \beta\cdot l_\alpha\cdot\sin\left(\frac{\pi}{2}\cdot\frac{2x_\alpha-l_\alpha}{L_\alpha-l_\alpha}\right) \tag{12.40}$$

for every $x_\alpha \in [l_\alpha/2, L_\alpha - l_\alpha/2]$, $\alpha = 1,2$, where $\beta \in [0,1]$. In Example 1 for $\beta_2 = 1$ we have dealt with biperiodic structure from which we can get the value of critical force $P_{cr\_per} = 1.552 \cdot 10^4\ kN/m$ for some special case. In this particular case the volume fraction of the beam material was 0.25 (because of $\beta = 0.25$ from that example).

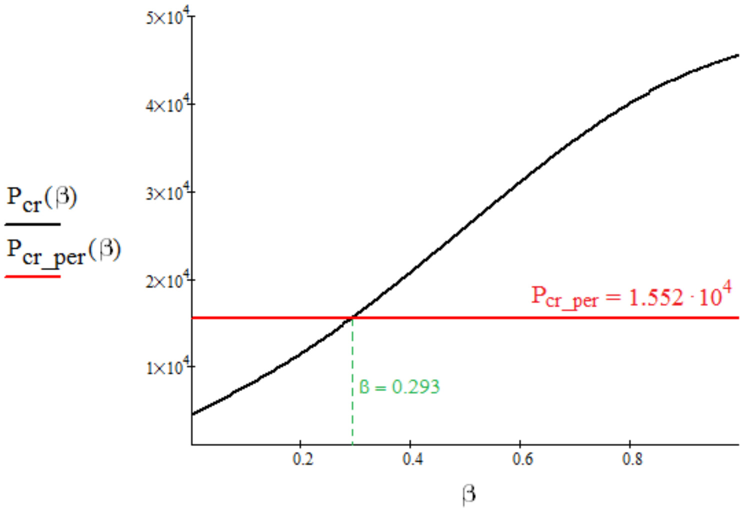

Fig. 12.9. Diagram of critical force in functionally graded plate in comparison to biperiodic plate

It occurs, Fig. 12.9, that the same value of critical force, but for the plate with variable beams width in both of directions, we obtained for $\beta = 0.293$. The beams material usage is 0.186 and its smaller then in biperiodic plate where it was 0.25. It means also that having variable beams width in our composite, by the same material usage in comparison to biperiodic structure, we get the greater values of critical force.

12.6. Summary

The problem of stability in two-component thin plates is described by the PDE with highly oscillating and discontinuous coefficients. Therefore, the tolerance technique was applied in order to obtain averaged PDEs with functional but smooth coefficients. Hence, the solution of specific boundary problems of stability of considered plates can be obtained using typical numerical method.

The validation process of the averaged model equations passed satisfactory. There is observed a smooth passage from non-uniform to uniform structure from the point of view of critical force value. It is obvious that reinforcement of the plate enlarge the value of this critical value but what is most important, the layout of these reinforcements (beams) plays crucial work in this analysis. It occurs that with non-uniform structure we can achieve up to 65% greater values of critical force the with biperiodic one. That information could be a crucial one in optimal control problems.

12.7. References

12.1 Baron E., On dynamic stability of an uniperiodic medium thickness plate band, J. Theor. Appl. Mech., Vol. 41, 2003, pp. 305-321.

12.2 Jędrysiak J., Michalak B., On the modelling of stability problems for thin plates with functionally graded structure. Thin-Walled Structures, Vol. 49, 2011, pp. 627-635.

12.3 Michalak B., Stability of elastic slightly wrinkled plates, Acta Mech., Vol. 130, 1998, pp. 111-119.

12.4 Perliński W., Gajdzicki M., Michalak B., Modelling of annular plates stability with functionally graded structure interacting with elastic heterogeneous subsoil, J. Theor. Appl. Mech., Vol. 52, 2014, pp. 485-498.

12.5 Rabenda M., Michalak B., Natural vibrations of prestressed thin functionally graded plates with dense system of ribs in two directions, Composite Structures, Vol. 133, 2015, pp. 1016-1023.

12.6 Tomczyk B., On stability of thin periodically densely stiffened cylindrical shells, J. Theor. Appl. Mech., Vol. 43, 2005, pp. 427-455.

12.7 Wierzbicki E., Woźniak Cz., Woźniak M., Stability of micro-periodic materials under finite deformations, Arch. Mech., Vol. 49, 1997, pp. 143-158.

12.8 Woźniak Cz., Michalak B.,Jędrysiak J., (eds.), Thermomechanics of Heterogeneous Solids and Structures, Wydawnictwo Politechniki Łódzkiej, Łódź 2008.

12.9 Woźniak Cz., et al., (eds.), Mathematical modeling and analysis in continuum mechanics of microstructured media, Wydawnictwo Politechniki Śląskiej, Gliwice 2010.

13.

On constitutive relations in the resultant non-linear theory of shells

13.1. Introduction

The resultant non-linear theory of elastic shells was proposed by Reissner [13.1], developed in a number of papers and summarised in monographs written by Libai and Simmonds [13.2] and Chróścielewski et al. [13.3]. In this formulation, the two dimensional (2D) non-linear shell equilibrium conditions are derived by the *exact* through-the-thickness integration of three dimensional (3D) equilibrium conditions of non-linear continuum mechanics. Then, the 2D virtual work identity allows one to construct *uniquely* the 2D shell kinematics consisting of the translation vector $\boldsymbol{u}$ and rotation tensor $\boldsymbol{Q}$ fields (six independent scalar variables) defined on the shell base surface. Because of this property the resultant shell model is also called the six-field or 6-parameter (6p) shell model. In this shell model the drilling rotation (about normal to the shell base surface) in this shell model remains as an independent kinematic variable, as well as two drilling couples and two work-conjugate drilling bending measures appear in the description of 2D stress and strain state. These features contradict all classical shell formulations of the Kirchhoff-Love and Timoshenko-Reissner type following from other 3D-to-2D reduction techniques.

The 2D stress resultants and couples $\boldsymbol{n}^{\alpha}, \boldsymbol{m}^{\alpha}$ as well as the resultant surface loads $\boldsymbol{f}, \boldsymbol{c}$ are exact resultant implications of corresponding 3D stress and load distributions in the shell space. The kinematic fields $\boldsymbol{u}, \boldsymbol{Q}$ defined only on the shell reference surface M describe an energetic through-the-thickness averaged gross displacement of the shell cross section. Also the 2D surface strain measures $\boldsymbol{\varepsilon}_{\alpha}, \boldsymbol{\kappa}_{\alpha}$ are defined only on M as unique surface fields work-conjugate to the stress resultants and stress couples $\boldsymbol{n}^{\alpha}, \boldsymbol{m}^{\alpha}$, but without any relation to 3D strains of continuum mechanics. Hence, the resultant non-linear theory of shells is briefly called dynamically exact and kinematically unique. The only approximations enter into this shell model through the constitutive equations relating 2D stress components with 2D strain components. But these are material laws based finally on experiments which are approximate anyway. As noted by Reissner [13.1] himself, cit.: “this problem may be considered in at least two distinct ways. One of these deals with the problem of devising suitable systems of physical experiments for elements of the two-dimensional continuum in order that a system of two-dimensional constitutive equations be established directly. The other deals with the problem of devising suitable mathematical methods to *deduce* constitutive equations for the shell as a *two*-dimensional continuum, as exact or asymptotic, or otherwise rationally approximate consequences of a *given* system of constitutive equations for the shell considered as a *three*-dimensional continuum."

In this chapter we discuss some rational procedures allowing one to deduce the 2D constitutive equations of the resultant shell theory from known systems of constitutive equations of the corresponding 3D solids. Three different material behaviours are analysed:

1 isotropic elastic shells undergoing small strains;
2 layered shells with different play sequences;
3 elasto-plastic FGM shells within small strains.

For each particular material behaviours some 3D-to-2D dimensional reduction procedures are discussed and the corresponding 2D constitutive equations are proposed.

13.2. Some exact shell relations

Let us recall some exact resultant relations of the non-linear theory of shells, see for example Libai and Simmonds [13.2], Chróścielewski et al. [13.3], Eremeyev and Pietraszkiewicz [13.4], or Pietraszkiewicz and Konopińska [13.5].

A shell is a 3D solid body identified in a reference (undeformed) placement with a region B of the physical space $\mathcal{E}$, having the translation vector space E. The shell boundary $\partial\mathrm{B}$ consists of three separable parts: the upper M^{+} and lower M^{-} shell faces, and the lateral shell boundary surface $\partial\mathrm{B}^{*}$. The position vectors $\mathbf{x}$ and $\mathbf{y}=\chi(\mathbf{x})$ of any material particle in the reference and deformed placements, respectively, can conveniently be represented by

$$\mathbf{x}=\boldsymbol{x}+\xi\boldsymbol{n}, \quad \mathbf{y}=\boldsymbol{y}(\boldsymbol{x})+\boldsymbol{\zeta}(\boldsymbol{x},\xi), \quad \boldsymbol{\zeta}(\boldsymbol{x},0)=\mathbf{0}. \tag{13.1}$$

Here $\boldsymbol{x}$ and $\boldsymbol{y}$ are the position vectors of some shell base surface M and $N=\chi(M)$ in the reference and deformed placements, respectively, ξ is the distance from M along the unit normal vector $\boldsymbol{n}$ orienting M such that $\xi\in[-h^{-},h^{+}]$, $h=h^{-}+h^{+}$ is the shell thickness, $\boldsymbol{\zeta}$ is a deviation vector of $\mathbf{y}$ from N, while χ and χ mean the 3D and 2D deformation functions, respectively.

Within the resultant non-linear theory of shells formulated in the referential description, the respective 2D internal contact stress resultant $\boldsymbol{n}_\nu$ and stress couple $\boldsymbol{m}_\nu$ vectors defined at the edge ∂R of an arbitrary part of the deformed base surface $R = \chi(P), P \subset M$, but measured per unit length of the undeformed edge ∂P having the outward unit normal vector $\boldsymbol{\nu}$, are defined by

$$\begin{aligned} \boldsymbol{n}_\nu &= \int_-^+ \mathbf{Pn}^* \mu \mathrm{d}\xi = \boldsymbol{n}^\alpha \nu_\alpha, \quad \boldsymbol{n}^\alpha = \int_-^+ \mathbf{p}^\alpha \mu \mathrm{d}\xi, \quad \int_-^+ \equiv \int_{-h^-}^{+h^+}, \\ \boldsymbol{m}_\nu &= \int_-^+ \boldsymbol{\zeta} \times \mathbf{Pn}^* \mu \mathrm{d}\xi = \boldsymbol{m}^\alpha \nu_\alpha, \quad \boldsymbol{m}^\alpha = \int_-^+ \boldsymbol{\zeta} \times \mathbf{p}^\alpha \mu \mathrm{d}\xi. \end{aligned} \tag{13.2}$$

Here $\mathbf{P} = \mathbf{p}^\varphi \otimes \mathbf{g}_\varphi + \mathbf{p}^3 \otimes \mathbf{g}_3$ is the Piola stress tensor in the shell space, $\mathbf{g}_i = \partial \mathbf{x} / \partial \theta^i$, $i = 1,2,3,$ are the base vectors in B, $\mathbf{n}^* = \mathbf{g}^\alpha \nu_\alpha$, $\alpha = 1,2,$ is the external normal to the reference shell orthogonal cross section $\partial \mathrm{P}^*$, $\mathbf{p}^\alpha = \delta^\alpha_\varphi \mathbf{p}^\varphi$, $\nu_\alpha = \boldsymbol{\nu} \cdot \boldsymbol{a}_\alpha$, $\boldsymbol{a}_\alpha = \partial \mathbf{x} / \partial \theta^\alpha$ are the base vectors of M, and $\mu^\alpha_\varphi = \delta^\alpha_\varphi - \xi b^\alpha_\varphi$ are geometric shifters in the undeformed shell space with b^α_φ the curvature tensor of M and $\mu = \det\left(\mu^\alpha_\varphi\right)$, see Naghdi [13.6] or Pietraszkiewicz [13.7].

The resultant 2D equilibrium equations satisfied for any part $P \subset M$ are

$$\boldsymbol{n}^\alpha|_\alpha + \boldsymbol{f} = \mathbf{0}, \quad \boldsymbol{m}^\alpha|_\alpha + \boldsymbol{y}_{,\alpha} \times \boldsymbol{n}^\alpha + \boldsymbol{c} = \mathbf{0}, \tag{13.3}$$

where $(\cdot)|_\alpha$ is the covariant derivative in the metric of M, while $\boldsymbol{f}$ and $\boldsymbol{c}$ are the external resultant surface force and couple vectors applied at N, but measured per unit area of M.

In order the conditions (13.3) to be satisfied, the resultant fields $\boldsymbol{n}^\alpha$ and $\boldsymbol{m}^\alpha$ require a unique 2D shell kinematics associated with the shell base surface M. Applying the virtual work identity Libai and Simmonds [13.2], Chróścielewski et al. [13.3], and Eremeyev and Pietraszkiewicz [13.4] proved that such 2D kinematics consists of the translation vector $\boldsymbol{u}$ and the proper orthogonal (rotation) tensor $\boldsymbol{Q}$, both describing the gross deformation (work-averaged through the shell thickness) of the shell cross section, such that

$$\boldsymbol{y} = \boldsymbol{x} + \boldsymbol{u}, \quad \boldsymbol{t}_\alpha = \boldsymbol{Q}\boldsymbol{a}_\alpha, \quad \boldsymbol{t} = \boldsymbol{Q}\boldsymbol{n}, \tag{13.4}$$

where $\boldsymbol{t}_\alpha, \boldsymbol{t}$ are three directors attached to any point of $N = \chi(M)$. In numerical FEM analyses [13.3] the undeformed base vectors $\boldsymbol{a}_\alpha, \boldsymbol{n}$ are usually taken to coincide with an orthonormal basis $\boldsymbol{t}^0_\alpha, \boldsymbol{t}^0$ of the arc-length orthogonal lines of principal curvatures of M . Then the rotated basis $\boldsymbol{t}_\alpha, \boldsymbol{t}$ becomes the orthonormal one as well.

The vectors $\boldsymbol{n}^\alpha, \boldsymbol{m}^\alpha$ and $\boldsymbol{f}, \boldsymbol{c}$ can naturally be expressed in components relative to the rotated basis $\boldsymbol{t}_\beta, \boldsymbol{t}$ by

$$\begin{aligned} &\boldsymbol{n}^\alpha = N^{\alpha\beta}\boldsymbol{t}_\beta + Q^\alpha \boldsymbol{t}, \quad \boldsymbol{m}^\alpha = \boldsymbol{t} \times M^{\alpha\beta}\boldsymbol{t}_\beta + M^\alpha \boldsymbol{t} = \varepsilon_{\lambda\beta} M^{\alpha\lambda}\boldsymbol{t}^\beta + M^\alpha \boldsymbol{t}, \\ &\boldsymbol{f} = f^\beta \boldsymbol{t}_\beta + f\boldsymbol{t}, \quad \boldsymbol{c} = \boldsymbol{t} \times c^\beta \boldsymbol{t}_\beta + c\boldsymbol{t} = \varepsilon_{\lambda\beta} c^\lambda \boldsymbol{t}^\beta + c\boldsymbol{t}, \end{aligned} \tag{13.5}$$

where $\varepsilon_{\alpha\beta}$ are components of the skew surface permutation tensor. The 2D components M^α are usually called the drilling couples.

The shell stretch $\boldsymbol{\varepsilon}_\alpha$ and bending $\boldsymbol{\kappa}_\alpha$ vectors associated with the 2D shell kinematics (13.4), which are work-conjugate to the respective stress resultant $\boldsymbol{n}^\alpha$ and stress couple $\boldsymbol{m}^\alpha$ vectors, are defined by

$$\begin{aligned} &\boldsymbol{\varepsilon}_\alpha = \boldsymbol{y},_\alpha - \boldsymbol{t}_\alpha = \boldsymbol{u},_\alpha + (\mathbf{1} - \boldsymbol{Q})\boldsymbol{a}_\alpha = E_{\alpha\beta}\boldsymbol{t}^\beta + E_\alpha \boldsymbol{t}, \\ &\boldsymbol{\kappa}_\alpha = \mathrm{ax}\left(\boldsymbol{Q},_\alpha \boldsymbol{Q}^T\right) = \boldsymbol{t} \times K_{\alpha\beta}\boldsymbol{t}^\beta + K_\alpha \boldsymbol{t} = \varepsilon_{\lambda\beta} K_\alpha^{\cdot\lambda} \boldsymbol{t}^\beta + K_\alpha \boldsymbol{t}, \end{aligned} \tag{13.6}$$

where $\mathbf{1}$ is the metric tensor of 3D space and $\mathrm{ax}(\cdot)$ is the axial vector of skew tensor $(\cdot)$. The 2D components K_α are usually called the drilling bending measures.

13.3. Isotropic elastic shells undergoing small strains

Let $\mathbf{S} = \mathbf{F}^{-1}\mathbf{P} = \mathrm{S}^{ij}\mathbf{g}_i \otimes \mathbf{g}_j = \mathbf{S}^T$, $i, j = 1,2,3$, be the 2nd Piola-Kirchhoff stress tensor, and $\mathbf{F} = \mathrm{Grad}\chi = \bar{\mathbf{g}}_i \otimes \mathbf{g}^i$ be the 3D deformation gradient tensor in the shell space, where $\bar{\mathbf{g}}_i$ is the spatial base vectors of convected coordinates in the deformed placement. Then $\mathbf{P} = \mathbf{FS} = \mathrm{S}^{ij}\bar{\mathbf{g}}_i \otimes \mathbf{g}_j$ and from Eq. (13.2) it follows that

$$\boldsymbol{n}^\alpha = \int_-^+ \mathrm{S}^{\alpha j}\mathbf{F}\mathbf{g}_j \mu \mathrm{d}\xi, \quad \boldsymbol{m}^\alpha = \int_-^+ \boldsymbol{\zeta} \times \mathrm{S}^{\alpha j}\mathbf{F}\mathbf{g}_j \mu \mathrm{d}\xi. \tag{13.7}$$

In the resultant shell model $\boldsymbol{n}^\alpha, \boldsymbol{m}^\alpha$ are the primary fields. Hence, for establishing 2D constitutive equations from their 3D form it is necessary to use the 3D complementary energy density W_c. When strains are small everywhere in the shell space, W_c is the quadratic function of components S^{ij},

$$\mathrm{W}_c = \frac{1}{2}\mathrm{K}_{ijkl}\mathrm{S}^{ij}\mathrm{S}^{kl}\ , \tag{13.8}$$

where K_{ijkl} are the elastic compliances which for an isotropic material are

$$\mathrm{K}_{ijkl} = \frac{1}{2E}\Big[(1+\nu)\big(\mathrm{g}_{ik}\mathrm{g}_{jl}+\mathrm{g}_{il}\mathrm{g}_{jk}\big)-2\nu\mathrm{g}_{ij}\mathrm{g}_{kl}\Big]\,, \tag{13.9}$$

with E the Young modulus and ν the Poisson ratio of the linear elastic material.

The resultants Eq. (13.7) are defined only through the stress components $\mathrm{S}^{\alpha\psi}, \mathrm{S}^{\alpha 3}$ alone, because only these stresses act on the shell cross section. The stress components S^{33} act only on the shell surfaces $\xi = \mathrm{const}$ parallel to the base surface M. They do not contribute to the effective part W_c^{eff} of the 3D complementary energy density associated with the resultants, which is defined by

$$\bar{\mathrm{W}}_c^{eff} = \frac{1}{2\mu^2}\Big[A_{\alpha\beta\lambda\mu}\mu_\varphi^\alpha\big(\mu\mathrm{S}^{\varphi\psi}\mu_\psi^\beta\big)\mu_\theta^\lambda\big(\mu\mathrm{S}^{\theta\sigma}\mu_\sigma^\mu\big)+4A_{\alpha3\lambda3}\mu_\varphi^\alpha\big(\mu\mathrm{S}^{\varphi3}\big)\mu_\theta^\lambda\big(\mu\mathrm{S}^{\theta3}\big)\Big], \tag{13.10}$$

where the following geometric relations have been used

$$\mathrm{K}_{\varphi\psi\theta\sigma} = A_{\alpha\beta\lambda\mu}\mu_\varphi^\alpha\mu_\psi^\beta\mu_\theta^\lambda\mu_\sigma^\mu\,, \quad \mathrm{K}_{\varphi3\theta3} = A_{\alpha3\lambda3}\mu_\varphi^\alpha\mu_\theta^\lambda\ , \tag{13.11}$$

$$A_{\alpha\beta\lambda\mu} = \frac{1}{2E}\Big[(1+\nu)\big(a_{\alpha\lambda}a_{\beta\mu}+a_{\alpha\mu}a_{\beta\lambda}\big)-2\nu a_{\alpha\beta}a_{\lambda\mu}\Big], \quad A_{\alpha3\lambda3} = \frac{1+\nu}{2E}a_{\alpha\lambda}\ . \tag{13.12}$$

The effective part of 2D complementary energy density may be obtained by direct through-the-thickness integration of Eq. (13.10). This results in the infinite series of terms of decreasing order. Pietraszkiewicz and Konopińska [13.5] estimated orders of all terms of this infinite series applying the concrete qualitative error estimates for stresses and their derivatives obtained by John [13.8] and Koiter [13.9] as well as consistently refined 3D kinematically admissible displacement fields and statically admissible stress fields obtained by Rychter [13.10]. The outcome of this complex procedure allowed them to distinguish in the series two principal terms and four secondary terms leading to (see [13.5], Eq. (47))

$$\Sigma_c^{eff} = \int_-^+ \mu \bar{\mathrm{W}}_c^{eff} \mathrm{d}\xi = \frac{1}{2h} A_{\alpha\beta\lambda\mu} \left(N^{\alpha\beta} N^{\lambda\mu} + \frac{12}{h^2} M^{\alpha\beta} M^{\lambda\mu} \right) +$$
$$+ \frac{1}{h} A_{\alpha\beta\lambda\mu} \left(b_\kappa^\kappa N^{\alpha\beta} M^{\lambda\mu} - N^{\alpha\beta} b_\rho^\lambda M^{\rho\mu} - M^{\alpha\beta} b_\rho^\lambda N^{\rho\mu} \right) + \frac{2}{h} A_{\alpha 3 \lambda 3} \frac{1}{\alpha_s} Q^\alpha Q^\lambda , \tag{13.13}$$

where $\alpha_s = 5/6$ is the shear correcting factor.

The Eq. (13.13) can be called the consistent second approximation to the complementary energy density of the geometrically non-linear isotropic elastic shells. The constitutive equations for $E_{\alpha\beta}$, $K_{\alpha\beta}$, E_α can now be calculated from (13.13) leading to

$$\begin{aligned} E_{\alpha\beta} &= \frac{\partial \Sigma_c^{eff}}{\partial N^{\alpha\beta}} = \frac{1}{h} A_{\alpha\beta\lambda\mu} \left(N^{\lambda\mu} - b_\rho^\lambda M^{\rho\mu} + b_\kappa^\kappa M^{\lambda\mu} \right) - \frac{1}{h} b_\alpha^\kappa A_{\kappa\beta\lambda\mu} M^{\lambda\mu} , \\ K_{\alpha\beta} &= \frac{\partial \Sigma_c^{eff}}{\partial M^{\alpha\beta}} = \frac{1}{h} A_{\alpha\beta\lambda\mu} \left(\frac{12}{h^2} M^{\lambda\mu} - b_\rho^\lambda N^{\rho\mu} + b_\kappa^\kappa N^{\lambda\mu} \right) - \frac{1}{h} b_\alpha^\kappa A_{\kappa\beta\lambda\mu} N^{\lambda\mu} , \end{aligned} \tag{13.14}$$

$$E_\alpha = \frac{\partial \Sigma^{eff}}{\partial Q^\alpha} = \frac{4}{\alpha_s h} A_{\alpha 3 \lambda 3} Q^\lambda . \tag{13.15}$$

For any particular choice of surface coordinates the Eqs. (13.14) can be inverted for $N^{\alpha\beta}, M^{\alpha\beta}$ provided that determinant of 8×8 matrix coefficients in Eqs. (13.14) does not vanish. For the arc-length orthogonal lines of principal curvatures of M such inversion was explicitly performed in [13.5]. This resulted in the following constitutive equations for the physical components of 2D shell stress and couple resultants

$$\begin{aligned} N_{11} &= C\left(E_{11} + \nu E_{22}\right) - D\left(\frac{1}{R_1} - \frac{1}{R_2}\right) K_{11} , \\ N_{22} &= C\left(E_{22} + \nu E_{11}\right) + D\left(\frac{1}{R_1} - \frac{1}{R_2}\right) K_{22} , \\ M_{11} &= D\left(K_{11} + \nu K_{22}\right) - D\left(\frac{1}{R_1} - \frac{1}{R_2}\right) E_{11} , \\ M_{22} &= D\left(K_{22} + \nu K_{11}\right) + D\left(\frac{1}{R_1} - \frac{1}{R_2}\right) E_{22} , \end{aligned} \tag{13.16}$$

$$
\begin{aligned}
N_{12} &= \frac{1}{2}C(1-\nu)\left(E_{12}+E_{21}\right)-D(1-\nu)\left(\frac{1}{R_1}-\frac{1}{R_2}\right)K_{12}\,,\\
N_{21} &= \frac{1}{2}C(1-\nu)\left(E_{12}+E_{21}\right)+D(1-\nu)\left(\frac{1}{R_1}-\frac{1}{R_2}\right)K_{21},\\
M_{12} &= \frac{1}{2}D(1-\nu)\left(K_{12}+K_{21}\right)-D(1-\nu)\left(\frac{1}{R_1}-\frac{1}{R_2}\right)E_{12},\\
M_{21} &= \frac{1}{2}D(1-\nu)\left(K_{12}+K_{21}\right)+D(1-\nu)\left(\frac{1}{R_1}-\frac{1}{R_2}\right)E_{21}\,,
\end{aligned}
\tag{13.17}
$$

$$
C=\frac{Eh}{1-\nu^2}\,,\quad D=\frac{Eh^3}{12\left(1-\nu^2\right)}\,,
\tag{13.18}
$$

where R_1 and R_2 are the principal radii of curvatures of M .

For the shear stress resultants by inverting Eq. (13.15) we obtain

$$
Q_1=\alpha_s\frac{Eh}{2(1+\nu)}E_1\,,\quad Q_2=\alpha_s\frac{Eh}{2(1+\nu)}E_2\,.
\tag{13.19}
$$

The constitutive equations for the drilling couples take the form

$$
M_1=\alpha_d D(1-\nu)K_1\,,\quad M_2=\alpha_d D(1-\nu)K_2\,,\quad \alpha_d=\frac{4}{15}\,.
\tag{13.20}
$$

It has been proved in [13.5] that within the error of small strain shell theory the drilling bendings K_α are entirely expressible through $K_{\alpha\beta}$, $1/R_\alpha$ and $(E_{11}+E_{22})_{,\alpha}$. Additionally, the M_α themselves have been estimated in [13.5] to be of negligible order in analyses of regular shells. But in solving non-linear problems of irregular shells with branching, intersections or junctions with beams for example, these small fields should be taken into account in order to preserve the structure of the resultant six-field non-linear shell theory.

13.4. Layered elastic shells with different play sequences

Composite shells, initially used in aeronautics, became popular recently in other fields of engineering and technology like aviation and marine industry, production of sport or home equipment and in civil engineering. Their safe and proper design is therefore a very important and responsible task, and the key current issue to consider is the failure analysis of laminates.

There are two main approaches allowing for load capacity estimation of laminates, namely First Ply Failure (FPF) and Last Ply Failure (LPF) methods, e.g. [13.11]. In the FPF concept the composite laminate loses its load resisting abilities at the moment of failure initiation (defined by some criteria), which can occur in an arbitrary point of the structure. In fact, the failure process is more complex. Although the initial failure occurs and material stiffness properties start to degrade, the structure is still able to carry some loads until its final destruction, which is the essence of the LPF approach. The choice whether to perform FPF or LPF calculations depends on the considered situation. For example, uncontrolled and progressive failure is not acceptable in design of civil engineering structures. On the other hand, new failure theories or practical design procedures can properly be formulated only on the basis of thorough experimental investigations and complex progressive failure simulations. Hence, introduction of new advanced theories, regarding load capacity estimation, provides the opportunity to improve properties of manufactured products that are commonly used in many fields of human activity.

Regardless whether the FPF or LPF approach is employed, the crucial role plays the choice of appropriate failure hypothesis. There exists a range of failure criteria established for laminates, but the universal failure theory has not been formulated until now, see e.g. [13.12]. Some of the criteria are relatively simple like maximum stress or strain hypotheses, whereas Tsai-Wu, Hashin or Puck theories represent more sophisticated descriptions of failure phenomenon [13.12]. All of these theories are developed under the assumption of stress tensor symmetry. Results of some FPF analyses using this approach are presented e.g. in [13.13÷13.15], whereas LPF method with symmetrical stress measures is studied in [13.16÷13.20].

The discussed resultant 6p shell theory can be successfully utilised in the analysis of modern shell structures with arbitrary geometry, [13.21-13.22]. As a consequence of presence of the sixth parameter (drilling rotation), the 2D strain and stress measures are not symmetric within this shell model. Therefore, the straightforward implementation of already developed 3D failure criteria into the 6p shell theory is not possible.

The proposed 6p shell model for thin laminated structures, utilizes the Equivalent Single Layer concept (see for instance [13.23]) as the 2D representation of 3D multilayered continuum. Consequently, the 2D constitutive law must give the relation between the 2D strain and stress measures

$$\boldsymbol{\varepsilon} = \{\varepsilon_{11}\ \varepsilon_{22}\ \varepsilon_{12}\ \varepsilon_{21} | \varepsilon_1\ \varepsilon_2 || \kappa_{11}\ \kappa_{22}\ \kappa_{12}\ \kappa_{21} | \kappa_1\ \kappa_2\}^T = \{\boldsymbol{\varepsilon}_m | \boldsymbol{\varepsilon}_s || \boldsymbol{\varepsilon}_b | \boldsymbol{\varepsilon}_d\}^T \quad (13.21)$$

$$\mathbf{s} = \{N^{11}\, N^{22}\, N^{12}\, N^{21} | Q^1 Q^2 || M^{11} M^{22} M^{12} M^{21} | M^1 M^2\}^T = \{\mathbf{s}_m | \mathbf{s}_s || \mathbf{s}_b | \mathbf{s}_d\}^T \quad (13.22)$$

The classical approach known for the nonpolar orthotropic linearly elastic continuum is used here for the 6p shell formulation. The 3D constitutive law is proposed in terms of five classical material engineering constants with one additional parameter describing the drilling stiffness [13.23]. Thus, the constitutive equation in an arbitrary point of the shell is formulated as follows

$$\left\{\begin{array}{c}\sigma_{aa}\\ \sigma_{bb}\\ \sigma_{ab}\\ \sigma_{ba}\\ \hline \sigma_{a}\\ \sigma_{b}\end{array}\right\}_k=\left[\begin{array}{cccc|cc}\dfrac{E_a}{1-\nu_{ab}\nu_{ba}} & \dfrac{\nu_{ab}E_b}{1-\nu_{ab}\nu_{ba}} & 0 & 0 & 0 & 0\\ \dfrac{\nu_{ba}E_a}{1-\nu_{ab}\nu_{ba}} & \dfrac{E_b}{1-\nu_{ab}\nu_{ba}} & 0 & 0 & 0 & 0\\ 0 & 0 & 2G_{ab} & 0 & 0 & 0\\ 0 & 0 & 0 & 2G_{ab} & 0 & 0\\ \hline 0 & 0 & 0 & 0 & 2G_{ac} & 0\\ 0 & 0 & 0 & 0 & 0 & 2G_{bc}\end{array}\right]_k\left\{\begin{array}{c}\varepsilon^{aa}\\ \varepsilon^{bb}\\ \varepsilon^{ab}\\ \varepsilon^{ba}\\ \hline \varepsilon^{a}\\ \varepsilon^{b}\end{array}\right\}_k \tag{13.23}$$

where E_a, E_b are the Young moduli in material axes, G_{ab} is the in-plane shear modulus in material axes, ν_{ab}, ν_{ba} are the Poisson ratios, and G_{ac}, G_{bc} are the transverse shear moduli.

The final form of the constitutive equation for shells is obtained by taking into account the assumptions of first order shear deformation (FOSD) kinematics

$$\begin{aligned}
\mathbf{s}_m &= \sum_{k=1}^{N_L}\left(\int_{\zeta_k^-}^{\zeta_k^+}\{\boldsymbol{C}_m\}_k\left(\boldsymbol{\varepsilon}_m+\zeta\boldsymbol{\varepsilon}_b\right)\mu\,d\zeta\right)=\underset{4\times4}{\mathbf{A}}\boldsymbol{\varepsilon}_m+\underset{4\times4}{\mathbf{B}}\boldsymbol{\varepsilon}_b\,,\\
\mathbf{s}_s &= \sum_{k=1}^{N_L}\left(\int_{\zeta_k^-}^{\zeta_k^+}(\alpha_s)_k\{\boldsymbol{C}_s\}_k\boldsymbol{\varepsilon}_s\,\mu\,d\zeta\right)=\underset{2\times2}{\mathbf{S}}\boldsymbol{\varepsilon}_s\,,\\
\mathbf{s}_b &= \sum_{k=1}^{N_L}\left(\int_{\zeta_k^-}^{\zeta_k^+}\{\boldsymbol{C}_m\}_k\left(\zeta\boldsymbol{\varepsilon}_m+(\zeta)^2\boldsymbol{\varepsilon}_b\right)\mu\,d\zeta\right)=\underset{4\times4}{\mathbf{B}}\boldsymbol{\varepsilon}_m+\underset{4\times4}{\mathbf{D}}\boldsymbol{\varepsilon}_b\,,\\
\mathbf{s}_d &= \alpha_t\sum_{k=1}^{N_L}\left(\int_{\zeta_k^-}^{\zeta_k^+}(\alpha_t)_k\{\boldsymbol{C}_d\}_k\boldsymbol{\varepsilon}_d\,\mu\,d\zeta\right)=\underset{2\times2}{\mathbf{G}}\boldsymbol{\varepsilon}_d\,,
\end{aligned} \tag{13.24}$$

where $\boldsymbol{C}_m$ and $\boldsymbol{C}_s$ are the sub-matrices of the local material matrix (13.23), transformed into the global shell axes [13.23] related to plane stress and transverse shear, respectively. The coefficients α_s and α_t are, correspondingly, the shear correction factor and the drilling stiffness parameter. In the matrix notation the obtained constitutive law has the following form

$$\underset{12\times1}{\begin{Bmatrix} \mathbf{s}_m \\ \mathbf{s}_s \\ \mathbf{s}_b \\ \mathbf{s}_d \end{Bmatrix}} = \underset{12\times12}{\begin{bmatrix} \underset{4\times4}{\mathbf{A}} & \mathbf{0} & \underset{4\times4}{\mathbf{B}} & \mathbf{0} \\ \mathbf{0} & \underset{2\times2}{\mathbf{S}} & \mathbf{0} & \mathbf{0} \\ \underset{4\times4}{\mathbf{B}} & \mathbf{0} & \underset{4\times4}{\mathbf{D}} & \mathbf{0} \\ \mathbf{0} & \mathbf{0} & \mathbf{0} & \underset{2\times2}{\mathbf{G}} \end{bmatrix}} \underset{12\times1}{\begin{Bmatrix} \boldsymbol{\varepsilon}_m \\ \boldsymbol{\varepsilon}_s \\ \boldsymbol{\varepsilon}_b \\ \boldsymbol{\varepsilon}_d \end{Bmatrix}} \tag{13.25}$$

The adopted assumptions of the FOSD kinematics allow one to approximately recalculate the unknown stress state in each layer from the obtained 2D stress measures at the reference surface. The recalculated stresses are transformed into the local material axes of the layer and are introduced into the failure criteria equations. Two of the existing 3D hypotheses have been adopted here in the framework of the described 6p shell theory, namely the Tsai-Wu criterion and the Hashin criterion.

Since in the applied 6p shell theory the stress tensor of the layer's material is not symmetric, it is not possible to apply a standard failure initiation criterion. Hence, the following form of the modified Tsai-Wu criterion is proposed

$$\begin{aligned} 1 = &\left(\frac{1}{X_t} - \frac{1}{X_c}\right)\sigma_1 + \left(\frac{1}{Y_t} - \frac{1}{Y_c}\right)\sigma_2 + \frac{1}{X_t X_c}\sigma_1^2 + \\ &+ \frac{1}{Y_t Y_c}\sigma_2^2 - \frac{1}{2\sqrt{X_t X_c Y_t Y_c}}\sigma_1\sigma_2 + \frac{\left[\max\left(|\tau_{12}|;|\tau_{21}|\right)\right]^2}{S^2}, \end{aligned} \tag{13.26}$$

where σ_1, σ_2, τ_{12}, τ_{21} ($\tau_{12}\neq\tau_{21}$) indicate the stress tensor components in the material coordinate system, X_t, Y_t, X_c, Y_c, S are the absolute values of tensile strengths in the 1st and 2nd material direction, compressive strengths in the 1st and 2nd material direction and shear strength in the 1-2 plane, respectively.

The difference between the proposed failure criterion and the classical one (see for instance [13.11]) concerns the in-plane shear contribution. Because the shear components are not symmetric in the proposed theory, the extreme value of shear stress affects the equation (13.26). Such an approach enables one a more precise description of the failure initiation. The effectiveness of this criterion was studied in [13.22].

Unlike to the Tsai-Wu criterion, the Hashin criterion predicts the mechanisms of damage. It consists of four expressions, corresponding to: fibre tension (F_f^t), fibre compression (F_f^c), matrix tension (F_m^t) and matrix compression (F_m^c). Four failure mode expressions incorporate normal and shear components of the stress tensor acting on particular failure planes. In accordance with the original work of Hashin [13.24], the fibre failure takes place in the plane with normal parallel to the 1st material axis, whereas matrix failure occurs in the plane with normal parallel to the 2nd material axis. This imposes the correct interpretation of shear components ($\sigma_{ab} \neq \sigma_{ba}$) associated with particular failure modes. For this reason σ_{ab} is correlated with the fibre failure and σ_{ba} with the matrix failure mechanism. Therefore, the modified Hashin criterion (analysed also in [13.21]), which we believe to be more suitable than the classical one, becomes

$$F_f^t = \left(\frac{\sigma_a}{X_t}\right)^2 + \left(\frac{\sigma_{ab}}{S_l}\right)^2 \quad \text{for } \sigma_a > 0, \tag{13.27}$$

$$F_f^c = \left(\frac{\sigma_a}{X_c}\right)^2 \quad \text{for } \sigma_a < 0, \tag{13.28}$$

$$F_m^t = \left(\frac{\sigma_b}{Y_t}\right)^2 + \left(\frac{\sigma_{ba}}{S_l}\right)^2 \quad \text{for } \sigma_b > 0, \tag{13.29}$$

$$F_m^c = \left(\frac{\sigma_b}{2S_t}\right)^2 + \left[\left(\frac{Y_c}{2S_t}\right)^2 - 1\right]\frac{\sigma_b}{Y_c} + \left(\frac{\sigma_{ba}}{S_l}\right)^2 \quad \text{for } \sigma_b < 0, \tag{13.30}$$

where S_t denotes the transverse shear strength. If one of the failure indices becomes equal to 1 the failure is detected. The expression for which the failure index is equal to 1 determines the failure mode.

Some results where the modified Tsai-Wu and Hashin criteria were used are published in [13.21, 13.22]. Some numerical examples considered by the authors in these works are described below.

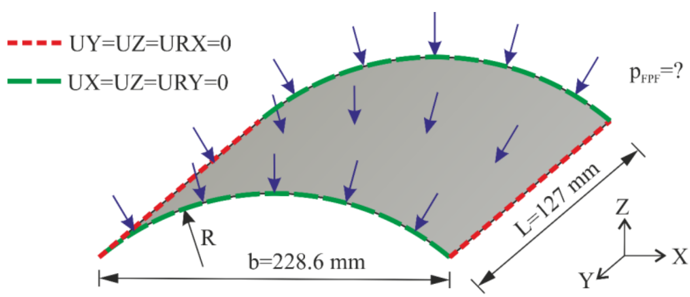

Fig. 13.1. Geometry, loads, BCs, of the elastic cylindrical panel subjected to pressure load

The finite element analyses are carried out with the use of CAM and Abaqus codes. We describe here, estimation of FPF loads of the cylindrical panel subjected to pressure load and the flat compressed plate, in order to assess the correctness of the proposed criteria modifications. The obtained numerical results are compared with solutions available in the literature.

The analysis of pressure loaded cylindrical panel is performed similarly as in [13.25]. Geometry, loads and boundary conditions (BCs) are depicted in Fig. 13.1. The Tsai-Wu criterion is used in order to predict FPF pressures.

The following elastic and strength properties of the considered lamina are applied into calculations: E_a = 132.4GPa, E_b = 10.7GPa, G_{ab} = G_{ac} = 5.6GPa, G_{bc} = 3.4GPa, ν_{ab} = 0.24, X_t = 1514MPa, X_c = 1696.7MPa, Y_t = 43.8MPa, Y_c = 43.8MPa, S_l = 87MPa. Three values of R/b ratio are considered: R/b=10^6, R/b = 100 and R/b = 10. The panel has $[0/90]_s$ layers sequence, with 0 matching the circumferential direction. The thickness of single lamina is equal to 0.127mm. The full panel is studied with 8x8 finite element mesh in both programs, as this is the discretization used in [13.25]. In Abaqus the S8R element is utilised, whereas in CAM the CAMe9FI element (9-node, fully integrated shell element), in which the locking effect is negligible. FPF loads corresponding to the classical Tsai-Wu criterion ([13.25] and Abaqus) and the modified Tsai-Wu criterion (CAM) are shown in Table 13.1. The failure indices are checked in the location of surface integration points and in the middle of each lamina, similarly to [13.25].

Table 13.1. FPF pressures according to Tsai-Wu criteria

R/b	[13.25]	Present Abaqus	Present CAM	Units
10	16.93	16.93	16.55	kPa
100	4.31	4.47	4.49	kPa
10^6	4.08 (10^{30})	4.23	4.21	kPa

Results presented in Table 13.1 are in a good agreement with the reference solution reported in [13.25]. The FPF pressures for R/b = 100 and 10^6 obtained with the CAM code are very close to the results following from Abaqus, because of negligible shear components asymmetry (the failure starts in the middle of the panel). On the other hand there is a slight difference between the present results if R/b = 10 (the failure initiates in the supporting area in the panel corner). It may be attributed to small asymmetry of the shear stress components and to the fact that the surface integration point of fully integrated element lies closer to the panel corner than the reduced integration one.

In the next example, analysis of the flat compressed plate as studied in [13.26] is described. Geometry, loads and BCs of the plate are depicted in Fig. 13.2. Hashin criterion is used in order to predict FPF P_{mag} loads.

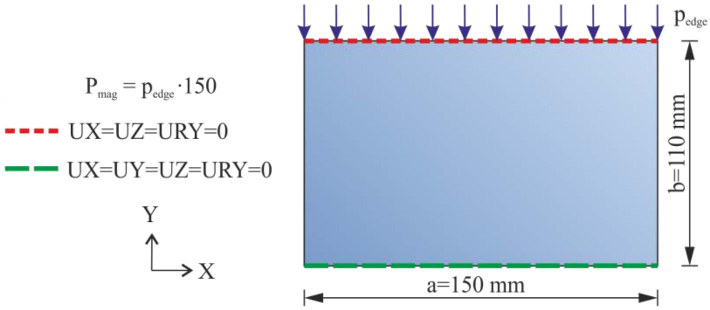

Fig. 13.2. Geometry, loads, BCs, elastic and strength properties of the flat compressed plate

The following elastic and strength properties of a single lamina are used during the analysis: $E_a = 37.24$GPa, $E_b = 10.04$GPa, $G_{ab} = G_{ac} = 4.92$GPa, $G_{bc} = 2.83$GPa, $\nu_{ab} = 0.24$, $X_t = 788.1$MPa, $X_c = 243.5$MPa, $Y_t = 43.45$MPa, $Y_c = 109.9$MPa, $S_l = 31.32$MPa, $S_t = 9.7$MPa. The plate has $[\pm45]_s$ sequence (0 is parallel to the "b" edge). The thickness of single lamina is equal to 0.25 mm. Geometrically non-linear calculations are performed. S4 and CAMe16FI (16-node, fully integrated shell element, in which locking effect is negligible) finite elements are used, respectively, in Abaqus 6.14-2 and in CAM. The structural mesh comprised of the same number of nodes (925) is used in both programs. Since the buckling effect is supposed to occur during the analysis, the negligibly small force imperfection is applied in order to enforce the panel deformation corresponding to the 1st buckling mode shape (the panel buckles into one half-wave along the shorter edge). The failure indices are checked in the integration points in 3 locations of each layer (in the middle and external fibres). The results obtained from the both codes revealed that the failure initiates due to the matrix tension (F_{mt}), in the external ply (+45), close to the free edge, just after buckling. The FPF load (P_{mag}, as defined in Fig. 13.2) obtained in Abaqus (classical Hashin criterion) is approximately 181.4N, while in CAM (modified Hashin criterion) it is close to 181.8N. The failure initiation indices are also similar. However, they are produced by different states of stress, i.e. namely $\sigma_b = 17.14$MPa, $\sigma_{ab} = \sigma_{ba} = -28.71$MPa in Abaqus and $\sigma_b = 15.45$MPa, $\sigma_{ba} = -29.26$MPa in CAM. Contours of matrix tension failure indices at the moment of failure initiation in the external +45 ply are shown in Fig. 13.3.

The FPF experimental load [13.26] is close to the buckling load, which is 195±12.3N, while the failure develops from the panel edges, according to [13.26]. The numerical FPF load calculated with the classical Hashin criterion is 307.34N [13.26]. Hence, the values and failure locations produced by the author calculations are in a good correspondence with the experimental data and are noticeably better than the numerical one given in [13.26], which seems to be overestimated.

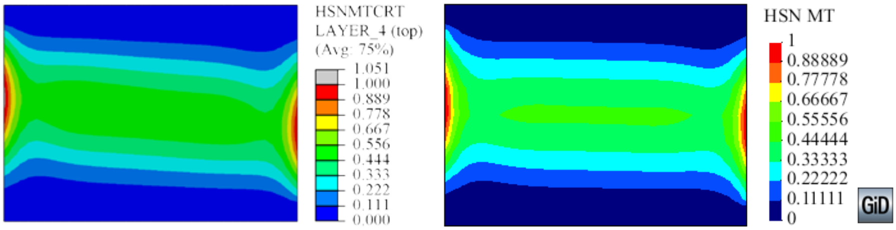

Fig. 13.3. Matrix tension failure indices obtained in Abaqus (left) and CAM (right), failure initiation in +45 ply

13.5. Elasto-plastic FGM shells

The composite shells, initially used in aeronautics, became in recent years more popular in other engineering fields. Shells with continuous change in microstructure, porosity and composition of constituent materials are known as shells made of the "functionally graded material" (FGM), which name was proposed by group of Japan investigators in 1984, [13.27]. Functionally graded materials are an innovative alternative for laminates suffering from intrinsic discontinuity of thermo-mechanical properties which may cause delamination. Combination of the high mechanical strength of metal constituent with the high heat-resistance of ceramic gives a desirable heat-shielding structural material with potential applications in various branches of engineering. The possibility to design material architecture at the microscopic level allows one for optimising some properties of FGM shells and improving its structural performance. Nowadays, the FGM shells are used in parts of machines, engines, high temperature thermal barrier coatings, spacecraft structural components, special nuclear components, etc. The FGM are also applied in biomechanical industry (e.g. in implants), in production of sensors, activators or optical fibres. The possible applications of FGM is nowadays less limited and its wide usage in the existing structures determines their innovative character. Therefore, there emerges the need to formulate suitable computational models of shells made of these materials.

Geometrically nonlinear analysis of simply supported square FGM plate under transverse mechanical load was performed for instance in [13.28]. Typical shell benchmark problems of FGM regular shells were solved using higher-order elements in [13.29]. The analysis of FGM regular and irregular shells in 6-parameter shell theory has been presented in [13.30]. Majority of recent papers in this field were dedicated to linear and geometrically nonlinear problems, vibration or buckling analyses of FGM shells and plates. Only in a few papers the problem of physically nonlinear analysis of functionally graded shells was discussed. The method of determination of material parameters for elasto-plastic model of functionally graded materials was presented in e.g. [13.31]. The 2D materially nonlinear analysis of FGM structures was first performed in [13.32]. Recently the elasto-plastic buckling analysis of functionally graded cylindrical shells has been presented in [13.33]. In papers [13.31÷13.33] the modified rule of mixture (Tamura-Tomota-Ozawa (TTO) model, see [13.34]) was used in contrary to papers [13.26÷13.28]. Since 3D analytical methods are very complex [13.35], and 3D analytical solutions of the considered FGM shells are still not available [13.36], the Finite Element Method (FEM) was chosen as the tool to analyse the complex FGM shell structures. The formulation of accurate elasto-plastic equations and determination of the plastic load capacity of FGM shells allow for applications of the functionally graded structures in many new fields.

The formulation of elasto-plastic constitutive equations with account of the FGM in shell structures belongs to still open problems of formulating the constitutive relations for Cosserat continua [13.37÷13.39]. Starting from asymmetric state of stress at the shell reference surface, natural conformity with the resultant asymmetric forces and the resultant asymmetric moments is obtained. In addition, it is possible to directly introduce the characteristic length which plays the regularizing role when damage/plastic localizations appear in numerical simulations.

Here an analysis of shells with power law variation of material constituents through the thickness is performed. In the formulas given below, subscripts *m*, *c* are describing metal and ceramic constituent, respectively. V_m and V_c denote the volume fraction of constituents, which vary along the thickness (coordinate ζ) according to

$$V_c = \left(0.5 + \zeta / h_0\right)^k , \quad V_m = 1 - V_c \tag{13.31}$$

Variation of material properties through the thickness is described with TTO model for elastic parameters

$$E\left(\zeta\right) = \left(\frac{q + E_c}{q + E_m} E_m V_m + E_c V_c \right) \Bigg/ \left(\frac{q + E_c}{q + E_m} V_m + V_c \right) \tag{13.32}$$

$$\nu\left(\zeta\right) = V_m \nu_m + V_c \nu_c \, , \tag{13.33}$$

and for plastic parameters [13.31]

$$\sigma_Y(\zeta)=\sigma_{Ym}\left(V_m+\frac{q+E_m}{q+E_c}\frac{E_c}{E_m}V_c\right) \tag{13.34}$$

$$E_T(\zeta)=\left(\frac{q+E_c}{q+E_{Tm}}E_{Tm}V_m+E_cV_c\right)\Big/\left(\frac{q+E_c}{q+E_{Tm}}V_m+V_c\right) \tag{13.35}$$

The formula (13.34) for the yield stress σ_Y may be questionable, because in known solutions (e.g. [13.31]) the pure ceramic layer ($V_c=1$) is assumed as the elastic one. To solve this issue we propose to use the relation

$$\sigma_Y(\zeta)=(1-k_Y)\sigma_{Ym}\left(V_m+\frac{q+E_m}{q+E_c}\frac{E_c}{E_m}V_c\right)+k_Y\frac{\sigma_{Ym}}{1-V_c} \tag{13.36}$$

where $1\geq k_Y>0$ denotes an additional non-dimensional parameter. When $V_c\to 1$, then $\sigma_Y(\zeta)\to\infty$, which fulfils the mentioned assumption.

Some preliminary analysis of the cylindrical shell under the shear load (Fig. 6) has been performed. Material parameters are: $E_c=6300$, $\nu_c=0.3$, $l_c=0.005$, $E_m=21000$, $\nu_m=0.3$, $l_m=0.005$, $E_{Tm}=0.0$, $\sigma_{Ym}=24$, $q=2100$, $k_Y=0.01$ and $n_G=1.0$. Upper clamped edge is moved towards *z* direction and the total reaction in this direction is measured. Due to symmetry, only half of the cylinder is taken into account.

Additional results, apart from the perfect solution, are solutions obtained with a small concentrated force as an assumed imperfection. The force is placed in the point (B) (Fig. 13.4) and is directed outward or inward, to impose different shell deformation scheme.

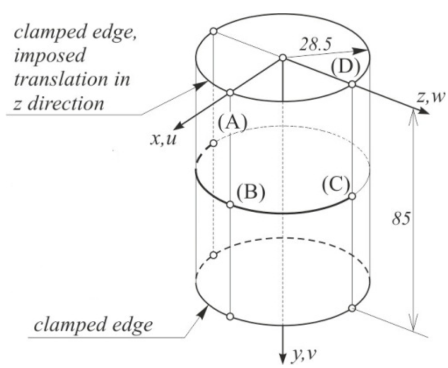

Fig. 13.4. Cylindrical shell under shear load

As a result of elasto-plastic analysis, equilibrium paths for different values of k parameter are given (Fig. 13.5). Results exhibit an interesting behaviour of sheared shell, with bifurcation points at the load level $RF = 5500$ for perfectly elastic behaviour (k = 0) and similar, suspected points for elastoplastic material (k = 0.1, 1.0). Secondary paths are suspected to exist, at a basis of imperfect solutions which tends to the perfect solution. Depending on k, displacement of the point (B) obtained directly in perfect solution is inward or outward. Fig. 8 preview shell deformations at same level of edge displacement, for different k value.

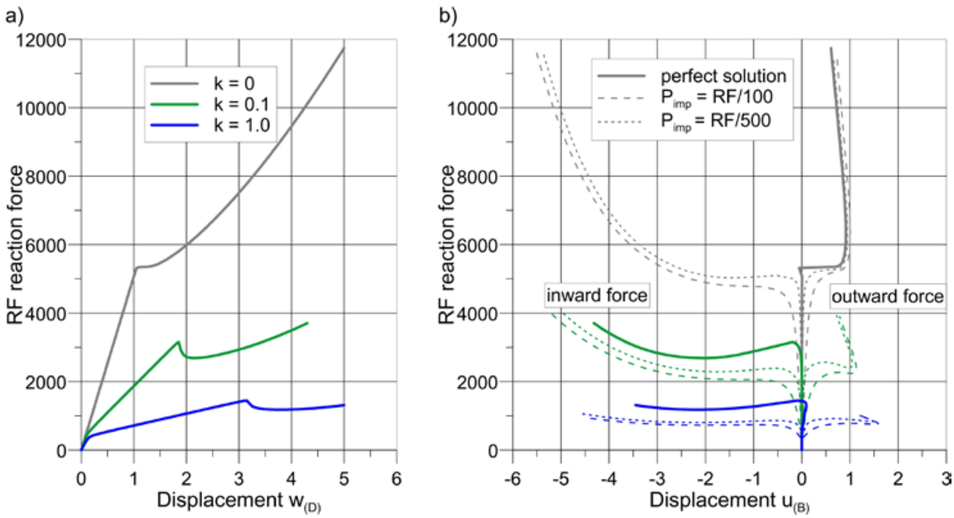

Fig. 13.5. Sheared cylinder - equilibrium paths for different k: a) reaction on upper edge versus displacement on this edge, and b) reaction on upper edge versus radial displacement of point B

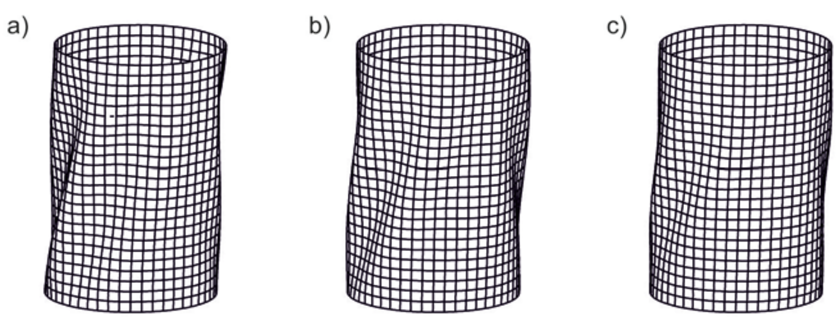

Fig. 13.6. Shell deformation at $w_{(D)}$ = 4.0: a) k = 0, b) k = 0.1, c) k = 1.0

Since ceramics are constituents of many FGMs and non-ductile damage lies in their nature, it is crucial to implement such effects into the material law. When the homogeneous structure is analyzed, use of the damage-plastic model for brittle materials is reasonable (e.g. [13.39]). In further research the combination of elasto-plastic metal behaviour and elasto-plastic damage model for ceramics into one material law is planned. Description of non-elastic effects in non-homogeneous shell layers, with partially ductile and brittle constituent is a demanding task.

13.6. Conclusions

We have discussed rational procedures allowing one to deduce the 2D constitutive relations of the resultant 6-parameter non-linear theory of shells from known constitutive relations of the corresponding 3D solids. Three different material behaviours have been analysed: 1) isotropic elastic shells undergoing small strains, 2) layered elastic shells with different play sequences, and 3) elasto-plastic shells composed of the functionally graded materials. For each material behaviour special 3D-to-2D reduction procedures have been worked out and the corresponding constitutive relations have been constructed. Accuracy of the constitutive relations for layered and FGM shells have been illustrated on examples of plates and shells analysed numerically by FEM.

The proposed constitutive relations complete the BVP of the resultant 6p shell model. It is hoped that they will make it possible to solve many complex problems of shell structures with the help of this most accurate 2D resultant shell model.

Acknowledgement

The research reported in this paper was supported by the National Science Centre, Poland with the grant 2015/17/B/ST8/02190.

13.7. References

13.1 Reissner E., Linear and nonlinear theory of shells, in: Thin Shell Structures, Fung Y.C., Sechler E.E. (eds.), Prentice-Hall, Englewood Cliffs, NJ, 1974, pp. 29-44.

13.2 Libai A., Simmonds J.G., The Nonlinear Theory of Elastic Shells, 2nd edition, Cambridge University Press, Cambridge UK, 1998.

13.3 Chróścielewski J., Makowski J., Pietraszkiewicz W., Statyka i Dynamika Powłok Wielopłatowych: Nieliniowa Teoria i Metoda Elementów

Skończonych (Statics and Dynamics of Multifold Shells: Nonlinear Theory and Finite Element Method), Wydawnictwo IPPT PAN, Warszawa 2004.
13.4 Eremeyev V.A., Pietraszkiewicz V., Local symmetry group in the general theory of elastic shells, Journal of Elasticity, Vol. 85, 2006, pp. 125-152.
13.5 Pietraszkiewicz W., Konopińska V., Drilling couples and refined constitutive equations in the resultant geometrically non-linear theory of elastic shells, International Journal of Solids and Structures, Vol. 51, 2014, pp. 2133-2143.
13.6 Naghdi P.M., Foundations of elastic shell theory, Progress in Solid Mechanics, Vol. 4, Sneddon I.N., Hill R. (eds.), North-Holland P.Co., Amsterdam 1963, pp. 3-90.
13.7 Pietraszkiewicz W., Finite Rotations and Lagrangean Descriptions in the Non-linear Theory of Shells, Polish Scientific Publishers, Warsaw-Poznań 1979.
13.8 John F., Estimates for the derivatives of the stresses in a thin shells and interior shell equations, Communications in Pure and Applied Mathematics, Vol. 18, 1965, pp. 235-267.
13.9 Koiter W.T., A consistent first approximation in the general theory of thin elastic shells, in: Proceeding of IUTAM Symposium on Theory of Thin Elastic Shells, North-Holland P.Co., Amsterdam 1960, pp. 12-32.
13.10 Rychter Z., Global error estimates in Reissner theory of thin elastic shells, International Journal of Engineering Science, Vol. 26, 1988, pp. 787-795.
13.11 Reddy J.N., Mechanics of Laminated Composite Plates and Shell: Theory and Analysis, second Edition, CRC Press, Philadelphia 2004.
13.12 Hinton M.J., Kaddour A.S., Soden P.D., Failure Criteria in Fibre Reinforced Polymer Composites: The World-Wide Failure Exercise. Elsevier, 2004.
13.13 Adali S., Izzet U. Cagdas, Failure analysis of curved composite panels based on first-ply and buckling failures, Procedia Engineering, Vol. 10, 2011, pp. 1591-1596.
13.14 Bakshi K., Chakravorty D., First ply failure study of thin composite conoidal shells subjected to uniformly distributed load, Thin-Walled Structures, Vol. 76, 2014, pp. 1-7.
13.15 Chróścielewski J., Kreja I., Sabik A., Sobczyk B., Witkowski W., Failure Analysis of footbridge made of composite materials, in: Shell Structures: Theory and Applications, CRC Press, Vol. 3, 2014, pp. 389-392,
13.16 Knight N.F., Rankin C.C., Brogan F.A., STAGS computational procedure for progressive failure analysis of laminated composite structures, International Journal of Non-Linear Mechanics, Vol. 37, 2002, pp. 833-849.
13.17 Ambur D.R., Jaunky N., Hilburger M., Dávila C.G., Progressive failure analyses of compression-loaded composite curved panels with and without cutouts, Composite Structures, Vol. 65, 2004, pp. 143-155.
13.18 Lee C.S., Kim J.H., Kim S.K., Ryu D.M., Lee J.M., Initial and progressive failure analyses for composite laminates using Puck failure criterion and damage-coupled finite element method, Composite Structures, Vol. 121, 2015, pp. 406-419.

13.19 Zhang Z., Chen H., Ye L., Progressive failure analysis for advanced grid stiffened composite plates/shells, Composite Structures, Vol. 86, 2008, pp. 45-54.
13.20 Ambur D.R., Jaunky N., Hilburger M.W., Progressive failure studies of stiffened panels subjected to shear loading, Composite Structures, Vol. 65, 2004, pp. 129-142.
13.21 Sobczyk B., Laminated plates and shells - first ply failure analysis within 6-parameter shell theory. In: S. Elgeti, J.-W. Simon (eds.), Proceedings of YIC GACM 2015: 3rd ECCOMAS Young Investigators Conference and 6th GACM Colloquium, 20.07-23.07.15 RWTH Aachen University, Aachen, Germany, 2015.
13.22 Chróścielewski J., Witkowski W., Sobczyk B., Sabik A., First ply failure analysis of laminated shells undergoing large displacements - 6 parameter shell theory approach, Proc. 3rd PCM & 21st CMM, Gdańsk, Poland, Vol. 1, pp. 323-324, Polish Society of Theoretical and Applied Mechanics, Gdańsk 2015.
13.23 Chróścielewski J., Kreja I., Sabik A., Witkowski W., Modeling of composite shells in 6-parameter nonlinear theory with drilling degree of freedom, Mechanics of Advanced Materials and Structures, Vol. 18, 2011, pp. 403-419.
13.24 Hashin Z., Failure criteria for unidirectional fiber composites, Journal of Applied Mechanics, Vol. 47, 1980, pp. 329-334.
13.25 Prusty B. G., Satsanagi S. K., Ray C., First ply failure analysis of laminated Panels Under Transverse Loading, Journal of Reinforced Plastics and Composites, Vol. 20(8), 2001, pp. 671-684.
13.26 Heidari-Rarani M., Khalkhali-Sharifi S.S., Shokrieh M.M., Effect of ply stacking sequence on buckling behavior of E-glass/epoxy laminated composites, Computational Materials Science, Vol. 89, 2014, pp. 89-96.
13.27 Koizumi M., FGM activities in Japan, Composites Part B, Vol. 28B, 1997, pp. 1-4.
13.28 Woo J., Meguid S.A., Nonlinear analysis of functionally graded plates and shallow shells, International Journal of Solids and Structures, Vol. 38, 2001, pp. 7409-7421.
13.29 Arciniega R.A., Reddy J.N., Large deformation analysis of functionally graded shells, International Journal of Solids and Structures, Vol. 44, 2007, pp. 2036-2052.
13.30 Daszkiewicz K., Chróścielewski J., Witkowski W., Geometrically nonlinear analysis of functionally graded shells based on 2-D Cosserat constitutive model, Engineering Transactions, Vol. 62(2), 2014, pp. 109-130.
13.31 Nakamura T., Wang T., Sampath S., Determination of properties of graded materials by inverse analysis and instrumented indentations, Acta Materialia, Vol. 48, 2000, pp. 4293-4306.
13.32 Eraslan A.N., Akis T., Plane strain analytical solutions for a functionally graded elastic-plastic pressurized tube, International Journal of Pressure Vessels and Piping, Vol. 83, 2006, pp. 635-644.

13.33 Huang H., Han Q., Elastoplastic buckling of axially loaded functionally graded material cylindrical shells, Composite Structures, Vol. 117, 2014, pp. 135-142.
13.34 Tamura I., Tomota Y., Ozawa H., Strength and ductility of Fe–Ni–C alloys composed of austenite and martensite with various strength. In: Proceeding of the Third International Conference on Strength of Metals and Alloys, Cambridge Institute of Metals, Vol. 1, 1973, pp. 611-615.
13.35 Jha D.K., Kant T., Singh R.K., A critical review of recent research on functionally graded plates, Composite Structures, Vol. 96, 2013, pp. 833-849.
13.36 Swaminathan K., Naveenkumar D.T., Zenkour A.M., Carrera E., Stress, vibration and buckling analyses of FGM plates - A state-of-the-art review, Composite Structures, Vol. 120, 2015, pp. 10-31.
13.37 Burzyński S., Chróścielewski J., Witkowski W., Geometrically nonlinear FEM analysis of 6-parameter resultant shell theory based on 2-D Cosserat constitutive model, Z. Angew. Math. Mech., 1-14, 2015, DOI 10.1002/zamm.201400092.
13.38 Eremeyev V.A., Pietraszkiewicz W., Material symmetry group and constitutive equations of micropolar anisotropic elastic solids, Mathematics and Mechanics of Solids, Vol. 21, 2016, SI, pp. 210-221, doi:10.1177/1081286515582862.
13.39 Addessi D., A 2D Cosserat finite element based on a damage-plastic model for brittle materials, Computers & Structures, Vol. 135, 2014, pp. 20-31.

14.

Stability and vibration of imperfect structures

14.1. Introduction

Taking into account the stiffness and inertia forces, dynamic behaviour of structures can be investigated. Dynamic investigation usually starts with an example of free vibration. It means to evaluate the natural frequency. The simplest stability problem of structures is buckling of a column. This problem can be arranged preparing the equilibrium conditions on a deformed structure. In general, however, for the evaluation of the stability problems strains should be evaluated for a deformed differential element what means to apply geometric non-linear theory.

Combination of dynamics and stability yields in a lot of problems: dynamic buckling, dynamic post buckling behaviour, parametric resonance, etc. Introduction example - vibration of a column loaded in compression is simple but its investigation still represents a lot of problems.

The natural frequency can be measured by using rather simple equipment. The comparison of frequencies measured experimentally and evaluated numerically is the basis of non-destructive methods for investigation of structure properties. Generally, it can be said that in structural design stability effects have to be taken into consideration. These two ideas are the reason for our investigation of the combination of vibration and stability.

Euler was probably the first scientist who had analyzed stability problems. The former solutions are supposed to be the linear stability. It means that we suppose an ideal structure. The differences between theory and reality inspired researchers to search for more accurate models. Especially the slender web as the main part of thin-walled structure has significant post-buckling reserves and it is necessary to accept a geometric non-linear theory for their description. The problem of the vibration of the non-linear system was formulated by Bolotin [14.2]. Burgreen [14.3] analysed the problem of the vibration of an imperfect column in early 50's. Some valuable results have been achieved by Volmir [14.8]. Combination of dynamics and stability is still a subject of research all over the world [14.1, 14.3, 14.4].

14.2. Dynamic Post-Bucklin Behaviour of Slender Web

14.2.1. Post-buckling behaviour of slender web - displacement model

As it was already mentioned, a slender web is the main constructional element of thin-walled structure. If we assume an "ideal" slender web and a distribution of the in-plane stresses are not the function of the out-of plane (the plate) displacements, the problem leads to eigenvalues and eigenvectors. From the obtained eigenvalues elastic critical load can be evaluated and eigenvector characterizes the mode of buckling.

Post-buckling behaviour can be assumed as follows (Fig.14.1).

Displacements of the point of the middle surface are

$$\mathbf{q} = [u, v, w]^T \tag{14.1}$$

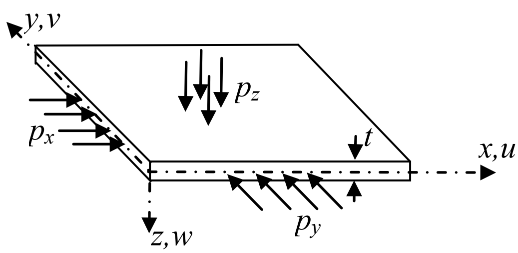

Fig. 14.1. Notation of quantities of slender web

In the post-buckling behaviour of the slender web the plate displacements are much larger than in-plane (web) displacements ($w >> u$, v) and so the strains are

$$\boldsymbol{\varepsilon} = \begin{Bmatrix} u_{,x} \\ v_{,y} \\ u_{,y} + v_{,x} \end{Bmatrix} + \frac{1}{2} \begin{Bmatrix} w_{,x}^2 \\ w_{,y}^2 \\ 2w_{,x} w_{,y} \end{Bmatrix} - z \begin{Bmatrix} w_{,xx} \\ w_{,yy} \\ w_{,xy} \end{Bmatrix} \tag{14.2}$$

where *"z"* is the coordinate of the thickness. The indexes *"x, y"* denote partial derivations.

For the next investigation, slender web with initial deformations is assumed. Initial deformations are the plate types only.

$$\mathbf{q_0} = [0, 0, w_0]^T \tag{14.3}$$

Due to that the initial strains are

$$\boldsymbol{\varepsilon}_0 = \frac{1}{2}\begin{Bmatrix} w_{0,x}^2 \\ w_{0,y}^2 \\ 2w_{0,x}w_{0,y} \end{Bmatrix} - z\begin{Bmatrix} w_{0,xx} \\ w_{0,yy} \\ 2w_{0,xy} \end{Bmatrix} \tag{14.4}$$

The *"w"* represents the global displacements and *"w_0"* is a part related to the initial displacement.

The linear elastic material has been assumed

$$\boldsymbol{\sigma} = \begin{Bmatrix} \sigma_x \\ \sigma_y \\ \tau \end{Bmatrix} = \mathbf{D}\left(\varepsilon - \varepsilon_0\right) + \boldsymbol{\sigma}_w, \quad \text{where } \mathbf{D} = \frac{E}{1-\nu^2}\begin{bmatrix} 1 & \nu & \\ \nu & 1 & \\ & & \dfrac{1-\nu}{2} \end{bmatrix} \tag{14.5}$$

and E, ν are the Young's modulus and Poisson's ratio, $\boldsymbol{\sigma}_w = \left[\sigma_{xw}, \sigma_{yw}, \tau_w\right]^T$ are the residual stresses.

The global potential energy of the slender web is

$$U = U_i + U_e \tag{14.6}$$

where: $U_i = \frac{1}{2}\int_V \left(\boldsymbol{\varepsilon} - \boldsymbol{\varepsilon}_0\right)^T \boldsymbol{\sigma}\, dV$ is the potential energy of the internal forces,

$U_e = -\int_\Gamma \left(\mathbf{q} - \mathbf{q_0}\right)^T \mathbf{p}\, d\Gamma$ - the potential energy of the external forces,

where V is the volume of the slender web, Γ is the in-plane surface.

The displacements are assumed as the product of the variational functions and the displacements parameters

$$\mathbf{q} = \mathbf{B}.\boldsymbol{\alpha} \tag{14.7}$$

The minimum of the global potential energy gives the system of conditional equations

$$\mathbf{K}_G(\boldsymbol{\alpha})\boldsymbol{\alpha} = \mathbf{f} \tag{14.8}$$

where $\mathbf{K}_G$ is the stiffness matrix as the function of the displacement parameters - non-linear stiffness matrix, $\mathbf{f}$ is the vector of the external load.

14.2.2. Post-buckling behaviour of slender web loaded in compression - illustrative example

For the simplification we suppose the square rectangular slender web loaded in compression simply supported all around. We do not need to suppose the external load as the constant along the edge. But the external force must be defined as $F = \int_0^b t\sigma dy$. Consequently, the average stress can be defined as $\sigma = F/b \cdot t$. For the approximate solution, we take a displacement functions as

$$w = \alpha S_{x1} S_{y1}\,,\; w_0 = \alpha_0 S_{x1} S_{y1}\,,\; u = \beta_1 \left(1 - \frac{2x}{b}\right) + \beta_2 S_{x2} C_{y2} + \beta_3 S_{x2}\,,$$

$$v = \gamma_1 \left(1 - \frac{2y}{b}\right) + \gamma_2 C_{x2} S_{y2} + \gamma_3 S_{y2}\,, \text{ where } S_{xi} = \sin\frac{i\pi x}{b}, \ldots\; C_{yi} = \cos\frac{i\pi y}{b}.$$

We have divided the variational parameters into: - plate $\boldsymbol{a}_D = \alpha$, - in-plane $\boldsymbol{a}_S = [\beta_1, \beta_2, \beta_3, \gamma_1, \gamma_2, \gamma_3]^T$. The in-plane displacements parameters are

$$\boldsymbol{a}_S = \frac{\pi}{16b}\left(\alpha^2 - \alpha_0^2\right)\left[\pi, 1, -1+\nu, \pi, 1, -1+\nu\right]^T$$

Introducing: $\sigma_E = \dfrac{\pi^2 E t^2}{12\left(1-\nu^2\right)b^2}$ (Euler's elastic critical stress),

the dimensionless load as $\overline{\sigma} = \dfrac{\sigma'}{4\sigma_E} = \dfrac{\sigma'}{\sigma_{cr}}$, ($\sigma_{cr} = 4\sigma_E$) and

the dimensionless parameters of the displacements function $\overline{\alpha} = \dfrac{\alpha}{t}, \overline{\alpha}_0 = \dfrac{\alpha_0}{t}$,

the result can be arranged into the final equation

$$0.34125\left(\overline{\alpha}^2 - \overline{\alpha}_0^2\right) + 1 - \frac{\overline{\alpha}_0}{\overline{\alpha}} = \overline{\sigma} \tag{14.9}$$

The parameters α and α_0 represent the amplitudes of the out of plate displacements of the slender web. Eq. (14.9) is arranged in Fig. 14.2.

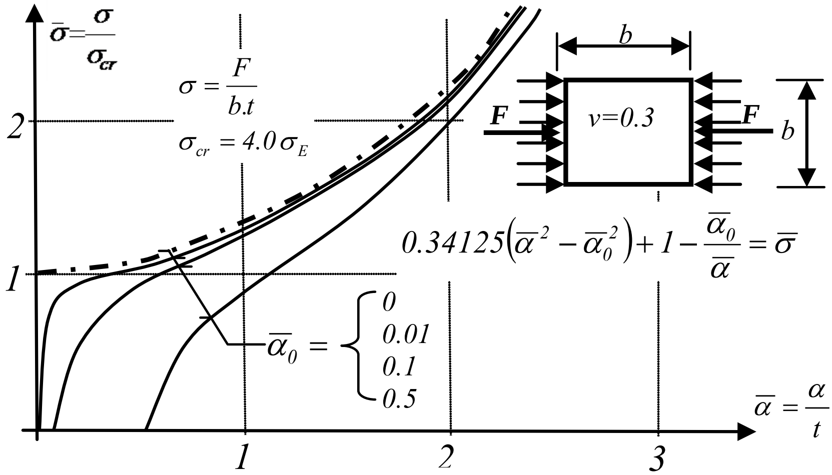

Fig. 14.2. Post-buckling behaviour of slender web loaded in compression

It is evident that the slender web could be loaded above the level of the elastic critical load. Due to that "the post-buckling behaviour" can be introduced. ***It has to be noted that the presented example represents an approximate solution.***

14.2.3. System of non-linear algebraic equations

First, we present a note related to the solution of geometric non-linear problems. We use (for example) the Ritz variational method. The functions of the displacements are sums of the products of the basic functions and the variational coefficients.

$$\boldsymbol{q} = \boldsymbol{B}.\alpha \tag{14.10}$$

These equations could be written in the mode as

$$u, w \Rightarrow \alpha \uparrow 1 \tag{14.11}$$

The sign „↑" is used as an exponent.

The elongations taking into account non-linear parts have the variational coefficients in quadrates and can be recorded as

$$\varepsilon = u_{,x} + \frac{1}{2} w_{,x}{}^2 - z.w_{xx} \Rightarrow \alpha \uparrow 2 \tag{14.12}$$

Assuming the linear elastic material, the stresses are in quadrates as well.

$$\sigma = E(\varepsilon - \varepsilon_0) \Rightarrow \quad \alpha \uparrow 2 \tag{14.13}$$

The potential energy of the internal forces is a product of the elongations and the stresses, then, finally, the variational coefficients are of the fourth power

$$U_i = \frac{1}{2}\varepsilon^T.\sigma = (\alpha \uparrow 2).(\alpha \uparrow 2) = \alpha \uparrow 4 \tag{14.14}$$

The system of conditional equations may be arranged as a partial derivation according to the variational coefficients

$$\frac{\partial U}{\partial \alpha_i} = \ldots = \alpha \uparrow 3 \tag{14.15}$$

Finally, we obtain the *system of cubic algebraic equations*.

A partial approval of our explanation can be seen in the example of the post bucking behaviour of the slender web. (Part 14.2.2, Eq.(14.9), where we have got the cubic algebraic equation.)

Note. In the example of the buckling of the column, the cubic terms have been eliminated. This “special case” is the consequence of the constant normal force along the column.

Let us continue with our former considerations.

The system of linear algebraic equations can be arranged as a matrix (two dimensional area). The system of quadratic algebraic equations could be arranged as a three dimensional matrix. The cubic algebraic equations are a four dimensional matrix. We are not able to imagine the four dimensional matrix, but modern computers are able to compile it.

One typical property of the finite element method is a large number of parameters (many thousands). To arrange 1000 cubic algebraic equations represents in computer memory $1000^4=1\times10^{12}$ real numbers and this is beyond possibilities.

The way how to solve these non-linear systems has been found. The idea is to use the Newton-Raphson iteration without compilation of the system of non-linear (cubic) algebraic equations. It will be explained in the following parts.

14.2.4. Incremental formulation

As it has been already explained in the previous part, we are forced to arrange the iterative method. It can be prepared from the incremental formulation and so we must prepare all the regulars in increments.

Note. All the rules for one dimensional problem (beams, columns) are prepared. For the solution of the two dimensional problems (webs, plates) the steps are similar [14.5, 14.7].

As the first step, the increments and variations for the elongations must be prepared.

If we have the linear function as

$$f\left(\frac{du}{dx}\right)=\frac{du}{dx}=u_{,x} \tag{14.16}$$

For the increments $u+\Delta u$, we get the increments of the function

$$\Delta f=f\left(\frac{d(u+\Delta u)}{dx}\right)-f\left(\frac{du}{dx}\right)=\frac{du}{dx}+\frac{d\Delta u}{dx}-\frac{du}{dx}=\frac{d\Delta u}{dx}=\Delta u_{,x} \tag{14.17}$$

We do the same steps for the non-linear function

$$f\left(\frac{dw}{dx}\right)=\frac{1}{2}\left(\frac{dw}{dx}\right)^2=\frac{1}{2}w_{,x}{}^2 \tag{14.18}$$

Then we have for the increment of this function

$$\begin{aligned}\Delta f&=f\left(\frac{d(w+\Delta w)}{dx}\right)-f\left(\frac{dw}{dx}\right)=\frac{1}{2}\left(\frac{d(w+\Delta w)}{dx}\right)^2-\frac{1}{2}\left(\frac{dw}{dx}\right)^2=\\&=\frac{1}{2}\left(\left(\frac{dw}{dx}\right)^2+2\frac{dw}{dx}.\frac{d\Delta w}{dx}+\left(\frac{d\Delta w}{dx}\right)^2\right)-\frac{1}{2}\left(\frac{dw}{dx}\right)^2=\frac{dw}{dx}.\frac{d\Delta w}{dx}+\frac{1}{2}\left(\frac{d\Delta w}{dx}\right)^2=\\&=w_{,x}.\Delta w_{,x}+\frac{1}{2}\Delta w_{,x}{}^2\end{aligned} \tag{14.19}$$

According to these rules the increment of the strain can be arranged as follows

$$\Delta\varepsilon_{,x}=\Delta u_{,x}+w_{,x}.\Delta w_{,x}+\frac{1}{2}\Delta w_{,x}{}^2-z.\Delta w_{xx} \tag{14.20}$$

Then the variation of the increment of the elongation is prepared

$$\delta\Delta\varepsilon_{,x}=\delta\Delta u_{,x}+w_{,x}.\delta\Delta w_{,x}+\delta\Delta w_{,x}.\Delta w_{,x}-z.\delta\Delta w_{xx} \tag{14.21}$$

14.2.5. The Hamilton's principle

In this step, we prepare the rules for the dynamic process. In order to neglect the inertial forces, we get the static problems.

The Hamilton's principle means: in each time interval, the variation of the kinetic and potential energy and the variation of the work of the external forces is equal to zero. This rule is valid for the increments as well

$$\int_{t_0}^{t_1} \delta(\Delta T - \Delta U)dt + \int_{t_0}^{t_1} \delta\Delta W dt = 0 \tag{14.22}$$

where $\Delta T = \int_V \frac{1}{2}\rho\Delta\dot{\boldsymbol{q}}^T\Delta\dot{\boldsymbol{q}}dV$ is the increment of the kinetic energy, $\Delta U = \int_V \left(\frac{1}{2}\Delta\varepsilon.\Delta\sigma + \Delta\varepsilon.\sigma\right)dV$ - the increment of the potential energy of the internal forces, $\Delta W = \int_V \Delta\boldsymbol{q}^T.(\boldsymbol{p} + \Delta\boldsymbol{p})dV$ - the increment of the work of the external forces, t_0, t_1 - the time intervals, ρ - the mass density, V - the volume (in our case it is the volume of the beam - column), $\boldsymbol{p}, \Delta\boldsymbol{p}$ - the external load, the increment of the external load. The dots mean the time derivation.

We assume the linear elastic material (Eq. (14.5)). For the increments, we have $\Delta\sigma = \boldsymbol{D}\Delta\varepsilon$.

In the case of the beam type of structures, the volume integration can be changed into the integration over the cross section and the integration over the length: *A, I* - the cross section area, the moment of inertia. The longitudinal axis is situated into centre of the gravity of the cross section.

We use the Ritz variational method

$$u = \boldsymbol{B}_S.\boldsymbol{\alpha}_S, \quad w = \boldsymbol{B}_D.\boldsymbol{\alpha}_D, \tag{14.23}$$

We have the incremental model and the variational coefficients $\boldsymbol{\alpha}_S$ and $\boldsymbol{\alpha}_D$ are timeless functions.

For the increments of the displacements functions, the independent basic variational functions can be used. The increments of the variational coefficients are the function of the time

$$\Delta u = \boldsymbol{B}_{S1}.\Delta\boldsymbol{\alpha}_S(t), \quad \Delta w = \boldsymbol{B}_{D1}.\Delta\boldsymbol{\alpha}_D(t) \tag{14.24}$$

Note. In some dynamic processes where there can be different boundary condition for the static behaviour and for the vibration, it is useful to have different basic variational functions for the displacements and for the increment of the displacements.

Finally, Eq. (14.22) leads to the system of conditional equation. This system could be arranged into the mode

$$\begin{aligned}&\boldsymbol{K}_{\boldsymbol{M-D}}\Delta\ddot{\alpha}_D + \boldsymbol{K}_{INC-D}\Delta\alpha_D + \boldsymbol{K}_{INC-DS}\Delta\alpha_S + \boldsymbol{f}_{\boldsymbol{INT-D}} - \boldsymbol{f}_{EXT-\boldsymbol{D}} - \Delta\boldsymbol{f}_{EXT-\boldsymbol{D}} = \boldsymbol{0}\\ &\boldsymbol{K}_{\boldsymbol{M}-S}\Delta\ddot{\alpha}_S + \boldsymbol{K}_{INC-S}\Delta\alpha_S + \boldsymbol{K}_{INC-SD}\Delta\alpha_D + \boldsymbol{f}_{\boldsymbol{INT}-S} - \boldsymbol{f}_{EXT-S} - \Delta\boldsymbol{f}_{EXT-S} = \boldsymbol{0}\end{aligned} \tag{14.25}$$

where: $\boldsymbol{K}_{\boldsymbol{M-D}} = \int_0^a \boldsymbol{B}_{\boldsymbol{D1}}^{\boldsymbol{T}}\rho A\boldsymbol{B}_{\boldsymbol{D1}}dx$ is the mass matrix of the “bendig” displacements,

$\boldsymbol{K}_{INC-D} = \boldsymbol{K}_{INC-DL} + \boldsymbol{K}_{INC-DG}$ - the incremental stiffness matrix of the bending,

$\boldsymbol{K}_{INC-DL} = \int_0^a \boldsymbol{B}_{\boldsymbol{D1}XX}^{\boldsymbol{T}} EI\boldsymbol{B}_{\boldsymbol{D1}XX}dx$ - the linear part,

$\boldsymbol{K}_{INC-DG} = \int_0^a \boldsymbol{B}_{\boldsymbol{D1}X}^{\boldsymbol{T}} EA\left(\frac{3}{2}w_{,x}^2 - \frac{1}{2}w_{0,x}^2\right)\boldsymbol{B}_{\boldsymbol{D1}X}dx$ - the non-linear part of the incremental stiffness matrix of the bending stiffness,

$\boldsymbol{K}_{INC-DS} = \int_0^a \boldsymbol{B}_{\boldsymbol{D1}X}^{\boldsymbol{T}} EA(w_{,x} + u_{,x}.w_{,x}.)\boldsymbol{B}_{S1X}dx$ - the incremental “bending - axial” stiffness matrix,

$\boldsymbol{f}_{\boldsymbol{INT-D}} = \int_0^a \boldsymbol{B}_{\boldsymbol{D1XX}}^{T} EI\left(w_{,xx} - w_{0,xx}\right)dx + \int_0^a \boldsymbol{B}_{\boldsymbol{D1X}}^{T} EA(u_{,x} + \frac{1}{2}w_{,x}^2u_{,x} - \frac{1}{2}w_{0,x}^2u_{,x} + \frac{1}{2}w_{,x}^3$
$+ w_{,x}u_{,x} - w_{,x}w_{0,x}^2)dx$ - the vector of the bending internal forces,

$\Delta\boldsymbol{f}_{\boldsymbol{EXT-D}} = \int_0^a \boldsymbol{B}_{\boldsymbol{D1}}^{\boldsymbol{T}}\Delta\boldsymbol{p}_{\boldsymbol{D}}dx$ - the increment of the vector of the bending external forces,

$\boldsymbol{K}_{\boldsymbol{M}-S} = \int_0^a \boldsymbol{B}_{S\boldsymbol{1}}^{\boldsymbol{T}}\rho A\boldsymbol{B}_{S\boldsymbol{1}}dx$ - the mass matrix of the “axial” displacements,

$\boldsymbol{K}_{INC-S} = \int_0^a \boldsymbol{B}_{SX\boldsymbol{1}}^{\boldsymbol{T}} EA\boldsymbol{B}_{SX\boldsymbol{1}}dx$ - the incremental stiffness matrix of the axial stiffness.

It can be proved that $\boldsymbol{K}_{INC-SD} = \boldsymbol{K}_{INC-DS}^{T}$ - the incremental “axial - bending” stiffness matrix,

$\boldsymbol{f}_{\boldsymbol{INT}-S} = \int_0^a \boldsymbol{B}_{\boldsymbol{S1X}}^T EA\left(u_{,x} + \frac{1}{2} w_{,x}^2 - \frac{1}{2} w_{0,x}^2 \right) dx$ - the vector of the axial internal forces,

$\boldsymbol{f}_{\boldsymbol{EXT}-S} = \int_0^a \boldsymbol{B}_{\boldsymbol{S1}}^{\boldsymbol{T}} \boldsymbol{p}_S dx$ - the vector of the axial external forces,

$\Delta \boldsymbol{f}_{\boldsymbol{EXT}-S} = \int_0^a \boldsymbol{B}_{\boldsymbol{S1}}^{\boldsymbol{T}} \Delta \boldsymbol{p}_S dx$ - the increment of the vector of the axial external forces.

It is evident that Eq.(14.25) represents the system of the differential equations of the second degree.

The axial and the bending displacement can be joined as

$$\Delta\boldsymbol{\alpha} = \begin{Bmatrix} \Delta\boldsymbol{\alpha}_D \\ \Delta\boldsymbol{\alpha}_S \end{Bmatrix}, \quad \boldsymbol{\alpha} = \begin{Bmatrix} \boldsymbol{\alpha}_D \\ \boldsymbol{\alpha}_S \end{Bmatrix}$$

The system of conditional equations (Eq. (14.25)) could be written as

$$\boldsymbol{K}_{\boldsymbol{M}} \Delta\ddot{\alpha} + \boldsymbol{K}_{INC} \Delta\alpha + \boldsymbol{f}_{INT} - \boldsymbol{f}_{EXT} - \Delta \boldsymbol{f}_{EXT} = \boldsymbol{0} \tag{14.26}$$

where:

$$\boldsymbol{K}_{\boldsymbol{M}} = \left[\begin{array}{c|c} \boldsymbol{K}_{\boldsymbol{M}-D} & \\ \hline & \boldsymbol{K}_{\boldsymbol{M}-S} \end{array} \right], \boldsymbol{K}_{INC} = \left[\begin{array}{c|c} \boldsymbol{K}_{INC-D} & \boldsymbol{K}_{INC-DS} \\ \hline \boldsymbol{K}_{INC-SD} & \boldsymbol{K}_{INC-S} \end{array} \right]$$

$$\Delta \boldsymbol{f}_{EXT} = \begin{Bmatrix} \Delta \boldsymbol{f}_{EXT-D} \\ \Delta \boldsymbol{f}_{EXT-S} \end{Bmatrix}, \quad \boldsymbol{f}_{EXT} = \begin{Bmatrix} \boldsymbol{f}_{EXT-D} \\ \boldsymbol{f}_{EXT-S} \end{Bmatrix} \quad \boldsymbol{f}_{INT} = \begin{Bmatrix} \boldsymbol{f}_{IND-D} \\ \Delta \boldsymbol{f}_{INT-S} \end{Bmatrix}$$

14.2.6. Static behaviour

The inertial forces can be neglected for the solution of the static behaviour of the structure

$$\boldsymbol{K}_{\boldsymbol{M}} . \Delta\ddot{\alpha} \cong \boldsymbol{0} \tag{14.27}$$

Note. In the case of the static behaviour, except the Hamilton's principle, (Eq. (14.22)) the principle of the minimum of the increment of the global potential energy can be applied.

The system of the differential equations (Eq. (14.25)) will be changed into the system of the linear algebraic equation related to the increments of the displacements

$$\boldsymbol{K}_{INC}\Delta\alpha + \boldsymbol{f}_{\boldsymbol{INT}} - \boldsymbol{f}_{EXT} - \Delta\boldsymbol{f}_{EXT} = \boldsymbol{0} \tag{14.28}$$

If the problem is not established in the increments, but in the displacement parameters, we get the system of the cubic algebraic equations in the mode

$$\boldsymbol{f}_{\boldsymbol{INT}} - \boldsymbol{f}_{EXT} = \boldsymbol{0} \tag{14.29}$$

As previously explained in the introduction Part 14.2.3, this system of cubic algebraic equations cannot be compiled. (Note. This system can be arranged in some simple examples only.)

Eq. (14.28) is the basis for the incremental solution and for the Newton-Raphson iteration as well.

14.2.7. Incremental solution

We assume the system in equilibrium represented by the parameters of the displacements "$\boldsymbol{\alpha}$". Then it is valid that

$$\boldsymbol{f}_{INT} - \boldsymbol{f}_{EXT} = \boldsymbol{0} \tag{14.30}$$

The increment of the external load is obtained. The increments of the parameters of the displacements can be obtained from Eq. (14.28)

$$\Delta\boldsymbol{\alpha} = \boldsymbol{K}_{INC}^{-1}\Delta\boldsymbol{f}_{EXT} \tag{14.31}$$

The displacement parameters of the new level are

$$\boldsymbol{\alpha}_D^{\;i} = \boldsymbol{\alpha}_D + \Delta\boldsymbol{\alpha}_D \tag{14.32}$$

14.2.8. Newton-Raphson iteration

We do not assume any system in equilibrium represented by the parameters of the displacements "$\boldsymbol{\alpha}^i$". Then we have the vector of residuum

$$\boldsymbol{r}^i = \boldsymbol{f}_{INT} - \boldsymbol{f}_{EXT} \tag{14.33}$$

For the correction of the roots (displacement parameters), we assume the constant level of the external load $(\Delta\boldsymbol{f}_{EXT} = 0)$. Then it can be evaluated from Eq. (14.28)

$$\Delta\boldsymbol{\alpha}^{i} = -\boldsymbol{K}_{INC}^{-1}.\boldsymbol{r}^{i} \tag{14.34}$$

The new approximation of the displacement parameters is

$$\alpha^{i+1} = \alpha^{i} + \Delta\alpha^{i} \tag{14.35}$$

Eqs. (14.33÷14.35) represent the Newton-Raphson iteration.

We have a large amount of parameters. For the completing the iterative process, it is necessary to use suitable norms. One of them could be

$$\|n\| = \frac{(\alpha^{i+1})^{T}.\alpha^{i+1} - (\alpha^{i})^{T}.\alpha^{i}}{(\alpha^{i+1})^{T}.\alpha^{i}} \leq 0.001,(0.0001) \tag{14.36}$$

Using the terminology of the Newton-Raphson iteration, we have

$$\boldsymbol{K}_{INC} = \boldsymbol{J} \tag{14.37}$$

The incremental stiffness matrix is the same as the Jacoby matrix of the Newton-Raphson iteration. The Jacoby matrix characterizes the tangent plane to the non-linear surface and is defined as

$$\boldsymbol{J}_{ij} \equiv \frac{\partial}{\partial\alpha_{i}}\boldsymbol{K}^{*}_{Gnel-ij} \tag{14.38}$$

where $\boldsymbol{K}^{*}_{Gnel}$ is the system of non-linear (in our case cubic) algebraic equations.

14.2.9. Bifurcation point

In the case of the non-linear problems, many results can be obtained represented by many paths (curves) illustrating relation of load versus the displacement parameters. Especially in the case of the stability problems, stable and unstable paths should be distinguished.

The global potential energy represents the surface. The local minimum of this surface is the point of stable path of the non-linear solution. From the theory of the quadratic surfaces for the local minimum, the Jacoby matrix (in our case, the incremental stiffness matrix) must be positively defined and all the principle minors must be positive as well

$$D = \left|\boldsymbol{K}_{INC}\right|_{\det} > 0,\ D_{k} > 0 \tag{14.39}$$

If any condition of Eq. (14.39) is not satisfied, the path is unstable. The point between the stable and unstable paths is called ***the bifurcation point***. In the bifurcation point, we have

$$D = \left| \boldsymbol{K}_{INC} \right|_{\det} = 0 \tag{14.40}$$

14.2.10. Vibration of the structure

The conditional equations have been arranged as a dynamic process. The static behaviour is taken as a partial problem. From the viewpoint of the dynamic, we consider only the problem of the vibration. We are able to evaluate the vibration of the structure in different load levels including the effects of initial imperfections.

We assume the structure in equilibrium and zero increment of the load

$$\Delta \boldsymbol{f}_{EXT} = \boldsymbol{0} \tag{14.41}$$

The system of conditional equations (Eq. 14.25) will be reduced

$$\boldsymbol{K_M} \Delta \ddot{\alpha} + \boldsymbol{K}_{INC} \Delta \boldsymbol{\alpha} = \boldsymbol{0} \tag{14.42}$$

Related to the increments of the displacements parameters, this system represents a homogeneous differential equation with constant coefficient. The solution has the mode

$$\Delta \boldsymbol{\alpha} = \Delta \overline{\boldsymbol{\alpha}} \sin(\omega t) \tag{14.43}$$

where ω is the circular frequency. Putting this into Eq. (14.42), we get

$$-\omega^2 \boldsymbol{K_M} \Delta \overline{\boldsymbol{\alpha}} \sin(\omega t) + \boldsymbol{K}_{INC} \Delta \overline{\boldsymbol{\alpha}} \sin(\omega t) = \boldsymbol{0} \tag{14.44}$$

The non-trivial solution leads to the problem of eigenvalues and eigenvectors

$$\left| \boldsymbol{K}_{INC} - \omega^2 \boldsymbol{K_M} \right|_{\det} = 0 \tag{14.45}$$

The eigenvalues represent the squares of circular frequencies, and eigenvectors are the parameters of the modes of the vibration.

Note. Incremental stiffness matrix includes level of the load, deformation of structure and initial imperfections as well.

14.3. Stability and vibration

14.3.1. Vibration of simply supported column loaded in compression

In Part 14.2.5, the derivation has been started by using the Hamilton's principle and generally prepared the conditional equation for the dynamic process. In Part 14.2.10., we have arranged the equations for the evaluation of the vibration.

Simple and interesting example is the vibration of the imperfect column. For the application of the action of the force, we must suppose one support as the hinge and the other support as the roller (the sliding support (Fig 14.3.)). (Note: The column is displayed in horizontal position.)

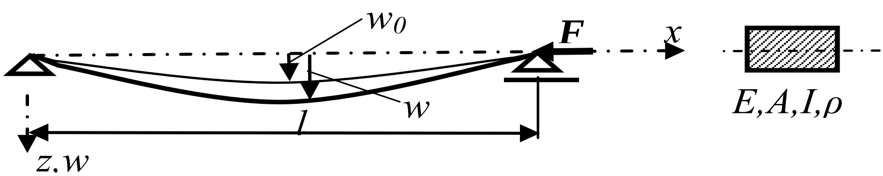

Fig. 14.3. Simply supported column with initial displacement

The axial inertial forces are neglected and the displacement functions are

$$w=\alpha_1 \sin\frac{\pi x}{l},\quad w_0=\alpha_0 \sin\frac{\pi x}{l},\quad u=\left[x, \sin\frac{2\pi x}{l}\right]\begin{Bmatrix}\alpha_2\\ \alpha_3\end{Bmatrix}$$

The parameters of axial displacements are

$$\alpha_2=-\frac{F}{EA}-\frac{\pi^2}{l^2}\left(\alpha_1^2-\alpha_0^2\right),\quad \alpha_3=-\frac{\pi}{8l}\left(\alpha_1^2-\alpha_0^2\right)$$

The equation of the static behaviour can be arranged in the form

$\overline{F}=\left(1-\dfrac{\alpha_0}{\alpha_1}\right)$, where $\overline{F}=\dfrac{F}{F_{EU}}$, $F_{EU}=\dfrac{\pi^2 EI}{l^2}$ is Euler's elastic critical force.

The incremental stiffness matrix is $\boldsymbol{K}_{INC}=\dfrac{\pi^4 EI}{l^4}\dfrac{l}{2}-\dfrac{\pi^2}{l^2}\dfrac{l}{2}F$.

Putting this into Eq. (14.45), obtained result is

$$\omega^2=\omega_0^2.\left(1-\overline{F}\right) \tag{14.46}$$

where $\omega_0^2 = \dfrac{\pi^4 EI}{\rho A l^4}$ is the square of the circular frequency of the simply supported column.

We have obtained a trivial result of the linear relation of the square of the circular frequency and the internal force. It can be seen that during the free vibration the initial displacements do not affect the free vibration.

14.3.2. Vibration of simply supported column loaded fixed supports

The result represented by Eq. (14.46) in the case of the level of the load as the elastic critical load gives the zero frequency. This is out of reality. For example, the miner foreman knocks on the columns. The low tone (the low frequency) means the small force inside the column and the column must be wedged. The high tone (the high frequency) means the high level of the load and the additional columns must be used.

To improve the obtained result the following arrangement must be done (Fig. 14.4)

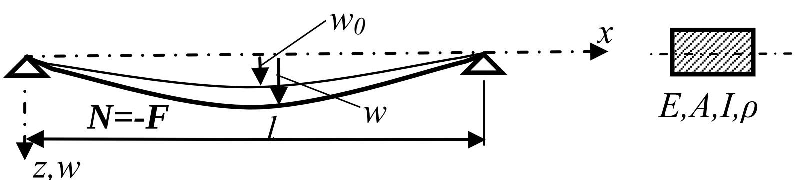

Fig. 14.4. Simply supported column with initial displacement - fixed support

For the displacements and the initial displacements, we take

$$w = \alpha_1 \sin(\pi x / l)\,,\; w_0 = \alpha_0 \sin(\pi x / l)\,,\quad u = \left[x, \sin(2\pi x / l)\right]\!.\!\left[\alpha_2, \alpha_3\right]^T$$

But for the increment of the displacement, we assume

$$\Delta w = \Delta\alpha_1 \sin(\pi x / l)\,,\quad \Delta u = \Delta\alpha_3 . \sin(2\pi x / l)$$

Now, different basic variational functions are used for the displacements and for the initial displacements.

Finally, the incremental stiffness matrix is

$$\boldsymbol{K}_{INC} = \frac{\pi^4 EI}{l^4}\frac{l}{2} - \frac{\pi^2}{l^2}\frac{l}{2}F + EA\frac{\pi^4}{l^4}\frac{l}{2}\frac{\alpha_1^2}{2}$$

Then we get the expression for the square of the circular frequency

$$\omega^2 = \omega_0^2 . \left(1 - \overline{F} + \frac{1}{2} \frac{\alpha_1^2}{r^2} \right) \tag{14.47}$$

where $r = \sqrt{\frac{I}{A}}$ is the radius of inertia.

Thus, the result close to reality has been obtained (Fig. 14.5). The displacement parameter „α_1“ is the function of the initial displacement and the level of the load. It means that the initial displacement enters the problem. If the load limits the level of the elastic critical load, the displacement and the frequency limits the infinity.

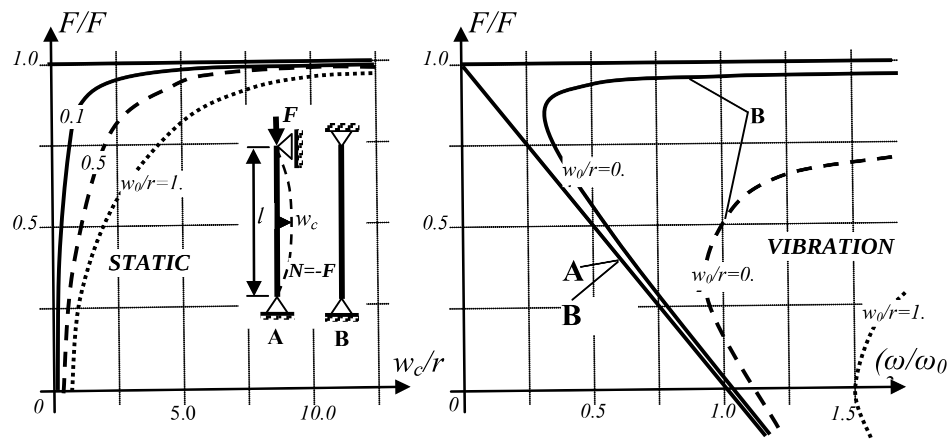

Fig. 14.5. Stability and vibration of imperfect column

This example represents an advantage of the separation of the basic variational functions for the displacements and for the increments of the displacements.

14.3.3. Initial displacement as the second mode of buckling

A particularly interesting problem is the influence of the mode of the initial displacement. In the previous part, we have supposed the initial displacement in the same mode as the first buckling mode (the mode of buckling related to the lowest elastic critical load). Due to that to obtain the solution by the analytical way was rather easy. The FEM has been used for the solution of more complicated examples.

Fig 14.6 presents the solution of the buckling and the vibration of the column when the initial displacement has the mode related to the second mode of buckling.

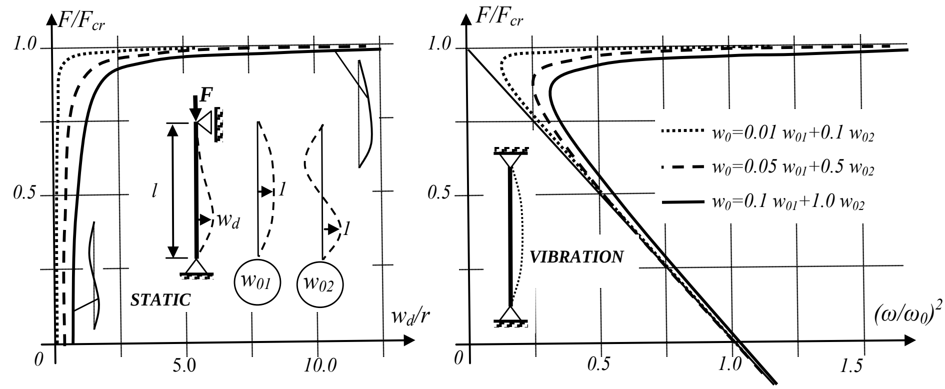

Fig. 14.6. Stability and vibration of imperfect column with the initial displacement as the second mode of buckling

Note. A lot of examples have been solved using the FEM. The obtained results can be presented in the dimensionless mode.

These results enable us to note some peculiarities. Even the initial displacement has the same mode as the second mode of the buckling ("*the mode 2*"), the collapse mode of the column is "*the mode 1*". The lowest elastic critical load is the maximum load. The mode of the vibration is "*the mode 1*" in all cases.

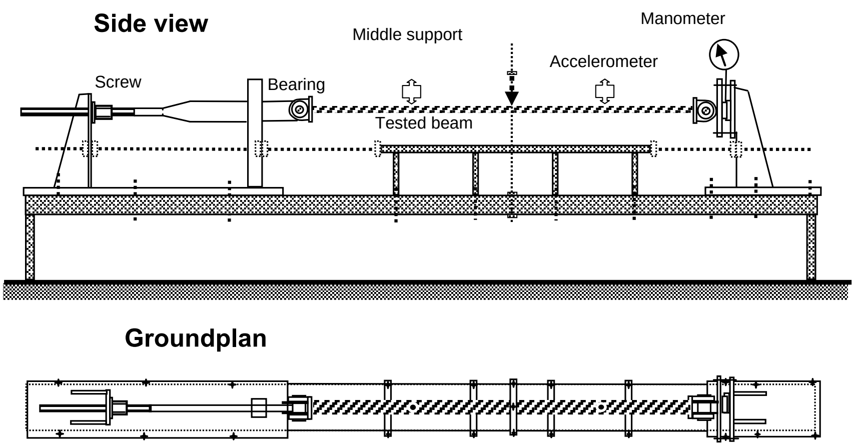

Fig. 14.7. Scheme of the test set-up

14.3.4. Experimental verification

The presented theoretical solutions are pointing to a substantial difference in the vibration of the beam at the moment when the critical load is reached. Considering sliding supports, the frequency should be zero. When supports are fixed, the frequency limits in infinity. This curiosity has been verified by an experiment.

The equipment for experimental verification of stability and vibration of beams loaded by pressure is shown in Fig. 14.7 and 14.8.

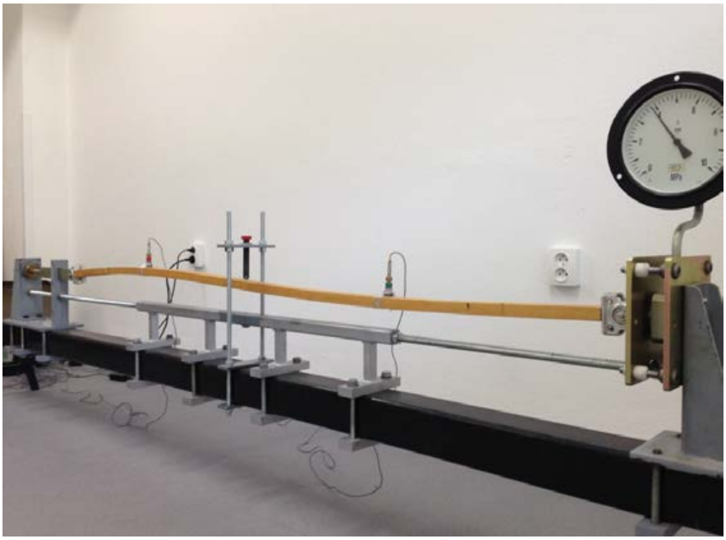

Fig. 14.8. General view of the test

The force (the load) is produced through the screw with a slight gradient (gradient 1.5 mm, average 30 mm), it means the load with the controlled deformation. The hinges are created by ball bearings in the jaw. The force is measured by manometer. The deflections are measured by mechanical displacement transducers fixed to the supporting steel structure. During measuring the frequency, the mechanical transducers are taken out and the accelerometer is attached.

Before the presentation of results, it is appropriate to make a note for specification of the mass matrixes due to end bearing (Fig. 14.9).

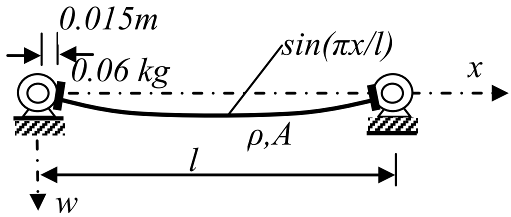

Fig. 14.9. Effects of end-bearing of beam to the mass matrix

The mass matrix taking into account the effect of the end bearing will be

$$\boldsymbol{K}_M = \rho A \frac{l}{2} + 2 * 0.06 * \sin \frac{\pi * 0.015}{l}$$

where the length of the beam is given in meters.

This effect of the end-bearing is dependent on the mass of the beam and is small (less than 1.5 %). To verify the dependence between the pressure force and frequency, the beams made of various types of materials have been analysed.

Steel hollow section profile Jäckl 30/15/1.5 mm

In the case of steel, the value of modulus of elasticity and the mass density are constant. When the exact dimensions of closed sections were measured, small problem occurred in measuring wall thickness.

The dimensions have been specified by measuring the weight of the profile. The rounded corners were considered in specification of cross-sectional characteristics. For further evaluation the following values were used:

Jäckl 29.9/14.8/1.53, $\mathrm{A} = 121.4\,\mathrm{mm}^2$, $\mathrm{I} = 4286.0\,\mathrm{mm}^4, \mathrm{r} = 5.94\,\mathrm{mm}, \mathrm{l} = 1450\,\mathrm{mm}$

$\mathrm{E} = 210000\,\mathrm{MPa}, \mu = 7850\,\mathrm{kg/m}^3, \mathrm{F}_{\mathrm{cr}} = 4225.1\,\mathrm{N},\ \omega_0 = 144.2\,\mathrm{s}^{-1}$

Timber beams

The modulus of elasticity of wood is an open question in the analyses of timber beams. In the presented measurements the critical load is identified at the moment of the increasing of the deformation without the increase of the force. Since the cross-sectional characteristics (the cross section, the moment of inertia) as well as the length of the beam have been known, using the Euler's elastic critical force, the modulus of elasticity can be evaluated. By measuring the weight of the profile, the mass density of wood has been easily and accurately evaluated. Subsequently, the natural circular frequency has been evaluated and two timber beams investigated.

$$Timber\,beam \quad 47/47\,mm,\ A = 2209\,mm^2,\ I = 406640\,mm^4,\ r = 13.57\,mm,$$
$$l = 2040\,mm, E = 10200\,MPa, \rho = 472\,kg/m^3, F_{cr} = 9836.7\,N,\ \omega_0 = 147.3\,s^{-1}$$
$$Timber\,beam \quad 42/32\,mm,\ A = 1344\,mm^2,\ I = 114888\,mm^4,\ r = 9.24\,mm,$$
$$l = 1650\,mm, E = 9750\,MPa, \rho = 454\,kg/m^3, F_{cr} = 4060.8\,N,\ \omega_0 = 1154.9\,s^{-1}$$

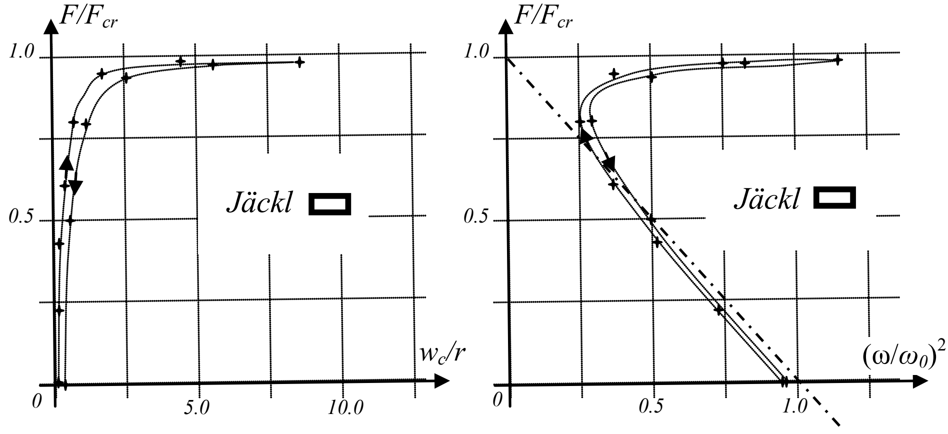

Fig. 14.10. Results from measurements of the steel hollow thin-walled section - Jäckl

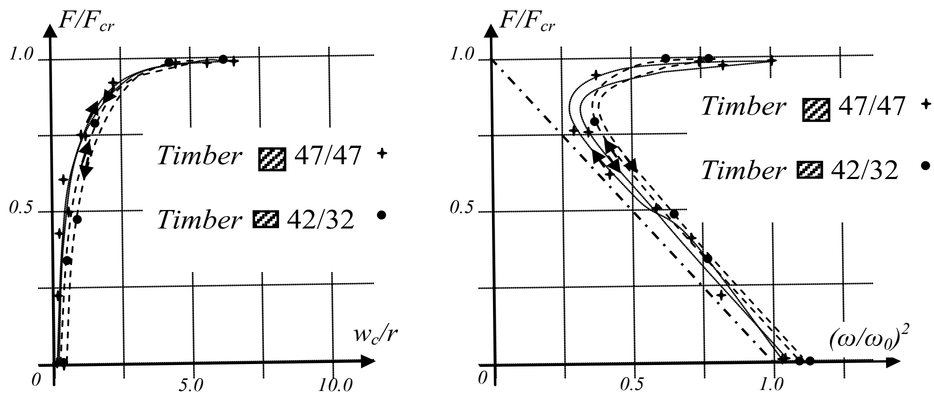

Fig. 14.11. Results from the measurements of the timber beams

The presented results confirmed undoubtedly a phenomenon that the frequency of the beam increases when the pressure force is near the critical level.

Continues beam

Fig. 14.12 presents the dimensions of investigated continues beam. Loading was implemented by steps (Fig. 14.13).

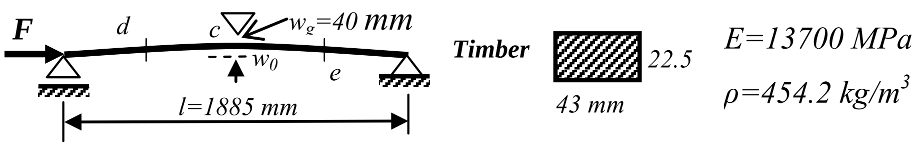

$$r = \sqrt{\frac{I}{A}} = 6.49\ mm \qquad F_{cr} = \frac{\pi^2 EI}{l^2} = 1661.8\ N \qquad \omega_0 = \sqrt{\frac{\pi^4 EI}{\rho A l^4}} = 100.2\ s^{-1}$$

Fig. 14.12. Dimension of continues timber beam

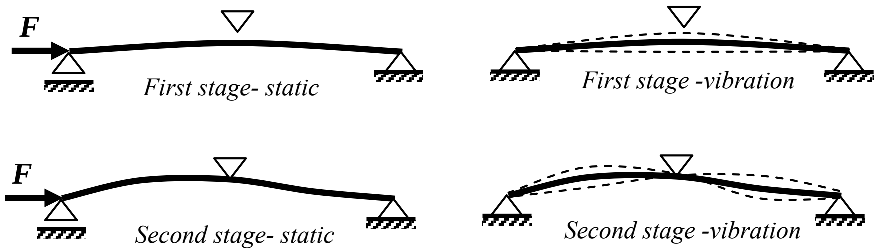

Fig. 14.13. Two states of continues beam behaviour

Figs. 14.14 and 14.15 present obtained results arranged in dimensionless form. Computers program had to be special improved for numerical evaluation of this example.

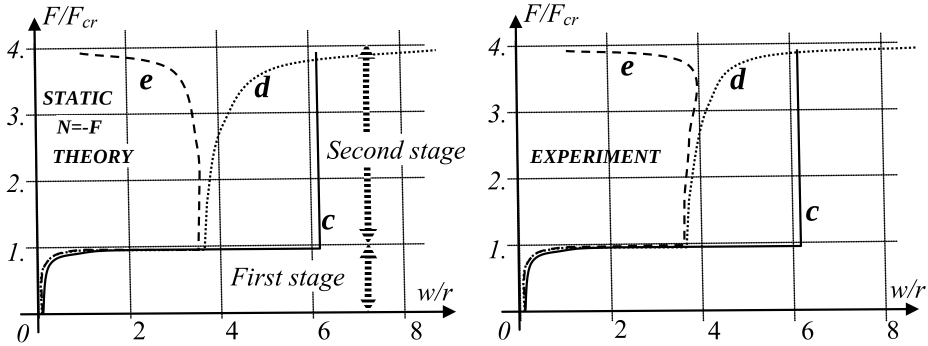

Fig. 14.14. Static behaviour of continues beam

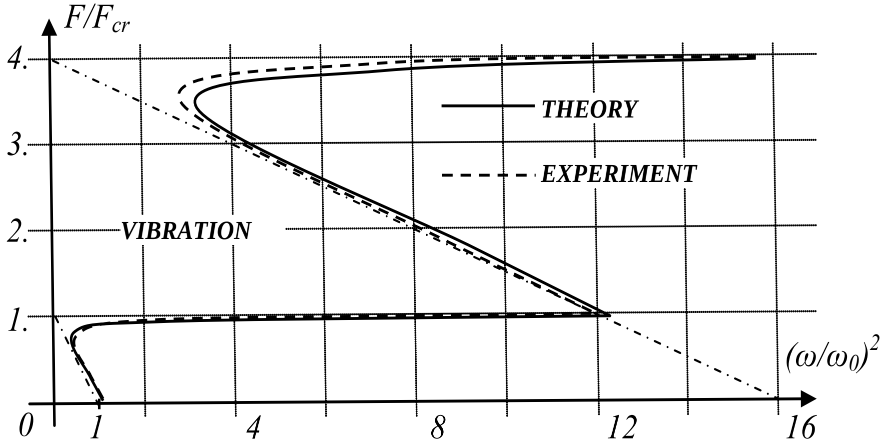

Fig. 14.15. Load versus square of circular frequency

14.4. Vibration and residual stresses

14.4.1. Vibration of simply supported column loaded in compression

Residual stresses (σ_w - Eq. (14.5)) are typical in the welded steel structures. Taking these stresses into increment of global potential energy and after doing variation we get term as product of increment of variation of derivation of displacement functions and residual stresses

$$\begin{aligned} &\ldots\int_V \delta\Delta\varepsilon.\sigma_w dV = \\ &\ldots\int_V \left(\delta\Delta u_{,x} + u_{,x}.\delta\Delta u_{,x} + w_{,x}.\delta\Delta w_{,x} + \delta\Delta w_{,x}.\Delta w_{,x} - z.\delta\Delta w_{xx}\right).\sigma_w dV \end{aligned} \tag{14.48}$$

In the case of the beam type of structures, the volume integration can be changed into the integration over the cross section and the integration over the length.

$$\ldots\int_0^a \left(\left(\delta\Delta u_{,x} + u_{,x}.\delta\Delta u_{,x} + w_{,x}.\delta\Delta w_{,x} + \delta\Delta w_{,x}.\Delta w_{,x}\right)\int_A \sigma_w dA - \delta\Delta w_{xx}\int_A z.\sigma_w dA \right) dx =$$

The residual stresses must be in equilibrium in the given cross section

$$\int_A \sigma_w dA = 0, \quad \int_A z.\sigma_w dA = 0 \quad \Rightarrow \quad \ldots\int_V \delta\Delta\varepsilon.\sigma_w dV = 0 \tag{14.49}$$

It is evident that *the residual stresses in the case of the beam structures have no influence on the circular frequency*.

Note. In the case of the statically indeterminate structure, Eq. (14.48) is not valid and the residual stresses could have the influence on the vibration.

There is much different situation in the case of the plate structures. In this case, the volume integration is divided into the integration over the thickness and the integration over the neutral surface. The integration of the residual stresses over the thickness is not zero and thus

$$\ldots\int_V \delta\Delta\varepsilon.\sigma_w dV = \int_\Gamma \left(\int_{-t/2}^{t/2} \delta\Delta\varepsilon.\sigma_w dz \right) d\Gamma = \int_\Gamma \left(\delta\Delta\varepsilon \int_{-t/2}^{t/2} \sigma_w dz \right) d\Gamma \neq 0$$

Finally, *in the case of the plate structures, the residual stresses have an influence on the circular frequency*.

Effect of residual stresses on circular frequency has been proved by experiment [14.5] (Fig. 14.16). Some results are presented in Figs. 14.17 and 14.18.

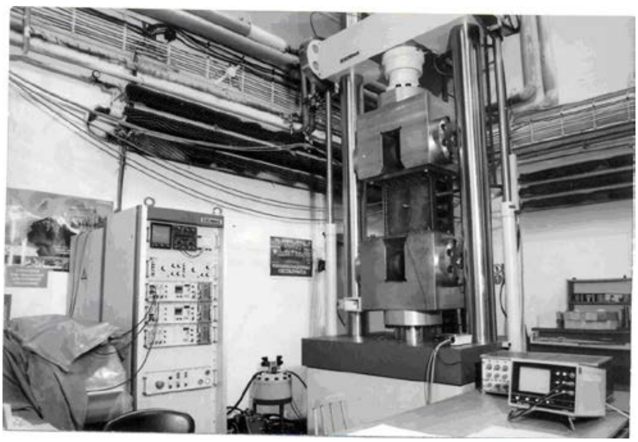

Fig. 14.16. General view of experimental arrangement for the test of thin-walled panel

14.5. Conclusion

The presented theory and results prove the influence of the natural frequency on the level of the load, on the geometrical imperfections and the residual stresses, too. This knowledge can be used as an inverse idea. Measuring of the natural frequencies provides a picture of the stresses and imperfections in a thin-walled structure. One idea how we can investigate the structure is presented in Fig. 14.19. Many times we are not able to measure the whole structure (global vibration) but even measuring local parts of structure (local vibration) can give us valuable results.

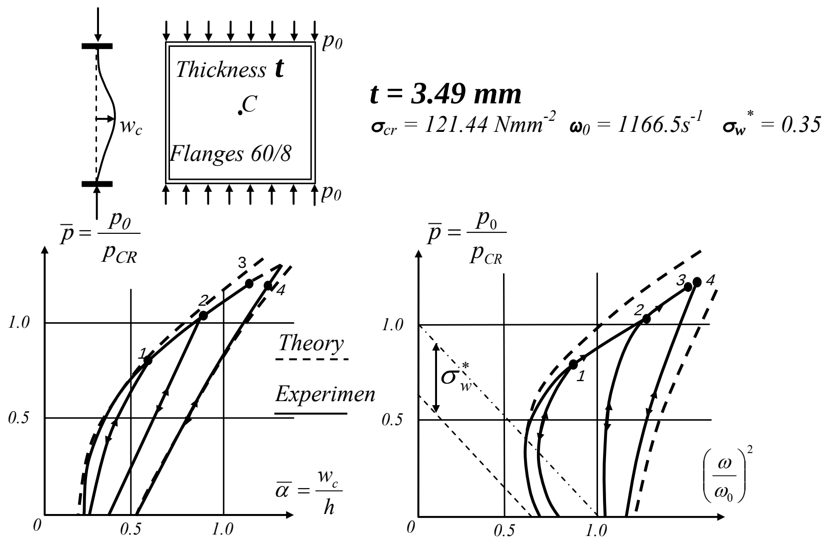

Fig. 14.17. Comparison of theoretical and experimental results for the steel panel with t = 3.49 mm thick web

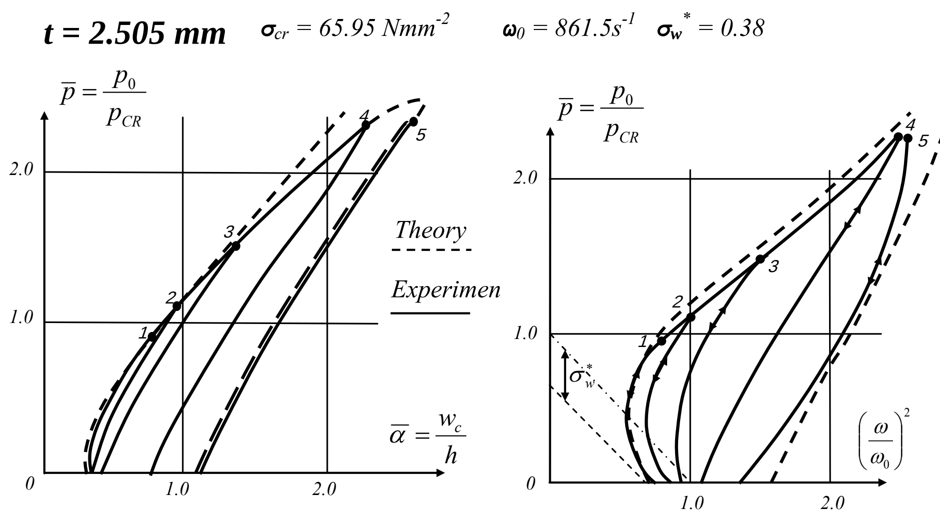

Fig. 14.18. Comparison of theoretical and experimental results for the steel panel with t = 2.505 mm thick web

It is true that the relation of frequencies versus stresses and imperfections represents a sophisticated theory, but it is unlikely an obstacle for further investigation.

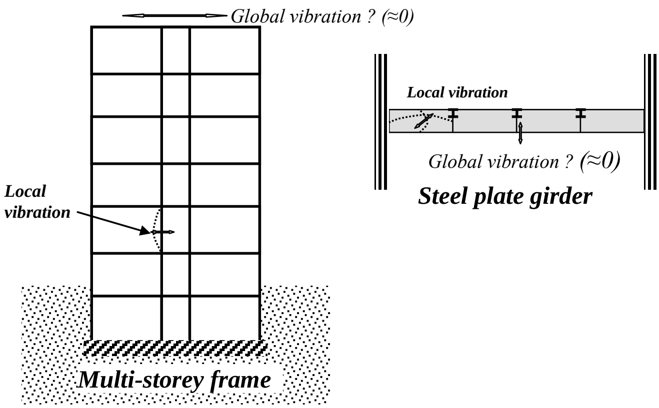

Fig. 14.19. Scheme for non-destructive investigation of structure properties

14.6. References

14.1 Bažant Z. P., Cedolin L., Stability of Structures: Elastic, Inelastic, Fracture and Damage Theories. Oxford University Press, New York, Oxford 1991.

14.2 Bolotin V.V., The Dynamic Stability of Elastic System. CITL. Moscow 1956 (In Russian. English translation by Holden Day. San Francisco 1994.)

14.3 Burgreen D., Free Vibration of Pined Column with Constant Distance Between Pin-ends. J. Appl. Mechan., 18, 1951, pp. 135-139.

14.4 Kolakowski K., Kowal-Michalska K., Statics, Dynamics and Stability of Structures, Vol. 2. Statics, Dynamics and Stabilty of Structural Elements and Systems. Quick-Druck, Lodz 2012.

14.5 Krolak M., Mania R.J., Statics, Dynamics and Stability of Structures, Vol. 1. Stability of Thin-Walled Plate Structures. Quick-Druck, Lodz 2011.

14.6 Ravinger J., Vibration of an Imperfect Thin-walled Panel. Part 1: Theory and Illustrative Examples. Part 2: Numerical Results and Experiment. Thin-Walled Structures, 19, 1994, pp. 1-36.

14.7 Ravinger J., Švolík J., Parametric Resonance of Geometrically Imperfect Slender Web, Acta Technica CSAV, 3, 1993, pp. 343-356.

14.8 Ravinger J., Stability & Vibration. SUT Bratislava 2012.

14.9 Volmir A.S., Non-Linear Dynamic of Plates and Shells, Nauka, Moscow 1972 (In Russian).

15.

Patch loading on steel girders

When an I-shaped or a box steel girder is subjected to a loading (or a reaction) which is acting over very small range on a web plate, generally, a transverse stiffener is to be installed at the location of the loading. However, in some cases, it is difficult to install a stiffener at the location of the loading. In such case, the girder falls into a very severe loading situation, and the strength of the girder under the severe situation becomes very important problem.

Such a problem is known as "the problem of a patch-loaded web plate". In this chapter, at first, the outline of the patch-loading problem on the steel girders is introduced, and then three procedures to estimate the strength of a patch-loaded web panel are described.

15.1. Outline of a patch loaded web panel

15.1.1. General view on a patch loaded plate

A patch-load on a steel girder is often found in the following two situations.

One of the examples of the patch-loaded web plate is a girder used as a crane rail. Fig. 15.1 shows a girder as a crane rail installed in a manufactory building. In this photo, we can find a crane beam is supported by rail girders, and it is running on the girder. The rail girder has, of course, transverse stiffeners. However, when the crane beam is running on the rail girders, the wheel of the crane beam shall be passing the location where no stiffener is installed. Thus, it becomes a typical "patch-loading" problem.

The second example is a steel girder erected with the launching method (or push-out method). With this erection method, a steel girder, which is assembled on the landside, is supported by a temporary launching shoe, and it will be sliding (or pushed) towards the opposite bank as shown in Fig. 15.2. This erection method is classified into some types. The typical types of the launching method are illustrated in Fig. 15.3. In Fig. 15.3(a) or Fig. 15.3(b), girder is on a roller or a sliding shoe, and is pushed by a jack. The method in Fig. 15.3(c) is somewhat complex. In this method, at first, the girder is supported by a temporary shoe on a sliding bed, and the horizontal jack pushes the shoe, and in the result the girder moves rightward in the figure. After pushing, the girder is jacked up by another jack for the vertical direction, and the horizontal jack and the shoe go back to their original locations. This method requires the complex equipment for pushing out, however, the equipment can keep on the same location throughout the erection process.

Fig. 15.1. Crane rail

Fig. 15.2. Box girder erected with launching method

The launching method, as the girder erection method, does not require a temporary support in the main span, because all equipment can be set on the landside. Therefore, this method is often adopted at the location where no scaffolding is available such as erection of an overbridge across a railway.

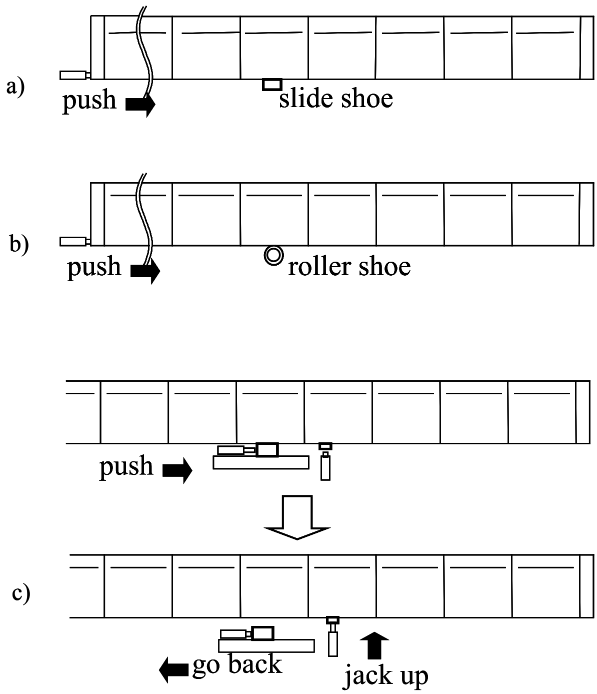

Fig. 15.3. Girder on launching shoe : a) sliding shoe, b) roller shoe, c) push-out equipment

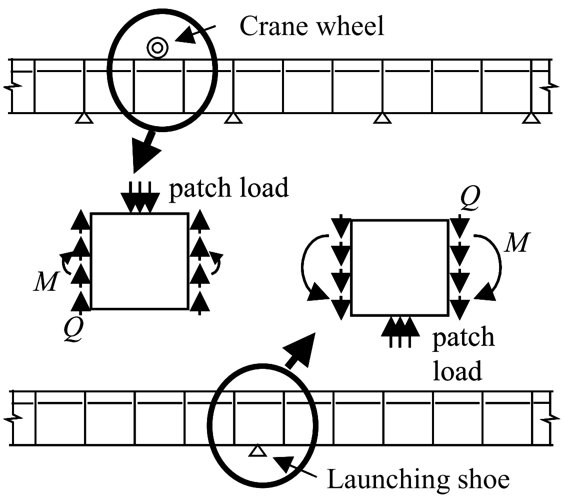

Fig. 15.4. Girder as crane rail and girder erected with launching method

To solve a patch-loading problem of a girder as a crane rail or a girder erected by the launching method, the stress in the web panel of the girder is to be known. Here, a difference is detected between above two examples when estimating stress in the web panel.

As it is found in the Fig. 15.1, a girder used as a crane rail is generally supported at many points with the short interval, and therefore, the web panel is subjected to very small bending moment. Thus, in a web panel in a crane rail, the normal stress for the vertical direction caused by the crane weight shall be dominant together with shear stress (upper part of Fig. 15.4). In the latter example, the girder is supported with longer span, and the web plate is subjected not only to the patch-load and shear but also to the relatively larger bending moment as illustrated in the lower part of Fig. 15.4. Therefore, in this case, behavior of the web panel may be influenced by the bending moment, and effect of the moment shall be an important problem.

15.1.2. Studies on patch loaded plate

In the earlier stage, the study on the patch-loading problem was made with a lone plate as illustrated in Fig. 15.5, i.e. a lone plate subjected to only a set of concentrated compression loadings or a set of concentrated load with shear. Studies of this stage are made by, for example, Wilkesmann [15.1] or Khan [15.2, 15.3].

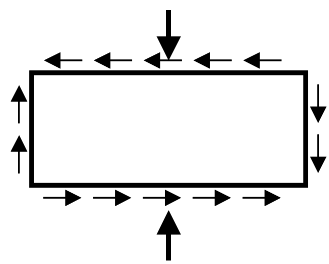

Fig. 15.5. Edge-loaded plate

After the above stage, studies on a patch-loaded girder, not a lone plate, with flanges and stiffeners can be found.

Herzog made studies on the patch loaded web plate with flanges [15.4, 15.5], and the patch loaded web plate in which stiffeners are installed is studied by Kutzelnigg [15.6]. Studies on a plate subjected to the patch load together with bending in the earlier stage are made by, for example, Rockey [15.7] or Warkenthin [15.8]. Roberts et al. presented a series of studies in which a simple procedure to estimate the strength of a patch loaded plate by using the mechanism solution [15.9, 15.10]. The mechanism solution on this problem is described in the next section of this chapter. Recently, Graciano et al. made a series of studies on the patch loaded web plate [15.11, 15.12, 15.13, 15.14], and Chacón presents a study on the stiffened girder [15.15]. In this chapter, first, the mechanism solution on the patch loaded plate is briefly introduced, and then design procedure on girders on launching shoe is described.

15.2. Collapse behaviour

15.2.1. Mechanism solution

In a guide book on the steel structures, the collapse pattern of a patch-loaded web panel is classified into two types; (1) web crippling, with which the web panel shall deform very locally near the loading, (2) web buckling over the full depth of the girder [15.16].

In 1964, Roberts and Rockey proposed a collapse mechanism of a patch-loaded web plate with considering the test results [15.9]. According to [15.9], a web plate collapses with the deformation pattern of crippling in the upper zone of the web panel, as illustrated in Fig. 15.6, and the plastic hinges arise in the upper flange. In this deformation pattern, out-of-plane deformation scarcely arises in the central part of the web panel. Therefore, Roberts et al. modelized the web deformation as shown in Fig. 15.7(a), and proposed the idealized collapse mechanism with three yield lines in Fig. 15.7(b).

On the other hand, a difference of the patch length, i.e. length of the patch-loading defined in Fig. 15.8, is found between two examples mentioned in the section 1 of this chapter. The patch length caused by a crane wheel is generally small. Therefore, many studies on the patch-loading adopt the ratio of the patch length against the web panel width as around 0.1.

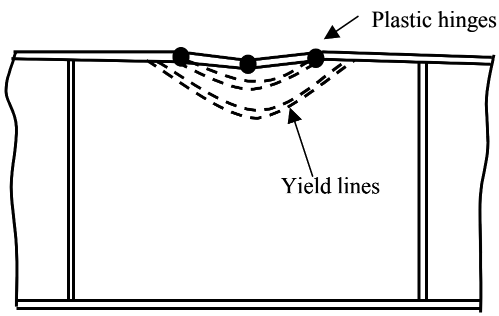

Fig. 15.6. Collapse mode by Rockey et al. [15.9]

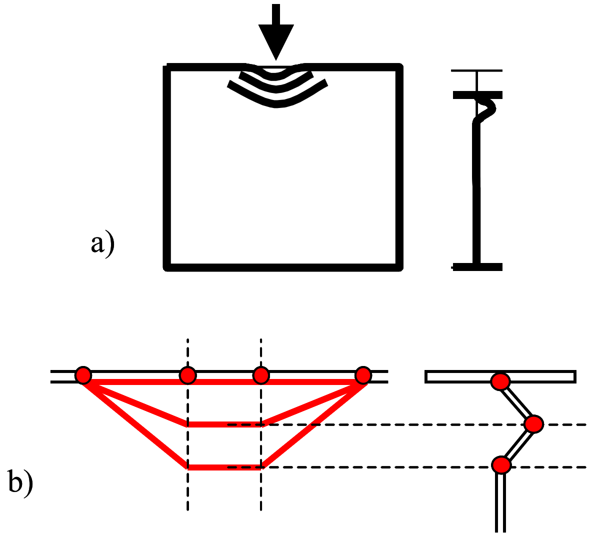

Fig. 15.7. Proposed collapse mode by Rockey et al. [15.9]:
a) collapse behaviour, b) idealized collapse mechanism

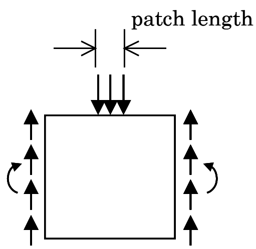

Fig. 15.8. Definition of Patch length

However, a launching shoe gives relatively larger patch length because a launching shoe generally has a certain dimension. This difference of the patch length often brings a difference of the collapse behaviour of the web panel. According to studies on the patch-loading problem by some researches including the author of this chapter, web crippling occurs mainly with the smaller patch length such as a crane wheel, and web buckling arises under the relatively large patch length.

Shimizu et al. carried out a series of experimental tests on the I-shaped steel girders on the launching shoe [15.17, 15.18]. The photo in Fig. 15.9 shows an example of the test setup by Shimizu and in Fig. 15.10 the layout of the test model is illustrated. In the test, the model girder is placed in the upside-down position and the patch-load as the reaction on the launching shoe is replaced with a loading by a jack on the bottom flange (placed on the upper side during the test) through a loading pad corresponding with the shoe. The patch length of the test is decided through the dimension of the launching shoe, and the ratio of the patch length against the web panel width is set as 0.3 or 0.5.

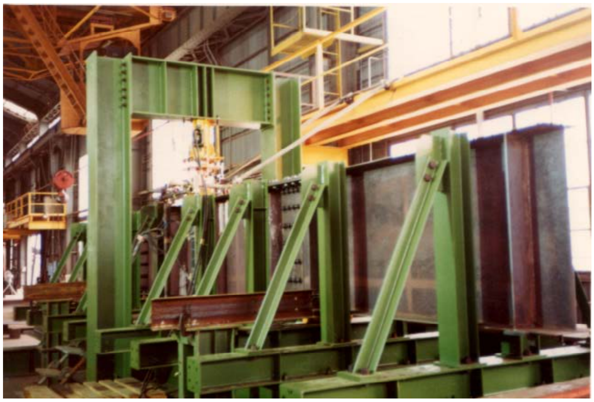

Fig. 15.9. Test setup of girder on launching shoe by Shimizu [15.17, 15.18]

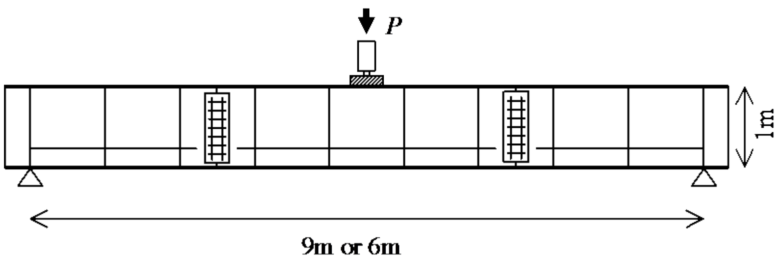

Fig. 15.10. Test layout of patch loaded girder [15.17, 15.18]

In Fig. 15.11, a typical web deformation pattern obtained through the test is shown. In this photo, the out-of-plane deformation is observed in the upper part of the web plate, and yield lines are found. However, unlike the deformation pattern in Fig. 15.6 or Fig. 15.7, the out-of-plane deformation of the web panel still arises just under the folded zone, and only two yield lines are found. Thus, this deformation pattern is modelized as in Fig. 15.12 with two yield lines [15.25, 15.26].

Using these collapse mechanisms, the ultimate load is obtained easily with the concept of the plastic design. That is, equating the external virtual work due to the vertical deformation of the flange multiplied by the patch-loading and the internal virtual work caused by rotation of the plastic hinges and the yield lines, the ultimate magnitude of the patch-loading can be estimated. In this method, effect of bending moment of the girder cannot be taken into account. Therefore, this method is applicable to the crane rail which may be subjected to small bending moment, however, for the girder erected with the launching method, it is not suitable to use the mechanism solution because a girder on a launching shoe generally is subjected to bending moment in addition to the patch-load.

Fig. 15.11. Typical failure mode of patch loaded girder [15.17, 15.18]

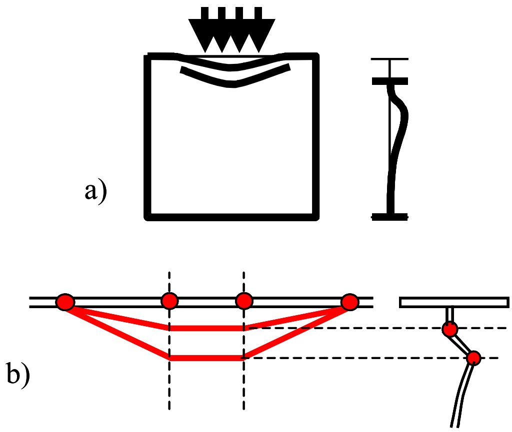

Fig. 15.12. Collapse model having two yield lines: a) collapse pattern, b) idealized collapse mechanism

15.2.2. Girders on launching shoe

A simple steel girder shall be subjected to the positive bending moment after the erection is completed. Therefore, when a longitudinal stiffener is installed on the web plate, the stiffener is arranged at the top part of the web, and on the bottom part of the web, longitudinal stiffener is not required. However, when a girder is erected with the launching method, the girder shall be subjected to negative bending moment temporary, and the compression stress for longitudinal direction arises in addition to the vertical compression caused by the reaction at the launching shoe. Therefore, the web plate on a launching shoe should be sometimes stiffened not only at its top part but also at its bottom part.

The “normal” longitudinal stiffener installed for the “normal” positive moment of the girder is generally the location at around 1/5 of the web depth from its top. However, on the “additional” stiffener at the bottom part of the web of the launching shoe, the location of 1/5 of the web depth from the bottom is not always optimum.

The collapse pattern on a launching shoe may be different with the existence and location of the longitudinal stiffener and the magnitude of the bending moment of the girder.

Fig. 15.13 shows the collapse pattern classification of a web plate on a launching shoe with the patch relatively large length (0.3 times of the panel width) [15.21]. This figure indicates that the collapse pattern can be classified into 4 types as “i”, “I”, “II” and “III”.

In the every case in Fig. 15.13, at the earlier stage, yielding caused by in-plane compression near the launching shoe arises. After the first stage, in the collapse pattern “i” and “I”, the web plate begins to deform for the out-of-plane direction, and the two yielded zones arise at the bottom part of the web near the launching shoe, and reaches to the final stage. These yielded zones are formed by out-of-plane bending of the plate for the alternate directions, and the in-plane yielding observed at the earlier stage vanishes after the first stage. In the collapse patterns “II” and “III”, the in-plane yielded zone develops, and in the pattern “II”, out-of-plane deformation begins to develop in the next stage. Finally, this pattern has three yielded zones; one is the in-plane yielding, and two are caused by out-of-plane bending as similar to the patterns “i” and “I”. In these patterns of “i”, “I” and “II” , two yield lines are formed at the final stage. In the pattern “III”, the out-of-plane deformation of the web plate scarcely arises, and reaches to the final stage with only the in-plane yielding at the bottom of the web panel.

The collapse pattern “i” is found only in the web plate with no additional stiffener.

When an additional longitudinal stiffener is installed in the web panel, collapse pattern “I”, “II” or “III” shall arise, according to the web thickness and the location of the additional stiffener. With the relatively large thickness, the collapse pattern III shall arise. When the web plate is having a little smaller thickness, collapse pattern II arises with the additional stiffener installed at the location of 1/10 of the web depth, and with the stiffener location of 1/5, pattern

III again appears. With much smaller thickness, pattern I with the stiffener location of 1/10 and pattern II with the location of 1/5 arise.

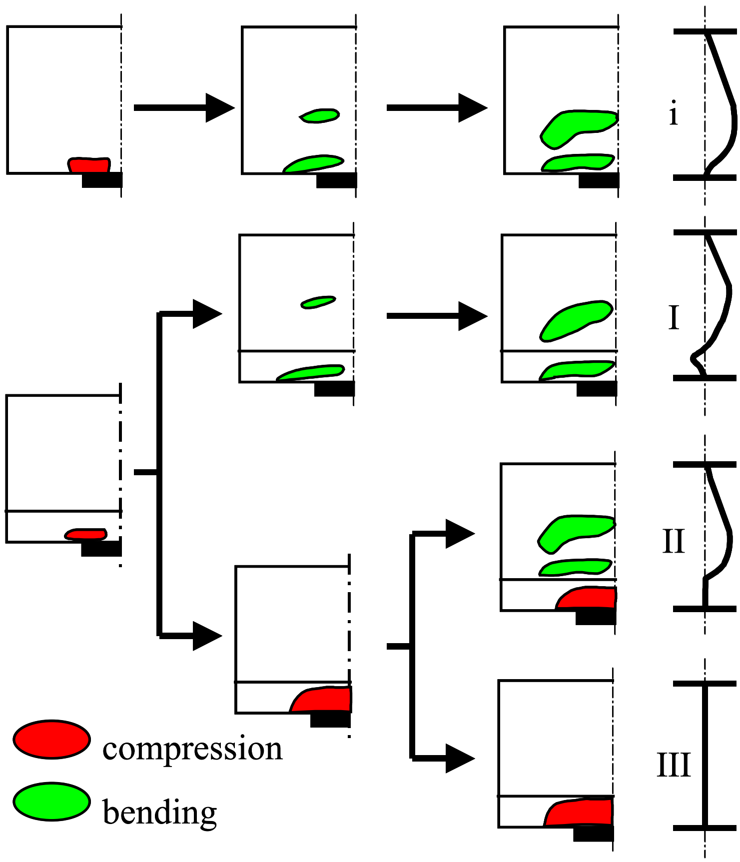

Fig. 15.13. Collapse mode classifications

Within these collapse patterns, for the pattern III, the plastic design concept cannot be applicable because no yield line arises and the collapse mechanism is not defined.

According to the results in [15.21], existence of the bending moment of the girder does not influence the collapse behaviour, and the web panel subjected to not only the reaction but also the bending moment shows the same collapse patterns to those with no moment. However, the strength of the web plate subjected the moment is smaller by around 10-20% than the strength with no bending.

15.2.3. Solution with the co-relation formula

For the web plate on the launching shoe which shall be subjected to not only the reaction force but also bending, the correlation formula is often used to verify the strength. This correlation formula is derived from von Mises's yield criterion which defines the equivalent stress. This method is generally used to verify the safety of the "normal" girder being subjected to bending and shear as illustrated in Fig. 15.14.

In the "normal" girder subjected to bending and shear, the normal stress σ_x for the x-axis (axis for the bridge) and the shear stress τ_{xy} arises, and the stress σ_y for the y-axis $\sigma_y = 0$. The well known Mises's formula of the equivalent stress for the 2-dimensions is Eq. (15.1).

$$\sigma_e = \sqrt{\sigma_x{}^2 - \sigma_x\sigma_y + \sigma_y{}^2 + 3\tau_{xy}{}^2} \tag{15.1}$$

Put σ_y= 0 in Eq. (15.1), it becomes Eq. (15.2).

$$\sigma_e = \sqrt{\sigma_x{}^2 + 3\tau_{xy}{}^2} \tag{15.2}$$

This must be less than the ultimate stress σ_r, and Eq. (15.3a) or (15.3b) can be obtained.

$$\sigma_e = \sqrt{\sigma_x{}^2 + 3\tau_{xy}{}^2} \le \sigma_r \tag{15.3a}$$

$$\sigma_e^2 = \sigma_x{}^2 + 3\tau_{xy}{}^2 \le \sigma_r{}^2 \tag{15.3b}$$

With this formula and the relation of the ultimate values of the normal stress and the shear stress $\sqrt{3}\tau_r = \sigma_r$, Eq. (15.3) becomes to Eq. (15.4).

$$\frac{\sigma_x{}^2}{\sigma_r{}^2} + \frac{3\tau_{xy}{}^2}{\sigma_r{}^2} = \frac{\sigma_x{}^2}{\sigma_r{}^2} + \frac{\tau_{xy}{}^2}{\tau_r{}^2} \le 1.0 \tag{15.4}$$

Replacing $\frac{\sigma_x}{\sigma_r} = \bar{\sigma}$, $\frac{\tau_{xy}}{\tau_r} = \bar{\tau}$, Eq. (15.4) can be rewritten as Eq. (15.5):

$$\frac{\sigma_x{}^2}{\sigma_r{}^2} + \frac{\tau_{xy}{}^2}{\tau_r{}^2} = \bar{\sigma}^2 + \bar{\tau}^2 \le 1.0 \tag{15.5}$$

This formula is very intuitional and easily understandable. That is, when the combination of the normal stress σ_x and the shear stress τ_{xy} falls within the circle illustrated in Fig. 15.15, it does not still reach to the ultimate state.

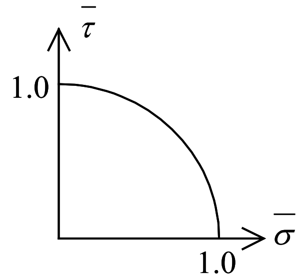

Fig. 15.14. Co-relation of normal stress and shear stress

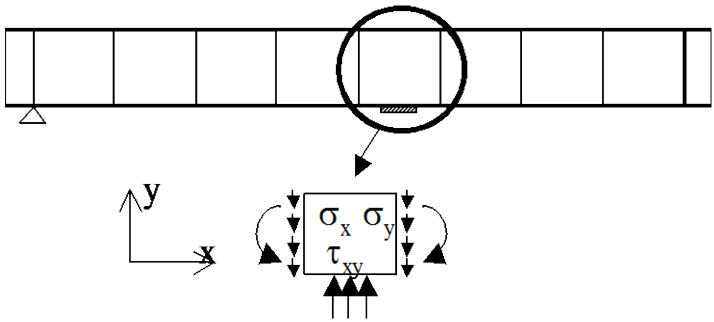

Fig. 15.15. Stresses in a web panel on a launching shoe

On the other hand, the web plate on the launching shoe in Fig. 15.15 is generally subjected to the normal stress for the vertical direction σ_y in addition to the normal stress caused by bending, σ_x, and the shear stress τ_{xy}. In this case, the formula corresponding with Eq. (15.3) becomes Eq. (15.6).

$$\sigma_e = \sqrt{\sigma_x^{\ 2} - \sigma_x\sigma_y + \sigma_y^{\ 2} + 3\tau_{xy}^{\ 2}} \leq \sigma_r \tag{15.6}$$

This formula can be rewritten as Eq. (15.7).

$$\frac{\sigma_x^{\ 2}}{\sigma_r^{\ 2}} - \frac{\sigma_x\sigma_y}{\sigma_r^{\ 2}} + \frac{\sigma_y^{\ 2}}{\sigma_r^{\ 2}} + \frac{\tau_{xy}^{\ 2}}{\tau_r^{\ 2}} \leq 1.0 \tag{15.7}$$

Thus on the web plate on the launching shoe, it does not become the "pure" correlation formula.

The principal design guidelines on the patch-loaded web plat on the launching shoe adopt the design formula with modified Eq. (15.7).

For example, DIN18800 Part 3 [15.22] specifies Eq. (15.8) to verify the strength of the web panel on the launching shoe.

$$\left(\frac{|\sigma_x|}{\sigma_{xpRC}}\right)^{e1} - V\left(\frac{|\sigma_x\sigma_y|}{\sigma_{xpRC}\cdot\sigma_{ypRC}}\right) + \left(\frac{|\sigma_y|}{\sigma_{ypRC}}\right)^{e2} + \left(\frac{|\tau|}{\tau_{pRC}}\right)^{e3} \leq 1.0 \qquad (15.8)$$

Here σ_{xpRC}, σ_{ypRC}, τ_{pRC} denote the ultimate stresses for the x, y directions and shear respectively, V denotes $V = \frac{|\sigma_x\sigma_y|}{\sigma_x\sigma_y}$, and e*1*, *e2*, *e3* are the reduction coefficients which defined with the table in the Code. It is found that this procedure is more complex than one with the "pure" correlation formula.

In the Japanese Guidelines for erection, design and installation of steel structures issued by JSCE (Japanese Society of Civil Engineers), Eq. (15.7) is rewritten simply and defines the verification formula as Eq. (15.9).

$$F_s\left\{\left(\frac{\sigma_b}{\sigma_{bcr}}\right)^2 + \left(\frac{\tau}{\tau_{cr}}\right) + \left(\frac{\sigma_p}{\sigma_{pcr}}\right)\right\} \leq 1.0 \qquad (15.9)$$

Here F_s denotes the safety factor, σ_b, σ_p, τ are stresses caused by the girder bending, reaction of the launching shoe and shear, and σ_{bcr}, σ_{pcr}, τ_{cr} are the buckling stresses [15.23].

Recently, in Japan, a new formula to verify the safety of the web plate on the launching shoe is proposed as Eq. (15.10) [15.24].

$$\left(\frac{\sigma_{xb}}{\sigma_{xbcr}}\right)^2 F_s^{\,2} + \left(\frac{\pm\sigma_{xc}}{\sigma_{xccr}}\right)F_s + \left(\frac{\gamma\sigma_y}{\sigma_{ycr}}\right)^2 F_s^{\,2} + \left(\frac{\gamma\tau}{\tau_{cr}}\right)^2 F_s^{\,2} \leq 1.0 \qquad (15.10)$$

This formula is similar to the Eq. (15.9), however, the normal stress for the x direction is separated into two parts; the stress caused by the girder bending, σ_{xb}, and the stress by the axial force for the x direction compression σ_{xc}. F_s denotes the safety factor and γ is the increase factor for the non-uniform distribution of the stress on the launching shoe.

While both Japanese formulae are simple, it seems to be lack in exactness because these procedures do not consider the term corresponding to $\frac{\sigma_x\sigma_y}{\sigma_r^{\,2}}$ in the Eq. (15.7).

Another problem in utilizing the formula based on Eq. (15.7) is how to deal the shear. The verification procedure based on the formula 15.7 supposes that the shear stress τ in the web panel distributes uniformly. This is generally true for the "usual" web panel subjected to bending and shear. This supposition can be considered with the shear force on the both edges of the web panel as illustrated in Fig. 15.16(a), and assumes that the shear is independent with the reaction of the launching shoe.

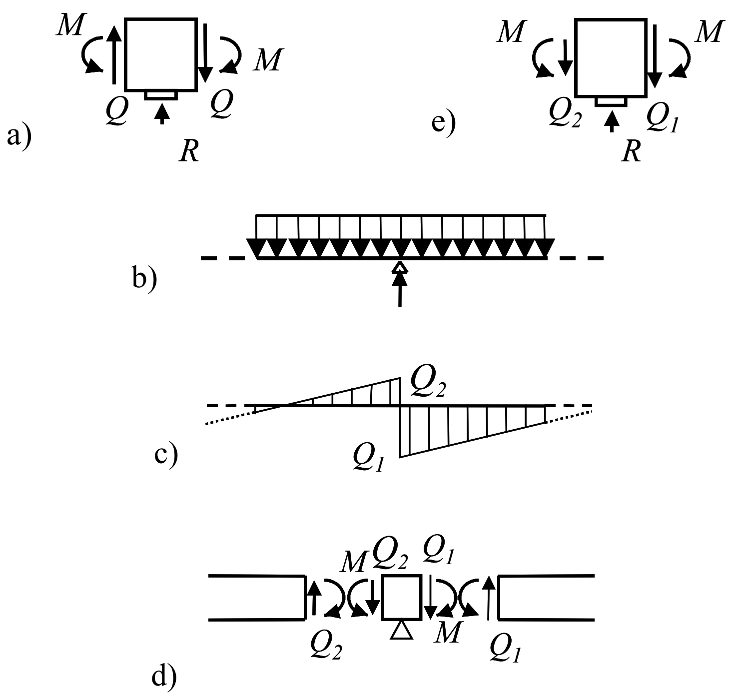

Fig. 15.16. Shear on launching shoe: a) "usual" forces on web panel, b) loading on launching shoe, c) shear diagram on launching shoe, d) forces near launching shoe, e) forces acting on web panel

Generally, a girder on a launching shoe is subjected to the reaction together with the dead load as illustrated in Fig. 15.16(b). Therefore, the shear force of the girder becomes as in Fig. 15.16(c). Thus, on the launching shoe, the moment and the shear become as shown in Fig. 15.16(d), and in the result the web panel on the launching shoe is subjected to the forces in Fig. 15.16(e). It should be noted that the sign of the shear changes in the panel, and the magnitude of the shear forces on the both edge of the panel, Q1 and Q2 in Fig. 15.16(d) or (e), not always equal to each other. In addition, this shear force is not independent to the reaction R, and $Q_1 + Q_2$ must be equal to R.

These facts suggest difficulty when Eq. (15.7) is utilized in this problem.

15.3. Buckling coefficient of web panel on launching shoe

In this section, the alternate idea to verify safety of a web panel on the launching shoe with using neither the plastic design procedure nor the correlation formula is introduced [15.25]. This method predicts the buckling coefficient of a web panel on the launching shoe.

It is supposed that a web panel on a launching shoe is being subjected to shear Q_1, Q_2 (corresponding to the reaction R of the shoe) and the bending moment M as mentioned in the previous section with Fig. 15.16(e). The reaction of the shoe R is R = Q1 + Q2. With these shear and moment, the web panel is receiving stresses σ_1, σ_2 and τ_1, τ_2 in Fig. 15.17(a), and the web width, web depth and the patch length are a, b and c respectively as in Fig. 15.17(b). Parameters used in this section are defined as follows:

- a aspect ratio of the panel, $a = a/b$;
- b patch length parameter (dimensionless patch length), $b = c/a$;
- ϕ moment-shear parameter, $\phi = \sigma_1/\tau_1$;
- γ shear parameter, $\gamma = \tau_1/\tau_2$;
- K_m buckling coefficient of the web panel subjected to no moment;
- K_R buckling coefficient of the web panel subjected to moment;
- μ reduction factor of the buckling coefficients, $K_R = \mu K_m$
- φ neutral axis parameter, $\varphi = \sigma_2/\sigma_1$.

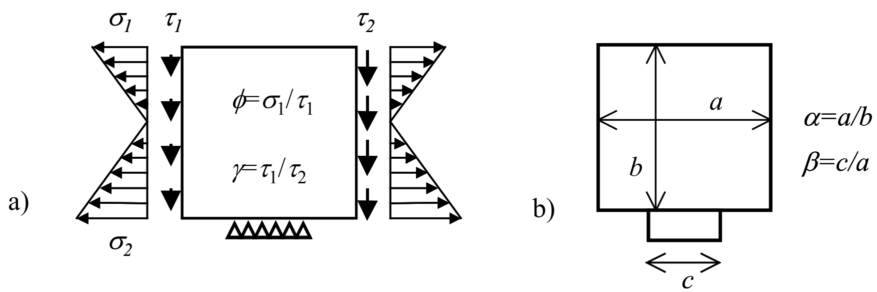

Fig. 15.17. Definitions used in this chapter: a) stresses, b) dimensions

The stress just above the shoe is defined as $\sigma_s = R/(c \times t_w)$ $= (|Q_1| + |Q_2|)/(c \times t_w)$, here c denotes the patch length, i.e. dimension of the launching shoe, and t_w the web thickness. When this stress reaches to the buckling stress $\sigma_{cr} = K_R \cdot \frac{\pi^2 E}{12(1-\nu^2)}\left(\frac{t_w}{b}\right)^2$, buckling of the web shall occur. K_R is the buckling coefficient of the web panel, and once K_R is obtained, buckling stress can be estimated.

In the study of [15.25], a series of numerical analyses are made on the web plate on a launching shoe with the various values of M, Q_1 and Q_2, aspect ratio of the web panel and the patch length (dimension of the launching shoe). In the analyses, the launching shoe is realized restraining the vertical displacement at the location of the shoe, and the reaction R is automatically introduced in the analyses.

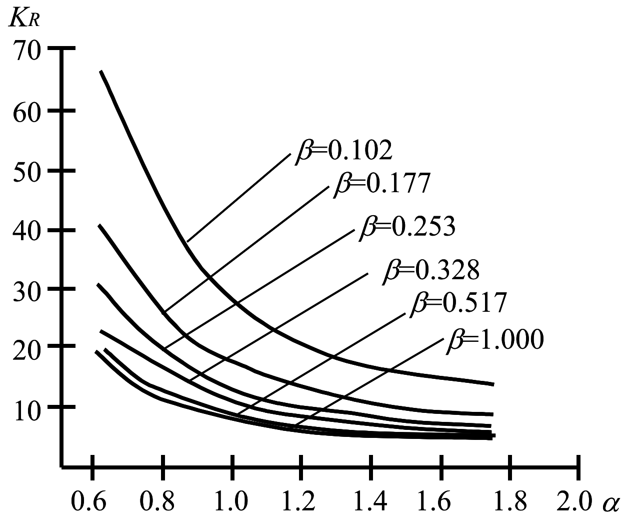

Fig. 15.18. Buckling coefficients for aspect ratio

In Figs. 15.18-15.19, demonstrative results on the buckling coefficients when the web panel is subjected to no moment, K_R, are plotted. These results are for the case that the web plate has the b depth of $b = 2200$ mm, web thickness t_w of $t_w = 11$ mm, and $E = 206$ GPa, $\nu = 0.3$, as summarized in Table 15.1, and subjected to no moment, i.e. $\sigma_1 = \sigma_2 = 0$ and in result $\phi = 0$. The web width a and the patch length c are variables, and the aspect ratio $\alpha = a/b$ and the dimensionless patch length $\beta = c/a$ are varied within $\alpha = 0.625 \div 1.750$ and $\beta = 0.102 \div 1.000$ respectively. The patch length $\beta = c/a = 1.000$ means that the launching shoe has the same dimension with the web width a.

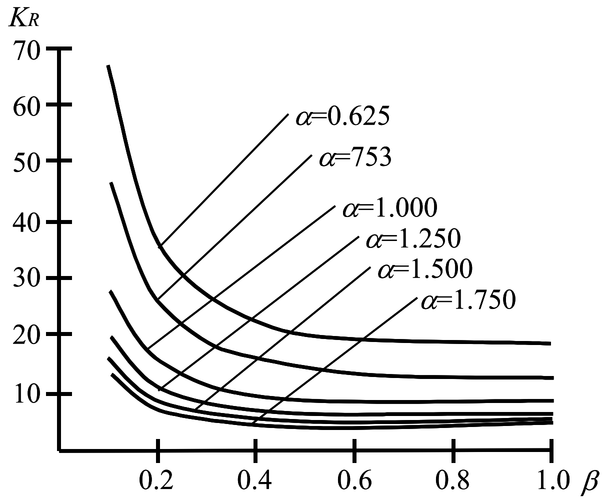

Fig. 15.19. Buckling coefficients for patch length

Table 15.1. Dimensions and material; properties of the demonstrative model [15.25]

Demonstrative model	Material parameters	Dimensions
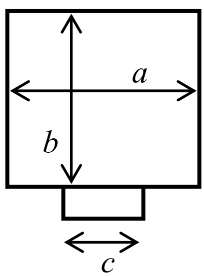	E = 206000 MPa γ = 0.3	a = variable b = 2200 mm c = variable t_w = 11 mm

When the web panel is subjected to the moment in addition to the shear (or the reaction), the strength of the panel shall become smaller. Fig. 15.20 shows the reduction factor μ for the moment-shear parameter ϕ. It is clearly found that the reduction factor μ decreases almost linearly for the magnitude of the moment. In Fig. 15.16 or Fig. 15.17, magnitude of shear on the both side Q_1 and Q_2, or τ_1 and τ_2 are different to each other. However, according to the study [15.25], the effect of the difference is very small, and therefore $\tau = (\tau_1 + \tau_2)/2$ can be used instead of τ_1 to estimate the moment-shear parameter $\phi = \sigma_1 / \tau_1$.

With these figures, formula to estimate the buckling coefficient is obtained empirically.

With referring Fig. 15.19, buckling coefficient of the web panel subjected no moment, K_R, can be expressed with the patch length parameter β as Eq. (15.11).

$$K_R = \frac{b_4}{\beta^4} + \frac{b_3}{\beta^3} + \frac{b_2}{\beta^2} + \frac{b}{\beta} + b_0 \tag{15.11}$$

The coefficients b_0-b_4 are estimated through Eq. (15.12) with the aspect ratio α.

$$b_i = C_{i3} \cdot \alpha^3 + C_{i2} \cdot \alpha^2 + C_{i1} \cdot \alpha + c_{i0} \tag{15.12}$$

The coefficients $C_{i,j}$ (i = 0-4, j = 0-3) are empirically defined as listed in Table 15.2 for the case that the web panel has been dimensioned as described above, by using the least square method.

Table 15.2. Coefficients $C_{i,j}$

b_i	C_{i3}	C_{i2}	C_{i1}	C_{i0}
b_4	-0.013	0.0840	-0.149	0.086
b_3	0.322	-1.954	3.354	-1.928
b_2	2.844	15.539	-25.751	14.653
b_1	2.379	-18.734	35.100	-21.844
b_0	-19.355	89.862	-136.979	76.399

The buckling coefficient when the web is subjected to moment, K_m, is calculated with multiplying the reduction factor μ to K_R. As shown in Fig. 15.20, the reduction factor is almost linear to the moment-shear parameter ϕ. The initial reduction factor μ_0 can be expressed with ϕ as Eq. (15.13).

$$\mu_0 = 1 - A\phi \tag{15.13}$$

The factor A also can be defined empirically with the least square method as Eq. (15.14) for the aspect ratio α and the patch length parameter β.

$$A = -0.040\alpha\beta - 0.033\alpha + 0.128\beta + 0.068 \tag{15.14}$$

When the stresses σ_1 and σ_2 in Fig. 15.16 are equal to each other, $\sigma_1 = \sigma_2$,i.e. the neutral axis parameter $\varphi = 1$, the reduction factor μ becomes μ_0 itself, i.e. $\mu = \mu_0$. If $\sigma_1 \neq \sigma_2$, the initial reduction factor μ_0 is modified with Eq. (15.15).

$$\mu = (e_1 . \varphi + e_2)\eta_0 \tag{15.15}$$

Here, e_1= -0.191β - 0.087 and e_2= -0.191β +0.913.

Now, using Eq. (15.11)÷Eq. (15.15), we can estimate the buckling coefficient of the web panel on a launching shoe. The values of the parameters and factors in these equations are obtained for the demonstrative model shown in Table 15.1.

In the paper [15.25], the numerical model which has its dimensions other than Table 15.1 is also studied, and it is indicated that the buckling coefficient can be obtained with the acceptable accuracy of the error of 8% in maximum.

This method does not require the formula based on Eq. (15.7), and does not give the theoretical solution, but is completely empirically. Therefore many other examples should be examined to verify effectiveness of this method.

15.4. Effect of flange plate

Expert bridge engineers often experientially point out that a web panel on a launching shoe designed with various verification formulas seems to have much more strength than the estimation.

This fact may be caused by stiffness of the flange plate, in particular torsional stiffness of the flange.

The studies on the patch loaded steel plate in the earlier stage deal with lone plate, and do not consider the effect of the flanges. However, a flange plate may influence the strength of the plate with its torsional stiffness. One example is shown below on the effect of flange on strength of a patch-loaded web of a box girder [15.26, 15.27].

In the report [15.26, 15.27], buckling stresses of a steel box girder are demonstrated. The demonstrated box girder has the web depth of 1800 mm, box width of 2100 mm as illustrated in Fig. 15.20(a), and the web and the top flange thickness of 12 mm and the bottom flange of 26 mm. On this box girder, 4 cases are compared as shown in Fig. 15.20(b)÷(d):1

a) full section box, i.e. the section with both top and the bottom flange;
b) top flange is removed, i.e. the section with only the bottom flange;
c) bottom flange is removed, i.e. the section with only the top flange;
d) lone web plate.

The buckling stresses for these four cases are summarized in Table 15.3.

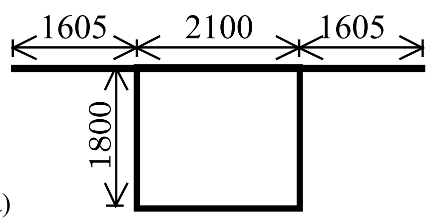

a)

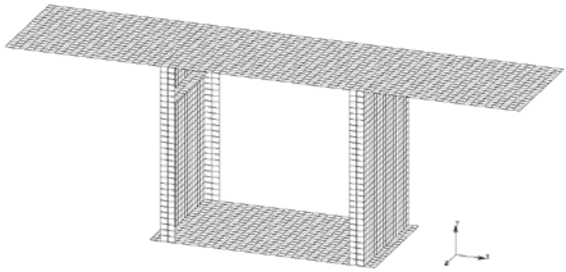

b)

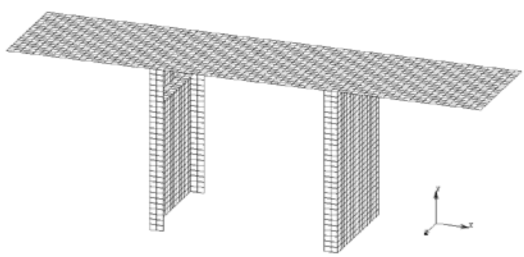

c)

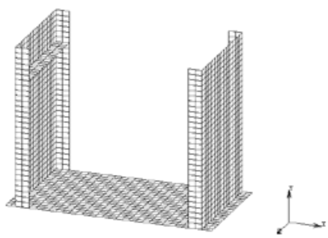

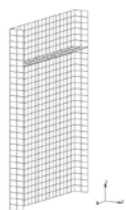

d) e)

Fig. 15.20. Flange effect examples: a) section dimensions, b) full section, c) with top flange, d) with bottom flange, e) only web plate

As shown in this table, the web panel with no bottom flange (cases b) and d) in the table) has the buckling stress of the web equal to 178 MPa, and with the bottom flange, it is 350 or 352 MPa. Thus the buckling stress of the web with the bottom flange is almost twice as large as the web with no bottom flange. This is owing to the fact that the bottom flange of a girder restricts the out-of-plane deformation of the bottom part of the web, and in the result it brings larger strength.

In [15.26], another example on an I-shaped steel girder is shown, and the larger buckling strength is also obtained for the I-shaped girder.

Table 15.3. Buckling strength with flange effect [15.27]

Pattern	Buckling strength [MPa]	Ratio
a) full section 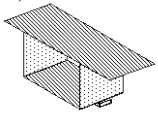	350	1.97
b) with top flange 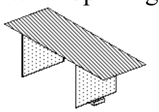	178	1.00
c) with bottom flange 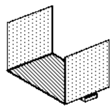	352	1.98
d) with no flange 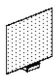	178	-

In the design procedure described in the sections 15.2 or 15.3, the effect of a flange is not taken into account.

Further studies are required on this problem to establish the design procedure with considering the effect of the bottom flange.

15.5. References

15.1 Wilkesmann F.W., Stegblechbeulung bei Längsrandbelastung, Der Stahlbau, Vol. 29, No. 10, 1960, pp. 314-322.

15.2 Khan Md.Z., Johns K.C., Hayman B., Buckling of plates with partially loaded edges, Jour. St. Division, ASCE, ST3, 1977, pp. 547-558.

15.3 Khan Md.Z., Walker A.C., Buckling of plates subjected to localized edge loading, The Structural Engineering, Vol. 50, 1972, pp. 225-232.

15.4 Herzog M., Die Krűppellast sehr dűnner Vollwandträgerstege nach Versuchen, Der Stahlbau, 1974, pp. 26-28.

15.5 Herzog M., Die Krűppellast von Blechträger- und Walzprofilstegen, Der Stahlbau, 1986, pp. 87-88.

15.6 Kutzelnigg E., Beulwerte nach der linearen Theorie fűr längsversteifte Platten unter Längsrandbelastung, Der Stahlbau, 1982, pp. 76-84.

15.7 Rockey K.C., El-Gaaly Md. A., Bagchi D.K., Failure of thin-walled members under partial edge loading, Jour. St. Division, ASCE, ST12, 1972, pp. 2739-2752.

15.8 Warkenthin W., Zur Beurteilung der Beulsicherheit querbelasterter Stegblechfelder, Der Stahlbau, 1965, pp. 28-29.
15.9 Roberts T.M., Rockey K.C., A mechanism solution for predicting the collapse loads of slender plate girders when subjected to in-plane patch loading, Proc. ICE, Part 2, Vol. 67, 1967, pp. 155-175.
15.10 Roberts T.M., Slender plate girders subjected to edge loading, Proc. ICE, Part 2, Vol. 71, 1981, pp. 805-819.
15.11 Graciano, C., Edlund, B., Nonlinear FE analysis of longitudinally stiffened girder webs under patch loading, Jour. Constructional Steel Research, Vol. 58, 2002, pp. 1231-1245.
15.12 Graciano C., Patch loading, Resistance of longitudinally stiffened steel girder webs, Doctoral thesis, Lueleä University of Technology, 2002.
15.13 Graciano C., Casanova E., Martĭnez J., Imperfection sensitivity of plate girder webs subjected to patch loading, Journal of Constructional Steel Research, Vol. 67, 2011, pp. 1128-1133.
15.14 Graciano C., Ayestarán A., Steel plate girder webs under combined patch loading, bending and shear, Journal of Constructional Steel Research, Vol. 80, 2013, pp. 202-212.
15.15 Chacón R., Mirambell E., Real E., Transversally stiffened plate girders subjected to patch loading, Part 1, Preliminary study, Journal of Constructional Steel Research, Vol. 80, 2013, pp. 483-491.
15.16 Maquoi R., Plate Girders, Chapter 2.6, Constructional Steel Design, An International Guide, Dowling P.J. et al. (eds.), Elsevier, 1992, ISBN 1-85166-895-0.
15.17 Shimizu S, Yoshida S., Okuhara H., An experimental study on patch-loaded web pate, Proc. of ECCS Colloquium on Stability of Plate and Shell Structures, Ghent, Belgium, 1987, pp. 85-94.
15.18 Shimizu S., Yabana H. Yoshida S., A new collapse model for patch-loaded web plates, Jour. Constructional Steel Research, Vol. 13, 1989, pp. 61-73.
15.19 Shimizu, S., Horii, S., Yoshida, S., The collapse mechanisms of patch loaded web plates, Jour. Constructional Steel Research, Vol. 14, 1989, pp. 321-337.
15.20 Shimizu S., The collapse behaviour of web plates on the launching shoe, Jour. Constructional Steel Research, Vol. 31, 1994, pp. 59-72.
15.21 Shimizu S., Effect of stiffener on the patch loaded plates, Proc. of 3rd International Conference on Computer-Aided Assessment and Control Localized Damage, 1994, pp. 505-512.
15.22 DIN18800 Part 3, Structural steelwork, Analysis of safety against buckling of plates, Deutsche Norm, 1990 (English version).
15.23 Guidelines for erection, design and installation of steel structures, JSCE, 2001(in Japanese).
15.24 Nogami K., Hirayama H., Shimizu S., Furuta T., Proposed stability verification method of web panel of steel girder bridges subjected to patch loadings, Jour. Structural Engineering, JSCE, Vol. 59A, 2013, pp. 56-69 (in Japanese).

15.25 Shimizu S., Yoshikawa K., Prediction of the buckling coefficients of a patch loaded web plate, Steel Construction Engineering, JSSC (Japanese Society of Steel Construction), Vol. 6, No. 24, 1999, pp. 111-122 (in Japanese).

15.26 Shimizu K., Shimizu S., Comparison and examination of verification procedures for a steel girder on a launching shoe, Proc. of Annual Meeting of the Chubu branch of JSCE, 2012.3 (in Japanese).

15.27 Nogami K., Shimizu S., Furuta T. et al., Standardization of verification procedure of buckling strength of web plate, Survey Report, Japan Bridge Association, 2012.3 (in Japanese).

16.

Local buckling and initial post-buckling behaviour of channel member flange - analytical approach

16.1. Introduction

Cold formed thin-walled channel members are widely applied in different kind of engineering structures. If the members are subjected to bending or compression stability problems, global, distortional or local buckling may be decisive in its designing [16.1, 16.2]. Usually the designing of the members is carried out in an elastic range of the material. Recent developments in theoretical and numerical stability analysis [16.3, 16.4] enable formulation and solution of optimal design of the channel beams [16.5, 16.6]. The analytical approximate solution of the local buckling of the compressed beam flange is very useful in formulation of the optimization problem [16.7]. The analytical formulae applied in these problems for the critical local buckling stress are derived with approximate assumptions: only the first buckling mode is taken into account and it is computed without accounting for a cooperation of the compressed flange with beam web.

The main purpose of the investigation is to give more rigorous analytical description of the local buckling and initial post-buckling behaviour of the member compressed flange within an elastic range of the material behaviour. The single and double sheet flanges are taken into consideration. The nonlinear governing differential equation of the stability problem is derived by means of the stationary total energy principle. In the total potential energy formulation a cooperation of the flange with web is taken into account. The perturbation approach applied to solve the equation leads to the buckling stresses related to the number of half-wave modes and the initial post-buckling equilibrium path. The critical buckling stress and corresponding mode are found as a minimum value of the buckling stresses obtained. Moreover the relation of the critical stress and the relative member length derived enables finding the number of half-waves of the buckling mode. The initial post-buckling equilibrium paths allows classifying all bifurcation points as symmetric and stable. Some numerical examples dealing with simply supported beams and columns are presented.

16.2. Total potential energy of member flange

Let us consider a channel beam undergoing pure bending or an axially compressed channel column as shown in Fig. 16.1. Local buckling of the compressed member flange and its initial post-buckling behaviour is investigated. It is assumed that the member material obeys the Hooke's low. The Cartesian coordinate system *x*, *y*, *z* is located at the centre of flange rotation. Additionally the parallel coordinate system x_0, y_0, z_0 is taken at the flange centre of gravity *B*. If the flange rotates about the line of connection with the web then the displacements *v*, *u* of an arbitrary point *x* of the flange may be written as

$$v = x\sin\theta, \quad u = -x(1-\cos\theta) \tag{16.1}$$

where the torsion angle is denoted as θ. Thus the displacements of the flange centre of gravity B are determined as

$$v_B = x_B \sin\theta, \quad u_B = -x_B(1-\cos\theta) \tag{16.2}$$

where the coordinate x_B of the point B is introduced. It should be noted that in formulas (16.2) the effect of the second coordinate y_B of point B is neglected since usually $y_B << x_B$.

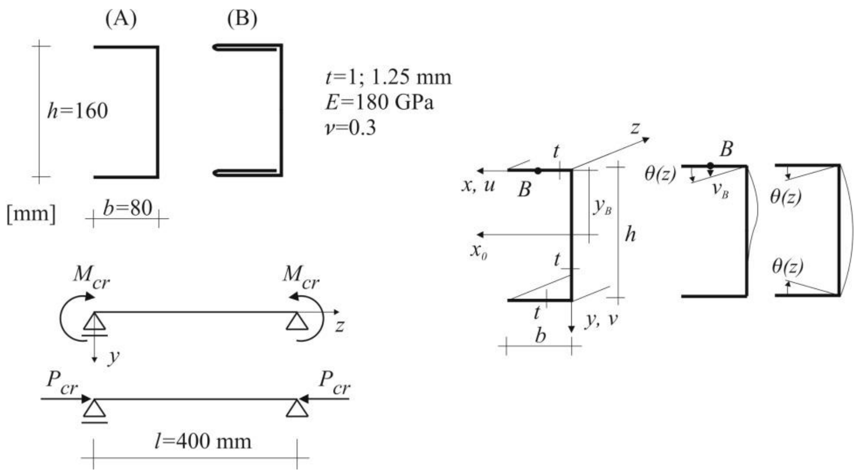

Fig. 16.1. Displacements of member's flanges and data of numerical examples

The flange-web cooperation is expressed by springs uniformly distributed along the connection line. The elastic modulus of the springs k_θ is different for the beam and the column and may be written as

$$k_\theta = \chi E I_w / h \tag{16.3}$$

where EI_w stands for the bending stiffness of the web, h denotes the web hight and the coefficient $\chi = 4$ for beams and $\chi = 2$ for columns.

The total potential energy of the flange V in the initial post-buckling state is considered as a sum of the elastic strain energy of the flange V_e , the potential energy of the springs V_s and the potential energy V_l of the applied uniformly distributed normal stresses σ_0

$$V = V_e + V_s + V_l \tag{16.4}$$

The elastic strain energy consists of effects of bending about axes x, y and free torsion and may following [16.8, 16.9] be expressed as

$$\begin{aligned} V_e = {} & 0.5EI_x \int_0^L \left[v''_B (1 - v'_B)^{-1} \right]^2 dz + 0.5EI_y \int_0^L \left[u''_B (1 - u'_B)^{-1} \right]^2 dz + \\ & + 0.5GI_d \int_0^L \theta'^2 dz + 0.125E\bar{I}_{00} L \int_0^L \theta'^4 dz \end{aligned} \tag{16.5}$$

where E is the Young's modulus, I_d stands for the free torsion moment of inertia of the flange cross-section, I_x, I_y denote the flange cross-section moment of inertia about x and y axes respectively. Moreover, by $\bar{I}_{00} = I_{00} - I_0^2 / A$ the reduced fourth moment of inertia of the flange cross-section is introduced. Here A stands for the area of the flange cross-section.

Using relations (16.2) and expanding the functions $\sin\theta$ and $\cos\theta$ into the Taylor's series after some algebra, Eq. (16.5) may be rewritten as

$$\begin{aligned} V_e = {} & 0.5EI_x \int_0^L x_B^2 \left[\theta''^2 + 2x_B^2 \theta'^2 \theta''^2 \right] dz + 0.5EI_y \int_0^L x_B^2 \theta'^4 dz + \\ & + 0.5E\left(I_y - I_x\right) \int_0^L x_B^2 \left(\theta''^2 \theta^2 + 2\theta\theta'' \theta'^2 \right) dz \\ & + 0.5GI_d \int_0^L \theta'^2 dz + 0.125E\bar{I}_{00} \int_0^L \theta'^4 dz \end{aligned} \tag{16.6}$$

where the powers of the rotation angle and its derivatives higher than fourth are omitted.

The potential energy of the applied normal stresses σ_0 uniformly distributed along the flange due to its rotation is

$$V_l = -\sigma_0 \left\{ \int_0^L \int_0^b t \left[1 - \left(1 - v'^2 \right)^{0.5} \right] dx dz + \int_0^L \int_0^b t \left[1 - \left(1 - u'^2 \right)^{0.5} \right] dx dz \right\} \tag{16.7}$$

where b is the flange width.

Similarly as above the relations (16.1) are applied in Eq. (16.7) and then we arrive at

$$V_l = -0.5\sigma_0 \int_0^L \left(I_{y_0} \theta'^2 + 0.5 I_{y_0 y_0} \theta'^4 \right) dz \tag{16.8}$$

where I_{y_0} and $I_{y_0 y_0}$ denote the second and fourth order moment of inertia of the flange cross-section about axis y_0 located in the rotation centre of the flange (see Fig. 16.1).

Last part of the total potential energy accounting for the uniformly distributed springs in accord with relation (16.3) may be written as

$$V_s = 0.5\chi \frac{EI_w}{h} \int_0^L \theta^2 dz \tag{16.9}$$

Having summed up all parts of the total potential energy (16.6), (16.7) and (16.9) the final form of V is a functional

$$V = 0.5 \int_0^L F(\theta, \theta', \theta'') dz \tag{16.10}$$

where the under-integral function is defined as

$$\begin{gathered} F(\theta,\theta',\theta'') = E\left[I_x x_B^2 \theta''^2 + I_y x_B^2 \theta'^4 + \left(I_y - I_x \right) x_B^2 \left(\theta''^2 \theta^2 + 2\theta\theta''\theta'^2 \right) + 0.25\bar{I}_{00} \theta'^4 \right] + \\ GI_d \theta'^2 + \chi I_w \theta^2 / h - \sigma_0 \left(I_{y0} \theta'^2 + 0.5 I_{y0y0} \theta'^4 \right) \end{gathered} \tag{16.11}$$

16.3. Local buckling and initial post-buckling behaviour

The nonlinear differential equation of equilibrium of the flange resulting from the Euler condition of stationary total potential energy (16.10) [16.10] can be written as

$$\begin{gathered} \theta^{IV} + 2\alpha\theta'' + \beta^2\theta = x_B^2 \left[-\left(I_y - I_x \right) \left(3\theta\theta''^2 + 6\theta'^2\theta'' + 4\theta\theta'\theta''' + \theta^2\theta^{IV} \right) + 6 I_y \theta'^2 \theta'' \right] \\ / \left(I_x x_B^2 \right) + \left[\left(1.5\bar{I}_{00} - 3\sigma_0 I_{y0y0} / E \right) \theta'^2 \theta'' - 2 x_B^4 I_x \left(\theta''^3 + 4\theta'\theta''\theta''' + \theta'^2 \theta^{IV} \right) \right] / \left(I_x x_B^2 \right) \end{gathered} \tag{16.12}$$

where

$$\begin{aligned} 2\alpha &= \left(\sigma_0 I_{y0} - GI_d \right) / E\left(I_x x_B^2 \right) \\ \beta^2 &= \chi I_w / h\left(I_x x_B^2 \right) \end{aligned} \tag{16.13}$$

The solution to Eq. (16.12) is determined by means of the perturbation approach [16.8, 16.11]. The torsion angle can be represented as the polynomial of the perturbation parameter *s*

$$\theta(z) = s\theta_1(z) + s^2\theta_2(z) + s^3\theta_3(z) + \dots \tag{16.14}$$

where $\theta_i(z)$ stand for functions of *z* that should fulfil suitable boundary conditions.

The stress σ_0 is also expressed in the same manner as

$$\sigma_0 = \sigma_{cr} + s\sigma^{(1)} + s^2\sigma^{(2)} + \dots \tag{16.15}$$

where σ_{cr} stands for the critical buckling stress and by $\sigma^{(i)}$ the *i*-th derivative of the stress σ with respect to *s* is denoted.

Moreover, it is assumed that the perturbation parameter is equal to the maximum torsion angle $s = \theta_0 = \theta(z_0)$ located at z_0 and hence using relation (16.14) some additional boundary conditions are established

$$\theta_1(z_0) = 1, \ \theta_i(z_0) = 0 \quad \text{for} \quad i \neq 1 \tag{16.16}$$

Utilizing relations (16.14) and (16.15) in the nonlinear differential equation (16.12) and coefficients of the first power of *s* equal to zero one can obtain the following linear differential equation

$$\theta_1^{IV} + 2\alpha\theta_1'' + \beta^2\theta_1 = 0 \tag{16.17}$$

where

$$\begin{aligned} 2\alpha &= \left(\sigma_{cr} I_{y0} - GI_d\right) / E\left(I_x x_B^2\right) \\ \beta^2 &= \chi I_w / h\left(I_x x_B^2\right) \end{aligned} \tag{16.18}$$

The solution to Eq. (16.17) can be written as

$$\theta_1 = C_1 \sin k_1 z + C_2 \cos k_1 z + C_3 \sin k_2 z + C_4 \cos k_2 z \tag{16.19}$$

where

$$k_1 = \sqrt{\alpha\left(1 - \sqrt{1 - (\beta/\alpha)^2}\right)}, \quad k_2 = \sqrt{\alpha\left(1 + \sqrt{1 - (\beta/\alpha)^2}\right)} \tag{16.20}$$

The constants C_1, C_2, C_3 and C_4 should be determined from suitable boundary conditions. Let us consider simply supported member as it is shown in Fig. 16.1. The boundary conditions defined as follows

$$\theta_1(z=0)=\theta_1''(z=0)=0, \quad \theta_1(z=L)=\theta_1''(z=L)=0 \tag{16.21}$$

together with the additional condition (16.16) enables obtaining the buckling stress

$$\sigma = E\left[I_x x_B^2 m^2 + \chi I_w / m^2 h + GI_d / E\right] / I_{y0} \tag{16.22}$$

and the buckling mode

$$\theta_1 = \sin mz \tag{16.23}$$

where $m = n\pi / L$ and n stands for number of the half waves of the buckling mode. The number n should be chosen to obtain minimum of the critical stress (16.22). Now it is possible to determine location of the maximum angle of torsion $z_0 = L/2n$ (16.16) in the middle of the half wave.

It is useful to know a relation between the critical stress and the member length that makes possible to find a number of the half waves n. As mentioned above, the critical stress should be determined to obtain minimum of the buckling stress (16.22). The necessary condition of the minimum of the buckling stress (16.22) with respect to the m is

$$\frac{d\sigma}{dm} = 2mI_x x_B^2 - 2\chi I_w / hm^3 = 0 \tag{16.24}$$

hence

$$m = \sqrt[4]{\frac{\chi I_w}{hI_x x_B^2}} \tag{16.25}$$

Equation (16.25) enables determining the member length corresponding to the stress minimum

$$L = n\pi \sqrt[4]{\frac{hI_x x_B^2}{\chi I_w}} \tag{16.26}$$

It is useful to define a characteristic member length L_0 as

$$L_0 = \pi \sqrt[4]{\frac{hI_x x_B^2}{\chi I_w}} \tag{16.27}$$

Substitution of Eq. (16.25) into the Eq. (16.22) leads to the minimum value of the stress which occurs in each member with the length $L=kL_0$

$$\sigma_{\min} = E\left[2\sqrt{\chi I_w I_x x_B^2 / h} + GI_d / E\right] / I_{y0} \tag{16.28}$$

The relation of the critical buckling stress and a scaling coefficient $k=L/L_0$ is shown in Fig. 16.2, where one can find not only the critical stress but also the number n of the half waves of the buckling mode.

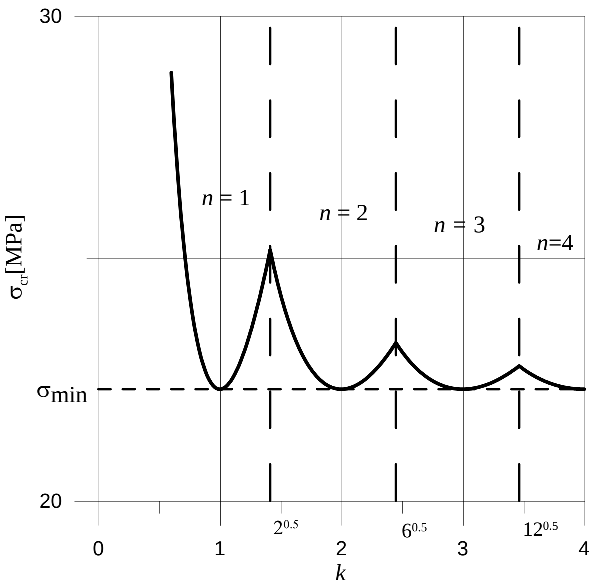

Fig. 16.2. Critical buckling stress vs. scaling coefficient k

The coefficient of the second power of s leads to the next differential equation

$$\theta_2^{IV} + 2\alpha\theta_2'' + \beta^2\theta_2 = -\sigma^{(1)} I_{y0}\theta_1'' / E\left(I_x x_B^2\right) \tag{16.29}$$

Utilizing the buckling mode (16.23) in (16.29) and noticing that left side of the equation (16.29) is the same as previous equation (16.17), it is easy to find

$$\theta_2 = 0 \quad \text{and} \quad \sigma^{(1)} = 0 \tag{16.30}$$

It means that the bifurcation point is symmetrical [16.11].

The next third term of the power series in s leads to the third linear differential equation

$$\begin{aligned}&\theta_3^{IV} + 2\alpha\theta_3'' + \beta^2\theta_3 = x_B^2\Big[-\left(I_y - I_x\right)\left(3\theta_1\theta_1''^2 + 6\theta_1'^2\theta_1'' + 4\theta_1\theta_1'\theta_1''' + \theta_1^2\theta_1^{IV}\right) + 6I_y\theta_1'^2\theta_1''\Big]\\ &/\left(I_x x_B^2\right) + \Big[\left(1.5\bar{I}_{00} - 3\sigma_0 I_{y0y0}/E\right)\theta_1'^2\theta_1'' - 2x_B^4 I_x\left(\theta_1''^3 + 4\theta_1'\theta_1''\theta_1''' + \theta_1'^2\theta_1^{IV}\right) - \sigma^{(2)} I_{y0}\theta_1''/E\Big]\\ &/\left(I_x x_B^2\right)\end{aligned} \tag{16.31}$$

Substituting the buckling mode (16.23) into Eq. (16.31) and using some trigonometric relations, Eq. (16.31) can be rewritten as

$$\theta_3^{IV} + 2\alpha\theta_3'' + \beta^2\theta_3 = k_3 \sin mz + l_3 \sin 3mz \tag{16.32}$$

where

$$\begin{aligned}
k_3 &= m^2\left[-0.5m^2\left(I_y / I_x - 1\right) - 3m^2\left(4I_y x_B^2 - 2\sigma_{cr} I_{y0y0} / E + \bar{I}_{00}\right)/8x_B^2\right] + \\
&- m^6 x_B^2 + m^2\sigma^{(2)} I_{y0} / I_x x_B^2 E \\
l_3 &= m^4\left[3.5x_B^2\left(I_y - I_x\right) - 3\left(4x_B^2 I_y - 2\sigma_{cr} I_{y0y0} / E + \bar{I}_{00}\right)/8 - 3m^2 x_B^4 I_x\right]/\left(I_x x_B^2\right)
\end{aligned} \tag{16.33}$$

The solution to equation (16.32) is

$$\theta_3 = C_1 \sin k_1 z + C_2 \cos k_1 z + C_3 \sin k_2 z + C_4 \cos k_2 z + K_3 \sin mz + L_3 \sin 3mz \tag{16.34}$$

where

$$\begin{aligned}
K_3 &= k_3 / \left(m^4 - 2\alpha m^2 + \beta^2\right) \\
L_3 &= l_3 / \left(81m^4 - 18\alpha m^2 + \beta^2\right)
\end{aligned} \tag{16.35}$$

The constants C_1, C_2, C_3 and C_4 should be established from boundary conditions (16.24) and the additional condition (16.16). Thus we arrive at

$$\theta_3 = L_3\left(\sin mz - \sin 3mz\right) \quad \text{and} \quad K_3 = 0 \tag{16.36}$$

The first relation (16.35) incorporated into the Eq. (16.14) and after substitution of the buckling mode (16.23) it leads to the initial post buckling shape of the torsional angle

$$\theta = \theta_0 \sin mz + \theta_0^{\,3} L_3\left(\sin mz - \sin 3mz\right) \tag{16.37}$$

The second equation (16.35) allows us to obtain $\sigma^{(2)}$ (see Eq.(16.15)) determining the initial curvature of the post-buckling equilibrium path

$$\sigma^{(2)} = EI_x m^2 x_B^2\left(2I_y / I_x - 0.5 - 0.75\sigma_{cr} I_{y0y0} / x_B^2 E I_x + 0.375\bar{I}_{00} / x_B^2 I_x + m^2 x_B^2\right)/ I_{y0} \tag{16.38}$$

Finally, the initial post-buckling equilibrium path may be written in approximated form as

$$\frac{\sigma}{\sigma_{cr}} = 1 + \frac{\sigma^{(2)}}{\sigma_{cr}}\theta^2 \tag{16.39}$$

The positive value of $\sigma^{(2)}$ together with $\sigma^{(1)} = 0$ (see (16.25)) shows the symmetrical stable point of bifurcation that is insensitive on inevitable geometrical imperfection. Otherwise the negative value of $\sigma^{(2)}$ shows that the symmetrical unstable point of bifurcation occurs and a decrease of the critical buckling stress arises.

16.4. Numerical examples

Let us consider an example of a simply supported beam undergoing pure bending and the axially compressed column as it is shown in Fig. 16.1. Two different shapes of flanges: single (A) and double bend (B) and two thicknesses t = 1 mm and t = 1.25 mm are taken into investigation. The critical buckling stresses and corresponding number of half waves are determined for all cases and shown in Table 16.1 and 16.2. In these tables the relative curvatures of the initial post-buckling paths (16.39) and the coefficients L_3 (16.35) determining the initial post-buckling behaviour of the flange rotation angle are presented as well.

Table 16.1. Critical local buckling stress of beam undergoing pure bending [MPa]

Flange	Number of half-waves n	Thickness [mm]	σ_{cr}[MPa]	$\dfrac{\sigma^{(2)}}{\sigma_{cr}}$	L_3
A	3	1	21.02	3995	190.2
	3	1.25	32.84	2555	121.7
B	2	1	26.37	1414	38.1
	2	1.25	41.21	904.4	24.2

Table 16.2. Critical local buckling stress of axially compressed column [MPa]

Flange	Number of half-waves n	Thickness [mm]	σ_{cr}[MPa]	$\dfrac{\sigma^{(2)}}{\sigma_{cr}}$	L_3
A	2	1	18.05	2068	216.5
	2	1.25	28.20	1322	138.5
B	1	1	22.50	414.4	36.7
	1	1.25	35.15	265.1	23.3

The graphical presentation of the post-critical stress vs. torsional angle amplitude is shown for beams in Figs. 16.3 and 16.4 and for columns in Fig. 16.5 and 16.6. Comparison of these results for both flange thicknesses is also provided.

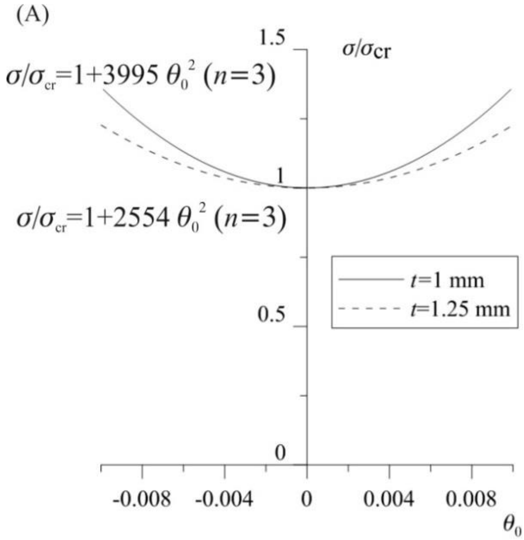

Fig. 16.3. Post-critical stresses σ vs. torsion angle amplitude for simply supported beam with single flanges

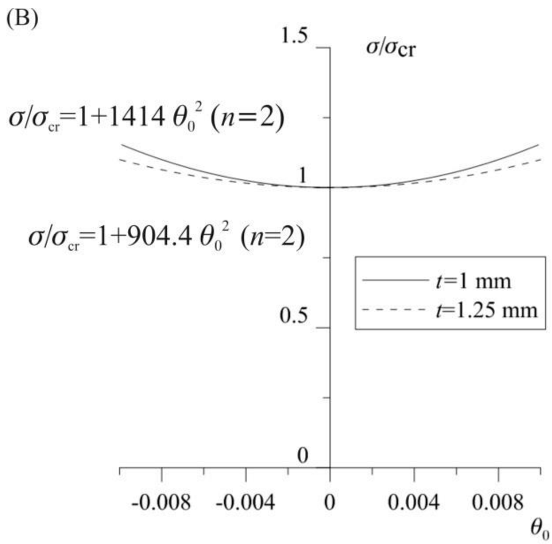

Fig. 16.4. Post-critical stresses σ vs. torsion angle amplitude for simply supported beam with double bend flanges

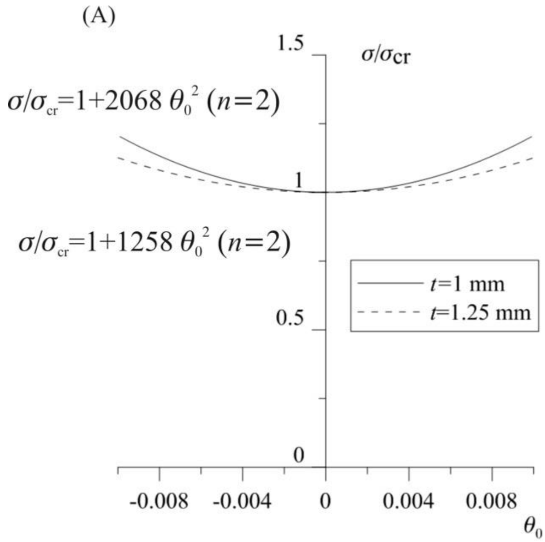

Fig. 16.5. Post-critical stresses σ vs. torsion angle amplitude for simply supported column with single flanges

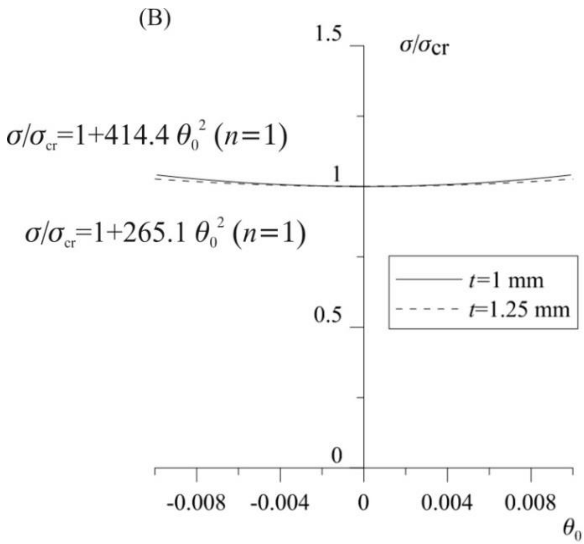

Fig. 16.6. Post-critical stresses σ vs. torsion angle amplitude for simply supported column with double bend flanges

Moreover the characteristic member lengths and the minimum critical buckling stresses for all cases of members and both thicknesses under investigation are determined and presented in Tables 16.3 and 16.4.

Table 16.3. Characteristic beam length and minimum critical stress

Flange	Thickness [mm]	Characteristic length [mm] L_0	Minimum critical stress [MPa]
A	1	149.44	20.76
	1.25	149.44	32.44
B	1	251.33	24.88
	1.25	251.33	38.88

Table 16.4. Characteristic column length and minimum critical stress

Flange	Thickness [mm]	Characteristic length [mm] L_0	Minimum critical stress [MPa]
A	1	177.72	17.85
	1.25	177.72	27.89
B	1	298.88	20.76
	1.25	298.88	32.44

The characteristic member length (16.27) may be determined directly by dimensions of the cross-section as

$$L_0 = \pi b \sqrt[4]{\frac{h}{4\chi b}} \tag{16.40}$$

for single flange and

$$L_0 = \pi b \sqrt[4]{\frac{2h}{\chi b}} \tag{16.41}$$

for double bend flanges.

Similarly the minimum buckling stress (16.28) may be expressed as

$$\sigma_{\min} = E\left(\frac{t}{b}\right)^2 \left(0.25\sqrt{\chi\frac{b}{h}} + \frac{G}{E}\right) \tag{16.42}$$

for single flange and as

$$\sigma_{\min} = E\left(\frac{t}{b}\right)^2 \left(0.5\sqrt{\frac{\chi b}{2h}} + \frac{G}{E}\right) \tag{16.43}$$

for double bend flanges.

It should be noted that the initial curvatures of the post-buckling equilibrium path in all cases under consideration are positive. This property together with (16.25) determines the symmetrical and stable points of bifurcations [16.8, 16.11], in which decrease of the buckling stresses is not possible. The critical stresses of beams undergoing pure bending are higher than the same stresses of axially compressed columns due to more effective flange-web cooperation. The greater thickness the higher critical stresses. Number of the mode half waves depends on the cross-section geometry and in beams is usually higher than in columns.

The buckling modes and initial post-buckling distribution of the flange angle along the beams axes are presented in Figs. 16.7 and 16.8 along the columns axes in Figs. 16.9 and 16.10. The amplitude of the buckling mode is assumed to be 0.05 [rad]. A strong increase of the post-buckling flange angle amplitude in accord with the half waves number should be noticed. The stiffer member flange the less amplitude of the post-buckling flange angle.

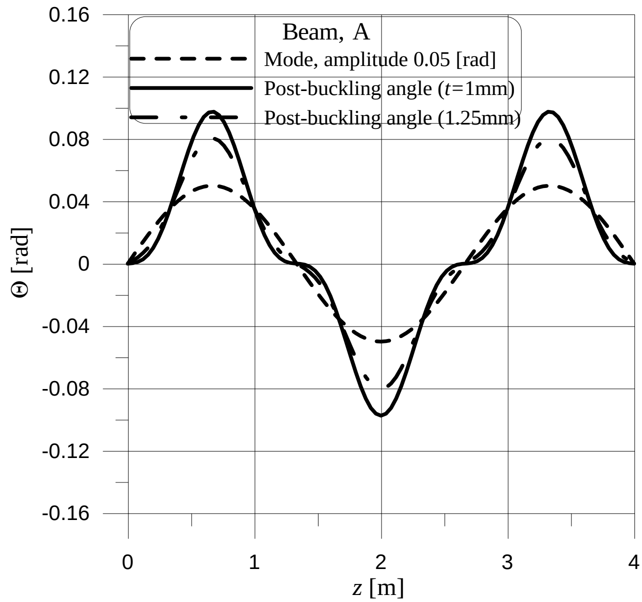

Fig. 16.7. Buckling mode and post-buckling shape of the flange angle of rotation vs. its amplitude for beam with single flange

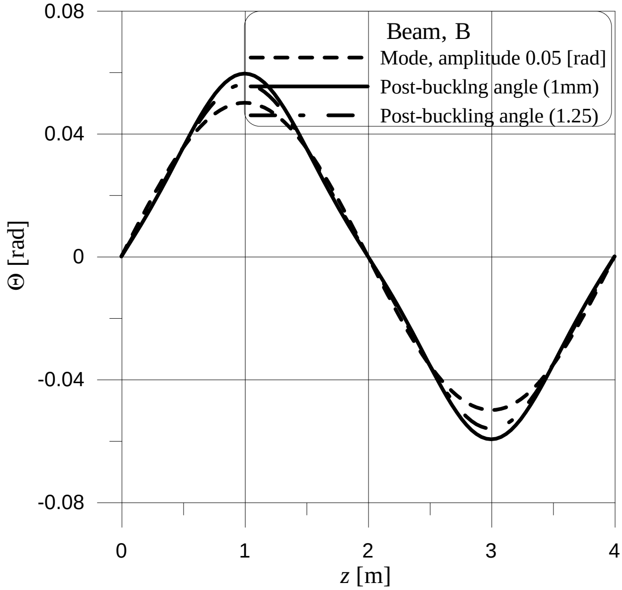

Fig. 16.8. Buckling mode and post-buckling shape of the flange angle of rotation vs. its amplitude for beam with double bend flange

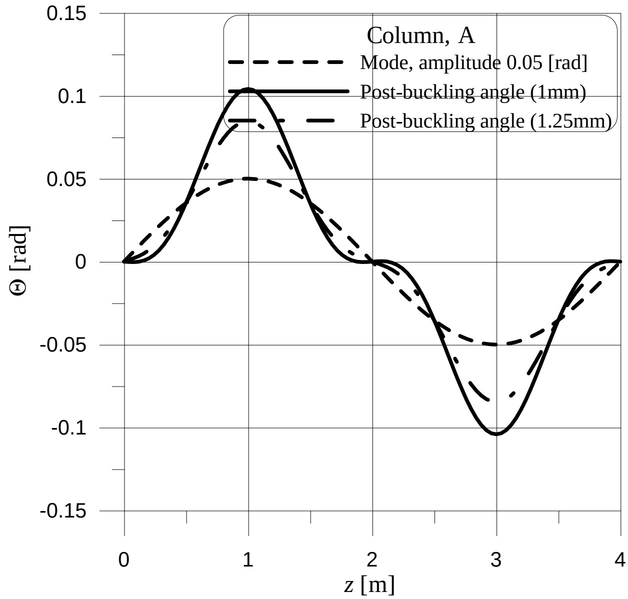

Fig. 16.9. Buckling mode and post-buckling shape of the flange angle of rotation vs. its amplitude for column with single flange

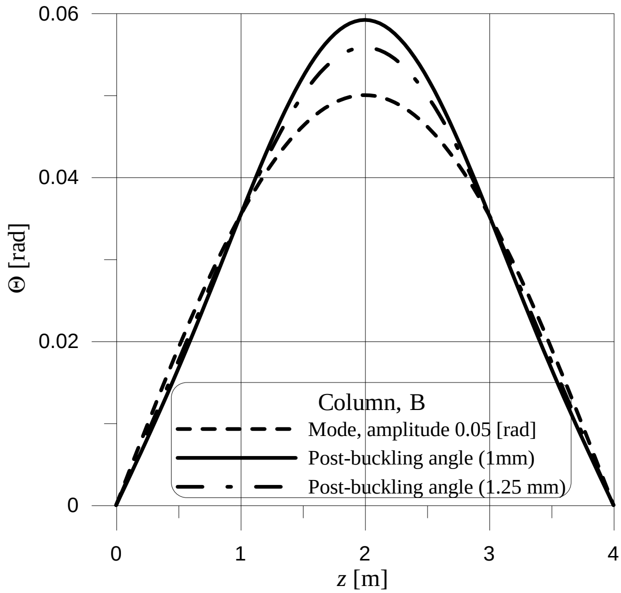

Fig. 16.10. Buckling mode and post-buckling shape of the flange angle of rotation vs. its amplitude for column with double bend flange

16.5. Conclusions

The local buckling of the compressed flanges of the cold formed channel beams undergoing pure bending and axially compressed columns are investigated. The total potential energy formulation allows one to derive the nonlinear differential equation governing the buckling and the initial post-buckling behaviour of the flanges. The simple model of the flange as the beam stiff in its plane and elastically connected with the member web is assumed. The solution of the equation is determined by means of the perturbation approach. The critical buckling stress and corresponding number of half-waves are determined. Moreover the characteristic member length is introduced that makes possible to obtain directly the number of the half waves related to the member length.

The theoretical and numerical investigation of the local buckling and initial post-buckling behaviour of the member flanges carried out enable us to draw some conclusions related to the problems under investigation:

- The points of bifurcation of the local buckling of the flanges are symmetrical and stable in all considered cases. The term $\sigma^{(2)}$ (16.38) denoting the curvature of the initial post buckling path is positive for beams and columns. This means that decrease of the critical stresses due to inevitable geometrical imperfections of the torsion angle of flange does not occur.

- The critical stresses of the beam flanges are higher than the same stresses of columns due to more effective the flange-web cooperation. The greater flange thickness leads to the higher critical buckling stresses.
- The number of the mode half waves depends on the flange bending stiffness and it is different for beams and columns with respect to the effect of the flange-web cooperation. The greater flange stiffness the less the half waves number. The number of the beams half waves is usually higher than for columns except the one half waves. It should be noticed that in many approximate solutions of the similar problems [16.12, 16.13] only the first mode is taken into account and no cooperation flange-web is included. Such assumptions may lead to qualitative and numerical errors. The analytical formulas of the critical buckling stress derived may be useful in preliminary design and optimization of this type of structures.

This paper is dedicated to the memory of Professor Katarzyna Kowal-Michalska, to her life, scientific achievements, our friendship and scientific cooperation.

16.6. References

16.1 Davies J.M., Recent advances in cold-formed steel structures, Journal of Constructional Steel Research, Vol. 55, 2000, pp. 267-288.

16.2 Hancock G.J., Cold-formed steel structures, Journal of Constructional Research, Vol. 59, 2003, pp. 473-487.

16.3 Mcdonald M., Heiyantuduwa M.A, Rhodes J., Recent developments in design of cold-formed steel members and structures, Thin-Walled Structures, Vol. 46, 2008, pp. 1047-1053.

16.4 Magnucki K., Szyc W., Stasiewicz P., Stress state and elastic buckling of a thin-walled beam with monosymmetric open cross-section, Thin-Walled structures, Vol. 42, 2008, pp. 25-38.

16.5 Magnucka-Blandzi E., Magnucki K., Buckling and optimal design of cold-formed beams; reviews of selected problems, Thin-Walled Structures, Vol. 46, 2011, pp. 554-561.

16.6 Magnucki K., Ostwald M., Optimal design of selected open-cross-sections of cold-formed thin-walled beams, Publishing House of Poznan University of Technology, 2005.
16.7 Magnucki K., Paczos P., Theoretical shape optimization of cold- formed thin-walled channel beams with drop flanges in pure bending, Journal of Constructional Steel research, Vol. 65, 2009, pp. 1731-1737.
16.8 Szymczak C., Buckling and initial post-buckling behavior of thin-walled I columns, Computers and Structures, Vol.11, 1980, pp. 481-487.
16.9 Szymczak C., Stan pokrytyczny dwuteowego pręta cienkościennego po wyboczeniu skrętnym (Post-critical state of thin-walled I bar after torsional buckling), Arch. Inż. Ląd., Vol. 25, 1999, pp. 399-411.
16.10 Gelfand I.M., Fomin S.W., Rachunek wariacyjny (Calculus of variations), PWN, Warsaw 1970.
16.11 Thompson J.M.T, Hunt G.W., A general theory of elastic stability, John Wiley and Sons, London 1973.
16.12 Magnucki K., Paczos P., Kasprzak K., Elastic buckling of cold formed thin-walled channel beams with drop flanges, Journal of Structural Mechanics ASCE, Vol. 136, 2010, pp. 886-896.
16.13 Paczos P., Stability and limit load of cold-formed thin-walled beams, Publishing House of Poznan University of Technology, 2014.

17.

Stability of columns with respect to their loads and specific disorders of their structure

17.1. Columns and disorders of their structures

The columns are slender systems subjected to a compressive load. Two basic types of columns can be distinguished:

- axially-symmetrical column built of a rod and concentric pipes. Buckling can take place in an optional plane if structure disorder does not force a specified buckling plane (cf. [17.38]),
- flat frame built of an even or odd number of rods in such a way that bending does not occur in the plane perpendicular to the buckling plane (cf. [17.35, 17.34]).

Supportive slender systems can be subjected to different kinds of structure disorders which influence the stability of the construction as well as the free vibrations of systems (changing frequencies and forms of free vibrations). These disorders can be divided into external and internal ones. Among external disorders the following can be distinguished:

- support of the system, which can be elastic, viscoelastic or elasto-plastic. Through the support of the system one can change the method of stability loss, for example instability of a divergence type into instability of a flutter type (cf. [17.37]);
- base of the system. (a one or multi parameter Winkler's base is the most common case. The system can have contact with the base along all its entire length (total base) or in a chosen fragment (local base) (cf. [17.22]);
- temperature of the system. As a result of a change in the temperature in the system, a change in material properties and the formation of an additional load takes place. A minor change can lead to a loss of stability. This type of disorder can be caused by a fire, and its impact on construction can have serious consequences (cf. [17.5]).

Internal disorders are connected to structure discontinuity inside the support element. Here the following can be distinguished:

- cracks (both open and open-closed ones). Occurrence of different kinds of cracks in the support structure weakens this structure - the ability to transfer compressive external loads decreases significantly. In the literature one can find works considering this type of disorder, and the results presented there have made a contribution to their detection. In such a case, the results connected to characteristic curves are especially suitable as they have substantial meaning in the diagnostics of support structures (cf. [17.20, 17.19]);
- additional elements in the complex support systems in the form of elastic, elasto-plastic or viscoelastic layers. In this case, the application of an element having an effect on the reciprocal deformation of the chosen elements of the support construction can have a positive influence on its stability or its vibrations (cf. [17.38]).

17.2. Loads of the columns

On the basis of the most general division of the external load of slender systems into conservative and non-conservative, the external load can be assigned to one of the following groups:

- conservative load
  - Euler's load (cf. [17.38]
  - generalized load (theoretical) (cf. [17.4])
  - a load generated by a force directed towards the pole (cf. [17.29])
  - specific load (cf. [17.23, 17.32, 17.24, 17.22])
- non-conservative load
  - Beck's load and Beck's generalised load (cf. [17.9, 17.35])
  - Reut's load and Reut's generalised load (cf. [17.8]).

Their characteristics are presented in brief below.

Euler's load is generated by an external force. The direction of this external force does not change during the deflection of the system from a rectilinear form of static equilibrium. The load capacity of a column subjected to this classic load is essentially dependent on the mounting methods (boundary conditions).

A generalised load should be treated as theoretical as there are no solutions of structures realising it in the literature. A generalised load makes it possible to formulate real loads through adequate selection of its characteristic parameters. A generalised load is caused by the simultaneous action of the axial force, lateral force and bending moment. The lateral force and bending moment are dependent on the axial force, the deflection and deflection angle of the loaded end of the column. The influence of the deflection and deflection angle on the lateral force and bending moment is realised by four coefficients, i.e. coefficients of the generalised load (two coefficients connected with lateral force and two coefficients connected with the bending moment).

The load generated by a force directed towards the pole is generated by a force whose course is determined by two points. The loaded end of the system is the first point and the second is the constant point (pole) on the non-deformed axis of the column (the pole can be placed above or below the loaded end of the column). The distance between the end of the system and the constant point (pole placed on non-deformed axis of the column) is the parameter of this load.

A specific load is the most recent conservative load of supported slender systems. This load was formulated and introduced into the literature by prof. Lech Tomski. It was created by different already existing loads. Several types of load can be distinguished, i.e. a generalised load with a force directed towards the pole and a load with a force directed towards the pole. The specific load is a real load and its realization is possible due to the application of adequately constructed loaded heads built of linear or curvilinear elements.

A characteristic of a specific load is the fact that displacement of the end of the column is strictly dependent on the parameters of the heads leading this end. It gives new possibilities for considering stability problems (possibility of controlling critical load) and the free vibrations of the system (change in free vibration frequency).

In the case of conservative loads, the stability of the systems can be determined on the basis of a static or kinetic stability criterion.

In the case of a non-conservative load in conditions in which the column is not subjected to stability loss of divergence type, the usage of kinetic stability criterion is essential to determine the critical load. In such a case the column undergoes destruction due to oscillatory vibrations of ascending amplitude (non-stability of a flutter type). A system subjected to a non-conservative load, where the type of stability loss (divergence or flutter) is dependent on structural parameters or parameters connected to the load, is called a hybrid system (cf. [17.10]). The rigidities of translational or rotational springs, constants of elasto-plastic or viscoelastic dampers, asymmetry coefficient of flexural rigidity (in a case of complex systems), mass and the mass moment of inertia of bodies connected to a column, can be structural parameters. The mentioned discrete elements can be present in different places of the considered system. They can be elements of the supported column (modelling impact of construction on the column) as well as elements present in the constructional nodes of the system, e.g. in the nodes of loaded structures (in this case they have an influence on the reciprocal translational or rotational displacement of cooperating elements). The parameters connected to a load are the coefficients which determine direction of non-conservative force action (e.g. in the case of Beck's generalised load) or the point of application of the force (e.g. in the case of Reut's generalised load).

17.3. A conservative condition of the load resulting from the field theory

A cantilever column subjected to a theoretical generalised load (cf. Fig. 17.1) is considered. The choice of this type of load was made due to the fact that all real cases of the load have to be expressed by an adequate selection of coefficients of generalised load (cf. [17.30]). The determined conservative condition of a generalised load can be compared with other cases. Lateral force H and bending moment M of the generalised load are dependent on axial force P, deflection $y(l)$ and deflection angle $y^I(l)$ of the loaded end of the column in the following way (P = const)

$$H = P\left[\left.\frac{dy(x)}{dx}\right|^{x=l}(1-\mu) - y(l)\gamma\right]; \quad M = P\left[\rho\left.\frac{dy(x)}{dx}\right|^{x=l} + \nu y(l)\right] \quad (17.1a,b)$$

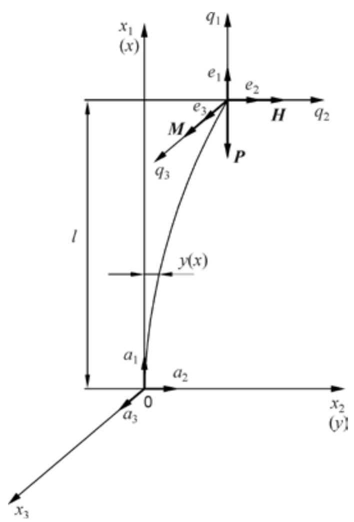

Fig. 17.1. Column subjected to a generalized load

The considered column is situated in a coordinate system $\{x_i\}$ with versors $\{\boldsymbol{a}_i\}$. Coordinates $\{x_i\}$ do not influence the external load, represented by vectors $\boldsymbol{P}$, $\boldsymbol{M}$ and $\boldsymbol{H}$, which are connected to the orthogonal coordinate system $\{q_i\}$ with versors $\{\boldsymbol{e_i}\}$. Lateral force $\boldsymbol{H}$ and bending moment $\boldsymbol{M}$ are dependent on the method of imposing the compressive external force $\boldsymbol{P}$ applied to the end of the column. The potential energy of generalised load is given by the following

$$V = -P\frac{1}{2}\int_0^l \left[\frac{dy(x)}{dx}\right]^2 dx + \frac{1}{2}Hy(l) + \frac{1}{2}M\frac{dy(x)}{dx}\Bigg|^{x=l} \tag{17.2}$$

The longitudinal displacement of the loaded end of the column, after using the theorem of integral mean-value, can be written in the form

$$\frac{1}{2}\int_0^l \left[\frac{dy(x)}{dx}\right]^2 dx = \frac{1}{2}\alpha y^I(l)y(l) \tag{17.3}$$

where: $\alpha \in (0,1)$.

The vector field of forces $\boldsymbol{C}$ is conservative if it is irrotational. Rotation of the considered vector field (force field) must be equal to zero

$$\operatorname{rot} \boldsymbol{C} = 0 \tag{17.4}$$

If the force field is conservative, the gradient of potential energy will be equal to the considered force field

$$\operatorname{grad} V = \boldsymbol{C}. \tag{17.5}$$

Coordinates of orthogonal system $\{q_i\}$ after considering equation (17.3) are as follows

$$q_1 = \frac{1}{2}\alpha q_2 q_3\,, \quad q_2 = y(l), \quad q_3 = \frac{dy(x)}{dx}\Bigg|^{x=l} \tag{17.6a-c}$$

The rotation of vector field $\boldsymbol{C}$ is equal to

$$\operatorname{rot} \boldsymbol{C} = \begin{vmatrix} \boldsymbol{e_1} & \boldsymbol{e_2} & \boldsymbol{e_3} \\ \dfrac{\partial}{\partial q_1} & \dfrac{\partial}{\partial q_2} & \dfrac{\partial}{\partial q_3} \\ P & H & M \end{vmatrix} \tag{17.7}$$

or after being rewritten

$$\operatorname{rot} \boldsymbol{C} = \boldsymbol{e_1}\left[\frac{\partial M}{\partial q_2} - \frac{\partial H}{\partial q_3}\right]. \tag{17.8}$$

Taking into account relationship (17.8), the final form of the conservative condition of the load can be expressed by

$$\frac{\partial M}{\partial y(l)} - \frac{\partial H}{\partial\left(\left.\frac{dy(x)}{dx}\right|^{x=l}\right)} = 0 \tag{17.9}$$

After substituting the relationship for lateral force H (17.1a) and bending moment M (17.1b), the final form of the conservative condition of the generalised load is obtained

$$\nu + \mu - 1 = 0 \tag{17.10}$$

Considering the derived conservative condition of the load (Eq. (17.10)) fulfilment of function (17.5) is obtained.

17.4. The course of the curve in the plane load - natural frequency

The equation describing the considered curve, that is $d\Omega^2/d\lambda$, should be derived to investigate the course of the characteristic curves in the plane: load λ - natural frequency Ω^2. This equation is derived on the basis of Leipholz's integro-differential relationship [17.11]

$$\Im = \int_0^l \left[y^{IV}(x) + \lambda\, y^{II}(x) - \Omega^2 y(x)\right] y(x)\,dx = 0 \tag{17.11}$$

The detailed derivation of the considered formula can be found in paper [17.11] considering a generalised active load and in [17.33] for an active and passive generalised load.

Taking into account publication [17.11] the equation describing the course of the curve in the plane load - natural frequency is in the following form

$$\frac{d\Omega^2}{d\lambda} =$$

$$= \frac{-\int_0^l \left[y^I(x)\right]^2 dx + \rho\left[y^I(l)\right]^2 - \gamma\left[y(l)\right]^2 + (\nu - \mu + 1) y(l) y^I(l)}{\int_0^l \left[y(x)\right]^2 dx + \frac{m\left[y(l)\right]^2}{\rho_0 A} - \lambda(\nu + \mu - 1)\left(y^I(l)\frac{\partial y(l)}{\partial \Omega^2} - y(l)\frac{\partial y^I(l)}{\partial \Omega^2}\right)} + \tag{17.12}$$

$$+ \frac{\lambda(\nu + \mu - 1)\left(y^I(l)\frac{\partial y(l)}{\partial \lambda} - y(l)\frac{\partial y^I(l)}{\partial \lambda}\right)}{\int_0^l \left[y(x)\right]^2 dx + \frac{m\left[y(l)\right]^2}{\rho_0 A} - \lambda(\nu + \mu - 1)\left(y^I(l)\frac{\partial y(l)}{\partial \Omega^2} - y(l)\frac{\partial y^I(l)}{\partial \Omega^2}\right)}$$

In the case of a conservative load (that is considering condition (17.11)) the examined equation can be written as

$$\frac{d\Omega^2}{d\lambda} = \frac{-\int_0^l \left[y^I(x)\right]^2 dx + \rho\left[y^I(l)\right]^2 - \gamma\left[y(l)\right]^2 + 2\nu\, y(l) y^I(l)}{\int_0^l \left[y(x)\right]^2 dx + \frac{m\left[y(l)\right]^2}{\rho_0 A}} \tag{17.13}$$

Equation (17.13) is valid for all types of conservative load mentioned in point 17.1 of this work. The values corresponding to any adequate case of a conservative load (every kind of load is characterised by different values of specified coefficients) should be substituted into parameters ρ, ν and γ.

If in the considerations, a non-conservative load is taken into account (condition (17.10) is not valid), the equations describing the considered curves are as follows (ρ, ν, μ, γ for adequate non-conservative loads are recorded in brackets):

– Beck's generalised load ($\rho = 0$, $\nu = 0$, $\mu = 1\text{-}\eta$, $\gamma = 0$)

$$\frac{d\Omega^2}{d\lambda} = \frac{-\int_0^l \left[y^I(x)\right]^2 dx + \eta\, y(l) y^I(l) - \lambda\eta\left(y^I(l)\frac{\partial y(l)}{\partial \lambda} - y(l)\frac{\partial y^I(l)}{\partial \lambda}\right)}{\int_0^l \left[y(x)\right]^2 dx + \frac{m\left[y(l)\right]^2}{\rho_0 A} + \lambda\eta\left(y^I(l)\frac{\partial y(l)}{\partial \Omega^2} - y(l)\frac{\partial y^I(l)}{\partial \Omega^2}\right)} \tag{17.14}$$

– Reut's generalised load ($\rho = 0$, $\nu = \eta$, $\mu = 1$, $\gamma = 0$)

$$\frac{d\Omega^2}{d\lambda} = \frac{-\int_0^l \left[y^I(x)\right]^2 dx + \eta\, y(l) y^I(l) + \lambda\eta \left(y^I(l)\frac{\partial y(l)}{\partial \lambda} - y(l)\frac{\partial y^I(l)}{\partial \lambda}\right)}{\int_0^l \left[y(x)\right]^2 dx + \frac{m\left[y(l)\right]^2}{\rho_0 A} - \lambda\eta \left(y^I(l)\frac{\partial y(l)}{\partial \Omega^2} - y(l)\frac{\partial y^I(l)}{\partial \Omega^2}\right)} \tag{17.15}$$

The terminology connected to the columns is given from the point of view of a curve course in the plane load - natural frequency.

In Fig. 17.2 possible cases of characteristic curves of systems subjected to conservative and non-conservative loads are presented.

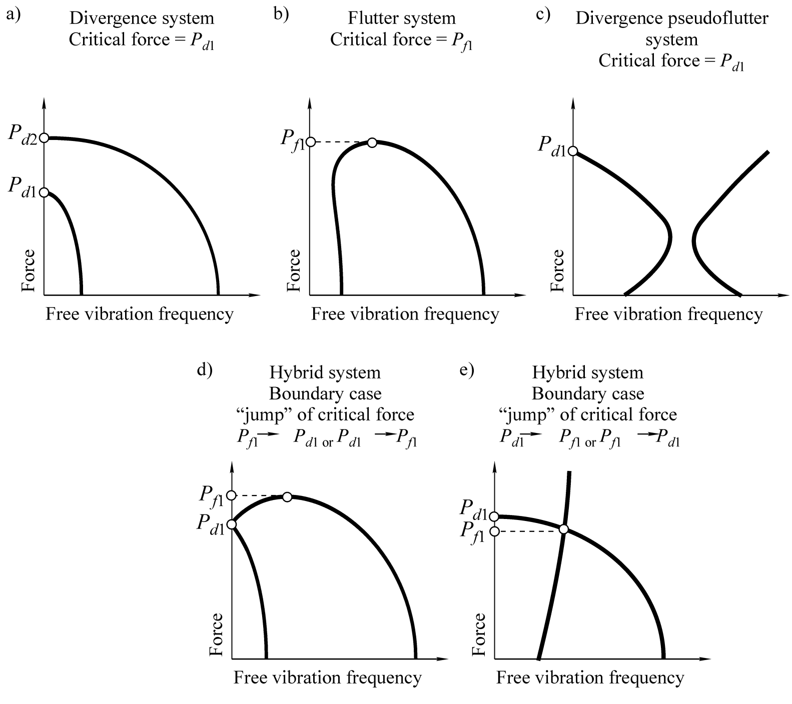

Fig. 17.2. The characteristic curves in the plane: load - natural frequency

For the presented courses the support systems can be divided into:

- divergence system (Fig. 17.2a). A system of this type undergoes destruction due to buckling at the critical divergence force, after reaching which the column movement stopped being restrained. The critical force corresponds to zero value of the first natural frequency (cf. [17.11, 17.38]);
- flutter system (Fig. 17.2b). A system of this type undergoes destruction due to oscillatory vibrations of ascending amplitude for the

critical flutter force. In this case one can distinguish two type of flutter instability: so-called quiet and violent flutter. The column is unlikely to undergo destruction for a quiet flutter of a short duration at the critical load (amplitude increases very slowly and the critical flutter force has a low value). It is the opposite in the case of violent flutter - the amplitude increases very quickly, so even a short load of the system by critical force can lead to its destruction (cf. [17.1, 17.8, 17.27]);

– divergence pseudo-flutter system (Fig.17.2c). This system undergoes destruction due to buckling. Stability loss is analogical to the divergence system. The difference between the divergence system and divergence pseudo-flutter consists of a change in buckling form. The divergence system is characterised by buckling form without nodal, while in a divergence pseudo-flutter system, nodal is present in the buckling form. In this case the slope of the characteristic curve can be positive, negative or zero, while a divergence system is characterised by a negative or zero slope of the considered curves (cf. [17.25, 17.26, 17.32]);
– hybrid system. A hybrid system can lose stability due to both buckling and oscillatory vibrations of growing amplitude. The type of stability loss is dependent on the values of the system parameters. The boundary course of curves in the plane load – natural frequency (Fig. 17.2d and 17.2e) is a characteristic feature of hybrid systems. In the boundary case (corresponding to adequately chosen parameters) there are simultaneously two critical forces: a buckling critical force and a flutter force. One can distinguish two types of hybrid systems. In the first one, the critical flutter force is higher than the critical buckling force considering the boundary course of the characteristic curves. In the second type, the relation between the critical forces is inverse (the critical divergence force is higher in comparison to the critical buckling force) (cf. [17.21, 17.28, 17.18]).

17.5. Modelling and analysis of slender structures under piezoelectric actuation

17.5.1. Introduction

Piezoelectric actuators, which utilize the inverse piezoelectric effect of piezoelectric materials to generate displacement and force, are characterised by a compact structure, very precise movement, high force generation and quick response time with low energy consumption.

Culshaw stated [17.2] that piezoactuators are able to perform 100-1000 times higher work per unit volume and to generate 10 times more energy per unit mass than conventional pneumatic, hydraulic or electromagnetic actuators. The maximal energy transfer from an actuator to the mechanical system occurs in the case when the rigidity of both components are comparable. These properties make them appropriate for micro positioning, structure shaping, vibration control, cancellation and generation as well as for fluid control functions as valves, dispensers and micro pumps. Many possible applications are given by the producers of actuators [17.40÷17.42], and they are also thoroughly discussed in review papers by Niezrecki et al. [17.12], Peng and Chen [17.13] and Wang and Wu [17.39]. Peng and Chen [17.13] presented recent achievements in the modelling and control of piezoelectric actuators (PEAs). They examined various methods for modelling the linear and nonlinear behaviours of PEAs, including hysteresis and creep. It should be added that contemporary material science and engineering produces piezoelectric materials which are characterized by a very low, and hence insignificant, hysteresis. These crystalic materials show 10-times higher linearity than classical materials (barium titanate, lead zirconate titanate - PZT) and can be applied for a very precise positioning without the necessity of open-loop control. Wang and Wu [17.39] described the role of piezoelectric materials on both the structural stability enhancement of engineering structures and the repair of delaminated structures under static and dynamic loadings.

As piezoceramic materials exhibit small strains - the ratio of displacement to thickness for PZT is in the range of 0.1÷0.2% - different actuator configurations have been developed. Niezrecki et al. [17.12] reviewed the architectural trends in amplifying small piezoelectric strains and categorized architectures of actuators into internally, externally and frequency-leveraged schemes. For an external scheme a direct extension of the material is amplified by the external mechanism. That idea has been a strong motivation because piezoceramic materials have one distinguishing attribute with regard to other smart materials - a Young's modulus of the value within the range of $6 \div 9 \cdot 10^{10}$ N/m^2. Such a high modulus is comparable to that of other engineering materials like aluminium, brass or bronze. This makes possible to discretely mount piezoceramic elements of different shapes and dimensions to the host structure to enhance its static or dynamic performance. The flextensional actuator (flexure guided actuator) is a very representative system of the externally leveraged scheme. In this device the beams and stiff link elements create an amplification frame including thin metal webs called flexural hinges or flexures. During the operation an excitation of the piezoelectric element (a monolithic bar or a stack), due to the applied voltage, results in its extensional in-plane motion in the axial direction, which is transformed into out-of-plane motion via the flexure of the surrounding frame - Fig. 17.3.

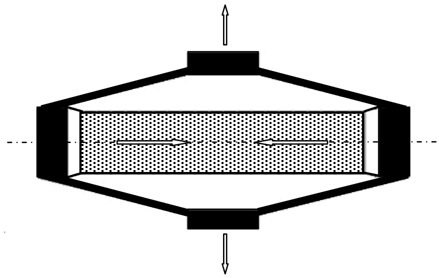

Fig. 17.3. Working principle of a flextensional actuator

Two piezoelectric effects related to piezoelectric coefficients d_{31} and d_{33} are utilised to generate the axial displacement of the active element, i.e. the transverse and longitudinal effects, which relate longitudinal and transverse deformations to the electric field applied along and perpendicular to the poling direction.

According to the IEEE Standard on Piezoelectricity [17.8] the constitutive equations for piezoceramic materials, which are transversely isotropic in the 12-plane and exhibits symmetry about the 3-axis, are given as

$$S_p = s_{pq}^E \, T_q + d_{ip} \, E_i \tag{17.16}$$

$$D_i = d_{iq} \, T_q + \xi_{ij}^T \, E_j \tag{17.17}$$

where: $i, j = 1, 2, 3$ and $p, q = 1, 2, ..., 6$.

In (Eq. 17.16, 17.17) $\boldsymbol{S}$ is the strain vector, $\boldsymbol{T}$ is the stress vector [N/m^2], $\boldsymbol{E}$ is the electric field vector [C/m^2], $\boldsymbol{D}$ is the electric displacement vector [V/m], s_{pq}^E is the elastic compliance matrix [m^2/N], d_{ip} is the piezoelectric constant matrix [m/V], ξ_{ij}^T is the permittivity coefficient matrix [F/m] and the superscripts E and T denote that the respective constants are evaluated at constant electric field and constant stress, respectively.

When a piezoceramic element is modelled as a Euler-Bernoulli beam or within the Rayleigh beam theory, all components of the stress vector with the exclusion of T_1 are treated as negligible

$$T_2 = T_3 = T_4 = T_5 = T_6 = 0 \tag{17.18}$$

and for a voltage along the 3-axis, Eq. 1 can be presented as follows

$$\begin{bmatrix} S_1 \\ D_3 \end{bmatrix} = \begin{bmatrix} s_{11}^E & d_{31} \\ d_{31} & \xi_{33}^T \end{bmatrix} \begin{bmatrix} T_1 \\ E_3 \end{bmatrix} \tag{17.19}$$

For piezoceramic stacks and the electric field vector parallel to the 3-axis, the constitutive equations are reduced to the form

$$\begin{bmatrix} S_3 \\ D_3 \end{bmatrix} = \begin{bmatrix} s_{33}^E & d_{33} \\ d_{33} & \xi_{33}^T \end{bmatrix} \begin{bmatrix} T_3 \\ E_3 \end{bmatrix} \tag{17.20}$$

(Eqs. 17.16,17.17,17.19 and 17.20) define electromechanical coupling in piezoceramic materials and establish the basis for a description of the static and dynamic behaviour of smart systems controlled by piezoelectric actuation.

17.5.2. Application of piezoceramic transducers for enhancing stability and dynamic control of structure

Piezoelectric control of slender structures with surface bonded piezo-patches or with piezoelectric rods discretely mounted to the host structure has been studied in the Institute of Mechanics and Machine Design Foundations of Czestochowa University of Technology for many years. These investigations have concerned among others the non-linear vibrations of a beam with a pair of piezoceramic patches [17.14], the stability of an articulated column with two collocated piezoelectric actuators [17.16], the static and dynamic analysis of a flextensional transducer with an axial piezoelectric actuation [17.17] and the shape control of an eccentrically loaded host column by means of a piezoceramic rod [17.15].

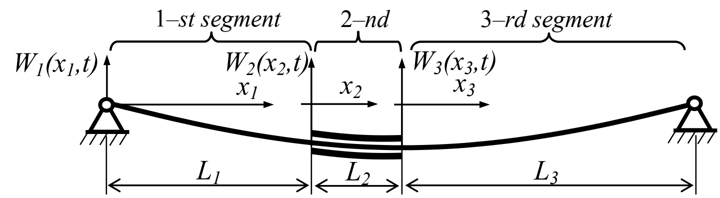

Fig. 17.4. Beam with piezoceramic patches [17.14]

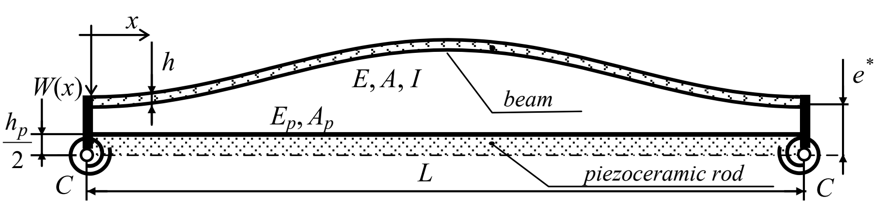

Fig. 17.5. Flextensional transducer with an axial piezoelectric actuation [17.17]

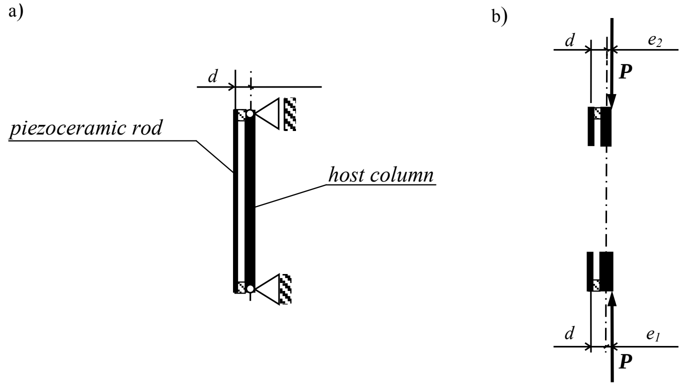

Fig. 17.6. Column with the piezoceramic rod [17.15]

The results of numerical simulations of the static behaviour of a column with a piezoelectric rod (Fig. 17.6) are presented in figures 17.7÷17.10. In Fig. 17.7 the transversal displacements of the host column midpoint are plotted for three values of *d* specifying the offset between the axis of the two members. Fig. 17.7a concerns the midpoint displacement due to the external load, while Fig. 17.7b shows its suppression as a result of piezoactuation. It can be concluded that an increase in distance *d* results in a greater initial displacement but simultaneously a smaller voltage is needed for the complete reduction of this displacement.

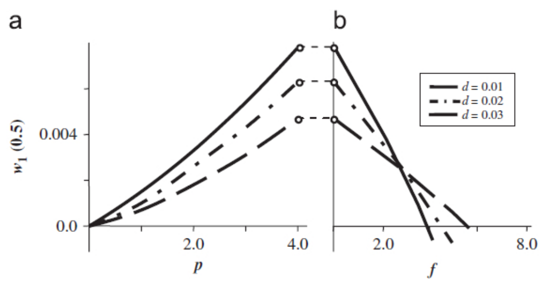

Fig. 17.7. The change in transversal displacement of the midpoint as a function of the external load (a) and the piezoforce (b) at different offset distance [17.15]

In Fig. 17.8 an increase in the transversal displacements of the midpoint with an external load are plotted. Independently from the value of the piezoelectric force, when the external load reaches its critical value, the displacement tends to infinity. Studying the change in the transversal displacement of the column (Fig. 17.9) it can be stated that the initial deflection, which is caused by the eccentrically applied load, can be gradually reduced by generating the piezoelectric force. For every configuration, a maximum reduction point can be found above which any further increase in the piezoelectric force results in over actuation causing a reverse deflection. In relation to the reduction of the displacements, a decrease in the bending moments along the length of the column have been presented in Fig. 17.10. In summary, it can be stated that proper actuation allows one to reduce both the deflection and the bending moment in the column at the same time.

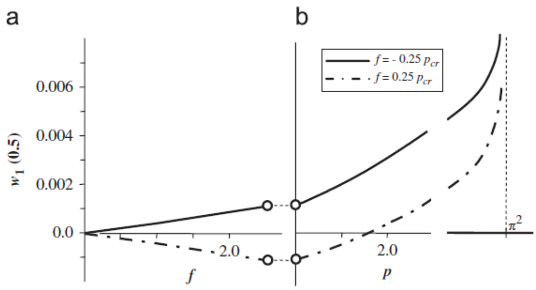

Fig. 17.8. The change in displacement of the midpoint as a function of the tensile and compressive piezoforce (a) and the external load (b) [17.15]

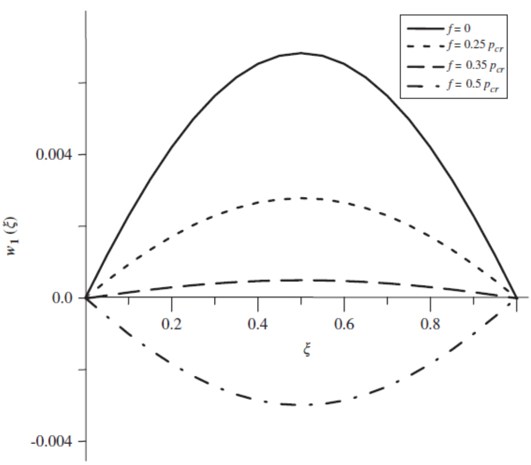

Fig. 17.9. Deflected axis of the column at different values of the piezoforce [17.15]

In the theoretical studies presented in this subchapter, it was shown that the deflection of the structure caused by an eccentrically applied external load can be controlled by a properly applied voltage to the piezoceramic bar. In the real construction the breakdown voltage must also be taken into account to prevent the depolarization of the piezoelement. The proper ratio of the flexural rigidity between the host column and piezo bar should also be selected to provide maximal energy transfer from the actuator to the system. The problem of over actuation can be solved by the close loop control strategy according to which the supplied voltage depends on the column bending being measured continuously by means of small piezo sensors or strain gauges. Instead of very long monolithic piezoceramic bars, production of which is rather expensive, one can apply segmented rods with/or piezo stack actuators. The stacks offer high energy density compared to other smart materials and can be effectively used for the purpose mentioned in this subchapter.

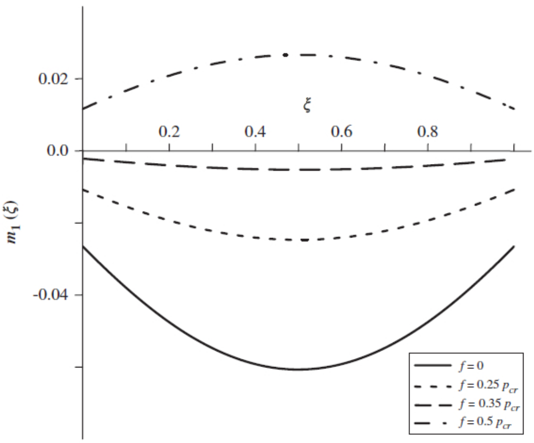

Fig. 17.10. Distribution of the bending moment along the column length for different values of the piezoforce [17.15]

17.6. Stability of a column resting locally on a Winkler type elastic base at specific load

The stability of a column loaded by a follower force directed towards the positive pole which rests locally on a Winkler type elastic base is considered (KLW system - Fig. 17.11b). The load is realized by a head inducing and taking a load of circular contour (constant curvature). The column was loaded by force P whose course of action goes through constant point O. Additionally, the course of action of the external loaded force is tangential to the bending line of the free end ($x = L$) of the system rod. The total length of the column equals L (while: $L = l_1 + l_2 + l_3$).

The system was divided into three elements with flexural rigidity $(EJ)_1$, $(EJ)_2$, $(EJ)_3$, (while: $(EJ)_1 = (EJ)_2 = (EJ)_3 = EJ$) to model an elastic base with coefficient of elasticity K (the base placed locally on a certain segment along the column length).

At the free end the column is connected to the head taking the load through an infinite rigid element of l_0 in length. Consideration of this element is essential due to the structural solution of the head realising the load. The flexural rigidity of the mentioned element is multiply higher than the flexural rigidity of the slender system. Pole O was placed within (R - l_0) of the free end of the column. The results obtained for the KLW system are compared to the KL system (Fig. 17.11a) - a comparative system without a base.

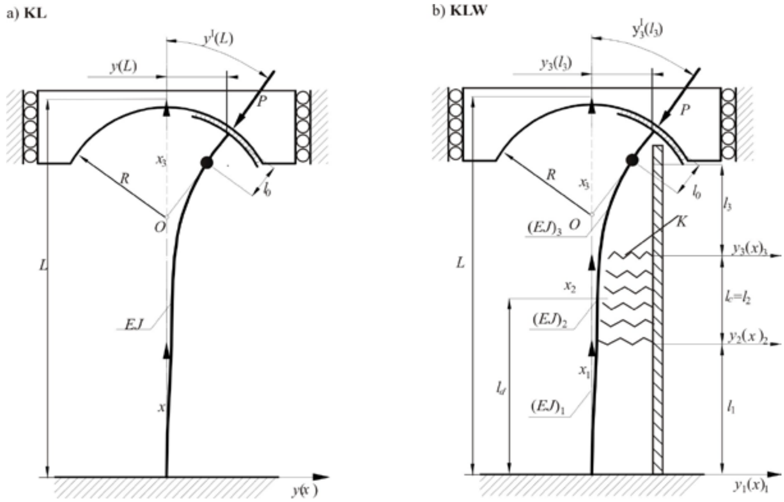

Fig. 17.11. Physical model of the column: a) linear column (KL), b) linear column resting locally on the Winkler type elastic base

The parameters describing the location and the size of the Winkler type elastic base in relation to the length of the column were introduced to describe this base (equations 17.21a,b).

$$l_c^* = \frac{l_2}{L} = \frac{l_c}{L}, \quad l_d^* = \frac{2l_1 + l_2}{2L} = \frac{l_d}{L} \tag{17.21a,b}$$

17.6.1. Potential energy of the system. Equations of displacement, boundary conditions

The components of potential energy are defined according to the Bernoulli-Euler bending theory taking into account the physical model of the column. The total potential energy V of the KLW system is as follows

$$\begin{aligned} V = \frac{EJ}{2}\sum_{i=1}^{3}\int_0^{l_i}\left[y_i^{II}(x_i)\right]^2 dx_i - \frac{P}{2}\sum_{i=1}^{3}\int_0^{l_i}\left[y_i^{I}(x_i)\right]^2 dx_i + \frac{P}{2}(R-l_0)\left[y_3^I(l_3)\right]^2 + \\ + \frac{1}{2}K\int_0^{l_2}\left[y_2(x_2)\right]^2 dx_2, \quad i = 1,2,3 \end{aligned} \tag{17.22}$$

The stability problem of a geometrically linear column was solved using the principle of minimum potential energy which consists of searching for the load at which the potential energy stopped being positively definite $\delta V = 0$, where: δ - variation operator.

Applying relationship (17.22), after computing the variation of potential energy and considering the dimensionless quantities in the form

$$\varphi_1 = \frac{l_2}{l_1}, \varphi_2 = \frac{l_3}{l_2}, (R-l_0)^* = \frac{R-l_0}{l_3}, \zeta_i = \frac{x_i}{l_i}, y_i(\zeta_i) = \frac{y_i(x_i)}{l_i},$$
$$K^*_{l_2} = \frac{Kl_2^4}{EJ}, \quad k_i^2 = \frac{Pl_i^2}{EJ}, \tag{17.23a-g}$$

The equations of lateral displacements were received

$$\begin{aligned} &y_j^{IV}(\xi_j) + k_j^2 y_j^{II}(\xi_j) = 0, j = 1,3 \\ &y_2^{IV}(\xi) + k_2^2 y_2^{II}(\xi) + K^*_{l_2} y_2(\xi) = 0 \end{aligned} \tag{17.24a-b}$$

the boundary conditions of the considered system KLW are

$$\begin{array}{ll} & y_1(0) = 0, \\ \varphi_1 y_1^{II}(1) = y_2^{II}(0), & y_1^{I}(0) = 0, \\ \varphi_2 y_2^{II}(1) = y_3^{II}(0), & y_1(1) = \varphi_1 y_2(0), \\ \varphi_1^2 y_1^{III}(1) = y_2^{III}(0), & y_2(1) = \varphi_2 y_3(0), \\ \varphi_2^2 y_2^{III}(1) = y_3^{III}(0) & y_1^{I}(1) = y_2^{I}(0), \\ (R-l_0)^* y_3^{III}(1) - y_3^{II}(1) = 0, & y_2^{I}(1) = y_3^{I}(0), \\ & y_3(1) = (R-l_0)^* y_3^{I}(1) \end{array} \tag{17.25a-l}$$

17.6.2. The results of numerical computations

Numerical computations were carried out on the basis of the stability of the considered system taking into account the solution to the boundary problem. The research results were presented giving consideration to the dimensionless parameters of the critical load of the system λ_c^* and an elastic base K^*

$$\lambda_c^* = \frac{P_{kr} L^2}{EJ}, \quad K^* = \frac{KL^4}{EJ} \tag{17.26a,b}$$

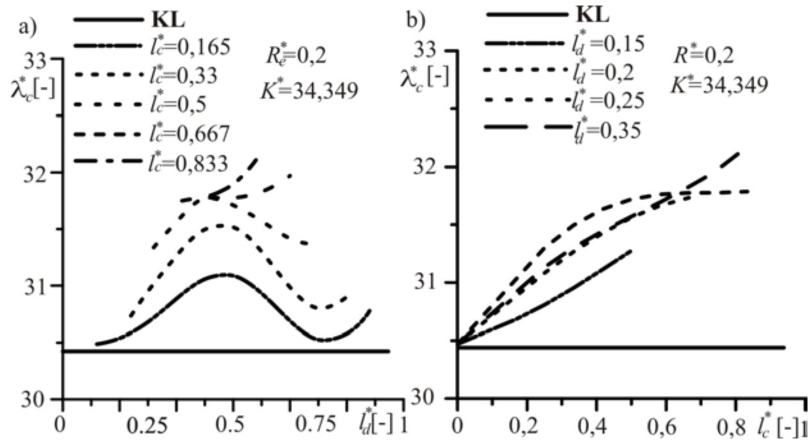

Fig. 17.12. Change in the dimensionless parameter of the critical load λ_c^* in relation to: a) placement of an elastic base l_d^* along the column length, b) the length of an elastic base l_c^*

The influence of the length of elastic base l_d^* on the dimensionless value of the critical load λ_c^* is presented in Fig 17.12, equation (17.26a). Numerical analysis was carried out for the chosen parameters of the head realising the load (R^* parameter - equation 17.27) and the elastic base (K^* - equation 17.26b).

$$R^* = \frac{R - l_0}{L} \tag{17.27}$$

The influence of the change in the value of R^* head parameter inducing the load on the critical value of the load parameter λ_c^* is presented in Fig. 17.12. The computations were carried out for the chosen parameters of rigidity of the elastic base K^* for a constant length of column L and the rigid element of the head realizing the load, being l_0 in length. All curves reach extreme values ($\left(R_e^*\right)_m$, where m = 1...6) in dependence on the parameters of rigidity of elastic base K^*. Together with an increase in the parameter of elastic base, the critical load reaches extremum for the smaller values of the radius of the head realizing the load. In the case of the KL column, the maximal value of the load occurs for $R_e^* = 0.5$.

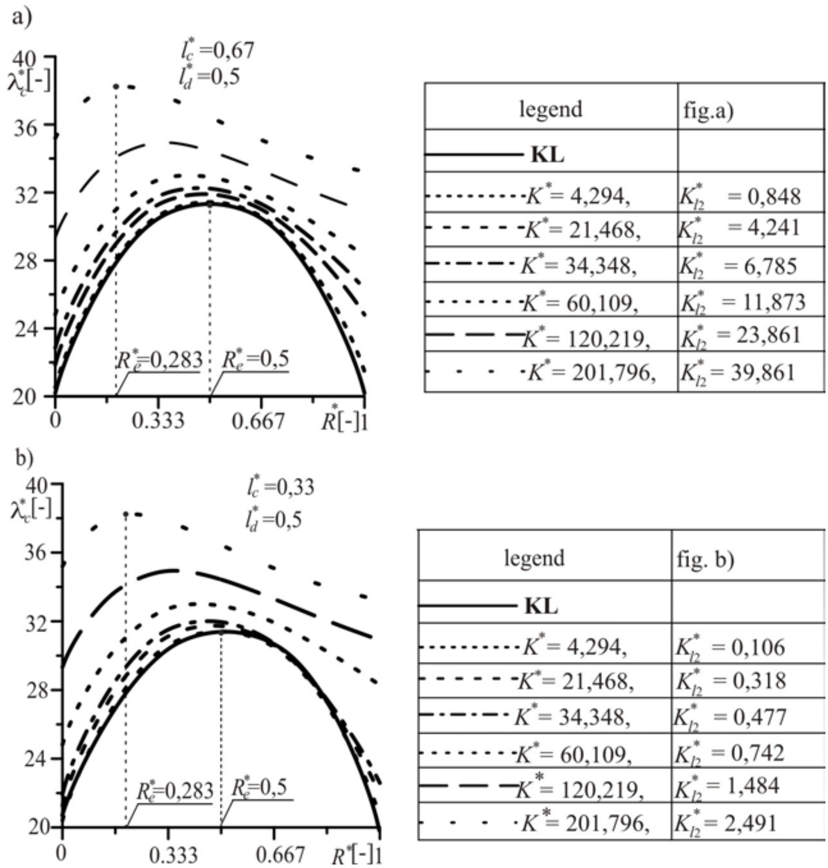

Fig. 17.13. Change in critical parameter of the load λ_c^* in relation to parameter R^* of the head inducing the load of the system for different values of rigidity coefficient of the elastic base K^*

A range of changes in the values of the parameters of head realising the load R_e^*, for which maximal values of the critical load were received for the given values of Winkler's base rigidity, is presented in Fig. 17.14. The computations were carried out for chosen parameters of elastic base l_c^* and its placement l_d^*.

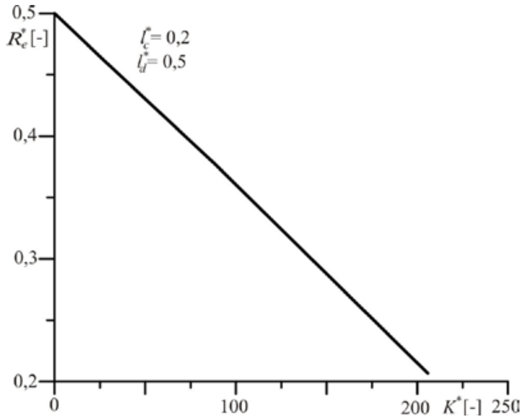

Fig. 17.14. Influence of the rigidity coefficient of elastic base K* on the value of the head parameter inducing the load R_e^*

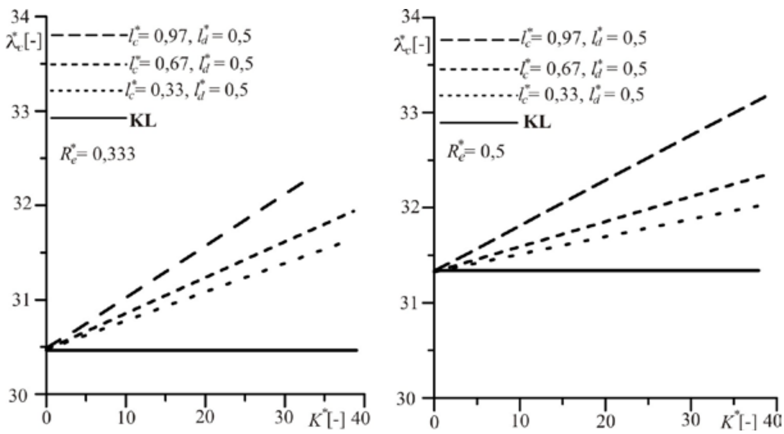

Fig. 17.15. Influence of the rigidity coefficient of elastic base K^* on the value of critical parameter of the load λ_c^* of KLW column

In Fig. 17.15, the influence of the rigidity coefficient of elastic base K^* on the value of the dimensionless parameter of critical load λ_c^* is shown. Computations were carried out for chosen parameters of head radius R^* and for chosen values of the location and placement of the elastic base. Together with an increase in the rigidity coefficient of the base at given lengths of the column, an increase in the value of the dimensionless parameter of load λ_c^* occurs.

A physical and a mathematical model of the system was built within theoretical research presented in this subsection. The boundary conditions of the considered column were determined on the basis of potential energy. Numerical simulations, concerning changes in the critical load in relation to chosen parameters of the heads realizing the load, were carried out. On the basis of the conducted numerical computations it can be stated that there are some values of the geometrical parameters of the heads for which the maximum of the critical load is obtained. Consideration of the Winkler type base in the physical model of the column increases the value of the critical load. The value of this load is dependent on the l_c^*, l_d^* parameters describing the base size and its location in relation to the system length. Maximal values are obtained for the base placement at the free end of the column.

17.7. References

17.1 Beck M., Die Knicklast des einseitig eingespannten, tangential gedrückten Stabes, ZAMM, 3, 1952, pp. 225-228.

17.2 Culshaw B., Smart Structures and Materials, Artech House Optoelectronics Library, Boston 1996.

17.3 Gajewski A., Życzkowski M., Optima shaping of an Elastic Homogeneous Bar Compresed by Polar Force, Biulletyn de L`Academie Polonaise des Sciences, Vol. XVII, No. 10, 1969, pp. 479-488.

17.4 Gajewski A., Życzkowski M., Optimal Design of Elastic Columns Subject to the General Conservative Behaviour of Loading, ZAMP, 21, 1970, pp. 806-818.

17.5 Hozjan T., Planinc I., Saje M., Srpcic S., Buckling of restrained steel columns due to fire conditions, Steel and Composite Structures, 8, 2008, pp. 159-178.

17.6 IEEE Standard on Piezoelectricity, Standards Committee of the IEEE Ultrasonics, Ferroelectrics and Frequency Control Society, IEEE, New York 1987.

17.7 Kounadis A.N., The existence of regions of divergence instability for nonconservative systems under follower forces, Int. Journal Solids Structures, 19, 8, 1983, pp. 725-733.

17.8 Langthjem M.A., Sugiyama Y., Dynamic stability of columns subjected to follower loads: a survey, Journal of Sound and Vibration, 238, 5, 2000, pp. 809-851.

17.9 Leipholz H., Piche R., Stability of follower-force rods with weight, J. Eng. Mech. Div., ASCE, 110(3), 1984, pp. 367-379.

17.10 Leipholz H.H.E., Aspects of Dynamic Stability of Structures, Journal of the Engineering Mechanics Division, April 1975, EM2, pp. 109-124.

17.11 Leipholz H.H.E., On Conservative Elastic Systems of the First and Second Kind, Ingenieur-Archiv, 43, 1974, pp. 255-271.

17.12 Niezrecki C., Brei D., Balakrishnan S., Moskalik A., Piezoelectric Actuation: State of the Art. Shock and Vibration Digest, Vol. 33, No. 4, 2001, pp. 269-280.

17.13 Peng J., Chen X., A Survey of Modeling and Control of Piezoelectric Actuators, Modern Mechanical Engineering, Vol. 3, 2013, pp. 1-20.
17.14 Przybylski J., Non-linear vibrations of a beam with a pair of piezoceramic actuators, Engineering Structures, Vol. 31, 2009, Issue: 11, pp. 2687-2695.
17.15 Przybylski J., Sokół K., Shape control of an eccentrically loaded column by means of piezoceramic rod, Thin Walled Structures, Vol. 49, 2011, pp. 652-659.
17.16 Przybylski J., Stability of an articulated column with two collocated piezoelectric actuators, Engineering Structures, Vol. 30, 2008, pp. 3739-3750.
17.17 Przybylski J., Static and dynamic analysis of a flextensional transducer with an axial piezoelectric actuation, Engineering Structures, Vol. 84, 2015, pp. 140-151.
17.18 Przybylski J. The role of prestressing in establishing regions of instability for a compound column under conservative or nonconservative load, Journal of Sound and Vibration, 231(2), 2000, pp. 291-305.
17.19 Qian G.L., GU. S.N., Jiang J.S., 1990, The dynamic behavior and crack detection of a beam with a crack, Journal of Sound and Vibration, 225(1), pp. 201-208.
17.20 Sokół K., Linear and Nonlinear Vibrations of a Column with an Internal Crack, Journal of Engineering Mechanics, 140, No. 5, 2014.
17.21 Sundararajan C., Influence of an elastic end support on the vibration and stability of Beck's column, Int. J. Mech. Sci. 18, 1976, pp. 239-241.
17.22 Szmidla J., Drgania swobodne i stateczność układów smukłych poddanych obciążeniu swoistemu, Częstochowa, 2009.
17.23 Tomski L., Przybylski J., Gołębiowska-Rozanow M., Szmidla J., Vibration and stability of columns to a certain type of generalised load, Journal of Theoretical and Applied Mechanics, 37, 2, 1999, pp. 283-299.
17.24 Tomski L., Przybylski J., Gołębiowska-Rozanow M., Szmidla J., Vibration and stability of a cantilever column subject to a follower force passing through a fixed point, Journal of Sound and Vibration, 214, 1, 1998, pp. 67-81.
17.25 Tomski L., Przybylski J., Gołębiowska-Rozanow M., Szmidla J., Vibration and stability of an elastic column subject to a generalized load, Archive of Applied Mechanics 67, 1996, pp. 105-116.
17.26 Tomski L., Przybylski J., Gołębiowska-Rozanow M., Szmidla J., Vibration and stability of a cantilever column subject to a follower force passing through a fixed point, Journal of Sound and Vibration, 214, 1, 1998, pp. 67-81.
17.27 Tomski L., Przybylski J., Flutter Instability of a Two Member Compound Column, Journal of Sound and Vibration, 146(1), 1991, pp. 125-133.
17.28 Tomski L., Przybylski J., Static Instability of an Elastically Restrained Cantilever Under a Partial Follower Force, AIAA Journal, 23(10), 1985, pp. 1637-1639.
17.29 Tomski L., Szmidla J., Badania teoretyczne drgań swobodnych i stateczności kolumn geometrycznie liniowych poddanych obciążeniu uogólnionemu, rozdział 2, Drgania i stateczność układów smukłych, Praca zbiorowa

wykonana pod kierunkiem naukowym i redakcją L. Tomskiego, WNT, Fundacja „Książka Naukowo-Techniczna", Warszawa 2004, pp. 40-67.

17.30 Tomski L., Szmidla J., Badania teoretyczne drgań swobodnych i stateczności kolumn geometrycznie liniowych poddanych obciążeniu uogólnionemu, rozdział 2, Drgania i stateczność układów smukłych, Praca zbiorowa wykonana pod kierunkiem naukowym i redakcją L. Tomskiego, WNT, Fundacja „Książka Naukowo-Techniczna", Warszawa 2004, pp. 68-133.

17.31 Tomski L., Szmidla J., Local and global instability and vibration of overbraced Euler's column, Journal of Theoretical and Applied Mechanics 41, 1, 2003, pp. 137-154.

17.32 Tomski L., Szmidla J., Vibration and Stability of Column Subjected to Generalised Load by a Force Directed Towards a Pole, Journal of Theoretical and Applied Mechanics 42, 1, 2004, pp. 163-193.

17.33 Tomski L., Uzny S., Badania teoretyczne drgań i stateczności kolumn poddanych swoistemu obciążeniu czynnemu i biernemu, rozdział 3, Drgania swobodne i stateczność układów smukłych poddanych obciążeniu konserwatywnemu i niekonserwatywnemu, red. L. Tomski, PWN, Warszawa 2012, pp. 59-78.

17.34 Tomski L., Uzny S., Free vibration and the stability of a geometrically non-linear column loaded by a follower force directed towards the positive pole, International Journal of Solids and Structures, 45, 1, 2008, pp. 87-112.

17.35 Tomski L., Uzny S., The regions of flutter and divergence instability of a column subjected to Beck's generalized load, taking into account the torsional flexibility of the loaded end of the column, Mechanics Research Communications, 38, 2011, pp. 95-100.

17.36 Tomski L., Uzny S., Vibration and stability of geometrically non-linear column subjected to generalised load by a force directed towards the positive pole, International Journal of Structural Stability and Dynamics 8, 1, 2008, pp. 1-24.

17.37 Uzny S., Free Vibrations of an Elastically Supported Geometrically Nonlinear Column Subjected to a Generalized Load with a Force Directed toward the Positive Pole, Journal of Engineering Mechanics-ASCE, 137(11), 2011, pp. 740-748.

17.38 Uzny S., Local and global instability and vibrations of a slender system consisting of two coaxial elements, Thin-Walled Structures, 49, 2011, pp. 618-626.

17.39 Wang Q., Wu N. A review on structural enhancement and repair using piezoelectric materials and shape memory alloys. Smart Materials and Structures, Vol. 21 (1), 2012, pp. 1-23.

17.40 www.dynamic-structures.com/actuators/

17.41 www.piceramic.com/applications.html

17.42 www.cedrat-technologies.com/en/mechatronic-products/actuators.html

18.

Elasto-plastic behaviour and load-capacity of multi-layered plated structures

18.1. Introduction

This chapter is a review of research realized in last decade mainly in collaboration with the late Professor Katarzyna Kowal-Michalska in the domain of elasto-plastic behaviour and ultimate strength of multi-layered plated structures. Thin plates consisting of several layers are widely used in modern thin-walled structure design. The layers are made of different materials. This concept is connected with common effort to reduce the weight of a structure while maintaining its strength properties. Since the mid-1980s, composite materials have been widely used in numerous engineering applications, also as materials of thin-walled beams and columns. Among them there are fiber composites, fiber metal laminates (FML), functionally graded materials (FGM). A separate class of multi-layered plated structures are sandwich plates: three-layered plates with different types of structural cores (honey comb, corrugated sheets, reinforced foam).

The fibrous composite material consists mostly of two components: the matrix and reinforcement i.e. fibres. The typical modern fibrous composite material is that belonging to the HCTL class (Hybrid Titanium Composite Laminate) and it consists of several layers of titanium and carbon fibres laid alternately [18.26].

Fibrous composites are non-homogenous and anisotropic materials. In particular cases, if fibres are orientated in the matrix in one or two perpendicular directions the composite is the orthotropic material with certain principal directions of orthotropy. If the reinforcement is distributed randomly in the matrix the composite material is isotropic one.

Fiber Metal Laminates (FMLs) are hybrid materials, built from thin layers of metal alloy and fiber reinforced epoxy resin. These materials are manufactured by bonding composite plies to metal ones. FMLs, with respect to metal layers, can be divided into FMLs based on aluminum alloys (ARALL reinforced with aramid fibers, GLARE - glass fibers, CARALL - carbon fibers) and others. Nowadays material such as GLARE (carbon fiber/aluminum) due to their very good fatigue and strength characteristics combined with the low density find increasing use in aircraft industry. The most common type of aluminium applied in Glare is 2024-T3 Alloy.

The safe work of thin-walled structures subjected to in-plane loading is often determined by local buckling. The methods allowing for estimation of ultimate strength of thin-walled plated structures can be classified into four categories:

- analytical-numerical methods where the equations describing the elastic post-buckling behaviour are found out analytically and next the elasto-plastic state is dealt with on the basis of the theory of plasticity by means of an iterative procedure [18.10],
- the effective width approach, which consists in reduction of the flexural stiffness of the cross-section after local buckling and subsequently - in the implementation of the first yield threshold criterion in order to estimate a load-carrying capacity of the structure (lower bound estimation) [18.10, 18.22],
- numerical methods - finite element methods and finite strip methods are both included in this category [18.25, 18.15],
- kinematical methods based on principle of virtual velocities, leading to the upper-bound estimation of ultimate load [18.13].

18.2. Problem formulation

The aim of the study is the estimation of the ultimate load for rectangular three-layered plates subjected to compression. The load carrying capacity of three-layered plated structures is determined by means of four methods mentioned above. The considered plate elements are simply supported and initially flat. The complex structure is assumed to be built of three-layered plates with metallic isotropic face layers and metallic or composite (orthotropic) core. The following core materials are taken into consideration:

a) metallic,
b) fibrous composite,
c) FML material,
d) honeycomb core.

The loading is applied in such a way that during analysis the response of the plate to the increment of its nodal displacements (Fig. 18.1) is searched for.

The plates are initially flat and stress free. It is assumed that the plate edges are simply supported and remain straight during loading. The plates are built of two identical isotropic layers (faces) that cover the middle layer (a core) of different material than faces.

The plates under consideration can be treated as individual elements (walls) of plated structures such as columns or beams (girders). Determining an ultimate strength of separate plate member allows one to estimate (approximately as a lower bound) the ultimate load of a whole structure.

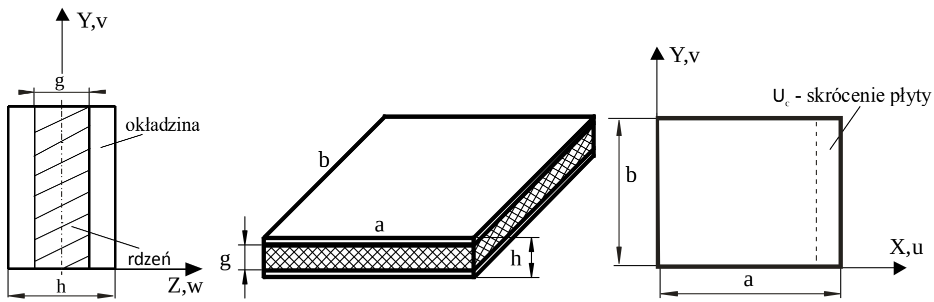

Fig. 18.1. Geometry of the plate

18.3. Review of applied methods of analysis

18.3.1. Analytical-numerical method

The method described below allows one to conduct the analysis of strains and stresses in the elastic and elasto-plastic range and to find out a load-displacement curve for the multi-layered plate. The analysis is carried out on the basis of nonlinear theory of thin plates involving plasticity [18.6, 18.8]. When mechanical properties of all layers are of the same range, the Kirchhoff's hypothesis can be applied for the entire section.

The elastic material properties are determined by following independent constants:

- for outer layers: E_m, ν_m,
- for middle layer (it can be orthotropic in such a way that there are only differences in strengths/yield limits due to positive and negative stresses) - E_c, ν_c,
- the pre-buckling displacement and stress fields of a plate are described by its nodal displacements in the *x* and *y* direction

$$u^o = U_c \frac{x}{a} \tag{18.1}$$

and additionally: $\sigma_x^o = const.$, $\sigma_y^o = 0$, $\tau_{xy}^o = 0$.

In the elastic range the solution of buckling problem and post-buckling behaviour has been obtained on the ground of the classical theory of thin laminated plates [18.10].

In order to obtain the approximate solution of the problem the expressions describing the forms of displacement fields in the elastic range have been found out (the detailed description of the method is given in Refs. [18.6, 18.7]).

The deflection function "*w*" has been assumed as

$$w = f \sin\frac{\pi x}{a}\sin\frac{\pi y}{b} \tag{18.2}$$

where f denotes the free parameter.

Assuming the in-plane displacements u and v in following forms

$$u = u^o + f^2\left(C_1 \sin\frac{2\pi x}{a} + B_1 \sin\frac{2\pi x}{a}\cos\frac{2\pi y}{b}\right) \tag{18.3}$$

$$v = v^o + f^2\left(C_2 \sin\frac{2\pi y}{b} + B_2 \sin\frac{2\pi y}{b}\cos\frac{2\pi x}{a}\right) \tag{18.4}$$

where C_1, C_2, B_1, B_2 are constants depending on the material and geometrical properties of layers that can be found out from equilibrium equations and taking into account boundary conditions. The displacement fields are determined for whole plate in the elastic range.

If the displacements "*u*", "*v*", "*w*" are known then using the von Karman's geometrical relations between strains and displacements and Hooke's law for orthotropic and/or isotropic material the elastic stresses can be determined in any point of a three layered plate.

In aim to determine the ultimate load the analysis of the post-buckling state has to be carried out in the elasto-plastic range. In the plastic range the following assumptions are made:

– the material properties of layers are known in the whole range of stresses,
– the appropriate yield criterion is applied for considered materials,
– all assumptions of non-linear plate theory still hold,
– the forms of displacement functions are the same in the elastic and elasto-plastic range but their amplitude "*f*" can vary arbitrarily,
– according to the plastic flow theory the increments of plastic strains are described by Prandtl-Reuss equations.

Additionally it has been assumed that the material characteristics of isotropic and orthotropic layers are elastic-perfectly plastic. Therefore the following material properties in plastic range are to be applied:

- for isotropic material (faces, core) - σ_{Ym}, σ_{Yc} - yield limit,
- for orthotropic material (a core) - T, C - yield limit in tensile and compression tests in x and y direction, respectively; and additionally S - yield stress in pure shear.

For orthotropic materials Tsai and Wu proposed the yield (failure) criterion that takes into account the difference in strengths due to positive and negative stresses. In case of a plane stress state Tsai-Wu criterion is formulated as follows

$$F = k_1\sigma_x + k_2\sigma_y + k_3\tau_{xy} + k_{11}\sigma_x^2 + k_{22}\sigma_y^2 - k_{12}\sigma_x\sigma_y + 3k_{33}\tau_{xy}^2 = 1 \tag{18.5}$$

where parameters k_1, k_2, k_3 and $k_{11}, k_{22}, k_{12}, k_{33}$ have to be determined by tensile, compressive and shear tests [18.10].

It is easy to notice that both Hill's yield criterion and Huber-Mises criterion can be obtained from the equation (18.5).

The associated flow rule for a given yield criterion can be expressed as [18.10]

$$d\varepsilon_{ij}^p = \Lambda S_{ij}; \qquad i, j = 1,2,3 \tag{18.6}$$

where: $S_{ij} = \dfrac{1}{3}\dfrac{\partial F}{\partial \sigma_{ij}}; \qquad i, j = 1,2,3$.

The relations (18.6) were formulated by Prandtl and Reuss [18.10].

In the calculations of elasto-plastic plates undergoing large deformations the infinitesimal increments in (18.6) have to be replaced by finite ones (denoted by Δ). Then the relations between stress and strain increments in the elasto-plastic range are described by Prandtl-Reuss equations in a form

$$\begin{aligned}
\Delta\sigma_{\mathrm{x}} &= \frac{E}{(1-\nu^2)}[\Delta\varepsilon_{\mathrm{x}} + \nu\Delta\varepsilon_{\mathrm{y}} - \Lambda(S_{\mathrm{xx}} + \nu S_{\mathrm{yy}})] \\
\Delta\sigma_{\mathrm{y}} &= \frac{E}{(1-\nu^2)}[\Delta\varepsilon_{\mathrm{y}} + \nu\Delta\varepsilon_{\mathrm{x}} - \Lambda(S_{\mathrm{yy}} + \nu S_{\mathrm{xx}})] \\
\Delta\tau_{\mathrm{xy}} &= G(\Delta\gamma_{\mathrm{xy}} - \Lambda S_{\mathrm{xy}})
\end{aligned} \tag{18.7}$$

where S_{xx}, S_{yy}, S_{xy} are defined as

$$S_{xx} = \frac{TC}{3}(k_1 + 2k_{11}\sigma_x - k_{12}\sigma_y)$$
$$S_{yy} = \frac{TC}{3}(k_2 + 2k_{22}\sigma_y - k_{12}\sigma_x) \tag{18.8}$$
$$S_{xy} = 2TCk_{33}\tau_{xy}$$

T and C denote the values of yield (failure) stress in tension and compression, respectively, determined for the characteristic of reference (see [18.10]).

For a material isotropic in the elastic range with the elastic-perfectly plastic characteristics the parameter Λ (which is a scalar, positively defined) is [18.10]

$$\Lambda = \frac{(S_{xx} + \nu S_{yy})\Delta\varepsilon_x + (S_{yy} + \nu S_{xx})\Delta\varepsilon_y + G^* S_{xy}\Delta\gamma_{xy}}{S_{xx}^2 + 2\nu S_{yy}S_{xx} + S_{yy}^2 + G^* S_{xy}^2} \tag{18.9}$$

where: $G^* = G\left(1 - \nu^2\right)/E$.

Rayleigh-Ritz variational method involving plasticity is applied to the problem. It was proved by Graves-Smith [18.8] that it is possible to apply the variational method to the plates undergoing finite deflections.

The potential energy in any point of a plate is a sum of elastic and plastic components. The plastic strain energy existing prior to the current strain increment bears no direct relation to the current state of stresses. For the purposes of minimisation this energy may arbitrarily be put to zero and only further changes of the strain energy have been taken into account.

$$\Delta W = \int_V \left[\left(\sigma_x + \frac{1}{2}\Delta\sigma_x \right)\Delta\varepsilon_x + \left(\sigma_y + \frac{1}{2}\Delta\sigma_y \right)\Delta\varepsilon_y + \left(\tau_{xy} + \frac{1}{2}\Delta\tau_{xy} \right)\Delta\gamma_{xy} \right] dxdydz \tag{18.10}$$

where: V - is a volume of the plate, $\sigma_x, \sigma_y, \tau_{xy}$ denote the stresses before the loading increment is applied and $\Delta\sigma_x, \Delta\sigma_y, \Delta\tau_{xy}$, $\Delta\varepsilon_x, \Delta\varepsilon_y, \Delta\gamma_{xy}$ denote the stress and strain increments produced by the increment of shortening ΔU_c.

In the elasto-plastic range the current state of stresses depends on the path of loading, so the solution of the problem can only be reached numerically. Therefore the numerical solution starts from the evaluation of the energy increment (10). In order to accomplish this, every layer is divided equally into $i \times j \times k$ appropriate cubicoids. The energy values calculated in each of cubicoids are summed for a whole structure.

Next, the numerical minimisation of the energy functional is performed versus independent parameter *f* of displacement functions. The average stress corresponding directly to the load applied to a considered structure is obtained numerically.

In each step of calculations active, passive and neutral processes and also the reduction of stress to the yield surface are taken into account.

18.3.2. Finite element method

The FE analysis of buckling, post-buckling and ultimate load of thin-walled members is usually solved in two steps:

- linear stability analysis (eigenvalue problem), which gives buckling loads (bifurcation points) and buckling modes (Fig. 18.3a [18.11]),
- non-linear stability analysis that allows to follow the behaviour of the structure in the post-buckling range and to find out the load carrying capacity.

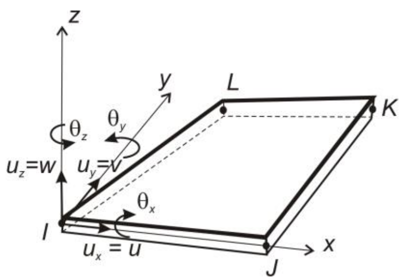

Fig. 18.2. Four-node shell element

Results of a linear buckling analysis (buckling loads and buckling modes) are used in the second step - non-linear analysis. The FE discrete model with the perturbation (geometric imperfections of the same shape as buckling modes determined in the first step) is applied. The analysis is carried out in order to determine the post-buckling path, the ultimate load and post-failure path. The imperfection amplitude is usually taken as 1/10 to 1/20 of the plate thickness. The FE model is built from shell elements. The simplest, typical shell element is shown in Fig. 18.2. It is a four-node element with six degrees of freedom at each node.

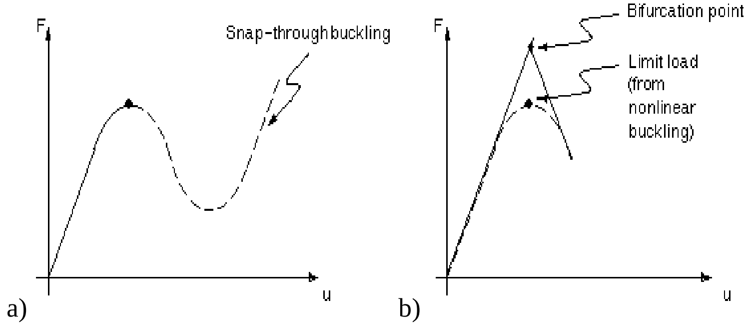

Fig. 18.3. Relations between forces and displacements in nonlinear and linear stability analysis using FEM [18.11]

In the present analysis the FE model was built of eight-node multi-layered shell elements of six degrees of freedom at each node (Fig. 18.4). This element allows to account for up to 100 layers of different thickness and material properties. In order to ensure the compatibility of boundary conditions considered in both methods the coupled degrees of freedom were assumed on the plate edges. It means that the distribution of applied compressive forces has to correspond to the uniform shortening of loaded edges and in the same time the unloaded edges should to remain straight and free of stresses. To describe a material stress - strain relationship the bilinear characteristic with plastic hardening [18.24, 18.25] was involved (Bilinear Kinematic Hardening option was used in ANSYS software).

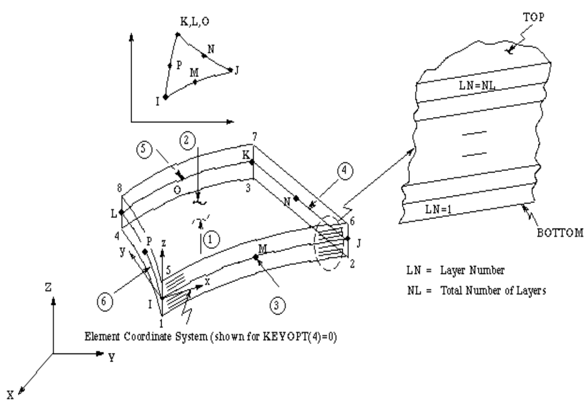

Fig. 18.4. Multi-layered shell element [18.24]

It should be added that in the post-buckling range the calculations were conducted using iteration scheme, the “arc-length” method, in order to avoid bifurcation points and track unloading. The applied iteration method is represented schematically in Fig. 18.5 [18.24].

The numerical calculations were conducted using FE commercial code ANSYS. The value of the imperfection amplitude was equal to 1/20 of the thickness of an analysed structure.

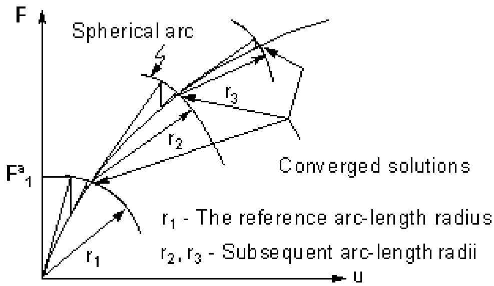

Fig. 18.5. Arc-length iteration method [18.24]

18.3.3. Plastic mechanism analysis

The kinematical method associated with the plastic mechanism approach (yield-line theory - YLT), has been used successfully to the analysis of ultimate load and post-failure behaviour of thin-walled structures since 60-ties of the 20th century [18.19]. This approach is attractive from some points of view, for it leads to relatively simple analytical or analytical-numerical solutions and provides not only with the upper-bound estimation of the ultimate load but with a knowledge about a rapidity of the failure process as well. The combination of the non-linear, post-buckling analysis with the analysis of the plastic mechanism allows one to establish a failure parameter approximately, i.e. to estimate the *upper bound* load-carrying capacity of the structure. Failure process in thin-walled, multi-layered structures may be of different character The failure modes of sandwich structures, depending on different layers configurations, materials of layers, span, etc., include face sheet yielding at large deformations (mainly for metal faces), face wrinkling, core shear leading to crack or yielding, core indentation. In the case of face sheets made of composite materials, one can detect delamination of faces. Another mode of failure is debonding on the contact surface between face sheet and core. Thus, among all failure modes mentioned above, a failure due to yielding (both in face sheets and core) can also take place in certain cases.

The kinematical method, based on the principle of virtual velocities [18.13, 18.19, 18.15], has been applied to the problem of the load-carrying capacity estimation of multi-layered plated structures in association with the rigid-plastic theory. Thus, the following additional assumptions are taken in the analysis:

- yield occurs in all layers simultaneously, so that the continuity of plastic strains takes place (it limits the analysis to certain “sets” of materials),
- layers lay-out is symmetrical with respect to the plate middle surface and yield stresses increase with the increase of the distance from the centre layer,
- yield zones are not only concentrated at yield lines, but also at plastic zones of tensile stresses (true or quasi-mechanisms are taken into account).

In the case of the multi-layered plate subject to compression, from the principle of virtual velocities we obtain the following variational relation

$$\delta W_{ext} = \delta W_b + \delta W_m \tag{18.11}$$

where δW_{ext} is the variation of work of external forces, δW_b is the variation of the energy of bending plastic deformation, δW_m - variation of the energy of membrane plastic deformation.

The fully plastic moment capacity [18.13, 18.15] at concentrated yield-lines has been evaluated for multi-layered walls of the global plastic mechanism, under assumptions mentioned above.

$$\overline{\tilde{\overline{m}}}_p = m^0_{p\beta} + \sum_{i=1}^{n} \left\{ t_i \sigma_{0i} \cdot [t_0 + \sum_{j=1}^{i-1} (2t_j) + t_i] \right\} \tag{18.12}$$

where $m^0_{p\beta}$ is a fully plastic moment at the centre layer (generally orthotropic) which is expressed as follows

$$m^0_{p\beta} = \frac{\sigma^k_{00} t_0^2}{4} \qquad k = 1,2 \tag{18.13}$$

for yield-line parallel to principal directions of orthotropy with corresponding yield stresses σ^k_{00},

$$m^0_{p\beta} = \frac{\sigma_{\gamma 00} t_0^2}{4} \tag{18.14}$$

for yield-line inclined at angle γ to principal directions of orthotropy whereas $\sigma_{\gamma 00}$ is the yield stress for the direction γ that can be evaluated according to Hill yield criterion [18.16]. The variation of the energy of bending plastic deformation dissipated at a yield-line amounts

$$\delta W_b = \sum_k l_k \overline{\overline{\tilde{m}}}_p \delta\beta_k \tag{18.15}$$

where l_k is a length of the yield-line and β_k is an angle of relative rotation of two walls of the global plastic hinge along that line.

In the case of three-layered wall with orthotropic core and taking into account the strain hardening phenomenon in face sheets, the plastic moment takes the form

$$\overline{\overline{\tilde{m}}}_p = m^0_{p\beta} + \left(\sigma_{01} + \frac{\overline{\sigma}_1 - \sigma_{01}}{2}\right) \cdot t_1(t_0 + t_1) \tag{18.16}$$

where $m^0_{p\beta}$ is a fully plastic moment at the center layer (core), generally orthotropic, t_1, t_0 are facings and core thickness, respectively, σ_{01} - yield stress of the facing material. The effective stress $\overline{\sigma}_1$ is evaluated under assumptions taken by Kotełko [18.13, 18.16]

$$\overline{\sigma}_1 = \sigma_{01} + E_t \cdot \frac{\beta}{2n} \le \sigma_{ult} \tag{18.17}$$

where E_t is a tangent modulus and σ_{ult} is an ultimate stress of the facing material, β is an angle of rotation as in [18.15] and n is a multiple of the wall thickness.

Variation of plastic strain energy dissipated at plastic zones of membrane stresses in i-th layer takes form

$$\delta W_{m,i} = (N_{xi}\delta\varepsilon^p_x + N_{yi}\delta\varepsilon^p_y)A_p \tag{18.18}$$

where: N_{xi}, N_{yi} are membrane forces per unit length, A_p is an area of membrane stresses plastic zones. Membrane forces N_{xi}, N_{yi} can be determined using the associated flow rule for Huber-Mises yield criterion.

The total plastic strain energy dissipated at plastic zones of membrane stresses through the whole plate thickness is expressed as

$$\delta W_m = \delta W_{m0} + 2\sum_{i=1}^{n} \delta W_{mi} \tag{18.19}$$

where: δW_{m0} - plastic strain energy in center layer, δW_{mi} - plastic strain energy in i-th layer.

Taking into account (18.12) to (18.19) in (18.11), a relation of compressive external force P in terms of shortening parameter (represented graphically as a *failure curve*) is evaluated.

An evaluation of the failure structural path (referred to as failure curve) can be used subsequently to the upper bound estimation of the load-carrying capacity of the plate or plated structure, namely an ordinate of the inter-section point of the failure curve with the post-buckling path obtained from the solution discussed in paragraph 3.2 is referred to as an upper bound ultimate load of the plate.

18.4. Selected numerical results

In this paragraph selected results of comparative numerical analysis carried out using three methods mentioned above, namely: analytical-numerical method (ANM), Finite Element Method (FEM) and kinematical method (KM) are presented for three-layered plates made of different materials. Point 4.9.3. concerns a particular problem of the three-layered plate with honeycomb core, solved using equivalent single plate models.

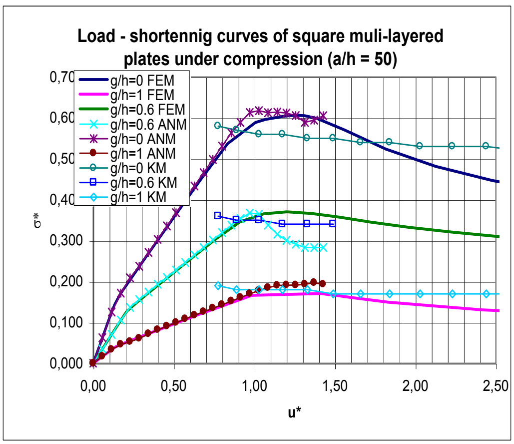

Faces - stainless steel
$E_m=2*10^5$ MPa; $\nu_m=0.3$
$\sigma_{Ym}=184$ MPa.

Core-aluminium
$E_c=7*10^4$ MPa $\nu_c=0.3$
$\sigma_{Yc}=123$ MPa.

Fig. 18.6. Load-shortening curves of square steel-aluminium-steel plate under compression [18.11]

18.4.1. Plates with metallic or fibrous composite core

Diagrams in Fig. 18.6 present the comparison of results obtained using different analytical methods and Finite Element Method for the plate with steel face sheets and aluminum core. Ratios g/h and a/h correspond to the notation in Fig. 18.1. The diagrams show the non-dimensional average stress normalized with respect to face sheets yield stress $\sigma^* = \sigma_{av}/\sigma_{Ym}$ in terms of non-dimensional shortening coefficient $u^* = (u_c/a)/(\sigma_{Ym}/E_m)$ in the whole range of loading, including the failure phase. Diagrams present FE results (curves FEM), results of calculations of the load-capacity in the elasto-plastic range, based on the method, described in paragraph 18.3.1 [18.17] (curves ANM) and failure curves for the pitched-roof plastic mechanism [18.15], obtained using kinematical method, described in paragraph 18.3.3 (curves KM). In the kinematical approach the pitched-roof plastic mechanism model has been applied [18.15]. Three sets of diagrams are presented, corresponding to three different core thickness to total plate thickness ratio g/h.

Analogous diagrams in co-ordinate system $\sigma^* = \sigma_{cv}/\sigma_{Ym}$ in terms of $u^* = (u_c/a)/(\sigma_{Ym}/E_m)$ for the plate with composite core are shown in Fig. 18.7.

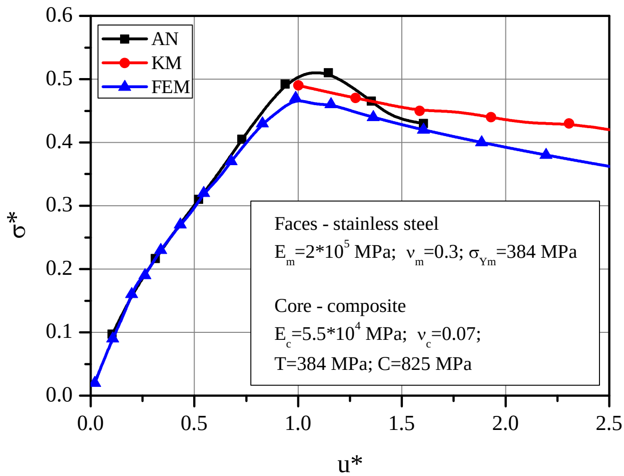

Fig. 18.7. Load-shortening curves of square metal-composite-metal plate under compression (a/h = 100) [18.11]

Analytical-numerical method (ANM) and FE simulations give very close results. The kinematical approach results, which are comparable with other results in the plastic range only, are also in relatively good agreement with two first methods.

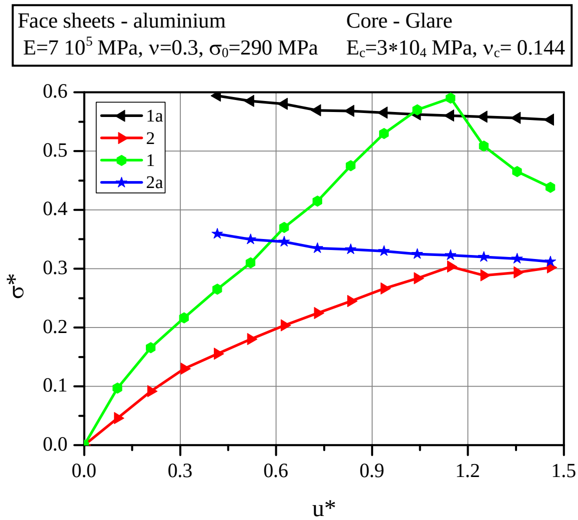

Fig. 18.8. Load-shortening diagrams of square metal-FML-metal plate under compression: a/h = 50; g/h = 0,4 (curves 1, 1a), g/h = 0,2 (curves 2, 2a); curves 1a,2a - kinematical method (KM), curves 1,2 - analytical-numerical method (ANM)

18.4.2. Plates with FML core

When a plate with GLARE core is subjected to the load, acting in its mid-plane, in the post-buckling state aluminium layers undergo yielding, while deformations of layers with glass fibers are still in the elastic range. Thus, structural behaviour of the plate with FML core differs substantially from the behaviour of the plate with homogeneous core [18.12]. In this paragraph very preliminary results of the analysis of structural behaviour of plates with FML core are presented. This analysis should be treated as a very far going approximation. The results concern also very particular parameters of plate layers and cannot be generalized. In Fig. 18.8 load-shortening diagrams in the coordinate system $\sigma^*=\sigma_{cv}/\sigma_{Ya}$ in terms of $u^* = (u_c/a)/(\sigma_{Ya}/E_a)$ are presented. Values of ultimate loads obtained using ANM and KM methods are very close (it should be underlined again, that equilibrium paths obtained from ANM and KM methods are comparable only in the plastic range). However, this agreement has to be confirmed in further analysis for wider range of plate dimensions, material parameters and layers configurations.

18.4.3. Plates with honeycomb core

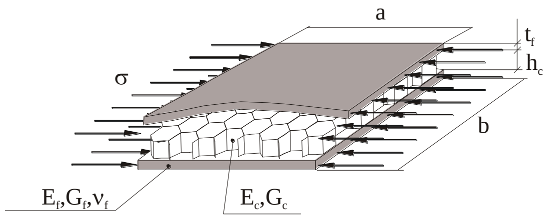

Fig. 18.9. Three-layered plate with honeycomb core

For inherently non-homogeneous structures like densely stiffened panel or three-layered plate with reinforced foam core, honeycomb core as well as corrugated metal sheet core a concept of structural orthotropy can be applied. It means, that one can calculate reduced orthotropic material parameters of the non-homogeneous structural member and subsequently consider the member as homogeneous but orthotropic one. Another words we can “smear” the non-homogeneity of the structure but take into account its orthotropy or generally, anisotropy. The problem of stability and load-capacity of sandwich structures with honeycomb core has been investigated by numerous researchers since 60-ties of the 20th century. Romanów [18.23] and Magnucki and Ostwald [18.17] carried out research in this domain. Romanów [18.11] has solved the problem of the sandwich plate with honeycomb core, using the energy method. Earlier Benson [18.20, 18.2] and Bert [18.3] worked on the same problem. The non-linear problem (of large deformations) of three-layered plate with orthotropic core have been solved by Alwan [18.1].

The problem of homogenisation of the honeycomb core strength characteristics was analyzed by Birger and Panovko [18.4] but has not been solved entirely so far. It seems that this problem as well as a homogenization of local failure phenomena could be solved using an averaging technique based on the asymptotic approach, however there has been very limited investigation into applications of this technique carried out.

Thus, simplified models that enable to avoid a complexity of the real sandwich structure are very much desirable and very attractive for designers under the circumstances discussed above. Two methods may be applied to replace the honeycomb sandwich panel by the equivalent single plate. There are namely: the equivalent rigidity method and the equivalent weight method (Vinson [18.26], Faulkner [18.5]), however limitations of these two approaches have not been entirely defined so far (Paik [18.21] and Kotełko and Mania [18.14]).

In the equivalent rigidity method the single plate equivalent thickness t_{eq} and equivalent Young modulus E_{eq} are defined such that the flexural rigidity of the equivalent plate given by the relation

$$D_{eq} = \frac{E_{eq} t_{eq}^3}{12(1-\nu_{eq}^2)} \tag{18.20}$$

(where $\nu_{eq} = \nu_f$) is equal to the flexural rigidity of the sandwich plate, calculated as (Paik [18.21])

$$D = \frac{E_f [(h_c + 2t_f)^3 - h_c^3]}{12(1-\nu_f^2)} \tag{18.21}$$

Additionally, the shear stiffness of the equivalent plate is equal to the shear stiffness of facings. Thus, the parameters of the single plate are as follows [18.21]

$$\begin{aligned} t_{eq} &= \sqrt{3h_c^2 + 6h_c t_f + 4t_f^2} \\ E_{eq} &= \frac{2t_f}{t_{eq}} E_f \\ G_{eq} &= \frac{2t_f}{t_{eq}} G_f \end{aligned} \tag{18.22}$$

In the equivalent weight method the weight of the equivalent plate equals that of the actual sandwich plate so that the equivalent thickness amounts

$$t_{eq} = \frac{2t_f \rho_f + h_c \rho_{cav}}{\rho_f} \tag{18.23}$$

where ρ_f is a density of the facing material and ρ_{cav} is an average density of the core. The Young and shear moduli are assumed to be equal to those of the facing material ($E_{eq} = E_f$, $G_{eq} = G_f$).

A more realistic and accurate model of the sandwich panel is the three-layered plate with homogenized orthotropic core. In this study the homogenisation of the honeycomb core strength characteristics has been carried out using relations derived by Birger and Panovko [18.4]. Reduced elastic parameters of the core are determined assuming relative displacements of facings of the honeycomb sandwich panel to be equal to the corresponding displacements of three-layered plate with homogeneous orthotropic core. For example, in order to determine a shear modulus G_{xz} one has to calculate (using a certain method) relative displacements of facings in their mid-surfaces subject to loads applied in these surfaces that cause distorsional (shear) relative displacements. The latter have to be compared with corresponding displacements in three-layered plate with homogeneous core. In an analogical way one can determine linear elastic moduli and Poisson ratios analyzing loads causing tension in the plate mid-surface or the normal direction.

Reduced elastic parameters used subsequently in FE analysis have been determined from following relations by Birger and Panovko [18.4]:

– shear moduli

$$G_{yz} = 0.576 G_c \frac{t_0}{r}; \quad G_{xz} = G_c \frac{t_0}{r} \xi \tag{18.24}$$

where t_0 is the thickness of the cell foil, $2r$ is the size of the hexagonal cell, ξ is a coefficient depending on structural parameters of the honeycomb core;

– linear module

$$E_x = E_y = 0 \qquad \text{for} \qquad \frac{h_c E_c t_0}{2 E_f t_f} < 0.25 \tag{18.25}$$

$$E_z = \frac{2 t_0 E_c}{1.3 r}$$

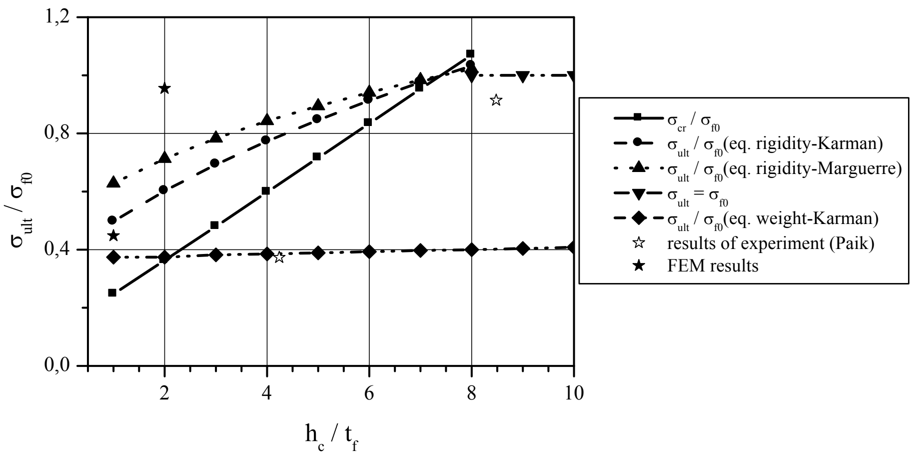

Fig. 18.10. Ultimate compressive stress predictions obtained from equivalent single plate models for square 500x500 mm sandwich plate with aluminium facings and honeycomb core made from aluminium foil t_f = 3 mm,
E_f = 71 070 MPa, σ_{f0} = 268 MPa, ρ_f = 2.7 g/cm^3, ρ_{cav} = 54.4.kg/m^3 [18.22]

The equivalent single plate models have been used by Kotełko and Mania [18.14] in order to determine buckling loads and load-bearing capacity of the sandwich three-layered plate with the honeycomb core subject to compression (Fig. 18.9). The load-bearing capacity of equivalent single plates was determined using the effective width approach. The exemplary results for plates with equivalent rigidity and weight together with FE results obtained for three-layered plate with homogenized core are shown in Fig. 18.10.

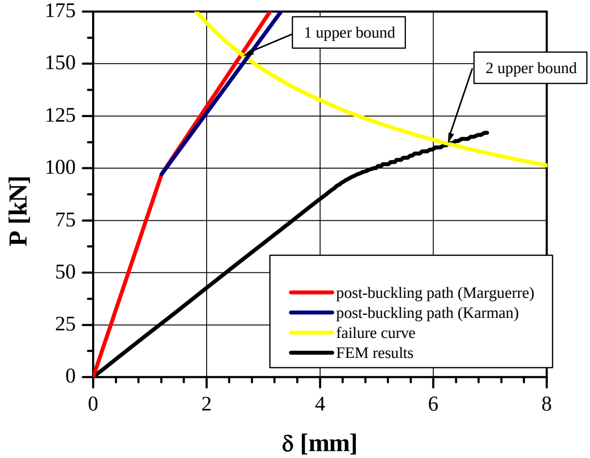

Fig. 18.11. Square plate 500x500 mm, h_C = 3, t_f = 1.5 mm, aluminium facings and honeycomb core made of aluminum foil (E_f = 71 070 MPa, σ_{f0} = 268 MPa), □cav = 54 kg/m^3

The diagrams represent ultimate stress normalized with respect to facings material yield stress σ_{f0}, in terms of core to face thickness ratio. Ultimate stress has been calculated using von Karman [18.9] and Marguerre [18.18] relations for the effective width reduction factor. Diagrams obtained for both equivalent plate models are compared with FE results and experimental results [18.21]. Diagram of the normalized buckling stress, calculated using classical solution for the thin plate under uniform compression, concerns only the model of equivalent rigidity.

The FE analysis was performed in that case using reduced parameters of orthotropy, given by relations (18.11) and (18.12) in section 18.3.3. Hence, the material of facings was assumed isotropic and the core was modelled as homogenous orthotropic layer. The overall critical load and buckling mode of the plate was determined in the linear buckling analysis (eigen-value buckling). The non-linear buckling approach was employed for post-buckling response of the plate. The initial geometric imperfection for non-linear analysis was set as a first buckling mode shape with appropriate reduction coefficient.

Predictions of ultimate stresses obtained for the single plate model of equivalent weight underestimate an actual load-capacity of the sandwich panel except the lowest values of h_c/t_f ratios, although experimental results even for $h_c/t_f = 4.35$ are very close to that prediction. However, it should be underlined here that both experimental ultimate loads indicated in the diagram concern the case of the failure initiated by the delamination while both theoretical models assume a perfect bonding between facings and the core. For higher values of h_c/t_f ratio greater than 3 the equivalent weight model is inadequate and gives ultimate load values more than two times lower than those obtained from equivalent rigidity model.

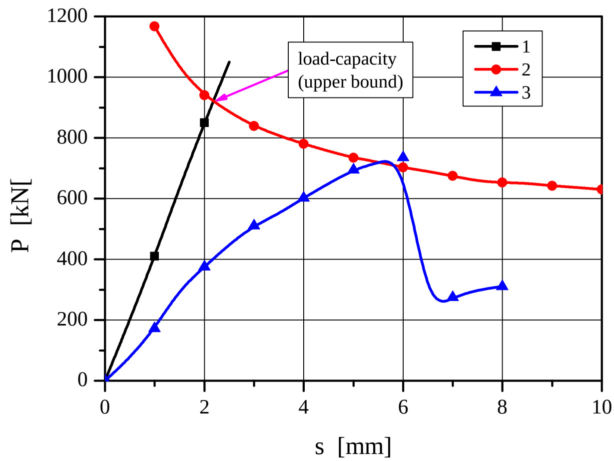

Fig. 18.12. Load-shortening diagram of square 500x500 mm sandwich plate with aluminium facings and honeycomb core made from aluminium foil t_f = 3 mm, h_c = 25.4 mm, E_f = 71 070 MPa, σ_{f0} = 268 MPa, ρ_f = 2.7 g/cm^3, ρ_{cav} = 54.4.kg/m^3

Structural behaviour of the sandwich plate in the entire range of loading (up to and beyond an ultimate load) has been examined using the effective width approach (for post-buckling state) and the kinematical approach (for the failure state). Pre-buckling paths were obtained taking into account compressive stiffness of facings only while compressive stiffness of the core was neglected. The single plate model of equivalent rigidity was applied as a more realistic one.

Post-buckling paths were calculated using the effective width approach with two different reduction factors, by von Karman [18.9] and Marguerre [18.18], respectively.

An exemplary diagram of the plate structural behaviour is shown in Fig. 18.11. Continuous straight line (1) represents the pre-buckling path, the failure curve (2) is obtained from the solution described in the previous paragraph (kinematical approach). The ordinate of the intersection point indicated in the diagram represents the upper-bound estimation of the load-capacity of the sandwich plate. Theoretical pre-buckling and post-failure paths together with the failure curve form an approximate structural behaviour characteristics of the sandwich plate.

The discrepancy of results obtained for the single plate of equivalent rigidity and those obtained from FE calculations for the three-layered plate with homogenized orthotropic core is significant. However, the discrepancy concerns the stiffness of both equivalent plate and the three-layered plate with homogenized core. On the contrary, it is worthy to notice that buckling loads (folding points in both diagrams) are nearly the same for both cases. The discrepancy in magnitudes of upper bound estimations of ultimate loads obtained using the pre- and post-buckling path for the single plate of equivalent rigidity and the failure curve (from kinematical approach) and using FE results and the same failure curve amounts about 36%. More safe seems to be the second estimation: compilation of the failure curve and the post-buckling path obtained from FE analysis.

In this study the same approach has been used in order to analyse the load-capacity and failure of the simplified, approximate model of the sandwich panel, i.e. the model of two-layered plate consisting of facings of the real sandwich plate, the distance of which is maintained constant and equals the core thickness. Thus, the load-carrying capacity of the core is entirely neglected. The model applied is in fact a very “rough” approximation of real phenomena occurring in sandwich panels. However it enables to determine effectively a load-capacity of the sandwich panel in relatively simple analytical-numerical procedure.

Comparison of theoretical and experimental results obtained from the calculations based on this simplified model are shown in Fig. 18.12. Continuous straight line (1) represents the pre-buckling path, the failure curve (2) is obtained from the solution described in paragraph 18.3 (kinematical approach). The ordinate of the intersection point indicated in the diagram represents the upper-bound estimation of the load-capacity of the sandwich plate. Theoretical pre-buckling and post-failure paths form an approximate structural behaviour characteristics of the sandwich plate that is compared with experimental results obtained by Paik [18.21] - curve (3). The agreement of theoretical and experimental values of ultimate loads is reasonably good, although many factors influencing the sandwich panel structural behaviour were not taken into account in this approximate theoretical analysis.

18.5. Final remarks

The above chapter presents some selected results of the structural behaviour analysis of three-layered plates made of widely treated composite materials. It contains also the review of analytical-numerical methods, which can be applied in this analysis and are competitive with Finite Element simulations. However, the authors are aware of many simplifications assumed in those analytical-numerical methods. First of all, yielding is assumed as an only mode of failure, while in real plated structures made of composite materials one has to do with some other complex modes of failure, like face wrinkling, core shear leading to crack, core indentation, debonding on the contact surface between face sheet and core, etc. Thus, further research should be continued to include into the analytical-numerical models some of these phenomena. Also extension of those models into multi-layered plates built of orthotropic layers of different configuration is an open question.

18.6. References

18.1 Alwan A.M., Large deflection of sandwich plates with orthotropic cores, AIAA J. 2,10, 1964.

18.2 Benson A.S., Mayers J., General instability and face wrinkling of sandwich plates. Unified theory and applications, AIAA J., 5, 4, 1967.

18.3 Bert C.W., Cho K.N., Uniaxial compressive and shear buckling in orthotropic sandwich plates by improved theory, AIAA/ASME/ASCE/AHS, 27th Struct., Dyn. and Mat. Conf.,San Antonio, Tex., 1986.

18.4 Birger A.A., Panovko A.B., Strength, Stability, Vibrations. (in Russian), Masinostrojenie, Moskva 1968.

18.5 Faulkner D., A review of effective plating for use in the analysis of stiffened plating in bending and compression, J. Ship Res., 19, 1, 1975, pp. 1-17.

18.6 Grądzki R., Kowal-Michalska K., Stability and ultimate load of multi-layered plates - a parametric study, Engineering Trans., 51, 4, 2003, pp. 445-459.

18.7 Grądzki R., Kowal-Michalska K., Stability and ultimate load of multi-layered plates of constant mass, Proceedings of Fourth Intern. Conf. CIMS'2004, edited by: M.Pignataro, J.Rondal, V.Gioncu, Timisoara 2006.

18.8 Graves-Smith T.R., A variational method for large deflection elasto-plastic theory and its application to arbitrary flat plates, in Structure, Solid Mechanics and Engineering Design, Te'eni, M. ED., Wiley-Interscience, 1971, pp. 1249-1255.

18.9 Kármán T., Sechler E., Donnell L.H., The strength of thin plates in compression, Trans. ASME, 54, 1932, pp. 53-57.

18.10 Kołakowski Z, Kowal-Michalska K. (eds.), Selected problems of instabilities in composite structures. Series of Monographs. Technical University of Łódź 1999.

18.11 Kotełko M., Kowal-Michalska K., et al., Estimation of load carrying capacity of multi-layered plated structures, Thin-Walled Structures, Vol. 46, No 7-9, 2008, pp. 1003-1010.
18.12 Kotełko M., Kowal-Michalska K., Oszacowanie nośności granicznej płyt typu FML przy zastosowaniu metod analityczno-numerycznych (in Polish: Load-carrying capacity estimation of FML plates), XI Konferencja „Nowe Kierunki Rozwoju Mechaniki", Sarbinowo 2015, pp. 51-52.
18.13 Kotełko M., Load-capacity estimation and collapse analysis of thin-walled beams and columns - recent advances. Special Issue - Cold formed steel structures: recent research advances in Central and Eastern Europe, ed. By D. Dubina, Thin-Walled Structures Vol. 42/2, Elsevier 2004, pp. 153-175.
18.14 Kotełko M., Mania R.J., Limitations of equivalent plate approach to the load-capacity estimation of honeycomb sandwich panels under compression, Proc. of Fourth Int. Conf. on Thin-Walled Struct., Thin-walled structures - advances in research, design and manufacturing technology, J. Loughlan (ed.), Inst. of Physics Publishing, Bristol and Philadelphia 2004, pp. 679-686.
18.15 Kotełko M., Nośność i mechanizmy zniszczenia konstrukcji cienkościennych (in Polish: Load-capacity and mechanisms of failure in thin-walled structures), WNT, Warszawa 2010, ISBN 9 78-83-204-3681-5.
18.16 Kotełko M., Ultimate load and post-failure behaviour of thin-walled orthotropic beams, Int. J. Applied Mechanics and Engineering, 2001, Vol. 6, No. 3, pp. 693-717.
18.17 Magnucki K., Ostwald M., Stability and optimization of three-layered structures. (in Polish), Poznań-Zielona Góra 2001.
18.18 Marguerre K., Die mittragende Breite des gedruckten Platten-Streifens, Luftfahrtforschung (in German: Effective width of plate strip under compression), 14, 3, 1937.
18.19 Murray N.W., Introduction to the theory of thin-walled structures, Clarendon Press, Oxford 1986.
18.20 Okuto K., at al., The analysis and design of honeycomb welded structures, J. Light Met. Welding, Vol. 29, 8, 1991, pp. 361-368.
18.21 Paik J.K. at al., The strength characteristics of aluminium honeycomb sandwich panels, Thin-Walled Struct., Vol. 35, 1999, pp. 205-231.
18.22 Rhodes J., Effective widths in plate buckling; contribution to: Developments in thin-walled structures-1, edited by J. Rhodes and A.C. Walker, Applied Science Publishers, London 1981.
18.23 Romanów F., Strength of multi-layered structures (in Polish), Wyd. WSI Zielona Góra 1995.
18.24 Structural Analysis Guide for ANSYS rev. 5.7, Ansys Inc., Houston, USA.
18.25 Theory References release 5.6, Ansys Inc., Houston, USA.
18.26 Vinson J.R., The behaviour of sandwich structures of isotropic and composite materials, Technomic Publ. Comp., 1999.

19.

Non-linear vibrations of a thin-walled composite column under periodically varied in time compression load

The phenomenon of a static buckling and post-buckling behaviour of thin-walled structures is well-known [19.3÷19.6, 19.10÷19.20, 19.30÷19.35]. In this case, the problem of interaction of the different buckling modes is very interesting and great significance. Thin-walled structures have many different local and global buckling modes. Such structures can sustain load after local buckling mode. This mode only cause a reduction in stiffness of the structures. While, the global buckling mode always causes a collapse of the structures. The interaction between buckling modes accelerates this process. This effect takes place when the global and local buckling modes are close each other [19.30, 19.35]. It can be achieved by selecting the appropriate length of the column. The local buckling takes place for the short columns. On the other hand, the long columns are subject to global buckling [19.2].

The problem of interactive buckling can be solved using asymptotic Koiter's theory [19.18÷19.19, 19.35] which is based on the asymptotic type expansion of the post-buckling path. The consideration of displacements and load components in the middle surface and precise geometrical relationships enabled an analysis of all possible buckling modes. The determination of the post-buckling equilibrium path requires the second order approximation to be taken into account. The two uncoupled modes are symmetric and stable, but on coincidence they are found to give rise to a symmetric unstable mixed form. The unstable coupled path will branch off the lower of the two uncoupled paths. The coupled post-buckling path can be important in continuous systems and it have an important effect on the type of instability which occurs. It enables determination of post-buckling equilibrium paths for the imperfect structure and to determine on them secondary bifurcation points or/and the limit point. If one takes into account the second order approximation, one can determine the limit load capacity of a structure in the elastic range. An assumption of one of the ”*engineering*” hypotheses of load carrying capacity allows for determination of the approximate estimation of load carrying capacity for the elastic-plastic range. Static interactive buckling of composite column has been described, among others, in books [19.12, 19.18, 19.35].

However, if the load depends on the time, then the strength of the structure may reduce. The dynamic behaviour of thin-walled structures, subjected to in–plane non-periodic and periodic loading can be considered using Koiter's theory [19.3, 19.20, 19.31÷19.34]. The asymptotic approximation leads to non-linear equations which can be solved with the Runge-Kutta method. The periodically changing load produces periodically changing coefficients in the mathematical model. The approximate analytical solutions can be determined by the multiple time scales of method [19.7÷19.8, 19.21÷19.23, 19.29, 19.37÷19.40]. The influence of different parameters of excitation on the structure response can be investigated. Additionally, a bifurcation scenario and a possible transition to chaotic oscillations can be also described. The response of structures subjected to oscillating loads can lead to vibration buckling [19.36]. Then, in certain frequency intervals, the trivial solution loses its stability and, the parametric resonance occurs. In such a case transverse vibrations become unacceptably large at critical combinations of amplitude, load frequency and damping. The most essential and dangerous, from the practical point of view, is the principal parametric resonance. This phenomenon appears for sufficiently small values of the axial force, when the loading frequency equals twice the natural bending frequency of the system (the column in our case). Apart from the principal also case the fundamental resonances may also appear, when the loading frequency coincides with the natural bending frequency of the column. Moreover the secondary parametric resonances may also occur. So, vibration buckling corresponds to the buckling resulting from parametric excitations. In paper [19.40], the authors deals with aspects of the parametric oscillations of thin-walled composite column under compression load, composed of static and periodic parts. The mathematical model of the structure considers geometrical nonlinear terms which couple considered global mode and the lowest local buckling one. The dynamic solutions were investigated around the principal parametric resonances.

The dynamic buckling of the structures under impact compression load can be treated as an amplification of initial displacements, or stresses [19.16]. For the dynamic buckling of a prefect structure, due to pulse loading, there is no exact counterpart in the static bifurcation load. Therefore dynamic bucking can be defined as the dynamic response of the structure which attains unacceptable level of displacements or stresses. In the analysis of dynamic buckling, a shape of pulse loading, pulse duration and a magnitude of its amplitude should be taken into account. The rectangular pulse is the most dangers. If the pulse duration is comparable to the period of natural vibrations, the dynamic buckling occurs. If the pulse duration is longer, the problem becomes quasi-static. Using the dynamic buckling criteria, it is possible to determine the dynamic critical load. When the displacement growth is assessed with time for different amplitude of load, buckling occurs when the dynamic load reaches a critical value associated with a maximum acceptable deformation (strain) or stress, the magnitudes of which are defined arbitrarily. Thus, there is no perfect criterion so far for dynamic buckling and no general guidelines for the design. Detailed reviews of problems of dynamic buckling under impact are presented in books [19.15÷19.17, 19.20, 19.25÷19.26]. The monographs [19.27÷19.28] deals with the experimental aspects of dynamic buckling.

19.1. An approximate method of analytical solutions for non-linear vibrations around the principal parametric resonances

The differential equations of motion can be obtained from the Hamilton's Principle. Under analysis, the plate model of a thin-walled structure [19.18÷19.19] was used. The rectangular plates are connected along longitudinal edges and supported at both ends. The constitutive equations of the material are assumed to be linear according to the classical theory of multi-layer plates [19.1, 19.9, 19.24]. The solution of these equations for each plate should satisfy: initial conditions, kinematic and static continuity conditions at the junctions of adjacent plates and the boundary conditions. The non-linear problem of multi-modes buckling has been solved with the asymptotic perturbation method in order to obtain an approximate analytical solution to the equations. The displacement fields and the sectional force fields were expanded in power series in the amplitudes of the buckling modes divided by the thickness of the first component plate. By substituting the displacement fields and the sectional force fields into the equations of equilibrium, junction conditions and boundary conditions, the boundary value problems of the zero, first and second order can be obtained. This method has allowed one to find the post-buckling coefficients which can be used in description of post-buckling equilibrium path for static load and in Lagrange equations for dynamic load. The details descriptions of this analytical-numerical method can be found in the monographs [19.18÷19.19]. In Poland, Kołakowski from the Department of Strength of Materials, Lodz University of Technology and co-workers developed this method and presented a lot of interesting results for problems of the coupled buckling of thin-walled plate structures with complex shapes of cross-sections, including an interaction of component plates.

In the case of the interaction of *n* buckling modes, the differential equations of motion can be written as [19.3÷19.6, 19.10÷19.20, 19.30÷19.35]

$$\frac{1}{\omega_{or}^2}\zeta_{r,tt}(t)+\left(1-\frac{\sigma(t)}{\sigma_r}\right)\zeta_r(t)+ + b_{pqr}\zeta_p(t)\zeta_q(t)+c_{pqsr}\zeta_p(t)\zeta_q(t)\zeta_s(t)=\frac{\sigma(t)}{\sigma_r}\zeta_r^* \quad \text{for } r=1,\dots,n \tag{19.1}$$

where: ζ_r is the dimensionless amplitude of the r-th buckling mode (maximum deflection referred to the thickness of the first plate);

σ_r, ω_{or}, ζ_r^* are the critical stress, circular frequency of free transverse vibrations corresponding to the r-th buckling mode when the compression stress is equal to 0 and dimensionless amplitude of the initial deflection corresponding to the r-th buckling mode; n is the number of interact buckling modes, respectively;

b_{pqr} are the non-linear coefficients in the first order approximations;

c_{pqsr} are the non-linear coefficients in the second approximations.

For the ideal structure (i.e. without initial imperfections) $\zeta_r^*=0$ and adopting the theory of the first order non-linear approximation (i.e. $c_{pqsr}=0$) Eq. (19.1) can be written as

$$\frac{1}{\omega_{or}^2}\zeta_{r,tt}(t)+\left(1-\frac{\sigma(t)}{\sigma_r}\right)\zeta_r(t)+b_{pqr}\zeta_p(t)\zeta_q(t)=0 \quad \text{for } r=1,\dots,n \tag{19.2}$$

The range of indexes p, q, r, s are (l, n). The summation is supposed on the repeated indexes. The coefficients b_{pqr} were determined with well-known formulae (see for example [19.3-19.6, 19.10-19.20, 19.30-19.35]).

The static problem of interactive buckling of thin-walled multilayer columns has been solved by the method presented in [19.12], while the frequencies of free vibrations have been determined in [19.33].

Let's consider the interaction of the global buckling mode and the lowest local one (i.e. $p=r=q=2$ in Eq.(19.2)). Introducing dimensionless time [19.7÷19.8, 19.21÷19.23, 19.37÷19.40]

$$\tau=\omega_{o2}t \tag{19.3}$$

And assuming that compression stress is composed of constant and periodic component

$$\sigma(\tau)=q_o+q\cos\Omega\tau \tag{19.4}$$

Eq. (19.2) can be written as

$$\begin{cases} \zeta_{1,\tau\tau}(\tau) + \dfrac{\omega_{o1}^2}{\omega_{o2}^2}\left(1 - \dfrac{q_o}{\sigma_1}\right)\cdot\zeta_1(\tau) - \dfrac{\omega_{o1}^2}{\omega_{o2}^2}\dfrac{q}{\sigma_1}\cos\Omega\tau\cdot\zeta_1(\tau) + \\ \qquad + \dfrac{\omega_{o1}^2}{\omega_{o2}^2}\left[b_{111}\zeta_1^2(\tau) + (b_{121} + \mathrm{b}_{211})\zeta_1(\tau)\zeta_2(\tau) + b_{221}\cdot\zeta_2^2(\tau)\right] = 0 \\ \zeta_{2,\tau\tau}(\tau) + \left(1 - \dfrac{q_o}{\sigma_2}\right)\cdot\zeta_2(\tau) - \dfrac{q}{\sigma_2}\cos\Omega\tau\cdot\zeta_2(\tau) + b_{112}\zeta_1^2(\tau) + \\ \qquad + (b_{212} + \mathrm{b}_{122})\zeta_1(\tau)\zeta_2(\tau) + b_{222}\cdot\zeta_2^2(\tau) = 0 \end{cases}$$

(19.5)

Introducing dimensionless natural frequencies $\Omega_{o1} = \omega_{o1}/\omega_{o2}$ and $\Omega_{o2} = \omega_{o2}/\omega_{o2} = 1$, Eq. (19.5) is written in the form

$$\begin{cases} \zeta_{1,\tau\tau} + \Omega_{01}^2\left[\beta_1\zeta_{1,\tau} + (1 - \delta\rho_o - \delta\rho\cos\Omega\tau)\,\zeta_1 + b_{111}\zeta_1^2 + b_{12}\zeta_1\zeta_2 + b_{221}\,\zeta_2^2\right] = 0 \\ \zeta_{2,\tau\tau} + \Omega_{02}^2\left[\beta_2\zeta_{2,\tau} + (1 - \rho_o - \rho\cos\Omega\tau)\zeta_2 + b_{112}\zeta_1^2 + b_{21}\zeta_1\zeta_2 + b_{222}\,\zeta_2^2\right] = 0 \end{cases}$$

(19.6)

where: $\zeta_{1,\tau}$, $\zeta_{2,\tau}$, $\zeta_{1,\tau\tau}$, $\zeta_{2,\tau\tau}$ denote the first and the second order time derivatives.

Parameter $\delta = \sigma_2/\sigma_1$ means the ratio of critical stresses; ρ_o represents a dimensionless constant load and ρ the amplitude of parametric excitation, defined as: $\rho_o = q_o/\sigma_2$, $\rho = q/\sigma_2$. Parameter Ω represents a dimensionless parametric excitation frequency. In Eq. (19.5) $b_{12} = b_{121} + b_{211}$, $b_{21} = b_{212} + b_{122}$ and furthermore modal viscous damping is introduced, by means of coefficients β_1 and β_2.

The differential equations of motion Eq. (19.5) constitutes a nonlinear system which includes nonlinear quadratic terms and parametric excitation. When we try to find solutions of such problem we have to assumed those nonlinear coupling terms are small [19.22-19.24]. Assuming that the nonlinear terms, the parametric excitation and the damping are all small, we express all those coefficients by a formal small parameter ε

$$\rho_o = \varepsilon\tilde{q}_o,\ \rho = \varepsilon\tilde{q},\ b_{111} = \varepsilon\tilde{b}_{111},\ b_{12} = \varepsilon\tilde{b}_{12},\ b_{221} = \varepsilon\tilde{b}_{221},\ b_{112} = \varepsilon\tilde{b}_{112},$$
$$b_{21} = \varepsilon\tilde{b}_{21},\ b_{222} = \varepsilon\tilde{b}_{222},\ \beta_1 = \varepsilon\tilde{\beta}_1,\ \beta_2 = \varepsilon\tilde{\beta}_2.$$

Thus, recalling that, the differential equations of motion take the form

$$\begin{cases} \zeta_{1,\tau\tau} + \Omega_{01}^2 \zeta_1 = \\ \quad = \varepsilon \Omega_{01}^2 \left[-\tilde{\beta}_1 \zeta_{1,\tau} + \delta(\tilde{\rho}_o + \tilde{\rho}\cos\Omega\tau)\,\zeta_1 - \tilde{b}_{111}\zeta_1^2 - \tilde{b}_{12}\zeta_1\zeta_2 - \tilde{b}_{221}\,\zeta_2^2 \right] \\ \zeta_{2,\tau\tau} + \zeta_2 = \\ \quad = \varepsilon \left[-\tilde{\beta}_2 \zeta_{2,\tau} + (\tilde{\rho}_o + \tilde{\rho}\cos\Omega\tau)\,\zeta_2 - \tilde{b}_{112}\zeta_1^2 - \tilde{b}_{21}\zeta_1\zeta_2 - \tilde{b}_{222}\,\zeta_2^2 \right] \end{cases} \tag{19.7}$$

To determine approximate analytical solutions we use the multiple time scale method [19.7, 19.21-19.23]. A solution of Eq. (19.7) is sought near the main parametric resonances in form of a series of the small parameter ε

$$\zeta_j(\tau,\varepsilon) = \zeta_{j0}(T_o,T_1) + \varepsilon\zeta_{j1}(T_o,T_1) + \ldots \quad \text{for} \quad j=1,2 \tag{19.8}$$

coordinates $\zeta_{j0}(T_o,T_1)$ and $\zeta_{j1}(T_o,T_1)$, are, respectively, the zero-th and first order functions of time. Dimensionless time is also expressed by a series for the small parameter,

$$\tau = T_o + \varepsilon T_1 \tag{19.9}$$

where T_o and T_1 are respectively the fast and slow time scales. Such time definitions results in the following formulae for the first and the second time derivatives [19.21-19.23]

$$\begin{aligned} \frac{d}{d\tau} &= \frac{\partial}{\partial T_o} + \varepsilon\frac{\partial}{\partial T_1} + \varepsilon^2\frac{\partial}{\partial T_2} = D_o + \varepsilon\, D_1 + \varepsilon^2 D_2 + \ldots \\ \frac{d^2}{d\tau^2} &= \frac{\partial^2}{\partial T_o^2} + 2\varepsilon\frac{\partial^2}{\partial T_o\,\partial T_1} + \varepsilon^2\left(2\frac{\partial^2}{\partial T_o\,\partial T_2} + \frac{\partial^2}{\partial T_1^2}\right) + \ldots = \\ &= D_o^2 + 2\varepsilon D_o D_1 + \varepsilon^2\left(2D_o D_2 + D_1^2\right) + \ldots \end{aligned} \tag{19.10}$$

where $D_n^m = \partial^m / \partial T_n$ means *m* order partial derivative with respect to the *n*-th time-scale.

19.1.1. Principal parametric resonances for Ω≈2Ω$_{01}$

Assuming that $\Omega \approx 2\Omega_{o1}$ [19.21÷19.23], we can write

$$\Omega_{o1}^2 = 0.25\Omega^2 - \varepsilon\nu_1 \tag{19.11}$$

where ν_1 is a frequency detuning parameter.

Substituting solution, taking into account the derivative definitions and expressing the natural frequency, after grouping terms with respect to order ε, we get a set of differential equations in the successive perturbation order

ε^{o} - order

$$D_o^2\zeta_{10} + 0.25\Omega^2\zeta_{10} = 0$$

$$D_o^2\zeta_{20} + \zeta_{20} = 0 \tag{19.12}$$

ε^{1} - order

$$\begin{aligned}
&D_o^2\zeta_{11} + 0.25\Omega^2\zeta_{11} = \nu_1\zeta_{10} - 2D_oD_1\zeta_{10} + \\
&\quad + 0.25\Omega^2\left[-\tilde{\beta}_1 D_o\zeta_{10} + \delta(\tilde{\rho}_o + \tilde{\rho}\cos\Omega T_o)\,\zeta_{10} - \tilde{b}_{111}\zeta_{10}^2 - \tilde{b}_{12}\zeta_{10}\zeta_{20} - \tilde{b}_{221}\,\zeta_{20}^2\right] \\
&D_o^2\zeta_{21} + \zeta_{21} = -2D_oD_1\zeta_{20} + \\
&\quad - \tilde{\beta}_2 D_0\zeta_{20} + (\tilde{\rho}_o + \tilde{\rho}\cos\Omega T_o)\,\zeta_{20} - \tilde{b}_{112}\zeta_{10}^2 - \tilde{b}_{21}\zeta_{1o}\zeta_{20} - \tilde{b}_{222}\,\zeta_{20}^2
\end{aligned} \tag{19.13}$$

ε^{2} - order

$$\begin{aligned}
&D_o^2\zeta_{12} + 0.25\Omega^2\zeta_{12} = -2D_oD_2\zeta_{10} - D_1^2\zeta_{10} - 2D_oD_1\zeta_{11} + \\
&\quad + 0.25\Omega^2[-\tilde{\beta}_1(D_o\zeta_{11} + D_1\zeta_{10}) + \delta(\tilde{\rho}_o + \tilde{\rho}\cos\Omega T_o)\,\zeta_{11} - 2\tilde{b}_{111}\zeta_{10}\zeta_{20} + \\
&\quad - \tilde{b}_{12}(\zeta_{11}\zeta_{20} + \zeta_{10}\zeta_{21}) - 2\tilde{b}_{221}\,\zeta_{20}\zeta_{21}\,] \text{-} \nu_1[\zeta_1 + \tilde{\beta}_1 D_o\zeta_{10} + \\
&\quad + \delta(\tilde{\rho}_o + \tilde{\rho}\cos\Omega T_o)\,\zeta_{10} + \tilde{b}_{111}\zeta_{10}^2 - \tilde{b}_{12}\zeta_{10}\zeta_{20} - \tilde{b}_{221}\,\zeta_{20}^2\,] \\
&D_o^2\zeta_{22} + \zeta_{22} = -2D_oD_1\zeta_{21} - 2D_0D_2\zeta_{20} - D_1^2\zeta_{20} + \\
&\quad - \tilde{\beta}_2(D_o\zeta_{21} + D_1\zeta_{20}) + (\tilde{\rho}_o + \tilde{\rho}\cos\Omega T_o)\,\zeta_{21} - 2\tilde{b}_{112}\zeta_{10}\zeta_{11} + \\
&\quad - \tilde{b}_{21}(\zeta_{11}\zeta_{20} + \zeta_{10}\zeta_{21}) - 2\tilde{b}_{222}\,\zeta_{20}\zeta_{21}\,]
\end{aligned} \tag{19.14}$$

We may write the solution in ε^{0}– order in the form

$$\zeta_{10}(T_o,T_1) = A_1(T_1)\cdot \mathrm{e}^{\left(i\cdot\frac{\Omega}{2}T_o\right)} + \overline{A}_1(T_1)\cdot \mathrm{e}^{\left(-i\cdot\frac{\Omega}{2}T_o\right)}$$

$$\zeta_{20}(T_o,T_1) = 0 \tag{19.15}$$

where: i is the imaginary unit, A_1 is the complex amplitude and $\overline{A}_1$ it's complex conjugate.

Solution (19.15) is substituted in ε^{1}- order. After grouping the terms in proper exponential functions, we get

$$D_o^2\zeta_{11} + 0.25\Omega^2\zeta_{11} =$$

$$= -0.5\Omega^2\widetilde{b}_{111}A_1\overline{A}_1 - 0.25\Omega^2\widetilde{b}_{111}A_1^2 e^{i\Omega T_o} - 0.125\delta\widetilde{\rho}_o\Omega^2 e^{\frac{3i\Omega T_o}{2}} + STe^{\frac{i\Omega T_o}{2}} + cc$$

$$D_o^2\zeta_{21} + \zeta_{21} = -2\widetilde{b}_{112}A_1\overline{A}_1 - \widetilde{b}_{112}A_1^2 e^{i\Omega T_o} + cc \tag{19.16}$$

where ST represent terms which generate secular terms in the solution of (19.16) and cc mean complex conjugate functions to those written in the equation. Therefore, to avoid this situation the ST have to be zero, thus we have

$$-i\Omega D_1 A_1 + A_1\nu_1 + 0.25\delta\Omega^2(\widetilde{\rho}_o A_1 + 0.5\widetilde{\rho}\overline{A}_1) - 0.125 i\widetilde{\beta}_1\Omega^3 A_1 = 0 \tag{19.17}$$

Next, rejecting the *ST* terms we may determine the particular solutions

$$\zeta_{11} = -2\widetilde{b}_{111}A_1\overline{A}_1 - \frac{1}{3}\widetilde{b}_{111}A_1^2 e^{i\Omega T_o} - \frac{1}{16}\delta\widetilde{\lambda}A_1 e^{\frac{3i\Omega T_o}{2}} + cc$$

$$\zeta_{21} = -2\widetilde{b}_{112}A_1\overline{A}_1 - \frac{\widetilde{b}_{112}A_1^2}{1-\Omega^2}e^{i\Omega T_o} + cc \tag{19.18}$$

Substituting this solutions into the second order equations (i.e. ε^2 - order) we get

$$D_o^2\zeta_{12} + 0.25\Omega^2\zeta_{12} = \{D_1^2 A_1 + 0.25\Omega^2\widetilde{\beta}_1 D_1 A_1 - i\Omega D_2 A_1 +$$
$$-\nu_1[\delta(\widetilde{\rho}_o A_1 + 0.5\widetilde{\rho}A_1) + 0.5 i\Omega\widetilde{\beta}_1 A_1] +$$
$$+\Omega^2[(\frac{5}{6}\widetilde{b}_{111} + 0.5\widetilde{b}_{112}\widetilde{b}_{12} + 0.25\frac{\widetilde{b}_{112}\widetilde{b}_{12}}{1-\Omega^2})A_1^2\overline{A}_1 - \frac{1}{128}\delta^2\widetilde{\rho}^2 A_1]\}e^{\frac{i\Omega T_o}{2}} +$$
$$+cc + NST$$

$$D_o^2\zeta_{22} + \zeta_{22} = NST \tag{19.19}$$

To avoid secular terms, thus we have

$$D_1^2 A_1 - 0.25\Omega^2\widetilde{\beta}_1 D_1 A_1 - i\Omega D_2 A_1 - \nu_1[\delta(\widetilde{\rho}_o A_1 + 0.5\widetilde{\rho}A_1) + 0.5 i\Omega\widetilde{\beta}_1 A_1] +$$
$$+\Omega^2[(\frac{5}{6}\widetilde{b}_{111} + 0.5\widetilde{b}_{112}\widetilde{b}_{12} + 0.25\frac{\widetilde{b}_{112}\widetilde{b}_{12}}{1-\Omega^2})A_1^2\overline{A}_1 - \frac{1}{128}\delta^2\widetilde{\rho}^2 A_1] = 0$$

(19.20)

where *NST* denotes nonsecular generating terms.

Applying the so called reconstitution method, we may formulate modulation equations for the complex amplitudes A_1. The amplitude derivative with respect to dimensionless time takes the form

$$\frac{dA_1}{d\tau} = \varepsilon\, D_1 A_1 + \varepsilon^2 D_2 A_1 \tag{19.21}$$

Expressing complex amplitude A_1 in the polar form

$$A_1 = 0.5 a_1 e^{i\Phi_1} \tag{19.22}$$

We can get the modulation equations for amplitude a_1 and phase ϕ_1

$$\begin{aligned}
2\Omega a_{1,\tau} &= -\varepsilon a_1 \Omega_{01}^2 (\tilde{\beta}\Omega + \delta\tilde{\rho}\sin 2\phi_1) \\
8\Omega\phi_{1,\tau} &= -2.5\Omega^2 + 12\Omega_{01}^2 - \frac{8\Omega_{01}^2}{\Omega^2} + \\
&\quad - \varepsilon\delta[\tilde{\rho}_o(\Omega^2 + 4\Omega_{01}^2) + 4\Omega_{01}^2\tilde{\rho}\cos 2\phi_1] + \\
&\quad + \varepsilon^2\{0.125\tilde{\beta}_1^2\Omega^4 + \frac{1}{16}\delta^2(3\tilde{\rho} - 8\tilde{\rho}_o)\Omega^2 + \\
&\quad - \frac{a_1^2\Omega^2[10\tilde{b}_{111}^2(1-\Omega^2) + 3\tilde{b}_{112}\tilde{b}_{12}(3-2\Omega^2)}{6(1-\Omega^2)}\}
\end{aligned} \tag{19.23}$$

In steady state $a_{1,\tau} = 0$, $\phi_{1,\tau} = 0$. We can find the resonance curve around the principal parametric resonance

$$\begin{aligned}
&-1 + \frac{\beta_1^2\Omega^2}{\delta^2\rho^2} + \frac{1}{[192\delta^2\rho\Omega^2(1-\Omega^2)\Omega_{01}^2]^2}\{-[120 + 16(5b_{111}^2 + 3b_{112}b_{12})a_1^2 - 6\beta_1^2 + \\
&-9\delta^2\rho^2 + 48\delta\rho_0 + 24\delta^2\rho_0^2]\Omega^6 - 6\beta_1^2\Omega^8 + 384\Omega_{01}^4 - 192\Omega^2\Omega_0^2(3 - \delta\rho_0 + 2\Omega_{01}^2) + \\
&+\Omega^4[8(10b_{111}^2 + 9b_{112}b_{12})a_1^2 + 3(\delta^2(-3\rho^2 + 8\rho_0^2) + 16\delta\rho_0(1-4\Omega_{01}^2) + 8(5 + 24\Omega_{01}^2))] = 0
\end{aligned} \tag{19.24}$$

We note that all the parameters in above equation have their original definitions, and are written without the tilde.

Finally, we can obtain approximate solutions for the first and second coordinate

$$\begin{aligned}
\zeta_1 &= a_1\cos(0.5\Omega\tau + \phi_1) - 0.5\varepsilon a_1[a_1\tilde{b}_{111} - \frac{1}{3}a_1\tilde{b}_{111}\cos(\Omega\tau + 2\phi_1) + \\
&\quad + 0.125\delta\tilde{\rho}\cos(1.5\Omega\tau + \phi_1)] + O(\varepsilon^2) \\
\zeta_2 &= -0.5\varepsilon a_1^2\tilde{b}_{112}[1 + \frac{1}{1-\Omega^2}\cos(\Omega\tau + 2\phi_1) + O(\varepsilon^2)
\end{aligned} \tag{19.25}$$

19.1.2. Principal parametric resonances for $\Omega \approx 2\Omega_{02}$

In this case, we can write [19.21÷19.23]

$$\Omega_{o2}^2 = 0.25\Omega^2 - \varepsilon\nu_2 \tag{19.26}$$

where: ν_2 is a frequency detuning parameter around the second natural frequency.

In this case the second coordinate dominates therefore, we seek solution in the form

$$\begin{aligned} \zeta_{10}(T_o, T_1) &= \varepsilon\zeta_{11}(T_o, T_1) + \ldots \\ \zeta_{20}(T_o, T_1) &= \zeta_{20}(T_o, T_1) + \varepsilon\zeta_{21}(T_o, T_1) + \ldots \end{aligned} \tag{19.27}$$

Repeating a similar procedure as in chapter 19.1.1, we get a set of equations in the ε^0, ε^1, ε^2 perturbation orders. Solving, them successively, and eliminating the secular generated terms, we get solutions for both coordinates

$$\begin{aligned} \zeta_1 &= -0.5\varepsilon a_2^2 \tilde{b}_{211}[1 + \frac{\Omega_{01}^2}{\Omega_{01}^2 - \Omega^2}\cos(\Omega\tau + 2\phi_2) + O(\varepsilon^2) \\ \zeta_2 &= a_2\cos(0.5\Omega\tau + \phi_2) - \frac{2\varepsilon a_2}{\Omega^2}[a_2\tilde{b}_{222} - \frac{1}{3}a_2\tilde{b}_{222}\cos(\Omega\tau + 2\phi_2) + \\ &+ 0.125\delta\tilde{\rho}\cos(1.5\Omega\tau + \phi_2)] + O(\varepsilon^2) \end{aligned} \tag{19.28}$$

Expressing complex amplitude A_2 in the polar form

$$A_2 = 0.5a_2 e^{i\phi_2} \tag{19.29}$$

We can get the modulation equations for amplitude a_2 and phase ϕ_2. In steady state $a_{2,\tau} = 0$, $\phi_{2,\tau} = 0$. We can find the resonance curve around the principal parametric resonance

$$\begin{aligned} &-1 + \frac{\beta_2^2\Omega^2}{\rho^2} + \frac{1}{[24\rho\Omega^2(\Omega_{01}^2 - \Omega^2)]^2}\{15\Omega^6 - 2(80b_{222}^2 a_2 - 9\rho^2 + 24(\rho\ \ -1)^2)\Omega_{01}^2 + \\ &+ 3\Omega^4(-24 + 8b_{221}b_{21}a_2^2 + 4\beta_2^2 + 24\rho_0 - 5\Omega_{01}^2) + 2\Omega^2[80b_{222}^2 a_2^2 - 3(3\rho^2 + 2(-4 - 4\rho_0^2 + \\ &+ (-6 + 3b_{221}b_{21}a_2^2 + \beta_2^2)\Omega_{01}^2) + \rho_0(8 + 6\Omega_{01}^2))]\}^2 = 0 \end{aligned} \tag{19.30}$$

19.2. Exemplary calculations and numerical studies

A detailed analysis of the calculations is conducted for compressed columns with the following dimensions of the channel cross-sections (Fig. 19.1):

$$b_1 = b_3 = 50 \text{ mm}, b_2 = 25 \text{ mm}, h = 0.927 \text{ mm}.$$

The length of the column is $L = 450$ mm.

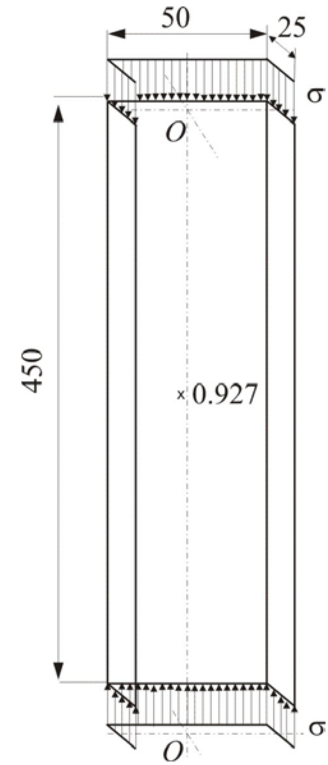

Fig. 19.1. Schematic view and dimensions in mm of the channel column

The column is made of a seven-layer composite with symmetric ply alignment $[0_7]$. Each layer of the thickness $h_{lay} = 0.131$ mm is characterized by the following mechanical properties: Young's elastic moduli in the 1 and 2 material directions $E_1 = 130$ GPa, $E_2 = 6.36$ GPa, Kirchhoff's modulus (shear modulus) in the 1, 2 plane $G_{12} = 4.18$ GPa, Poisson's ratio in the 1, 2 plane $\nu_{12} = 0.32$ and the density 2000 kg/m^3.

The static problem of buckling of thin-walled multilayer columns has been solved (Fig. 19.2) and the frequencies of free vibrations have been determined.

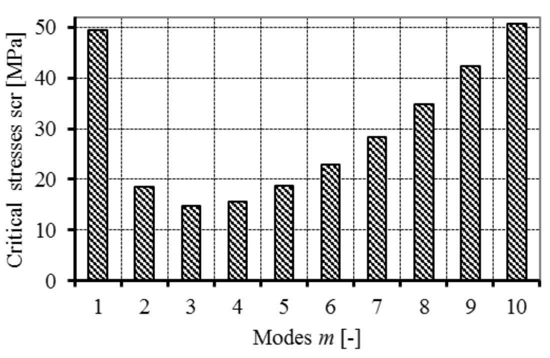

Fig. 19.2. Values of buckling stresses versus the number of half-waves *m* for the uniformly compressed channel column

(a) 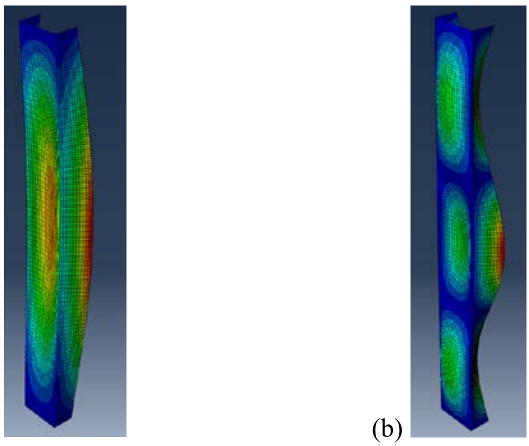 (b)

Fig. 19.3. Buckling modes:
a) global buckling mode (m =1), b) lowest local buckling mode (m =3)

The frequency of free vibration ω_{or} and critical stresses σ_r (r=1,2) for global (Fig. 19.3a) and the lowest local buckling modes (Fig. 19.3b) are:

$$\omega_{o1} = 1098.50 \text{ rad/s}, \ \omega_{o2} = 1796.22 \text{ rad/s}, \ \sigma_1 = 49.518 \text{ MPa}, \ \sigma_2 = 14.711 \text{ MPa}$$

The values of nonlinear coefficients b_{ijr} of the first order approximation are:

$$b_{111} =-0.0126409, \ b_{221} =-0.0563475, \ b_{12} =0.0273859,$$

$$b_{112} =0.00520127, \ b_{222} =-0.00306516, \ b_{21} =-0.0428073$$

Modal damping of the structure has been assumed to be arbitrary with coefficients $\beta_1 = 0.01$ and $\beta_2 = 0.01$.

Solving modulations equations (19.24) in the first order perturbation near the first natural frequency, we can determine the relation between the parameters which has to be satisfied in order to get periodic oscillations

$$\rho = \sqrt{\frac{4(1+\delta\rho_0)^2\Omega^2 - 32(1+\delta\rho_0)\Omega^2\Omega_{01}^2 + 64\Omega_{01}^2 + \beta_1^2\Omega^2}{\delta^2\Omega^4}} \tag{19.31}$$

The above equation allows to determine stability zones in a two parameters plane (ρ, Ω) i.e. amplitude and frequency of excitation. In a similar way we may find the stability zone near the second natural frequency

$$\rho = 0.5\sqrt{16 - 32\rho_0 + 16\rho_0^2 + \rho_0\Omega^2 + \Omega^4 + 4\beta_2^2\Omega^2} \tag{19.32}$$

Unfortunately, the first perturbation order does not allow to determine the amplitudes as a function of frequency or another bifurcation parameter. To get these dependencies we have to examine the modulation equations taking into account the second order terms.

Solving the equations (19.24) and (19.30) representing the resonance curves in the second perturbation order, around the first and the second principal parametric resonance, we find amplitudes a_1 and a_2, respectively. The resonance curves, calculated around the first (Fig. 19.4a) and the second (Fig. 19.5a) principal parametric resonance, exhibit the softening effect. The influence of the added constant load component, $\rho_0 = 0.1$, is presented by red curves. This parameter shifts the resonance zones into the lower frequency direction.

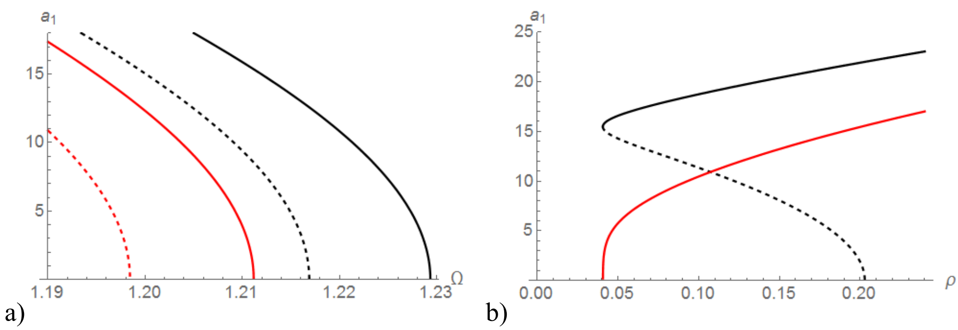

Fig. 19.4. The resonance curves (a) for $\rho_0 = 0$, $\rho = 0.08$ (black colour), $\rho_0 = 0.1$, $\rho = 0.08$ (red colour), and amplitude of the column response versus amplitude of parametric excitation (b) for $\rho_0 = 0$, $\Omega = 1.205$ (black colour), for $\rho_0 = 0.1$, $\Omega = 1.205$ (red colour), around the first natural frequency

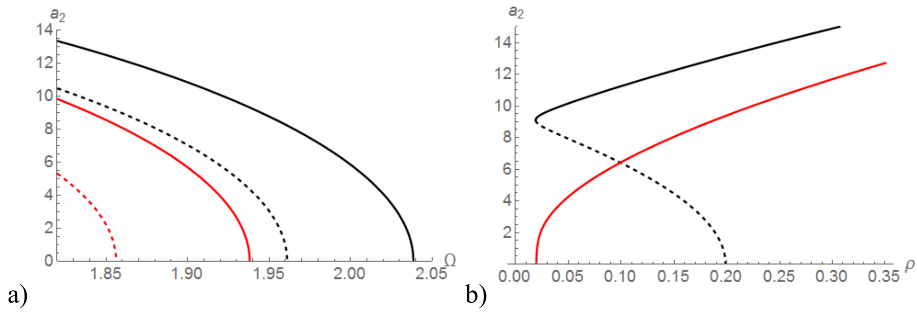

Fig. 19.5. The resonance curves (a) for $\rho_0 = 0$, $\rho = 0.08$ (black colour), $\rho_0 = 0.1$, $\rho = 0.08$ (red colour), and amplitude of the column response versus amplitude of parametric excitation (b) for $\rho_0 = 0$, $\Omega = 1.9$ (black colour), $\rho_0 = 0.1$, $\Omega = 1.9$ (red colour), around the second natural frequency

On the basis of the approximate analytical solutions, the bifurcation diagrams for fixed frequency and varying amplitude of excitation ρ are computed. Trivial solutions go to periodic oscillations after the subcritical or supercritical Hopf bifurcation. This phenomenon is presented in Fig. 19.4b around the first natural frequency and in Fig. 19.5b around the second natural frequency. The scenario is different for different values of constant load. If $\rho_0 = 0$ (black curve) then the subcritical Hopf bifurcation takes place. While for $\rho_0 = 0.1$ the supercritical Hopf bifurcation occurs (red curve). Similar behaviour have been observed around the first and the second resonance zones (Fig. 19.4b and Fig. 19.5b). Comparing Fig. 19.4b and Fig. 19.5b we may conclude that for the assumed configuration of the composite column, the second (local) mode loses stability of its equilibrium position earlier then the first (global) mode.

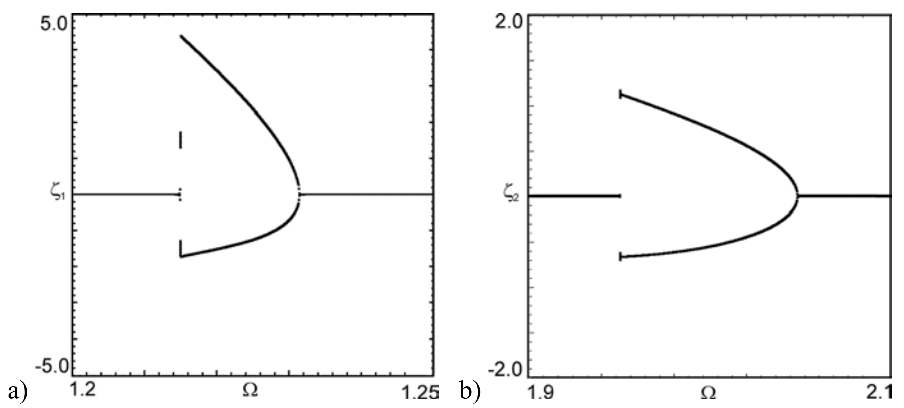

Fig. 19.6. Bifurcation diagrams near the first principal resonance, (a) coordinate ζ_1, and (b) coordinate ζ_2, $\rho = 0.1$ [19.40]

In order to verify analytical solutions the bifurcation diagrams near the first and the second principal parametric resonance are computed directly from the ordinary differential equations of motion (19.6). Curves in Fig. 19.6 confirm the analytical prediction very well. Moreover on the basis of the direct numerical simulation we see that dynamics of the structure is very sensitive to the initial conditions. The increase in the dynamic load amplitude ρ leads to a period doubling bifurcation (Fig. 19.7), and then the solution transits to chaotic oscillations after the cascade of period doublings. Another scenario is observed while varying excitation frequency. Around the first resonance zone for ρ=0.1 the subcritical Hopf bifurcation occurs (Fig. 19.8a) which is in agreement with the analytical prediction. But around the second resonance zone, apart from periodic solutions also irregular oscillations arise (back region in Fig. 19.8b).

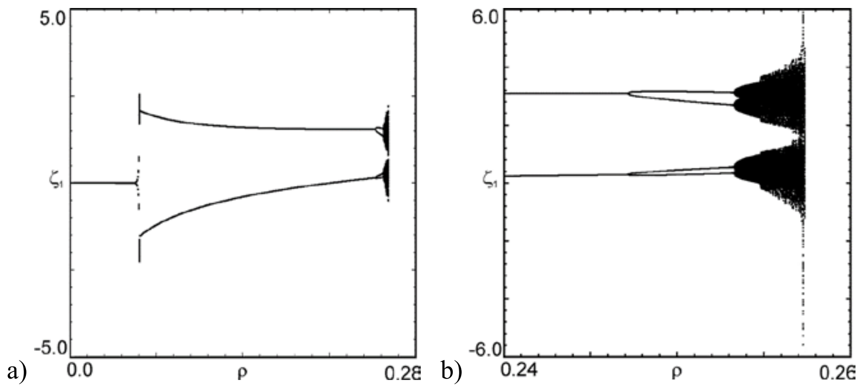

Fig. 19.7. Bifurcation diagrams of coordinate ζ_1 versus amplitude of parametric excitation ρ near the first principal resonance $\Omega = 1.22$, (a) full diagram and (b) zoom near the period doubling bifurcation [19.40]

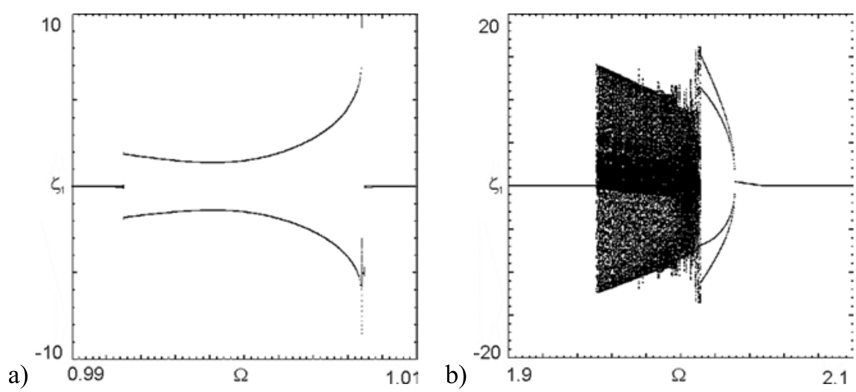

Fig. 19.8. Bifurcation diagrams near the first, (a) and the second (b) principal parametric resonance; coordinate ζ_1, $\rho = 0.1$

Acknowledgements

This paper was financially supported by the Ministerial Research Project No. DEC-2012/07/B/ST8/03931 financed by the Polish National Science Centre.

19.3. References

19.1 Altenbach H, Altenbach J, Kissing W., Structural analysis of laminate and sandwich beams and plates, An introduction into the mechanics of composite, Lubelskie Towarzystwo Naukowe, Lublin 2001.

19.2 Bazant Z.P., Cedolin L., Stability of structures. Elastic, inelastic, fracture and damage theories. Oxford University Press 1991.

19.3 Budiansky B., Hutchinson J.W., Dynamic buckling of imperfection-sensitive structures, Proceedings of the Eleventh International Congress of Applied Mechanics, Goetler H. (Ed), Munich, 1966, pp. 636-651.

19.4 Byskov E, Hutchinson J.W., Mode interaction in axially stiffened cylindrical shells. AIAA J. Vol. 15(7), 1977, pp. 941-948.

19.5 Byskov E., Elastic buckling problem with infinitely many local modes. The Danish Centre for Applied Mathematics and Mechanics, The Technical University of Denmark, Report No. 327, 1986.

19.6 Byskov E., Elastic buckling problem with infinitely many local modes, Mechanics of Structures and Machines, Vol. 15(4), 1987-8, pp. 413-435.

19.7 Cartmell M.P., Introduction to Linear, Parametric and Nonlinear Vibrations, Chapman and Hall, London 1990.

19.8 Evan-Iwanowski R.M., On the parametric response of structures. Applied Mechanics Reviews, Vol. 18, 1965, pp. 699-702.

19.9 Jones M.J., Mechanics of composite materials. Taylor and Francis, 1999.

19.10 Koiter W.T., Pignataro M., An alternative approach to the interaction between local and overall buckling in stiffened panels. In: "*Buckling of Structures*" /Proc. of IUTAM Symposium, Cambridge, 1974, pp.133-148.

19.11 Kołakowski Z., Interactive buckling of thin-walled beams with open and closed cross-sections, Thin-Walled Structures, Vol. 15, 1993, pp. 159-183.

19.12 Kołakowski Z., Kowal-Michalska K., (Eds), Selected problems of instabilities in composite structures. Technical University of Lodz, Poland 1999.

19.13 Kołakowski Z., Kowal-Michalska K., (eds.), Statics, Dynamics and Stability of Structures, Vol. 2, Static, Dynamics and Stability of Structural Elements and Systems, Wydawnictwa Politechniki Łódzkiej, Monografie, Łódź 2012.

19.14 Kołakowski Z., Teter A., Interactive buckling of thin-walled beam-columns with intermediate stiffeners or/and variable thickness, Int. J. Solids Structures, Vol. 37(24), 2000, pp. 3323-3344.

19.15 Kowal-Michalska K., Mania R.J. (eds.), Statics, Dynamics and Stability of Structures, Vol. 3, Review and Current Trends in Stability of Structures, Wydawnictwa Politechniki Łódzkiej, Monografie, Łódź 2013.

19.16 Kowal-Michalska K. (ed.), Stateczność dynamiczna kompozytowych konstrukcji płytowych, WNT Warszawa 2007.
19.17 Królak M., Mania R.J. (eds.), Statics, Dynamics and Stability of Structures, Vol. 1, Stability of Thin-walled Plate Structures, Wydawnictwa Politechniki Łódzkiej, Monografie, Łódź 2011.
19.18 Królak M. (ed.), Stany zakrytyczne i nośność graniczna cienkościennych dźwigarów o ścianach płaskich, PWN Warszawa-Łódź 1990.
19.19 Królak M. (ed.), Stateczność, stany zakrytyczne i nośność cienkościennych konstrukcji o ortotropowych ścianach płaskich, Monografie. Wydawnictwo Politechniki Łódzkiej, 1995.
19.20 Kubiak T., Interakcyjne wyboczenie dynamiczne cienkościennych słupów, Zeszyty Naukowe Politechniki Łódzkiej nr 998, Łódź 2007.
19.21 Nayfeh A. H., Nonlinear Interactions, Analytical, Computational, and Experimental Methods. John Willey and Sons, Inc., 2000.
19.22 Nayfeh A. H., Pai, F.P., Linear and Nonlinear Structural Mechanics, John Wiley and Sons Inc., 2004.
19.23 Nayfeh A., Problems in perturbations, John Wiley & Sons, 1985.
19.24 Reddy J.N., Mechanics of laminate composite plates, theory and analysis. CRC Press, 2004.
19.25 Simitses G.J., Dynamic stability of suddenly loaded structures. Springer Verlag, New York 1990.
19.26 Simitses G.J., Hodges D.H., Fundamentals of structural stability. Butterworth-Heinemann 2006.
19.27 Singer J, Arbocz J, Weller T, Buckling Experiments. Experimental methods in buckling of thin-walled structure. Basic concepts, columns, beams, and plates, Volume 1, John Wiley & Sons Inc. New York 1998.
19.28 Singer J, Arbocz J, Weller T., Buckling Experiments. Experimental methods in buckling of thin-walled structure, Shells built-up structures, composites and additional topics, Volume 2, John Wiley & Sons Inc. New York 2002.
19.29 Sinha S.K., Dynamic stability of a Timoshenko beam subjected to an oscillating axial force. Journal of Sound and Vibration, Vol. 131, 1989, pp. 509-14.
19.30 Sridharan S., Benito R., Columns: Static and Dynamic Interactive Buckling, J. Engineering Mechanics, ASCE, Vol. 110-1,1984, pp. 49-65.
19.31 Teter A., Dynamic critical load based on different stability criteria for coupled buckling of columns with stiffened open cross-sections. Thin-Walled Structures Vol. 49, 2011, pp. 589-595.
19.32 Teter A., Kolakowski Z., Buckling of thin-walled composite structures with intermediate stiffeners, Composite Structures, Vol. 60, 2005, pp. 421-428.
19.33 Teter A., Kolakowski Z., Natural frequencies of thin–walled structures with central intermediate stiffeners or/and variable thickness, Thin–Walled Structures, Vol. 41, 2003, pp. 291-316.
19.34 Teter A., Review. Dynamic, multimode buckling of the thin-walled columns with subjected to in-plane pulse loading, Int. J. Non-Linear Mechanics, Vol. 45, 2010, pp. 207-218.

19.35 van der Heijden A.M.A. (Ed), W.T. Koiter's Elastic Stability of Solids and Structures. Cambridge University Press, 2009.
19.36 Virgin L.N., Vibration of axially loaded structures. Cambridge University Press 2007.
19.37 Warmiński J., Kecik K., Instabilities in the main parametric resonance area of a mechanical system with a pendulum, Journal of Sound and Vibration, Vol. 332, 2009, pp. 612-628.
19.38 Warmiński J., Nonlinear Normal Modes of a Self-Excited System Driven by Parametric and External Excitations, Nonlinear Dynamics, Vol. 61, 2010, pp. 677-689.
19.39 Warmiński J., Nonlinear normal modes of coupled self-excited oscillators in regular and chaotic vibration regimes. Journal of Theoretical and Applied Mechanics Vol. 46(3), 2008, pp. 693-714.
19.40 Warmiński J., Teter A., Non-linear parametric vibrations of a composite column under uniform compression, Proceedings of the Institution of Mechanical Engineers, Part C: Journal of Mechanical Engineering Science, Vol. 226(8), 2012, pp. 1921-38.

20.

Research and design of thin-walled steel structures by FEM. Part I- Stability of slender steel structures: A short review and guidance for numerical modelling

20.1. Introduction

Scientifically, *buckling* is a mathematical instability, leading to a failure mode. The formal meaning of the notion is found in engineering and sciences, concerning stability of *systems*. Broadly speaking, structural stability can be defined as *the power to recover equilibrium* [20.1]. It is an essential requirement for all structures. Theoretically, for a structural system, buckling is caused by a *bifurcation* in the solution to the equations of *static equilibrium*. At a certain stage under an increasing load, further load is able to be sustained in one of two states of equilibrium: an undeformed state, or a laterally-deformed state. In practice, buckling is characterized by a sudden failure of a structural member subjected to high compressive stress, where the actual compressive stress at the point of failure is less than the ultimate compressive stresses that the material is capable of withstanding.

To evaluate the behaviour of a slender structure, which might loss its stability, according to previous definition, needs for the control by design the three characteristic ranges of load-deformation, as shown in Figure 20.1:

– Pre-critical range, e.g. $P \in (0, P_{cr}]$ defining the domain of *Structural stability*;
– Critical point (bifurcation of equilibrium);
– Post-critical range, e.g. $P > P_{cr}$, the *Structural instability* domain.

Although the stability of bars was firstly studied over 250 years ago (Euler's paper was published in 1744), adequate solutions are still not available for many problems in structural stability. So much has been and being studied and written in the field of structural stability, that one may well wonder why, after such intellectual and financial efforts, there are no definite solutions to these problems. Numerical facilities and advanced FE codes make possibly today to calculate and/or simulate accurately the behaviour of complex structures. However, for slender structures highly sensitive to buckling, still there are difficulties for a reliable evaluation of the buckling load.

Why? Because determining the load under which a structure collapses due to the loss of stability still remains one of the most sensitive problems of structural design!

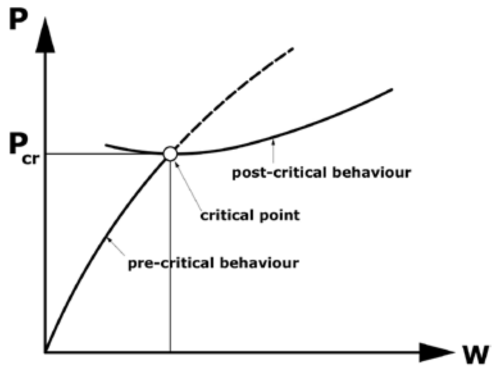

Fig. 20.1. Critical and post-critical behaviour

This is due to the following factors [20.2]:

a) The loss of stability depends on numerous factors, some of which are very difficult to control. This is confirmed by a number of recent structural accidents. Faulty design and execution, overstressing or the use of inadequate materials have been shown to be mainly responsible for these accidents. It should be noted that these accidents practically cover the entire range of structures. Today, only a specialist can carry out stability checks in complete agreement with the actual behaviour of the structure;
b) Instability occurs in a region with both strong geometrical and material nonlinearities. For pre-critical range an extensive literature provides effective solutions. For post-critical range, the theoretical background was significantly developed within second half of last century, but only after remarkable progress in the field of electronic computing equipment, and nonlinear analysis using FE (e.g. GMNIA - Geometrical and Material Nonlinear with Imperfection Analysis) and some special numerical techniques (such as the Arc-Length Method) in the neighbourhood of the limit point, has made possible to correctly describe the behaviour of structure, shortly before its failure and after. However, such analyses are difficult and costly and they are not accessibly for many designers;
c) In no other field of structural mechanics the influence of imperfections due to the execution is not as significant as in the field of instability. In strength analysis the stress-strain state is determined by means of an

idealized scheme of the structure, neglecting the geometrical and mechanical imperfections, compared to the actual structure, differences are relatively small. However, in the case of slender structures, highly sensitive to nonlinear effects and imperfections, due to instability the real capacity might drops up to 50%-80% compared with the one of ideal structure, if that is evaluated using a simplified elastic eigenvalue buckling approach;

d) Checking the buckling of structure experimentally is very difficult because it is impossible to test the actual structure just until it collapse. In strength analysis, the reduced model tests are used for checking the validity of theoretical values. In stability analysis, testing on reduced models is irrelevant in most cases, because a correct modelling of the effect of imperfections is practically impossible;

e) In the last decades, a lot of information has become available through scientific papers and books related to the progress in research on stability and instability of structures; however the design codes and standards with modern conceptions for stability checking remained at the level of classical formulation.

Why such a delay between the advances in research and update of the codes? This is because, trying to integrate the research results related to the complex problems of stability and, particularly, instability of structures, into the actual format of design codes, using analytical formulations, sometimes leads to really complicate formulas, difficult to understand and difficult to apply. At the end, even these analytical approaches are not applied through hand calculations, since they can be solved using Excel calculation sheets, Mathcad or other computational tools, their use in practical design still remains difficult.

One speaks, more and more, that the future design codes will be mostly based on application of numerical tools than on the code based analytical methods. However, the availability of numerical tools, e.g. computer and software, it is not enough, since applying correctly these tools needs for a deep understanding of the problem and, for that, a good theoretical background and experience are necessary.

To support these ideas, the authors attempt to prepare to the readers of this volume, the title of above for their contribution, divided in two parts. The present one, aiming to make a review of classical problems of stability and instability of steel structures (however, even not exhaustively, but still aiming to give a light guidance for the application of Finite Element Method-FEM to the problems of slender structures) and, the second part, which summarises two case studies devoted to solve two complex problems using advanced FE analyses.

In a large extend, this work has a monograph character, based on cited contributions, collected from available literature. However, some relevant contributions of the authors are integrated too.

20.2. Stability of slender steel structures. A short review

20.2.1. Basic assumptions for elastic theory of stability

Definition of stability of equilibrium of a structure, regarded as a *mechanical system*, is basically related to the "*quality*" of the equilibrium configuration possibly to be achieved by that system. Intuitively, stability might be defined as the ability of the system to return to equilibrium when slightly disturbed. According to the theorem Dirichlet: *"The equilibrium of a mechanical system is stable if, moving out the points of the system from their equilibrium positions by an infinitesimal amount, and giving each one a small initial velocity, the displacements of different points of the system remain, throughout the course of the motion, contained within small prescribed limits"*. So, the stability is a *quality* of one solution - *an equilibrium solution* - of the system, and that the problem of ascertaining the stability of a solution is concerned with the "*neighbourhood*" of this particular solution. It applies for both rigid bodies and elastic or even nonlinear systems, which can be classified on the basis of their possible evolution after a small (finite) perturbation on the system, while resting in its equilibrium condition.

Testing the sensitivity to the loss of stability of equilibrium, one considers an elastic conservative system, which is initially in a state of equilibrium under the action of a set of forces; the system will move-out from its equilibrium state only if acted upon by some transient perturbation force. To formulate mathematically, the applied force (or forces) is characterized by a *loading parameter* λ, also called a *load factor*. Setting $\lambda = 0$, it means the structure is *unloaded*, at which it takes up an equilibrium configuration $C_0 = (0)$, called the *undeformed state*. This state is *stable.* As the forces λ is varied from 0 the structure deforms and assumes equilibrium configurations $C(\lambda)$. These are assumed to be (i) continuously dependent on λ and (ii) stable for sufficiently smaller values of λ. How the stability of the system can be proved? Freeze λ at a specific value, say λ_d, where d connotes "deformed." The associated equilibrium configuration is $C_d = C(\lambda d)$. Apply an *admissible perturbation* to C_d, and *remove* it.

The perturbation triggers subsequent motion of the system. Three possible equilibrium configurations, namely **S**, **N** and **U** are sketched in Figure 20.2 [20.1]:

S: Stable. For *all* admissible perturbations, the structure either returns to the examined configuration C_d or executes bounded oscillations about it. If so, the equilibrium is called *stable*.

U: Unstable. If for at least *one* admissible perturbation the structure moves to (decays to, or oscillates about) another configuration, or "takes off" in an unbounded motion, the equilibrium is *unstable*.

N: Neutral. The transition from stable to unstable occurs at a value λ_{cr}, which is called the *critical load factor*. The configuration $C_{cr} = C(\lambda_{cr})$ at the critical load factor is said to be in *neutral* equilibrium. The quantitative determination of this transition is a key objective of the stability analysis.

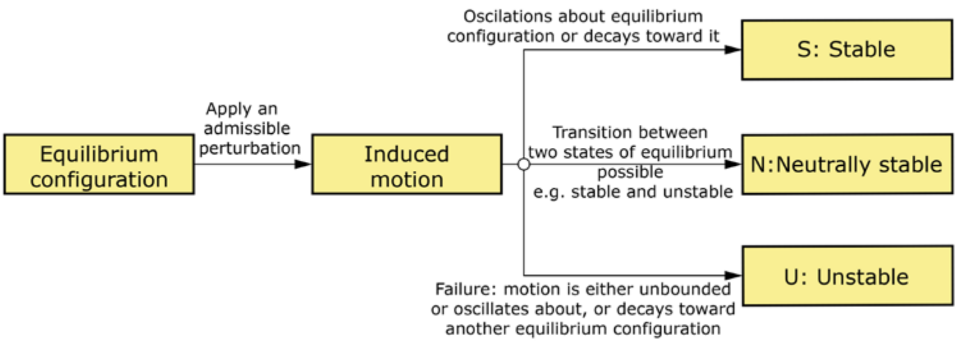

Fig. 20.2. Equilibrium states

Even the equilibrium problems can be solved in terms of balance between force acting and reaction forces, between external and internal forces, according to the *static approach,* terms as *perturbation, oscillation* and *motion* are used to define stability of equilibrium state. That leads to the idea the stability concept rather is *dynamic* in its nature because, in fact, "*the failure of structures is a dynamical process, and so it is obviously more realistic to approach buckling and instability from a dynamical point of view*." [20.3]. *Stability of motion (e.g. the equilibrium of dynamic state)* is a more general topic, considering the static case as a particular one.

A *dynamic approach* for equilibrium offers the means to better characterise the system behaviour and "*quality*" of solutions (e.g. criteria) for stability state, in the sense reported above. Equation of motions can be written for the system starting from its current equilibrium condition to ascertain whether it tends to come back to the original condition or evolves towards other more stable ones. But, the *dynamic approach*, despite to be *closer-to-the-nature* of phenomenon, and more accurate, usually results in more complicated mathematical procedures, making it more difficult to apply for current engineering stability problems.

Equilibrium of bodies or structures can be studied within the framework of various hypotheses. Considering the *material is linear elastic* and the applied forces are *conservative*, a relevant class of equilibrium problems are usually named *Euler-model problems* and are based upon the two following hypotheses:

- *small strains* of the structures starting from a reference equilibrium configuration; however, the displacement and rotations are not necessarily very small, they are *finite;*
- *perfect or "ideal" systems*, namely absence of geometric, material, and mechanical imperfections (initial bow or lack of straightness of centroid axis, initial vertical slope, initial distortion of cross-section, non-homogeneous material, initial induced stresses, eccentricity centrically applied loads and supports etc.).

A conservative load is that which can be derivable from a potential. For example, gravity and hydrostatic loads are conservative. On the other hand, aerodynamic and propulsion loads (wind gusts on a bridge, rocket thrust etc.) are often non-conservative. The loss of stability under non-conservative loads is inherently dynamic in nature.

20.2.2. Continuous and discrete models

Physical models applied in stability analysis are framed models of actual into two categories i.e.:

Continuous models. Such models have an *infinite* number of degrees of freedom (DOF). This is the case of deformable structures, either of elastic or plastic behaviour. They lead to ordinary or partial differential equations, generally defined in 3D in space, from which stability equations may be derived by perturbation techniques. Obtaining nontrivial solutions of the perturbed equations generally leads to transcendental eigenvalue problems, even if the underlying model is linear.

Discrete models. These models have a *finite* number of DOF in space. Often, such models are discrete approximations to the underlying continuum models. For instance, if a structure is assumed to be composed by rigid body-type members, interconnected by spring elements, this is a discrete model.

Two common discretization techniques can be applied:

- *Lumped parameter models*, in which the flexibility of the structure is localized at a finite number of places. One common model of this type for columns is joint-hinged rigid struts supported by extensional or torsional springs at the joints;
- *Finite element models* that include the so-called *geometric stiffness* properties.

Stability equations for discrete models may be constructed using various devices. For lumped parameter models one may resort to either perturbed equilibrium equations *(these equations are written taking as reference the deformed shape of given structure*), or to energy methods. For FEM models only energy methods are practical. All techniques eventually lead to matrix stability equations that take the form of an algebraic eigenvalue problem.

20.2.3. Bifurcation and limitation of equilibrium

Euler definition of stability will be firstly referred to discrete structures pointing out the condition of possible alternative equilibrium configuration available for the system (affected by no imperfections and in equilibrium in its reference position) when the compression axial load achieve a certain "critical" value: this possible availability of more than one equilibrium configuration (e.g. "bifurcation" of equilibrium). Moreover, imperfections do play a relevant role in the so called "equilibrium path" (namely the relationship between the current value of loads and the corresponding equilibrium configuration of the system) and their influence will be analysed in this chapter with reference to the mentioned discrete systems.

Two basic models are used to describe the instability state: *Bifurcation of equilibrium* and *Limitation of equilibrium.* Related to the Limitation model, for the particular case of imperfect bar, there is also the divergence of equilibrium model.

Bifurcation of equilibrium

Currently, structural engineers associate bifurcation of equilibrium with buckling. The structure reaches a *bifurcation point* (see Figure 20.3), at which two or more equilibrium paths intersect. What happens after the bifurcation point is traversed is called *post-buckling* behaviour. According to *bifurcation* model, the equilibrium equation can be directly written on a deformed configuration in the neighbours of the reference undeformed one, considering the effect of displacements of the forces applied of the structure.

Limitation of equilibrium

This is the case when the structure reaches a *limit point* at which the load, or the loading parameter, reaches a maximum value. Figure 20.3 shows comparatively the *bifurcation* and *limitation* models, for the case of an axially compressed member, in terms of compression force *P* and member axial shortening, *u*.

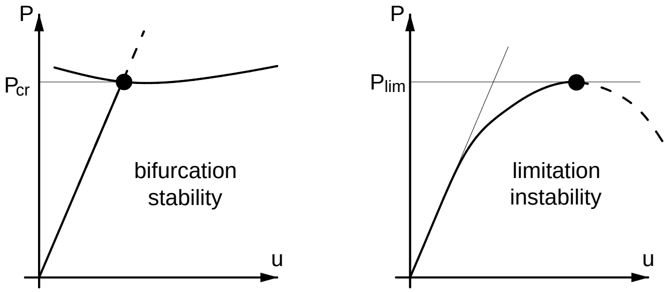

Fig. 20.3. Limitation of equilibrium

The phenomenon is also known as *limit point* or *snap buckling*. What happens after the limit point is traversed is called *post-buckling* or *post-snapping* behaviour.

Divergence of equilibrium

The physical model which is closest to real phenomenon of instability is the so called *divergence of equilibrium* (“divergence” is term lent from French and the model itself was proposed by Dutheil [20.4]). Maquoi and Rondal [20.5] applied Ayron-Perry equation [20.6] to calibrate experimentally the equations of actual European buckling curves.

The model itself is simple; it assumes the imperfect slender member in axial compression starts continuously deform from the initial moment of load application due to second order effect (see Figure 20.4a). Until point ***E*** ($P = Pe$), the behaviour of the slender member is geometrically nonlinear only (e.g. elastically nonlinear). Since in point ***E*** the elastic limit is attained in the outer fibre of section, if the load still increases, the behaviour becomes elastically-plastic nonlinear until arrive at the apex point of the curve, corresponding to the ultimate capacity, P_n (see Figure 20.4b). In this point the internal stresses equilibrate the external ones. After, if the load continues to increase, it cannot be equilibrated by internal stresses and the so called divergence between internal and external stresses occurs, the member undergoes into the post-critical range, following descending (softening) path, until the moment when full pacification of the section occurs, appears the plastic hinge and the member collapses.

The *divergence* model is fact a limit point model, which assumes the elastic-plastic behaviour of the compression member [20.7].

Bifurcation points and *limit points* are instances of *critical points*. The importance of correct estimation of critical points, at least in terms of corresponding critical or limit loads, in static stability analysis terms is crucial because the *transition from stability to instability can only occur at the critical points*!

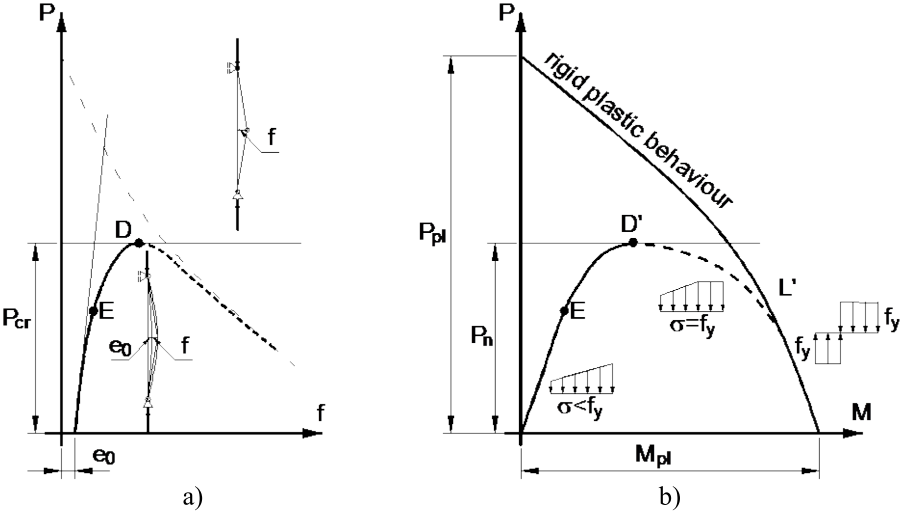

Fig. 20.4. Divergence of equilibrium [20.7]

Reaching a critical point may lead to unforeseen collapse of the structure. This depends on its *post-buckling* or *post-snapping* behaviour, but also on the ductile or fragile nature of the material. For some scenarios the knowledge of such behaviour is important since a sudden collapse may lead to the loss of the structure. On the other hand, there are some configurations where the structure keeps resisting - or even increasing - loads after traversing a critical point. It is important for the structural system to possess redundancy in order to offer alternate paths for stresses redistribution in case of stability loss of a member. Of the most dangerous phenomenon is the so called *dynamic propagation of instability*, from a member to the entire structure which collapses, and, of course, such a phenomenon has to be prevented by correct evaluation and appropriate design.

To illustrate the occurrence of static instability as well as critical points we will often display load-deflection response curve, which plots the successive *equilibrium configurations* taken by a structure, as a load or loading parameter (starting from zero is gradually and continuously varied). The load, or the loading parameter λ, is plotted along the vertical axis while a judiciously chosen representative deflection, which could be an angle, is plotted along the horizontal axes. A common convention is to take zero deflection at zero load. This defines the *initial state.*

A continuous set of equilibrium configurations forms an *equilibrium path*. Such paths are illustrated in Figure 20.5. The load-deflection curve in Figure 20.5a shows a response path with no critical points. On the other hand, that in

Figure 20.5b depicts the occurrence of two critical points: one bifurcation and one limit point, labelled as ***B*** and ***L***, respectively [20.1].

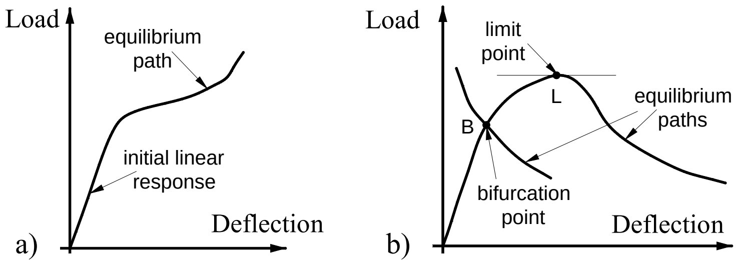

Fig. 20.5. Graphical representation of static equilibrium paths and their critical points: (a) a response path with no critical points; (b) multiple response paths showing occurrence of two critical points types: bifurcation point, *B*, and limit point, *L*

However, in case of complex structures multiple critical points might be identified along the load-defection equilibrium paths, with a sequence of bifurcation and limit points. In such cases an important question raised by structural engineer is *which critical point should be chosen as determining the critical or limit load to be used for estimating the safety factor against instability of given structure*?

In current design practice it is recommended to take the lowest critical load or load factor. When the analysis is limited to pre-critical range, up to attainment of critical or limit load that is the correct answer.

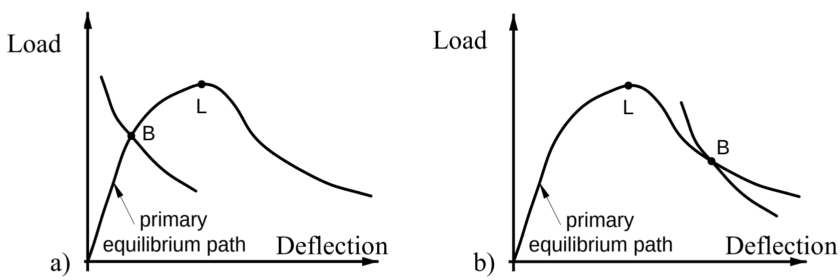

Fig. 20.6. Primary Equilibrium Path and the Design Critical Load: a) Bifurcation point located on the primary equilibrium path, before limit point; b) Limit point is attained before bifurcation

However, for a more comprehensive answer, it is useful to define first the *primary equilibrium path,* which is the one that passes through the reference state (often this is the undeformed or unloaded state).Then, the *design critical load* will be taken the one *located on the primary equilibrium path that is nearest to* *the reference state*. This choice makes engineering sense since most structures are designed to operate on the primary equilibrium path while in service. In fact, for design purposes, a critical load is that associated with the critical point first encountered when traversing the primary equilibrium path from the reference state. Figure 20.6 illustrates such two situations. In Figure 20.6b, for instance, the limit point ***L*** defines the design critical load because it is encountered first while traversing the primary equilibrium path, starting from initial state, and that does not matter that the bifurcation point ***B*** occurs at a lower load factor unless post-critical behaviour is important in design, which rarely is the case [20.1].

20.2.4. Post-buckling behaviour

The equilibrium paths of the three cases described in Figure 20.2, can be schematized for both ideal (with no imperfections) and imperfect structures, as shown Figure 20.7, to summarize some basic examples [20.8].

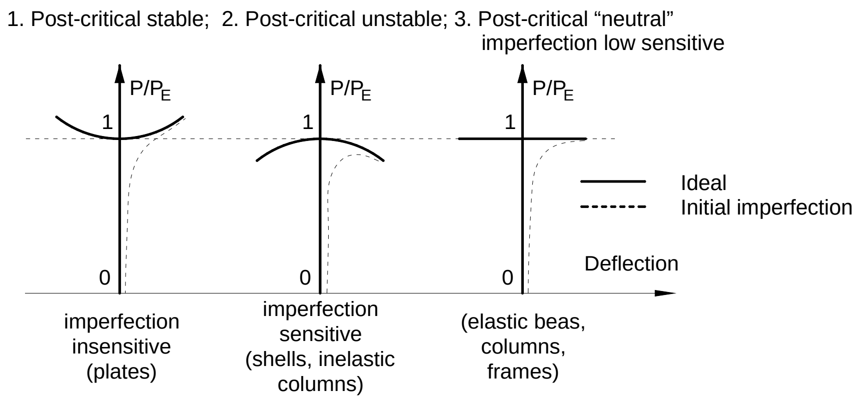

Fig. 20.7. Perfect and imperfect post-critical behaviour

20.3. Instability types

The contents of this section, is composed as follows:

- sub-chapters 20.3.1-20.3.3, which are mainly based on *Chapter 2: Phenomenological Modelling of Instability*, authored by Professor Victor Gioncu, of the Lecture Note No. 470 entitled *Phenomenological and Mathematical Modelling of Structural Instabilities* [20.2]; however, other references cited in the text have been used, too;
- sub-chapters 20.3.4-20.3.5, based on the authors previous works [20.9, 20.10].

20.3.1. Structures undergoing instability by bifurcation

Considering the bifurcation instability model described in Figure 20.1, such type of behaviour may happen in one of the following situations:

- When the pre-critical deformations do not correspond with the instability deformations; this is the case portal frame which has a symmetrical pre-critical deformation, while the post-critical deformation is asymmetrical (see Figure 20.8a);
- When the structure is perfect, as in case of compression bar, the bar in the pre-critical state is straight, while the post-critical form is bent (see Figure 20.8b);
- When the structure is an actual one with geometrical imperfections, but these are not affine with the post-critical deformations. As example, the pin-supported arch can have a symmetrical deviation from the designed form, but the post-critical deformation is asymmetrical one (see Figure 20.8c).

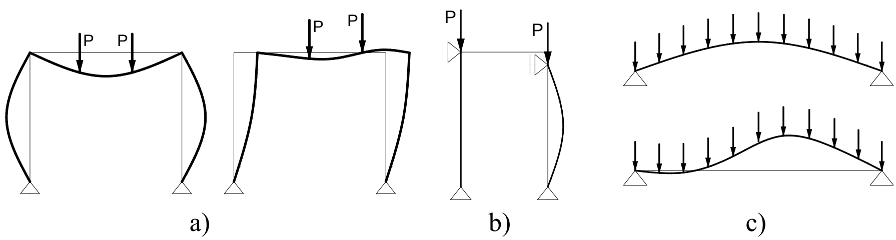

Fig. 20.8. Bifurcation cases

The bifurcation models are classified according to the shape of post-critical path. When traverse the critical point, from pre-critical range (e.g. *primary path*) to post-critical one (*secondary path)*, the system changes its rigidity (n.b.: in the critical point the stiffness is null, corresponding to the neutral stability state), two situation may appear:

- Stable when the stiffness is increasing, because the nonlinear deformations have a stabilizing effect;
- Unstable when the stiffness of system is decreasing, the nonlinear deformations inducing a destabilizing effect.

There are *simple* and *coupled* (multiple) bifurcation instabilities. *Simple bifurcation* instabilities are those cases when a given structure undergoes a *single mode* of bifurcation. There are three distinct situations:

Asymmetric bifurcation, which are stable in one side and unstable in the other (see Figure 20.9a), and occurs when for positive or negative deformations the stiffness of members having contrary effects, as in cases of the three-hinged arch, two bars frame (“Lee” frame), or bridge-type truss (see Figure 20.9b). Such type of behaviour also appears in case of latticed planar space structure and in case of unsymmetrical cross-section compression bar of fixed end-supports; cylindrical compressed shells are very sensitive for such a type of instability. This type of post-critical behaviour is very unstable, with high sensitivity to imperfections, of which correct estimation, both for amplitude and sign is crucial. *An imperfection applied on the wrong sense stabilizes the structure, when in fact it is severely unstable.*

Symmetric stable bifurcation, for which post-critical stiffness increases in the post-critical range for both, positive or negative displacements, is presented in Figure 20.10a; as in the case of the portal frame or a ring see (Figure 20.10b). Such type of behaviour also occurs in case of flexural buckling of double symmetric cross-section columns, for lateral-torsional buckling of beams, rectangular and circular compression plates, for sphere under concentrated loads. The sensitivity to imperfections of structures framed into such type of behaviour, even not negligible, is quite low.

a)

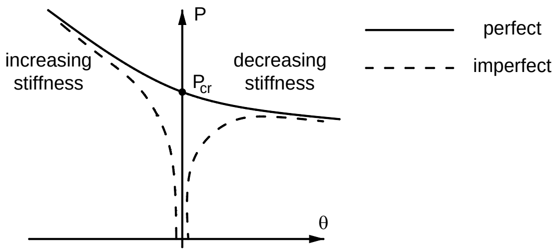

b)

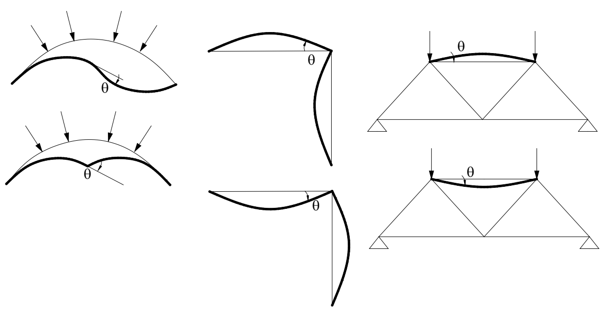

Fig. 20.9. Asymmetric bifurcations

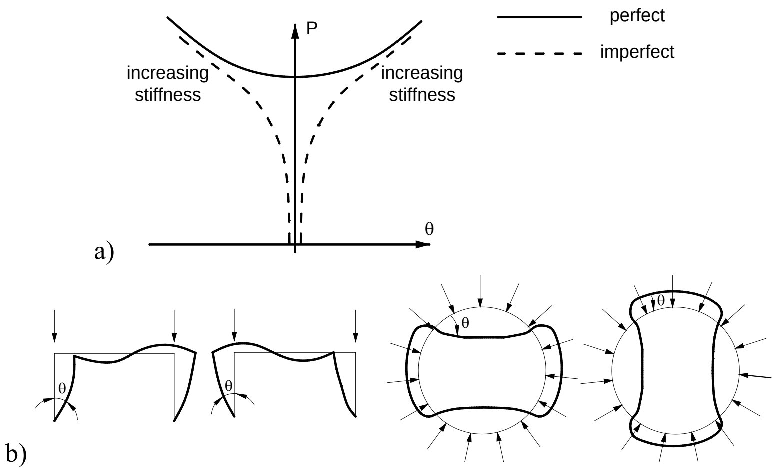

Fig. 20.10. Symmetric stable bifurcation

Symmetric unstable bifurcation (see Figure 20.11a) which occurs when for both positive or negative displacement the post-critical stiffness decreases, as in the cases of two-hinged arch and compressed beam on elastic foundation (see Figure 20.11b). This behaviour occurs also for a compression bar with elastic end-supports, for a ring under variable pressure, axially compressed cylinders undergoing axially symmetric buckling. Structures framed in this type of behaviour are characterized by a moderate sensitivity to imperfections.

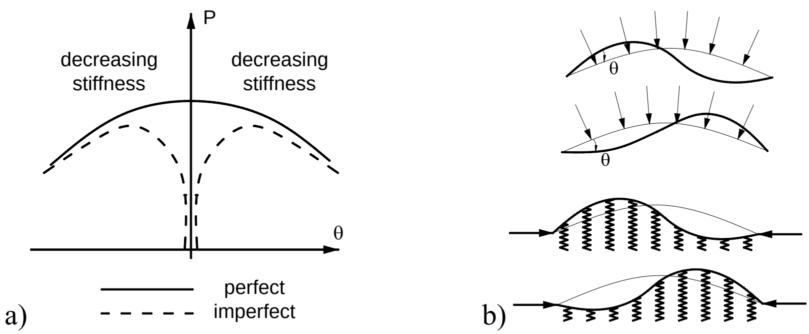

Fig. 20.11. Symmetric unstable bifurcation

Coupled bifurcation instabilities are characteristic for the structures for which, at the same critical load, there are possible two or more (*multiple bifurcation*) instability modes. In these cases some additional unstable paths corresponding to the coupled instability might occur. This subject will be discussed later on for interactive buckling.

20.3.2. Structures undergoing instability by limitation

The instability by limitation occurs in two situations, i.e.:

a) *Limitation due to geometrical imperfections.* A *perfect structure* which, *theoretically*, loses its stability by *bifurcation*, under de effect of initial imperfections is prone to second order effects and switch into a *limitation instability*. In fact, if examine all those cases the conclusion is simple: Perfect structures buckle in general by bifurcation, while imperfect structures undergo instability by limitation. However, the buckling resistance of structures framed as being of stable symmetrical post-critical bifurcation, even imperfect, due to their lower sensitivity to imperfections, could be approximated by a bifurcation analysis.

b) *Limitation due to nonlinear deformations.* It is not happened often for current structures; it is the case of some structural typologies for which, under the effect load the change of geometry becomes significant and the structure, *still remaining elastic*, exhibits geometrical nonlinear load-deflection relationship. In principle, the response of an imperfect system is similar to that of the corresponding perfect system (see Figure 20.12a). In case of shallow arches, shallow trusses and spherical domes, characterized by high compression stresses, *snap-through* buckling can occur where the initially stable path loses its stability when reaching the locally maximum value of the load, in the *limit point of equilibrium*, to *jump* suddenly in another equilibrium point, from where the structure (largely deformed) being able to take again loading. Figure 20.12b shows the jump of equilibrium phenomenon for the well-known *toggle* frame.

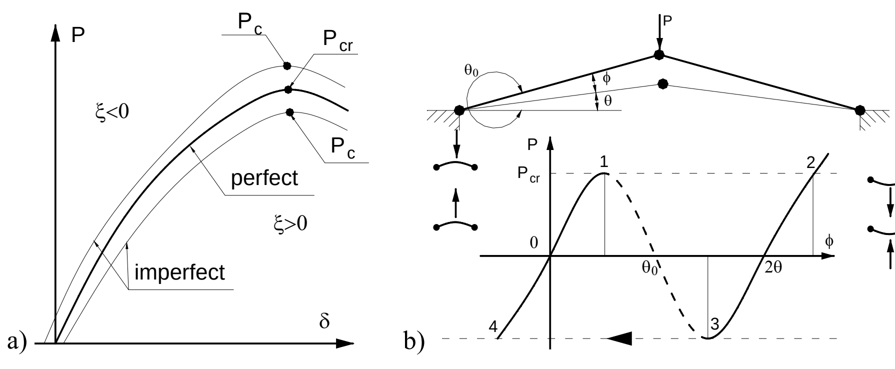

Fig. 20.12. a) Limitation instability due geometrical nonlinear deformations;
b) Snap-trough instability of toggle frame

It can be observed that from the limit point 1 the structure suddenly passes to the point 2, corresponding to another position of stable equilibrium loading.

The rate at which the equilibrium jump takes place is very high and large inertial forces appear. When the external load *N* reach the limit value the geometry suddenly changes with dynamic effects.

20.3.3. Dynamic instability

The transition of a structure from a stable state into an unstable one is a dynamic process and should be analysed accordingly; this is an aspect which was already tackled. However, in most of practical load cases, even the action has a dynamic character the problem can be solved using a *static equivalent* approach, amplifying the corresponding static load with a dynamic amplification factor. This is, for instance, the method applied in design of running beam of a bridge crane. However, there are some cases, almost always when apply *non-conservative actions*, when the static equivalent approach is not suitable. Three types of dynamic loads, for which the *dynamic stability approach* must be applied, can be met:

- step load when the time of action is very small, infinitesimal; blast is such a load;
- impulsive loads, it is a step load type, but with a finite duration, the structure undergoing vibrations; impact is such a load;
- time dependent or periodic loads, which may cause instability by flutter or divergence, as wind gust for example.

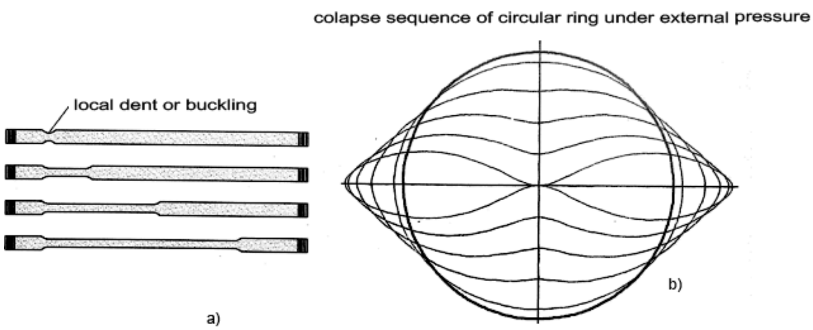

Fig. 20.13. Progressive propagation of a local dent in case of pipelines under external pressure

A very particular and dangerous case is the dynamic propagation or progressive instability. A local instability of a member in a structure occurs, caused, for instance, by a static load, and following to the redistribution of stresses in the neighbored zone, other members will buckle, and so one, till the overall collapse of the structure. The problem is such a phenomenon - dynamic in its nature - takes place with a very high speed! Such phenomena might appear in cases pipelines (see Figure 20.13), for double-layer grids (see Figure 20.14) and reticulated shells (see Figure 9.15).

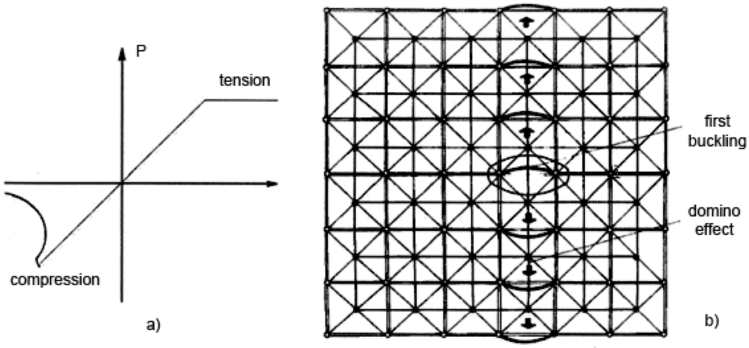

Fig. 20.14. The domino effect in case of double-layer grids

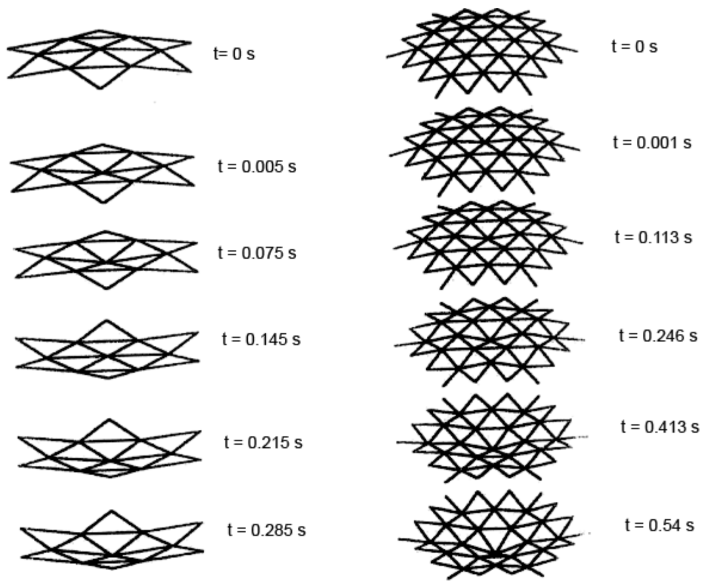

Fig. 20.15. Dynamic propagation of instability in case of reticulated domes

For double-layer grids (see Figure 20.14) and reticulated shells (see Figure 20.15), two types of local instabilities might occur: compression member buckling and node instability, the last being the most dangerous. It can be initiated by a variety of causes such as material defects, fabrication errors, impact, and deviations in the geometry of the ideal form or abnormal concentrated forces in nodes. A nodal *snap-trough* failure undergoes, it extends to a small surrounding portion of the structure initially, but has potential to propagate in the structure and cause a *line instability* or even the total collapse. The two examples in Figure 20.15, show the numerical simulation performed with Ansys of phenomenon, with the time steps, from initiation to the collapse [20.11].

20.3.4. Interactive buckling. The phenomenon

This subject refers to coupled bifurcation already introduced in §§20.3.1. In the case of an ideal structure, the theoretical equilibrium bifurcation point and corresponding load, P_{cr}, are observed at the intersection of the pre-critical (primary) force-displacement curve with the post-critical (secondary) curve as shown in Figure 20.16.

For a real structure, affected by a generic imperfection (δ_0), the bifurcation point does not appear anymore and, instead, the equilibrium *limit point* is the one characterizing the ultimate capacity (P_u) of the structure. The difference between P_{cr} and P_u represents the *Erosion of the Critical Bifurcation Load* (*ECBL*), due to the imperfections.

This model applies in the instability *mode interaction*. The meaning of the *mode interaction* refers to the *erosion* of critical bifurcation load in case of interaction of two (or more) buckling modes associated with the same, or nearly the same, critical load; it happens when the mode simultaneity is due to the results of design and/or imperfections. A well-known example of *mode interaction* are the coupling of local or distortional buckling with overall buckling in the case of thin-walled cold-formed members, or the coupling between local buckling of class 4 web with the lateral-torsional buckling of plated beam.

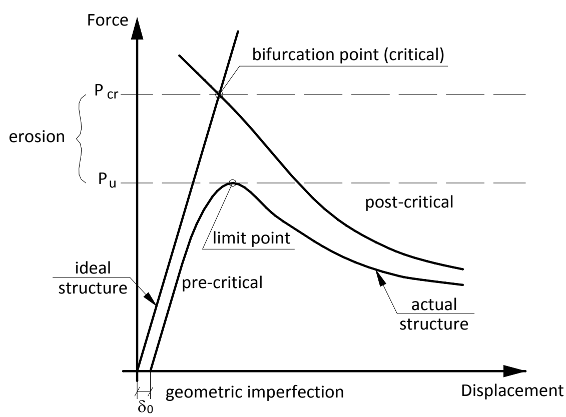

Fig. 20.16. Critical and post-critical behaviour

One of the pioneering studies devoted to local-overall mode interaction was conducted by Van der Neut [20.12]. In this case, the interaction occurred between the local buckling of the flanges and flexural buckling of a column of square box plated section; only the flanges have been considered to be active, while the web role was to connect them.

Figure 20.17a shows the buckling curve of the Van der Neut column without local or overall imperfections. For lengths greater than L_1 the column fails in overall Euler buckling, $N_E = \pi^2 EI / L^2$. For shorter lengths, the local buckling load $N_{cr,L} = 2\dfrac{k_\sigma \pi^2 E}{12(1-\nu^2)}\left(\dfrac{t}{d}\right)^2$, is reached before Euler buckling takes place (t is the thickness and d is the width of flanges, ν is the Poisson's ratio and $k_\sigma = 4$, the plate buckling coefficient). In the locally buckled shape, a reduced bending stiffness of the column, given by ηEI, is considered, where η is the slope of the load-strain diagram of the flange plate in the post-local buckling range. Van der Neut has considered the results of work by Hemp [20.13], who demonstrated that η is fairly constant over an extended strain range past the local buckling point and can be taken as $\eta = 0.4083$ for plates of which the longitudinal edges are free to pull in. As a result, the reduced overall buckling load in the post-local buckling range is given by $N_u = \eta N_E$, with $N_E = \pi^2 EI / L^2$. For column lengths between L_1 and L_2, equilibrium at a load N_L is stable if:

$$\frac{2\eta}{1+\eta}\pi^2\frac{EI}{L^2} > N_L \tag{20.1}$$

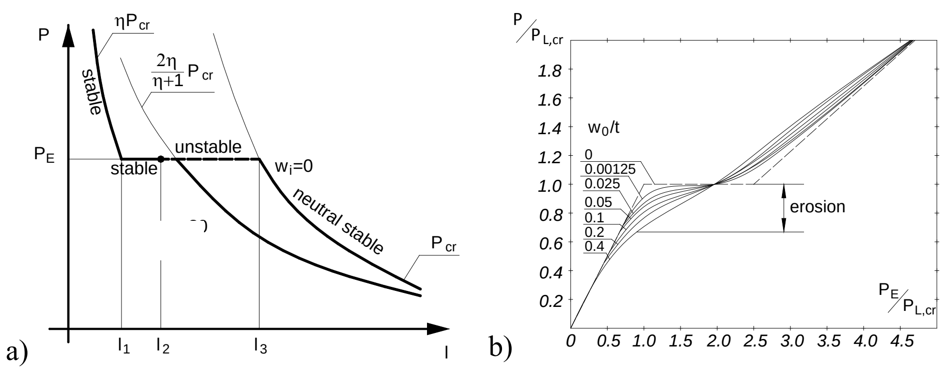

Fig. 20.17. a) The van der Neut model;
b) Local imperfection effect on the buckling load

Eq. (20.1) expresses that the column post-buckling capacity, given by Engesser's double modulus formula, has to be greater than the local buckling load N_L, and results in: $L_2 < L < L_0$, with $L_0 = 0.761L_1$. Columns with $L_0 < L < L_1$ are in a state of unstable equilibrium once the local buckling load is reached and collapse explosively (e.g. snap through effect).

In a second step, Van der Neut considered a local imperfection affine with the local buckling mode. Figure 20.17b displays the non-dimensional buckling load $N/N_{L,cr}$ function of $P_E/P_{L,cr}$ for different values of w_0/t, where w_0 is the local imperfection amplitude and t, is the flange thickness. It is seen that the local imperfection can cause a severe reduction in column capacity, and that the effect is most pronounced in the vicinity of the point where $P_E = P_{L,cr}$. For instance, a reduction (e.g. erosion) of 30% was calculated for $w_0/t = 0.2$. It was also demonstrated that, in the region where the perfect column displays unstable collapse, the peak of the load-bar shortening curve gets smoothened out as a result of the imperfection and the instability almost vanishes for $w_0/t = 0.2$. Van der Neut [20.12] also investigated the effect of an overall imperfection. The research concluded that the presence of an overall imperfection (e.g. bar deflection) has a similar negative effect on the column strength, the most significant erosion being obtained again in the point $P_E = P_{L,cr}$, but extending its influence over a larger zone (compared to the local imperfection) into the region where $P_E > P_{L,cr}$. At the end, the most important observation of this study is the reduction of P, due to the initial imperfection of flanges which is most significant when $P_E = P_{L,cr}$.

Another relatively recent design method, which can be framed in the class of semi-analytical methods, is *Direct Strength Method* [20.14] which practically replace the "effective width" concept with the "effective stress" one. The method explicitly incorporates local or distortional and Euler buckling resistances, which are evaluated numerically, and does not require calculations of the effective properties. The procedure is an alternative to the "effective width method". Direct Strength Method has been adopted in 2004 as design method in Appendix 1 to the *North American Specification for the Design of Cold-Formed Steel Structural Members* [20.15].

The *General method* in EN 1993-1-1 [20.16], applied for lateral-torsional buckling problems operates, in some way, similarly.

20.3.5. Interaction classes and erosion of critical bifurcation load

In almost all practical cases, the mode interaction, obtained by coupling of a local instability with an overall one, is a result of design (e.g. calibration of mechanical and geometrical properties of member) and has a nonlinear nature:

- Coupling by design occurs when the geometric dimensions of structure are chosen such as two or more buckling modes are simultaneously possible. For this case, the optimization based on the simultaneous mode design principle plays a very important role and the attitude of the designer towards this principle is decisive. This type of coupling is the most interesting in practice because, even the erosion of critical buckling load is maximum in the interactive range, the ultimate buckling strength still remain maximum in this range;

– Nonlinearity characterizes the post-buckling behaviour of coupling of instability modes and is due to design and the presence of the geometrical imperfections which is indispensable for coupling; this coupling doesn't exist for ideal structure. For instance, this is the case of the interaction between flexural buckling and torsional-flexural buckling of some mono-symmetrical cross-section.

Figure 20.18 illustrates such a case for a mono-symmetrical T section in compression, which is prone to the mode interaction between flexural and flexural-torsional modes [20.17, 20.18].

Due to the imperfections, an interaction erosion of critical bifurcation load occurs. This erosion is maximum in the coupling point vicinity. For bar members, an interactive slenderness range, in which sensitivity to imperfections is increased, may be identified. Depending on imperfection sensitivity, classes of interaction types, characterized by specific levels of erosion intensity, may be defined.

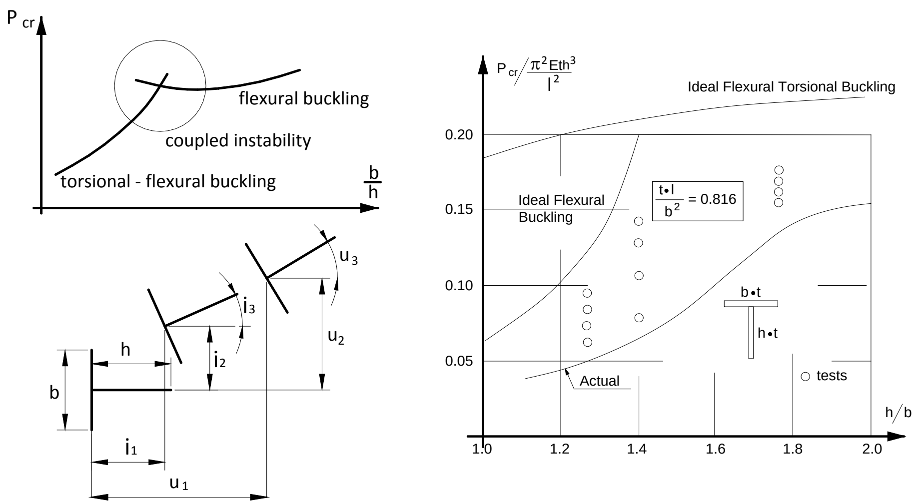

Fig. 20.18. Coupled instability by design: example for T section with test evidence [20.18]

Given a compression member and assuming two simultaneous buckling modes which might couple, the perfect member prone to interactive critical buckling load, N_{cr}, while the actual member to ultimate load, N_u, the erosion, ψ, can be expressed as follows:

$$\psi = \overline{N}_{cr} - \overline{N}_u \tag{20.2}$$

and

$$\overline{N}_u = (1-\psi)\overline{N}_{cr} \tag{20.3}$$

The *erosion factor* ψ was introduced as a *measure* of erosion of critical load. Gioncu [20.18] has ranked the mode interaction types in terms of erosion factor in four classes (see Figure 20.19).

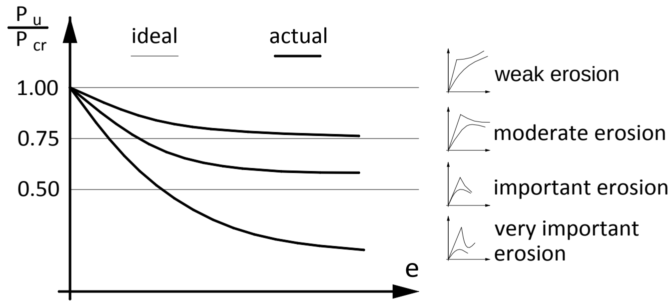

Fig. 20.19. Erosion classes

Obviously, an appropriate framing of each mode interaction into a relevant class is very important because the methods of analysis used for design have to be different from one class to another. In case of week or moderate interaction, structural reliability will be provided by simply using of design code safety coefficients, while in case of strong or very strong interaction, special methods are needed. Interaction classes can be associated with erosion levels or classes (see Figure 20.19) i.e. week weak erosion - low interaction of low sensitivity to imperfections; strong erosion - high interaction of high sensitivity to imperfections; a.s.o.

In case of thin-walled members, two types of interaction might occur. The first one is due to multiple local modes, which leads to a so called *localized* mode, and gives rise to an unstable post-critical behaviour. The second interaction between the localized buckling mode with the overall buckling mode yields to a very unstable post-critical behaviour, with great erosion due to the imperfections. This case of multiple local buckling mode interaction causes in the second case (local-overall) very destabilizing effects. Strong and very strong interactions are the result of this type of coupled instability. In such a case, very special design methods must be developed. Usually, this is the case of thin-walled columns in compression.

Stiffened plates in compression are prone to the interaction between overall flexural buckling with local buckling of stiffeners in compression or compression-bending. This is a high interaction characterised by high sensitivity to imperfections and strong erosion. Very strong erosion, due to the high sensitivity to imperfections can be encountered in case of cylinders or dome shells, continuous or reticulated were bi- or multi-modal interaction might occur.

To take into account properly for such a type of interaction in practical design, the FEM is actually the only effective tool!

20.4. Principles and general recommendations for numerically-based buckling analysis of thin-walled steel structures

20.4.1. Finite Element Methods (FEM) for analysis and design

The Finite Element Method (FEM) is widely used in design of structures. Annex C of EN 1993-1-5 [20.19] gives guidance on the use of FE-methods for ultimate limit state design, serviceability limit state design and fatigue verifications of plated structures. The FE-modelling may be carried out either for: (1) the component as a whole or (2) a substructure as a part of the whole structure. Also, design of members and details can be assisted by numerical simulations (e.g. numerical testing). The choice of the FE-method depends on the problem to be analysed.

The key categories of computational analysis that were first devised for use in EN 1993-1-6 [20.20] are recommended for wide use for all structures [20.21]:

LBA: Linear elastic bifurcation analysis, obtaining the lowest eigenvalue for the system;

MNA: Materially nonlinear analysis, using small displacement theory (no change of geometry), and an ideal elastic-plastic constitutive model for the material;

GNA: Geometrically nonlinear analysis of the elastic perfect structure;

GMNA: Geometrically and materially nonlinear analysis of the perfect structure;

GMNIA: Geometrically and materially nonlinear analysis with explicit imperfections.

Geometrically nonlinear means an analysis that takes full account of the change in geometry, both in kinematic and equilibrium relationships, whether this be a small change in one dimension or a gross inversion of the complete structure. Similarly it is expected that in a GMNA or GMNIA analysis, the material model will be fully nonlinear and not simply an ideal elastic-plastic model, unless this truly represents the material response. The classic image of the load-displacement curves given by these analyses is shown in Figure 20.20.

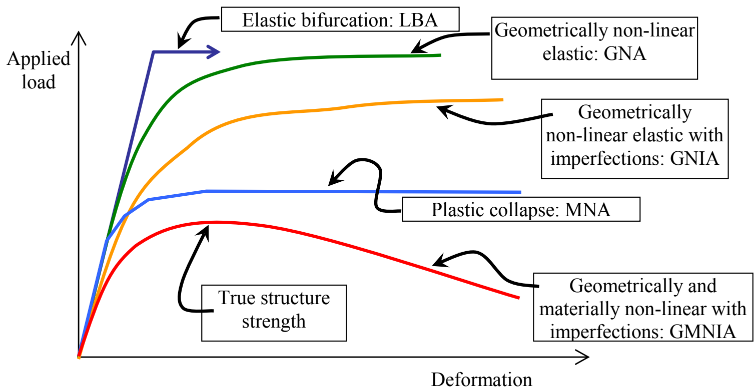

Fig. 20.20. Load-displacement curves found using different analyses of the same structure [20.21]

In using FEM for design special care should be taken in:
– the modelling of the structural component and its boundary conditions;
– the choice of software and documentation;
– the modelling of imperfections;
– the modelling of material properties;
– the modelling of loads;
– the choice of limit state criteria;
– the choice of partial factors to be applied.

The choice of FE-models (shell models or volume models) and the size of mesh determine the accuracy of results. For validation, sensitivity checks with successive refinement may be carried out.

The boundary conditions for supports, interfaces and applied loads should be chosen such that results obtained are conservative. Geometric properties should be taken as nominal.

Where imperfections need to be included in the FE-model these imperfections should include both geometric and structural imperfections. Unless a more refined analysis of the geometric imperfections and the structural imperfections is carried out, equivalent geometric imperfections may be used. The direction of the applied imperfection should be such that the lowest resistance is obtained. In combining imperfections a leading imperfection should be chosen and the accompanying imperfections may have their values reduced to 70%.

Material properties should be taken as characteristic values. Depending on the accuracy and the allowable strain required for the analysis the following assumptions for the material behaviour may be used:

a) elastic-plastic without strain hardening;
b) elastic-plastic with a nominal plateau slope;
c) elastic-plastic with linear strain hardening;
d) true stress-strain curve modified from test results.

The loads applied to the structures should include relevant load factors and load combination factors. For simplicity a single load multiplier α may be used.

Thin-walled cold-formed steel members are characterised by the following instability modes: local buckling of the walls, distortional buckling of the cross-section or global buckling of the member. For relevant member lengths an interaction of these modes can occur. The structural design of thin-walled cold-formed steel members is strongly dependent on the analysis of the stability and, consequently, the elastic stability behaviour has to be obtained as accurate as possible, in order to produce safe and reliable results to be applied in design procedures.

For this, one can apply direct formulations previously obtained from the theory of elastic stability, as for the case of the global buckling, or take advantage of computational programs that allow general stability analysis by solving the fundamental eigenvalue problem, related to the bifurcation-type stability behaviour. The general solution of the first order stability problem for the case of thin-walled members can be easily accessed, with the help of finite element method – based programs.

Alternative computational solutions have been developed, on the basis of numerical models other than the FEM, such as the general beam theory method (GBT) and the finite strip method (FSM).

Generalized Beam Theory is an extension to conventional engineering beam theory that allows cross-section distortion to be considered. Stability analysis of thin-walled members may also be performed using GBT. GBT was originally developed by Schardt [20.22], then extended by Davies et al. [20.23], and has over the last several years been an active focus of Silvestre & Camotim [20.24, 20.25, 20.26]. It has a short solution time and the method is applicable for both pin-ended and fixed-ended members. Generalized Beam Theory has a user friendly program for use developed at the TU Lisbon called GBTUL (http://www.civil.ist.utl.pt/gbt/), that performs elastic buckling (bifurcation) and vibration analyses of prismatic thin-walled members.

Another alternative to determine the elastic buckling loads of thin-walled cold-formed members is the freely available open source program CUFSM tool (http://www.ce.jhu.edu/bschafer/cufsm/). CUFSM employs the semi-analytical finite strip method to provide solutions for the cross-section stability of such members [20.27]. The new version CUFSM 4.04 applies to members with general end boundary conditions. The constrained finite strip method (cFSM) is also fully implemented in this version. Other software packages that provide the same solutions are available e.g. CFS (www.rsgsoftware.com) and THIN-WALL (http://sydney.edu.au/ engineering/civil/case/thinwall.shtml).

In case of thin-walled cold-formed members, when the interaction of local-overall or distortional-overall buckling is the purpose of an analysis, GNIA or GMNIA, with shell finite elements are recommended. For connecting details, in almost all the cases, MNA with 3D finite elements can be used. A useful reference for a good guidance in design of steel structures using FEM is the book of Kidmann and Krauss [20.28].

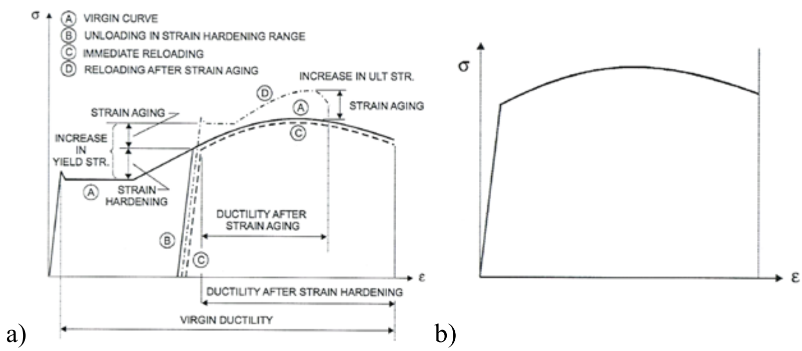

Fig. 20.21. Effects of cold straining and strain aging on σ-ε characteristics of carbon steel: a) global σ-ε diagram; b) apparent σ-ε diagram for a cold-formed member

20.4.2. Modelling of material properties and imperfections for numerical analysis

Material properties and modelling

Thin-walled steel sections are fabricated by means of cold-rolling of coils or press-braking of plates made by carbon steel. However, for these members, frequently used in modern steel construction, the initial σ-ε relation of the steel is considerably changed by the cold-straining due to the manufacturing processes. Figure 20.21a shows the modification of the σ-ε diagram when a carbon steel specimen is first strained beyond the yield plateau and then unloaded. For modern steel the strain aging effect is now very rare, or at least limited.

Therefore, only the cold-forming effect has to be considered in the computation and on this purpose the apparent σ-ε diagram (see Figure 20.21b) can be used.

Due to the forming process strain-hardening can vary considerably along the cross-section as shown in Table 20.1 and Figure 20.22.

Table 20.1. Influence of manufacturing process on the basic strengths of hot and cold-formed profiles [20.29]

Forming process		Cold rolling	Press braking
Yield strength (f_y)	Corner	high	high
	Flat faces	moderate	--
Ultimate strength (f_u)	Corner	high	high
	Flat faces	moderate	--

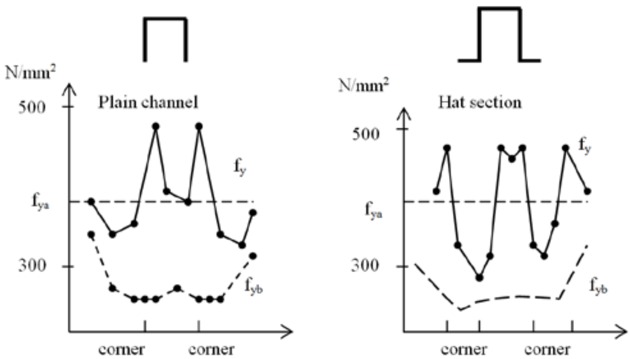

Fig. 20.22. Influence of manufacturing process on yield strength [20.30]

Eurocode 3-Part 1.3 [20.31] gives the following formula to evaluate the average yield strength, f_{ya}, of the full section:

$$f_{ya} = f_{yb} + (C \cdot n \cdot t^2 / A_g) \cdot (f_u - f_{yb}) \tag{20.4}$$

where A_g is the gross cross sectional area and n is the number of 90° bends in the section, with an internal radius $r < 5t$. In this formula, $C = 7$ for cold-rolling and $C = 5$ for other methods of forming, but

$$f_{ya} \leq 0.5 \cdot (f_{yb} + f_u) \tag{20.5}$$

or

$$f_{ya} \leq 1.25 \cdot f_{yb} \tag{20.6}$$

The average yield strength, f_{ya}, can be used in numerical analysis when a bilinear stress-strain model approximates the material behaviour. However, if tests results are available, the input parameters for material model needed to describe the stress-strain behaviour, directly obtained from tensile coupon tests from different portions of the member cross-section.

The increase of the yield strength is due to strain hardening and depends on the type of steel used for cold rolling. On the contrary, the increase of the ultimate strength is related to strain aging that is accompanied by a decrease of the ductility and depends on the metallurgical properties of the material.

Material modelling represents one of the most important aspects of the FE simulation. If tests results are not available, an idealisation of the material model, that is elastic-plastic with strain hardening, can be conveniently approximated by Ramberg-Osgood or Powell equations.

In [20.32] very accurate tests, performed at University of Sydney [20.33], on compressed cold-formed steel lipped channels, have been selected to investigate the influence of material models. The L36 test series, on pin-ended members, was chosen to calibrate the FEM model. The nominal cross-section dimensions for the series specimen are: thickness of 1.5 mm, web width of 96 mm, flange width of 36 mm and lip width of 12 mm. The lipped channels were brake-pressed from zinc-coated structural steel sheets grade G450 (nominal yield stress of 450 MPa). Material properties, determined from coupon tests, are: measured static 0.2% ($\sigma_{0.2}$) tensile proof stresses of 500 MPa, tensile strength (σ_u) of 540 MPa and Young's modulus E = 195 GPA.

Using Ansys, the ideally elastic-plastic material model can be implemented by means of bilinear isotropic plastic model (BISO), and Ramberg-Osgood model by means of multi-linear model (MISO). Table 20.2 and Figure 20.23 shown the numerical results obtained with Ansys large-deformation elastic-plastic analysis using the two material loads [20.32]. One can see that both characteristic values and the shape of load-deflection curves do not differ significantly in the models.

Table 20.2. Limit loads in kN [20.32]

Specimen	Tests	Ansys with bilinear material model		Ansys with R-O model
		measured imperfections	equivalent imperfections	measured imperfections
L36P0280-	83.5	-	85.87	81.41
L36P0815+	67.9	70.5	72.08	69.8
L36P1315-	41.1	41.42	38.56	40.75

An important role plays the corner properties. Due to the manufacturing process the material exhibits significant strain hardening in corner regions of the cold-formed section. They are characterised by a yield strength much higher than in the flat zone, and simultaneously by a reduced ductility. For stainless steel, [20.34] proposed a simple model which can be applied to all types of corners to predict $\sigma_{0.2,c}$ by knowing the ultimate strength of virgin material, $\sigma_{u,v}$, i.e. $\sigma_{0.2,c} = 0.85 \cdot \sigma_{u,v}$.

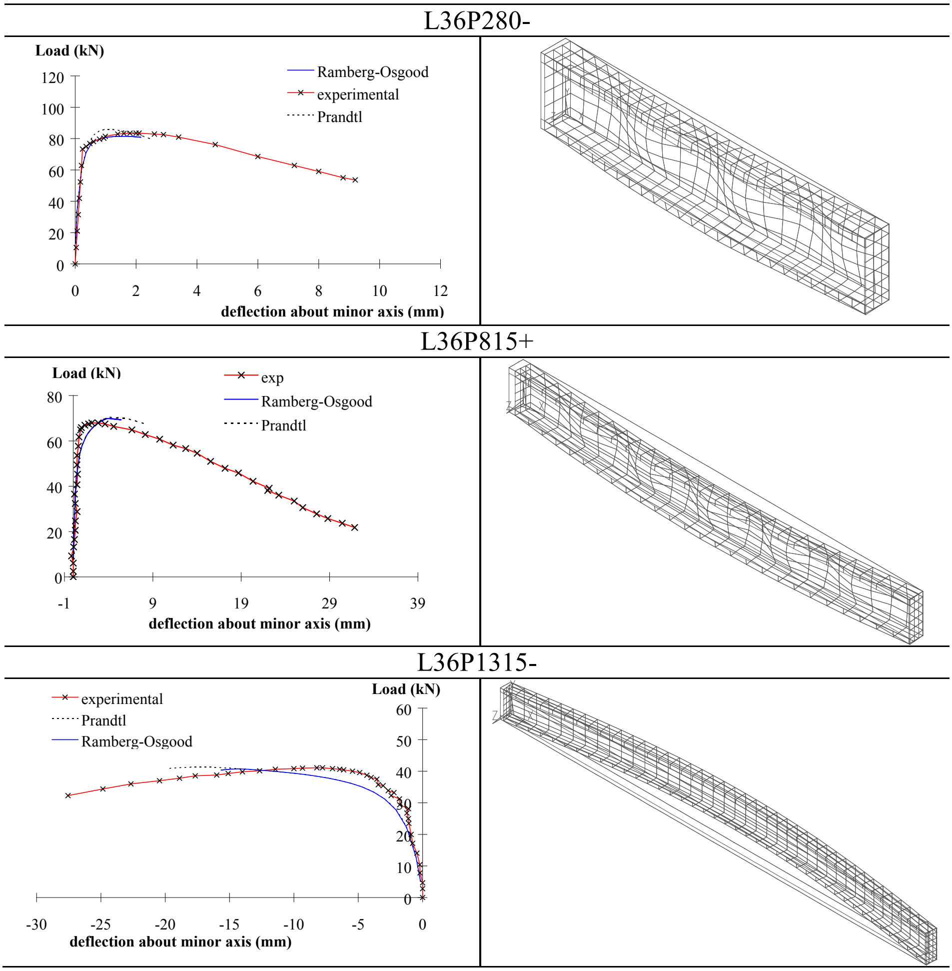

Fig. 20.23. Load versus mid-length deflection about minor axis and deformed shapes at the limit load [20.32]

Residual stresses

In cold-formed steel members, both residual stresses and increase in yield strength are due to the manufacturing process and tend to compensate each other.

Hot-rolled profiles are affected by residual stresses, which result from air cooling after hot-rolling. These stresses are mostly of membrane type; they depend on the shape of sections and have a significant influence on the buckling strength. Therefore, residual stresses are the main factor which causes the design of hot-rolled sections to use different buckling curves in European design codes [3.16].

In the case of cold-formed sections the residual stresses are mainly of flexural type, as Figure 20.24 demonstrates [20.35], and their influence on the buckling strength is less important than membrane residual stresses as Table 20.3 shows. On the other hand, cold rolling process produces different residual stresses in the section when compared with press braking, as shown in Table 20.3, so the section strength may be different in cases where buckling and yielding interact [20.29].

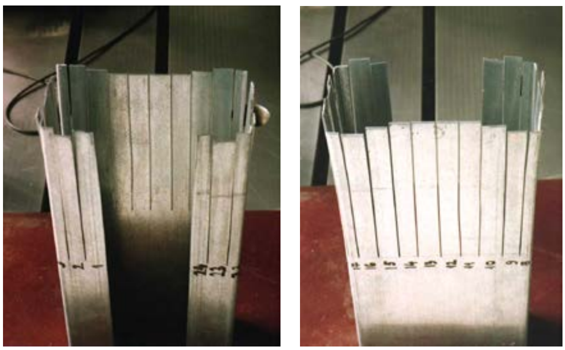

Fig. 20.24. Evidence of flexural residual stresses in a lipped channel cold-formed steel section [20.35]

Table 20.3. Type magnitude of residual stress in steel sections [20.29]

<table>
<tr><th rowspan="2">Forming method</th><th rowspan="2">Hot rolling</th><th colspan="2">Cold forming</th></tr>
<tr><th>Cold rolling</th><th>Press braking</th></tr>
<tr><td>Membrane residual stresses (σ_{rm})</td><td>high</td><td>low</td><td>low</td></tr>
<tr><td>Flexural residual stresses (σ_{rf})</td><td>low</td><td>high</td><td>low</td></tr>
</table>

Adequate computational modelling of residual stresses is troublesome. Inclusion of residual stresses (at the integration points of the model for instance) may be complicated, and selecting an appropriate magnitude is made difficult by the lack of data. As a result, residual stresses are often excluded altogether, or the stress-strain behaviour of the material is modified to approximate the effect of residual stresses.

In hot-rolled steel members, residual stresses do not vary markedly through the thickness, which means the membrane residual are dominant, while in cold-formed members residual stresses are dominated by a "flexural", or through thickness variation. This variation of residual stresses leads to early yielding at the faces of cold-formed steel plates. Through-thickness residual stresses are implicitly considered when obtaining the stress-strain curve from coupon tests, and lead to a roundedness of the stress-strain curve near the yield point.

Residual stress can be idealised as a summation of two types: flexural and membrane (see Figure 20.25).

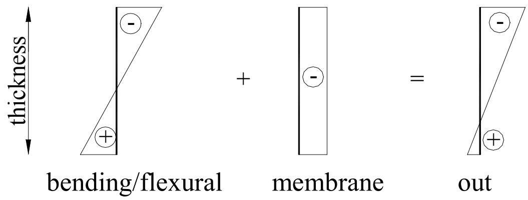

Fig. 20.25. Idealisation of residual stress [20.36]

Membrane residual stresses are more prevalent in roll-formed members than press-braked members. Compressive membrane residual stresses cause a direct loss in compressive strength. Significant membrane residual stresses exist primarily in corner regions. Counteracting this effect, the yield stress, f_y, is enhanced in corner regions due to significant cold work during forming. If large membrane residual stresses are modelled in the corners or other heavily worked zones, then increased yield stress in these regions should be modelled as well. Conversely, if membrane residual stresses are ignored, the enhancement of the yield stress should not be included. Further study is needed to assess how much these two effects counteract one another.

Flexural residual stresses. Flexural residual stresses are much more significant in cold-formed steel sections than the membrane ones. For member buckling (overall modes) their influence is usually not important. However, sectional buckling strengths, mainly the local and distortional buckling strengths can be significantly influenced.

Large magnitudes of flexural residual stresses in cold-formed sections are regularly observed - residual stresses equal to 50% f_y are not uncommon. Measured flexural residual stresses also experience a large degree of variability. For the purpose of numerical analysis Schafer and Peköz [20.36] proposed the approximate and conservative average distributions of flexural residual stresses, as shown in Figure 20.26.

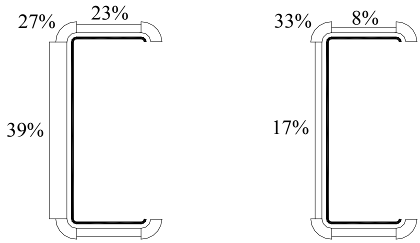

a) Roll-formed b) Press-braked

Fig. 20.26. Average flexural residual stress as percentage of f_y [20.36]

When a highly refined numerical analysis is performed, both residual stresses and actual distribution of yield strength over the full cross-section, taking into account the influence of cold-forming have to be considered. Numerical studies have shown the reduced influence of flexural residual stresses on the ultimate strength of sections [20.37]. Moreover, Rasmussen and Hancock [20.38] observed that tension and compression coupons cut from finished tubes curved longitudinally as a result of through-thickness flexural residual stresses, and that straightening of the coupons as part of the testing procedure approximately reintroduced the flexural residual stresses. Therefore, when the material properties of the cross-section are established from coupons cut from within the section, the effect of flexural residual stresses is inherently present, and is not require to be explicitly defined in the finite element model [20.39].

Geometrical imperfection

Geometric imperfections refer to the deviation of member from the *perfect* or *nominal* geometry. Imperfections of cold-formed steel members include bowing, warping, and twisting as well as local deviations.

When a geometrical nonlinear analysis is performed, some kind of initial disturbances (e.g. imperfection) are necessary when the strength of the member is studied [20.40]. In case of cold-formed steel sections, two kinds of imperfections are characteristic, i.e.:

– geometrical imperfections, sectional and along the member;
– residual stress and change of yield strength due to cold forming effect.

When initial imperfections are used to invoke geometric nonlinearity, the shape of imperfections can be determined with a linear buckling analysis and must be affine with the relevant local, sectional or overall buckling modes of the cross-section. Consequently, until now the geometrical imperfections are introduced in numerical models using equivalent sine shapes with half-wavelength corresponding to relevant instability modes. Rasmussen and Hancock [20.41] and Schafer and Peköz [20.36] proposed numerical models to generate automatically geometrical imperfection modes. Schafer et al. [20.42] used the probabilistic analysis in order to evaluate the frequency and magnitude of imperfections.

Maximum measured imperfections can be conservatively used as amplitude in sine shape to predict by analysis lower bound strength [20.41]. While it is true that larger imperfections do not always mean lower strength, if the eigenmode shape used in the analysis does not characterise the most unfavourable imperfect shape of the member, generally the strength decreases as the magnitude of the imperfection increases. However, different shapes of local/sectional imperfections have different effect on the buckling strength of the member and, not always, the sine shape of geometrical imperfections represents the most relevant mode to be considered in the analysis. Since maximum imperfections are not periodic along the length, using the maximum amplitude of imperfection as for the buckled shape is rather conservative. Despite these drawbacks, the maximum imperfection approach is simply to apply and provides a reasonable criterion for a lower bound strength analysis. At this point, it is also useful to underline a conclusion by Bernard et al. [20.43], who demonstrated statistically that a significant influence of geometrical imperfections exists in thin-walled members at short and medium wave-lengths, leading to reduction of the load carrying capacity. This means the sectional buckling modes, singly or coupled with overall ones are mainly affected.

Appropriate allowance must be made to account for the effects of practical imperfections in the global analysis, in the analysis of bracing systems and in member design. Practical imperfections, which include residual stresses, are geometrical imperfections such as lack of verticality, lack of straightness, lack of fit and unavoidable eccentricities present in practical joints. Allowance for these imperfections may be achieved by incorporating suitable geometric imperfections with values which reflect all types of imperfection. According to EN1993-1-1 [20.16] the following imperfections should be taken into account in the global analysis of all frames:

a) global imperfections for frames and bracing systems,

b) local imperfections for individual members.

The effects of member imperfections may neglected when carrying out the analysis of non-sway frames. For sway frames with slender columns it may be required to incorporate member imperfections in the analysis.

The effects of global frame imperfections must be accounted for in the global analysis in the form of an equivalent geometric imperfection, i.e. an initial sway [20.16]. The assumed shape of global imperfections and local imperfections may be derived from the elastic buckling mode of a structure in the plane of buckling considered. Both in- and out-of-plane buckling including torsional and flexural-torsional buckling with symmetric and asymmetric buckling shapes should be taken into account in the most unfavourable direction and form. The resulting forces and moments shall be used for member design. These global imperfections can also be accounted for by introducing equivalent lateral loads at the floor levels.

For frames sensitive to buckling in a sway mode, the effect of imperfections should be allowed for in frame analysis by means of an equivalent imperfection in the form of an initial sway imperfection and individual bow imperfections of members. The recommended values given by EN1993-1-1 [20.16] are presented in Table 20.4, with reference to the column buckling curves.

Table 20.4. Design values of initial local bow imperfection for elastic analysis [20.16]

Buckling curve	e_0/L
a_0	1/350
a	1/300
b	1/250
c	1/200
d	1/150

The appropriate equivalent bow imperfection for a given member depends on the relevant buckling curve, the method of analysis and the type of cross-section verification used.

In what concern the overall sinusoidal imperfections (bar deflection), with the maximum amplitude of 1/1500 times the member length, (L), which corresponds to statistical mean of imperfections of carbon steel columns, as suggested by Bjorhovde [20.44], can be used, or more conservatively, L/1000, as proposed by ECCS Recommendation [20.45].

In case of lateral-torsional buckling of thin-walled beams, both initial deflection and initial twisting may be significant. On this purpose, the Australian Standard AS 4100 [20.46] proposes recommendations for the initial deflection, (f_o), and initial twist, (ϕ_o), as follows:

$$1000 \cdot f_o / L = 1000 \cdot \varphi_o \cdot (M_{cr} / N_{cr} L) = -1 \quad \text{for} \quad \overline{\lambda}_{LT} \geq 0.6 \qquad (20.7)$$

$$1000 \cdot f_o / L = 1000 \cdot \varphi_o \cdot (M_{cr} / N_{cr} L) = -0.001 \quad \text{for} \quad \overline{\lambda}_{LT} < 0.6 \qquad (20.8)$$

where N_{cr} is the column elastic critical buckling (Euler) load about minor axis, M_{cr} is the elastic critical moment for lateral-torsional buckling, $\overline{\lambda}_{LT}$ is the flexural-torsional slenderness and L is the length of the member.

Local deviations are characterised by dents and regular undulation on the plate. Collected data on geometric sectional imperfections are sorted by Schafer and Peköz [20.36] in two categories (see Figure 20.27): *type 1*, maximum local imperfection in a stiffened element (e.g. local buckling type imperfection), and *type 2*, maximum deviation from straightness for a lip stiffened or unstiffened flange (e.g. distortional type imperfection).

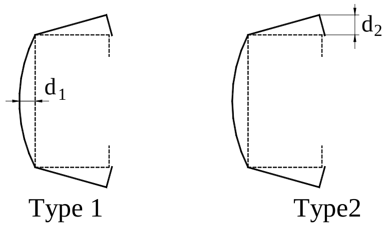

Fig. 20.27. Sectional imperfections

Based on statistical analysis of actual measurements, Schafer and Peköz [20.36] proposed the following simple rules to apply when width/thickness (*b/t*) less than 200 for *type 1* imperfections and, (*b/t*) less than 100 for *type 2* imperfections, respectively. Thickness should be less than 3 mm. For *type 1* imperfections, a simple linear regression based on the plate width yields to the approximate expression

$$d_1 \approx 0.006 \cdot b \tag{20.9}$$

where *b* is width or depth of the web.

An alternative rule based on an exponential curve fit to the thickness (*t*)

$$d_1 \approx 6 \cdot t \cdot e^{-2t} \ (d_1 \ and \ t \ in \, mm) \tag{20.10}$$

For *type 2* imperfections the maximum deviation from straight is approximately equal to the plate thickness:

$$d_2 \approx t \tag{20.11}$$

20.5. Conclusions

There is a large variety of instability problems which can be encountered in practice; most of them are covered by the codes provisions but, however, still being some aspects which cannot be properly solved by codified approaches. Numerical advanced FE codes, such as Ansys, Abaqus, Nastran, etc., make possibly today to calculate and/or simulate accurately the behaviour of complex problems. The choice of the FE-method depends on the problem to be analysed. Particularly, for slender structures, highly sensitive to buckling, still there are difficulties for a reliable evaluation of the buckling load. On the other hand, since there are several ways to model and to analyse the stability problems, it is important to make the appropriate choice of the model and procedure to apply to the given problem.

The stability issues for structures with reduced sensitivity to imperfections and stable post-critical behaviour can be addressed in a simplified way, using LBA analyses, treated as bifurcation problems. Those, which are sensitive to second order effects and, therefore, to imperfections, that develop plastic mechanisms only in the failure stage (the case of cold-formed sections of class 4), GNIA can be applied. If the behaviour in the post-buckling range is investigated (local plastic mechanism primarily occurs and the behaviour in the post-elastic stage is of interest when follows the post-critical path), GMNIA must be used. If elastic-plastic problems are investigated, GMNIA have to be used in all cases. In case of interactive buckling problems GMNIA is recommended to be used in all cases.

Stability analysis of thin-walled members may also be performed using specialised software, such as: Generalized Beam Theory (GBTUL - http://www.civil.ist.utl.pt/gbt/), open source program CUFSM tool (http://www.ce.jhu.edu/bschafer/cufsm/), CFS (www.rsgsoftware.com) and THIN-WALL (http://sydney.edu.au/ engineering/civil/case/thinwall.shtml). These specialised programs enable to determine the elastic buckling loads of thin-walled cold-formed members, to perform vibration analyses and modal decomposition. The main problems of these programs are that they do not cover post-critical range, do not include imperfections and are not developed to analyse the structure as a whole. For such problems, GNIA or GMNIA, with shell finite elements is recommended.

What is important to be underlined is that the numerical models, together with the solver procedures, particularly for complex nonlinear analyses, must be always calibrated and validated through experimental results or validated benchmark numerical examples.

20.6 References

20.1 Felippa C.A., Lecture Notes, Part VI: Introduction to structural stability. University of Colorado, 2015 (http://www.colorado.edu/engineering/CAS/courses.d/Structures.d/Home.html).

20.2 Gioncu V., Phenomenological modelling of instability. Phenomenological and mathematical modelling of structural instabilities, Pignataro M., Gioncu V. (eds.), CISM International Centre for Mechanical Sciences, No. 470, Springer-Verlag Wien 2005, pp. 85-134.

20.3 Bazant Z.B., Cedolin L., Stability of Structures: Elastic, Inelastic, Fracture and Damage Theories, Dover Publication Inc., New York 2003.

20.4 Dutheil J., Vérification des pièces comprimées. Principes Fondamentaux. Construction Métallique, Nos. 2-3, 1966, pp. 3-11.

20.5 Maquoi R., Rondal J., Mise en equation des nouvelles courbes Europeenes de flambement, Construction Metallique, Vol. 1, 1978, pp. 17-30.

20.6 Ayron W.E., Perry J., On struts, The Engineer, Vol. 62, 1886.

20.7 Mateescu D., Appeltauer J., Cuteanu E., Stability of compression members in steel structures (in Romanian), Publishing House of R.S.R. Academy, Bucharest 1980.

19.8 Galabos T.V., Surovek A.E., Structural Stability of Steel: Concepts and Applications for Structural Engineers, John Wiley & Sons, 2008.

20.9 Dubina D., Ungureanu V., Crisan A., Experimental Evidence of Erosion of Critical Load in Interactive Buckling, Journal of Structural Engineering, Vol. 139, 2013, pp. 705-716.

20.10 Dubina D., Ungureanu V., Instability mode interaction: From Van Der Neut model to ECBL approach, Thin-Walled Structures, Vol. 81, 2014, pp. 39-49.

20.11 Ivan A., Gioncu V., Dynamic propagation of local instability for single-layer reticulated domes. Coupled Instabilities in Metal Structures, Camotim D., Dubina D., Rondal J. (eds.), London, Imperial College Press, 2000, pp. 515-522.

20.12 van der Neut A. The interaction of local buckling and column failure of thin-walled compression members. Report VTH 149, Delft University of Technology, Department of Aeronautical Engineering, The Netherlands, 1968.

20.13 Hemp W.S., The Theory of Flat Panels Buckled in Compression. Reports and Memoranda, Aeronautical Research Council, No. 2178, 1945.

20.14 Schafer B.W., Designing cold-formed steel using the Direct Strength Method, Proceeding of the 18th International Specialty Conference on Cold-Formed Steel Structures, Orlando, USA, 2006.

20.15 AISI:2004. Supplement 2004 to the North American Specification for the Design of Cold-Formed Steel Structural Members, 2001 Edition: Appendix 1, Design of Cold-Formed Steel Structural Members Using Direct Strength Method. American Iron and Steel Institute, Washington, D.C., SG05-1, 2004.

20.16 EN1993-1-1, Eurocode 3: Design of steel structures - Part 1-1: General rules and rules for buildings, ECS, Brussels, 2005.

20.17 Gioncu V., General Theory of Coupled Instability, Thin-Walled Structures (Special Issue on Coupled Instability in Metal Structures – CIMS’92), Vol. 19, Nos. 2-4, 1994, pp. 81-128.

20.18 Gioncu V., Balut N., Dubina D., Moldovan A., Pacoste C., Coupled instabilities in mono-symmetrical steel compression members, Journal of Constructional Steel Research, Vol. 21, Nos. 1-3, 1992, pp. 71-95.

20.19 EN1993-1-5, Eurocode 3: Design of steel structures - Part 1-5: Plated structural elements, ECS, Brussels 2006.

20.20 EN1993-1-6, Eurocode 3: Design of steel structures - Part 1.6: General rules. Strength and stability of shell structures, ECS, Brussels 2007.

20.21 Rotter J.M., Challenges in the generalisation of structural buckling assessments to all structures and load cases. Proceedings of the 6th International Conference on Thin Walled Structures – ICTWS 2011, Dubina D., Ungureanu V. (eds.), Timisoara, Romania 2011, pp. 71-86.
20.22 Schardt R., Verallgemeinerte Technische Biegetheorie, Springer-Verlag, Berlin 1989.
20.23 Davies J.M., Leach P., First-order generalised beam theory, Journal of Constructional Steel Research, Vol. 31, Nos. 2-3, 1994, pp. 187-220. Second-order generalised beam theory. Journal of Constructional Steel Research, Vol. 31, Nos. 2-3, 1994, pp. 221-241.
20.24 Silvestre N., Camotim D., First-order generalised beam theory for arbitrary orthotropic materials, Thin-Walled Structures, Vol. 40, No. 9, 2002, pp. 755-789.
20.25 Silvestre N., Camotim D., Second-order generalised beam theory for arbitrary orthotropic materials, Thin-Walled Structures, Vol. 40, No. 9, 2002, pp. 791-820.
20.26 Silvestre N., Camotim D., Nonlinear Generalized Beam Theory for Cold-formed Steel Members, International Journal of Structural Stability and Dynamics, Vol. 3, No. 4, 2003, pp. 461-490.
20.27 Schafer B.W., Ádány S., Buckling analysis of cold-formed steel members using CUFSM: conventional and constrained finite strip methods. Proceeding of the 18th International Specialty Conference on Cold-Formed Steel Structures, Orlando, USA, 2006.
20.28 Kidmann R., Krauss M., Steel Structures. Design using FEM, Ernst & Sohn, Berlin 2011.
20.29 Rondal J., Thin-walled structures – General Report. Stability of Steel Structures, Ivanyi M. (ed.), Akademiai Kiado, Budapest, Vol. 2, 1988, pp. 849-866.
20.30 Batista E., Essais de profils C et U en acier plies a froid. Rep. No. 157, Universite de Liege, Laboratoire de Stabilite des Constructions, 1986.
20.31 EN1993-1-3, Eurocode 3: Design of steel structures. Part 1-3: General Rules. Supplementary rules for cold-formed thin gauge members and sheeting, ECS, Brussels 2006.
20.32 Dubina D., Goina D., Zaharia R., Ungureanu V., Numerical Modelling of Instability Phenomena of Thin-walled Steel Members, Proceedings of the 5th International Colloquium on Stability and Ductility of Steel Structures - SDSS'97, Nagoya, Japan, 29-31 July 1997, Vol. 2, pp. 755-762.
20.33 Young B., Rasmunssen K.J.R., Compression tests of fixed-ended and pin-ended cold-formed lipped channels, Research Report, School of Civil and Mining Engineering, University of Sydney, Australia 1995.
20.34 Gardner L., Nethercot D.A., Numerical modeling of stainless steel structural components - A consistent approach, Journal of Structural Engineering, ASCE, Vol. 130, No. 10, 2004, pp. 1586-1601.
20.35 Rondal J., Dubina D., Bivolaru D., Residual stresses and the behaviour of cold-formed steel structures. Proceedings of the 17th Czech and Slovak

International Conference on Steel Structures and Bridges, Bratislava, Slovakia, September 7-9, 1994, pp. 193-197.
20.36 Schafer B.W., Peköz T., Computational modelling of cold-formed steel characterising geometric imperfections and residual stresses, Journal of Constructional Steel Research, Vol. 47, 1998, pp. 193-210.
20.37 Dubina D., Rondal J., Ungureanu V., Numerical modelling and codification of imperfections for cold-formed steel members analysis, Steel Composite Structures - An International Journal, Vol. 5, No. 6, 2005, pp. 515-533.
20.38 Rasmussen K.J.R., Hancock G.J., Design of cold-formed stainless steel tubular members. I: Columns, Journal of Structural Engineering, ASCE, Vol. 119, No. 8, 1993, pp. 2349-2367.
20.39 Gardner L., Nethercot D.A., Behaviour of cold-formed stainless steel cross-sections. Proceeding of the 9th Nordic Steel Construction Conference - NSCC2001, Helsinki, Finland, 18-20 June 2001, pp. 781-789.
20.40 Dubina D., Peculiar problems in cold-formed steel design - Chapter 2. Light gauge metal structures. Recent advances, Rondal J., Dubina D. (eds.), CIMS Udine Courses and Lectures - No. 455, Springer-Verlag Wien, 2005, pp. 5-15.
20.41 Rasmussen K.J.R., Hancock G.J., Geometric imperfections in plated structures subject to interaction between buckling modes, Thin-Walled Structures, Vol. 6, 1988, pp. 433-452.
20.42 Schafer B.W., Grigoriu M., Peköz T., A probabilistic examination of the ultimate strength of cold-formed steel elements, Thin-Walled Structures, Vol. 31, 1998, pp. 271-288.
20.43 Bernard E.S., Coleman R., Bridge R.Q., Measurement and assessment of imperfections in thin-walled panels, Thin-Walled Structures, Vol. 33, 1999, pp. 103-126.
20.44 Bjorhovde R., Deterministic and probabilistic approaches to the strength of steel columns, PhD Dissertation, Lehigh University, PA, 1972.
20.45 ECCS_49, European recommendations for design of light gauge steel members, Publication P049, European Convention for Constructional Steelwork, Brussels 1987.
20.46 AS4100-1990, Australian Standard: Steel Structures, Homebush, Australia.

ISBN 978-83-7283-758-5